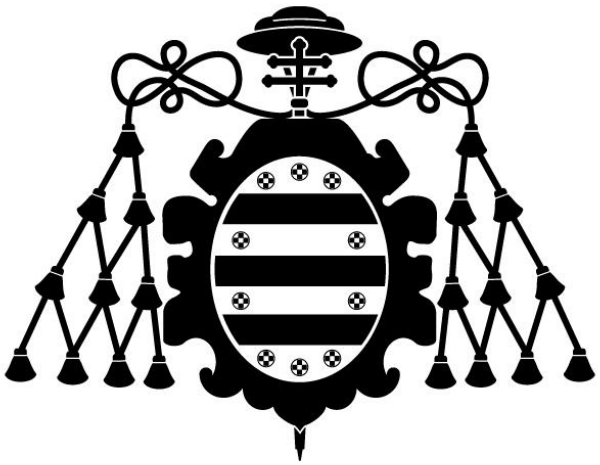

Universidad de Oviedo

Universidá d'Uviéu

University of Oviedo

Programa de Doctorado en Materiales

MATERIALES BIDIMENSIONALES EN DISPERSIÓN COLOIDAL. PREPARACIÓN ESCALABLE, CARACTERIZACIÓN Y APLICACIONES

TESIS DOCTORAL

Jose María Munuera Fernández

Junio 2019

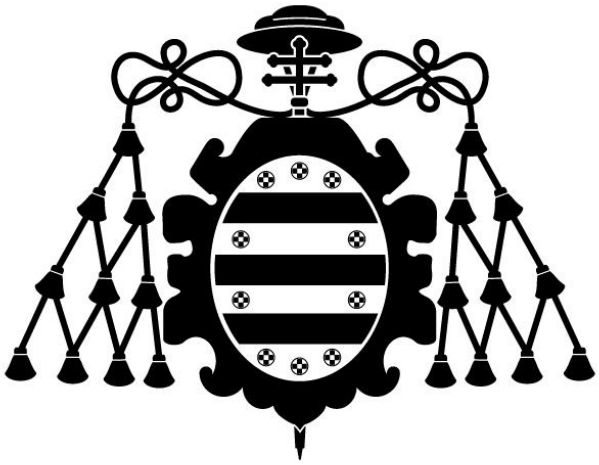

Universidad de Oviedo
Universidá d'Uviéu
University of Oviedo

Programa de Doctorado en Materiales

MATERIALES BIDIMENSIONALES EN DISPERSIÓN COLOIDAL. PREPARACIÓN ESCALABLE, CARACTERIZACIÓN Y APLICACIONES

TESIS DOCTORAL

Juan Ignacio Paredes Nachón
Juan Manuel Diez Tascón

Universidad de Oviedo
Universidá d'Uviéu
University of Oviedo

RESUMEN DEL CONTENIDO DE TESIS DOCTORAL

1.- Título de la Tesis	
Español: Materiales bidimensionales en dispersión coloidal: preparación escalable, caracterización y aplicaciones.	Inglés: Colloidal dispersions of 2D materials: scalable preparation, characterization and applications.

2.- Autor	
Nombre: José María Munuera Fernández	DNI:
Programa de Doctorado: Materiales	
Órgano responsable: Comisión Académica del Programa de Doctorado en Materiales	

RESUMEN (en español)

La presente tesis tiene como objetivo central el desarrollo de métodos de preparación y funcionalización en fase líquida de materiales bidimensionales (2D), concretamente grafeno, disulfuro de molibdeno (MoS_2) y óxido de cobalto (Co_3O_4). Se ha estudiado la exfoliación electroquímica anódica de grafito para obtener grafeno con sulfato potásico como electrolito, investigándose el uso de diferentes grafitos como ánodo y su influencia en las características del grafeno resultante. Entre los materiales estudiados, el grafito flexible mostró los mejores resultados. Asimismo, se utilizaron como electrolitos en exfoliación anódica sulfonatos aromáticos, que actúan como agentes intercalantes, estabilizantes, antioxidantes y centros de anclaje para la preparación de materiales híbridos basados en grafeno con un grado de oxidación muy bajo (~2%). Se estudió también el pretratamiento del grafito flexible con ácido sulfúrico, lo que permitió aumentar el rendimiento de exfoliación electroquímica anódica del ~10% a más del 50%. En el contexto de la exfoliación anódica se indentificó a los halogenuros de sodio como electrolitos eficientes de exfoliación, con resultados similares a los sulfatos utilizados habitualmente, pero con un grado de oxidación menor. Este descubrimiento llevó al desarrollo de aditivos de electrolito con función antioxidante, destacando entre ellos el anión cloruro, para obtener grafeno anódico de muy alta calidad con un grado de oxidación muy limitado Se estudió también la funcionalización de MoS_2 obtenido mediante la ruta de intercalación de litio con grupos de ácido acético, obteniéndose láminas en fase 1T coloidalmente estables a largo plazo que se utilizaron como catalizadores de la reducción de nitroarenos, reteniendo su actividad durante más tiempo que las láminas no funcionalizadas. Por último, mediante un proceso solvotérmico en medio micelar laminar se prepararon láminas 2D de Co_3O_4 activado sin necesidad de activación posterior. Este material se utilizó como electrodo para almacenamiento de carga, como catalizador de la reducción de nitroarenos y como adsorbente de colorantes en disolución acuosa, con resultados comparables o superiores en todos los casos a los de materiales nanoestructurados basados en óxido de cobalto.

RESUMEN (en Inglés)

The main objective of this thesis is the development of preparation and functionalization methods of liquid phase 2D materials, particularly graphene, molybdenum disulfide (MoS_2) and cobalt oxide (Co_3O_4). Anodic electrochemical exfoliation of graphite using potassium sulfate as the electrolyte was studied, evaluating the use of different graphites and the impact of the choice over the characteristics of the obtained graphene. Among the materials studied, graphite foil showed the best results. Aromatic sulfonates were also studied as electrolytes for the preparation of graphene, acting as the intercalating agents, colloidal stabilizers, antioxidants and anchoring points for the formation of graphene-based hybrids with very low oxidation degree (~2%). A pretreatment of the graphite foil with sulfuric acid was studied, and it increased the yield of electrochemical exfoliation from ~10% to more than 50%. Sodium halides were identified as efficient anodic exfoliation electrolytes, yielding graphenes with lower oxygen content than those obtained using sulfate. This discovery led to the development of electrolyte additives acting as antioxidants, with chloride anion standing out, allowing to obtain very high quality anodic graphene with a very limited degree of oxidation. Functionalization of MoS_2

obtained through the lithium intercalation route with acetic acid groups was studied, obtaining 1T phase nanosheets with long-term colloidal stability in water that were tested as catalysts for the reduction of nitroarenes, maintaining their catalytic activity longer than the non-functionalized material. Finally, activated Co_3O_4 2D nanosheets were synthesized through a micellar phase directed solvothermal process. This material was tested as charge storage electrode, catalyst in the reduction of nitroarenes and dye adsorbant in water solutions, showing comparable or better results in all cases compared to those of other nanostructured cobalt oxide materials.

SR. PRESIDENTE DE LA COMISIÓN ACADÉMICA DEL PROGRAMA DE DOCTORADO EN MATERIALES

Universidad de Oviedo
Universidá d'Uviéu
University of Oviedo

FORMULARIO RESUMEN DE TESIS POR COMPENDIO

1.- Datos personales solicitante	
Apellidos: Munuera Fernández	Nombre: Jose María

Curso de inicio de los estudios de doctorado	2014

	SI	NO
Acompaña acreditación por el Director de la Tesis de la aportación significativa del doctorando		
Acompaña memoria que incluye		
Introducción justificativa de la unidad temática y objetivos	X	
Copia completa de los trabajos *	X	
Resultados/discusión y conclusiones	X	
Informe con el factor de impacto de la publicaciones	X	
Se acompaña aceptación de todos y cada uno de los coautores a presentar el trabajo como tesis por compendio		
Se acompaña renuncia de todos y cada uno de los coautores a presentar el trabajo como parte de otra tesis de compendio		

* Ha de constar el nombre y adscripción del autor y de todos los coautores asi como la referencia completa de la revista o editorial en la que los trabajos hayan sido publicados o aceptados en cuyo caso se aportará justificante de la aceptación por parte de la revista o editorial

FOR-MAT-VOA-033

Artículos, Capítulos, Trabajos

Trabajo, Artículo 1

Titulo (o título abreviado)	High quality, low oxygen content and biocompatible graphene nanosheets obtained by anodic exfoliation of different graphite types
Fecha de publicación	17/Julio/2015
Fecha de aceptación	15/Julio/2015
Inclusión en Science Citation Index o bases relacionadas por la CNEAI (indíquese)	Sí (*Carbon*, SCI)
Factor de impacto	7.082

Coautor2 x Doctor □ No doctor . Indique nombre y apellidos	Juan Ignacio Paredes
Coautor3 x Doctor □ No doctor . Indique nombre y apellidos	Silvia Villar-Rodil
Coautor4 x Doctor □ No doctor . Indique nombre y apellidos	Miguel Ayán-Varela
Coautor5 x Doctor □ No doctor . Indique nombre y apellidos	Ana Pagán
Coautor6 x Doctor □ No doctor . Indique nombre y apellidos	Salvador D. Aznar-Cervantes

Coautor7 x Doctor □ No doctor . Indique nombre y apellidos	José L. Cenis
Coautor8 x Doctor □ No doctor . Indique nombre y apellidos	Amelia Martínez-Alonso
Coautor9 x Doctor □ No doctor . Indique nombre y apellidos	Juan M. D. Tascón

Trabajo, Artículo 2

Titulo (o título abreviado)	Electrolytic exfoliation of graphite in water with multifunctional electrolytes: en route towards high quality, oxide-free graphene flakes
Fecha de publicación	05/enero/2016
Fecha de aceptación	04/enero/2016
Inclusión en Science Citation Index o bases relacionadas por la CNEAI (indíquese)	Sí (*Nanoscale*, SCI)
Factor de impacto	7.233

Coautor2 x Doctor □ No doctor . Indique nombre y apellidos	Juan Ignacio Paredes
Coautor3 x Doctor □ No doctor . Indique nombre y apellidos	Silvia Villar-Rodil
Coautor4 x Doctor □ No doctor . Indique nombre y apellidos	Miguel Ayán-Varela
Coautor5 x Doctor □ No doctor . Indique nombre y apellidos	Amelia Martínez-Alonso
Coautor6 x Doctor □ No doctor . Indique nombre y apellidos	Juan M. D. Tascón

Trabajo, Artículo 3

Titulo (o título abreviado)	A simple strategy to improve the yield of graphene nanosheets in the anodic exfoliation of graphite foil
Fecha de publicación	17/enero/2017
Fecha de aceptación	13/enero/2017
Inclusión en Science Citation Index o bases relacionadas por la CNEAI (indíquese)	Sí (*Carbon*, SCI)
Factor de impacto	7.082

Coautor2 □ Doctor □ No doctor . Indique nombre y apellidos	Juan Ignacio Paredes
Coautor3 □ Doctor □ No doctor . Indique nombre y apellidos	Silvia Villar-Rodil
Coautor4 □ Doctor □ No doctor . Indique nombre y apellidos	Amelia Martínez-Alonso
Coautor5 □ Doctor □ No doctor . Indique nombre y apellidos	Juan M. D. Tascón

Trabajo, Artículo 4

Titulo (o título abreviado)	Electrochemical Exfoliation of Graphite in Aqueous Sodium Halide Electrolytes toward Low Oxygen Content Graphene for Energy and Environmental Applications
Fecha de publicación	23/junio/2017
Fecha de aceptación	23/junio/2017

Inclusión en Science Citation Index o bases relacionadas por la CNEAI (indíquese)	Sí (ACS Applied Materials & Interfaces, SCI)
Factor de impacto	8.097

Coautor2 x Doctor □ No doctor . Indique nombre y apellidos	Juan Ignacio Paredes
Coautor3 x Doctor □ No doctor . Indique nombre y apellidos	Marina Enterría
Coautor4 x Doctor □ No doctor . Indique nombre y apellidos	Ana Pagán
Coautor5 x Doctor □ No doctor . Indique nombre y apellidos	Silvia Villar-Rodil
Coautor6 x Doctor □ No doctor . Indique nombre y apellidos	Manuel F. R. Pereira
Coautor7 x Doctor □ No doctor . Indique nombre y apellidos	José I. Martins
Coautor8 x Doctor □ No doctor . Indique nombre y apellidos	José L. Figueiredo
Coautor9 x Doctor □ No doctor . Indique nombre y apellidos	José L. Cenis
Coautor10 x Doctor □ No doctor . Indique nombre y apellidos	Amelia Martínez-Alonso
Coautor11 x Doctor □ No doctor . Indique nombre y apellidos	Juan M. D. Tascón

Trabajo, Artículo 5

Titulo (o título abreviado)	High quality, low-oxidized graphene via anodic exfoliation with table salt as an efficient oxidation-preventing co-electrolyte for water/oil remediation and capacitive energy storage applications
Fecha de publicación	14/marzo/2018
Fecha de aceptación	5/marzo/2018
Inclusión en Science Citation Index o bases relacionadas por la CNEAI (indíquese)	No (Applied Materials Today)
Factor de impacto	-

Coautor2 x Doctor □ No doctor . Indique nombre y apellidos	Juan Ignacio Paredes
Coautor3 x Doctor □ No doctor . Indique nombre y apellidos	Silvia Villar-Rodil
Coautor4 x Doctor □ No doctor . Indique nombre y apellidos	Alberto Castro-Muñiz
Coautor5 x Doctor □ No doctor . Indique nombre y apellidos	Amelia Martínez-Alonso
Coautor6 x Doctor □ No doctor . Indique nombre y apellidos	Juan M. D. Tascón

Trabajo, Artículo 6

Titulo (o título abreviado)	Impact of Covalent Functionalization on the Aqueous Processability, Catalytic Activity, and Biocompatibility of Chemically Exfoliated MoS_2 Nanosheets
Fecha de publicación	5/octubre/2016
Fecha de aceptación	23/septiembre/2016
Inclusión en Science Citation Index o bases relacionadas por la CNEAI (indíquese)	Sí (ACS Applied Materials & Interfaces, SCI)
Factor de impacto	8.097

Coautor2 x Doctor □ No doctor . Indique nombre y apellidos	Juan Ignacio Paredes
Coautor3 x Doctor □ No doctor . Indique nombre y apellidos	Silvia Villar-Rodil
Coautor4 x Doctor □ No doctor . Indique nombre y apellidos	Laura Guardia
Coautor5 x Doctor □ No doctor . Indique nombre y apellidos	Miguel Ayán-Varela
Coautor6 x Doctor □ No doctor . Indique nombre y apellidos	Ana Pagán
Coautor7 x Doctor □ No doctor . Indique nombre y apellidos	Salvador D. Aznar-Cervantes
Coautor8 x Doctor □ No doctor . Indique nombre y apellidos	José L. Cenis
Coautor9 x Doctor □ No doctor . Indique nombre y apellidos	Amelia Martínez-Alonso
Coautor10 x Doctor □ No doctor . Indique nombre y apellidos	Juan M. D. Tascón

Trabajo, Artículo 7

Titulo (o título abreviado)	A direct route to activated two-dimensional cobalt oxide nanosheets for electrochemical energy storage, catalytic and environmental applications
Fecha de publicación	15/diciembre/2018
Fecha de aceptación	14/diciembre/2018
Inclusión en Science Citation Index o bases relacionadas por la CNEAI (indíquese)	Sí (Journal of Colloid and Interface Science, SCI)
Factor de impacto	5.091

Coautor2 x Doctor □ No doctor . Indique nombre y apellidos	Juan Ignacio Paredes
Coautor3 x Doctor □ No doctor . Indique nombre y apellidos	Silvia Villar-Rodil
Coautor4 □ Doctor x No doctor . Indique nombre y apellidos	Sergio García-Dalí
Coautor5 x Doctor □ No doctor . Indique nombre y apellidos	Alberto Castro-Muñiz
Coautor6 x Doctor □ No doctor . Indique nombre y apellidos	Amelia Martínez-Alonso
Coautor7 x Doctor □ No doctor . Indique nombre y apellidos	Juan M. D. Tascón

En caso de compendio de un número de artículos superior a seis, se incorporarán hojas suplementarias conforme a este modelo

Tabla de contenido

Agradecimientos

Creo que no es de recibo empezar el desarrollo de la perorata científica que resume y condensa los años de tesis doctoral sin antes agradecer a quien lo ha hecho posible, llevadero e incluso divertido.

Como no podría ser de otra manera, antes de nada debo agradecerle a mis directores Nacho y Tascón el haber depositado su confianza en un individuo como yo para trabajar con ellos, cuando estaba huyendo de la facultad de Química aterrado por mi futuro inmediato. Y no solo por eso, sino por su tremendo esfuerzo en sacar adelante el trabajo que se realiza en nuestro grupo. También al resto de personas pertenecientes al grupo de Materiales Carbonosos, que han tenido a bien no sólo enseñarme todo lo que necesitaba saber y no sabía sobre la investigación en ciencia de materiales, sino que año tras año han aguantado mis divagaciones, peroratas, anécdotas, estupideces y despropósitos en general. Silvia, Fabián, Amelia, Rubén, Laura, Miguel, Tomás, Óscar, Bárbara y Sergio, gracias. El primer nombre de esta tesis es el mío, pero (casi) todos los vuestros están recogidos en los trabajos, y con buena razón.

A mi familia cercana en general y muy en especial a Luján, mi señora madre. A ella, que se ha preocupado por mí (y sigue haciéndolo) más allá de toda cordura y necesidad, y me ha hecho convertirme en el hombre que soy. Pero también a mi padre José, de quien he heredado muchas cosas, entre ellas mi carácter, mis gestos y andares. Y a mis hermanas Amaya e Itziar, y a mi hermano Aitor, que siempre han estado pendientes de mi bienestar y mi aprendizaje.

A mis amigos, tanto los más veteranos (Chus, Pablo, Víctor, Sarah, Julio y Andrés) como los más recientes (Franchi, Helio, Rut, Pei, Pepe y Pablón), porque sois la gente que me conecta al mundo real, y quienes más han aguantado mis despropósitos y defectos de carácter, y aun así seguís dirigiéndome la palabra.

A quien ha pasado fugazmente por mi vida estos últimos años, en ocasiones dejando recuerdos gratos y en muchas otras un sabor agridulce. Gracias por enseñarme involuntariamente a apreciar lo que tengo, lo que me pierdo y lo que he perdido.

Y por último a quien está leyendo esta tesis, porque no es una molestia menor navegar entre estas páginas y espero que, aunque larga y tediosa, la lectura sea interesante.

“Y el árbol se planta,

la flor vuelve y crece,

somos la estrella que alumbra,

aunque estemos sin luz seis meses.”

-Benito Antonio Martínez Ocasio

Resumen

La presente tesis tiene como objetivo central el desarrollo de métodos de preparación y funcionalización en fase líquida de materiales bidimensionales (2D), concretamente grafeno, disulfuro de molibdeno (MoS_2) y óxido de cobalto (Co_3O_4). Se ha estudiado la exfoliación electroquímica anódica de grafito para obtener grafeno con sulfato potásico como electrolito, investigándose el uso de diferentes grafitos como ánodo y su influencia en las características del grafeno resultante. Entre los materiales estudiados, el grafito flexible mostró los mejores resultados. Asimismo, se utilizaron como electrolitos en exfoliación anódica sulfonatos aromáticos, que actúan como agentes intercalantes, estabilizantes, antioxidantes y centros de anclaje para la preparación de materiales híbridos basados en grafeno con un grado de oxidación muy bajo (~2%). Se estudió también el pretratamiento del grafito flexible con ácido sulfúrico, lo que permitió aumentar el rendimiento de exfoliación electroquímica anódica del ~10% a más del 50%. En el contexto de la exfoliación anódica se indentificó a los halogenuros de sodio como electrolitos eficientes de exfoliación, con resultados similares a los sulfatos utilizados habitualmente, pero con un grado de oxidación menor. Este descubrimiento llevó al desarrollo de aditivos de electrolito con función antioxidante, destacando entre ellos el anión cloruro, para obtener grafeno anódico de muy alta calidad con un grado de oxidación muy limitado. Se estudió también la funcionalización de MoS_2 obtenido mediante la ruta de intercalación de litio con grupos de ácido acético, obteniéndose láminas en fase 1T coloidalmente estables a largo plazo que se utilizaron como catalizadores de la reducción de nitroarenos, reteniendo su actividad durante más tiempo que las láminas no funcionalizadas. Por último, mediante un proceso solvotérmico en medio micelar laminar se prepararon láminas 2D de Co_3O_4 activado sin necesidad de activación posterior. Este material se utilizó como electrodo para almacenamiento de carga, como catalizador de la reducción de nitroarenos y como adsorbente de colorantes en disolución acuosa, con resultados comparables o superiores en todos los casos a los de materiales nanoestructurados basados en óxido de cobalto.

Abstract

The main objective of this thesis is the development of preparation and functionalization methods of liquid phase 2D materials, particularly graphene, molybdenum disulfide (MoS_2) and cobalt oxide (Co_3O_4). Anodic electrochemical exfoliation of graphite using potassium sulfate as the electrolyte was studied, evaluating the use of different graphites and the impact of the choice over the characteristics of the obtained graphene. Among the materials studied, graphite foil showed the best results. Aromatic sulfonates were also studied as electrolytes for the preparation of graphene, acting as the intercalating agents, colloidal stabilizers, antioxidants and anchoring points for the formation of graphene-based hybrids with very low oxidation degree (~2%). A pretreatment of the graphite foil with sulfuric acid was studied, and it increased the yield of electrochemical exfoliation from ~10% to more than 50%. Sodium halides were identified as efficient anodic exfoliation electrolytes, yielding graphenes with lower oxygen content than those obtained using sulfate. This discovery led to the development of electrolyte additives acting as antioxidants, with chloride anion standing out, allowing to obtain very high quality anodic graphene with a very limited degree of oxidation. Functionalization of MoS_2 obtained through the lithium intercalation route with acetic acid groups was studied, obtaining 1T phase nanosheets with long-term colloidal stability in water that were tested as catalysts for the reduction of nitroarenes, maintaining their catalytic activity longer than the non-functionalized material. Finally, activated Co_3O_4 2D nanosheets were synthesized through a micellar phase directed solvothermal process. This material was tested as charge storage electrode, catalyst in the reduction of nitroarenes and dye adsorbant in water solutions, showing comparable or better results in all cases compared to those of other nanostructured cobalt oxide materials.

1. Introducción

1.1 Materiales bidimensionales (2D)

Los materiales nanoestructurados o nanomateriales, son una familia de sólidos que se caracterizan por tener una morfología en la que al menos una de sus dimensiones se encuentra en la escala de los nanómetros, o bien por poseer poseen una estructura interna en dicha escala. Así, los materiales con 3 dimensiones nanométricas se denominan cero-dimensionales (0D, como los puntos cuánticos), y materiales unidimensionales (1D) y bidimensionales (2D) para aquellos sólidos con dos y una dimensiones nanométricas, respectivamente (como nanotubos y nanoláminas) [1]. La escala nanométrica en la estructura no es trivial, sino que afecta a las propiedades de estos materiales y los distingue de los correspondientes sólidos no nanoestructurados. Como ejemplo, el grafito, un material blando en su estado *bulk*, presenta una dureza extremadamente alta al ser exfoliado hasta monocapas de grafeno [2]. El descubrimiento de este material en 2004 por los físicos Geim y Novoselov dio pie al estudio del caso que centra esta tesis, a saber, los materiales 2D [3]. Estos materiales presentan una morfología laminar con espesores del orden de pocos nanómetros o angstroms y tamaños laterales de entre decenas de nanómetros y centímetros, en función del material y el método de preparación. En muchos casos, los materiales 2D están directamente relacionados con los materiales laminares, una familia de sólidos (naturales y artificiales) compuestos por capas apiladas que presentan enlaces fuertes (p. e. covalentes) en el plano y que están unidas entre sí por fuerzas débiles tipo van der Waals [4]. A raíz del descubrimiento del grafeno se ha desatado una enorme actividad investigadora, que continúa a día de hoy, en torno a los materiales 2D, de los que han sido documentados diferentes familias, como se indica en la Figura 1. Partiendo de los materiales laminares conocidos, como el grafito, nitruro de boro hexagonal y los dicalcogenuros de metales de transición (TMDs, transition metal dichalcogenides) se han desarollado métodos de preparación, tanto de síntesis a partir de precursores moleculares (bottom-up) como de exfoliación a partir de dichos materiales laminares (top-down) para obtener los correspondientes materiales 2D [5-8].

<table>
<tr><td>Familia de grafeno</td><td>Grafeno</td><td colspan="2">hBN</td><td>BCN</td><td>Fluorografeno</td><td>Óxido de grafeno</td></tr>
<tr><td rowspan="2">Calcogenuros 2D</td><td colspan="2" rowspan="2">MoS_2, WS_2, $MoSe_2$, WSe_2</td><td colspan="2" rowspan="2">Dicalcogenuros semiconductores: $MoTe_2$,WTe_2, ZrS_2, $ZrSe_2$, etc.</td><td colspan="2">Dicalcogenuros metálicos: $NbSe_2$, NbS_2, TaS_2, TiS_2, $NiSe_2$, etc.</td></tr>
<tr><td colspan="2">Semiconductores laminares: GaSe, GaTe, InSe, Bi_2Se_3, etc.</td></tr>
<tr><td rowspan="2">Óxidos 2D</td><td>Micas, BSCCO</td><td colspan="2">MoO_3, WO_3</td><td colspan="2" rowspan="2">Tipo Perovskita: $LaNb_2O_7$, $(Ca,Sr)_2Nb_3O_{10}$, $Bi_4Ti_3O_{12}$, $Ca_2Ta_2TiO_{10}$, etc.</td><td>Hidróxidos: $Ni(OH)_2$, $Eu(OH)_2$, etc.</td></tr>
<tr><td>Óxidos de Cu laminares</td><td colspan="2">TiO_2, MnO_2, V_2O_5, TaO_3, RuO_2, etc.</td><td>Otros</td></tr>
</table>

Figura 1. Clases de materiales 2D. Adaptado de [8].

En el desarrollo de esta tesis se ha trabajado fundamentalmente con materiales 2D, en concreto grafeno, disulfuro de molibdeno y óxido de cobalto.

1.1.1 Grafeno

El grafeno, por definición, consiste en una lámina plana formada por átomos de carbono unidos covalentemente en estructura hexagonal, con anillos de 6 átomos en hibridación sp^2, cuyo espesor es 0.34 nm. A pesar de esta definición estricta, es habitual considerar grafeno a láminas de entre 2 y 10 capas, debido a que sus propiedades son marcadamente diferentes a las del grafito *bulk* (<10 capas), y a que estos materiales tienen un gran interés práctico en aplicaciones (Figura 2) [9-13].

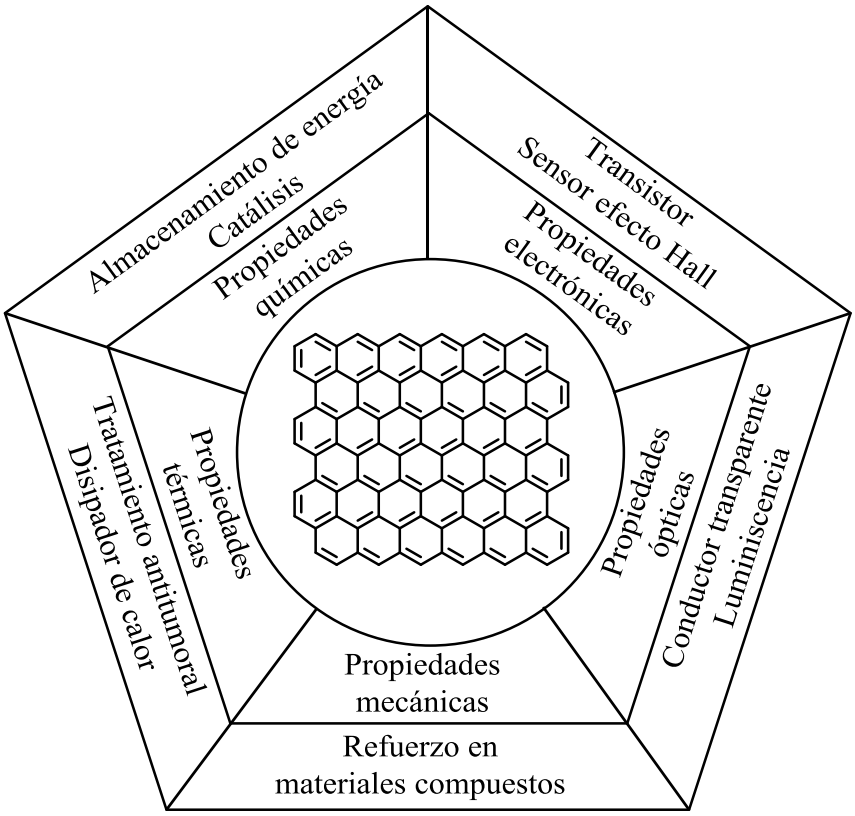

Figura 2. Propiedades del grafeno y sus aplicaciones relacionadas.

De esta estructura se derivan sus **propiedades electrónicas**. Debido a la hibridación sp^2 de los átomos de carbono, se establecen enlaces covalentes sencillos entre átomos vecinos (red hexagonal representada en la Figura 3a). Perpendiculares al plano se encuentran los orbitales $2p_z$, que forman enlaces dobles que se conjugan a lo largo de la estructura en una nube electrónica π a ambos lados del plano basal (Figura 3b). Esta deslocalización permite una gran movilidad de cargas (2.5×10^5 cm^2 V^{-1} s^{-1}) y conductividad eléctrica un millón de veces superior a la del cobre [14]. La razón de esta movilidad viene dada por su estructura de bandas. La estructura de la celda unitaria del grafeno hace que las bandas de valencia y conducción intersecten en un punto (el punto de Dirac), donde está situado el nivel de Fermi de los electrones. Esta característica de las bandas convierte al grafeno en un semiconductor de *gap* de banda cero y con propiedades semimetálicas, que pueden ser modificadas a través de su funcionalización [15].

Otra de las propiedades debidas a la naturaleza 2D del grafeno es el efecto Hall cuántico. Este fenómeno consiste en la aparición de una diferencia de potencial en un material sometido a una corriente eléctrica y un campo magnético perpendiculares. En

el fenómeno clásico existe una relación lineal entre el voltaje de Hall y el campo magnético aplicado, mientras que en el fenómeno cuántico la relación es escalonada y, en el caso particular del grafeno, está cuantizada en números semienteros [16,17]. Debido a estas propiedades, así como a su estabilidad química y las posibilidades de modificación y funcionalización, se han documentado aplicaciones del grafeno en baterías, condensadores de doble capa eléctrica (EDLC, electrostatic double layer capacitors, denominados habitualmente supercondensadores), pilas de combustible, celdas solares, transistores y sensores electroquímicos y de efecto Hall [18,19, 20, 21]

También son relevantes las **propiedades ópticas** del grafeno. Una monocapa (0.34 nm de espesor) posee una transmitancia del 97.7% de luz visible y una reflectancia del 0.1%. Para filmes más gruesos la transmitancia disminuye linealmente con el espesor, hasta un 70% para 10 nm [22]. El grafeno absorbe radiación en el espectro visible e infrarrojo (IR) cercano sin rasgos distintivos, y de forma casi constante entre 300 y 2500 nm. También presenta absorción en el ultravioleta (UV) con un pico característico a ~270 nm, que corresponde a transiciones $\pi \rightarrow \pi^*$ de los orbitales moleculares de la estructura [22]. Estas características, junto a la conductividad eléctrica mencionada antes, hacen al grafeno un buen candidato como conductor transparente, un posible sustituto del óxido de indio y estaño (ITO, indium tin oxide) de uso común a día de hoy en dispositivos electrónicos [23]. Por otra parte, mediante la modificación de las dimensiones de las láminas de grafeno (para tener nanocintas o puntos cuánticos) o modificando la estructura del plano basal, es posible modificar sus características como el gap de banda, lo que permite obtener materiales luminiscentes que permiten fabricar sensores y visualizar tejidos vivos [24].

En cuanto a las **propiedades mecánicas** del grafeno, destaca particularmente su excepcional rigidez. El módulo de Young para este material es de ~1 TPa, 5 veces superior al del acero estructural estándar. Además, su resistencia a la tracción es de 130 GPa, muy superior a la de ese mismo acero (0.4 GPa) o la del kevlar (0.38 GPa) [25]. Estas propiedades hacen del grafeno un gran candidato como refuerzo de materiales compuestos con diferentes matrices (poliméricas, cerámicas, metálicas), dando como resultado una gran mejora en las propiedades mecánicas con cargas de grafeno relativamente bajas [26].

Otro apartado en el que el grafeno destaca y es candidato a diversas aplicaciones es el referente a sus **propiedades térmicas**. En su forma prístina, este material posee una conductividad térmica de ~5000 W m^{-1} K^{-1}, más de 10 veces superior a la del cobre [27], lo que lo hace idóneo como componente disipador de calor en componentes electrónicos [28]. Es posible también su incorporación en materiales compuestos para mejorar su conductividad y estabilidad térmicas, además de modificar las temperaturas de transición de fase [29]. Por otra parte, estas propiedades térmicas y de absorción IR permiten la aplicación de láminas de grafeno en nanomedicina, por ejemplo para la destrucción de células cancerígenas mediante calentamiento por láser (terapia fototérmica), reduciendo el daño a los tejidos colindantes en comparación con el uso de otros materiales[30].

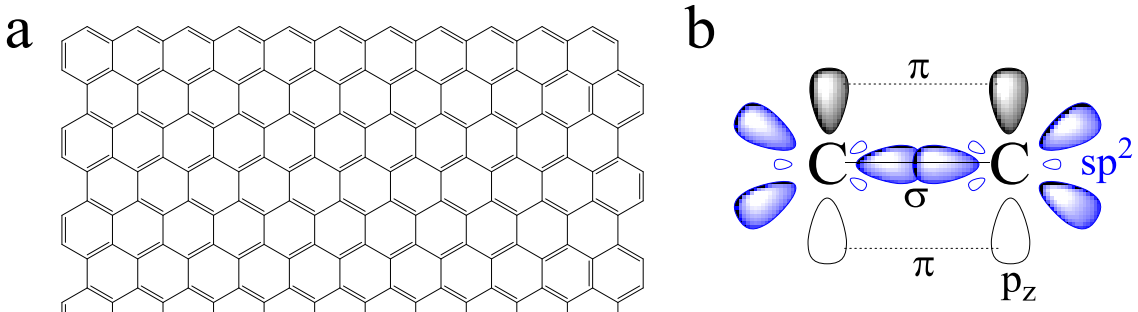

Figura 3. **(a)** Estructura de una monocapa de grafeno. **(b)** Hibridación sp2 y enlace doble entre átomos de carbono.

Es importante destacar también las **propiedades químicas** de este material, que proporcionan oportunidades para otras aplicaciones. El procesado del grafeno en fase líquida para diversos usos requiere la preparación de dispersiones coloidales estables del material, y para ello existen metodologías de funcionalización de las láminas, orientadas tanto a facilitar su estabilidad coloidal como a modificar sus propiedades (hidrofobia/hidrofilia, *gap* de banda, superficie específica, actividad catalítica, almacenamiento de carga, etc.). Existen dos enfoques cualitativamente diferentes para abordar esta funcionalización: la vía covalente y la no covalente.

La primera de estas dos vías implica la formación de enlaces covalentes entre las láminas del grafeno y una especie externa, como pueden ser átomos, moléculas pequeñas o macromoléculas [31,32]. Los bordes del grafeno son la zona más reactiva de

las láminas, y por tanto los centro más propensos a la funcionalización covalente. No obstante, es posible modificar el plano basal mediante sustitución atómica, de manera que átomos de carbono se intercambian por heteroátomos, siendo los más habituales nitrógeno y azufre. De esta manera, es posible modificar la estructura electrónica de las láminas, mejorando sus características en aplicaciones como catalizador de la reacción de reducción de oxígeno (ORR, oxygen reduction reaction), electrodos de baterías y de pilas de combustible [33,34].

Por otra parte es posible la funcionalización no covalente del grafeno, que habitualmente implica la adsorción de moléculas por interacciones dispersivas o π-π con el plano basal del grafeno. De esta manera la estructura del material permanece inalterada, aunque permite modificar su estructura electrónica mediante la transferencia de carga con la especie adsorbida [35], lo que facilita la fabricación de sensores [36], catalizadores [37] y electrodos de supercondensadores [38].

La funcionalización puede tener como objetivo mejorar la estabilidad coloidal en disolventes orgánicos o en agua, tanto mediante la modificación covalente como mediante la adsorción no covalente de moléculas anfifílicas (surfactantes) [39-41]. Esta mejora facilita el procesado del material en fase líquida, lo que a su vez permite una diversidad de aplicaciones mediante la preparación de materiales híbridos, composites, recubrimientos, filmes y estructuras 3D a partir de las dispersiones coloidales de grafeno. Así, es posible obtener materiales con actividad catalítica [42], electrodos para supercondensadores [43] y baterías [44], dispositivos electrónicos flexibles [45], filmes para el estudio de proliferación celular [46] y espumas para tratamiento de aguas contaminadas [47].

1.1.2 Disulfuro de molibdeno (MoS_2)

Los dicalcogenuros de metales de transición (TMDs, transition metal dichalcogenides), son compuestos de fórmula general MX_2, donde M es un metal de transición (Mo, W, Ti, Nb, etc.) y X es un calcógeno (S, Se, Te). Esta familia de materiales laminares ha sido partícipe del auge del grafeno y los materiales 2D en los últimos años, debido a la variedad de combinaciones que permite y sus diferentes características. Por ejemplo, existen TMDs semiconductores (MoS_2, WS_2, etc.),

metálicos (p. e. NbS_2, VSe_2), semimetálicos (p. e. WTe_2, $TiSe_2$), magnéticos ($CrSe_2$) y superconductores ($PdTe_2$). Entre ellos, el MoS_2 es el material que más intensamente está siendo investigado, debido a sus propiedades químicas, ópticas, mecánicas y sus posibles aplicaciones [48,49], y sobre todo debido a su relativa abundancia [50].

El MoS_2 *bulk* posee una estructura tridimensional compuesta por láminas unidas débilmente por fuerzas de van der Waals. Las láminas están formadas por una monocapa de átomos de molibdeno situada entre dos monocapas de átomos de azufre. Existen dos coordinaciones de los átomos de azufre alrededor del molibdeno (Figura 4), en forma de prisma trigonal (fase 2H, termodinámicamente estable) y octaédrica (fase 1T, metaestable) [51,52].

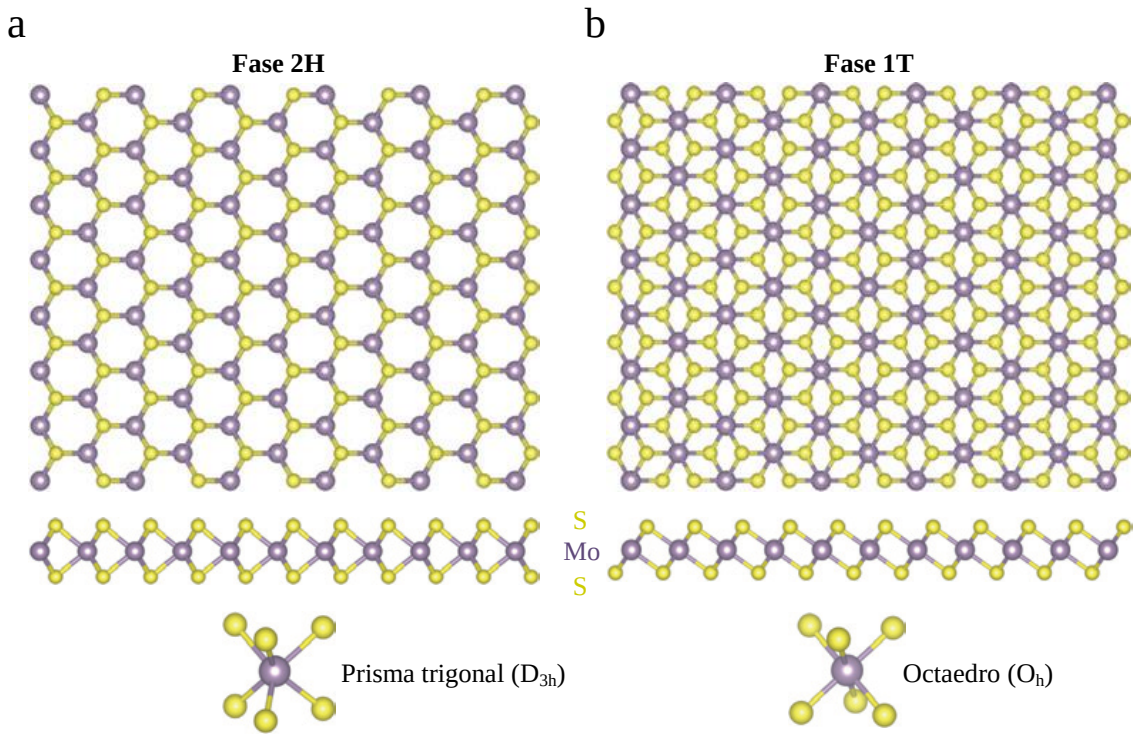

Figura 4. Fases **(a)** 2H y **(b)** 1T del MoS_2. Adaptado de [51].

Las **propiedades electrónicas y ópticas** del MoS_2, al igual que las de otros materiales 2D, dependen sensiblemente del número de capas. En su forma *bulk* este material es un semiconductor de *gap* de banda indirecto de 1.29 eV, mientras que al ser exfoliado en monocapas el gap se hace directo y tiene un valor de ~1.9 eV [53]. Este gap de banda dependiente del número de capas permite el uso del material en

dispositivos electrónicos, como transistores de efecto de campo [54], dispositivos bioelectrónicos [55] y sensores [56].

Las **propiedades mecánicas** del MoS_2 lo hacen apropiado para su uso en dispositivos electrónicos flexibles [57] y como refuerzo en materiales compuestos [58]. Su módulo de Young es comparable al del acero (270 frente a 400 GPa) [59], y los filmes de MoS_2 2D son marcadamente elásticos, con deformaciones de 10 nm para espesores de 5 a 25 láminas [60].

En cuanto a las **propiedades térmicas**, su conductividad térmica a lo largo del plano es de ~ 18 W m^{-1} K^{-1}, con variaciones en función del grado de exfoliación [61]. Así, es posible utilizar el MoS_2 en materiales compuestos para mejorar tanto sus propiedades térmicas como su estabilidad a temperaturas altas [62].

Por último, las **propiedades químicas** del MoS_2 son también relevantes. Las vacantes de azufre en la red atómica, relativamente abundantes debido a su baja energía de formación, provocan la existencia de centros catalíticamente activos de molibdeno, de manera que el material puede utilizarse como catalizador en reacciones como evolución de hidrógeno (HER, hydrogen evolution reaction) [63], hidrodesulfuración [64], reducción de óxido de azufre [65] y reducción de nitroarenos [66]. La exfoliación química del material bulk mediante la intercalación de litio permite la transformación de la fase 2H (semiconductora) en fase 1T (metálica) con un exceso de electrones, lo que mejora la estabilidad coloidal de las láminas en dispersión acuosa, y contribuye también a una mejora de la actividad catalítica [66] y de sus prestaciones cuando se usa como electrodo para almacenamiento electroquímico de energía [67].

La modificación de láminas de MoS_2 por vía no covalente permite obtener, entre otros, híbridos con nanopartículas metálicas catalíticamente activos [68,69] o aptos como sensores de espectroscopía Raman amplificada por superficie [70]. Es posible también mejorar la estabilidad coloidal de láminas en fase 2H mediante el uso de surfactantes [71,72] o biomoléculas [73] lo que permite su uso como catalizadores para HER en el primer caso, y mejora su biocompatibilidad y permite el uso en terapia quimiofototérmica en el segundo.

Por otra parte, la modificación covalente permite el dopaje mediante heteroátomos para la fabricación de transistores y dispositivos optoelectrónicos [74],

debido, por ejemplo, a la sustitución de átomos de molibdeno por niobio. Además, es posible la funcionalización del MoS2 2D a través de los átomos de azufre con complejos metálicos coordinados [75] y con grupos moleculares provenientes de compuestos organoyodados, que reaccionan por sustitución nucleófila, mejorando en ambos casos la estabilidad coloidal de las láminas y facilitando su uso en aplicaciones [76].

1.1.3 Óxido de cobalto (Co_3O_4)

En la familia de los materiales 2D, buena parte de ellos se pueden obtener mediante exfoliación de los correspondientes materiales laminares, esto es, aquellos cuya estructura está compuesta de capas unidas débilmente entre sí. No obstante, para la mayoría de los materiales, como muchos óxidos de metales de transición M_xO_y (M= Ti, Fe, Co, Ni, etc.) no existe esa posibilidad, ya que en su forma *bulk* presentan una estructura de enlaces iónicos y/o covalentes 3D, no compuesta por capas susceptibles de ser separadas. Estos materiales, y en particular los óxidos metálicos son de gran interés tanto en su estado *bulk* como en forma de láminas 2D, debido a sus posibles aplicaciones en campos como la conversión y el almacenamiento de energía y a su relativa abundancia y bajo coste [77,78].

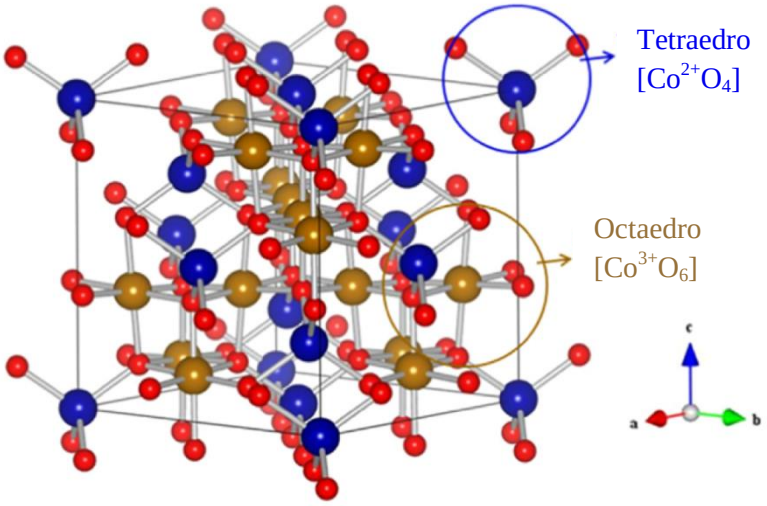

Figura 5. Celda unitaria del Co_3O_4. Adaptado de [79].

El óxido de cobalto (Co_3O_4) tiene una estructura cristalina 3D de espinela (Figura 5) compuesta por cationes Co^{2+} y Co^{3+} rodeados en disposición tetraédrica y octaédrica respectivamente por aniones O^{2-}. Esta estructura cristalina no está organizada en capas, y por tanto no es posible su exfoliación. Por tanto su obtención en forma de láminas 2D hace que sea necesario recurrir a otras estrategias de preparación [77].

Debido a la presencia de iones Co^{2+} con electrones desapareados, este óxido posee **propiedades magnéticas** que han sido ampliamente estudiadas tanto en el material *bulk* como en formas nanoestructuradas, con vistas a su aplicación como materiales magnéticos [79].

En cuanto a las **propiedades ópticas y eléctricas**, el Co_3O_4 presenta absorción tanto en el espectro visible como en el ultravioleta, con bandas características. Esta absorción, debida al gap de banda ensanchado por la preparación en forma de láminas 2D, permiten el uso del óxido en fotodetectores, dando una respuesta lineal de corriente al ser irradiados con luz UV [77].

Por último, son las **propiedades químicas** de este material las que lo hacen apto para sus aplicaciones más habituales. Por su morfología, las láminas 2D de Co_3O_4 poseen una gran proporción de superficie frente a volumen, y en consecuencia gran cantidad de centros activos superficiales. Estos sitios activos son centros de Co^{2+} que, por su densidad electrónica, son catalíticamente activos y permiten el uso de este material en procesos de electrorreducción [80], fotocatálisis [81] y ORR [82]. El control de la morfología y la porosidad durante la síntesis del óxido en forma de láminas permite la preparación de sensores de gases [83] y, junto a la presencia de centros electroactivos, hace que sea posible su uso como electrodo en almacenamiento de energía en condensadores [78] y baterías de litio [84].

Sin embargo, y como es habitual en el caso de óxidos metálicos en aplicaciones electroquímicas, una de las mayores limitaciones de la eficiencia del material es su conductividad eléctrica relativamente baja [85]. Las soluciones habituales a este problema pasan por la preparación de híbridos con la adición de materiales conductores como níquel [86] o grafeno [87], o bien por la modificación química del Co_3O_4. Esta modificación puede llevarse a cabo a través del dopaje para obtener óxidos mixtos, MCo_2O_4 [88], o mediante la activación del material por reducción parcial, obteniéndose

así materiales con vacantes de oxígeno y con mayor proporción de Co^{2+} [89], que presentan mejores características en las aplicaciones relacionadas.

1.2 Métodos de obtención de materiales 2D

Como sucede con todos los nanomateriales, las propiedades de los materiales 2D suelen ser sustancialmente diferentes de las de sus equivalentes *bulk* 3D. Estas propiedades son generalmente dependientes del grosor de las láminas, y por tanto es crucial controlar el grado de exfoliación en los materiales 2D obtenidos a partir de materiales laminares, así como el espesor en materiales 2D no laminares, de cara a obtener materiales útiles en aplicaciones tecnológicas. Teniendo esto en cuenta, es importante señalar que no existe un único método de preparación de materiales 2D, sino que durante los últimos años se han ido desarrollando técnicas fundamentadas en diferentes metodologías, con diferentes características en cuestión de precio, cantidad obtenida, rendimiento, escalabilidad, control de las características del material (espesor, tamaño lateral, oxidación, defectos, grupos funcionales, morfología, etc.), rapidez y subproductos contaminantes generados. Es necesario, por tanto, seleccionar el método apropiado de preparación de láminas 2D en función de los requerimientos de la aplicación concreta que se busque. De forma general, los métodos de obtención de materiales 2D se pueden clasificar en dos grandes familias: los métodos *bottom-up* o ascendentes y *top-down* o descendentes.

1.2.1 Métodos *bottom-up*

Esta familia de métodos de preparación se basa en la síntesis de láminas 2D a partir de precursores atómicos o moleculares mediante reacciones químicas que permiten la formación del material con morfología 2D. Entre ellos, los que destacan en fase líquida son la síntesis de TMDs y de óxidos metálicos a partir de precursores moleculares por vía solvotérmica.

Síntesis de TMDs a partir de precursores moleculares: es posible sintetizar láminas 2D de TMDs como el MoS_2 a partir de precursores moleculares, aprovechando

la ventaja de que su estructura en capas favorece el crecimiento en forma laminar [90]. Mediante este método se obtienen láminas de MoS_2 ejerciendo control sobre la proporción de las fases 1T y 2H en función de las condiciones de preparación [91], y los materiales obtenidos muestran una actividad mejorada en su uso como catalizadores de HER [91], electrodos de baterías de ión litio [92] y en terapias antitumorales [93].

Síntesis de láminas 2D controlada por fases micelares: los materiales que por no estar constituidos por capas en su estructura 3D no pueden ser exfoliados (como los óxidos metálicos) se pueden sintetizar en forma de láminas delgadas (2D) a partir de precursores moleculares en fase líquida. Los precursores utilizados habitualmente son sales metálicas que, por tratamiento solvotérmico y mediante el uso de agentes directores de la estructura tipo surfactante, dan lugar a láminas nanométricos (Figura 6) [77]. La función de estos agentes directores es la formación de fases micelares en las que tiene lugar la nucleación y crecimiento a partir de los precursores, de manera que los productos obtenidos son láminas 2D. Existen procedimientos generales para la preparación de óxidos metálicos basados en el uso de fases micelares de morfología laminar en las que se utilizan como agentes directores polímeros anfifílicos [77] y surfactantes [94], o bien el uso de otros materiales 2D como óxido de grafeno [95]. Las láminas obtenidas por estos métodos se han empleado como fotodetectores [77], catalizadores de ORR [94] y en almacenamiento de carga eléctrica [95].

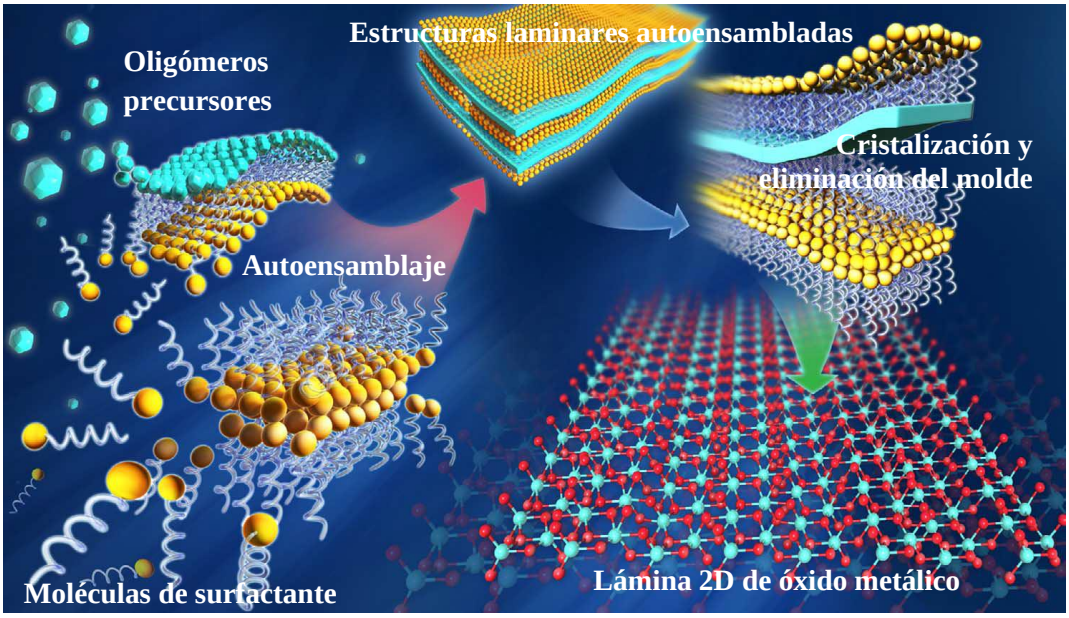

Figura 6. Síntesis de láminas 2D de óxidos metálicos dirigida por fases micelares de morfología laminar. Adaptado de [77].

1.2.2 Métodos *top-down*

Esta familia de métodos se basa en la obtención de láminas 2D (tanto materiales monocapa como multicapa) mediante la exfoliación de un material laminar *bulk*. Estos materiales están formados por láminas individuales que se mantienen unidas por fuerzas débiles tipo van der Waals, formando estructuras 3D por apilamiento. Dichas fuerzas débiles entre capas deben ser superadas para aislar las láminas individuales, de manera que es necesario aplicar algún tipo de estímulo o fuerza externa que aumente el espaciado interlaminar. Las interacciones involucradas son proporcionales a $1/d^6$ (siendo *d* la distancia interlaminar) y se vuelven despreciables por encima de distancias de ~5 Å [96]. Las estrategias que se utilizan para separar las láminas se basan en aplicar fuerzas a través de procesos como cambios de temperatura, intercalación de especies químicas, ultrasonidos o fuerzas de cizalla, con diferentes condiciones y mecanismos asociados en cada caso.

Históricamente, el primer método utilizado para aislar monocapas de un material 2D a partir de un material fue el **método de la cinta adhesiva** (***Scotch tape***, o de forma general, **exfoliación micromecánica**), mediante el cual se obtuvieron láminas de

grafeno a partir de grafito pirolítico altamente orientado (HOPG, highly oriented pyrolitic graphite) en 2004 [3]. En ese trabajo, los autores llevaron a cabo la exfoliación pegando y despegando la cinta adhesiva a una pieza de grafito. Al repetir este proceso un gran número de veces se va reduciendo progresivamente el número de capas del material, de manera que es posible obtener monocapas. Como el proceso no involucra reactivos ni condiciones agresivas, los materiales obtenidos tienen una altísima calidad estructural, por lo que es posible utilizarlo para estudios fundamentales y desarrollo de prototipos. Además, por su propia naturaleza, es un proceso aplicable a cualquier material laminar *bulk* en forma de cristales a partir de pocos mm^2 de tamaño, por lo que su uso se ha extendido a otros materiales como MoS_2, WS_2, $NbSe_2$, fósforo negro, hBN y otros [97].

No obstante, y como cabe esperar, la productividad de este método es muy baja, por lo que ha sido necesario desarrollar otras estrategias que sean capaces de producir mayores cantidades de materiales 2D. Los métodos más habituales son los que se llevan a cabo en fase líquida, ya que permiten grandes números de láminas del material 2D en dispersión coloidal, lo que facilita su procesado. En función de la fuerza impulsora de la exfoliación (ultrasonidos, modificación química, intercalación), tenemos diferentes clases de métodos de preparación. Las más relevantes son las siguientes:

a) Exfoliación por ultrasonidos/cizalla

Una de las vías más extendidas para la preparación de dispersiones coloidales de láminas 2D es la exfoliación de materiales *bulk* mediante sonicación o fuerzas de cizalla [98]. El fundamento de este método es la aplicación de fuerzas laterales y verticales a los planos basales que separen las capas en el material *bulk*, provocando su exfoliación hasta obtener láminas 2D de pocas capas de espesor. Estas fuerzas pueden ser generadas por las burbujas de cavitación que se generan al aplicar ultrasonidos en fase líquida, así como por fuerzas de cizalla generadas por un rotor que gira sumergido en un disolvente [99,100] (Figura 7). Para obtener resultados satisfactorios en cualquiera de los dos casos es necesario llevar a cabo el proceso en un medio líquido cuya energía superficial sea muy similar a la del plano basal del material a exfoliar, de manera que se minimice la energía requerida para la exfoliación y solvatación de las láminas 2D. Es habitual el uso de disolventes orgánicos como la N-metilpirrolidona (NMP), el isopropanol (IPA) y la N,N-dimetilformamida (DMF), tanto para la exfoliación de grafeno [99] como de otros materiales 2D como MoS_2, WS_2, $MoSe_2$, $MoTe_2$, $TaSe_2$, $NbSe_2$, $NiTe_2$, BN, y Bi_2Te_3

[101]. Es posible además utilizar mezclas de agua y otras sustancias, como otros disolventes o moléculas anfifílicas, para minimizar la energía requerida en la exfoliación. Así, se han usado mezclas agua/alcohol [102], así como surfactantes [103], polímeros [104] y biomoléculas [105].

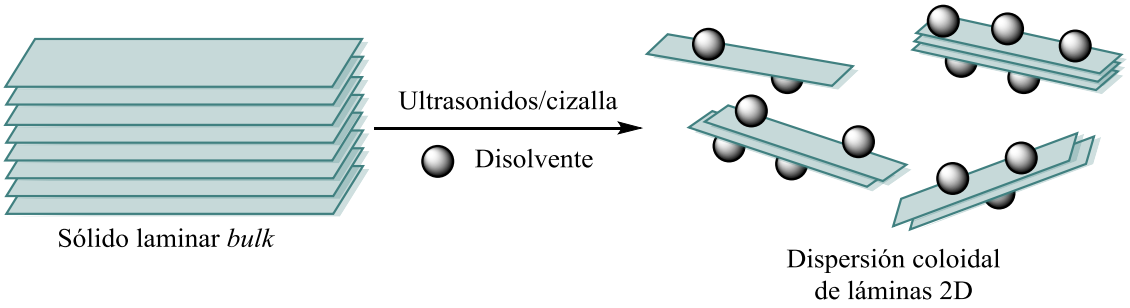

Figura 7. Exfoliación mediante ultrasonidos/cizalla de un material laminar para obtener dispersiones de láminas 2D.

El resultado de este método son dispersiones coloidales de láminas 2D formadas por pocas capas (habitualmente entre 3 y 10 capas, en diferentes proporciones) y con un rendimiento de exfoliación habitualmente por debajo del 1% en peso [99]. Por norma general, la calidad estructural de los materiales 2D obtenidos es muy alta, ya que el proceso no implica una modificación química significativa de la estructura, sino que la fuerza directora de la exfoliación proviene de fenómenos físicos esencialmente mecánicos. Las dispersiones obtenidas son fácilmente procesables, y han sido utilizadas para preparar, entre otros, materiales compuestos [106], electrodos de supercondensadores [107] y transistores [108].

b) Ruta del óxido de grafeno

Otra de las vías más populares para la preparación de láminas 2D en dispersión coloidal es la modificación química de materiales laminares. El mejor ejemplo es la ruta del óxido de grafeno (GO, graphene oxide, Figura 8). El GO se puede preparar mediante la oxidación de grafito por el método de Hummers o modificaciones del mismo [109,110]. En una primera etapa, se oxida el grafito mediante el uso de oxidantes fuertes como el $KMnO_4$ en medio ácido, obteniéndose así óxido de grafito. Este óxido presenta gran proporción de grupos oxigenados tanto en el plano basal como en los bordes de lámina, lo que aumenta su espaciado interlaminar y disminuye la energía requerida para

separar unas capas de otras. Ello permite dispersar el material tanto en agua como en disolventes orgánicos [110,111], ya que la presencia de grupos oxigenados capaces de desprotonarse hace que el material tenga buena dispersabilidad coloidal, obteniéndose fácilmente suspensiones de láminas monocapa de GO mediante sonicación. Por último es necesario llevar a cabo una reducción del GO para obtener el denominado óxido de grafeno reducido (rGO, reduced graphene oxide), con la intención de recuperar en l medida de lo posible la estructura y las propiedades del grafeno prístino. De hecho, una conversión completa a grafeno prístino solo se puede alcanzar en filmes a muy altas temperaturas [112], mientras que en dispersión coloidal es posible solamente reducir parcialmente el material y por tanto sólo recuperar parcialmente sus propiedades. Existen muchas metodologías para la obtención de rGO, entre ellos el uso de reductores químicos como hidracina [113], vitamina C [114], hidrógeno [115] o biomoléculas [116], así como procesos de reducción térmica [117], electroquímica [118] y fotorquímica [119].

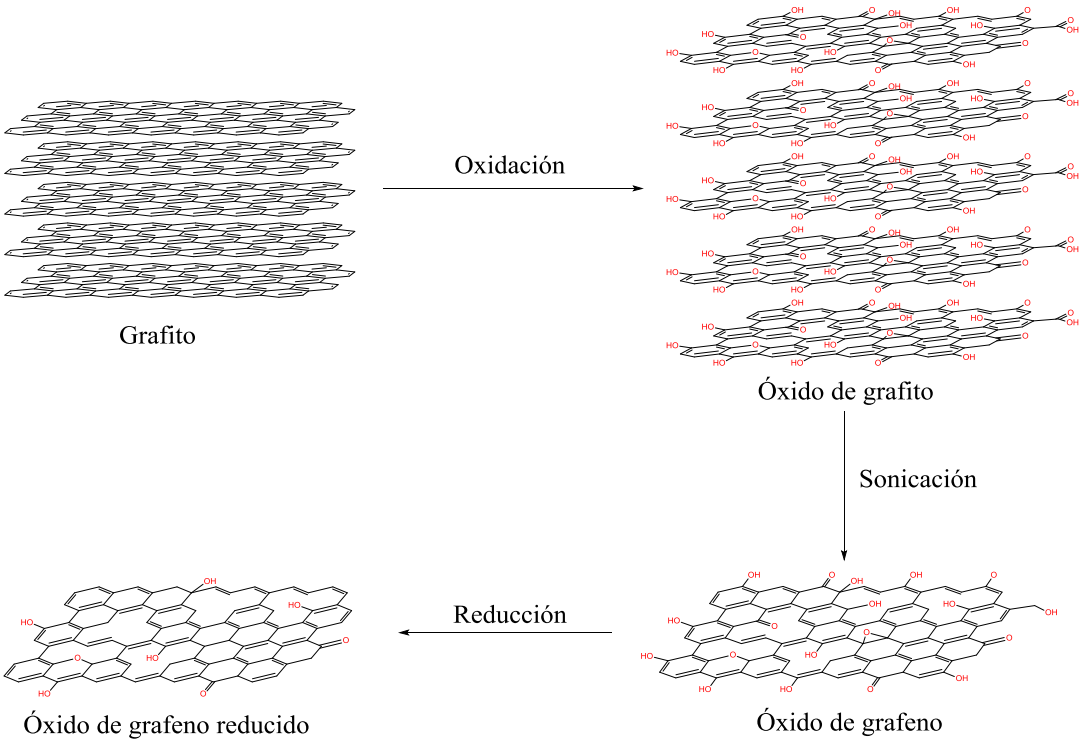

Figura 8. Proceso de preparación de rGO.

Se ha utilizado rGO preparado por estos métodos en materiales híbridos para aplicaciones como el almacenamiento y conversión de energía [120,121], electrocatálisis [118] y tratamiento de aguas [119].

c) Exfoliación química

Una de las posibles fuerzas directoras de la exfoliación de materiales laminares como los TMDs es la intercalación de especies químicas que aumenten el espaciado interlaminar y por tanto faciliten la deslaminación al debilitar las interacciones cohesivas del material [122]. En la exfoliación de MoS_2 y otros TMDs esta estrategia se lleva a cabo habitualmente mediante la intercalación de metales alcalinos en forma de compuestos como el n-butil-litio, de manera que se obtienen compuestos de intercalación (p. e. Li_xMoS_2), en los que tiene lugar una transferencia de electrones del litio al metal, que en muchos casos induce un cambio de la fase original 2H (semiconductora) a la 1T (metálica) [123,124,125]. Estos compuestos de intercalación suelen ser es altamente reactivos, y al hacerse reaccionar con agua dan lugar a la formación de LiOH e hidrógeno gaseoso, de manera que se produce la exfoliación del material (Figura 9). Esta exfoliación química da lugar a una dispersión coloidal acuosa de láminas 2D formadas por monocapas del TMD cargadas negativamente debido al exceso de electrones, lo que les proporciona estabilidad coloidal en el medio acuoso. No obstante, el exceso de electrones de las láminas las hace bastante reactivas, y su tendencia a oxidarse por reacción con el agua provoca que pierdan la carga eléctrica y por tanto precipiten irreversiblemente en cuestión de pocas semanas [126].

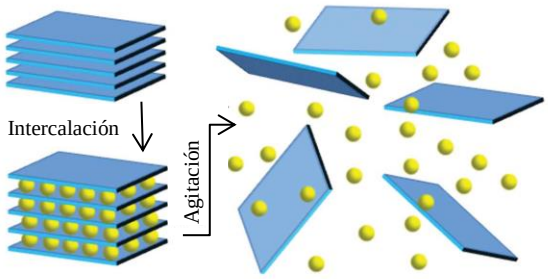

Figura 9. Exfoliación de un material laminar mediante intercalación de una especie química. Adaptado de [122].

La transformación del MoS_2 y otros TMDs a la fase metálica 1T y el correspondiente aumento de la densidad electrónica hacen apropiado el uso de láminas 2D de estos materiales en aplicaciones como el almacenamiento de energía en supercondensadores [124], catalizador de HER [125] y de reducción de nitroarenos [127], mostrando en muchos casos mejores resultados que la fase 2H.

d) Exfoliación electroquímica

Uno de los métodos más recientes y prometedores para llevar a cabo la preparación de grafeno en fase líquida de forma escalable y en cantidades más allá de la escala de laboratorio es la exfoliación de grafito por vía electroquímica [128,129]. La fuerza directora del proceso es la aplicación de un voltaje a un electrodo de grafito sumergido en un electrolito líquido. Este voltaje aplicado induce la intercalación de especies iónicas solvatadas en la estructura del grafito, aumentando el espaciado interlaminar y facilitando por tanto su deslaminación para obtener grafeno (Figura 10). Existen dos variantes de esta técnica, en función del signo positivo o negativo del potencial aplicado al electrodo de grafito, y esta elección tiene consecuencias en términos de los electrolitos apropiados, así como en las características del grafeno obtenido [128].

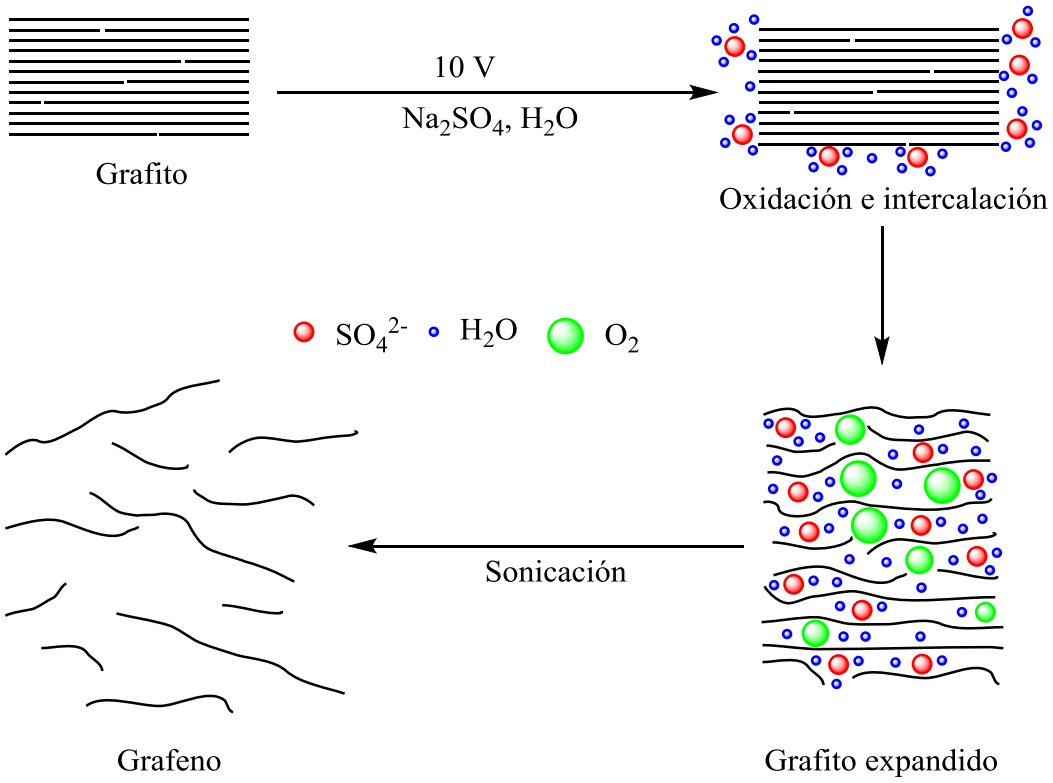

Figura 10. Exfoliación electroquímica de un ánodo de grafito.

En la **exfoliación catódica** el electrodo de grafito se somete a un potencial negativo (típicamente de -2 a -10 V), y por tanto tiene lugar la intercalación de cationes en la estructura [130]. Este proceso suele llevarse a cabo utilizando como electrolitos sales de Li^+ [131], de alquilamonio [132,133] o líquidos iónicos [134], habitualmente en disolventes orgánicos como dimetilsulfóxido (DMSO) o carbonato de propileno (PC). A

continuación, es habitual someter al electrodo expandido a un proceso de sonicación que complete la deslaminación del material, de manera que se obtienen dispersiones coloidales de láminas de grafeno. Por norma general, los materiales obtenidos están constituidos por láminas relativamente delgadas (entre 5 y 10 capas), con poco contenido en oxígeno y defectos [130], y han sido utilizados en aplicaciones como el almacenamiento y la conversión de energía [129], sensores y LEDs [130].

Por otra parte, la **exfoliación anódica** se fundamenta en la aplicación de un potencial positivo en un ánodo de grafito y la consiguiente intercalación de aniones. En esta variante de exfoliación es habitual utilizar agua como disolvente y electrolitos como ácido sulfúrico [135], ácido fosfórico [136], sales de sulfato [137], sulfonatos orgánicos [138] y líquidos iónicos [139]. Como se detalla en la Figura 10, al someter al electrodo de grafito a un potencial positivo (entre 4 y 30 V, siendo lo más común aplicar 10 V) tiene lugar la oxidación de los bordes de grano y lámina del grafito, lo cual facilita la intercalación de los aniones presentes en el electrolito. Debido a que este potencial es superior al de oxidación del agua, el proceso genera especies altamente reactivas como el radical OH·, que atacan (oxidan) el ánodo de grafito tanto en los bordes como en el plano basal y generan especies gaseosas. Este proceso induce la expansión del ánodo, dando lugar a un grafito expandido que puede terminar de ser exfoliado en láminas de grafeno mediante sonicación. Los materiales grafénicos obtenidos mediante exfoliación aniónica están compuestos generalmente por láminas muy delgadas (entre 1 y 3 monocapas en su mayoría). Sin embargo, la naturaleza oxidativa del proceso hace que el contenido en oxígeno sea relativamente alto, con porcentajes típicos entre el 10 y el 30% [129].

Durante el proceso de exfoliación electroquímica anódica es posible la utilización de electrolitos y aditivos de electrolito especiales, con objeto de cumplir dos funciones: disminuir la oxidación del grafeno anódico y/o promover su funcionalización [140]. El control de la oxidación se lleva a cabo mediante el uso de sustancias susceptibles de ser oxidadas en el proceso electrolítico en lugar del grafeno (es decir, sustancias antioxidantes, ya sean el electrolito intercalante o aditivos añadidos al electrolito intercalante). Algunas de las sustancias utilizadas como aditivos de electrolito son la melamina [141], el 2,2,6,6-tetrametilpiperidin-1-il)oxil (TEMPO) [142] y el benzoato de sodio [143], con contenidos de oxígeno en el grafeno anódico resultante de aproximadamente 4% en los tres casos, y utilizados en aplicaciones como relleno de materiales compuestos [141], electrodos de supercondensadores [142] y

electrocatalizadores [143]. Por otra parte, es posible la funcionalización del grafeno en el proceso, tanto de forma no covalente con el propio electrolito [138] como covalentemente, mediante dopaje atómico. Este dopaje suele llevarse a cabo con átomos de nitrógeno [144], azufre [145] o ambos [146], y mejora sus propiedades en el uso del grafeno en supercondensadores [144,145] y catalizador de ORR [146].

Bibliografía

[1] International Organization for Standardization, ISO/TS 80004:2015 Nanotechnologies-Vocabulary.
[2] Lee, J.-U.; Yoon, D.; Cheong, H. Estimation of young's modulus of graphene by Raman spectroscopy. *Nano Lett*., **2012**, 12, 4444-4448.
[3] Novoselov, K. S.; Geim, A. K.; Morozov, S. V.; Jiang, D.; Zhang, Y.; Dubonos, S. V.; Grigorieva, I.V.; Firsov, A.A.; Electric field in atomically thin carbon films. *Science*, **2004**, 306, 666-669.
[4] Butler, S. Z.; Hollen, S. M.; Cao, L.; Cui, Y.; Gupta, J.A.; Gutiérrez, H.R.; Heinz, T.F.; Hong, S. S.; Huang, J.; Ismach, A. F.; Johnston-Halperin, E.; Kuno, M.; Plashnitsa, V. V.; Robinson, R. D.; Ruoff, R. S.; Salahuddin, S.; Shan, J.; Shi, L.; Spencer, M. G.; Terrones, M.; Windl, W.; Goldberger, J. E. Progress, Challenges, and Opportunities in Two-Dimensional Materials Beyond Graphene. *ACS Nano*, **2013**, 7, 2898-2926.
[5] Bhimanapati, G. R.; Lin, Z.; Meunier, V.; Jung, Y.; Cha, J.; Das, S.; Xiao, D.; Son, Y.; Strano, M. S.; Cooper, V. R.; Liang, L.; Louie, S. G.; Ringe, E.; Zhou, W.; Kim, S. S.; Naik, R. R.; Sumpter, B. G.; Terrones, H.; Xia, F.; Wang, Y.; Zhu, J.; Akinwande, D.; Alem, N.; Schuller, J. A.; Schaak, R. E.; Terrones, M.; Robinson, J.A. Recent Advances in Two-Dimensional Materials beyond Graphene. *ACS Nano*, **2015**, 9, 11509-11539.
[6] Mas-Ballesté, R.; Gómez-Navarro, C.; Gómez-Herrero, J.; Zamora, F. 2D materials: To graphene and beyond. *Nanoscale*, **2011**, 3, 20-30.
[7] Lv, R.; Robinson, J. A.; Schaak, R. E.; Sun, D.; Sun, Y.; Mallouk, T. E.; Terrones, M. Transition metal dichalcogenides and beyond: Synthesis, properties, and applications of single- and few-layer nanosheets. *Acc. Chem. Res*., **2015**, 48, 56-64.
[8] Geim, A. K.; Grigorieva, I. V. Van der Waals heterostructures. *Nature*, **2013**, 499, 419-425.
[9] Rao, C. N. R.; Sood, A. K.; Subrahmanyam, K. S .; Govindaraj, A. Graphene: The new two-dimensional nanomaterial. *Angew. Chem. Int. Ed*., **2009**, 48, 7752-7777.
[10] Ohta, T.; Bostwick, A.; Seyller, T.; Horn, K.; Rotenberg, E. Controlling the Electronic Structure of Bilayer Graphene. *Science*, **2006**, 313, 951-954.
[11] Zhang, Y.; Tang, T.-T.; Girit, C.; Hao, Z.; Martin, M. C.; Zettl, A.; Crommie, M. F.; Shen, Y. R.; Wang, F. Direct observation of a widely tunable bandgap in bilayer graphene. *Nature*, **2009**, 459, 820-823.
[12] Shahil, K. M. F.; Balandin, A. A. Graphene-Multilayer Graphene Nanocomposites as Highly Efficient Thermal Interface Materials. *Nano Lett*., **2012**, 12, 861-867.
[13] Tan, P. H.; Han, W. P.; Zhao, W. J.: Wu, Z. H.; Chang, K.; Wang, H.; Wang, Y. F.; Bonini, N.; Marzari, N.; Pugno, N.; Savini, G.; Lombardo, A.; Ferrari, A.C. The shear mode of multilayer graphene. *Nat. Mat*., **2012**, 11, 294-300.
[14] Novoselov, K. S.; Fal'Ko, V. I.; Colombo, L.; Gellert, P. R.; Schwab, M. G.; Kim, K. A roadmap for graphene. *Nature*, **2012**, 490, 192-200.
[15] Weiss, N. O.; Zhou, H.; Liao, L.; Liu, Y.; Jiang, S.; Huang, Y.; Duan, X. Graphene: An emerging electronic material. *Adv, Mater*., **2012**, 24, 5782-5825.
[16] Zhang, Y.; Tan, Y.-W.; Stormer, H. L.; Kim, P. Experimental observation of the quantum Hall effect and Berry's phase in graphene. *Nature*, **2005**, 438, 201-204.
[17] Novoselov, K. S.; Jiang, Z.; Zhang, Y.; Morozov, S. V.; Stormer, H. L.; Zeitler, U.; Maan, J. C.; Boebinger, G. S.; Kim, P.; Geim, A. K. Room-temperature quantum hall effect in graphene. *Science*, **2007**, 315, 1379.

[18] Sun, Y.; Wu, Q.; Shi, G. Graphene based new energy materials, *Energy Environ. Sci.*, **2011**, 4, 1113-1132.
[19] Bonaccorso, F.; Colombo, L.; Yu, G.; Stoller, M.; Tozzini, V.; Ferrari, A. C.; Ruoff, R. S.; Pellegrini, V. Graphene, related two-dimensional crystals, and hybrid systems for energy conversion and storage. *Science*, **2017**, 347, 1246501.
[20] Schwierz, F. Graphene transistors, *Nat. Nanotechnol.*, **2010**, 5, 487-496
[21] Novoselov, K. S.; Fal'Ko, V. I.; Colombo, L.; Gellert, P. R.; Schwab, M. G.; Kim, K. A roadmap for graphene. *Nature*, **2012**, 490, 192-200.
[22] Bonaccorso, F.; Sun, Z.; Hasan, T.; Ferrari, A. C. Graphene photonics and optoelectronics. *Nat. Photonics*, **2010**, 4, 611-622.
[23] Shuping Pang, S.; Hernandez, Y.; Feng, X.; Müllen, K. Graphene as Transparent Electrode Material for Organic Electronics. *Adv. Mater*., **2011**, 23, 2779-2795.
[24] Prezzi, D.; Varsano, D.; Ruini, A.; Marini, A.; Molinari, E. Optical properties of graphene nanoribbons: The role of many-body effects. *Phys. Rev. B.* **2008**, 77, 041404(R).
[25] Lee, C.; Wei1, X.; Kysar, J. W.; Hone1, J. Measurement of the Elastic Properties and Intrinsic Strength of Monolayer Graphene. *Science*, **2008**, 321, 385-388.
[26] Graphene Reinforced Metal Matrix Composite (GRMMC): A Review. *Procedia Eng*., **2014**, 97, 1033-1040.
[27] Balandin, A. A.; Thermal properties of graphene and nanostructured carbon materials. *Nat. Mater*., **2011**, 10, 569-581.
[28] Weiss, N.O.; Zhou, H.; Liao, L.; Liu Y.; Jiang, S.; Huang, Y.; Duan, X. Graphene: an emerging electronic material. *Adv Mater*., **2012**, 24, 5782-825.
[29] Pottsa, J. R.; Dreyerb, D. R.; Bielawski, C. W.; Ruoff, R. S. Graphene-based polymer nanocomposites. *Polymer*, **2011**, 52, 5-25.
[30] Yang, K.; Feng, L.; Shi, X.; Liu, Z. Nano-graphene in biomedicine: theranostic applications. *Chem. Soc. Rev*., **2013**,42, 530-547
[31] Georgakilas, V.; Otyepka, M.; Bourlinos, A. B.; Chandra, V.; Kim, N.; Kemp, K. C.; Hobza, P.; Zboril, R.; Kim, K. S. Functionalization of Graphene: Covalent and Non-Covalent Approaches, Derivatives and Applications. *Chem. Rev*., **2012**, 112, 6156-6214.
[32] Kuilaa, T.; Bose, S.; Mishra, A. K.; Khanraa, P.; Kim, N. H.; Lee, J. H. Chemical functionalization of graphene and its applications. *Prog. Mater Sci*., **2012**, 57, 1061-1105.
[33] Chua, C. K.; Pumera, M. Covalent chemistry on Graphene. *Chem. Soc. Rev*., **2013**,42, 3222-3233.
[34] Paredes, J. I.; Munuera, J. M. Recent advances and energy-related applications of high quality/chemically doped graphenes obtained by electrochemical exfoliation methods. *J. Mater. Chem. A*, **2017**, 5, 7228-7242
[35] Uddin, M. U.; Kuila, T.; Nayak, G. C.; Kim, N. H.; Ku, B-C.; Lee, J. H. Effects of various surfactants on the dispersion stability and electrical conductivity of surface modified Graphene. *J. Alloys Compd*., **2013**, 562, 134-142.
[36] Liu, Y.; Wang, R.; Zhu, Y.; Li, R.; Zhang, J. Photoelectrochemical sensing of catechol based on CdS-DNA-pristinegraphene nanocomposite film. *Sens. Actuators, B*, **2015**, 210, 355-361.
[37] Bin, D.; Ren, F.; Wang, Y.; Zhai, C.; Wang, C.; Guo, J.; Yang, P.; Du, Y. Pd-nanoparticle-supported, PDDA-functionalized graphene as a promising catalyst for alcohol oxidation. *Chemistry - An Asian Journal*, **2015**, 10, 667-673.

[38] Lü, Q.-F.; Chen, G.; Lin, T.-T.; Yu, Y. Dye-functionalized graphene/polyaniline nanocomposite as an electrode for efficient electrochemical supercapacitor. *Composites Science and Technology*, **2015**, 115, 80-86.
[39] Choudhary, S.; Mungse, H. P.; Khatri, O. P. Dispersion of alkylated graphene in organic solvents and its potential for lubrication applications. *J. Mater. Chem*., **2012**, 22, 21032-21039.
[40] Hou, S.; Cuellari, R.D.; Hakimi, N.H.H.; Patel, K.; Shah, P.; Gorring, M.; Brachfeld, S. Amino Terminated Polyethylene Glycol Functionalized Graphene and Its Water Solubility. *Mater. Res. Soc. Symp. Proc*., **2010**, 1205, 13-19.
[41] Ayán-Varela, M.; Paredes, J. I.; Guardia, L.; Villar-Rodil, S.; Munuera, J. M.; Díaz-González, M.; Fernández-Sánchez, C.; Martínez-Alonso, A.; Tascón, J. M. D. Achieving extremely concentrated aqueous dispersions of graphene flakes and catalytically efficient graphene-metal nanoparticle hybrids with flavin mononucleotide as a high-performance stabilizer. ACS Appl. Mater. Interfaces, 2015, 7, 10293−10307
[42] Ayán-Varela, M.; Ruiz-Rosas, R.; Villar-Rodil, S.; Paredes, J. I.; Cazorla-Amorós, D.; Morallón, E.; Martínez-Alonso, A.; Tascón, J. M. D. Efficient Pt electrocatalysts supported onto flavin mononucleotide–exfoliated pristine graphene for the methanol oxidation reaction, *Electrochimica Acta*, **2017**, 231, 386-395.
[43] Martinez, J.G.; Ayán-Varela, M.; Paredes, J. I.; Villar-Rodil, S.; Aznar-Cervantes, S. D.; Otero, T. F. Electrochemical synthesis and characterization of flavin mononucleotide-exfoliated pristine graphene/polypyrrole composites. *ChemElectroChem*, **2017**, 4, 1487-1497.
[44] Xing, X.; Liu, R.; Liu, S.; Xiao, S.; Xu, Y.; Wang, C.; Wu, D. Surfactant-assisted hydrothermal synthesis of cobalt oxide/nitrogen-doped graphene framework for enhanced anodic performance in lithium ion batteries. *Electrochimica Acta*, **2016**, 194, 310-316.
[45] Torres Alonso, E.; Karkera, G.; Jones, G. F.; Craciun, M. F.; Russo, S. Homogeneously Bright, Flexible, and Foldable Lighting Devices with Functionalized Graphene Electrodes. *ACS Applied Materials and Interfaces*, **2016**, 8, 16541-16545.
[46] Parandhaman, T.; Das, S. K. Facile synthesis, biofilm disruption properties and biocompatibility study of a poly-cationic peptide functionalized graphene-silver nanocomposite. *Biomaterials Science*, **2018**, 6, 3356-3372.
[47] Cao, J.; Wang, Z.; Yang, X.; Tu, J.; Wu, R.; Wang, W. Green synthesis of amphipathic graphene aerogel constructed by using the framework of polymer-surfactant complex for water remediation. *Applied Surface Science*, **2018**, 444, 399-406.
[48] Ganatra, R.; Zhang, Q. Few-layer MoS_2: A promising layered semiconductor. *ACS Nano*, **2014**, 4074-4099.
[49] Huang, X.; Zeng, Z.; Zhang, H. Metal dichalcogenide nanosheets: preparation, properties and applications. *Chem. Soc. Rev*., **2013**, 42, 1934-1946.
[50] Winer, W.O. Molybdenum disulfide as a lubricant: A review of the fundamental knowledge. *Wear*, **1967**, 10, 422-452.
[51] Chhowalla, M.; Shin, H. S.; Eda, G.; Li, L.-J.; Loh, K. P.; Zhang, H. The chemistry of two-dimensional layered transition metal dichalcogenide nanosheets. Nat. Chem., 2013, 5, 263-275.
[52] Benavente, E.; Santa Ana, M.A.; Mendizábal, F.; González, G. Intercalation chemistry of molybdenum disulfide. *Coord. Chem. Rev*., **2002**, 224, 87-109.
[53] Mak, K.F.; Lee, C.; Hone, J.; Shan, J.; Heinz, T.F. Atomically thin MoS_2: a new direct-gap semiconductor. *Phys Rev Lett*., **2010**, 105, 136805.
[54] Ghatak, S.; Pal, A.N.; Ghosh, A. Nature of electronic states in atomically thin MoS_2 field-effect transistors. *ACS Nano*, **2011**, 5, 7707-7712.

[55] Kang, P.; Wang, M. C.; Nam, S. Bioelectronics with two-dimensional materials, *Microelectron. Eng*., **2016**, 161, 18–35.
[56] Zhang, W.; Zhang, P.; Su, Z.; Wei, G. Synthesis and sensor applications of MoS_2-based nanocomposites. *Nanoscale*, **2015**, 7, 18364-18378.
[57] Lembke, D.; Bertolazzi, S.; Kis, A. Single-Layer MoS_2 Electronics. *Acc. Chem. Res*., **2015**, 48, 100-110.
[58] Wang, X.; Kalali, E. N.; Wang, D-Y. An in situ polymerization approach for functionalized MoS_2/nylon-6 nanocomposites with enhanced mechanical properties and thermal stability. *J. Mater. Chem. A*, **2015**, 3, 24112-24120.
[59] Bertolazzi, S.; Brivio, J.; Kis, A. Stretching and breaking of ultrathin MoS_2. *ACS Nano*, **2011**, 5, 9703-9709.
[60] Castellanos-Gomez, A.; Poot, M.; Steele, G.A.; van der Zant, H.S.J.; Agraït, N.; Rubio-Bollinger, G. Elastic properties of freely suspended MoS2 nanosheets, *Adv. Mater*, **2012**, 24, 772-775.
[61] Kim, J.-Y.; Choi, S.M.; Seo, W.-S.; Cho, W.-S. Thermal and Electronic Properties of Exfoliated Metal Chalcogenides. *Bull. Korean Chem. Soc*., **2010**, 31, 3225-3227.
[62] Zhou, K.; Liu, J.; Zeng, W.; Hu, Y.; Gui, Z. In situ synthesis, morphology, and fundamental properties of polymer/MoS_2 nanocomposites. *Compos. Sci. Technol*., **2015**, 107, 120-128.
[63] Jaramillo, T.F.; Jørgensen, K.P.; Bonde, J.; Nielsen, J.H.; Horch, S.; Chorkendorff, I. Identification of active edge sites for electrochemical H_2 evolution from MoS_2 nanocatalysts. *Science*, **2007**, 317, 100-102.
[64] Grange, P.; Delmon, B. The role of cobalt and molybdenum sulphides in hydrodesulphurisation catalysts: A review. *J. Less Common. Met*., **1974**, 36, 353-360.
[65] Zhang, X.; Hayward, D.O.; Lee, C.; Mingos, D.; Michael, P. Microwave assisted catalytic reduction of sulfur dioxide with methane over MoS_2 catalysts. *Appl. Catal., B*, **2001**, 33, 137-148.
[66] Guardia, L.; Paredes, J. I.; Munuera, J. M.; Villar-Rodil, S.; Ayán-Varela, M.; Martínez-Alonso, A.; Tascón, J. M. D. Chemically exfoliated MoS_2 nanosheets as an efficient catalyst for reduction reactions in the aqueous phase. *ACS Appl. Mater. Interfaces* **2014**, 6, 21702−21710.
[67] Acerce, M.; Voiry, D.; Chhowalla, M. Metallic 1T phase MoS_2 nanosheets as supercapacitor electrode materials. *Nat. Nanotech*., **2015**, 10, 313-318.
[68] Kim, J.; Byun, S.; Smith, A.J.; Yu, J.; Huang, J. Enhanced Electrocatalytic Properties of Transition-Metal Dichalcogenides Sheets by Spontaneous Gold Nanoparticle Decoration. *J. Phys. Chem. Lett*., **2013**, 4, 1227-1232.
[69] Yuwen, L.; Xu, F.; Xue, B.; Luo, Z.; Zhang, Q.; Bao, B.; Su, S.; Weng, L.; Huang, W.; Wang, L. General synthesis of noble metal (Au, Ag, Pd, Pt) nanocrystal modified MoS_2 nanosheets and the enhanced catalytic activity of Pd–MoS_2 for methanol oxidation. *Nanoscale*, **2014**, 6, 5762-5769.
[70] Lu, J.; Lu, J.H.; Liu, H.; Liu, B.; Gong, L.; Tok, E.S.; Loh, K.P.; Sow, C.H. Microlandscaping of Au Nanoparticles on Few-Layer MoS_2 Films for Chemical Sensing. *Small*, **2015**, 11, 1792-1800.
[71] Varrla, E.; Backes, C.; Paton, K.R.; Harvey, A.; Gholamvand, Z.; McCauley, J.; Coleman, J.N. Large-Scale Production of Size-Controlled MoS_2 Nanosheets by Shear Exfoliation. *Cem. Mat.*, **2015**, 27, 1129-1139.

[72] Guardia, L.; Paredes, J.I.; Rozada, R.; Villar-Rodil, S.; Martínez-Alonso, A.; Tascón, J.M.D. Production of aqueous dispersions of inorganic graphene analogues by exfoliation and stabilization with non-ionic surfactants. *RSC Adv*., **2014**, 4, 14115-14127.
[73] Chen, L.; Feng, W.; Zhou, X.; Qiu, K.; Miao, Y.; Zhang, Q.; Qin, M.; Li, L.; Zhang, Y.; He, C. Facile synthesis of novel albumin-functionalized flower-like MoS_2 nanoparticles for in vitro chemophotothermal synergistic therapy. *RSC Adv*., **2016**, 6, 13040-13049.
[74] Suh, J.; Park, T.-E.; Lin, D.-Y.; Fu, D.; Park, J.; Jung, H.J.; Chen, Y.; Ko, C.; Jang, C.; Sun, Y.; Sinclair, R.; Chang, J.; Tongay, S.; Wu, J. Doping against the Native Propensity of MoS_2: Degenerate Hole Doping by Cation Substitution. *Nano Lett*., **2014**, 14, 6976-6982.
[75] Backes, C.; Berner, N.C.; Chen, X.; Lafargue, P.; LaPlace, P.; Freeley, M.; Duesberg, G.S.; Coleman, J.N.; McDonald, A.R. Functionalization of Liquid-Exfoliated Two-Dimensional 2H-MoS_2. *Angew. Chem. Int. Ed*., **2015**, 54, 2638-2642.
[76] Voiry, D.; Goswami, A.; Kappera, R.; Castro e Silva, C. C.; Kaplan, D.; Fujita, T.; Chen, M.; Asefa, T.; Chhowalla, M. Covalent functionalization of monolayered transition metal dichalcogenides by phase engineering. *Nat. Chem.*, **2015**, 7, 45-49.
[77] Sun, Z.; Liao, T.; Dou, Y.; Hwang, S. M.; Park, M.-S.; Jiang, L.; Kim, J. H.; Dou, S. X. Generalized self-assembly of scalable two-dimensional transition metal oxide nanosheets. *Nat. Commun.*, **2014**, 5, 3813-3822.
[78] Tan, H. T.; Sun, W.; Wang, L.; Yan, Q. 2D transition metal oxides/hydroxides for energy-storage applications. *ChemNanoMat*, **2015**, 2, 562–577.
[79] Seidov, Z.; Açıkgöz, M.; Kazan, S.; Mikailzade, F. Magnetic properties of Co_3O_4 polycrystal powder. *Ceramics International*, **2016**, 42, 12928-12931.
[80] Gao, S.; Jiao, X.; Sun, Z.; Zhang, W.; Sun, Y.; Wang, C.; Hu, Q.; Zu, X.; Yang, F.; Yang, S.; Liang, L.; Wu, J.; Xie, Y. Ultrathin Co_3O_4 Layers Realizing Optimized CO_2 Electroreduction to Formate. *Angew. Chem. Int. Ed.*, **2016**, 55, 698–702.
[81] Zheng, Y.; Wang, W.; Jiang, D.; Zhang, L.; Li, X.; Wang, Z. Ultrathin mesoporous Co_3O_4 nanosheets with excellent photo-/thermo-catalytic activity. *J. Mater. Chem. A*, **2016**,4, 105-112.
[82] Du, S.; Ren, Z.; Qu, Y.; Wu, J.; Xi, W.; Zhu, J.; Fu, H. Co_3O_4 nanosheets as a high performance catalyst for oxygen evolution proceeding via a double two electron process, *Chem. Commun.*, **2016**, 52, 6705–6708.
[83] Wang, X.; Yao, S.; Wu, X.; Shi, Z.; Sun, H.; Que, R. High gas-sensor and supercapacitor performance of porous Co3O4 ultrathin nanosheets. *RSC Adv*., **2015**, 5, 17938-17944.
[84] Mei, J.; Liao, T.; Kou, L.; Sun, Z. Two-dimensional metal oxide nanomaterials for next-generation rechargeable batteries. *Adv. Mater.*, **2017**, 29, 1700176.
[85] Kou, T.; Yao, B.; Liu, T.; Li, Y. Recent advances in chemical methods for activating carbon and metal oxide based electrodes for supercapacitors. *J. Mater. Chem. A*, **2017**, 5, 17151–17173.
[86] Yuan, C.; Yang, L.; Hou, L.; Shen, L.; Zhang, X.; Lou, X. W. Growth of ultrathin mesoporous Co_3O_4 nanosheet arrays on Ni foam for high-performance electrochemical capacitors. *Energy Environ. Sci.*, **2012**, 5, 7883–7887.
[87] Yao, Y.; Zhu, Y.; Zhao, S.; Shen, J.; Yang, X.; Li, C. Halide ion intercalated electrodeposition synthesis of Co_3O_4 nanosheets with tunable pores on graphene foams as free-standing and flexible Li-ion battery anodes. *ACS Appl. Energy Mater.*, **2018**, 1, 1239–1251.
[88] Kaneti, Y. V.; Salunkhe, R. R.; Septiani, N. L. W.; Young, C.; Jiang, X. C.; He, Y. B.; Kang, Y. M.; Sugahara, Y.; Yamauchi, Y. General template-free strategy for fabricating mesoporous two-dimensional mixed oxide nanosheets via self-deconstruction/reconstruction of monodispersed metal glycerate

Nanospheres. *J. Mater. Chem. A*, **2018**, 6, 5971–5983.
[89] Yang, M.-Q.; Wang, J.; Wu, H.; Ho, G. W. Noble metal-free nanocatalysts with vacancies for electrochemical water splitting. *Small*, **2018**, 14, 1703323.
[90] Chua, C. K.; Loo, A. H.; Pumera, M. Top-Down and Bottom-Up Approaches in Engineering 1 T Phase Molybdenum Disulfide (MoS2): Towards Highly Catalytically Active Materials. *Chemistry - A European Journal*, **2016**, 22, 14336-14341.
[91] Sun, K.; Liu, Y.; Pan, Y.; Zhu, H.; Zhao, J.; Zeng, L.; Liu, Z.; Liu, C. Targeted bottom-up synthesis of 1T-phase MoS_2 arrays with high electrocatalytic hydrogen evolution activity by simultaneous structure and morphology engineering. *Nano Research*, **2018**, 11, 4368–4379.
[92] Gong, Y.; Yang, S.; Zhan, L.; Ma, L.; Vajtai, R.; Ajayan, P. M. A bottom-up approach to build 3D architectures from nanosheets for superior lithium storage. *Advanced Functional Materials*, **2014**, 24, 125-130.
[93] Wang, S.; Li, K.; Chen, Y.; Chen, H.; Ma, M.; Feng, J.; Zhao, Q.; Shi, J. Biocompatible PEGylated MoS_2 nanosheets: Controllable bottom-up synthesis and highly efficient photothermal regression of tumor. *Biomaterials*, **2015**, 39, 206-217.
[94] Zhuang, L.; Ge, L.; Yang, Y.; Li, M.; Jia, Y.; Yao, X.; Zhu, Z. Ultrathin iron-cobalt oxide nanosheets with abundant oxygen vacancies for the oxygen evolution reaction. *Adv. Mater.*, **2017**, 1606793.
[95] Chen, P.-Y.; Liu, M.; Valentin, T. M.; Wang, Z.; Steinberg, R. S.; Sodhi, J.; Wong, I. Y.; Hurt, R. H. Hierarchical metal oxide topographies replicated from highly textured graphene oxide by intercalation templating. *ACS Nano*, **2016**, 10, 10869-10879.
[96] From graphite to graphene: direct liquid-phase exfoliation of graphite to produce single- and few layered pristine graphene. *J. Mater. Chem. A*, **2013**, 1, 10592-10606.
[97] Novoselov, K.S.; Jiang, D.; Schedin, F.; Booth, T.J.; Khotkevich, V.V.; Morozov, S.V.; Geim, A.K. Two-dimensional atomic crystals. *Proc. Natl. Acad. Sci. U.S.A.*, **2005**, 102, 10451-10453.
[98] Coleman, J.N.; Lotya, M.; O'Neill, A.; Bergin, S.D.; King, P.J.; Khan, U.; Young, K.; Gaucher, A.; De, S.; Smith, R.J.; Shvets, I.V.; Arora, S.K.; Stanton, G.; Kim, H.-Y.; Lee, K.; Kim, G.T.; Duesberg, G.S.; Hallam, T.; Boland, J.J.; Wang, J.J.; Donegan, J.F.; Grunlan, J.C.; Moriarty, G.; Shmeliov, A.; Nicholls, R.J.; Perkins, J.M.; Grieveson, E.M.; Theuwissen, K.; McComb, D.W.; Nellist, P.D.; Nicolosi, V. Two-dimensional nanosheets produced by liquid exfoliation of layered materials. *Science*, **2011**, 331, 568-571.
[99] Hernandez, Y.; Nicolosi, V.; Lotya, M.; Blighe, F. M.; Sun, Z.; De, S.; McGovern, I. T.; Holland, B.; Byrne, M.; Gun'Ko, Y. K.; Boland, J. J.; Niraj, P.; Duesberg, G.; Krishnamurthy, S.; Goodhue, R., Hutchison, J.; Scardaci, V.; Ferrari, A. C.; Coleman, J. N. High-yield production of graphene by liquid-phase exfoliation of graphite. *Nature Nanotechnology*, **2008**, 3, 563–568.
[100] Paton, K. R.; Varrla, E.; Backes, C.; Smith, R. J.; Khan, U.; O'Neill, A.; Boland, C.; Lotya, M.; Istrate, O. M.; King, P.; Higgins, T.; Barwich, S.; May, P.; Puczkarski, P.; Ahmed, I.; Moebius, M.; Pettersson, H.; Long, E.; Coelho, J.; O'Brien, S. E.; McGuire, E. K.; Sanchez, B. M.; Duesberg, G. S.; McEvoy, N.; Pennycook, T. J.; Downing, C.; Crossley, A.; Nicolosi, V.; Coleman, J. N. Scalable production of large quantities of defect-free few-layer graphene by shear exfoliation in liquids. *Nature Materials*, **2014**, 13, 624–630.
[101] Coleman, J. N.; Lotya, M.; O'Neill, A.; Bergin, S. D.; King, P. J.; Khan, U.; Young, K.; Gaucher, A.; De, S.; Smith, R. J.; Shvets, I. V.; Arora, S. K.; Stanton, G.; Kim, H.-Y.; Lee, K.; Kim, G. T.; Duesberg, G. S.; Hallam, T.; Boland, J. J.; Wang, J. J.; Donegan, J. F.; Grunlan, J. C.; Moriarty, G.; Shmeliov, A.; Nicholls, R. J.; Perkins, J. M.; Grieveson, E. M.; Theuwissen,

K.; McComb, D. W.; Nellist, P. D.; Nicolosi, V. Two-dimensional nanosheets produced by liquid exfoliation of layered materials. *Science*, **2011**, 331, 568-571.
[102] Halim, U.; Zheng, C. R.; Chen, Y.; Lin, Z.; Jiang, S.; Cheng, R.; Huang, Y.; Duan, X. A rational design of cosolvent exfoliation of layered materials by directly probing liquid–solid interaction. *Nature Commun.*, **2013**, 4, 2213-2020.
[103] Lotya, M.; Hernandez, Y.; King, P. J.; Smith, R. J.; Nicolosi, V.; Karlsson, L. S.; Blighe, F. M.; De, S.; Zhiming, W.; McGovern, I. T.; Duesberg, G. S.; Coleman, J. N. Liquid phase production of graphene by exfoliation of graphite in surfactant/water solutions. *J. Am. Chem. Soc*., **2009**, 131, 3611-3620.
[104] Bourlinos, A. B.; Georgakilas, V.; Zboril, R.; Steriotis, T. A.; Stubos, A. K.; Trapalis, C. Aqueous-phase exfoliation of graphite in the presence of polyvinylpyrrolidone for the production of water-soluble graphenes. *Solid State Communications*, **2009**, 149, 2172-2176.
[105] Caridad, B.; Paredes, J. I.; Pérez-Vidal, O.; Villar-Rodil, S.; Pagán, A.; Cenis, J. L.; Martínez-Alonso, A.; Tascón, J. M. D. A biosupramolecular approach to graphene: Complementary nucleotide-nucleobase combinations as enhanced stabilizers towards aqueous-phase exfoliation and functional graphene-nucleotide hydrogels. *Carbon*, **2018**, 129, 321-334.
[106] Shahil, K. M. F.; Balandin, A. A. Graphene-multilayer graphene nanocomposites as highly efficient thermal interface materials. *Nano Letters*, **2012**, 12, 861-867.
[107] Bissett, M. A.; Kinloch, I. A.; Dryfe, R. A. W. Characterization of MoS_2-Graphene Composites for High-Performance Coin Cell Supercapacitors. *ACS Appl. Mater. Interfaces*, **2015**, 7, 17388-17398.
[108] Kelly, A. G.; Hallam, T.; Backes, C.; Harvey, A.; Esmaeily, A. S.; Godwin, I.; Coelho, J.; Nicolosi, V.; Lauth, J.; Kulkarni, A.; Kinge, S.; Siebbeles, L. D. A.; Duesberg, G. S.; Coleman, J. N. All-printed thin-film transistors from networks of liquid-exfoliated nanosheets. *Science*, **2017**, 356, 69–73.
[109] Dreyer, D.R.; Park, S.; Bielawski, C.W.; Ruoff, R.S. The chemistry of graphene oxide. *Chem. Soc. Rev*., **2010**, 39, 228-240.
[110] Zhu, Y.; Murali, S.; Cai, W.; Li, X.; Suk, J.W.; Potts, J.R.; Ruoff, R.S. Graphene and Graphene Oxide: Synthesis, Properties, and Applications. *Adv. Mater*., **2010**, 22, 3906-3924.
[111] Paredes, J. I.; Villar-Rodil, S.; Martínez-Alonso, A.; Tascón, J. M. D. Graphene oxide dispersions in organic solvents. *Langmuir*, **2008**, 24, 10560-10564.
[112] Rozada, R.; Paredes, J. I.; López, M. J.; Villar-Rodil, S.; Cabria, I.; Alonso, J. A.; Martínez-Alonso, A.; Tascón, J. M. D. From graphene oxide to pristine graphene: Revealing the inner workings of the full structural restoration. *Nanoscale*, **2015**, 7, 2374-2390.
[113] Stankovich, S.; Dikin, D.A.; Piner, R.D.; Kohlhaas, K.A.; Kleinhammes, A.; Jia, Y.; Wu, Y.; Nguyen, S.T.; Ruoff, R.S. Synthesis of graphene-based nanosheets via chemical reduction of exfoliated graphite oxide. *Carbon*, **2007**, 45, 1558-1565.
[114] Fernández-Merino, M.J.; Guardia, L.; Paredes, J.I.; Villar-Rodil, S.; Solís-Fernández, P.; Martínez-Alonso, A.; Tascón, J.M.D. Vitamin C Is an Ideal Substitute for Hydrazine in the Reduction of Graphene Oxide Suspensions. *J. Phys. Chem. C*, **2010**, 114, 6426-6432.
[115] Pham, V.H.; Pham, H.D.; Dang, T.T.; Hur, S.H.; Kim, E.J.; Kong, B.S.; Kim, S.; Chung, J.S. Chemical reduction of an aqueous suspension of graphene oxide by nascent hydrogen. *J. Mater. Chem.*, **2012**, 22, 10530-10536.
[116] Aunkor, M.T.H.; Mahbubul, I.M.; Saidur, R.; Metselaar, H.S.C. The green reduction of graphene oxide. *RSC Adv*., **2016**, 6, 27807–27828.

[117] Acik, M.; Lee, G.; Mattevi, C.; Pirkle, A.; Wallace, R.M.; Chhowalla, M.; Cho, K.; Chabal, Y. The Role of Oxygen during Thermal Reduction of Graphene Oxide Studied by Infrared Absorption Spectroscopy. *J. Phys. Chem. C*, **2011**, 115, 19761-19781.
[118] Guo, H.-L.; Wang, X.-F.; Qian, Q.-Y.; Wang, F.-B.; Xia, X.-H. A Green Approach to the Synthesis of Graphene Nanosheets. *ACS Nano*, **2009**, 3, 2653-2659.
[119] Guardia, L.; Villar-Rodil, S.; Paredes, J.I.; Rozada, R.; Martínez-Alonso, A.; Tascón, J.M.D. UV light exposure of aqueous graphene oxide suspensions to promote their direct reduction, formation of graphene–metal nanoparticle hybrids and dye degradation. *Carbon*, **2012**, 50, 1014-1024.
[120] Huang, X.; Qi, X.; Boey, F.; Zhang, H. Graphene-based composites. *Chemical Society Reviews*, **2012**, 41, 666-686.
[121] Huang, X.; Yin, Z.; Wu, S.; Qi, X.; He, Q.; Zhang, Q.; Yan, Q.; Boey, F.; Zhang, H. Graphene-based materials: Synthesis, characterization, properties, and applications. *Small*, **2011**, 7, 1876-1902.
[122] Nicolosi, V.; Chhowalla, M.; Kanatzidis, M. G.; Strano, M. S.; Coleman, J. N. Liquid Exfoliation of Layered Materials. *Science*, **2013**, 340, 1226419.
[123] Joensen, P.; Frindt, R. F.; Morrison, S. R. Single-layer MoS2. *Materials Research Bulletin*, **1986**, 21, 457-461.
[124] Acerce, M., Voiry, D., Chhowalla, M. Metallic 1T phase MoS2 nanosheets as supercapacitor electrode materials. *Nature Nanotechnology*, **2015**, 10, 313-318.
[125] Lukowski, M.A., Daniel, A.S., Meng, F., Forticaux, A., Li, L., Jin, S. Enhanced hydrogen evolution catalysis from chemically exfoliated metallic MoS2 nanosheets. *J. Am. Chem. Soc*., **2013**, 135, 10274-10277.
[126] Chou, S. S.; De, M.; Kim, J.; Byun, S.; Dykstra, C.; Yu, J.; Huang, J.; Dravid, V. P. Ligand conjugation of chemically exfoliated MoS_2. *J. Am. Chem. Soc.*, **2013**, 135, 4584−4587.
[127] Guardia, L.; Paredes, J. I.; Munuera, J. M.; Villar-Rodil, S.; Ayán-Varela, M.; Martínez-Alonso, A.; Tascón, J. M. D. Chemically exfoliated MoS_2 nanosheets as an efficient catalyst for reduction reactions in the aqueous phase. *ACS Appl. Mater. Interfaces*, **2014**, 6, 21702-21710.
[128] Abdelkader, A. M.; Cooper, A. J.; Dryfe, R. A. W.; Kinloch, I A. How to get between the sheets: a review of recent works on the electrochemical exfoliation of graphene materials from bulk graphite. *Nanoscale*, **2015**, 7, 6944-6956.
[129] Yang, S.; Lohe, M. R.; Müllen, K.; Feng, X. New-generation graphene from electrochemical approaches: production and applications. *Adv. Mater.*, **2016**, 28, 6213–6221.
[130] Low, C. T. J.; Walsh, F. C.; Chakrabarti, M. H.; Hashim, M. A.; Hussain, M. A. Electrochemical approaches to the production of graphene flakes and their potential applications. *Carbon*, **2013**, 54, 1-21.
[131] Wang, J.; Manga, K. K.; Bao, Q.; Loh, K. P. High-yield synthesis of few-layer graphene flakes through electrochemical expansion of graphite in propylene carbonate electrolyte. *J. Am. Chem. Soc.*, **2011**, 133, 23, 8888-8891.
[132] Cooper, A. J.; Velický, M.; Kinloch, I. A.; Dryfe, R. A. W. On the controlled electrochemical preparation of R4N+ graphite intercalation compounds and their host structural deformation effects. *Journal of Electroanalytical Chemistry*, **2014**, 730, 34-40.
[133] Cooper, A. J.; Wilson, N. R.; Kinloch, I. A.; Dryfe, R. A. W. Single stage electrochemical exfoliation method for the production of few-layer graphene via intercalation of tetraalkylammonium cations. *Carbon*, **2014**, 66, 340-350.
[134] Yang, Y.; Lu, F.; Zhou, Z.; Song, W.; Chen, Q.; Ji, X. Electrochemically cathodic exfoliation of graphene sheets in room temperature ionic liquids N-butyl, methylpyrrolidinium

bis(trifluoromethylsulfonyl)imide and their electrochemical properties. *Electrochimica Acta*, **2013**, 113, 9–16.

[135] Parvez, K.; Li, R.; Puniredd, S. R.; Hernandez, Y.; Hinkel, F.; Wang, S.; Feng, X.; Müllen, K. Electrochemically exfoliated graphene as solution-processable, highly conductive electrodes for organic electronics. *ACS Nano*, **2013**, 7, 3598–3606.

[136] Liu, J. L.; Yang, H. P.; Zhen, S. G.; Poh, C. K.; Chaurasia, A.; Luo, J. S.; Wu, X. Y.; Yeow, E. K. L.; Sahoo, N. G.; Lin, J. Y.; Shen, Z. X. A green approach to the synthesis of high-quality graphene oxide flakes via electrochemical exfoliation of pencil core. *RSC Adv.*, **2013**, 3, 11745-11750.

[137] Parvez, K.; Wu, Z.-S.; Li, R.; Liu, X.; Graf, R.; Feng, X.; Müllen, K. Exfoliation of graphite into graphene in aqueous solutions of inorganic salts. *J. Am. Chem. Soc.*, **2014**, 136, 6083−6091.

[138] Alanyalıoğlu, M.; Segura, J. J.; Oró-Solè, J.; Casañ-Pastor, N. The synthesis of graphene sheets with controlled thickness and order using surfactant-assisted electrochemical processes. *Carbon*, **2012**, 50, 142-152.

[139] Liu, N.; Luo, F.; Wu, H.; Liu, Y.; Zhang, C.; Chen, J. One-step ionic-liquid-assisted electrochemical synthesis of ionic-liquid-functionalized graphene sheets directly from graphite. *Adv. Funct. Mater.*, **2008**, 18, 1518–1525.

[140] Paredes, J. I.; Munuera, J. M. Recent advances and energy-related applications of high quality/chemically doped graphenes obtained by electrochemical exfoliation methods. *J. Mater. Chem. A*, **2017**, 5, 7228-7242.

[141] Chen, C.-H.; Yang, S.-W.; Chuang, M.-C.; Woon, W.-Y.; Su, C.-Y. Towards the continuous production of high crystallinity graphene via electrochemical exfoliation with molecular in situ encapsulation. *Nanoscale*, **2015**, 7, 15362-15373.

[142] Yang, S.; Brüller, S.; Wu, Z.-S.; Liu, Z.; Parvez, K.; Dong, R.; Richard, F.; Samorì, P.; Feng, X.; Müllen, K. Organic Radical-Assisted Electrochemical Exfoliation for the Scalable Production of High-Quality Graphene. *J. Am. Chem. Soc.*, **2015**, 137, 13927-13932.

[143] Kurys, Y. I.; Ustavytska, O. O.; Koshechkoa, V. G.; Pokhodenko, V. D. Structure and electrochemical properties of multilayer graphene prepared by electrochemical exfoliation of graphite in the presence of benzoate ions. *RSC Adv.*, **2016**, 6, 36050-36057.

[144] Yang, Y.; Shi, W.; Zhang, R.; Luan, C.; Zeng, Q.; Wang, C.; Li, S.; Huang, Z.; Liao H.; Ji, X. Electrochemical exfoliation of graphite into nitrogen-doped graphene in glycine solution and its energy storage properties. *Electrochim. Acta*, **2016**, 204, 100–107.

[145] Parveen, N.; Ansari, M. O.; Ansari, S. A.; Cho, M.H. Simultaneous sulfur doping and exfoliation of graphene from graphite using an electrochemical method for supercapacitor electrode materials. *J. Mater. Chem. A*, **2016**, 4, 233–240.

[146] Parvez, K.; Rincón, R. A.; Weber, N.-E.; Cha, K. C.; Venkataraman, S. S. One-step electrochemical synthesis of nitrogen and sulfur co-doped, high-quality graphene oxide. *Chem. Commun.*, **2016**, 52, 5714–5717.

1. INTRODUCCIÓN

2. Objetivos y planteamiento de la memoria

2.1 Objetivos

Como se ha descrito en el capítulo previo, los materiales 2D poseen un gran interés científico en términos de sus propiedades y aplicaciones, pero actualmente su uso está severamente limitado fuera del ámbito de la investigación. Esta limitación se debe en gran parte a la falta de métodos de preparación escalables y que permitan obtener materiales 2D de alta calidad y en grandes cantidades de manera asequible. En este sentido, la preparación de dispersiones de materiales 2D en fase líquida por vías como la exfoliación electroquímica permiten cumplir en gran medida estas premisas, por lo que su estudio permitirá avanzar no solo en el conocimiento *per se*, sino en la implementación del material en aplicaciones prácticas. Por otra parte, el estudio de la activación y funcionalización de materiales por vía química y térmica constituye una manera viable de mejorar sus propiedades con vistas a su implementación en aplicaciones.

Como objetivo general de esta tesis se ha planteado el desarrollo de metodologías de preparación y funcionalización de materiales 2D,concretamente grafeno, MoS_2 y Co_3O_4, así como su caracterización y el estudio de algunas aplicaciones potenciales. Los objetivos específicos son los siguientes:

- Estudio de la exfoliación de grafeno por vía electroquímica, con las siguientes variables:
    - Tipo de grafito de partida.
    - Uso de electrolitos que posean funcionalidades adicionales al efecto exfoliante.
    - Pretratamiento del grafito de partida.
    - Uso de aditivos de electrolito que permitan limitar el grado de oxidación del grafito resultante.
- Estudio de la funcionalización covalente de MoS_2 2D preparado mediante exfoliación química por intercalación de litio.
- Desarrollo de metodologías directas de preparación de Co_3O_4 2D activado.
- Caracterización de los materiales obtenidos.
- Ensayo en aplicaciones de almacenamiento de energía (grafeno y Co_3O_4), catálisis (grafeno, MoS_2 y Co_3O_4), eliminación de contaminantes del agua (grafeno y Co_3O_4) y estudios de biocompatibilidad (grafeno y MoS_2).

2.2 Organización de la memoria

En el primer capítulo de esta tesis (introducción) se describen de forma general los materiales 2D y de forma más detallada aquellos en los que se ha trabajado, es decir, grafeno, MoS_2 y Co_3O_4, así como los métodos de preparación de estos materiales. En el presente capítulo se describen los objetivos y la organización de la memoria. En el tercer capítulo se recogen los métodos de preparación y caracterización de los materiales empleados en la tesis. El cuarto capítulo contiene una recopilación de los fundamentos y aplicaciones de las técnicas de caracterización empleadas. En el quinto capítulo se recopilan los resultados de la tesis en forma de los artículos publicados y enviados, precedidos en cada bloque de resúmenes detallados para cada artículo. La tabla mostrada a continuación recoge los artículos publicados y enviados a revistas, junto al nombre de las mismas, su índice de impacto (ISI JCR 2017) y valor de CiteScore de Scopus 2017, así como su posición frente al número total de revistas y el área de publicación relevante en ambas bases de datos. Las publicaciones se han agrupado en tres bloques, coincidiendo con los tres materiales estudiados. Un bloque de grafeno con seis artículos, y otros dos bloques para MoS_2 y Co_3O_4, con un artículo cada uno. Las conclusiones de esta tesis están descritas en el capítulo sexto, y se ha incluido un anexo que recoge las publicaciones relacionadas que no pertenecen a la tesis, así como una compilación de las comunicaciones a congresos.

Título	**Revista**	**Índice de impacto**	**Posición/ nº de revistas total**	**CiteScore**	**Posición/ nº de revistas total**	**Áreas**
High quality, low oxygen content and biocompatible graphene nanosheets obtained by anodic exfoliation of different graphite types	Carbon	7.082	32/285	7.42	25/371	Materials Science, General Chemistry
Electrolytic exfoliation of graphite in water with multifunctional electrolytes: en route towards high quality, oxide-free graphene flakes	Nanoscale	7.233	30/285	7.17	37/439	Materials Science, General Materials Science
A simple strategy to improve the yield of graphene nanosheets in the anodic exfoliation of graphite foil	Carbon	7.082	32/285	7.42	25/371	Materials Science, General Chemistry
Electrochemical Exfoliation of Graphite in Aqueous Sodium Halide Electrolytes toward Low Oxygen Content Graphene for	ACS Applied Materials & Interfaces	8.097	26/285	8.69	24/439	Materials Science, General Materials Science

Energy and Environmental Applications						
High quality, low-oxidized graphene via anodic exfoliation with table salt as an efficient oxidation-preventing co-electrolyte for water/oil remediation and capacitive energy storage applications	Applied Materials Today	-	-	8.10	28/439	General Materials Science
Impact of covalent functionalization on the aqueous processability, catalytic activity, and biocompatibility of chemically exfoliated MoS2 nanosheets	ACS Applied Materials & Interfaces	8.097	26/285	8.69	24/439	Materials Science, General Materials Science
A direct route to activated two-dimensional cobalt oxide nanosheets for electrochemical energy storage, catalytic and environmental applications	Journal of Colloid and Interface Science	5.091	33/147	5.93	9/116	Chemistry, Surfaces

2. OBJETIVOS Y PLANTEAMIENTO DE LA MEMORIA

3. Materiales y métodos

3.1 Grafeno

3.1.1 Exfoliación electroquímica con electrolito de sulfato de potasio

Se ha preparado grafeno mediante exfoliación electroquímica. El método consiste en utilizar grafito como ánodo en una celda electroquímica, usando platino como cátodo y disoluciones acuosas de sales como electrolito. En el caso de grafito en polvo (grado 2910, Mersen) y en copos (Ref. 332461, Sigma–Aldrich) se compactan 500 mg en forma de pastilla de 12 mm de diámetro a una presión de 1 tonelada, y se perfora un agujero en la misma por el que se introduce un hilo de platino que se conecta a la fuente de corriente como ánodo. En el caso de HOPG (grado ZYH, Advanced Ceramics) o grafito flexible (Papyex I980, Mersen), la pieza se conecta directamente a la fuente de corriente mediante una pinza. El cátodo es un hilo de platino que se conecta mediante una pinza a la fuente (Agilent 6614C). Se pesan 1.394 g de sulfato de potasio (Ref. P0072, Sigma Aldrich) y se disuelven en 80 mL de agua milli-Q. Se sumergen los electrodos en la disolución acuosa separados a una distancia de ~2 cm uno de otro y se aplica un potencial de 10 V con una corriente máxima de 0.5 A durante un tiempo fijado de 3, 15 o 60 minutos. Durante este tiempo se desprenden del ánodo partículas de grafito expandido. El grafito expandido se filtra y lava con abundante agua, y a continuación se seca a vacío y temperatura ambiente durante 18 horas, si se va a utilizar sin procesar.

Para preparar dispersiones de grafeno a partir del material tratado electroquímicamente, se toma el producto lavado y se sonica durante 3 h en baño de ultrasonidos (JP Selecta Ultrasons system, 40 KHz, 20 W L^{-1}) en una disolución de sal sódica de riboflavina 5′-monofosfato (pureza de 73-79%, Sigma Aldrich, F6750) a 1 mg mL^{-1} o en N, N-dimetilformamida (Ref. 103053, Merck). A continuación, para descartar el material sin exfoliar se centrifuga a 200 g durante 20 min (Eppendorf 5424). Si se ha dispersado el material en sal de riboflavina se hacen dos ciclos de centrifugado a 20000 g durante 20 min y redispersión en agua milli-Q para eliminar el exceso de dicha sal.

La concentración de grafeno en dispersión se determina mediante espectroscopía UV-Vis usando la ley de Lambert-Beer, $A/l = \alpha C$, donde A es la absorbancia medida a

660 nm para la dispersión de grafeno, l es el paso óptico, α es el coeficiente de extinción a esa longitud de onda (2440 mL mg^{-1} m^{-1}) y C es la concentración de grafeno.

3.1.2 Exfoliación electroquímica con electrolitos de sulfonatos aromáticos

El procedimiento para la exfoliación electroquímica con sulfonatos aromáticos sigue el proceso general descrito en el apartado anterior con las siguientes particularidades. Se utiliza una pieza de grafito flexible de 35×25×0.5 mm^3 como ánodo y un hilo de platino como cátodo. Los electrodos se sumergen en 20 mL de disolución del sulfonato (Sigma Aldrich) en agua milli-Q a una concentración entre 0.001 y 0.2 M y se aplica un voltaje de 10 V durante 1 h. El material expandido se sonica en la propia disolución durante 3 h, se centrifuga dos veces a 20000 g durante 20 min redispersando en agua milli-Q, y por último se centrifuga a 200 g durante 20 min, recuperando el sobrenadante.

3.1.3 Pretratamiento con ácido sulfúrico

Con el objetivo de aumentar el rendimiento de la exfoliación anódica, se realiza un pretratamiento consistente en sumergir una pieza de grafito flexible (55×30×0.5 mm^3) en ácido sulfúrico (95-98%, Sigma Aldrich) durante tiempos de 1 a 72 h. A continuación se lleva a cabo la exfoliación de la misma manera a la descrita en el apartado 3.1.1. El material expandido resultante se sonica en una mezcla de agua y 2-propanol 65/35 % en volumen durante 3 h y se dializa durante 72 h. A continuación, se centrifuga como ha sido descrito previamente.

3.1.4 Exfoliación electroquímica con electrolitos de halogenuros

La exfoliación electroquímica con halogenuros de sodio sigue el mismo procedimiento general que el seguido para el sulfato de potasio. Se utilizan piezas de grafito flexible de 35×25×0.5 mm^3 como ánodo y una lámina de platino (cuadrada, 25 mm de lado) como cátodo, y ambos electrodos se sumergen en disoluciones 0.01 a 1.0 M de NaCl, NaBr y NaI (Sigma Aldrich). Los materiales expandidos se lavan con abundante agua y etanol y se sonican y centrifugan como está descrito en el apartado 3.1.1.

3.1.5 Exfoliación electroquímica con aditivos de electrolito de carácter antioxidante

Con objeto de impedir la oxidación del grafeno durante la exfoliación electroquímica, se lleva a cabo el proceso descrito en 3.1.1, utilizando sulfato de sodio 0.1 M y añadiendo especies antioxidantes (etanol, cloruro de potasio, cloruro, bromuro, yoduro, citrato, ascorbato, sulfito y borohidruro de sodio) en concentraciones de 0.01 a 0.70 M.

3.2 Disulfuro de molibdeno

3.2.1 Exfoliación química

En caja seca bajo atmósfera de argón, se añaden 3 mL de *n*-butil-litio (1.6 M en hexano, Sigma Aldrich, 186171) a 300 mg de MoS_2 en polvo (Sigma Aldrich, 69860). Se deja reaccionar durante 48 h, se filtra y lava con 60 mL de hexano (pureza 95%, Sigma Aldrich, 296090). Se extrae el producto de la caja seca y se sumerge inmediatamente en agua Milli-Q. Se sonica en baño de ultrasonidos durante 1 h para obtener una dispersión de MoS_2 exfoliado químicamente (ce-MoS_2). La dispersión se dializa durante 48 h para eliminar restos de litio e impurezas presentes. Para determinar la concentración del ce-MoS_2 se utiliza espectroscpía UV-Vis, midiendo la absorbancia a 450nm y utilizando un coeficiente de extinción de 5045 m^{-1} g^{-1} L para aplicar la ley de Lambert-Beer.

3.2.2 Funcionalización con grupos de ácido acético

Para funcionalizar el ce-MoS_2, se añade ácido yodoacético (1.1 mmol) a 40 mL de una dispersión ácida (pH ~4) de ce-MoS_2 a 0.44 mg mL^{-1}, que se mantiene con agitación a temperatura ambiente durante 5 días. A continuación la dispersión se lava con isopropanol, etanol y agua mediante ciclos de centrifugación a 1743g durante 30 min y redispersión (3 ciclos para cada disolvente). La dispersión resultante se dializa durante 72 h para eliminar las impurezas restantes, obteniéndose ce-MoS_2 funcionalizado (f-MoS_2)

3.3 Óxido de cobalto

3.3.1 Síntesis de Co_3O_4

Para sintetizar el óxido amorfo precursor CoO, se disuelven 200 mg del copolímero tribloque Pluronic 123 (Sigma Aldrich) en 14 mL de agua/etanol (33/2 v/v) con agitación. A esta mezcla se le añaden a continuación 125 mg de acetato de cobalto (II) tetrahidrato (Sigma Aldrich) y 70 mg de hexametilentetraamina (Sigma Aldrich). Se agita la mezcla durante 15 minutos, para después añadir 13 mL de etilenglicol y agitar durante otros 30 minutos. Se deja reposar durante 24 h la mezcla y a continuación se calienta en autoclave de teflón a 170 ºC durante 2 h. El sólido verde resultante se lava mediante ciclos de 2000 g durante 20 min y redispersión en agua y etanol (3 ciclos cada disolvente), para después secar a vacío y temperatura ambiente durante 24 h. Para obtener Co_3O_4, el sólido obtenido previamente se calcina a temperaturas de 250, 350 y 450 ºC durante 2 h.

3.4 Preparación de híbridos de material bidimensional-nanopartículas metálicas

3.4.1 Híbridos de grafeno/surfactante con nanopartículas de platino

Se calientan 9 mL de una dispersión 0.2 mg mL^{-1} de grafeno/surfactante (naftaleno 1,5-disulfonato de sodio o pireno 1,3,6,8-tetrasulfonato de sodio) a 85 ºC y se añade 1 mL de K_2PtCl_4 (99.99%, Sigma Aldrich) 1.1 mM en disolución acuosa. La mezcla se mantiene en agitación a esta temperatura 2 h, y posteriormente se centrifuga a 200 g durante 20 min y se redispersa en agua milli-Q. Se añaden 20 µL de una disolución acuosa de $NaBH_4$ de concentración 1.5 M y se deja a temperatura ambiente sin agitación durante 45 min. A continuación, para purificar los híbridos se realizan dos ciclos de centrifugación a 20000 g durante 20 min y redispersión en agua milli-Q.

3.4.2 Híbridos de f-MoS_2 con nanopartículas de plata

Se mezclan disoluciones acuosas de nitrato de plata 0.5 mM, borohidruro de sodio 22.5 mM y dispersión acuosa de f-MoS_2 0.1 mg mL^{-1}, y se dejan reaccionar sin

agitación durante 2 h. El producto de la reacción se purifica mediante dos ciclos de centrifugado a 20000 g durante 20 min y redispersión en agua milli-Q.

3.5 Preparación de electrodos para caracterización electroquímica

3.5.1 Electrodos de grafeno

Para preparar los electrodos de trabajo de las celdas electroquímicas se utilizó el grafito expandido producido en la exfoliación electroquímica tras un lavado y secado, sin posteriores tratamientos.

En el caso de las medidas con dos electrodos, se toman dos porciones de 7 mg de una pasta de grafito expandido y politetrafluoroetileno (PTFE) en proporción 8 a 1 en masa, y se presionan a 1 tonelada durante 15 segundos, formando discos de ~0.78 cm^2. Los electrodos se desgasifican a 100 ºC durante 4 h y se sumergen en el electrolito (H_2SO_4 1M) durante 24 horas. Los electrodos, separados por una membrana de fibra de vidrio (grado 934-AH, Whatman), se colocan en una celda tipo Swagelok y se conectan al potenciostato (PGZ 402 Voltalab, from Radiometer Analytical) para llevar a cabo la caracterización electroquímica.

Para medidas con tres electrodos, el grafeno se utiliza como electrodo de trabajo tomando 10 mg y prensando (1 tonelada, 15 s) sobre una pieza de grafito flexible de 0.78 cm^2. El contraelectrodo consiste en una mezcla de carbón activado comercial (ACF A20), PTFE y negro de carbono en proporción en peso de 95:5:5. Los electrodos se sumergen en el electrolito (H_2SO_4 1M) durante 24 h, se desgasifican a vacío durante 1 min y se colocan en una celda Swagelok separados por una membrana de fibra de vidrio (grado 934-AH, Whatman). El electrodo de referencia es Ag/AgCl (KCl 3M) y la celda se conecta a un potenciostato Biologic VSP para realizar las medidas.

3.5.2 Electrodos de óxido de cobalto

Las medidas electroquímicas realizadas sobre los óxidos de cobalto se llevan a cabo según el mismo procedimiento descrito para el grafeno en configuración de tres electrodos, con la diferencia de que se deposita un volumen de dispersión (400 μL, 0.5 mg mL^{-1}) sobre el grafito flexible, dejando evaporar 24 h a temperatura ambiente. El

electrolito en este caso es KOH 6M y el electrodo de referencia de Hg/HgO (NaOH 1M).

4. Técnicas de caracterización

4.1 Espectroscopías

La espectroscopía es la disciplina que estudia el intercambio de energía que se produce por interacción de la radiación electromagnética con la materia. Debido a los niveles cuantizados de los estados energéticos de la materia, ésta solo puede absorber o emitir radiación con determinados valores de energía [1], como se expresa en la ecuación de Plank-Einstein:

$$E_{superior} - E_{inferior} = \Delta E = h\nu \quad (1)$$

donde $E_{superior}$ es la energía del estado más alto, $E_{inferior}$, la del estado más bajo, h es la constante de Plank y ν es la frecuencia de la radiación emitida o absorbida. Esa frecuencia de la radiación por tanto corresponde a una diferencia energética característica del material, por lo que esta técnica puede utilizarse para caracterizarlo. Por otra parte, la absorción de radiación de un material a cualquier frecuencia dada se puede relacionar con su concentración en un medio según la ley de Lambert-Beer [2]:

$$A = \varepsilon l c \quad (2)$$

donde A es la absorbancia a una determinada longitud de onda, ε es el coeficiente de extinción molar a esa longitud de onda, l es la longitud de paso óptico y c la concentración. De esta manera, además, la medida de la absorbancia de un material permite cuantificar su concentración siempre y cuando la medida se realice en el rango lineal de aplicación de la ecuación.

4.1.1 Espectroscopía de absorción ultravioleta-visible (UV-vis)

La caracterización mediante absorción UV-vis recogida en esta tesis se ha realizado en un espectrofotómetro dispersivo de doble haz Helios α (Thermo Spectronic). La Figura 11 muestra el esquema de funcionamiento del equipo. Se mide al mismo tiempo el haz que atraviesa la referencia (P_0) y el haz que atraviesa la muestra (P), lo que permite calcular la absorbancia, que viene dada por la ecuación $A=-log\ (P/P_0)$. Las medidas de absorbancia de dispersiones coloidales se realizan diluyendo las

dispersiones hasta el rango lineal de la ecuación de Lambert-Beer, sin ninguna otra preparación.

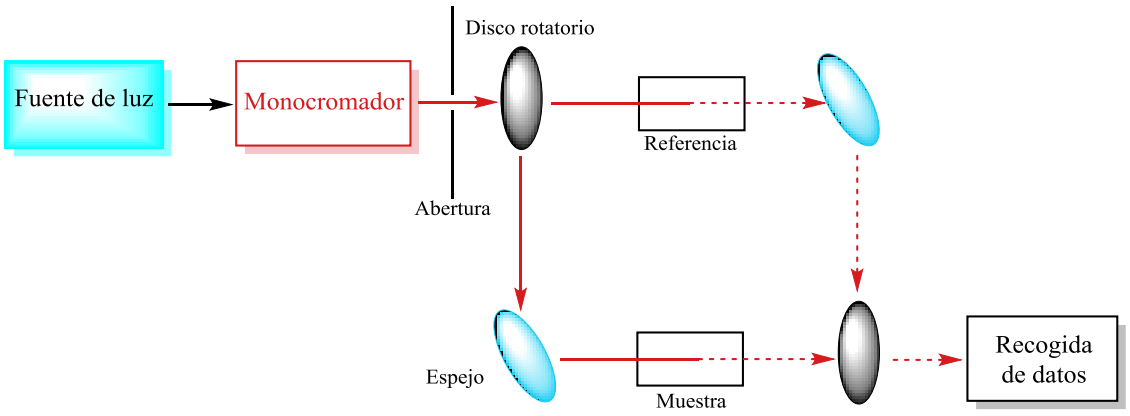

Figura 11. Esquema de funcionamiento de un espectrofotómetro UV-vis de doble haz.

En este tipo de equipos se mide típicamente la absorbancia de radiación con logitudes de onda entre 200 y 1100 nm, lo que corresponde a energías entre ~1 y 6 eV. Estas energías son propias de transiciones entre niveles energéticos poco separados, como son orbitales moleculares tipo π insaturados, pares de electrones no enlazantes u orbitales *d* y *f* en los casos de metales de transición y transición interna respectivamente [3].

Estos niveles energéticos no son estados únicos, sino que a su vez incorporan estados vibracionales y rotacionales asociados. De esta manera, para cada transición no existe un único salto energético entre niveles sino que los diferentes estados vibracionales y rotacionales permiten diferentes transiciones. La consecuencia inmediata de esto es que los espectros de absorción de las especies que poseen niveles vibracionales y rotacionales no tienen longitudes de onda perfectamente definidas (bandas tipo función delta), sino bandas ensanchadas debido a las diferentes combinaciones de transiciones [4]. Por otra parte, la interacción de los materiales con el medio, por ejemplo el disolvente en fase líquida, contribuye también a ensanchar la señal debido a los cambios que introducen en los niveles energéticos [1,5]. Estos hechos provocan que la técnica tenga una resolución limitada y que el espectro de UV-Vis por sí solo sea insuficiente para identificar unívocamente una sustancia. No obstante, esta técnica es ampliamente utilizada y permite detectar la presencia de ciertos grupos funcionales [6,7], complejos organometálicos [8,9] o nanoestructuras [10,11], a partir de la forma y posición de las bandas del espectro de absorción. En esta tesis, los espectros

de absorción UV-Vis de materiales bidimensionales en dispersión coloidal se han utilizado para determinar de forma cualitativa:

- La efectividad del proceso de purificación de grafenos dispersos con surfactantes. Al utilizar especies anfifílicas como agentes dispersantes del grafeno, es necesario efectuar un paso de purificación después de la preparación para eliminar el exceso de dichas sustancias. Este paso se lleva a cabo mediante diálisis o ciclos de centrifugado y redispersión, y puede monitorizarse mediante UV-Vis, ya que los surfactantes muestran en muchos casos bandas de absorción en la zona UV del espectro (~200-400 nm). Esto se observa en la Figura 12a, donde están representados espectros antes y después del proceso de purificación.

- La formación de nanopartículas de plata sobre la superficie de láminas de MoS_2. En nanopartículas metálicas puede darse el fenómeno de resonancia plasmónica superficial, cuando la frecuencia de una radiación incidente coincide con la frecuencia de oscilación colectiva de los electrones en el material. Esta frecuencia viene determinada por el tamaño y forma de las nanopartículas y en el caso de nanopartículas de plata sobre MoS_2 se pudo comprobar su formación al aparecer una banda a ~400 nm asociada al plasmón superficial.

- El cambio de fase 2H a 1T y viceversa en dispersiones de MoS_2 exfoliado por intercalación de litio. Estas dos fases implican diferentes coordinaciones de los átomos de azufre alrededor del molibdeno en la estructura (trigonal prismática en 2H y octaédrica en 1T). Estas diferentes coordinaciones tienen diferente simetría, lo que origina diferentes niveles energéticos para cada estructura, y particularmente un mayor número de transiciones posibles en la estructura menos simétrica (2H) [12] La Figura 12b muestra espectros UV-Vis de dispersiones en fase 1T y 2H.

- La formación de óxido de cobalto (II) mediante un proceso solvotérmico. Las especies $Co(OH)_2$, CoO y Co_3O_4 presentan bandas de absorción a diferentes longitudes de onda en el espectro visible, que corresponden con sus diferentes colores rosa, verde y negro respectivamente [13].

Esta técnica es también aplicable a la cuantificación de especies absorbentes siempre y cuando el disolvente sea transparente (no absorba radiación) en el rango de medida y la concentración de la especie se encuentre dentro del rango lineal de la ecuación de Lambert-Beer. En esta tesis se ha utilizado la espectroscopía UV-Vis para cuantificar:

- La concentración de grafeno y MoS_2 en dispersión coloidal. Utilizando los coeficientes de extinción molar documentados en la literatura a diferentes longitudes de onda [14,15] y la ecuación de Lambert-Beer, se pudieron calcular las concentraciones de las dispersiones utilizadas.

- Seguimiento de reacciones en las cuales alguno de los reactivos o productos tienen un espectro característico. La reacción de reducción de nitroarenos puede estudiarse mediante esta técnica, ya que los reactivos 4-nitrofenol y 4-nitroanilina tienen bandas de absorción a ~400 y ~380 nm respectivamente, y por tanto la disminución de la absorbancia a esas longitudes de onda permite medir los tiempos de reacción [6].
- La adsorción de colorantes sobre materiales bidimensionales. Dado que los colorantes son moléculas que presentan espectros de absorción con bandas muy intensas en el rango visible, es posible cuantificar con precisión la cantidad adsorbida sobre láminas de grafeno u óxidos de cobalto midiendo la absorbancia de una disolución de colorante antes y después de estar en contacto con el material.

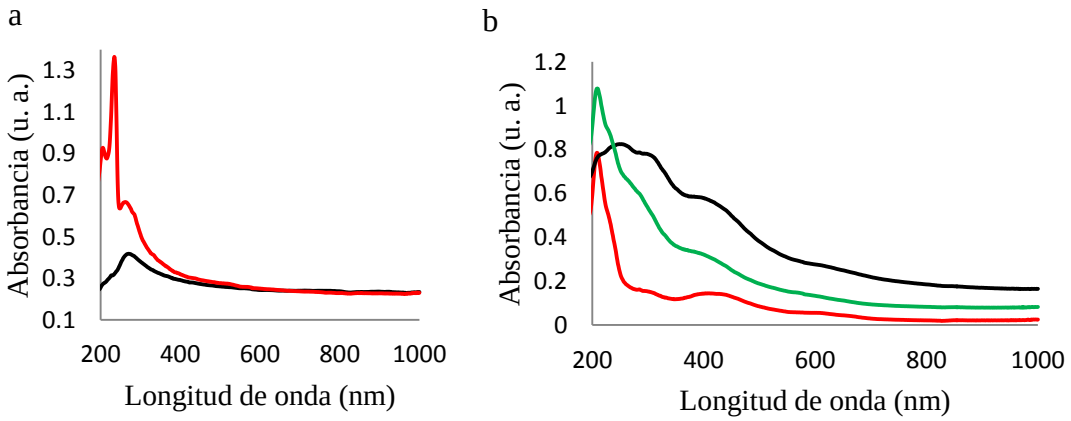

[16].

Figura 12. Espectros de **(a)** grafeno exfoliado con surfactantes anfifílicos antes (rojo) y después (negro) del proceso de lavado y **(b)** MoS2 en fase 1T sin funcionalizar (negro) y funcionalizado (verde) y en fase 2H (rojo)

4.1.2 Espectroscopía infrarroja (IR)

La radiación electromagnética de longitudes de onda entre 2.5 y 25 μm (números de onda entre ~400 y 4000 cm^{-1}) constituye el espectro infrarrojo medio, y su interacción con la materia se corresponde con las transiciones entre estados energéticos vibracionales [1,5]. No todos los modos de vibración son activos en IR sino que, para que la absorción sea permitida por las leyes de la mecánica cuántica, el momento dipolar de la especie debe cambiar con el modo de vibración [1]. La frecuencia

correspondiente a un modo de vibración es tanto mayor cuanto más fuertes son los enlaces implicados y cuanto menor es la masa reducida de los átomos implicados. Por esta razón, los grupos funcionales con enlaces muy polares y aquellos unidos a hidrógeno suelen tener frecuencias de vibración altas y desacopladas de las del resto de la sustancia, apareciendo sus bandas características en el espectro IR en rangos de número de ondas generalmente independientes de la sustancia. De esta manera es posible la identificación de grupos funcionales de un material mediante el espectro de IR medio, aunque debido a la menor resolución y sensibilidad en comparación con la espectroscopía UV-Vis, su cuantificación no suele ser posible.

Para la obtención de medidas de IR, en esta tesis se ha utilizado un espectrómetro infrarrojo de transformada de Fourier (Fourier transform infrared spectroscopy, FTIR) modelo Nicolet 8700 (Thermo Scientific). Las medidas se realizaron en modo de reflexión total atenuada (attennuated total reflectance, ATR). Se utilizaron las medidas de IR para comprobar la presencia de grupos funcionales oxigenados en grafenos exfoliados anódicamente a partir de diferentes materiales grafíticos. Aquellos grafenos más oxidados presentan bandas en la región de ~3000-3500 cm^{-1}, características de los grupos funcionales –OH (Fig. XX).

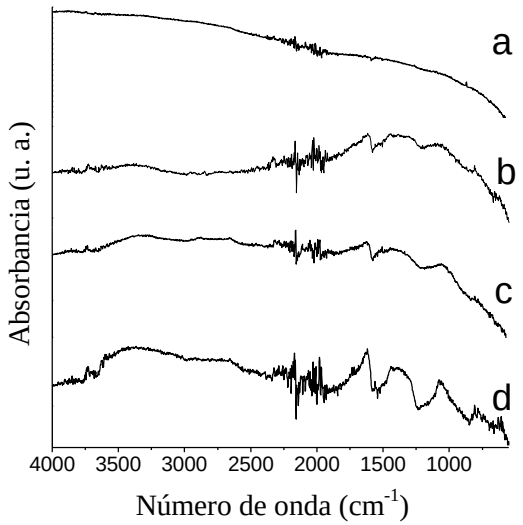

Figura 13. Espectro ATR-FTIR de muestras de grafeno obtenidas a partir de (a) grafito en polvo (3 min de exfoliación), (b) grafito flexible (15 min), (c) grafito flexible (60 min) y (d) HOPG (60 min).

4.1.3 Espectroscopía Raman

La espectroscopía Raman, al igual que la espectroscopía IR, estudia las transiciones entre niveles vibracionales en la materia [1, 5,17]. Sin embargo, mientras que en la segunda se hace incidir radiación del IR medio sobre la muestra y se estudia su absorción, en la espectroscopía Raman la radiación incidente es de mayor energía (habitualmente una fuente láser visible) y se mide la radiación dispersada inelásticamente. Al irradiar una sustancia con radiación electromagnética cuya frecuencia no corresponda con ninguna transición energética, la gran mayoría de los fotones incidentes serán dispersados elásticamente (sin cambio en su frecuencia), lo que constituye la dispersión Rayleigh (Figura 14). Sin embargo, una pequeña fracción de la radiación incidente experimenta dispersión inelástica, el fenómeno de la dispersión Raman. Esta dispersión puede producir fotones de menor energía que la luz incidente (transición Stokes) o, si la población de estados de energía superiores es alta, puede dar lugar a fotones de mayor energía (anti-Stokes). Para que estas transiciones sean permitidas y por tanto se puedan observar, el modo de vibración tiene que provocar un cambio en la polarizabilidad de la sustancia. Por todas estas razones, a pesar de que el rango de energías de los espectros Raman es similar al de IR, la información que contienen es muy distinta. Mientras que el IR aporta información sobre los grupos funcionales presentes en una sustancia, las bandas del espectro Raman se asocian a modos de vibración colectivos de un sólido [17].

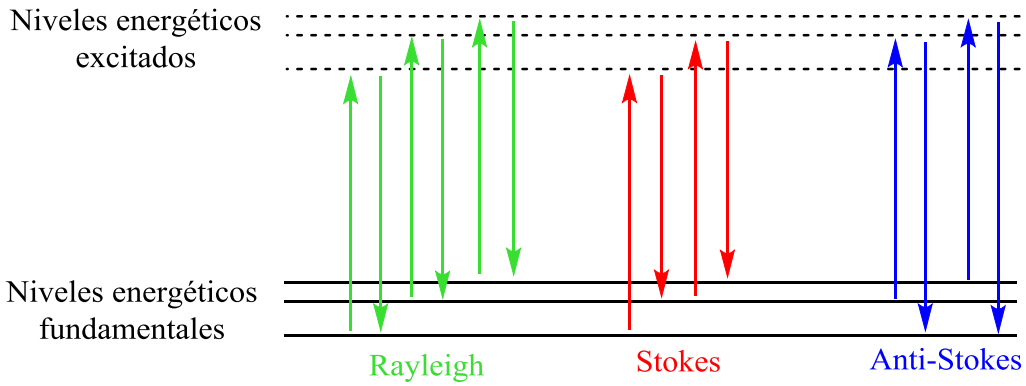

Figura 14. Transiciones entre niveles energéticos que dan lugar a los fenómenos Rayleigh, Stokes y anti-Stokes.

Las medidas de espectroscopía Raman en esta tesis fueron realizadas en un espectrómetro Horiba Jobin-Yvon LabRam con una fuente láser de 532 nm y 2 mW de potencia. Los espectros registrados corresponden a transiciones Stokes, y fueron registrados:

- Como pastilla, en el caso de tratarse de muestras sólidas (grafito, disulfuro de molibdeno, óxidos de cobalto).
- En muestras depositadas a partir de dispersiones, mediante la evaporación del disolvente a 50–60 ºC sobre discos de acero inoxidable, o bien en forma de filmes preparados mediante filtración de las dispersiones.

La espectroscopía Raman se usa rutinariamente para caracterizar las propiedades de materiales carbonosos [18-22] y materiales bidimensionales como el grafeno [21,23] y óxidos metálicos [13]. En el trabajo contenido en esta tesis se ha empleado para:

- Evaluar la calidad estructural de las láminas de grafeno midiendo la relación de intensidades integradas de las bandas denominadas G y D, características de materiales grafíticos, situadas en números de onda ~1582 cm^{-1} y 1348 cm^{-1}, respectivamente. Por ejemplo, en el espectro Raman de grafeno preparado por exfoliación anódica con NaCl, NaBr y NaI como electrolitos (Figura 15a), la relación entre las intensidades de ambas bandas (I_D/I_G) se toma como medida del desorden estructural presente en el material [24-30], tomando en este caso valores entre 0.8 y 1.4, que varían en función del electrolito y su concentración.
- Estudiar la naturaleza amorfa o cristalina de láminas de CoO y Co_3O_4 respectivamente, así como la presencia de defectos. Estos compuestos se sintetizaron por un proceso solvotérmico y posterior calcinación en aire, y el análisis de sus espectros de Raman permitió confirmar que se trataba de esas especies así como descartar la presencia de otras, como el $Co(OH)_2$, debido a las bandas características presentes (Figura 15b).

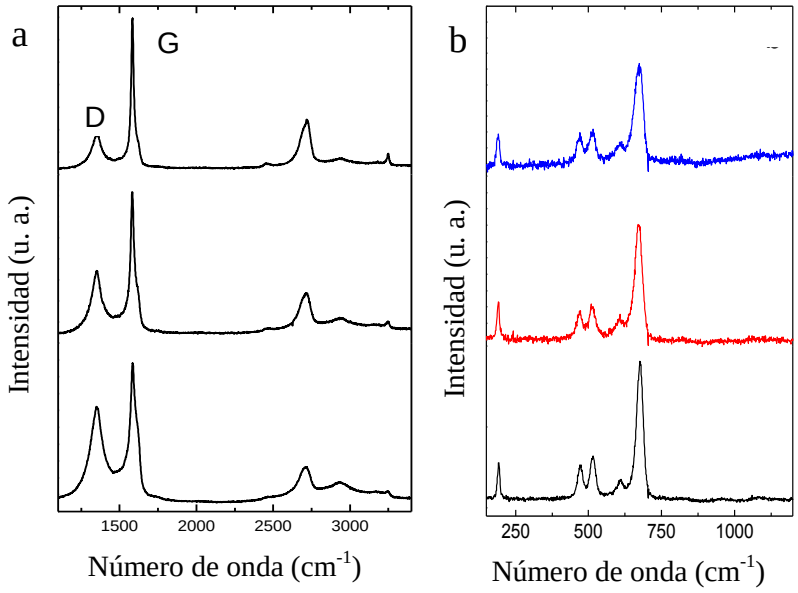

Figura 15. Espectros Raman de (a) grafeno exfoliado con NaCl (superior), NaBr (medio) y NaI (inferior) y (b) Co3O4 preparado a 250 (azul), 350 (rojo) y 450ºC (negro).

4.1.4 Espectroscopía fotoelectrónica de rayos X (XPS)

La espectroscopía fotoelectrónica de rayos X (XPS), a diferencia de los tipos de espectroscopías antes mencionados, estudia las transiciones de electrones desde niveles internos del átomo al continuo de energía, esto es, electrones arrancados del material debido al efecto fotoeléctrico [1,5,31]. Para que tenga lugar este efecto, es necesario irradiar la muestra con fotones de energía superior a la suma de la energía de ligadura del electrón al atómo (binding energy, BE) y la función de trabajo del equipo (Φ, la energía necesaria para llevar el electrón al nivel de Fermi del vacío cercano a la muestra). El resto de la energía correspondiente a la radiación incidente se transfiere al electrón en forma de energía cinética (kinetic energy, KE), de manera que la ecuación de Plank-Einstein se puede escribir en la forma:

$$\Delta E = h\nu = BE + \Phi + KE \qquad (3)$$

En esta espectroscopía se utilizan rayos X que expulsan electrones de capas internas de los átomos de la muestra a analizar y se obtiene su energía de ligadura a través de la medida de su energía cinética. En el espectro XPS se representa la intensidad de la señal (número de electrones emitidos) en función de la energía de ligadura. Solo aquellos electrones procedentes de átomos situados en las capas más

superficiales de la muestra pueden escapar de ésta y ser detectados por el equipo, ya que los generados a mayores profundidades son reabsorbidos por la muestra tras sufrir colisiones inelásticas. Por tanto, los espectros de XPS solamente proporcionan información de la superficie de la muestra, con un espesor de análisis de unos pocos nanómetros. Mediante XPS es posible detectar todos los elementos salvo H y He, por lo que es posible obtener la composición superficial de una muestra. Además, la energía de ligadura de los electrones internos se ve afectada por el entorno químico de los átomos, de modo que también es posible obtener información acerca de los estados de oxidación y los enlaces entre átomos a partir de la forma detallada del espectro correspondiente a cada elemento (espectros de alta resolución).

El equipo en el que se han realizado las medidas de esta tesis es un espectrómetro XPS de marca SPECS que utiliza fuentes de rayos X tanto Al Kα monocromática como Mg Kα no monocromática. El equipo se opera a presiones inferiores a 10^{-7} Pa durante las medidas, y las muestras analizadas fueron preparadas de la misma manera que las utilizadas en análisis Raman. En esta tesis se ha empleado XPS para:

- Estudiar el contenido en oxígeno de los grafenos preparados mediante exfoliación anódica. El proceso provoca la oxidación del material [32], y la proporción entre las señales de oxígeno y carbono se toma como indicador del contenido global en oxígeno. (Figura 16a).
- Confirmar la formación de híbridos de materiales bidimensionales con nanopartículas metálicas (grafeno-Pt, MoS_2-Ag) y comprobar que los metales se encuentran en estado de oxidación 0 [33].
- Calcular la proporción de las fases 2H y 1T en MoS_2 exfoliado químicamente, funcionalizado y tratado térmicamente. Estos tres procesos alteran la fase del material, y mediante el análisis del espectro de alta resolución del Mo 3d es posible estimar la proporción de cada una [12] (Figura 16b).
- Estudiar la composición de óxidos de cobalto antes y después del tratamiento de calcinación, en concreto la proporción entre Co(II) y Co(III) [13].

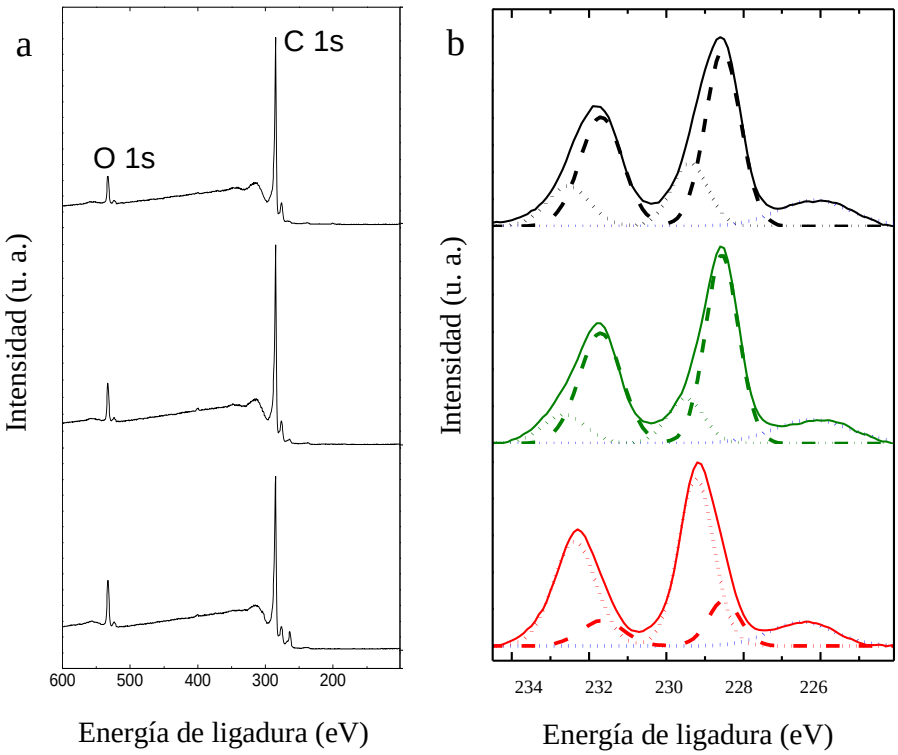

Figura 16. Espectros XPS de **(a)** grafeno exfoliado con NaCl (arriba), NaBr (medio) y NaI (abajo) y **(b)** MoS2 1T (rojo, verde) y 2H (rojo).

4.2 Microscopías

4.2.1 Microscopía electrónica de transmisión (TEM)

Debido a las limitaciones de resolución de la microscopía óptica (resolución del orden de la longitud de onda de la luz visible, ~400 nm), es necesaria una técnica con mayor poder de resolución. Dado que los electrones pueden comportarse de manera similar a fotones cuando son emitidos por un filamento y acelerados por un campo electromagnético (a voltajes de 100-1000 kV), su uso constituye la base de la microscopía electrónica [1]. Si se trabaja con muestras delgadas (espesor menor de 200 nm), los electrones pueden ser transmitidos a su través de forma análoga a lo que ocurre con los fotones en microscopía óptica, lo cual permite obtener imágenes con mucha mayor resolución que dicha técnica. La Figura 17 representa esquemáticamente los componentes de un equipo de microscopía electrónica de transmisión (transmission electron microscopy, TEM). En la parte superior se sitúa la fuente de electrones, y estos

se concentran hacia la muestra por acción de las lentes electromagnéticas. Tras atravesar la muestra, los electrones transmitidos pasan por otro juego de lentes que los dirigen al detector, donde se registran. El equipo utilizado en las medidas para esta tesis es un microscopio JEOL 200 EX-II operado a 160 kV. Para su medida, las muestras se han preparado depositando 40 µL de una mezcla 1:1 de dispersión acuosa y etanol sobre rejillas de cobre recubiertas de un filme delgado de carbono (Electron Microscopy Sciences), dejando evaporar los disolventes a temperatura ambiente.

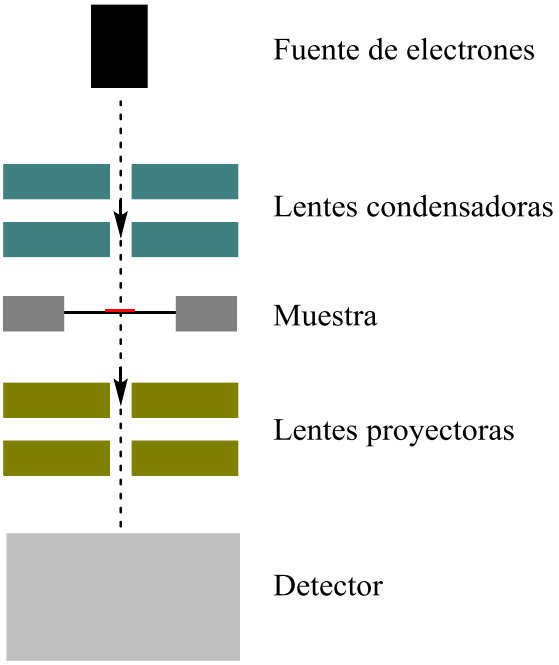

Figura 17. Esquema de los componentes de un microscopio TEM.

En la presente tesis se han analizado mediante TEM láminas de MoS_2, así como los híbridos de grafeno-Pt y MoS_2-Ag. En ambos casos, las imágenes obtenidas permiten observar la morfología de las láminas (delgadas, constituidas por muy pocas capas), así como el tamaño y la distribución de las nanopartículas metálicas depositadas sobre los materiales [33,34]. En la Figura 18 se pueden observar imágenes típicas de estos materiales.

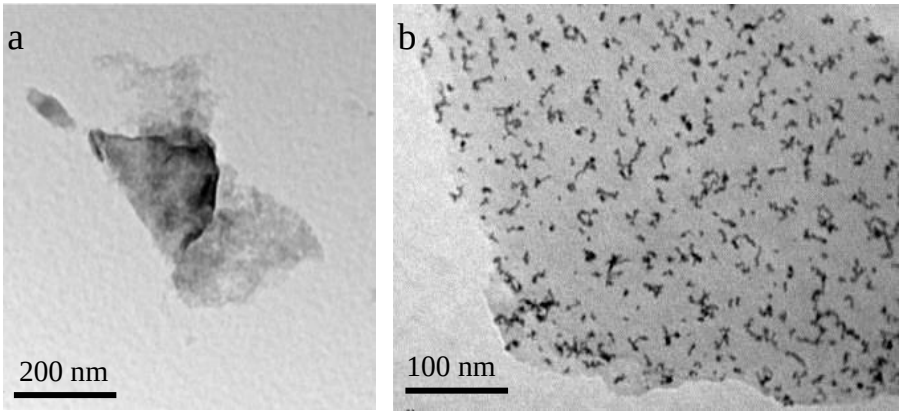

Figura 18. Imágenes TEM de **(a)** MoS2 y **(b)** híbrido grafeno-PtNPs.

4.2.2 Microscopía electrónica de barrido (SEM)

De forma similar a un microscopio TEM, un equipo de microscopía electrónica de barrido (scanning electron microscopy, SEM), utiliza una fuente de electrones (acelerados en este caso por voltajes menores, de ~40 kV) y los concentra mediante lentes electromagnéticas sobre la muestra [1,35] Un esquema de la operación de este equipo se puede ver en la Figura 19a:

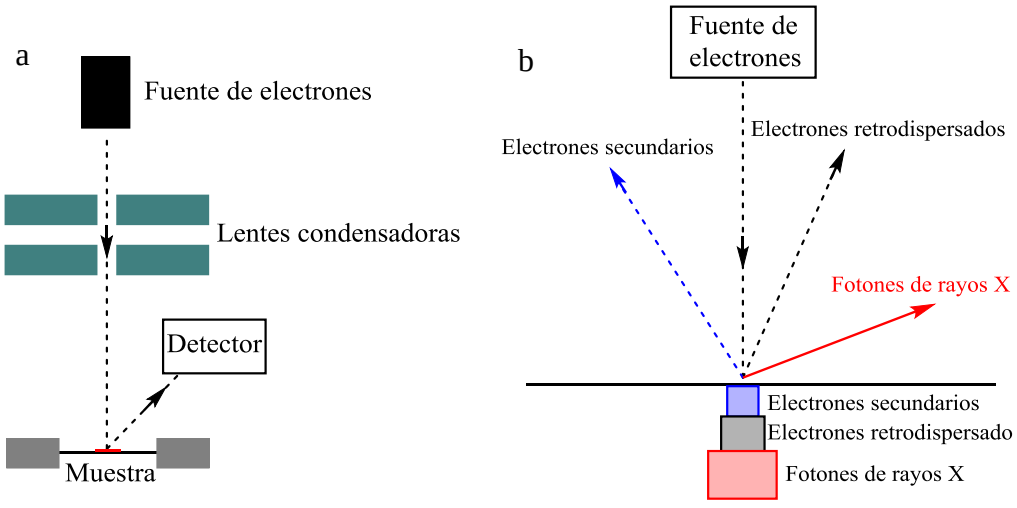

Figura 19. (a) Esquema de un microscopio electrónico de barrido (SEM). **(b)** Diferentes tipos de emisión al hacer incidir un haz de electrones sobre la superficie de la muestra.

Los electrones incidentes sobre la muestra pueden:

- Experimentar choques elásticos, "rebotando" en la superficie de la muestra sin perder energía. Estos son los llamados electrones retrodispersados.
- Interaccionar con los electrones de la banda de conducción, dando lugar a la expulsión de estos últimos. Debido a esta interacción de tipo inelástico la energía de estos electrones, llamados secundarios, es menor que la de los retrodispersados. Como los electrones procedentes de capas internas del sólido pierden energía por choques inelásticos, los que se detectan en este rango de energía son superficiales, razón por la que los electrones secundarios son los que se utilizan habitualmente para obtener imágenes de la superficie de sólidos.
- Expulsar los electrones de capas internas de los átomos de la muestra. Esta interacción provoca estados electrónicos excitados, que se relajan mediante la caída de electrones a niveles internos y la consiguiente emisión de fotones de rayos X. Éstos, al sufrir menos interacciones que los electrones, salen de la muestra sin ser alterados desde profundidades mayores.

En la Figura 19b se representan los electrones incidentes, los distintos tipos de señales procedentes de la muestra y la profundidad de la zona de procedencia. Los detectores recogen las diferentes señales, sean electrones o fotones, y a partir de ella se construye punto a punto la imagen de la superficie de la muestra. Esta técnica, debido a que es capaz de enfocar superficies de tamaños muy diferentes (desde pocas decenas de nm a varios mm), es tremendamente útil para estudiar la morfología de materiales.

Para tomar las imágenes de esta tesis se ha utilizado un microscopio Quanta FEG 650 (FEI Company), operado a 25 kV y utilizando la señal de electrones secundarios.

Se ha estudiado por SEM la morfología de:

- Diferentes tipos de grafito (polvo, copos, HOPG, grafito flexible) utlizados como material de partida en la exfoliación anódica para obtener grafeno. (Figura 20a)
- Los mismos materiales después del tratamiento electroquímico. (Figura 20b)
- Grafeno obtenido en dispersión coloidal a partir de los materiales anteriores.
- CoO y Co_3O_4 obtenido a diferentes temperaturas, en estado sólido (Figura 20c) y en dispersión coloidal (Figura 20d).

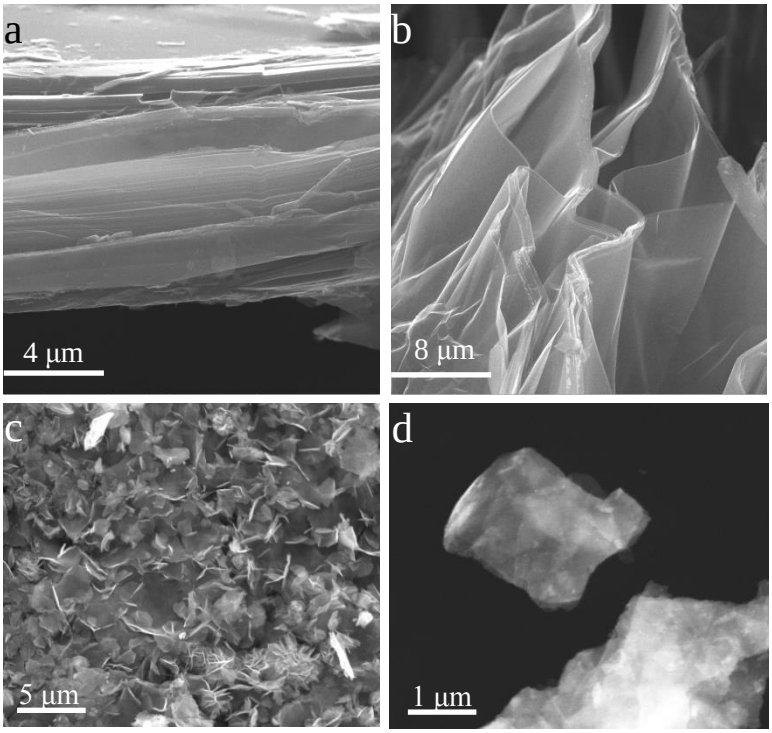

Figura 20. Imágenes SEM de copo de grafito natural **(a)** sin tratar, **(b)** exfoliado con K_2SO_4, Co_3O_4 preparado a 250 ºC **(c)** sólido y **(d)** láminas en dispersión coloidal (imagen de STEM).

Los materiales sólidos utilizados, ya fueran grafitos de partida o productos obtenidos, no requieren de especial preparación para ser estudiados. Las muestras de dispersiones coloidales se prepararon de la misma manera que aquellas medidas en TEM (ver sección anterior).

Si el equipo incorpora un detector de electrones situado bajo la muestra, como se puede ver en la Figura 19, y la muestra es suficientemente delgada para permitir la transmisión de electrones (como en el caso de láminas de materiales bidimensionales), se pueden registrar imágenes de microscopía electrónica de barrido por transmisión (scanning tranmission electron microscopy, STEM) con muy alta resolución, mayor que la que permiten los electrones secundarios [36]. El microscopio SEM utilizado en esta tesis permite este tipo de técnica, lo que permitió visualizar láminas individuales de materiales bidimensionales (Figura 20d).

4.2.3 Microscopía de fuerza atómica (AFM)

Se denominan microscopías de proximidad a aquellas técnicas microscópicas que, acercando una punta a la muestra a escala de nanómetros o angstroms y midiendo las interacciones resultantes, permiten obtener imágenes de su superficie. En el caso de la microscopía de fuerza atómica (atomic force microscopy, AFM) se detecta la fuerza que experimenta una punta al interactuar con la superficie de la muestra en función de la distancia que las separa, como se representa en la Figura 21a [1]. La punta está situada de manera perpendicular al final de una palanca flexible (cantilever), que puede oscilar verticalmente. Sobre el cantilever se hace incidir un láser, cuya señal reflejada se recoge en un fotodetector dividido en secciones, de manera que el movimiento de flexión queda registrado y puede ser representado en un mapa topográfico para la superficie de la muestra al hacer barridos sobre la misma (Figura 21b).

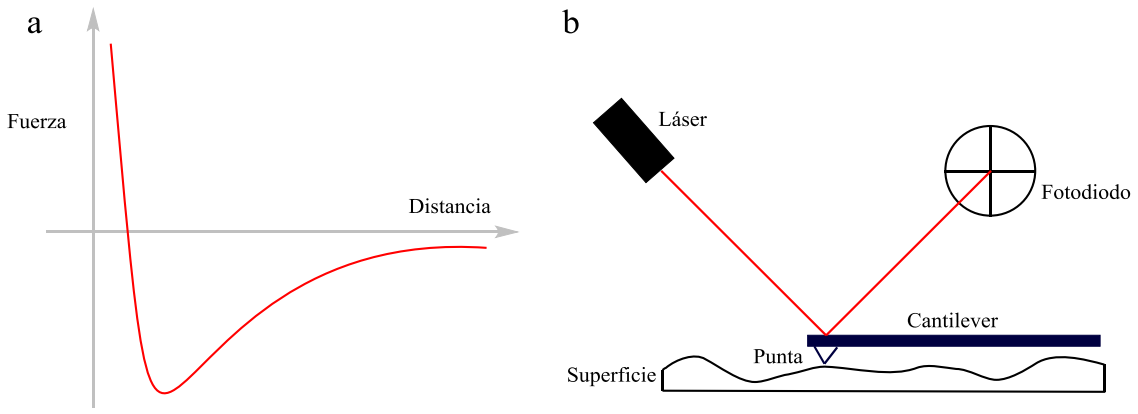

Figura 21. (a) Interacción punta-muestra en función de la distancia. **(b)** Esquema de operación de un microscopio AFM.

La técnica AFM tiene como ámbito de aplicación el estudio de superficies de materiales, y debido a que la interacción se da con cualquier sólido, es aplicable a cualquier muestra con una superficie relativamente plana [37-40]. La interacción punta-muestra medida en AFM puede ser repulsiva a distancias muy cortas y atractiva a distancias ligeramente superiores. Así, esta técnica se puede utilizar en modo de contacto, donde la interacción punta-muestra es repulsiva, o en modo de contacto intermitente (tapping) [41]. Este segundo modo es mucho menos agresivo con la superficie de la muestra, y por ello es posible utilizarlo para estudiar materiales bidimensionales depositados sobre sustratos planos, tales como grafeno sobre HOPG [42]. El fundamento de este modo de AFM consiste en la oscilación del cantilever con

una amplitud de ~100-200 nm por la aplicación de un voltaje a un elemento piezoeléctrico situado en su extremo. Cuando la punta se acerca a la superficie de la muestra a distancias inferiores a esta oscilación, la interacción con la superficie hace que se reduzca la amplitud de oscilación. Manteniendo la amplitud de oscilación constante y registrando los cambios en la posición vertical del cantilever, esta técnica permite generar mapas topográficos de la superficie de la muestra mediante barridos lineales.

Para la obtención de imágenes de AFM en modo tapping, en esta tesis se ha utilizado un microscopio Nanoscope IIIa Multimode de Veeco Instruments, utilizando cantilevers de silicio de constante de fuerza ~40 N m^{-1} y frecuencia de resonancia ~250–300 kHz (Bruker Corporation). Para preparar las muestras a medir, se depositaron pequeños volúmenes (10 μL) de una dispersión acuosa diluida (~0.05 mg mL^{-1}) del material sobre un sustrato de HOPG, mica o silicio recubierto de SiO_2 (300 nm de espesor) precalentado a 50-60 ºC.

A diferencia de las microscopías antes mencionadas (TEM y SEM), la microscopía AFM posee un gran poder de resolución en la dirección perpendicular a la superficie de la muestra, lo que permite determinar el espesor de láminas de grosor atómico, además de su morfología y tamaño lateral [42]. En esta tesis se ha utilizado extensamente AFM para obtener imágenes de láminas de materiales bidimensionales (grafeno, MoS_2 y óxidos de cobalto) depositadas desde dispersión coloidal, y de esta manera determinar su grosor, número de capas (en el caso de grafeno y MoS_2) y dimensiones laterales, como se ejemplifica en la Figura 22.

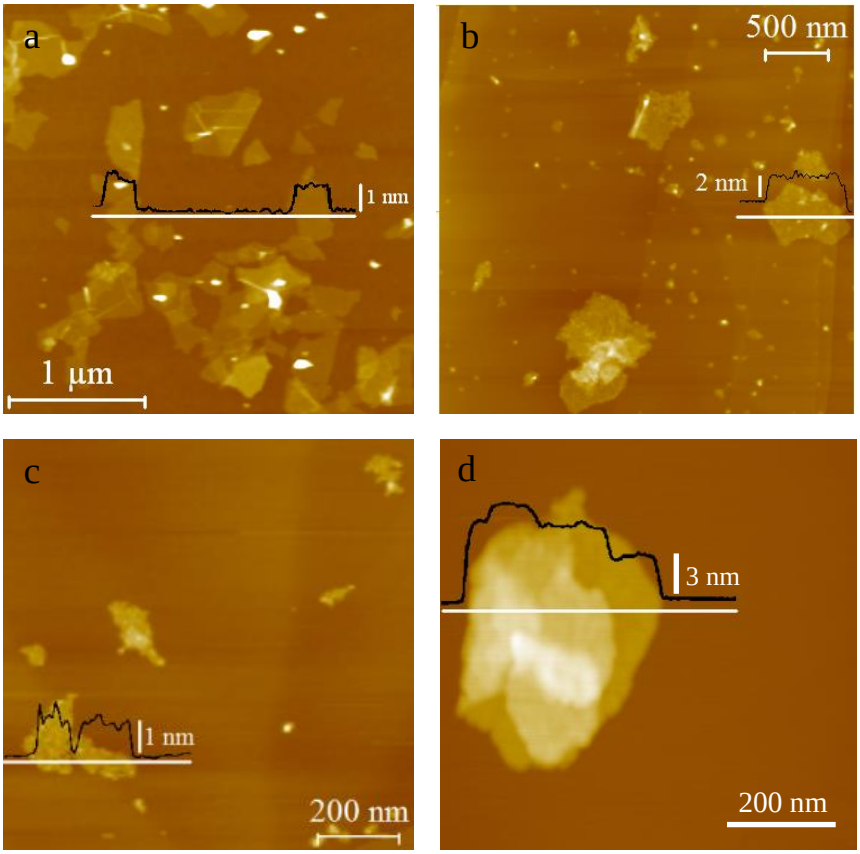

Figura 22. Imágenes de AFM de **(a)** grafeno obtenido por exfoliación de HOPG con K_2SO_4, **(b)** grafeno obtenido por exfoliación de grafito flexible con pireno 1,3,6,8–tetrasulfonato de sodio, **(c)** MoS_2 exfoliado químicamente y **(d)** CoO preparado por método solvotérmico.

4.3 Técnicas electroquímicas

4.3.1 Voltamperometría

Esta técnica consiste en medir la intensidad de corriente (I) que tiene lugar al aplicar un voltaje (V) entre un electrodo de trabajo (WE) y un contraelectrodo (CE) impregnados de un electrolito. Este voltaje se aplica a una velocidad de barrido (v) constante, típicamente entre 1 mV s^{-1} y 1V s^{-1}, y la curva de I en función de V obtenida se denomina voltamperograma [43,44]. Se denomina voltamperometría lineal al proceso de barrido en sentido creciente o decreciente de potencial, y voltamperometría cíclica (CV) si se realizan ciclos de barrido en ambos sentidos, lo que permite explorar la evolución de las curvas con el tiempo debido a procesos que pueden tener lugar por acción del potencial aplicado. Esta técnica es la base del análisis electroquímico, y la

facilidad con la que se pueden modificar sus parámetros le confiere mucha versatilidad. Experimentos de CV permiten, entre otras cosas, estudiar procesos redox, adsorción sobre superficies, intercalación de iones, procesos catalíticos, cinéticas de reacción y almacenamiento de energía [43,44].

Las medidas de voltamperometría cíclica se realizaron en dos potenciostatos, un equipo PGZ 402 Voltalab, de Radiometer Analytical y otro VSP, de Bio-Logic Science Instruments. Se realizaron estudios en configuración de dos electrodos simétricos y de tres electrodos. En la segunda configuración se usaron electrodos de trabajo con el material activo, contraelectrodos de pasta de carbón activado y electrodos de referencia de Ag/AgCl o Hg/HgO dependiendo del tipo de electrolito. Los materiales utilizados como electrodos de trabajo se utilizaron en estado sólido presionados contra grafito flexible o depositando dispersiones sobre el mismo grafito flexible y dejando evaporar el disolvente a temperatura ambiente.

En esta tesis se realizaron experimentos de voltamperometría para caracterizar la respuesta electroquímica y la capacidad de almacenamiento de energía de materiales de grafeno y óxidos de cobalto. La Figura 23 muestra voltamperometrías cíclicas de grafeno preparado por exfoliación electroquímica con NaI.

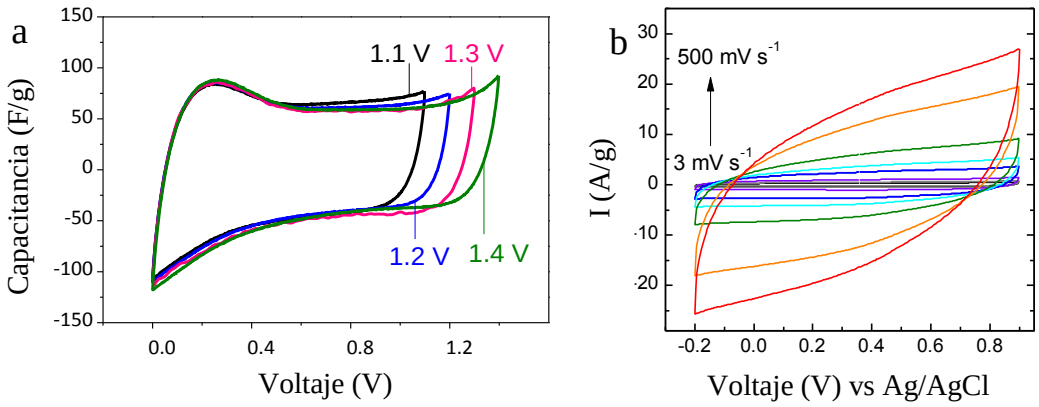

Figura 23. Voltamperogramas de grafeno exfoliado electroquímicamente con **(a)** NaI con diferentes ventanas de voltaje y **(b)** Na_2SO_4 y NaCl a diferentes velocidades de barrido.

4.3.2. Carga-descarga galvanostática

Si a un electrodo de trabajo se le aplica una intensidad de corriente constante (habitualmente entre 0.1 y 20 A g^{-1}), y se mide el voltaje creciente de la celda en función del tiempo, se obtiene una curva de carga galvanostática (o de descarga si la corriente es negativa y el voltaje es decreciente). Al aplicar la corriente, y dependiendo de las características químicas, morfológicas y superficiales del electrodo, en él tienen lugar procesos de adsorción del electrolito y/o redox que implican el almacenamiento de energía (carga eléctrica) en el material (procesos denominados capacitivos y pseudocapacitivos/tipo batería respectivamente) [43,44]. El análisis de estas curvas de carga y descarga permite caracterizar el tipo de procesos que tienen lugar en el material, así como evaluar su capacitancia en diferentes condiciones.

Los experimentos de carga y descarga galvanostáticos fueron llevados a cabo en los mismos potenciostatos y las mismas condiciones que las voltamperometrías cíclicas. Esta técnica se utilizó para calcular la capacitancia de materiales grafénicos y óxidos de cobalto. La Figura 24 muestra curvas de carga-descarga de grafeno exfoliado con Na_2SO_4 y NaCl.

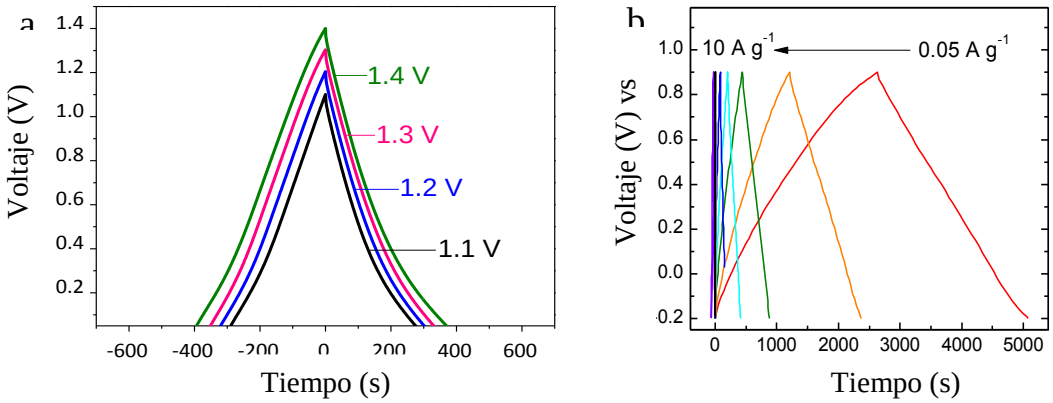

Figura 24. Curvas de carga-descarga galvanostática de grafeno exfoliado con **(a)** NaI a diferentes ventanas de voltaje y **(b)** Na_2SO_4 y NaCl a diferentes densidades de corriente.

4.3.3 Espectroscopía de impedancia electroquímica (EIS)

Se define la impedancia electroquímica Z para una celda electroquímica como el cociente entre el potencial aplicado V y la corriente I que circula (Z= V/I) [43,44]. La espectroscopía de impedancia electroquímica consiste en someter a la celda con la muestra a un potencial que varía sinusoidalmente en un rango de frecuencias y registrar la corriente que circula por dicha celda. La impedancia obtenida es dependiente de la frecuencia del voltaje, y esta relación proporciona información acerca de los procesos de transferencia de carga y masa que puedan tener lugar en el electrodo. En esta tesis se usó la EIS para caracterizar los procesos que tienen lugar en los dispositivos de almacenamiento de energía (ya fueran tipo condensador o tipo batería) de forma complementaria a las otras técnicas electroquímicas. Los equipos utilizados para este análisis fueron los mismos que en los apartados anteriores y con la misma preparación de las muestras. Como ejemplo, en la Figura 25 están representados espectros de EIS de muestras de óxidos de cobalto.

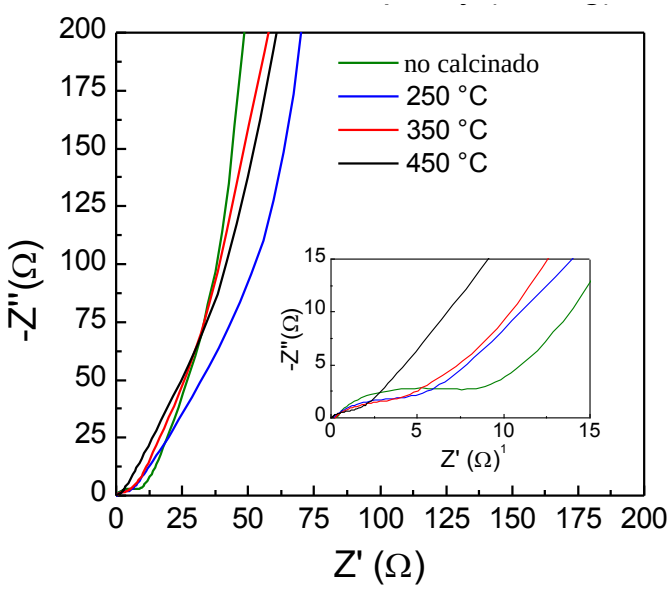

Figura 25. Espectros de EIS de óxidos de cobalto.

4.4 Medida de conductividad eléctrica de filmes

Se define la conductividad eléctrica como la facilidad que tiene un material para dejar fluir la corriente a su través cuando está sometido a un potencial eléctrico. Esta propiedad depende de la facilidad que tienen los electrones para moverse por su estructura, y por tanto depende de su composición y morfología. Existen diversos métodos para medir la conductividad de materiales, y entre ellos el de van der Pauw es de gran utilidad para medidas precisas de muestras altamente conductoras, ya que su diseño minimiza la influencia de los puntos de contacto del equipo con la muestra [45]. Se utilizó este método para determinar la conductividad eléctrica de filmes de grafeno (12×12 mm^2, con espesores del orden de micras) usando como fuente de corriente continua un equipo Agilent 6614C y un multímetro Fluke 45, como se describe en la Figura 26.

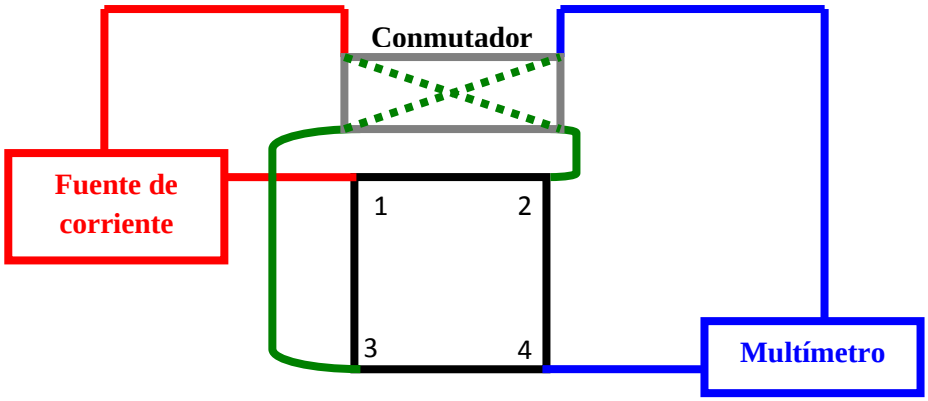

Figura 26. Esquema para la medida de la conductividad eléctrica de filmes con el método de Van der Paw.

Con una configuración como la representada en la Figura 26 se aplica una corriente entre los puntos 1 y 2 y se mide el voltaje inducido (por el efecto Hall) entre los puntos 3 y 4. A continuación, gracias al conmutador, se aplica corriente entre los puntos 1 y 3, y se mide el voltaje entre 2 y 4. De esta manera obtenemos $R_A=V_{43}/I_{12}$ y $R_B=V_{42}/I_{13}$, que nos permiten obtener la resistencia del material (Rs) según la ecuación XX:

$$e^{-\frac{\pi RA}{Rs}} + e^{-\frac{\pi RB}{Rs}} = 1 \qquad (4)$$

Con este valor de resistencia y conocidas la longitud (L) y el área de la sección (A) del filme se puede calcular la conductividad σ según la ecuación XX:

$$\sigma = \frac{L}{Rs\ A} \tag{5}$$

4.5 Estudios de biocompatibilidad y proliferación

En esta tesis se han realizado estudios de biocompatibilidad de grafeno y disulfuro de molibdeno mediante el método MTT (bromuro de 3-(4,5-dimetiltiazol-2-ilo)-2-5-difeniltetrazol). Estos ensayos consisten en pruebas de proliferación celular de fibroblastos de ratón L-929 en presencia de los materiales a ensayar y habitualmente se utilizan como medida del posible efecto citotóxico de dichos materiales.

El fundamento del ensayo es la reducción de MTT que tiene lugar por acción de una enzima mitocondrial (la succinato-deshidrogenasa) para generar formazán, una especie coloreada cuya concentración se puede medir mediante su absorbancia a 570 nm [46-48]. La concentración de formazán es proporcional al número de células vivas, de manera que se puede cuantificar así la proliferación celular en presencia de los materiales a ensayar (Figura 27). Las medidas de absorbancia del formazán se llevaron a cabo en un equipo BMG FLUOstar Galaxy (MTX Lab Systems, Inc).

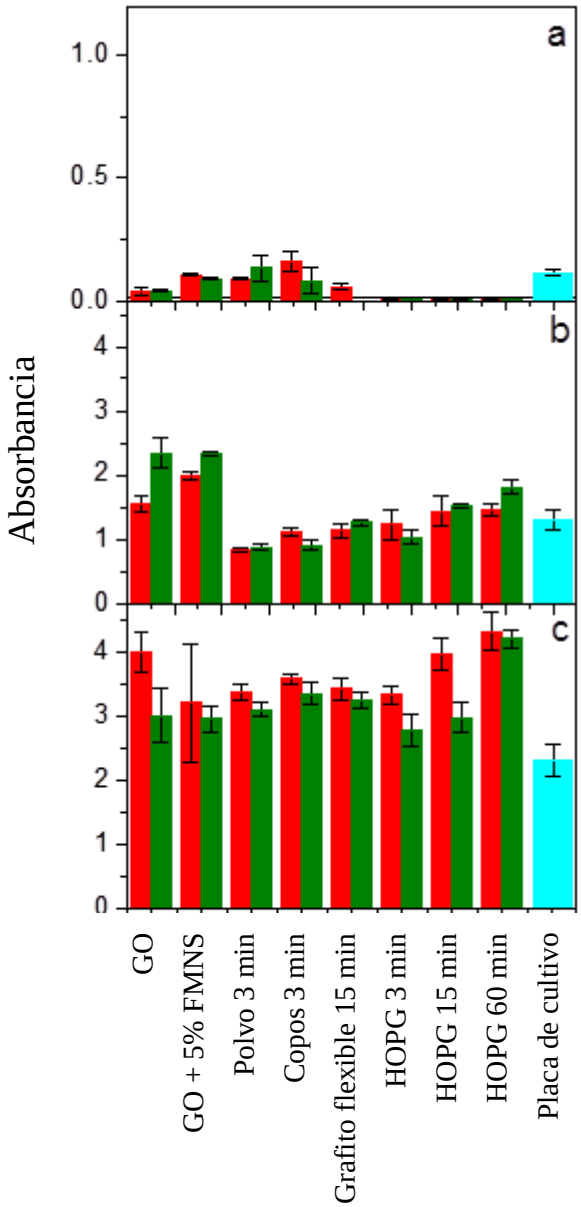

Figura 27. Estudios de proliferación celular L-929 por el método MTT para filmes delgados de grafenos preparados a partir de diferentes grafitos.

4.6 Actividad catalítica

Se ha estudiado la actividad catalítica de híbridos grafeno-nanopartículas de Pt y disulfuro de molibdeno. Para ello se han utilizado dos reacciones modelo para el ensayo de catalizadores, las de reducción de 4-nitrofenol (4-NP) y 4-nitroanilina (4-NA) con borohidruro de sodio [6]. Como los reactivos son especies que poseen bandas de

absorción características en el espectro visible, estas reacciones se pueden seguir de manera conveniente mediante espectroscopía UV-Vis. Para llevar a cabo el ensayo, se toman cantidades fijas de reactivo (4-NP o 4-NA) y un exceso de $NaBH_4$, y se hacen reaccionar en presencia de una cantidad variable del material catalítico a estudiar. Se mide la absorción del medio de reacción a 400 y 380 nm para 4-NP y 4-NA, respectivamente, y se determina el punto final de la reacción. Conociendo el tiempo de reacción y las cantidades de reactivo y catalizador es posible determinar la actividad catalítica. En la Figura 28 se representan espectros de absorción de reactivos y productos y el seguimiento de la reacción para el ensayo de catálisis de los híbridos grafeno-nanopartículas de Pt.

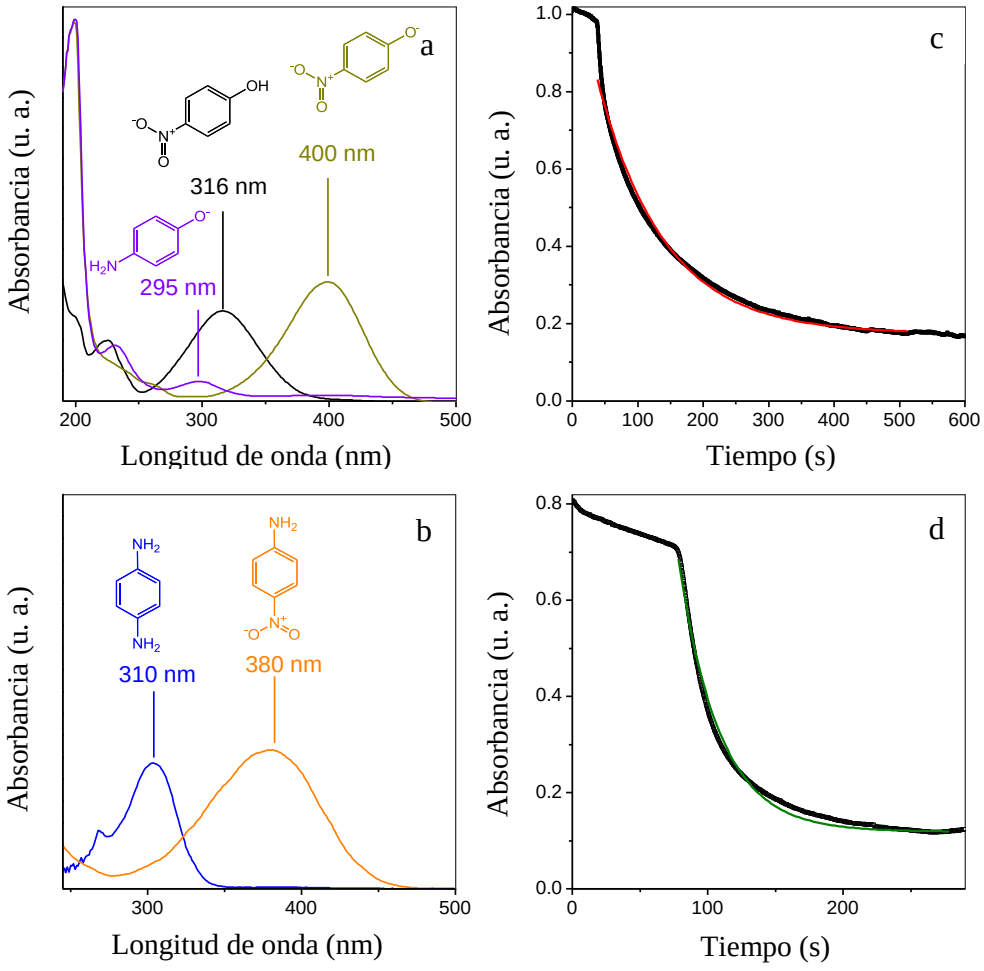

Figura 28. Espectros UV-Vis de **(a)** 4-nitrofenol (negro), 4-nitrofenóxido (ocre) y 4-aminofenóxido (violeta); **(b)** 4-nitroanilina (naranja) y p-fenilendianilina (azul). Evolución temporal de la absorción a **(c)** 400 nm para la reducción de 4-nitrofenóxido con NaBH4 y **(d)**

380 nm para la reducción de 4-nitroanilina, ambos en presencia de híbrido grafeno-nanopartículas de Pt.

4.7 Difracción de rayos X

Una de las técnicas más comunes para el estudio de sólidos cristalinos, y particularmente en el caso de materiales laminares, es la difracción de rayos X (DRX) [1]. El fundamento de esta técnica es la irradiación de una muestra cristalina con rayos X y el posterior estudio de la radiación difractada. Al hacer incidir la radiación sobre el material cristalino, ésta es reflejada por la red. Esta reflexión tiene lugar en los diferentes planos de la red cristalina, lo que provoca que la radiación reflejada tenga un desfase correspondiente a la separación entre planos, y a su vez que se produzca un fenómeno de interferencia en función del ángulo de incidencia de la radiación, lo que origina un patrón de difracción (Figura 29).

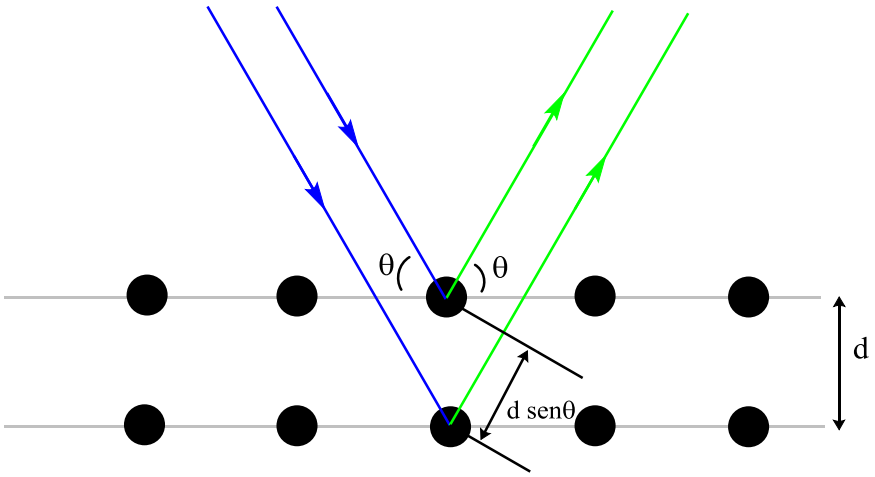

Figura 29. Esquema de la radiación incidente y reflejada sobre un cristal. La diferencia de caminos origina el patrón de difracción por la interferencia.

La relación entre el ángulo de la radiación incidente y la separación entre los planos cristalinos viene dada por la ley de Bragg:

$$2d\ sen\ (\theta) = n\lambda \tag{6}$$

, donde d es la distancia entre planos cristalinos, θ el ángulo entre la dirección de la radiación y el plano, n un número entero positivo y λ la longitud de onda de la radiación

incidente. Si se hace incidir radiación sobre la muestra en un rango de ángulos θ (habitualmente se utiliza 2θ en el equipo y en el tratamiento de datos), se obtiene un patrón de difracción, que puede ser transformado en un difractograma cuando se representa la intensidad de la radiación reflejada frente a 2θ. La presencia de picos (interferencia constructiva de la difracción) permite deducir las distancias interplanares de la red cristalina, y por tanto obtener información sobre su estructura.

En esta tesis se utilizó un equipo de difracción Bruker D8 Advance, usando Cu K_α (λ= 0.154 nm) como fuente de rayos X. Se utilizó esta técnica para determinar si el tratamiento del grafito flexible por inmersión en ácido sulfúrico provoca la separación de los planos del grafito y para el estudio de la cristalinidad de óxidos de cobalto. En la Figura 30 se observan los difractogramas de Co_3O_4 obtenidos por calentamiento de CoO amorfo a diferentes temperaturas y de distintos tipos de grafito flexible.

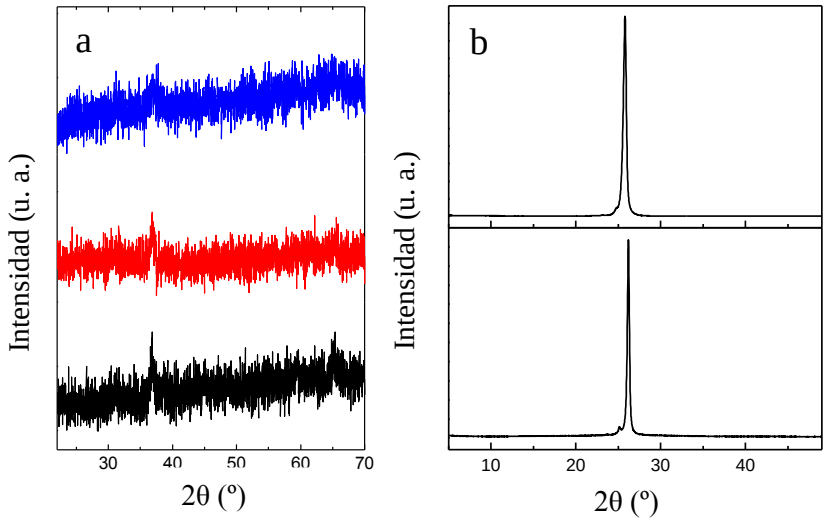

Figura 30. Difractogramas de **(a)** Co_3O_4 obtenidos a 250 (azul), 350 (rojo) y 450ºC (negro) y **(b)** grafito flexible antes (arriba) y después (abajo) de 24h de inmersión en H_2SO_4.

BIBLIOGRAFÍA

[1] Faraldos, M.; Goberna C. Técnicas de análisis y caracterización de materiales. Madrid: Consejo Superior de Investigaciones Científicas, **2011**.

[2] Beer, A. Determination of the absorption of red light in colored liquids, *Annalen der Physik und Chemie*, **1852**, 86, 78–88.

[3] Jentoft, F. C. Characterization of solid materials and heterogeneous catalysts: from structure to surface reactivity. Wiley-VCH, **2012**, Volume 1.

[4] Pino, F.; Pérez, M. D., Análisis de elementos-traza por espectrofotometría de absorción molecular ultravioleta-visible. Universidad de Sevilla. **1983**.

[5] Skoog, D. A.; Holler, F. J.; Nieman, T. A. Principles of instrumental analysis. Belmont (USA): Thomson Brooks/cole. **2007**.

[6] Hervés, P.; Pérez-Lorenzo, M.; Liz-Marzán, L.M.; Dzubiella, J.; Lu, Y.; Ballauff, M. Catalysis by metallic nanoparticles in aqueous solution: Model reactions. *Chem. Soc. Rev*., **2012**, 41, 5577-5587.

[7] Preat, J.; Michaux, C.; Jacquemin, D.; Perpèt, E. A. Enhanced efficiency of organic dye-sensitized solar cells: triphenylamine derivatives. *J. Phys. Chem. C*, **2009**, 113, 16821-16833.

[8] Liu, M.; Wang, L.; Meng, Y.; Chen, Q.; Li, H.; Zhang, Y.; Yao, S. (4-Ferrocenylethyne) phenylamine functionalized graphene oxide modified electrode for sensitive nitrite sensing. *Electrochim. Acta*, **2014**, 116, 504-51.

[9] Deka, M. J.; Chowdhury, D. Tuning electrical properties of graphene with different π-stacking organic molecules. *J. Phys. Chem. C*, **2016**, 120, 4121-4129.

[10] Panáček, A.; Kvítek, L.; Prucek, R.; Kolář, M.; Večeřová, R.; Pizúrová, N.; Sharma, V. K.; Nevěčná, T.; Zbořil, R. Silver colloid nanoparticles: synthesis, characterization, and their antibacterial activity. *J. Phys. Chem. B*, **2006**, 110, 16248-16253.

[11] Haiss, W.; Thanh, N. T. K.; Aveyard, J.; Fernig, D. G. Determination of size and concentration of gold nanoparticles from UV−Vis spectra. *Anal. Chem*., **2007**, 79, 4215-4221.

[12] Eda, G.; Yamaguchi, H.; Voiry, D.; Fujita, T.; Chen, M.; Chhowalla, M. Photoluminescence from chemically exfoliated MoS_2. *Nano Lett*., **2011**, 11, 5111-5116.

[13] Sun, Z.; Liao, T.; Dou, Y.; Hwang, S. M.; Park, M-S.; Jiang, L.; 4, Kim, J. H.; Dou, S. X. Generalized self-assembly of scalable two-dimensional transition metal oxide nanosheets. *Nat. Commun.*, **2014**, 5, 3813-3822.

[14] Hernandez, Y.; Nicolosi, V.; Lotya, M.; Blighe, F. M.; Sun, Z.; De, S.; McGovern, I. T.; Holland, B.; Byrne, M.; Gun'ko, Y. K.; Boland, J. J.; Niraj, P.; Duesberg, G.; Krishnamurthy, S.; Goodhue, R.; Hutchison, J.; Scardaci, V.; Ferrari, A. C.; Coleman, J. N.; High-yield production of graphene by liquid-phase exfoliation of graphite. *Nat. Nanotechnol*., **2008**, 3, 563-568.

[15] Ayán–Varela, M.; Paredes, J. I.; Guardia, L.; Villar–Rodil, S.; Munuera, J. M.; Díaz–González, M.; Fernández–Sánchez, C.; Martínez–Alonso, A.; Tascón, J. M. D. Achieving extremely concentrated aqueous dispersions of graphene flakes and catalytically efficient graphene-metal nanoparticle hybrids with flavin mononucleotide as a high-performance stabilizer. *ACS Appl. Mater. Interfaces*, **2015**, 7, 10293–10307.

[16] Ramesha, G. K.; Kumara, A. V.; Muralidhara, H. B.; Sampath, S. Graphene and graphene oxide as effective adsorbents toward anionic and cationic dyes. J. Colloid Interface Sci., 2011, 361, 270-277.

[17] Smith, BC. Modern Raman spectroscopy: a practical approach. John Wiley & Sons, **2005**.

[18] Ferrari, A. C.; Robertson J. Interpretation of Raman spectra of disordered and amorphous carbon. *Phys. Rev. B,* **2000**, 61, 14095.
[19] Kataura, H.; Maniwa, Y.; Kodama, T.; Kikuchi, K.; Hirahara, K.; Suenaga, K.; Iijima, S.; Suzuki, S.; Achiba, Y.; Krätschmer, W. High-yield fullerene encapsulation in single-wall carbon nanotubes. *Synth. Met*., **2001**, 121, 1195-1196.
[20] Dresselhaus, M. S.; Dresselhaus, G.; Saito, R.; Jorio, A. Raman spectroscopy of carbon nanotubes. *Phys. Rep*., **2005**, 409, 47-99.
[21] Ferrari, A.C. Raman spectroscopy of graphene and graphite: Disorder, electron-phonon coupling, doping and nonadiabatic effects. *Solid State Commun*., **2007**, 143, 47-57.
[22] Knight, D.S.; White, W.B. Characterization of diamond films by Raman spectroscopy. *J. Mater. Res*., **1989**, 4, 385-393.
[23] Ferrari A. C.; Meyer, J. C.; Scardaci, V.; Casiraghi, C.; Lazzeri, M.; Mauri, F.; Piscanec, S.; Jiang, D.; Novoselov, K. S.; Roth, S.; Geim A. K. Raman spectrum of graphene and graphene layers. *Phys Rev Lett*., **2006**, 97, 187401.
[24] Paton, K. R.; Varrla, E.; Backes, C.; Smith, R. J.; Khan, U.; O'Neil, A.; Boland, C.; Lotya, M.; Istrate, O. M.; King, P.; Higgins, T.; Barwich, S.; May, P.; Puczkarski, P.; Ahmed, I.; Moebius, M.; Pettersson, H.; Long, E.; Coelho, J.; O'Brien, S. E.; McGuire, E. K.; Mendoza Sanchez, B.; Duesberg, G. S.; McEvoy, N.; Pennycook, T. J.; Downing, C.; Crossley, A.; Nicolosi, V.; Coleman, J. N. Scalable production of large quantities of defect-free few-layer graphene by shear exfoliation in liquids. *Nature Mater*., **2014**, 13, 624-630.
[25] Guardia, L.; Fernández-Merino, M. J.; Paredes, J. I.; Solís-Fernández, P.; Villar-Rodil, S.; Martínez-Alonso, A.; Tascón, J. M. D. High-throughput production of pristine graphene in an aqueous dispersion assisted by non-ionic surfactants. *Carbon*, **2011**, 49, 1653-1662.
[26] Sun, Z.; Masa, J.; Liu, Z.; Schuhmann, W.; Muhler, M. Highly concentrated aqueous dispersions of graphene exfoliated by sodium taurodeoxycholate: dispersion behavior and potential application as a catalyst support for the oxygen-reduction reaction. *Chem. Eur. J*. **2012**, 18, 6972-6978.
[27] Zhang, L.; Zhang, Z.; He, C.; Dai, L.; Liu, J., Wang L. Rationally designed surfactants for few-layered graphene exfoliation: ionic groups attached to electron deficient π-conjugated unit through alkyl spacers. *ACS Nano*, **2014**, 8, 6663-6670.
[28] Buzaglo, M.; Shtein, M.; Kober, S.: Lovrinčić, R.: Vilan, A.; Regev, O. Critical parameters in exfoliating graphite into graphene. *Phys. Chem. Chem. Phys*., **2013**, 15, 4428-4435.
[29] Bourlinos, A. B.; Georgakilas, V.; Zboril, R.; Steriotis, T. A.; Stubos, A. K.; Trapalis, C. Aqueous-phase exfoliation of graphite in the presence of polyvinylpyrrolidone for the production of water-soluble graphenes. *Solid State Commun*., **2009**, 149, 2172- 2176.
[30] Notley, S. M. Highly Concentrated suspensions of graphene through ultrasonic exfoliation with continuous surfactant addition. *Langmuir*, **2012**, 28, 14110-14113.
[31] Van der Heide, P. X-ray photoelectron spectroscopy: an introduction to the principles and practices; John Wiley & Sons: Hoboken, NJ, **2012**.
[32] Paredes, J. I.; Munuera, J. M. Recent advances and energy-related applications of high quality/chemically doped graphenes obtained by electrochemical exfoliation methods, *J. Mat. Chem. A*, **2017**, 16, 7228-7242.
[33] Ayán-Varela, M.; Fernández-Merino, M. J.; Paredes, J. I.; Villar-Rodil, S.; Fernández-Sánchez, C.; Guardia, L.; Martínez-Alonso, A.; Tascón, J. M. D. Highly efficient silver-assisted reduction of graphene oxide dispersions at room temperature: Mechanism, and catalytic and electrochemical performance of the resulting hybrids, *J. Mat. Chem. A*, **2014**, 20, 7295-7305.

[34] Guo, S.; Wang, E. Noble metal nanomaterials: controlable synthesis and application in fuel cells and analytical sensors. *Nano Today*, **2011**, 6, 240-264.
[35] Spence, J. C. H. High-Resolution Electron Microscopy, Oup Oxford, **2014**.
[36] Egerton, R. F. Physical principles of electron microscopy. Springer. **2008**.
[37] Biris, A. R.; Dervishi, E.; Ardelean, S.; Lazar, M. D.; Watanabe, F.; Biris, G. L.; Misan, I.; Biris, A. S.; Giessibl, F. J. Advances in atomic force microscopy. *Rev. Mod. Phys*., **2003**, 75, 949-983.
[38] Abu-Lail, N. I., Camesano, T. A. Polysaccharide properties probed with atomic force microscopy. *J. Microsc.*, **2003**, 212, 217-238.
[39] Kuznetsov, Y. G.; Malin, A. J.; Lucas, R. W.; Plomp, M.; McPherson, A. Imaging of viruses by atomic force microscopy. *J. Gen. Virol*., **2001**, 82, 2025-2034.
[40] Jalili, N. ; Laxminarayana, K. A review of atomic force microscopy imaging systems: Application to molecular metrology and biological sciences. *Mechatronics*, **2004**, 14, 907-945.
[41] Haugstad, G. Atomic Force Microscopy: Understanding Basic Modes and Advanced Applications. Wiley. **2012**.
[42] Paredes, J. I.; Villar-Rodil, S.; Solís-Fernández, P.; Martínez-Alonso, A.; Tascón, J. M. D. Atomic force and scanning tunneling microscopy imaging of graphene nanosheets derived from graphite oxide. *Langmuir*, **2009**, 25, 5957-5968.
[43] Scholz, F. Electroanalytical methods: guide to experiments and applications. Springer. **2010**.
[44] Zoski, C. G. Handbook of electrochemistry. Elsevier. **2007**.
[45] Van der Paw, L. A method of measuring the resistivity and Hall coefficient on lamellae of arbitrary shape. *Philips Tech. Rev*., **1958**, 20, 220-224.
[46] Carmichael, J.; Gazdar, A. F. Evaluation of a tetrazolium-based semiautomated colorimetric assay: assessment of chemosensitivity testing. *Cancer Research*, **1987**, 47, 936-942.
[47] Denizot, F.; Lang, R. Rapid colorimetric assay for cell growth and survival. Modifications to the tetrazolium dye procedure giving improved sensitivity and reliability. *J. Immunol. Methods*, **1986**, 89, 271-277.
[48] Hansen, M. B.; Nielsen, S. E.; Berg, K. Re-examination and further development of a precise and rapid dye method for measuring cell growth/cell kill. *J. Immunol. Methods*, **1989**, 119, 203-210.

5. Resúmenes y artículos

5.1 Exfoliación electroquímica de grafeno

Artículo I

High quality, low oxygen content and biocompatible graphene nanosheets obtained by anodic exfoliation of different graphite types, Munuera, J.M. , Paredes, J.I., Villar-Rodil, S., Ayán-Varela, M., Pagán, A., Aznar-Cervantes, S.D., Cenis, J.L., Martínez-Alonso, A., Tascón, J.M.D., Carbon, 2015, 94, 729-739.

Artículo II

Electrolytic exfoliation of graphite in water with multifunctional electrolytes: En route towards high quality, oxide-free graphene flakes, Munuera, J.M., Paredes, J.I., Villar-Rodil, S. , Ayán-Varela, M., Martínez-Alonso, A., Tascón, J.M.D. Nanoscale, 2016, 8, 5, 2982-2998.

Artículo III

A simple strategy to improve the yield of graphene nanosheets in the anodic exfoliation of graphite foil, Munuera, J.M. , Paredes, J.I., Villar-Rodil, S., Martínez-Alonso, A., Tascón, J.M.D., Carbon, 2017, 115, 625-628.

Artículo IV

Electrochemical exfoliation of graphite in aqueous sodium halide electrolytes toward low oxygen content graphene for energy and environmental applications, Munuera, J. M.; Paredes, J. I.; Enterría, M.; Pagán, A.; Villar-Rodil, S.; Martins, M. F. R.; Figueiredo, J. I.; Cenis, J. L.; Martínez-Alonso, A.; Tascón, J. M. D.; ACS Applied Materials and Interfaces, 2017, 9, 24085-24099.

Artículo V

High quality, low-oxidized graphene via anodic exfoliation with table salt as an efficient oxidation-preventing co-electrolyte for water/oil remediation and capacitive energy storage applications, Munuera, J. M.; Paredes, J. I.; Villar-Rodil, S.; Castro-Muñiz, A.; Martínez-Alonso, A.; Tascón J. M. D.,Applied Materials Today, 2018, 11, 246–254.

La exfoliación electroquímica de grafito es una técnica emergente de preparación de grafeno que posee rasgos atractivos como versatilidad, potencial escalabilidad y la calidad del grafeno obtenido. Esto queda evidenciado en el número de publicaciones en las que se describe la preparación de grafeno por diferentes variaciones de este método. No obstante, es necesario un estudio exhaustivo de cada una de las variables del proceso, esto es, el voltaje y la corriente aplicados, el tiempo de exfoliación, el tipo y morfología del grafito de partida, los posibles pretratamientos del mismo, el electrolito y su concentración, la presencia de aditivos de electrolito y sus concentraciones, y también en menor medida el tamaño del electrodo de grafito, así como el volumen de electrolito. El estudio de estas variables es de gran importancia debido a su influencia en las características del producto final, en términos de rendimiento, grado de exfoliación, tamaño de las láminas, oxidación, así como cantidad y tipos de defectos. Debido a la falta de estudios exhaustivos a fecha de inicio de la presente tesis, se tomó como objetivo estudiar diferentes variaciones de algunos de los parámetros mencionados, concretamente el material de partida en el **artículo I**, el uso de diferentes electrolitos en los **artículos II**, **IV** y **VI**, un pretratamiento en el **artículo III** y el uso de aditivos de electrolito como agentes antioxidantes en el **artículo V**.

La variable a considerar en el **artículo I** fue el grafito utilizado como ánodo en la exfoliación anódica. Estudios previos a la publicación de este trabajo utilizaban indistintamente grafitos de diferente morfología a conveniencia (grafito en polvo, en copos, HOPG, grafito flexible) sin que hubiera un estudio de la posible influencia de esta elección en las características del grafeno obtenido. Para evaluar esta influencia, se procedió a estudiar la exfoliación anódica de grafitos con diferentes morfologías en un mismo proceso, esto es, sometidos al mismo voltaje durante tiempos iguales, sumergidos en disoluciones de sulfato de potasio de concentración 0.1 M, un electrolito estándar y de eficacia ampliamente comprobada. Se exfolió grafito en polvo y copos compactado en forma de pastilla en una prensa a baja presión, conectado a la fuente de corriente mediante un hilo de platino. Se exfoliaron también grafito flexible y HOPG, sujetados por medio de una pinza a la fuente de corriente. En todos los casos el grafito se utilizó como ánodo en una celda electroquímica, utilizando como cátodo un hilo de platino. Se aplicó un potencial de 10 V a la celda durante tiempos de 3, 15 y 60 minutos y en todos los casos la aplicación del potencial condujo a la intercalación del electrolito en el ánodo de grafito, produciendo una expansión muy marcada y el desprendimiento

de partículas expandidas que, tras un proceso de sonicación (bien en N,N-dimetil formamida (DMF), bien en agua con un dispersante) produjo dispersiones de nanoláminas de grafeno.

No obstante, ya en el proceso de exfoliación se aprecian claras diferencias entre los cuatro tipos de grafito. En el caso de grafitos de pequeño tamaño de partícula como son el polvo y los copos (con partículas de tamaños del orden de decenas y cientos de micras respectivamente), los ánodos en forma de pastilla se deshacen en tiempos del orden de 3 a 6 minutos durante la exfoliación, ya que la intercalación del electrolito y la posterior expansión hacen que las partículas se disgreguen del ánodo y pierdan contacto eléctrico con la fuente. La consecuencia inmediata de esto es que el grado de intercalación y exfoliación son limitados, apareciendo nanoláminas de grosores entre 3 y 5 nanómetros medidas por AFM, lo que corresponde a entre 6 y 12 capas de grafeno. Por otra parte, el grafito flexible y HOPG, con tamaños de partícula del orden de milímetros, que no requieren ser compactados, permiten tiempos de exfoliación superiores. En ambos casos la aplicación del voltaje conduce a la intercalación del electrolito y la expansión del electrodo, así como al desprendimiento de partículas de grafito expandido. Sin embargo, a diferencia de los otros materiales, en estos casos el ánodo de grafito sigue siendo estructuralmente sólido, manteniendo el contacto eléctrico durante tiempos largos y permitiendo así una exfoliación más eficiente. Las nanoláminas producidas usando estos materiales son más delgadas, con grosores típicos por AFM de 1 a 2 nanómetros, lo que corresponde a 1 a 3 capas de grafeno.

Los grafenos obtenidos a partir de los cuatro tipos de grafito se analizaron mediante espectroscopías Raman y fotoelectrónica de rayos X (XPS). En concreto, para evaluar la presencia de defectos se estudió la relación de intensidades integradas de las bandas D y G del espectro de Raman, y para determinar el grado de oxidación se midió la proporción atómica de oxígeno respecto al carbono por medio de XPS. Los grafenos obtenidos a partir de grafito en polvo y en copos presentan valores bajos de oxidación y defectos, consistentes con los tiempos cortos de exfoliación (como se ha comentado previamente, la exfoliación anódica es un proceso oxidativo, y mayores tiempos de exfoliación implican generalmente mayor oxidación y más aparición de defectos en la red del grafeno). Los grafenos obtenidos a partir de grafito flexible y HOPG, en cambio, presentan cantidades de defectos y de oxidación relativamente altos en comparación con los anteriores, particularmente a tiempos de exfoliación más largos. No obstante, estos

dos materiales no se comportan igual, teniendo el grafeno derivado de HOPG un grado de oxidación superior al del grafeno proveniente del grafito flexible (casi el doble para tiempos iguales de exfoliación). Esta diferencia de comportamiento puede explicarse una vez más por sus diferentes morfologías. Como se observó en las imágenes de FE-SEM de los materiales de partida, el HOPG así como los grafitos en polvo y copos presentan una estructura marcadamente laminar, con una morfología compacta. Sin embargo el grafito flexible tiene una estructura menos densa, con multitud de arrugas, huecos y recovecos debido al proceso de preparación del mismo (grafito en copos expandido y posteriormente laminado entre rodillos). Esta morfología poco densa y desordenada facilita enormemente la acción del electrolito puesto que, como se ha comentado, la intercalación es un proceso que se origina en los bordes del grafito, y los huecos y arrugas proporcionan muchos más puntos de entrada al electrolito que una estructura densa de láminas perfectamente apiladas

En conjunto, todas las características de los grafenos obtenidos están dentro de los valores habituales para grafenos exfoliados anódicamente, y queda patente la relevancia de elegir uno u otro material de partida. Vistas en conjunto las características, los materiales particulados (polvo y copos) se descartan como materiales idóneos por la incomodidad que supone su uso, así como por el hecho de que las láminas producidas son relativamente gruesas. Respecto al HOPG y grafito flexible, la elección es fácil por dos motivos. El primero es el grado de oxidación. A pesar de que sus valores para tiempos de tratamiento electrolítico de 60 minutos son aceptables y están dentro de lo habitual para este tipo de grafenos (18% de oxígeno para HOPG, 11% para grafito flexible), la menor oxidación de este último hace que el grafito flexible resulte más atractivo. El segundo motivo y muy relevante, es el precio. El HOPG es un material de muy alta calidad e incluso los grados más baratos tienen precios del orden de 100 € por gramo, frente a los ~0.1 € por gramo para el grafito flexible. Por tanto, y considerando todas estas variables, el material que exhibe las mejores características para ser usado como ánodo en la exfoliación electroquímica es el grafito flexible, y así se ha seguido utilizando en posteriores trabajos.

Debido a los potenciales usos en aplicaciones biomédicas de los materiales grafénicos, se realizaron ensayos de biocompatibilidad de los grafenos producidos en este trabajo. Estos ensayos consisten en pruebas de proliferación celular de fibroblastos de ratón L-929, y aunque se aprecian leves diferencias según el contenido en oxígeno de

los materiales grafénicos, todos ellos permiten la proliferación celular y por tanto se consideran biocompatibles.

El uso del anión sulfato en forma de ácido o sales como electrolito está ampliamente extendido en la exfoliación anódica de grafito, y ha demostrado sobradamente su eficiencia en este proceso. No obstante su uso tiene limitaciones, como son la oxidación significativa del grafeno producido y la necesidad de lavar extensamente el material expandido para eliminar el sulfato y después dispersarlo en un disolvente orgánico o agua (que requiere la adición de un surfactante). Por estas razones, en el **artículo II** se explora el uso de compuestos aromáticos sulfonados como electrolitos multifuncionales en la exfoliación anódica acuosa de grafito, utilizando el mismo procedimiento que en el trabajo anterior. Estos compuestos, consistentes en uno o varios grupos sulfonato anclados a anillos mono o poliaromáticos se emplearon para corregir los problemas y deficiencias de los electrolitos habituales. Se estudiaron gran cantidad de compuestos del mencionado tipo.

Debido a sus características, estos compuestos actúan como agentes intercalantes de la misma manera que el anión sulfato, produciendo la expansión del grafito que permite la obtención de grafeno mediante una posterior sonicación. En el caso del anión sulfato, es necesario efectuar la sonicación en un medio dispersante apropiado, bien sea un disolvente como el DMF o en agua mediante la adición de un surfactante. Sin embargo, debido a la naturaleza anfifílica de los sulfonatos aromáticos, es posible usarlos también como surfactantes, dando lugar a dispersiones de grafeno estabilizadas por la propia acción de estos compuestos. Una vez preparadas estas dispersiones estables de grafeno, la presencia de los sulfonatos aromáticos adsorbidos en la superficie de las láminas sirve como punto de anclaje para la síntesis de nanopartículas, lo que permitió la formación de híbridos grafeno-nanopartículas de platino, que demostraron una excelente capacidad catalítica en la reducción de nitroarenos (4-nitrofenol y 4-nitroanilina) con borohidruro de sodio.

Uno de los grandes inconvenientes de la exfoliación anódica de grafeno en medio acuoso es la oxidación del producto final. Debido a la naturaleza oxidativa del proceso electroquímico anódico, así como a la necesidad de oxidar los bordes de grano del grafito para facilitar la intercalación de los aniones, existe la creencia extendida de que es inevitable que se produzca una oxidación significativa del grafeno durante el

proceso de exfoliación anódica. No obstante, la utilización de electrolitos multifuncionales en la exfoliación puede afectar en gran medida a la calidad del grafeno obtenido. La exfoliación anódica tiene lugar a potenciales muy superiores al de la oxidación del agua, lo cual provoca la aparición de especies como el radical hidroxilo (·OH). Estas especies son altamente inestables y tienden a oxidar cualquier compuesto o material presente en el lugar de su formación, bien sea el electrolito o el ánodo de grafito. En el caso de la exfoliación con sulfato, al no poder éste ser oxidado, las especies oxidantes atacan los bordes y planos basales del grafito (y menor medida el plano basal), dando lugar a grafenos oxidados. Sin embargo, si durante el proceso el electrolito intercalante es un compuesto oxidable, estas especies lo atacarán y por tanto la oxidación del grafeno será previsiblemente menor.

Se estudió el uso de varios sulfonatos aromáticos, determinándose que, en general, todos ellos fueron eficientes en la exfoliación de grafeno, salvo aquellos que por tener una parte hidrófoba demasiado grande son poco solubles en agua. Además, todos los electrolitos con una componente apolar lo suficientemente grande como para adsorberse sobre las láminas produjeron dispersiones estables en agua formadas por grafeno de pocas capas. En lo que respecta a la presencia de oxidación y defectos, la mayoría de electrolitos conducen a grafeno muy similar al obtenido usando el anión sulfato, con un contenido en oxígeno de ~11% y una relación de intensidades de las bandas D y G de Raman (I_D/I_G) de ~1.0. Sin embargo, como cabría esperar por la capacidad de los anillos aromáticos para ser oxidados, algunos de estos electrolitos permiten obtener grafenos con mucha menor oxidación y defectos. En concreto para el 1,3,6,8-pirenotetrasulfonato y el 1,5-naftalenodisulfonato se obtuvieron valores tan bajos como 6 y 2% de oxígeno y relaciones I_D/I_G de 0.3 y 0.2 respectivamente, siendo los segundos los menores documentados hasta la fecha para grafenos exfoliados anódicamente.

Utilizando los grafenos preparados con estos dos electrolitos como soporte, se prepararon nanopartículas de platino por reducción de tetracloroplatinato de potasio (K_2PtCl_4) con borohidruro de sodio ($NaBH_4$). La presencia de los aniones aromáticos sulfonados adsorbidos en la superficie de las láminas no solo contribuye a estabilizar las dispersiones acuosas, sino que facilita el anclaje de las nanopartículas, produciendo híbridos con mayor cantidad y mejor distribución que en experimentos de control sin la presencia de los electrolitos adsorbidos. Estos híbridos fueron estudiados como

catalizadores de las reacciones de reducción de 4-nitrofenol y 4-nitroanilina, de las cuales se sabe que el platino es un excelente catalizador. La distribución de las nanopartículas sobre las láminas contribuye a una mayor eficiencia en la catálisis, y esto se constata al determinar la actividad catalítica para ambos grafenos. Se obtuvieron valores de 11-14 min^{-1} para la reducción de 4-nitrofenol y de 23-57 min^{-1} para la de 4-nitroanilina, valores del mismo orden o superiores a los documentados para nanopartículas de platino en dispersión coloidal.

Queda constatado, por tanto, que estos electrolitos son capaces de cumplir las cuatro funcionalidades propuestas para ellos (intercalación, estabilidad coloidal, remediar la oxidación y anclaje de nanopartículas) de forma excepcional, obteniendo por este método grafeno comparable con el obtenido por sonicación directa mediante ultrasonidos.

Uno de los mayores retos en cuanto a los métodos de producción de grafeno es el rendimiento del proceso. Si el objetivo es disponer de grandes cantidades (o al menos pasar de la escala de miligramos a la de gramos), es necesario que los procesos de preparación tengan una capacidades de producción y rendimientos altos. La capacidad de producción requiere procesos escalables, y aunque apenas se han publicado estudios en los que se describen procesos a escala industrial, la exfoliación electroquímica se plantea como uno de los métodos con mayor potencial de escalabilidad. Si pensamos en términos de rendimiento, la mayor parte de métodos en fase líquida (sonicación directa, cizalla) tienen rendimientos inferiores al 1%, considerando las masas de grafeno obtenido y de grafito de partida. Por otra parte, los rendimientos de grafenos exfoliados electroquímicamente, aunque son mayores que los anteriores, suelen ser relativamente limitados. En el **artículo III** se describe el uso de un pretratamiento del grafito flexible que permite incrementar el rendimiento del proceso hasta un 50%.

El pretratamiento se basa en la inmersión de las piezas de grafito flexible en ácido sulfúrico concentrado durante tiempos de 1 a 72 horas. A continuación se lleva a cabo el proceso de exfoliación electroquímica descrito previamente, esto es, se emplea el grafito como ánodo, un hilo de platino como cátodo y se aplica un potencial de 10 V durante una hora mientras ambos electrodos permanecen sumergidos en una disolución de sulfato potásico 0.1 M.

Durante el tiempo que el grafito flexible está sumergido en ácido sulfúrico se aprecia una leve expansión que aumenta con el tiempo, debido a que este ácido tiene gran afinidad por el grafito y se inserta en los huecos y arrugas propios de su morfología. Mediante difracción de rayos X se puede comprobar que el espaciado de las capas del grafito se mantiene constante durante el proceso, lo cual confirma que no se produce un compuesto de intercalación como tal, sino la acumulación de ácido sulfúrico en los huecos del grafito. Al utilizar el grafito como ánodo en la exfoliación electroquímica descrita arriba, el efecto que tiene el ácido sulfúrico acumulado es de acelerar enormemente el proceso, llegando a un rendimiento del 50% para 48 h de inmersión, en comparación con un rendimiento del 10% para el grafito sin tratar con ácido sulfúrico.

Dado que la exfoliación anódica es un proceso oxidativo y que genera defectos en el grafeno producido, cabe preguntarse si aumentar el rendimiento mediante este tratamiento tiene algún efecto sobre el producto. Para evaluar este efecto, se estudiaron el porcentaje de oxígeno, el espectro Raman y la conductividad del grafeno pretratado, y se compararon los valores con aquellos de grafeno exfoliado anódicamente documentados en la literatura. En efecto, el porcentaje de oxígeno es relativamente alto (~20%, frente a ~10% en el grafeno sin tratar). Sin embargo, esta cifra entra dentro del rango de valores habituales para grafenos preparados anódicamente, que oscilan entre el 10 y el 30%. Por otra parte, los espectros Raman del grafeno preparado con y sin pretratamiento apenas se diferencian, lo que indica que no hay un incremento muy alto en la cantidad de defectos introducidos. Esto se corrobora con la medida de conductividad, de ~35000 S m^{-1}, un valor muy alto y que implica la existencia de dominios de grafeno prístino abundantes y extensos en las láminas. Por otra parte, se estudiaron mediante AFM el grosor de las láminas y se descubrió que no hay variaciones significativas respecto al grafeno obtenido sin pretratamiento, encontrando láminas de menos de 4 capas de grafeno, como es habitual.

En conclusión, al aplicar este pretratamiento sencillo se ha incrementado 5 veces el rendimiento (del 10 al 50%) sin alterar muy sustancialmente las características del grafeno producido.

Si bien los electrolitos más utilizados en la exfoliación anódica de grafeno son sales de sulfato en disolución acuosa, existe la posibilidad de utilizar otras sales, como

se explora en el **artículo IV**. Existen en la literatura trabajos que describen el uso, con diversos grados de éxito, de sales comunes como electrolitos, entre ellos fosfatos, nitratos y halogenuros. Estos últimos han sido sistemáticamente desechados por los grupos de investigación por no ser capaces de dar lugar a la exfoliación. No obstante, habida cuenta de la experiencia de nuestro grupo al evaluar la influencia de las variables del proceso de exfoliación anódica (en concreto el tipo de grafito y la concentración del electrolito), decidimos explorar la posibilidad de exfoliar grafeno utilizando como electrolitos las sales más sencillas que encontramos: halogenuros de sodio.

El primer paso para evaluar el uso de estos electrolitos fue explorar el tipo de grafito usado. Se utilizaron grafito en copos, HOPG y grafito flexible como ánodos en experimentos de exfoliación, y como electrolito una disolución de cloruro de sodio 0.1 M, aplicando un voltaje de 10 V durante una hora. Los tres materiales experimentan una expansión visible, pero el análisis de la morfología de los materiales expandidos muestra que solo en el caso del grafito flexible la expansión da lugar a láminas delgadas (de nanómetros de grosor), que tras sonicación en un medio apropiado producen dispersiones de grafeno. Por el contrario, los otros dos materiales producen láminas muy gruesas que no son estables coloidalmente (por estar compuestas de grafito de muchas capas).

Tras comprobar la importancia del material a exfoliar, se utilizaron como electrolitos disoluciones de cloruro, bromuro y yoduro de sodio en concentraciones desde 0.01 a 1.0 M utilizando como ánodo el grafito flexible. Así, se observó que los tres halogenuros tienen diferentes rangos de concentración en los que producen una exfoliación efectiva del grafito. A concentraciones bajas del electrolito la intercalación es muy débil y apenas se observa expansión del ánodo ni desprendimiento de fragmentos de grafito expandido. A concentraciones superiores se empieza a apreciar la exfoliación, desprendiéndose materiales expandidos que, tras sonicación, producen dispersiones estables de grafeno de pocas capas. No obstante, aunque mayores concentraciones de electrolito generalmente conducen a un aumento de la cantidad de material expandido (ya que aumenta la conductividad de la disolución), esto no redunda directamente en un mayor rendimiento de la producción de grafeno, puesto que se observa que a partir de un cierto umbral de concentración los materiales expandidos ya no producen dispersiones estables tras sonicación, sino que están formados por placas gruesas de grafito en lugar de grafeno de pocas capas. Este rango de concentraciones es

diferente para cada electrolito y relativamente estrecho, y parece ser la razón por la cual estos electrolitos habían sido desechados previamente, ya que habían sido usados en concentraciones demasiado altas.

Si bien los tres halogenuros pueden ser usados como electrolitos en la exfoliación, los grafenos obtenidos no tienen las mismas características en cuanto a oxidación y presencia de defectos, como se comprueba analizándolos mediante XPS y espectroscopía Raman. Estos grafenos tienen porcentajes de oxígeno de 6% (NaCl), 7-8% (NaBr) y 8-11% NaI), valores en general bajos comparados con el valor típico para el grafeno obtenido con Na_2SO_4 (11% de oxígeno). Es importante destacar también que, gracias a las medidas de XPS, sabemos que los grafenos no están funcionalizados con ningún halogenuro, ya que no aparece señal de estos elementos. Esto hace pensar que los halogenuros, además de actuar como electrolitos intercalantes, tienen algún efecto en el mecanismo de la oxidación del grafeno durante la exfoliación. Como se describe en el **artículo II**, durante el proceso de exfoliación se originan especies oxidantes, como el radical hidroxilo (·OH), que dan lugar a la oxidación del grafeno. Estas especies pueden reaccionar mediante diferentes rutas, bien oxidando al ánodo (dando lugar a grafeno oxidado), bien oxidando el electrolito para dar en este caso especies X_2 (X= Cl, Br, I) que contribuyen a la expansión o bien continuar oxidándose para dar O_2, que también contribuye a la expansión del material. Ya que se observa que el contenido en oxígeno de los grafenos obtenidos es en general menor al de referencia (el obtenido con Na_2SO_4, un electrolito que no puede experimentar oxidación), parece evidente que estas rutas que evitan la oxidación del material y promueven su expansión están teniendo lugar en cierta medida al usar los halogenuros como electrolitos. Cabe por tanto plantearse el uso de estas especies (y posiblemente otras) como aditivos de electrolito que sean capaces de evitar la oxidación del grafeno durante la exfoliación anódica, utilizando un electrolito eficiente para la intercalación y exfoliación como es el Na_2SO_4.

El material expandido obtenido de la exfoliación con NaI 0.1 M, lavado y secado sin ningún tratamiento posterior fue utilizado para su evaluación en potenciales aplicaciones energéticas y medioambientales: electrodo para supercondensadores y adsorbente para tratamiento de aguas (retención de disolventes y adsorción de colorante). En el primer caso se obtuvieron valores de capacitancia de ~50 F g^{-1} a 0.1 A g^{-1}, un valor relativamente bajo, pero que junto a una ventana de potencial relativamente alta en medio acuoso (1.4 V frente a ~1 V), proporciona unos valores de densidad de

energía y potencia específicas de 15.3 Wh kg^{-1} y 3220 W kg^{-1} respectivamente. Estos valores se comparan favorablemente con aquellos documentados para materiales de grafeno basados en óxido de grafito que habitualmente requieren procesos de preparación mucho más costosos, laboriosos y complejos. Para el caso de la retención de disolventes, el material expandido tiene capacidades del orden de ~12 a 24 g g^{-1}, similares a los que se obtienen, una vez más, con materiales grafénicos más complejos y menos densos. Por último, su uso como adsorbente de tintes proporcionó valores de capacidad de adsorción de hasta ~920 mg g^{-1}, entre los valores más altos documentados para materiales grafénicos.

En vista de que existen rutas para evitar la oxidación del grafeno obtenido por exfoliación anódica y que hay especies que las promueven, en el **artículo V** se estudió el uso de aditivos de electrolito como especies antioxidantes durante el proceso de exfoliación.

Se llevaron a cabo experimentos de exfoliación anódica en las condiciones habituales: grafito flexible, Na_2SO_4 0.1 M, 10 V durante 1 hora. A este electrolito acuoso estándar se le añadieron diversas especies en diferentes concentraciones como posibles antioxidantes. Los potenciales antioxidantes que se usaron fueron etanol y sales sódicas de citrato, ascorbato, borohidruro y sulfito, así como también los halogenuros de sodio utilizados en el **artículo IV** y cloruro de potasio. Los resultados son muy variados, y en muchos casos se observa una tendencia a aumentar la oxidación del grafeno producido. Sin embargo, en el caso particular de los cloruros de sodio y potasio, para concentraciones de 0.05 M y superiores se obtienen grafenos muy poco oxidados, con contenidos en oxígeno tan bajos como 2%, que es el valor más bajo que se ha descrito para grafeno preparado por exfoliación anódica. Medidas de AFM muestran que las láminas tienen las mismas dimensiones laterales y de grosor que aquellas exfoliadas utilizando solamente Na_2SO_4 (unos pocos cientos de nanómetros y <5 capas de grosor), y el alto valor de conductividad eléctrica (34000 S cm^{-1}) corrobora su alta calidad estructural y baja oxidación. Además, mediante XPS sabemos que las láminas no están funcionalizadas ni con sulfato ni con cloruro, por lo que podemos hablar de grafeno comparable al que se obtiene mediante sonicación de grafito en disolventes orgánicos, o agua con surfactantes.

Al igual que en el trabajo anterior y debido a la similitud de los materiales obtenidos, se estudió el uso del grafito expandido preparado usando Na_2SO_4 y NaCl 0.1 M sin ningún procesado posterior como electrodo para supercondensador y como adsorbente en tratamiento de aguas. La capacitancia de los supercondensadores en electrolito ácido es de 120 F g^{-1} a 0.05 A g^{-1}, mientras que la capacidad de retención de disolventes es de ~15-30 g g^{-1} y la capacidad de adsorción de tintes presenta valores de 130 a 450 mg g^{-1}. Todos estos valores se comparan favorablemente y en algunos casos superan a los documentados en la literatura para materiales grafénicos de características similares, todos ellos con procesos de preparación más complejos y costosos que los materiales aquí descritos.

High quality, low oxygen content and biocompatible graphene nanosheets obtained by anodic exfoliation of different graphite types

J.M. Munuera[a*], J.I. Paredes[a], S. Villar-Rodil[a], M. Ayán-Varela[a], A. Pagán[b], S.D. Aznar-Cervantes[b], J.L. Cenis[b], A. Martínez-Alonso[a], J.M.D. Tascón[a]

[a]*Instituto Nacional del Carbón, INCAR-CSIC, Apartado 73, 33080 Oviedo, Spain*

[b]*Instituto Murciano de Investigación y Desarrollo Agrario y Alimentario (IMIDA), C/Mayor 1, 30150 La Alberca (Murcia), Spain*

[*]Corresponding author. Tel: (+34) 985 11 90 90. E-mail: j.munuera@incar.csic.es (J.M: Munuera)

Abstract

Anodic exfoliation of graphite has emerged as an attractive method to access graphene nanosheets in large quantities, but oxidation reactions associated to this process compromise the structural quality of the resulting materials. Here, we demonstrate that the type of starting graphite material impacts the oxygen and defect content of anodically exfoliated graphenes obtained thereof. We investigated highly oriented pyrolytic graphite (HOPG) as well as graphite foil, flakes and powder as electrode in the anodic process. Importantly, materials with low levels of oxidation and disorder (similar to those typically achieved with cathodic exfoliation approaches) could be attained through proper choice of the graphite electrode. Specifically, using graphite foil afforded nanosheets of higher quality than that of HOPG-derived nanosheets. This discrepancy was interpreted to arise from the structural peculiarities of the former, where the presence of folds, voids and wrinkles would make its exfoliation process to be less reliant on oxidation reactions. Furthermore, cell viability tests carried out with murine fibroblasts on thin graphene films suggested that the anodically exfoliated graphenes investigated here (possessing low or high oxidation levels) are highly biocompatible. Overall, control upon the extent of oxidation and disorder should expand the scope of anodically exfoliated graphenes in prospective applications.

1. Introduction

More than ten years after it could be first isolated by a relatively straightforward exfoliation approach [1], graphene has become one of the most intensively studied objects from the condensed matter physics and materials science fields [2–4]. Although research efforts were originally focused for the most part on purely fundamental aspects related to the exceptional electronic, mechanical, thermal and optical properties of this two-dimensional carbon structure, more recent years have witnessed a shift in emphasis towards its implementation in a wide variety of relevant target applications [4]. However, fulfilling the promise of graphene as a disruptive material in real-life

applications will first and foremost require its large-scale production by methods that should ideally be simple, inexpensive and versatile enough to afford products with characteristics tailored to each intended use. Because no single method known to date can deliver cost-effective graphene materials with high yields and on-demand characteristics at the same time, researchers have directed their efforts towards the development of a pool of bottom-up and top-down fabrication approaches, each of which exhibits its own advantages and drawbacks and is therefore best suited to certain applications [4,5].

Bottom-up production methods are dominated by chemical vapor deposition (CVD) of hydrocarbons onto suitable metal substrates (e.g., copper), which gives access to high quality graphene wafers appropriate for applications in electronics and photonics [5,6]. Unfortunately, issues related to the use of high temperatures and a sacrificial metal or the need of subsequent transfer processes hamper its widespread adoption. Among top-down methods, which are based on the exfoliation of graphite and graphite derivatives [7,8], the so-called graphite oxide route has received a great deal of attention, as it can provide single-layer sheets of graphene oxide (GO) and reduced graphene oxide (RGO) with high throughput and yield [9,10]. Nevertheless, the obtained materials are typically very defective; as a result, many of the attractive physical properties observed in pristine graphene have been found to degrade in GO/RGO [11]. While full structural restoration of the latter has been shown to be feasible, the process relies on the use of very high temperatures (>1500 ºC), making it impractical for most applications [12,13]. Alternatively, defect-free graphene flakes can be procured by direct exfoliation of graphite in the liquid phase, usually with the assistance of ultrasound or shear forces [14–16]. This method readily lends itself to the preparation of colloidal graphene dispersions that can be further processed into useful materials, such as thin films, composites or hybrids, but usually suffers from low yields and relatively limited exfoliation degrees (multilayer graphene), as well as small flake sizes.

Another top-down approach to graphene production that has emerged in recent years is the one based on electrochemical exfoliation of graphite, which boasts such appealing features as simplicity and speed of operation or a strong potential to be scaled-up [17–19]. Although a variety of electrochemical processes have been successfully tested towards this end [19], they can be broadly classified into either (1) cathodic exfoliation in organic solvents (propylene carbonate, dimethyl sulfoxide, etc) containing lithium or alkylammonium salts as the electrolyte [20–24], or in water in some specific cases [25]

or (2) anodic exfoliation in ionic liquid-water mixtures or aqueous solutions of acids (mainly H_2SO_4) or inorganic salts [26–33]. The anodic exfoliation protocols are particularly attractive due to their greener character (use of water/ionic liquids vs. organic solvents) and generally higher and faster production rates. However, contrary to the case of cathodic exfoliation, the obtained graphene materials tend to be decorated with significant amounts of oxygen functional groups that compromise their structural quality [25,28–33]. Such functionalization is thought to be the result of oxidation processes inherent to the application of anodic potentials to the graphite electrode. To alleviate this problem, some researchers have proposed using aqueous solutions of inorganic salts instead of acids as the electrolyte (e.g., K_2SO_4 rather than H_2SO_4) [28,31], but the data available in the literature still reveal a wide variability in oxygen content for anodically exfoliated graphenes prepared through such a strategy [31,33,34].

In addition to the electrolyte nature, we hypothesize that other factors such as the type of graphite used for exfoliation could be critical in determining the oxygen content, and thus the structural quality, of anodically derived graphenes. It is well-known in carbon science that oxidation and intercalation of graphitic materials, the two main processes that are thought to drive anodic exfoliation [27,31], are greatly dependent on their specific microstructure (particle/grain size, presence of imperfections, etc) [35,36]. Consequently, graphene materials with different characteristics and thus a variety of potential uses should be expected when different graphite types are employed, but to the best of our knowledge this question has not yet been studied and elucidated, let alone taken advantage of. In the present work, we address this issue by investigating the anodic exfoliation of several different types of graphite to give graphene nanosheets. The results indicate that the oxygen and defect contents of such graphenes are highly dependent on graphite type, which could be mainly attributed to their morphological peculiarities. More importantly, graphenes with minimized content of oxygen and structural defects can be obtained through judicious choice of the starting graphite. Finally, materials based on anodically exfoliated graphenes could be promising for biomedical applications, but their biocompatibility has not yet been investigated. Hence, we also report here cell proliferation tests on thin films of anodically exfoliated graphenes of different characteristics towards the murine fibroblast cell line L-929, which suggest these types of graphene to be highly biocompatible.

2. Experimental

2.1. Preparation of graphene by anodic exfoliation of different graphite types

Four different types of graphite were used in the present study: highly oriented pyrolytic graphite (HOPG; grade ZYH, obtained from Advanced Ceramics), graphite foil (Papyex I980, obtained from Mersen), natural graphite flakes (ref. 332461, from Sigma-Aldrich) and natural graphite powder (grade 2910, from Mersen). For the electrochemical exfoliation experiments, ~10×10×2 mm^3 pieces of HOPG and graphite foil were employed, whereas the graphite powder and flake materials were pressed into circular pellets (12 mm in diameter, 2 mm in thickness) by means of a hydraulic press. Exfoliation was conducted in a two-electrode system by immersing a graphite piece/pellet and a Pt wire into an aqueous 0.1 M K_2SO_4 solution, which were used as working and counter electrodes, respectively. The Pt wire was placed parallel to the graphite sample at a distance of about 2 cm. Then, a positive voltage (10 V, 0.5 A) was applied to the graphite electrode using a DC power supply (Agilent 6614C apparatus) for periods of time that typically ranged between a few and several minutes. Such a process led to the continuous expansion and detachment of graphite fragments from their parent piece/pellet, which tended to float on the electrolyte solution. This expanded product was then collected, thoroughly rinsed off with copious amounts of Milli-Q water to remove residual salts and dried overnight at room temperature under reduced pressure. Colloidal dispersions of the resulting expanded materials, either in water assisted by flavin mononucleotide (FMN) as an efficient stabilizer or in *N*,*N*-dimethylformamide (DMF), were obtained either through bath sonication (Selecta Ultrasons system, 40 kHz) or, alternatively, by shear mixing (IKA T-25 Ultra-Turrax high-speed homogenizer; rotor diameter: 12.7 mm; rotor-stator gap: 300 μm; rotor speed: 9000 rpm) for 1 h, followed by centrifugation at 200 *g* for 20 min (Eppendorf 5424 microcentrifuge) to sediment the non fully exfoliated or poorly exfoliated graphite fraction. Finally, the top ~75% of the obtained supernatant was collected and stored for further use. In the case of the FMN-stabilized aqueous dispersions, this supernatant was further subjected to two cycles of sedimentation (20000 *g*, 20 min) and resuspension in Milli-Q water to remove the free (non-adsorbed) FMN fraction.

2.2. Characterization techniques

Characterization of the anodically exfoliated graphenes was carried out by UV-vis absorption spectroscopy, field-emission scanning electron microscopy (FE-SEM), atomic force microscopy (AFM), X-ray photoelectron spectroscopy (XPS), attenuated

total reflection Fourier transform infrared (ATR-FTIR) spectroscopy, Raman spectroscopy as well as electrical conductivity measurements. UV-vis absorption spectra were recorded with a double-beam Heλios α spectrophotometer (Thermo Spectronic). FE-SEM images were acquired on a Quanta FEG 650 microscope (FEI Company) at 25 kV. AFM imaging was accomplished with a Nanoscope IIIa Multimode apparatus (Veeco) under ambient conditions in the tapping mode of operation, using Si cantilevers with nominal spring constant and resonance frequency of ~40 N m^{-1} and about 250-300 kHz, respectively. Specimens for AFM were prepared by drop-casting colloidal graphene dispersions (~0.1-0.2 mg mL^{-1}) onto pre-heated (50-60 ºC) SiO_2/Si or freshly cleaved HOPG substrates, which were then allowed to dry. XPS measurements were performed on a SPECS system under a pressure of 10^{-7} Pa with a monochromatic Al K_α X-ray source operated at 100 W. ATR-FTIR spectra were obtained with a Nicolet 3700 spectrometer (Thermo Scientific) using diamond as ATR crystal. Raman spectra were recorded on a Horiba Jobin-Yvon LabRam instrument at a laser excitation wavelength and incident power of 532 nm and 2 mW, respectively. Electrical conductivity measurements were carried out by the van der Pauw method using a home-built setup (Agilent 6614C DC power supply and Fluke 45 digital multimeter). Graphene samples for XPS, ATR-FTIR and Raman spectroscopy, as well as electrical conductivity measurements were prepared in the form of free-standing, paper-like films by vacuum filtration of the corresponding FMN-stabilized aqueous dispersions through either silver or polycarbonate membrane filters 47 mm in diameter and 0.2 μm of pore size (Sterlitech Corporation).

2.3. L-929 cell line viability tests for thin films of anodically exfoliated graphene

The biocompatibility of the anodically exfoliated graphenes was evaluated on the basis of cell proliferation assays carried out on polystyrene culture plates covered by a thin film of the different graphene specimens. Murine fibroblasts (L-929 cell line, ECACC No 85011425) were chosen for these studies, because such a cell type is highly stable, fast-growing and commonly used in cytotoxicity experiments. 48-well tissue culture plates were coated with either ~0.25 or 0.50 mg of each graphene sample by depositing, respectively, 125 or 250 μL of the corresponding FMN-stabilized aqueous dispersion at a concentration of ~2 mg mL^{-1}. Such a procedure led to films with approximate thickness of 1 μm (0.25 mg) and 2 μm (0.50 mg). Following sterilization,

the culture plates were incubated only with pure fetal bovine serum (FBS) at 37 ºC for 2 h to facilitate the initial fibroblast adhesion. Then, the FBS was removed and the culture plates were seeded with the L-929 cells at a density of 5000 cells per well. Dulbecco´s modified Eagle´s medium (DMEM) supplemented with 10% FBS, penicillin (100 U mL^{-1}) and streptomycin (100 mg mL^{-1}) was used as culture medium at 37 ºC in a 7.5% CO_2 atmosphere. This medium was carefully replaced twice a week during the cell growth experiments. Cell proliferation was determined by means of the MTT assay, which is based on the enzymatic reduction of the tetrazolium dye 3-(4,5-dimethylthiazol-2-yl)-2,5-diphenyltetrazolium bromide (MTT) to its corresponding purple formazan. The assays were accomplished 1, 4 and 7 days after cell seeding, each experiment being performed in triplicate. To this end, each well from the seeded culture plates was incubated for 4 h in 500 μL of MTT solution (1 mg mL^{-1}) at 37 ºC under 7.5% CO_2 atmosphere [37]. Then, the MTT solution was removed, 200 μL of dimethyl sulfoxide were added to solubilize the water-insoluble purple formazan crystals formed by reduction of MTT, and the absorbance of the resulting solution was measured with a BMG FLUOstar Galaxy microplate reader (MTX Lab Systems, Inc) at 570 nm as well as 690 nm as the reference wavelength.

3. Results and discussion

3.1. Morphological evolution of different graphite types upon anodic treatment

For our study on the influence of the type of graphite starting material on the characteristics of the graphene obtained from it by electrochemical exfoliation, we applied a positive potential (10 V) to a graphite working electrode in a 0.1 M K_2SO_4 aqueous electrolyte. These specific values were chosen on the basis of very recent studies on the anodic exfoliation of graphite in aqueous solutions of sulfate-based salts [31,38] where such parameters were reported to be optimal for graphite exfoliation. In line with these previous reports [31,33,38], application of such potential to a graphite anode in aqueous electrolyte led to the expansion and detachment of small (up to a few millimetres) fragments of the material. Evidence for such an expansion could be gathered by examining the morphology of these fragments by FE-SEM, with noticeable differences being observed depending on the type of graphite used. Fig. 1a-d shows representative FE-SEM images of the starting HOPG (a,b) and graphite foil (c,d) samples, both for basal plane (a,c) and edge (i.e., prismatic) plane (b,d) views. As could be expected, the basal surface of HOPG appeared essentially flat and featureless (Fig.

1a). In agreement with previous results for this type of graphite [39], more detailed visualization by AFM (Fig. 2a) confirmed a surface topography made up of atomically flat terraces separated by step edges with heights between ~0.35 nm (corresponding to a monolayer-high step) and several nanometers (a few tens of monolayers). This result indicates that the graphene layers in HOPG are very tightly packed with each other, leaving little room, if any, to such imperfections in its structure as voids, ripples or wrinkles. The edge plane surface of the HOPG pieces tended to exhibit a rather compact and relatively rough morphology (Fig. 1b). The latter can be ultimately ascribed to the fact that the edge terminations in the individual graphene layers are typically ill-defined, with a random/uneven combination of zig-zag and armchair configurations that lend a rough profile, as opposed to the atomically flat surface characteristic of the basal plane [40]. On the other hand, the basal surface of the graphite foil samples was seen to be comprised of a disordered stacking of micrometer-sized graphitic platelets that exhibited many flaws such as folds, overlaps or wrinkles (Fig. 1c), whereas their edge surfaces were apparently rather similar to those observed in the case of HOPG (Fig. 1d). AFM imaging (Fig. 2b) corroborated the topographically rugged nature of this type of graphite (compare the magnitude of the vertical scale in the overlaid line profile with that of HOPG in Fig. 2a). As will be discussed below, such differences in the packing configuration of the graphitic layers between HOPG and graphite foil are believed to lead to anodically exfoliated graphene materials with distinct characteristics.

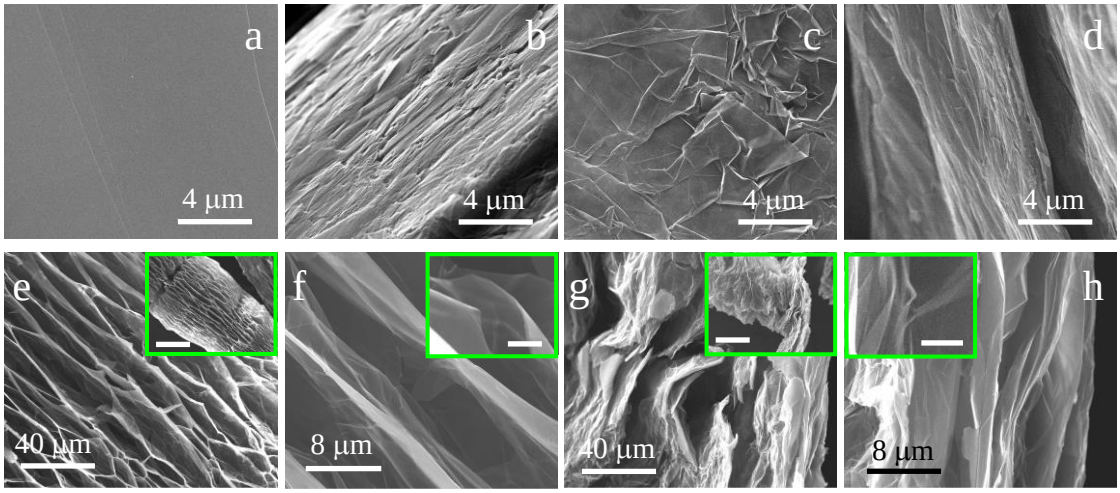

Figure 1. Representative FE-SEM images of the basal (a,c) and edge (b,d) surfaces of the starting HOPG (a,b) and graphite foil (c,d) materials as well as of the edge surfaces of HOPG (e,f) and graphite foil (g,h) after electrochemical exfoliation treatment for 15 min. Scale bars of the inset images: 200 μm (e and g) and 1 μm (f and h).

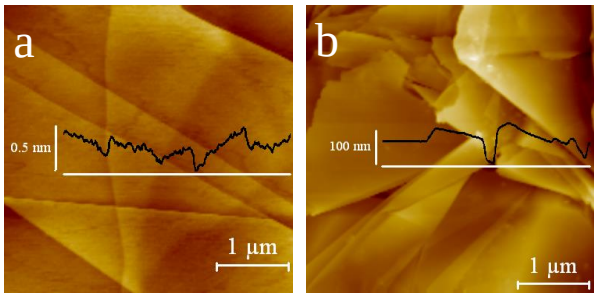

Figure 2. AFM images of the basal surface of the starting HOPG (a) and graphite foil (b) materials. Representative line profiles taken along the marked white lines are shown overlaid on the images.

Following anodic treatment, both the HOPG and graphite foil materials showed evidence of highly expanded structures. Fig. 1e-h presents FE-SEM images of the prismatic surface of detached graphite fragments after 15 min of electrochemical exfoliation for HOPG (e,f) and graphite foil (g,h). The HOPG fragments were frequently found in a more or less uniform, accordion-like expanded form (Fig. 1e and its inset), with large voids many micrometers wide having developed between the cleaved layers. As noticed from Fig. 1f, this type of structure tended to replicate on smaller length scales, so that higher resolution imaging often revealed thinner layers separated by narrower voids (inset to Fig. 1f). Indeed, FE-SEM inspection at the highest

possible magnification disclosed split layers that were at least as thin as a few to several nanometers, indicating that the electrochemical exfoliation process was quite efficient. In the case of the graphite foil samples, the electrochemical expansion led to detached fragments with a much more ill-defined structure on large length scales (Fig. 1g and its inset). We attribute such a result to the particular configuration of this type of graphite discussed above, where the disordered packing of folded and/or wrinkled graphitic platelets would not favor a homogeneous expansion of the layers in an accordion-like fashion similar to that observed for HOPG. Nevertheless, more detailed scrutiny of the expanded structures (Fig. 1h and its inset) indicated that on a local scale very thin layers were effectively separated from one another also in this case, thus suggesting a degree of exfoliation comparable to that attained with the HOPG samples. Further analysis of the exfoliated products by AFM confirmed that this was indeed the case (see below).

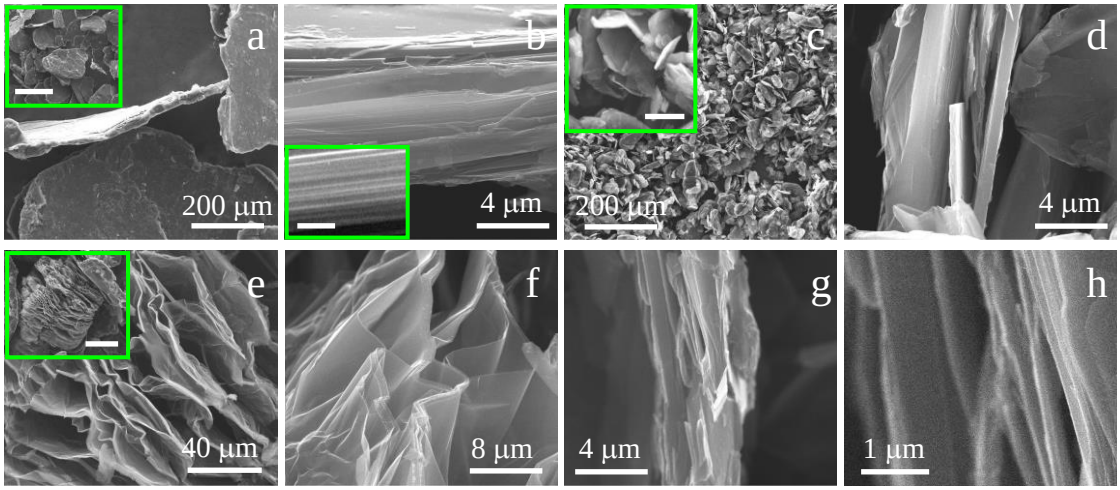

Figure 3. Typical FE-SEM images of the starting graphite flakes (a,b) and powder (c,d), as well as graphite flakes (e,f) and powder (g,h) after electrochemical exfoliation treatment for 3 min. Scale bars of the inset images: 1 mm (a), 250 nm (b), 20 μm (c) and 200 μm (e).

Fig. 3 shows representative results from the FE-SEM observations carried out for the graphite flake and powder samples. The former material was seen to be comprised of slabs ~10-40 μm thick and typical lateral dimensions between 500 and 1000 μm (Fig. 3a and inset). Edge plane views of these slabs (Fig. 3b and inset) indicated that their graphitic planes were organized in a compact, well ordered fashion. The graphite powder material was made up of much smaller particles (Fig. 3c and inset), with typical thickness and lateral dimensions of about 1-4 and 10-50 μm, respectively, and their

graphitic planes displayed a compact arrangement as well (Fig. 3d). For both types of graphite, anodic exfoliation times of 3 min were employed. Due to their small size (especially in the case of the powder samples), the individual graphite particles in the pelletized working electrode tended to expand very quickly during the electrolytic process. This led in turn to the prompt detachment of the particles from the pellet, so that a graphite electrode with a mass comparable to that of the HOPG and graphite foil electrodes used here (~0.5 g) was completely taken apart in 3 min. Such a length of time was sufficient to induce a large, accordion-like expansion of the graphite flakes (Fig. 3e and inset), yielding very thin separated layers (Fig. 3f) similar to those observed for HOPG pieces after 15 min of electrochemical treatment (Fig. 1e and f). Furthermore, we note that the same type of expanded structures was brought about with only 3 min of treatment in HOPG (images not shown). However, the electrochemical expansion was much more limited when using graphite powder (Fig. 3g). In this case, no accordion-like structures were developed and only relatively narrow voids were generated between the thin cleaved layers (Fig. 3h). This result suggests that exfoliation was significantly less efficient with graphite powder compared to the other three types of graphite. We interpret that, due to their small size, the individual graphite particles that comprise a pellet of the powder material are in contact with neighboring particles only at a relatively limited number of points. Thus, a graphite particle on the surface of the pellet that is expanding as a result of the electrochemical treatment in contact with the electrolyte will rapidly loose (electrical) contact with the pellet, so that its expansion will become arrested at a relatively early stage of the process. Hence, the resulting product can be expected to exhibit a limited extent of expansion, as it was indeed the case (Fig. 3g and h). For pellets with much larger particle sizes (i.e., flakes) or monolithic graphite samples (i.e., the HOPG and graphite foil pieces), the expanding particles/fragments will be in contact with the rest of the electrode for longer times, thus enabling higher degrees of expansion. Support for this interpretation was gathered from the observation that detachment of graphitic fragments/particles from the electrodes proceeded at the slowest pace for the HOPG and graphite foil samples, was somewhat faster when using the flake material, and was the fastest with the graphite powder.

3.2. Processing and characteristics of graphene materials derived from anodically exfoliated graphites

Irrespective of the specific morphologies developed during the anodic treatment, the four types of graphite employed here required an additional processing step to complete the exfoliation process. This is the case with almost all the electrochemical exfoliation methods (both anodic and cathodic) that have been reported to this day, and such a step is usually accomplished via sonication in suitable aqueous or organic solvents to afford stable colloidal dispersions of thin, well-exfoliated graphene flakes [19]. We tested the formation of colloidal graphene suspensions from the anodically expanded products both in water assisted by the biomolecule FMN and in the organic solvent DMF. The latter is well known to efficiently stabilize pristine as well as graphite oxide-derived graphene flakes [41–43], whereas FMN, a phosphorylated derivative of riboflavin (vitamin B_2), has been identified as a particularly efficient dispersant of graphene flakes in aqueous medium, delivering high flake concentrations at low FMN/graphene mass ratios [44,45]. The anodically expanded graphites were subjected either to sonication in an ultrasound bath cleaner or to shear mixing in a high speed homogenizer (see Experimental section). We note that shear mixing has been recently put forward as a competitive alternative to sonication in the exfoliation of graphite particles to yield graphene flakes [16,46], but to the best of our knowledge it has not yet been used for the dispersion of electrochemically exfoliated samples.

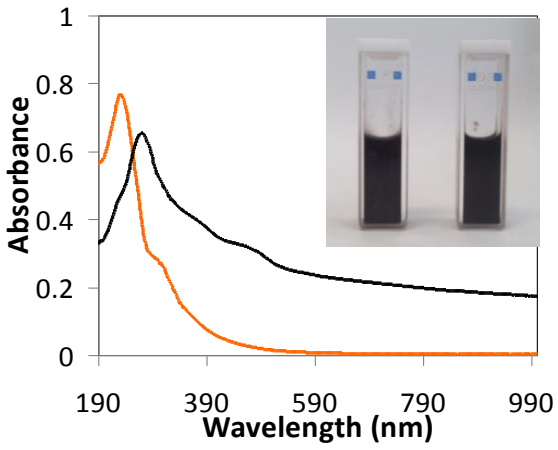

Figure 4. Typical UV-vis absorption spectra of anodically exfoliated graphene dispersed in water with the assistance of FMN as a stabilizer (black trace) and unreduced GO, also dispersed in water (orange trace). Inset: digital photograph of colloidal dispersions of anodically exfoliated graphene derived from graphite foil in water-FMN solution (left cuvette) and DMF (right cuvette).

In our case, both sonication and shear mixing led to the attainment of opaque black dispersions (following a centrifugation step to sediment insufficiently exfoliated fractions) with the four graphite types employed here, and both in FMN/water solution and in DMF. Such dispersions remained visually homogeneous and colloidally stable at least for several weeks, if not months. Two examples of such dispersions (for anodically exfoliated graphite foil after sonication in DMF and FMN/water) are given in Fig. 4 (inset). From UV-vis absorption measurements [45], concentrations of suspended graphitic material between a few tenths of milligram and a few milligrams per milliliter were readily achieved. Fig. 4 (black trace) shows an UV-vis absorption spectrum that was representative of those recorded for the water-based suspensions regardless of graphite type and dispersion method used. All the spectra were dominated by an absorption peak located at ~268-270 nm and strong absorbance in the whole wavelength range above 270 nm, along with two weak shoulders at about 370 and 450 nm. The former two features are known to be characteristic of graphitic, sp^2-based carbon structures [47,48], suggesting the presence of well-exfoliated products in the aqueous medium, whereas the weak shoulders can be attributed to the stabilizing FMN molecules adsorbed onto the graphitic materials [45]. More specifically, the peak at 268-270 nm can be ascribed to $\pi \rightarrow \pi^*$ transitions from electronically conjugated domains in carbon materials [47–49]. The actual position of such a peak is dependent on the size of the conjugated domains (provided that they are of nanometer-sized dimensions), so that a blue-shift in peak position can be expected for domains of decreasing size as a result of quantum confinement effects [49]. This point is relevant for the present anodically exfoliated materials, because the anodic process tends to oxidize the resulting graphene flakes to some extent [19]. For instance, if the graphene lattice became very heavily oxidized, we would expect its structure to contain only tiny conjugated domains, similar to those observed in, e.g., GO sheets prepared by harsh oxidation of graphite in acidic medium [50]. For comparison purposes, the typical UV-vis absorption spectrum of the latter is given in Fig. 4 (orange trace), its absorption peak being located at ~231 nm. From absorbance data taken from the literature [51,52], the peak position at 268-270 nm measured here for all the electrochemically exfoliated materials would be consistent with graphene flakes having oxygen contents similar to or lower than those of well reduced GO samples. As will be shown below, the XPS results were consistent with this conclusion.

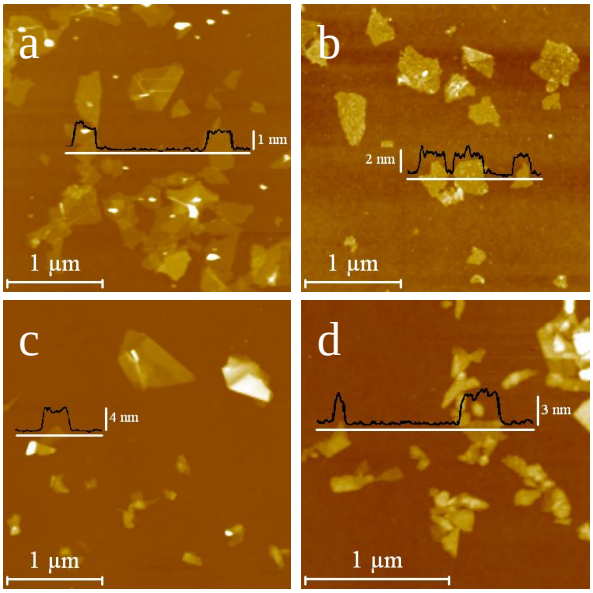

Figure 5. AFM images of anodically exfoliated graphenes obtained from HOPG (a) as well as graphite foil (b), flakes (c) and powder (d). A typical line profile taken along the marked white line is shown superimposed on each image.

The exfoliation degree and lateral size of the graphitic products present in the final colloidal suspensions (i.e., after electrochemical expansion and sonication-/shear mixing-assisted dispersion) was investigated by AFM. Fig. 5 shows typical height images recorded for dispersions derived from HOPG (a) as well as from graphite foil (b), flakes (c) and powder (d), which were drop-cast onto SiO_2/Si substrates. It was observed that both HOPG and graphite foil afforded very thin nanosheets or platelets with lateral dimensions in the 200-600 nm range and apparent thickness mostly between 1 and 2 nm (see representative line profiles overlaid on the AFM images). Considering that AFM measurements of thickness for both pristine and oxidized forms of graphene supported onto SiO_2/Si generally include an artifactual contribution amounting to ~1 nm [53,54], we conclude that the actual thickness of the sheets obtained from HOPG and graphite foil is not greater than about 1 nm, i.e., the sheets comprise no more than three or four monolayers. We note that such a high extent of exfoliation was attained irrespective of treatment time in the electrochemical expansion step. For example, the AFM image of Fig. 5a corresponds to a treatment time of the HOPG piece of 15 min, but the same results were obtained for 3 and 60 min of electrolytic treatment (images not shown). On the other hand, the graphene platelets derived from graphite flakes and

powder (Fig. 5c and d, respectively) tended to be somewhat smaller and thicker. In both cases, their lateral dimensions were between 100 and 400 nm, although larger platelets (up to about 1μm) were occasionally observed, with apparent thickness values mostly in the ~3-4 nm range (for powder) and ~4-5 nm range (for flakes), implying that the exfoliated products were made up of several (typically 6-12) monolayers, even though thicker objects (up to 10-15 nm) were also sometimes present. The typical lateral size and apparent thickness values for the graphene nanosheets obtained from the different graphite types are collected in Table 1.

Because the exfoliated products obtained in the final colloidal dispersions had undergone a sonication/shear-mixing step in addition to the electrolytic process, and the former is known to directly induce the cleavage of graphite to give graphene platelets by itself [14–16], the actual role of the electrochemical treatment in attaining an effective exfoliation was a priori unclear. To address this issue, as a control experiment the different as-received graphites (i.e., those without prior electrochemical expansion) were subjected to the same sonication procedure as that applied to the anodically expanded materials. For HOPG and graphite foil, hardly any material could be exfoliated and dispersed in the liquid phase, and the exfoliated objects were much thicker than 1-3 monolayers, implying that the electrolysis step was critical in the exfoliation process. For graphite flakes and powder the amount of exfoliated material was significant, but estimated to be only about 1/8 of that achieved when the electrochemical expansion step was included, which indicates that such a step was still the main driving force towards exfoliation. However, the apparent thickness of the sonicated-only platelets was mostly ~5-6 nm, compared with ~3-5 nm measured for products with prior electrochemical expansion, suggesting that electrolysis did not have a very strong effect on the exfoliation degree of platelets derived from these two graphite types.

Table 1. Characteristics of anodically exfoliated graphenes obtained from different types of graphite. For each graphene material, the anodic exfoliation time of the corresponding graphite is given in parenthesis.

Graphene material	Lateral size (AFM) (nm)	Apparent thickness (AFM) (nm)	O/C atomic ratio (XPS)	I_D/I_G (Raman)	Electrical conductivity ($S\ m^{-1}$)
Graphite powder (3 min)	100-400	3-4	0.041	0.21	22100
Graphite flakes (3 min)	100-400	4-5	0.068	0.11	57200
Graphite foil (15 min)	200-600	1-2	0.058	0.38	13300
Graphite foil (60 min)	200-600	1-2	0.110	0.82	10300
HOPG (3 min)	200-600	1-2	0.055	0.17	7590
HOPG (15 min)	200-600	1-2	0.091	1.35	4130
HOPG (60 min)	200-600	1-2	0.180	1.23	7910

As mentioned previously, anodic exfoliation of graphite generally leads to oxidation of the resulting graphene materials. Because oxidation can seriously compromise the performance of many graphene-based materials and devices [55], it is important to develop an understanding of the different factors that have a bearing on such a process. To elucidate the possible effects of graphite type and electrolysis time on oxidation, the chemical composition and nature of functional groups present in the different exfoliated products were analyzed by XPS and ATR-FTIR spectroscopy. Fig. 6a,b shows two illustrative XPS survey spectra, corresponding to graphene platelets derived from (a) HOPG (60 min of electrochemical treatment) and (b) graphite powder (3 min of electrochemical treatment). As could be expected, although carbon was the dominant element in all the samples (C 1s peak located at ~285 eV), oxygen was also present to a significant extent (O 1s peak at ~532 eV). However, the amount of oxygen was also seen to differ considerably between the different samples, as can be noticed from their

corresponding O/C atomic ratios given in Table 1. For graphene platelets derived from graphite flakes and powder, the measured O/C ratios (~0.068 and 0.041, respectively) were among the lowest that have ever been reported for anodically exfoliated graphenes. This result could be reasonably anticipated, taking into account the short electrolysis time applied in both cases and the fact that the individual graphite particles were quickly detached from their pellet once they became exposed to the electrolyte solution, thus arresting their oxidation process. Nonetheless, such a limited extent of oxidation was attained at the expense of a comparatively low degree of platelet exfoliation, as noted above. The most enlightening results, though, were those obtained for graphene samples derived from the HOPG and graphite foil materials. First, the oxidation degree of the platelets was seen to increase with increasing electrolysis time. For example, the measured O/C atomic ratios were 0.055, 0.091 and 0.180 for samples derived from HOPG after 3, 15 and 60 min of electrolysis, respectively, even when highly exfoliated platelets were brought about in all cases. Second, and more significantly, for a given electrolysis time the graphene platelets obtained from graphite foil were considerably less oxidized than their HOPG-derived counterparts (e.g., O/C ratios of 0.058 vs. 0.091 and 0.110 vs. 0.180 for 15 and 60 min, respectively, of electrolysis). We note that in all cases the reported amounts of oxygen must have been necessarily introduced during the electrochemical treatment, because the O/C ratios measured for all the as-received graphite types were very small (<0.01).

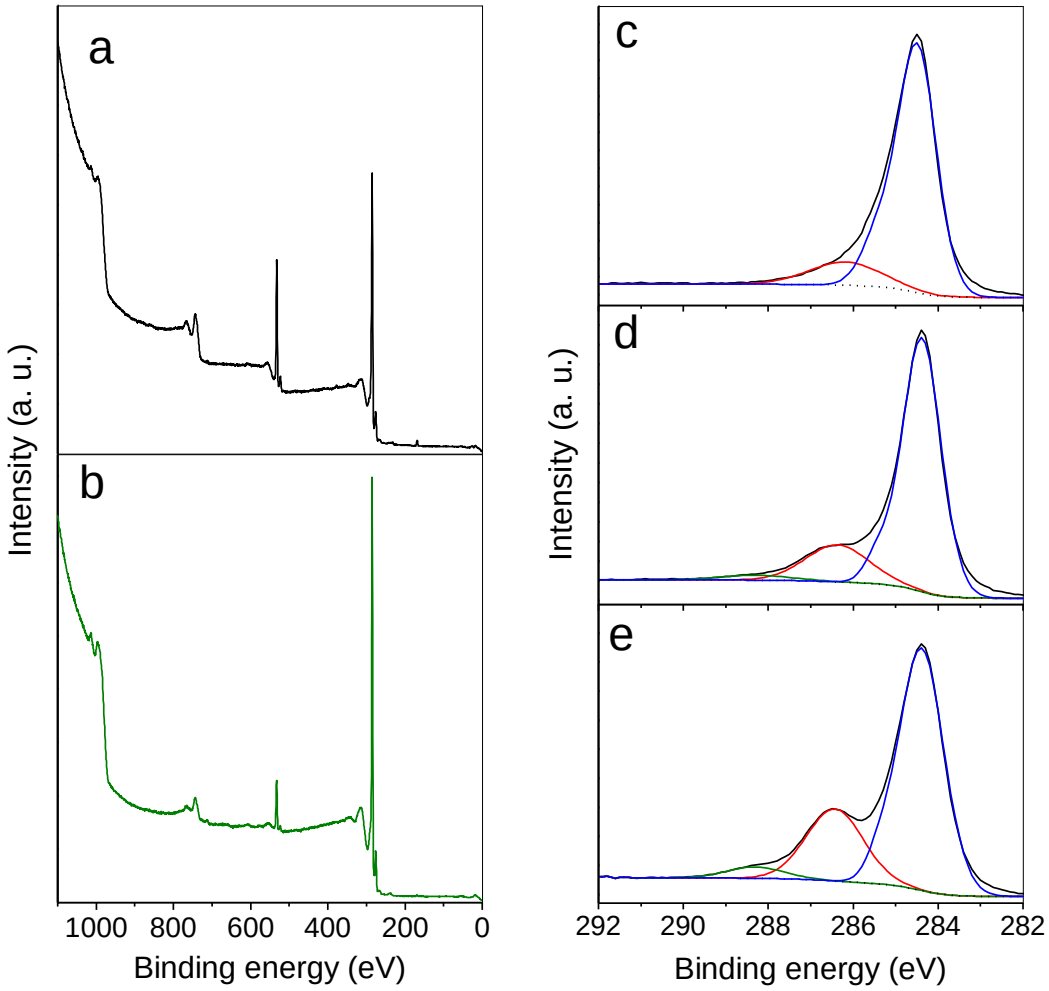

Figure 6. (a,b) Survey XPS spectra of anodically exfoliated graphenes obtained from (a) HOPG (60 min of exfoliation time) and (b) graphite powder (3 min). (c-e) High resolution core level C 1s spectra for graphenes obtained from graphite foil after 15 (c) and 60 (d) min of exfoliation time and (e) HOPG (60 min). In (c-e), components obtained by peak-fitting the experimentally obtained envelopes are indicated by blue, red and green traces.

Information on the specific types of oxygen functional groups generated upon exfoliation was gathered from the high resolution core level C 1s spectra of the samples, as illustrated in Fig. 6c-e for graphenes derived from graphite foil [15 (c) and 60 min (d) of electrolysis] and HOPG [60 min of electrolysis (e)]. The C 1s profiles were dominated by a peak located at ~284.6 eV, which can be ascribed to carbon atoms in unoxidized graphitic environments (C=C species), together with some additional components at higher binding energies that can be attributed to oxidized carbon atoms. More specifically, peak-fitting of these profiles yielded two components in addition to

the main peak at 284.6 eV: one component was centered at about 286.5 eV, associated to C-O species (e.g., hydroxyl or epoxide groups) and the other one was located at ~288.0 eV, which can be assigned to C=O species (e.g., carbonyl groups) [51,56]. The high resolution C 1s spectra of the other graphene samples yielded the same components (results not shown), but as could be expected, it was generally observed that the weight of the C-O and C=O components relative to the main C=C graphitic peak tended to diminish as the O/C atomic ratio of the samples decreased. ATR-FTIR spectroscopy corroborated the presence of these oxygen functional groups, as exemplified in Fig. 7 for some of the graphene samples, derived from graphite powder [3 min of electrochemical exfoliation (a)], graphite foil [15 min (b) and 60 min (c)] and HOPG [60 min (d)]. The following bands were observed for those samples with the highest O/C ratios: 3000-3500 cm^{-1} (O-H stretching vibrations from hydroxyl or carboxyl groups), ~1620 cm^{-1} (C=C stretching, skeletal vibrations from unoxidized graphitic domains) with a shoulder at about 1720 cm^{-1} (C=O stretching vibrations from carbonyl and carboxyl groups), 1300-1450 cm^{-1} (O-H bending vibrations and C-OH stretching vibrations from hydroxyl groups) with a shoulder/edge at ~1260 cm^{-1} (breathing vibrations from epoxy groups) and ~1070 cm^{-1} (C-O stretching in ethers or epoxides) [28,51,57]. Such bands were seen to strongly decline in intensity with decreasing O/C atomic ratio, and were barely discernible for graphene samples with the lowest O/C ratios [e.g., spectrum (a) in Fig. 7].

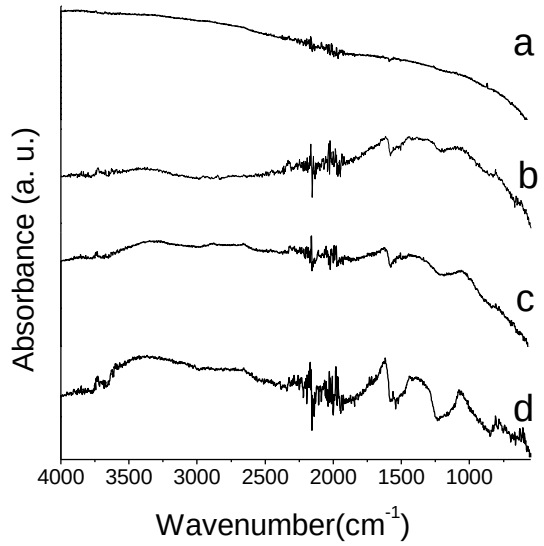

Figure 7. ATR-FTIR spectra of graphene samples obtained from (a) graphite powder (3 min of exfoliation time), (b) graphite foil (15 min), (c) graphite foil (60 min) and (d) HOPG (60 min).

As is well known from some chemically derived forms of graphene (i.e., GO and RGO) [9,11–13,50], oxidation is usually associated to the introduction of a significant amount of defects and structural imperfections in the carbon lattice of graphene sheets, which in turn has an impact on such relevant properties as their electrical conductivity. The structural quality of the anodically exfoliated graphenes was evaluated by means of Raman spectroscopy, as illustrated in Fig. 8 for some of the samples, specifically those derived from graphite powder [3 min (e)], graphite foil [15 min (f) and 60 min (g)] and HOPG [60 min (h)]. The Raman spectra of the starting graphite materials are shown in Fig. 8a-d as a reference. The first-order region of the spectra (1100-1700 cm^{-1}) comprised three peaks with different relative intensities depending on the specific sample: a strong peak located at about 1582 cm^{-1}, the so-called graphitic G band, which is the only band present in completely defect-free graphite/graphene, and two defect-related bands, D and D´, which appear at ~1350 and 1620 cm^{-1}, respectively [58–60]. The starting graphites were seen to have increasing structural quality in the following order: graphite powder, flakes, foil and HOPG. This was numerically reflected in the integrated intensity ratio of the D and G bands (I_D/I_G ratio), which is widely adopted as a quantitative measure of the amount of defects present in graphitic structures [59,60]. Indeed, the I_D/I_G ratios for the starting graphites were 0.10, 0.02, 0.01 and 0, respectively, in the order given above. Generally speaking, the Raman spectra of the graphene samples revealed that the D and D´ bands were typically more intense for those possessing higher O/C ratios, which can be generally taken as a clear indication of their larger extent of structural disorder. The calculated I_D/I_G values of the different graphene samples are given in Table 1, and contrast with the comparatively smaller values obtained for the starting graphites. There were, however, some exceptions to the direct correlation between O/C atomic ratio and I_D/I_G value. For instance, the I_D/I_G ratio measured for graphene obtained by 60 min of electrolysis from HOPG was similar (slightly smaller) that that of the sample prepared by 15 min of electrolysis (1.23 vs. 1.35), even though the O/C ratio was much higher for the former (0.180 vs. 0.091). This result could be due to the fact that, above a certain defect density in the graphene/graphite lattice (in our case, defects are assumed to be mostly generated by oxygen groups covalently attached to carbon atoms), the intensity of the D band decreases, rather than increases, with increasing disorder [59,60]. Likewise, the spatial distribution of the defects, and not just their overall density, is known to have a bearing on the D band intensity, so that, e.g., a graphene sheet with scattered defects can yield a

very different I_D/I_G value compared to that obtained for a sheet where the defects are closely aggregated, even though the overall defect density is the same in both cases [60]. This point could tentatively explain why graphene samples from different graphite types but having similar O/C ratios gave rather different I_D/I_G values in some cases: we speculate that the spatial distribution of their oxygen functional groups, and consequently of their defects, could be affected by the specific type of graphite used.

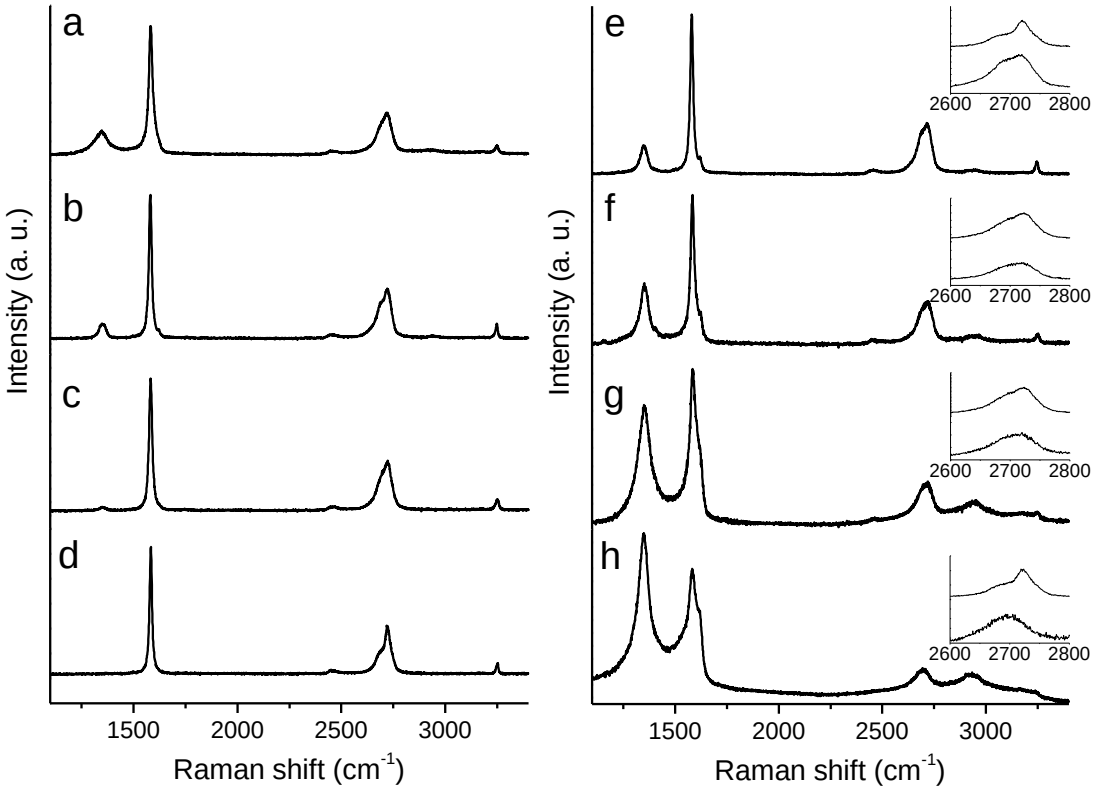

Figure 8. Raman spectra of (a) graphite powder, (b) graphite flakes, and (c) graphite foil, and of (d) HOPG, as well as Raman spectra of graphene samples obtained from (e) graphite powder (3 min of exfoliation time), (f), graphite foil (15 min), (g) graphite foil (60 min) and (h) HOPG (60 min). In the insets, magnified G´ band range for corresponding sample (lower trace) and its parent, non exfoliated graphite (upper trace).

The second-order region of the Raman spectra (2300-3300 cm^{-1}) was dominated by the G´ (or 2D) band, located at about 2700 cm^{-1}. As previously documented in the literature [58] and noticed here from the plots shown in the different insets to Fig. 8e-h, the shape of the G´ band for high quality graphites in bulk, non-exfoliated form was markedly asymmetrical (upper trace in each of the insets). By contrast, this band

became more symmetrical and was slightly down-shifted upon anodic exfoliation to yield the different graphene samples (lower trace in the inset plots). Such features were consistent with these samples being comprised of few- to several-layered sheets [16,59–61], which in turn was in general agreement with the results obtained by AFM and discussed above (Fig. 5).

The starting graphites possess high electrical conductivity values, namely, 1.69×10^6 S m^{-1} in the case of HOPG and 9.84×10^4 S m^{-1} in that of graphite foil. The significant difference in conductivity between these two types of graphite derives from their distinct morphology (see Fig. 1a and 1c, and Fig. 2) and structural quality (Fig. 8c and 8d). Indeed, the already mentioned abundant folds, overlaps and wrinkles present in the platelets of graphite foil must act as dispersion sites for charge carriers, which would limit its conductivity. The electrical conductivity of the graphene samples after their processing into free-standing, paper-like films by vacuum filtration of the corresponding FMN-stabilized aqueous dispersions was also determined, and the results are listed in Table 1. The conductivities of the graphene samples are notably lower than those of their corresponding parent graphites, being dominated by the relatively smaller size of their nanosheets and their relatively high content in oxygen. As could be expected, graphenes with lower O/C and I_D/I_G ratios, and therefore with smaller amounts of structural disorder, tended to be more electrically conductive. Values between ~4000 and 57000 S m^{-1} were measured, which compare favorably with those reported beforehand for other (non-annealed) anodically exfoliated graphenes (4000-25000 S m^{-1}) [29,31,56] and also for high quality graphenes prepared by direct exfolitation of graphite in the aqueous phase using sonication or shear-mixing and colloidally stabilized by surfactants (2000-5000 S m^{-1}) [48,62,63]. We attribute such a positive outcome not only to the relatively low defect content of some of our graphene samples, but also to the fact that FMN was used as a dispersant. It has just been demonstrated that small amounts of this vitamin B_2 derivative are able to colloidally stabilize large quantities of graphene flakes, so that the electrical conductivity of films obtained therefrom is not very significantly degraded by the use of this dispersant, contrary to the case of many surfactants investigated before [45].

The previous results comparing the characteristics of graphene nanosheets derived from different types of graphite are significant in that they suggest that the oxidation degree of the nanosheets can be minimized to a relevant extent simply by a proper choice of the graphite type. This finding would constitute an important asset in the

anodic preparation of graphene, which has been regarded of relatively limited utility (compared to, e.g., cathodic exfoliation approaches) in the pursuit of high quality materials as a result of its extensive introduction of oxygen and related structural defects [17–19]. More to the point, the present results indicate that graphene nanosheets obtained from graphite foil are significantly less oxidized than their HOPG-derived counterparts (see Table 1), even though they are prepared under exactly the same conditions and exhibit the same (high) degree of exfoliation. For instance, the O/C ratio of graphene obtained by 15 min of electrolysis of graphite foil was as low as 0.058, compared with 0.091 for its HOPG-derived equivalent, the former figure being similar to, or even lower than, the values that have been reported for many cathodically exfoliated graphenes [21–24,64,65]. Another advantage of using graphite foil vs. HOPG lies in its much lower price (~$0.1 per gram compared with ~$100 per gram for HOPG).

There still remains the question of why the HOPG and graphite foil materials led to graphene samples with so different degrees of oxidation and structural disorder, considering that both starting graphites were essentially devoid of heteroatoms, oxygen in particular, and defects (as judged by XPS and Raman spectroscopy). We believe that the nanometer- and/or micrometer-scale morphology of the graphite pieces has some influence on their exfoliation process. According to earlier reports [27,31], the anodic exfoliation of graphite in aqueous electrolytic solution proceeds through the following steps: (i) Hydroxyl and oxygen radicals are generated at the graphite anode by the oxidation of water molecules. The anode is then attacked by these radicals, initially at the highly reactive edge sites, leading to an initial expansion of the graphite layers from their edges. (ii) The oxidative expansion of the layer edges facilitates the intercalation of anions from the electrolyte (SO_4^{2-} in our case). These anions can subsequently decompose to give gaseous species (e.g., SO_2), which force the graphite layers apart, leading to their exfoliation. Thus, for HOPG, which is made up of perfectly packed layers with little or no voids in between, we interpret that a sizable intercalation of anions to prompt an effective exfoliation should heavily rely on the oxidation step to open up the layers at their edges and allow the anions in. This inevitably leads to a significant oxidation of the resulting graphene flakes. On the other hand, graphite foil is produced by roll compaction of expanded graphite particles; thus, we can expect it to be riddled with voids and packing imperfections, as was indeed evident from the recorded FE-SEM and AFM images (e.g., Fig. 1c and 2b). Such pre-formed voids would facilitate the direct penetration of anions into this material without requiring some

preliminary oxidation of the graphite layers. As a result, exfoliation of the graphite foil could be readily completed with a limited extent of oxidation compared to the case of HOPG, which would be much more dependent on oxidation for its exfoliation to proceed.

3.3. Biocompatibility of anodically exfoliated graphene films towards the L-929 cell line

Finally, graphene and graphene-based materials are currently the focus of increasing research attention regarding their potential application in biomedicine [4,66,67]. For example, graphene and graphene-containing (bio)polymer films could be used as substrates for cell growth and differentiation or tissue regeneration, with a high biocompatibility of such films being an obvious and necessary pre-requisite. Although previous studies have revealed GO, RGO and CVD-derived graphene substrates to be generally biocompatible towards a number of human and animal cell lines [66–70], to the best of our knowledge no biocompatibility studies are available for electrochemically exfoliated graphenes in general and anodically exfoliated graphenes in particular. Because the latter can be prepared with different physicochemical characteristics (e.g., a range of oxygen and defect contents, as shown above), which in turn can differ significantly from those of GO, RGO and CVD-derived graphene, it is unclear that the results of biocompatibility tests for these types of graphene can be generalized to anodically exfoliated graphenes. Hence, we carried out a preliminary biocompatibility assessment for thin films of several of the graphene samples prepared in this work towards the murine fibroblast cell line L-929. This cell line is commonly employed in the cytotoxicity screening of prospective biomaterials [71], and has already been tested on a number of graphene-based and other carbon substrates [72–78]. The biocompatibility tests were accomplished on thin graphene films deposited from their corresponding FMN-stabilized aqueous dispersions onto polystyrene culture plates. FMN is an innocuous and safe biomolecule used as a food additive, and therefore constitutes an a priori very attractive dispersant of graphene sheets with a view to bio-related applications of this material [45].

The results of the L-929 cell viability tests for several graphene samples, based on the MTT assay and performed 1, 4 and 7 days after cell seeding on ~1 and 2 μm thick graphene films, are summarized in Fig. 9a, b and c, respectively. For comparison purposes, tests were also carried out on thin GO films obtained from aqueous dispersions that were either free of FMN and any other stabilizer (positive control) or

incorporated about the same amount of FMN as that present in the dispersions of anodically exfoliated graphenes (~5 wt. % relative to the graphene content), as well as on the bare culture plates (negative control). The GO dispersions were prepared by oxidation of graphite powder via the Hummers method as described previously [51,52]. In general terms, all the anodically exfoliated graphenes afforded good cell proliferation rates, implying that they are highly biocompatible materials. After 7 days (Fig. 9c), cell proliferation was conspicuously higher for all the graphene samples (including the two GO specimens) compared with the bare culture plate. There were not large differences between the 1 and 2 μm thick films or between the different graphene samples, although some subtle trends could be noticed. For example, comparison of the three graphene samples obtained from HOPG with different exfoliation times (see Table 1) suggested cell proliferation after both 4 and 7 days to increase somewhat with increasing oxygen content of the flakes. This observation would be consistent with the idea that hydrophilic surfaces tend to be better substrates for cell growth because they favour the cell-material interaction [73,79]. Such an effect appeared to be most obvious for the intermediate testing time of 4 days (Fig. 9b), with the highest cell proliferation being detected on the extensively oxidized, and thus more hydrophilic, GO samples (O/C atomic ratios ~0.40-0.45) and the lowest proliferation occurring on the less oxidized and hence more hydrophobic graphenes (e.g., the sample derived from graphite powder). However, factors other than oxygen content/hydrophilicity are also thought to play a role in the promotion of L-929 cell growth on carbon substrates, in particular their electrical conductivity (more conductive substrates allowing for higher proliferation of L-929 cells) [78]. Thus, the fact that the anodically exfoliated graphenes afforded highly conductive films while GO is an electrical insulator could help to explain why cell proliferation on the former eventually caught up with that on GO films after a 7 day period.

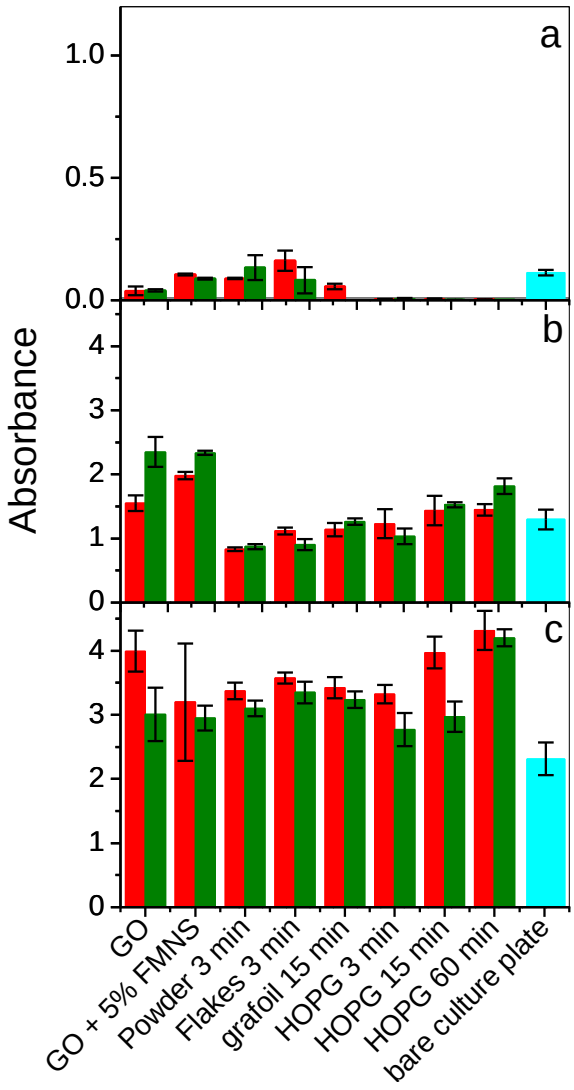

Figure 9. Results of L-929 cell proliferation tests, based on the MTT assay, for thin films of different anodically exfoliated graphenes, as well as GO, deposited from their corresponding aqueous dispersions onto polystyrene culture plates. The anodically exfoliated graphene dispersions used for the tests were colloidally stabilized in water by FMN molecules (FMN/graphene mass ratio of ~0.05), whereas GO dispersions both in the absence and presence of FMN were assessed. Red and green bars indicate ~1 and 2 μm thick films, respectively. The light blue bars correspond to tests performed on the bare culture plate. Results of the MTT assay 1 (a), 4 (b) and 7 (c) days after L-929 cell seeding are shown.

4. Conclusions

We have demonstrated that anodically exfoliated graphenes exhibiting a range of oxygen and defect contents can be attained through the use of starting graphite materials of different characteristics. Significantly, graphene nanosheets with high structural quality and minimized amount of oxygen functional groups (e.g., O/C atomic ratios of

~0.04-0.06) could be obtained by selecting appropriate types of graphite, such as graphite foil. This result was rationalized in terms of the specific microstructure of the starting graphite material and the exfoliation mechanism that is thought to be in place during the anodic process, and provides an avenue to access graphenes of similar quality to that achieved with cathodic exfoliation approaches, while avoiding the use of organic solvents at the same time. The implementation of anodically exfoliated graphenes in a range of potential uses could benefit from the ability to control their extent of oxidation and disorder. For example, graphenes with high oxygen/defect content would be suitable for the nucleation and growth of nanoparticles to produce hybrids for catalytic and biomedical applications, whereas the use of high quality materials would be preferable when good electrical conductivity is required. Irrespective of their oxygen and defect content, the anodically exfoliated graphenes were seen to be highly biocompatible when processed into thin films from their corresponding aqueous dispersions stabilized by the innocuous and safe biomolecule flavin mononucleotide, as determined by cell proliferation tests performed with murine fibroblasts (L-929 line). Finally, the fact that the oxidation degree of anodically exfoliated graphene can be controlled (minimized) by means of some process variables (e.g., graphite type in the present case) suggests that other strategies could also be effective in the pursuit of very high quality nanosheets based on the aqueous anodic approach, and therefore they will be worth exploring in the future.

Acknowledgements

Financial support from the Spanish MINECO and the European Regional Development Fund (projects MAT2011-26399) is gratefully acknowledged. The authors also acknowledge partial funding of this work by Plan de Ciencia, Tecnología e Innovación 2013-2017 del Principado de Asturias and European Regional Development Fund through project GRUPIN14-056. M.A.-V. thanks the receipt of a pre-doctoral contract (FPI) from MINECO.

References

[1] Novoselov KS, Geim AK, Morozov SV, Jiang D, Zhang Y, Dubonos SV, et al. Electric field effect in atomically thin carbon films. Science 2004; 306: 666-9.

[2] Novoselov KS, Fal´ko VI, Colombo L, Gellert PR, Schwab MG, Kim K. A roadmap for graphene. Nature 2012; 490: 192-200.

[3] Randviir EP, Brownson DAC, Banks CE. A decade of graphene research: production, applications and outlook. Mater Today 2014; 17(9): 426-32.

[4] Ferrari AC, Bonaccorso F, Fal'ko VI, Novoselov KS, Roche S, Bøggild P et al. Science and technology roadmap for graphene, related two-dimensional crystals, and hybrid systems. Nanoscale 2015; 7: 4598-810.

[5] Bonaccorso F, Lombardo A, Hasan T, Sun Z, Colombo L, Ferrari AC. Production and processing of graphene and 2d crystals. Mater Today 2012; 15: 564-89.

[6] Zhang Y, Zhang L, Zhou C. Review of Chemical Vapor Deposition of Graphene and Related Applications. Acc Chem Res 2013; 46(10): 2329-39.

[7] Cai M, Thorpe D, Adamson DH, Schniepp HC. Methods of graphite exfoliation. J Mater Chem 2012; 22: 24992-5002.

[8] Zhong YL, Tian Z, Simon GP, Li D. Scalable production of graphene via wet chemistry: progress and challenges. Mater Today 2015; 18(2): 73-8.

[9] Park S, Ruoff RS. Chemical methods for the production of graphenes. Nat Nanotech 2009; 4: 217-24.

[10] Dreyer DR, Park S, Bielawski CW, Ruoff RS. The chemistry of graphene oxide. Chem Soc Rev 2010; 39: 228-40.

[11] Mattevi C, Eda G, Agnoli S, Miller S, Mkhoyan KA, Celik O, et al. Evolution of Electrical, Chemical, and Structural Properties of Transparent and Conducting Chemically Derived Graphene Thin Films. Adv Funct Mater 2009; 19(16): 2577-83.

[12] Rozada R, Paredes JI, Villar-Rodil S, Martínez-Alonso A, Tascón JMD. Towards full repair of defects in reduced graphene oxide films by two-step graphitization. Nano Res 2013; 6(3): 216-33.

[13] Rozada R , Paredes JI, López MJ, Villar-Rodil S, Cabria I, Alonso JA et al. From graphene oxide to pristine graphene: revealing the inner workings of the full structural restoration. Nanoscale 2015; 7: 2374-90.

[14] Coleman JN. Liquid exfoliation of defect-free graphene. Acc Chem Res 2013; 46(15): 14-22.

[15] Ciesielski A, Samorì P. Graphene via sonication assisted liquid-phase exfoliation. Chem Soc Rev 2014; 43: 381-98.

[16] Paton KR, Varrla E, Backes C, Smith RJ, Khan U, O'Neill A, et al. Scalable production of large quantities of defect-free few-layer graphene by shear exfoliation in liquids. Nature Mater 2014; 13: 624-30.

[17] Low CTJ, Walsh FC, Chakrabarti MH, Hashim MA, Hussain MA. Electrochemical approaches to the production of graphene flakes and their potential applications. Carbon 2013; 54: 1-21.

[18] Salavagione HJ. Promising alternative routes for graphene production and functionalization. J Mater Chem A 2014; 2: 7138-46.

[19] Abdelkader AM, Cooper AJ, Dryfe R, Kinloch IA. How to get between the sheets: a review of recent works on the electrochemical exfoliation of graphene materials from bulk graphite. Nanoscale 2015; 7, 6944-56.

[20] Wang J, Manga KK, Bao Q, Loh KP. High-yield synthesis of few-layer graphene flakes through electrochemical expansion of graphite in propylene carbonate electrolyte. J Am Chem Soc 2011; 133(23): 8888-91.

[21] Zhou M, Tang J, Chg Q, Xu G, Cui P, Qin LC. Few-layer graphene obtained by electrochemical exfoliation of graphite cathode. Chem Phys Lett 2013; 572: 61-5.

[22] Abdelkader AM, Kinloch IA, Dryfe RAW. Continuous electrochemical exfoliation of micrometer-sized graphene using synergistic ion intercalations and organic solvents. ACS Appl Mater Interfaces 2014; 6(3): 1632-9.

[23] Cooper AJ, Wilson NR, Kinloch IA, Dryfe RAW. Single stage electrochemical exfoliation method for the production of few-layer graphene via intercalation of tetraalkylammonium cations. Carbon 2014; 66: 340-50.

[24] Zhao M, Guo XY, Ambacher O, Nebel CE, Hoffmann R. Electrochemical generation of hydrogenated graphene flakes. Carbon 2015; 83: 128-35.

[25] Morales GM, Schifani P, Ellis G, Ballesteros C, Martínez G, Barbero C, et al. High-quality few layer graphene produced by electrochemical intercalation and microwave-assisted expansion of graphite. Carbon 2014; 49: 2809-16

[26] Liu N, Luo F, Wu H, Liu Y, Zhang C, J. Chen. One-step ionic-liquid-assisted electrochemical synthesis of ionic-liquid-functionalized graphene sheets directly from graphite. Adv Func Mater 2008; 18(10): 1518-25.

[27] Lu J, Yang J, Wang J, Lim A, Wang S, Loh KP. One-pot synthesis of fluorescent carbon nanoribbons, nanoparticles, and graphene by the exfoliation of graphite in ionic liquids. ACS Nano 2009; 3(8): 2367-75.

[28] Su CY, Lu AY, Xu Y, Chen FR, Khlobystov AN, Li LJ. High-quality thin graphene films from fast electrochemical exfoliation. ACS Nano 2011; 5(3): 2332-9.

[29] Parvez K, Li R, Puniredd SR, Hernandez Y, Hinkel F, Wang S, et al. Electrochemically exfoliated graphene as solution-processable, highly conductive electrodes for organic electronics. ACS Nano 2013; 7(4): 3598-606.

[30] Liu J, Yang H, Zhen SG, Poh CK, Chaurasia A, Luo J, et al. A green approach to the synthesis of high-quality graphene oxide flakes via electrochemical exfoliation of pencil core. RSC Adv 2013; 3(29): 11745-50.

[31] Parvez K, Wu ZS, Li R, Liu X, Graf R, Feng X, et al. Exfoliation of graphite into graphene in aqueous solutions of inorganic salts. J Am Chem Soc 2014; 136(16): 6083-91.

[32] Najafabadi AT, Gyenge E. High-yield graphene production by electrochemical exfoliation of graphite: Novel ionic liquid (IL)–acetonitrile electrolyte with low IL content. Carbon 2014; 71: 58-69.

[33] Rao KS, Sentilnathan J, Cho HW, Wu JJ, Yoshimura M. Soft processing of graphene nanosheets by glycine-bisulfate ionic-complex-assisted electrochemical exfoliation of graphite for reduction catalysis. Adv Funct Mater 2015; 25(2): 298-305.

[34] Liu J, Notarianni M, Will G, Tiong VT, Wang H, Motta N. Electrochemically exfoliated graphene for electrode films: effect of graphene flake thickness on the sheet resistance and capacitive properties. Langmuir 2013; 29(43): 13307-14.

[35] Lang FM, Magnier P, Action of oxygen and carbon dioxide above 100 millibars on "pure" carbon. In: Walker PA, editor. Chemistry and physics of carbon, vol 3, New York; Dekker; 1968 p. 121-209.

[36] Inagaki M, Kang F, Toyoda M. Exfoliation of graphite via intercalation compounds. Chem Phys Carbon 2004; 29: 1-69. In: Radovic LR, editor. Chemistry and physics of carbon, vol 29, New York; Dekker; 2004 p. 1-69.

[37] Vistica DT, Skehan P, Scudiero D, Monks A, Pittman A, Boyd MR. Tetrazolium-based assays for cellular viability: a critical examination of selected parameters affecting formazan production. Cancer Res 1991; 51: 2515-20.

[38] Chen K, Xue D. Preparation of colloidal graphene in quantity by electrochemical exfoliation. J Colloid Interface Sci 2014; 436: 41-6.

[39] Paredes JI, Martínez-Alonso A, Tascón JMD. Multiscale imaging and tip-scratch studies reveal insight into the plasma oxidation of graphite. Langmuir 2007; 23(17): 8932-43.

[40] Warner JH, Schäffel F, Rümmeli MH, Büchner B. Examining the edges of multi-layer graphene sheets. Chem Mater 2009; 21(12): 2418-21.

[41] Park S, An J, Jung I, Piner RD, An SJ, Li X, et al. Colloidal suspensions of highly reduced graphene oxide in a wide variety of organic solvents. Nano Lett 2009; 9(4); 1593-7.

[42] Villar-Rodil S, Paredes JI, Martínez-Alonso A, Tascón JMD. Preparation of graphene dispersions and graphene-polymer composites in organic media. J Mater Chem 2009; 19: 3591-3.

[43] Hernandez Y, Lotya M, Rickard D, Bergin SD, Coleman JN. Measurement of multicomponent solubility parameters for graphene facilitates solvent discovery. Langmuir 2010; 26(5): 3208-13.

[44] Yoon W, Lee Y, Jang H, Jang M, Kim JS, Lee HS, et al. Graphene nanoribbons formed by a sonochemical graphene unzipping using flavin mononucleotide as a template. Carbon 2015; 81: 629-38.

[45] Ayán-Varela M, Paredes JI, Guardia L, Villar-Rodil S, Munuera JM, Díaz-González M, et al. Achieving extremely concentrated aqueous dispersions of graphene flakes and catalytically efficient graphene-metal nanoparticle hybrids with flavin mononucleotide as a high-performance stabilizer. ACS Appl. Mater. Interfaces 2015; 7: 10293−307.

[46] Varrla E, Paton KR, Backes C, Harvey A, Smith RJ, McCauley J, et al. Turbulence-assisted shear exfoliation of graphene using household detergent and a kitchen blender. Nanoscale 2014; 6: 11810-9.

[47] Li D, Müller MB, Gilje S, Kaner RB, Wallace GG. Processable aqueous dispersions of graphene nanosheets. Nature Nanotech 2008; 3: 101-5.

[48] Guardia L, Fernández-Merino MJ, Paredes JI, Solís-Fernández P, Villar-Rodil S, Martínez-Alonso A, et al. High-throughput production of pristine graphene in an aqueous dispersion assisted by non-ionic surfactants. Carbon 2011; 49: 1653-62.

[49] Skoog DA, Holler FJ, Nieman TA, Principles of Instrumental Analysis, Hartcourt Brace & Company, Philadelphia, 1998, ch. 13.

[50] Erickson K, Erni R, Lee Z, Alem N, Gannett W, Zettl A. Determination of the local chemical structure of graphene oxide and reduced graphene oxide. Adv Mater 2010; 22(40): 4467-72.

[51] Fernández-Merino MJ, Guardia L, Paredes JI, Villar-Rodil S, Solís-Fernández P, Martínez-Alonso A, et al. Vitamin C is an ideal substitute for hydrazine in the reduction of graphene oxide suspensions. J Phys Chem C 2010; 114: 6426-32.

[52] Fernández-Merino MJ, Villar-Rodil S, Paredes JI, Solís-Fernández P, Guardia L, García R, et al. Identifying efficient natural bioreductants for the preparation of graphene and graphene-metal nanoparticle hybrids with enhanced catalytic activity from graphite oxide. Carbon 2013; 63: 30-44.

[53] Nemes-Incze P, Osváth Z, Kamarás K, Biró LP. Anomalies in thickness measurements of graphene and few layer graphite crystals by tapping mode atomic force microscopy. Carbon 2008; 46(11): 1435-42.

[54] Solís-Fernández P, Paredes JI, Villar-Rodil S, Martínez-Alonso A, Tascón JMD. Determining the thickness of chemically modified graphenes by scanning probe microscopy. Carbon 2010; 48: 2657-60.

[55] Gómez-Navarro C, Weitz RT, Bittner AM, Scolari M, Mews A, Burghard M, et al. Electronic transport properties of individual chemically reduced graphene oxide sheets. Nano Lett 2007; 7(11): 3499-503.

[56] Wu L, Li W, Li P, Liao S, Qiu S, Chen M, et al. Powder, paper and foam of few-layer graphene prepared in high yield by electrochemical intercalation exfoliation of expanded graphite. Small 2014; 10(7): 1421-9.

[57] Liu J, Poh CK, Zhan D, Lai L, Lim SH, Wang L, et al. Improved synthesis of graphene flakes from the multiple electrochemical exfoliation of graphite rod. Nano Energy 2013; 2(3): 377-86.

[58] Pimenta MA, Dresselhaus G, Dresselhaus MS, Cançado LG, Jorio A, Saito R. Studying disorder in graphite-based systems by Raman spectroscopy. Phys Chem Chem Phys 2007; 9: 1276-91.

[59] Saito R, Hofmann M, Dresselhaus G, Jorio A, Dresselhaus MS. Raman spectroscopy of graphene and carbon nanotubes. Adv Phys 2011; 60(3): 413-550.

[60] Ferrari AC, Basko DM. Raman spectroscopy as a versatile tool for studying the properties of graphene. Nature Nanotech 2013; 8: 235-46.

[61] Hao Y, Wang Y, Wang L, Ni Z, Wang Z, Wang R, et al. Probing layer number and stacking order of few-layer graphene by raman spectroscopy. Small 2010; 6(2): 195-200.

[62] De S, King PJ, Lotya M, O´Neill A, Doherty EM, Hernandez Y, et al. Flexible, transparent, conducting films of randomly stacked graphene from surfactant-stabilized, oxide-free graphene dispersions. Small 2010; 6(3): 458-64.

[63] Zhang L, Zhang Z, He C, Dai L, Liu J, Wang L. Rationally designed surfactants for few-layered graphene exfoliation: ionic groups attached to electron-deficient π-conjugated unit through alkyl spacers. ACS Nano 2014; 8(7): 6663-70.

[64] Huang H, Xia Y, Tao X, Du J, Fang J, Gan Y, et al. Highly efficient electrolytic exfoliation of graphite into graphene sheets based on Li ions intercalation–expansion–microexplosion mechanism. J Mater Chem 2012; 22: 10452-6.

[65] Najafabadi AT, Gyenge E. Synergistic production of graphene microsheets by simultaneous anodic and cathodic electro-exfoliation of graphitic electrodes in aprotic ionic liquids. Carbon 2015; 84: 449-59.

[66] Mao HY, Laurent S, Chen W, Akhavan O, Imani M, Ashkarran AA, et al. Graphene: promises, facts, opportunities, and challenges in nanomedicine. Chem Rev 2013; 113(5): 3407-24.

[67] Zhang H, Grüner G, Zhao Y. Recent advancements of graphene in biomedicine. J Mater Chem. B 2013; 1: 2542-67.

[68] Sanchez VC, Jachak A, Hurt RH, Kane AB. Biological interactions of graphene-family nanomaterials: an interdisciplinary review. Chem Res Toxicol 2012; 25(1): 15-34.

[69] Yang K, Li Y, Tan X, Peng R, Liu Z. Behavior and toxicity of graphene and its functionalized derivatives in biological systems. Small 2013; 9(9-10): 1492-503.

[70] Akhavan O, Ghaderi E, Abouei E, Hatamie S, Ghasemi E. Accelerated differentiation of neural stem cells into neurons on ginseng-reduced graphene oxide sheets. Carbon 2014; 66: 395-406.

[71] Biological evaluation of medical devices. Part 5: Tests for in vitro cytotoxicity. ISO 10993-5: 2009.

[72] Chen H, Müller MB, Gilmore KJ, Wallace GG, Li D. Mechanically strong, electrically conductive, and biocompatible graphene paper. Adv Mater 2008; 20(18): 3557-61.

[73] Yan X, Chen J, Yang J, Xue Q, Miele P. Fabrication of free-standing, electrochemically active, and biocompatible graphene oxide−polyaniline and graphene−polyaniline hybrid papers. ACS Appl Mater Interfaces 2010; 2(9): 2521-9.

[74] Fan H, Wang L, Zhao K, Li N, Shi Z, Ge Z, et al. Fabrication, mechanical properties, and biocompatibility of graphene-reinforced chitosan composites. Biomacromolecules 2010; 11(9): 2345-51.

[75] Sayyar S, Murray E, Thompson BC, Gambhir S, Officer DL, Wallace GG. Covalently linked biocompatible graphene/polycaprolactone composites for tissue engineering. Carbon 2013; 52: 296-304.

[76] Correa-Duarte MA, Wagner N, Rojas-Chapana J, Morsczeck C, Thie M, Giersig M. Fabrication and biocompatibility of carbon nanotube-based 3d networks as scaffolds for cell seeding and growth. Nano Lett 2004; 4(11): 2233-6.

[77] Lobo AO, Corat MAF, Antunes EF, Palma MBS, Pacheco-Soares C, Garcia EE, et al. An evaluation of cell proliferation and adhesion on vertically-aligned multi-walled carbon nanotube films. Carbon 2010; 48 (1): 245-54.

[78] Kim SI, Sahu BB, Kim SE, Ali A, Choi EH, Han JG. Controlling conductivity of carbon film for L-929 cell biocompatibility using magnetron sputtering plasmas. J Mater Chem B 2015; 3(16): 3267-78.

[79] Akhavan O, Ghaderi E. The use of graphene in the self-organized differentiation of human neural stem cells into neurons under pulsed laser stimulation. J Mater Chem B 2014; 2(34): 5602-11.

ARTÍCULO II

Electrolytic exfoliation of graphite in water with multifunctional electrolytes: en route towards high quality, oxide–free graphene flakes†

J.M. Munuera, J.I. Paredes, S. Villar–Rodil,* M. Ayán–Varela, A. Martínez–Alonso, J.M.D. Tascón

Instituto Nacional del Carbón, INCAR-CSIC, Apartado 73, 33080 Oviedo, Spain

* E–mail: silvia@incar.csic.es

† Electronic Supplementary Information (ESI) available: Experimental set–up for the electrolytic anodic treatments; visual and microscopic evidence for the expansion of graphite foil upon anodic treatment; evidence for the electrolytic treatment being the critical step in the exfoliation; additional AFM characterization of the samples; additional XPS characterization of the samples; measurement of film thickness by FE–SEM; derivatization and XPS analysis of the graphene flakes obtained by anodic treatments using SS as electrolyte; UHPLC/MS of the product of SNDS oxidation; demonstration for starting graphites other than graphite foil; growth of Pt NPs on electrolytically exfoliated graphene in the absence of amphiphile electrolyte/dispersants.

Abstract

Electrolytic – usually referred to as electrochemical – exfoliation of graphite in water under anodic potential holds enormous promise as a simple, green and high–yield method for the mass production of graphene, but currently suffers from several drawbacks that hinder its widespread adoption, one of the most critical being the oxidation and subsequent structural degradation of the carbon lattice that is usually associated to such a production process. To overcome this and other limitations, we introduce and implement the concept of multifunctional electrolytes. The latter are amphiphilic anions (mostly polyaromatic hydrocarbons appended with sulfonate groups) that play different relevant roles: (1) intercalating electrolyte to trigger exfoliation of graphite into graphene flakes, (2) dispersant to afford stable aqueous colloidal suspensions of the flakes suitable for further use, (3) sacrificial agent to prevent graphene oxidation during exfoliation and (4) linker to promote nanoparticle anchoring on the graphene flakes, yielding functional hybrids. The implementation of this strategy with some selected amphiphiles even furnishes anodically exfoliated graphenes of a quality similar to that of flakes produced by direct, ultrasound– or shear–induced exfoliation of graphite in the liquid phase (i.e., almost oxide- and defect–free). These high quality materials were used for the preparation of catalytically efficient graphene–Pt nanoparticle hybrids, as demonstrated by model reactions (reduction of nitroarenes). The multifunctional performance of these electrolytes is also discussed and rationalized, and a mechanistic picture of their oxidation–preventing ability is proposed. Overall, the present results open the prospect of anodic exfoliation as a competitive method for the production of very high quality graphene flakes.

1. Introduction

Boasting exceptional physical properties and a strong potential for application in many critical technological areas, including electronics, photonics, energy conversion/storage, catalysis and biomedicine, graphene is set to become one of the key materials of the next few decades.[1–4] However, despite the enormous progress attained over the last years, issues related to the mass production of this two–dimensional form of carbon with on–demand specifications by cost–effective means have not yet been settled and constitute a significant obstacle in the path of graphene-based disruptive technologies.[4] In this endeavor, top–down fabrication approaches, which rely on the exfoliation of graphite and graphite derivatives, are the focus of considerable research

efforts, as they offer the opportunity to access very large quantities of graphene flakes suitable for a wide range of prospective applications starting from an abundant and affordable source material.[4–6]

Currently, three main top–down methods of graphene production that are particularly promising in terms of scalability can be identified:[7] (i) exfoliation and subsequent reduction of graphite oxide, (ii) direct exfoliation of graphite in the liquid phase, and (iii) electrolytic exfoliation of graphite. The graphite oxide route is particularly attractive in that it can provide very large quantities of single–layer sheets, in the form of both graphene oxide (GO) and reduced graphene oxide (RGO), which have been found useful in a range of potential applications.[8–12] Nevertheless, the carbon lattice in GO and RGO is generally riddled with oxygen groups and structural defects derived from the harsh oxidation process, which have traditionally limited their wider utility in the graphene realm.[7,13,14] On the other hand, very high quality graphene can be obtained by direct liquid–phase exfoliation of graphite, usually triggered by ultrasound waves or shear forces.[15–17] This method naturally affords colloidal dispersions of defect–free graphene flakes that can be further processed into valuable materials, such as thin conductive films, polymer composites or hybrid structures, but on the downside it suffers from low exfoliation yields (typically <1 wt. %) and the as–prepared materials are frequently dominated by multilayer (mostly 3–8) rather than single– or few–layer (<4) flakes.[16,17] By contrast, electrolytic exfoliation of graphite has been shown to overcome, at least in part, some of the main limitations of the two previous approaches.[18–20] Specifically, this method can provide graphene samples at relatively high yields consisting of single– and few–layer flakes of a structural quality better than that of reduced graphene oxide. As a result, electrolytically exfoliated graphenes have recently started to be explored towards their use as, e.g., electrodes for supercapacitors[21,22] and lithium–sulfur batteries,[23] metal–free catalysts,[24] catalyst supports[25] or electromagnetic interference shielding devices.[26]

Overall, electrolytic processes for the exfoliation of graphite into graphene can be of either cathodic or anodic nature.[20] Cathodic exfoliation is mostly based on the use of lithium or alkylammonium salts dissolved in organic solvents (e.g., propylene carbonate or dimethyl sulfoxide) as the electrolytic medium,[27–31] whereas anodic exfoliation is usually carried out in water in the presence of ionic liquids, acids or inorganic salts,[24,25,32–36] being therefore more attractive from an environmental standpoint and also generally in terms of production rates. Nevertheless, the anodic approach currently

suffers from some significant drawbacks. First, to be useful for further processing purposes the exfoliated materials frequently need to be dispersed in the liquid phase to afford colloidal suspensions. Due to their predominant hydrophobic nature, anodically exfoliated graphenes are typically dispersed in organic solvents such as *N*,*N*–dimethylformamide,[24,25,33–35] whose efficiency to colloidally stabilize graphene flakes has been established in earlier studies.[37–39] For many prospective uses of this type of graphene, however, water would be the preferred dispersing medium, and in such a case the use of surfactants or other stabilizers becomes essential.[15,16] Thus, the anodic preparation of graphene could be deployed to a greater advantage if chemical species with the ability to act efficiently both as an electrolyte during the anodic exfoliation and as a dispersant to stabilize the resulting graphene flakes in water were identified. Some previous work using, e.g., sodium dodecyl sulfate or copper phthalocyanine tetrasulfonic acid has suggested such a strategy to be feasible.[40–42] However, systematic studies to identify effective species for this dual role, as well as to rationalize their performance and compare it by some quantifiable metric would be needed to make the most of this approach, but have not yet been undertaken.

Second, anodically exfoliated graphenes tend to be significantly oxidized due to the generation of reactive oxygen species from water at the graphite anode, their oxidation degree being generally comparable to that found for RGO.[19,20] Similar to the case of the latter, this generally unwanted effect induces structural degradation in the resulting graphenes and compromises their application scope. To address this issue, researchers have explored some approaches to curtail the extent of graphene oxidation, for example the use of inorganic salts instead of acids as the electrolyte,[34] certain additives in combination with the electrolyte[43] or specific types of graphite as the anode.[44] Nevertheless, when these improved graphenes are compared with their corresponding reference samples, such efforts are seen to be successful only to a limited degree. Indeed, no anodic exfoliation strategy reported to date has afforded graphene flakes that exhibit a quality similar to that of flakes obtained by direct liquid–phase exfoliation of graphite, i.e. graphenes that are essentially oxide– and defect–free. Attaining such a goal would thus constitute a significant step forward.

With the aim of providing a unified solution to the abovementioned issues, we have conducted an investigation into a pool of electrolytes towards the anodic exfoliation of graphite into graphene, the results of which are reported here. First, a number of readily available amphiphilic anions are demonstrated to be effective as both exfoliating

electrolyte and dispersant, easily affording aqueous colloidal suspensions of well–exfoliated graphene flakes. The performance of these chemical species in such a dual role is quantitatively compared and rationalized. Second, several of the newly identified electrolytes are also shown to prevent oxidation of the graphene flakes to a large extent, an ability that can be related to their propensity to get themselves oxidized by reactive oxygen species. Moreover, graphene flakes with chemical make–up and structural quality comparable to those typical of samples produced by direct ultrasonic or shear exfoliation of graphite are obtained using the best electrolytes. Finally, adding to the multifunctional nature of these electrolytes, we demonstrate the growth of Pt nanoparticles (NPs) onto the electrolyte–stabilized graphene flakes. The resulting graphene-Pt NP hybrids were seen to possess a remarkably high catalytic activity, as evaluated on the basis of model reduction reactions with nitroarenes.

2. Experimental

2.1. Materials and reagents

High purity graphite foil (Papyex I980, acquired from Mersen) was used as starting material throughout the study. The following chemical species were tested as electrolyte in the anodic exfoliation of graphite in aqueous medium: sodium sulfate (SS), sodium dodecyl sulfate (SDS), sodium methanesulfonate (SMS), sodium benzenesulfonate (SBS), disodium benzene–1,3–disulfonate (SBDS), sodium *p*–toluenesulfonate (STS), sodium *p*–toluate (SPT), sodium dodecylbenzene sulfonate (SDBS), disodium naphthalene–1,5–disulfonate (SNDS), disodium naphthalene–2,6–dicarboxylate (SNDC), trisodium naphthalene–1,3,(6,7) –trisulfonate (SNTS), sodium pyrene–1–sulfonate (SPS) and tetrasodium pyrene–1,3,6,8–tetrasulfonate (SPTS). These chemicals were obtained from Sigma–Aldrich, either as such or in their corresponding acid form, which was then converted to the sodium salt by mixing with the appropriate molar amount of NaOH.

2.2. Anodic exfoliation and dispersion of graphite in water with different electrolytes

The anodic exfoliation process was carried out in a two–electrode configuration, using a graphite foil piece (40×25×0.5 mm^3) as working electrode and a platinum wire as counter electrode. The two electrodes were submerged in an aqueous solution (20

mL) of a given electrolyte at a certain concentration (specified below), and then a positive voltage (10 V) was applied to the graphite electrode for 60 min using an Agilent 6614C DC power supply. The platinum wire was placed parallel to the graphite foil surface at a distance of about 2 cm. A digital photograph of the experimental set–up is depicted in Fig. S1 of the ESI†. During the electrolytic treatment, the graphite sample was typically seen to swell and expand. Visual and microscopic evidence for such expansion are given in Fig. S2 of the ESI†. After the 60 min electrolysis period, the resulting expanded product was gently scraped with a spatula from its parent graphite piece and transferred directly to the working aqueous solution. The latter was subsequently sonicated for 3 h in an ultrasound bath cleaner (J.P. Selecta Ultrasons system, 40 kHz). The obtained dispersion was purified by two cycles of sedimentation via centrifugation (20000*g*, 20 min; Eppendorf 5424 microcentrifuge) and re-suspension in Milli–Q water with a brief (2–3 min) sonication, and finally subjected to a mild centrifugation step (200*g*, 20 min) to remove the non–exfoliated or poorly exfoliated graphite fraction from the resulting supernatant, which was collected for further use. The concentration of graphene in the final supernatant was taken as a metric for the overall efficiency of the investigated chemical species in the dual role of exfoliating (intercalating) electrolyte and dispersant. Following previously reported protocols, the concentration was determined by UV-vis absorption spectroscopy (double-beam Heλios α instrument, from Thermo Spectronic) based on the Lambert-Beer law and using a value of 2440 mL mg^{-1} m^{-1} for the extinction coefficient at the measured wavelength of 660 nm.[45,46]

2.3. Synthesis and catalytic activity of anodically exfoliated graphene–Pt NP hybrids

Graphene–Pt NP hybrids were prepared from several of the previously obtained aqueous graphene dispersions by the following procedure: 9 mL of a given anodically exfoliated graphene suspension (0.2 mg mL^{-1}) were heated at 85 ºC under magnetic stirring in a 20 mL test tube sealed with a septum. Then, 1 mL of 1.1 mM aqueous K_2PtCl_4 solution was added and the mixture was magnetically stirred at the mentioned temperature for 2 h. To remove unreacted Pt salt, the resulting product was centrifuged at 20000 *g* for 20 min and resuspended in Milli–Q water via sonication for 1–2 min. Subsequently, 20 μL of 1.5 M $NaBH_4$ were added to the suspension and allowed to react for 45 min at room temperature. Following this step, the final product was purified

by two cycles of sedimentation via centrifugation (20000 *g*, 20 min) and resuspension in Milli–Q water. The catalytic activity of the obtained graphene–Pt NP hybrids was evaluated on the basis of two model reactions with nitroarenes: the reduction of 4–nitrophenol (4–NP) and 4–nitroaniline (4–NA) to 4–aminophenol (4–AP) and *p*–phenylenediamine (*p*–PDA), respectively, in aqueous medium at room temperature using $NaBH_4$ as a reductant. To this end, mixed aqueous solutions containing 0.06 mM of the nitroarene, 36 mM of $NaBH_4$ and 1.8–4.8 μg mL^{-1} of graphene flakes decorated with Pt NPs (amounting to concentrations of the latter of 0.8–2.1 μM) were freshly prepared and the reaction progress was monitored by measuring their optical density at a given wavelength at 0.25 s intervals with UV–vis absorption spectroscopy. For reasons that will be discussed below, the monitored wavelengths were 400 and 380 nm in the case of 4–NP and 4–NA, respectively.

2.4. Characterization techniques

Characterization of the samples was accomplished by UV–vis absorption spectroscopy, Raman spectroscopy, X–ray photoelectron spectroscopy (XPS), scanning transmission electron microscopy (STEM), transmission electron microscopy (TEM), atomic force microscopy (AFM), inductively coupled plasma-mass spectrometry (ICP–MS) and measurement of electrical conductivity. Raman spectra were recorded with a Horiba Jobin–Yvon LabRam instrument using a laser excitation wavelength of 532 nm at an incident power of 2.5 mW. XPS measurements were performed on a SPECS apparatus under a pressure of 10^{-7} Pa with a non-monochromatic Mg K_α X–ray source (11.81 kV, 150 W). Samples for both Raman spectroscopy and XPS were prepared by drop-casting the corresponding suspension onto a pre-heated (~50–60 ºC) circular stainless steel sample-holder 12 mm in diameter and allowing it to dry. STEM imaging was accomplished with a Quanta FEG 650 system (FEI Company) operated at 30 kV, while TEM images were acquired on a JEOL 2000 EX–II instrument operated at 160 kV. For STEM and TEM, specimens were prepared by mixing the corresponding suspension with an equal volume of ethanol, and then 40 μL of the resulting dispersion were drop-cast onto a copper grid (200 square mesh) covered with a carbon film (Electron Microscopy Sciences) and allowed to dry under ambient conditions. AFM imaging was conducted with a Nanoscope IIIa Multimode apparatus (Veeco Instruments) under ambient conditions in the tapping mode of operation. To this end,

rectangular silicon cantilevers with nominal spring constant and resonance frequency values of 40 N m^{-1} and 250–300 kHz, respectively, were employed. Either highly oriented pyrolytic graphite (HOPG) pieces or SiO_2 (300 nm)/Si wafers were used as substrates for AFM. The substrates were pre–heated at ~50–60 ºC and then a small volume (20–40 μL) of graphene dispersion (~0.05 mg mL^{-1}) was drop–cast and allowed to dry. ICP-MS analysis of graphene–Pt NP hybrids was carried out with a 7500ce apparatus (Agilent) furnished with an octopole collision/reaction cell to destroy interfering ions. Before analysis, the samples were subjected to microwave-assisted acid digestion. To measure electrical conductivity, the graphene samples were processed into free–standing paper–like films by vacuum filtration of the corresponding colloidal dispersions through silver membrane filters 25 mm in diameter and 0.2 μm of pore size (Sterlitech Corporation). Then, 12×12 mm^2 square pieces were cut from the films and their conductivity was determined through the van der Pauw method by means of a homemade setup (Agilent 6614C potentiostat and Fluke 45 digital multimeter). The thickness of the films was estimated by field–emission scanning electron microscopy (FE–SEM, Quanta FEG 650 system, from FEI Company).

3. Results and discussion

3.1. Electrolytes with dual functionality towards the anodic exfoliation and dispersion of graphite in water

As a first step in the investigation, we sought to identify chemical species that function both as efficient electrolytes to promote the anodic exfoliation of graphite in water and as dispersants to colloidally stabilize the resulting graphene flakes. Therefore, some rationale had to be first established in the selection of the potential candidates that were subsequently evaluated. To this end we note that, according to previous reports,[32,34] the anodic exfoliation of graphite in aqueous electrolytic solution relies on the following two basic processes: (1) pre–expansion of the graphite layers, starting at edge sites, through attack by hydroxyl and oxygen radicals generated from the oxidation of water molecules at the anode; (2) subsequent separation of the pre–expanded layers (i.e., exfoliation) as a result of the intercalation of anions from the electrolyte. This mechanism implies that successful chemical species that can both exfoliate and colloidally stabilize graphite by the approach investigated here have to be of anionic nature. In addition, it is well known that the essentially hydrophobic character of graphene requires the use of amphiphilic molecules for it to be colloidally stabilized in

water, and anodically exfoliated graphene is no exception in this regard.[15,16] Such amphiphilic dispersants typically consist of a non–polar, hydrophobic component that adsorbs onto the graphene surface and a polar, hydrophilic moiety that extends into the aqueous medium.[16,47,48] With these considerations in mind, we selected a number of molecules incorporating a hydrophobic (aromatic– and/or alkyl–containing) section appended with one or several anionic groups that were intended to serve both as the polar moiety required to make up the amphiphilic structure and as the anions that drive the intercalation of the molecule during the electrolytic process. Although several anions have been previously tested for electrolytic intercalation of graphite (e.g., sulfate, phosphate, nitrate or tetrafluoroborate),[24,32–34,49] sulfates and sulfonates were mostly chosen for the present work, as they are known to be particularly efficient towards this purpose and can also be readily combined with organic moieties to form amphiphilic molecules.

Table 1 lists the name, chemical structure and acronym used for the species tested here as potential electrolyte/dispersant, which generally comprise an alkyl (e.g., dodecyl) or aromatic (benzene, naphthalene or pyrene) moiety appended with one, two, three or four sulfonate groups. We note that some of these molecules have already been used as dispersants in the direct exfoliation (via sonication) of graphite to give graphene.[47,50,51] However, the high efficacy of a given amphiphile as a graphene dispersant is not expected to guarantee its success as intercalating electrolyte and, therefore, that it can be considered an efficient electrolyte/dispersant overall. To provide some quantitative measure of overall performance, we carried out benchmark tests based on a protocol that comprised the following steps (described in detail in the Experimental section): (1) anodic treatment of a graphite piece of set dimensions in aqueous solution of a given chemical species; (2) bath sonication of the anodically expanded product in the same solution; (3) purification of the resulting dispersion by sedimentation via centrifugation and subsequent re–suspension in Milli-Q water; (4) determination of the concentration of graphene material in the final dispersion by UV-vis absorption spectroscopy. The results of such tests performed for the different chemical species at various molar concentrations are summarized in Table 1. Before discussing them in detail, we note that in many cases the described preparation protocol led to homogeneous, opaque black suspensions, as exemplified in Fig. 1a with SNTS, SPTS and SNDS, which were seen to be colloidally stable for weeks to months. Fig. 1b shows some representative UV–vis absorption spectra of the dispersions. The spectra

were dominated by an intense band located at ~270 nm, together with strong absorbance in the 300–1000 nm wavelength range. These features were nearly identical to those observed previously for both reduced graphene oxide and pristine graphene flakes,[47,52,53] and are known to reveal the presence of graphitic material possessing extended electronically conjugated domains. Additional bands of varied intensity located in the 200–400 nm wavelength range were also quite frequently noticed in the spectra of the obtained suspensions. Control experiments indicated that they were associated to the chemical species used as electrolyte/dispersant, and more specifically to their aromatic moieties ($\pi \rightarrow \pi^*$ transitions).[54]

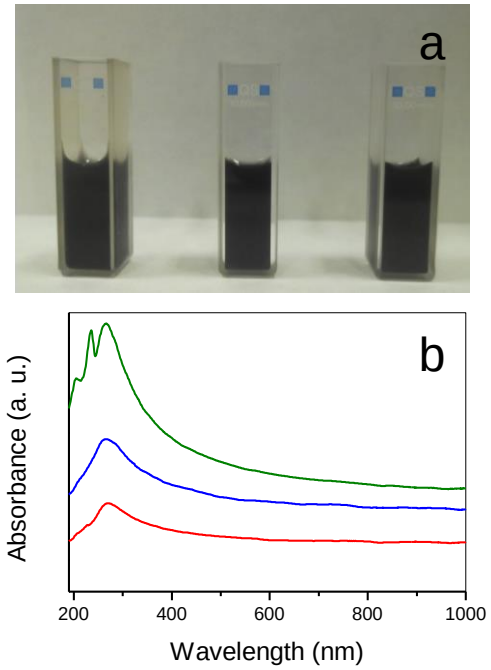

Figure 1. (a) Digital photograph of graphene suspensions obtained in the presence of different electrolytes (from left to right): SNTS, SPTS, and SNDS. **(b)** UV-vis absorption spectra of the graphene suspensions in (a): SNTS (green trace), SPTS (blue trace), and SNDS (red trace).

Focusing now on the results of the tests (Table 1), we first note that a number of the assayed chemical species were not successful in yielding aqueous dispersions with non–negligible content of graphitic material (i.e., entries in Table 1 that indicate zero graphene concentration), even though some of these species were known to be very efficient either as electrolyte in the anodic exfoliation of graphite or as graphene dispersant. For example, SS afforded a large amount of expanded product upon anodic treatment, in agreement with previous results from the literature,[21,34] but the sulfate

anion alone failed to colloidally stabilize the resulting graphene sheets due to the lack of a hydrophobic moiety that could adsorb onto the sheets. Incorporation of a methyl unit to the anion did not suffice to provide the electrolyte with the sought–after quality of colloidal stabilizer, as demonstrated by the fact that SMS, while inducing also a vigorous anodic expansion of the graphite piece (see Fig. S2 in ESI†), was not able to afford final aqueous dispersions possessing any significant amount of graphitic product. We interpret that, having such a short alkyl chain, SMS is only very weakly adsorbed on the graphene sheets and thus cannot confer them enough colloidal stability. Likewise, SPS, which is made up of a sulfonate group appended to a pyrene unit, has been shown to be a powerful dispersant of graphene flakes in aqueous medium,[50,51] but in the present work could not be put to good use as electrolyte for the anodic expansion of graphite. The graphite foil sample did not expand to any significant extent in aqueous solutions of this species, and its surface was just seen to roughen after the 60 min electrolytic treatment. We note that, due to solubility limitations, SPS could be tested only at concentrations of up to 0.01 M, whereas sulfate salts (e.g., SS and others) in successful anodic exfoliations have been typically used at concentrations in the range of 0.1 M.[33–35] We conclude that just a very limited degree of intercalation is possible with SPS at the attainable concentrations, being clearly insufficient to induce a significant expansion, and then exfoliation, of the graphite anode.

Table 1. Characteristics of anodically exfoliated graphenes obtained with several intercalating electrolytes. The apparent thickness of the graphene flakes was gathered by AFM. The O/C atomic ratio was obtained from XPS survey spectra. I_D/I_G values were obtained from the Raman spectra. The name, chemical structure and acronym and the different concentrations assayed for each species tested here as potential electrolyte/dispersant electrolyte are indicated. The concentration of graphene material in the final dispersion measured by UV–vis absorption spectroscopy is also given.

Electrolyte (acronym)	Structure	[electrolyte] (M)	[graphene] (mg mL^{-1})	Apparent thickness (nm)	O/C	I_D/I_G
Sodium sultate (SS)	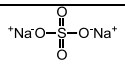	0.10	0.00	2.1	0.11	1.0
Sodium methane		0.10	0.00	-	-	-

sulfonate (SMS)						
Sodium bencene sulfonate (SBS)	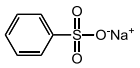	0.01 0.05 0.10 0.20	0.02 0.19 0.40 0.58	2.0	0.07 0.08 0.07 0.09	0.8 1.1 1.1 0.8
Sodium bencene 1,3–disulfonate (SBDS)	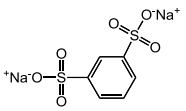	0.01 0.05 0.10 0.20	0.16 0.20 0.42 0.15	1.6	0.10 0.11 0.12 0.10	0.9 1.2 1.0 0.9
Sodium *p*–toluene sulfonate (STS)	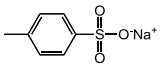	0.01 0.05 0.10 0.20 0.50	0.04 0.13 0.14 0.51 0.55	2.4	0.07 0.08 0.08 0.07 0.07	0.4 0.7 0.6 0.8 0.8
Sodium *p*–toluate (SPT)	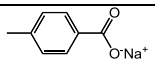	0.10	0.00	-	-	-
Sodium naphtalene 1,5–disulfonate (SNDS)	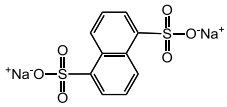	0.01 0.05 0.10 0.20	0.04 0.19 0.17 0.84	2.5	0.06 0.06 0.04 0.02	0.4 0.4 0.3 0.2
Sodium naphtalene 2,6–dicarboxylate (SNDC)	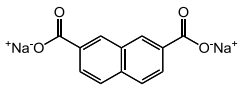	0.10	0.00	-	-	-
Sodium naphtalene 1,3,(6,7)–trisulfonate (SNTS)	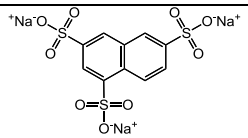	0.01 0.05 0.10 0.20	0.06 0.37 0.32 0.40	1.9	0.05 0.06 0.05 0.05	0.3 0.4 0.3 0.3
Sodium pyrene 1–sulfonate (SPS)	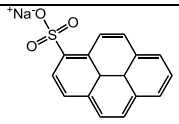	0.01	0.00	-	-	-
Sodium pyrene 1,3,6,8–	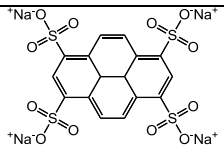	0.005 0.01	0.12 0.33	1.8	0.08 0.06	0.6 0.6

tetrasulfonate (SPTS)		0.05	0.14		0.06	0.3
Sodium dodecyl sulfate (SDS)	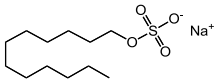	0.05	0.04	2.1	0.10	1.1
		0.10	0.18		0.09	0.9
		0.20	0.71		0.08	1.0
Sodium dodecyl bencene sulfate (SDBS)	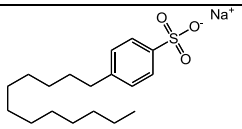	0.01	0.05	1.9	0.06	0.7
		0.05	0.16		0.10	0.9
		0.10	0.42		0.09	1.0
		0.20	0.29		0.07	1.1

The previous results suggest that chemical species must possess appropriate combinations of certain characteristics to be successful in the dual role of electrolyte and dispersant. For instance, their hydrophobic moiety should be large enough to allow sufficiently strong adsorption on the graphene flakes, but not too bulky so as to hamper the electrophoretic mobility of the amphiphilic anion during the electrolytic process (as determined by its charge/mass ratio) and/or its ability to intercalate between the graphene layers. In this regard, a single benzene unit coupled to the sulfonate anion was already seen to furnish the resulting amphiphilic molecule (i.e., SBS) with a non–negligible stabilizing capability, presumably due to the establishment of a relatively strong interaction (π–π), while retaining at the same time the ability of SS and SMS to expand graphite upon electrolytic treatment. As a result, SBS yielded stable aqueous suspensions of graphitic material at significant concentrations. A similar result was obtained with a sulfonate group attached to a toluene moiety (STS). Likewise, using amphiphiles that incorporate several, rather than one, ionic groups could be an effective strategy to settle the aforementioned issues, at least in part. Support for such a hypothesis was obtained by noting that, contrary to the case of SPS, SPTS (i.e., a pyrene molecule with four sulfonate groups attached; see Table 1) afforded large amounts of anodically expanded material, even if working at SPTS concentrations of 0.01 M and below. The expanded product could then be colloidally stabilized at reasonable concentrations. It is worth mentioning that SPTS is substantially less efficient than SPS as a graphene dispersant,[50,51] but this relative drawback was more than outweighed by the fact that it was quite effective in inducing the anodic expansion of graphite, whereas SPS was not.

Similarly, SBDS (a benzene ring coupled to two sulfonate groups) tended to outperform SBS as electrolyte/dispersant overall (higher concentration of graphitic material in the final dispersion) at electrolyte concentrations of 0.01 and 0.05 M; however, the use of higher electrolyte concentrations (i.e., 0.1 and 0.2 M) led to similar or even better performance for SBS. To shed an understanding on this question, we carried out a control experiment to determine which of the two amphiphiles performs better as a graphene dispersant. To this end, we first prepared a certain amount of anodically expanded graphite using SS (0.1 M) as the electrolyte. After extensive washing and drying, equal amounts of the obtained product were dispersed in aqueous solutions of SBS and SBDS at different concentrations between 0.01 and 0.2 M, bath–sonicated for 3 h and finally centrifuged. It was apparent to the naked eye, but also confirmed by UV–vis absorption spectroscopy, that the amount of graphitic material retained in the resulting supernatants was substantially larger when using SBS for all the tested concentrations, i.e. this amphiphile was far superior to SBDS as a dispersant. Such a result parallels the observations on the performance of SPS and SPTS as graphene dispersants reported and rationalized by other authors, as mentioned above, and can be explained by invoking a similar line of reasoning:[51] the ability of these amphiphilic anions to colloidally stabilize graphene sheets in aqueous medium is expected to be governed by the strength of their adsorption onto the sheets, i.e., by their adsorption free energy. The latter is in turn determined by the interplay between the solvation free energy of the amphiphile in water and the interaction free energy of the amphiphile with the graphene surface. The interaction free energy of SBS and SBDS with graphene can be assumed to be similar or even somewhat larger for SBDS on account of its additional sulfonate group. However, this additional group would make the solvation free energy of SBDS to be substantially larger and hence its adsorption free energy to be smaller than their counterparts for SBS. As a result, SBDS would exhibit a weaker ability to colloidally stabilize graphene in water, as was indeed observed in the control experiment.

In the light of the previous discussion, the following rationale can be put forward to account for the observed behavior of SBS and SBDS towards their combined role of electrolyte/dispersant. At low electrolyte concentration, the expected higher electrophoretic mobility of SBDS will lead to a larger extent of intercalation of the graphite anode, and consequently to a much larger amount of expanded product (as was visually evident), compared with the case of SBS. As a result, SBDS will afford more

graphitic material in the final dispersion simply because there was very little expanded product available for dispersion with SBS (see Table 1). On the other hand, it can be argued that the low intercalation rate of the SBS molecule arising from its comparatively low mobility can be compensated for when working at high electrolyte concentrations. In such a case, the sheer amount of SBS used would be enough to induce a sizable intercalation and expansion of the graphite anode, as was also observed in the experiments. With a significant amount of expanded graphite in the aqueous medium, the concentration of graphitic material in the final suspension after the sonication step will most probably be dictated by the ability of the amphiphile to act as a dispersant, so in this case higher concentrations would be expected when using SBS compared to SBDS, as it was indeed observed.

A limited electrophoretic mobility of amphiphiles that incorporate a single anion and a relatively bulky hydrophobic moiety, therefore possessing relatively low charge/mass ratios, can also be invoked to explain why SDS (sulfate group with a dodecyl chain) and SDBS (sulfonate group with a dodecylbenzene moiety), which are known to be reasonably efficient surfactants for graphene,[47, 55] did not succeed in expanding the graphite anode to any significant extent at low electrolyte concentration (0.01 M), similar to what was observed for SPS. However, contrary to the case of the latter species and due to their ability to assemble into micelles, both SDS and SDBS could be tested as electrolytes at concentrations well above 0.01 M. In line with the ideas discussed in the preceding paragraph for SBS, the use of sufficiently high concentrations of these species (e.g., 0.05 M for both SDS and SDBS) led to a substantial expansion of the graphite anode and finally to aqueous dispersions containing considerable amounts of graphitic material (see Table 1). We note that all the concentrations tested for SDS and SDBS (see Table 1) were above their corresponding critical micelle concentration values,[56] which warranted the effectiveness of both surfactants in the colloidal stabilization of the expanded graphitic products.

The information obtained from the experimental results presented above can be used as a guide to select further amphiphiles that are effective in the sought–after dual role of electrolyte and dispersant. Such results suggest that successful candidates must strike an appropriate balance between their net charge and the mass of their hydrophobic moiety. On one hand, the net charge should be high enough to promote efficient intercalation/ expansion of the graphite anode but not too high so as to critically weaken the free energy of adsorption of the amphiphile on the graphene surface. On the other hand, the

hydrophobic component should be large enough to favour its adsorption onto the graphene surface, but not too large so as to hamper the electrophoretic mobility of the molecule. More specifically, if SPS suffers from solubility and electrophoretic mobility limitations, but both SPTS and SBS possess appropriate combinations of the desired characteristics, then it is reasonable to expect that amphiphilic anions comprising two or three benzene rings as the hydrophobic moiety and two or three sulfonate groups should also perform efficiently as electrolyte and dispersant. To corroborate this point, we tested two chemical species that consisted of a naphthalene unit appended with either two or three sulfonate groups (i.e., SNDS and SNTS, respectively), and in both cases stable aqueous suspensions containing significant amounts of graphitic material could be readily obtained even at low electrolyte concentrations (see Table 1). As a final comment on the competence of the tested species to act as efficient electrolytes, it is worth mentioning that the nature of the anionic group present in the amphiphile was central to its ability to intercalate the graphite electrode. We selected sulfonate– and sulfate–containing amphiphiles based on the known propensity of graphite to be intercalated by such anions, both electrolytically and by other means.[57–59] Indeed, as exemplified with the case of SPT (toluene with a carboxylate) and SNDC (naphthalene with two carboxylates), replacement of the sulfonate groups by carboxylates led to chemical species that could not efficiently intercalate and expand the graphite anode, even under basic conditions to ensure that they were in a fully deprotonated, negatively charged state. This result is in agreement with previous results indicating that the use of, e.g., acetic or formic acid as electrolyte did not result in any significant exfoliation of the graphite anode.[24]Finally, the exfoliation yield for the electrolytic process investigated here with the best performing electrolytes was ~10 wt. % which significantly exceeded that obtained by liquid phase exfoliation of graphite via ultrasonication in sodium cholate (SC) aqueous solutions for similar treatment times of 4 hours (~0.5 wt. %).[60]

3.2. Chemical and structural characterization of the exfoliated products: evidence for high quality graphene flakes with very low oxygen content

To elucidate the morphological (exfoliation degree, object shape/size), chemical (e.g., oxidation level) and structural characteristics of the exfoliated materials using the electrolytes/dispersants discussed above, STEM, AFM, XPS and Raman spectroscopy measurements were carried out. Fig. 2a and b shows STEM images of the dispersions

obtained with 0.2 M SNDS (a) and 0.01 M SPTS (b), where the effective exfoliation of the starting graphite into thin flakes was made evident. This was further supported by AFM imaging, as illustrated in Fig. 2c–f for selected dispersions after being drop–cast onto HOPG substrates, more to the point those prepared with 0.1 M SS (c, dispersion prepared in water–isopropanol mixture and shown for comparison purposes), 0.01 M SPTS (d), 0.05 M SBDS (e) and 0.2 M SNDS (f). For all the successful electrolytes/dispersants, the resulting suspensions were comprised of very thin and flat objects displaying irregular polygonal shapes, consistent with them being well exfoliated graphene flakes. We note that in Fig. 2d–f a high density of small rounded (as opposed to polygonal) features decorate the HOPG surface. These can be attributed to the amphiphilic dispersants, which are expected to strongly adsorb onto the HOPG surface as well as onto the graphene flakes. The flakes exhibited typical lateral dimensions between a few and several hundred nanometers, and their apparent thickness, determined as flake height relative to the substrate (see exemplary line profiles in Fig. 2d–f), ranged between ~0.5 and 2.5 nm, although the specific values differed slightly depending on the particular electrolyte/dispersant used (see Table 1 and Fig. S4 of the ESI†). These values were very similar to the ones reported here and in the literature for graphene flakes anodically exfoliated in sulphuric acid or sulfate salts (e.g., SS),[33,44,61,62] suggesting that intercalation of the graphite electrode was not critically hampered by the larger size of the (amphiphilic) anions used here. We also note that the apparent thickness values were well below those usually reported for surfactant–stabilized graphene dispersions obtained by direct exfoliation of graphite via sonication or shear mixing (~3–8 nm),[17,46] thus suggesting a much better degree of exfoliation. In fact, taking into account that the typical thickness of the patches of amphiphilic molecules adsorbed onto the HOPG surface (Fig. 2d–f) was slightly above 1 nm and that these molecules are expected to contribute to the measured thickness of the flakes, we conclude that all the samples obtained here are mostly made up of single– to few–layer (<5) flakes.

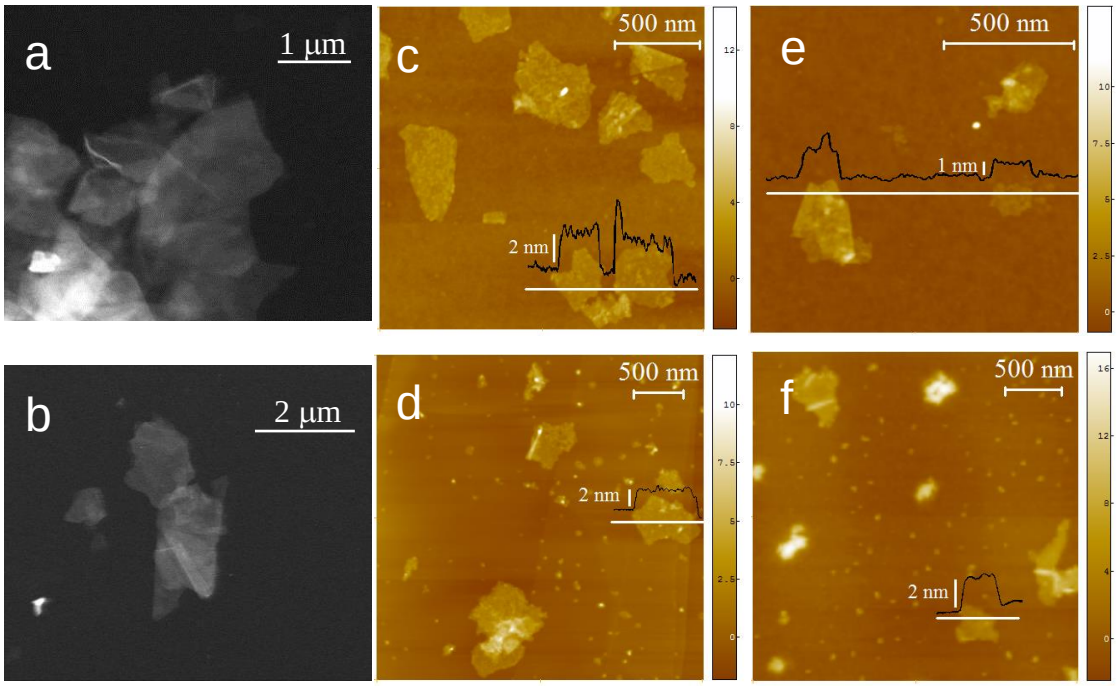

Figure 2. Representative STEM images of the graphene dispersions obtained with 0.2 M SNDS **(a)** and 0.01 M SPTS **(b).** Representative AFM images of graphene dispersions prepared with 0.1 M SS **(c,** dispersion prepared in water-isopropanol mixture and shown for comparison purposes), 0.01 M SPTS **(d)**, 0.05 M SBDS **(e)** and 0.2 M SNDS **(f)**. A typical line profile taken along the marked white line is shown superimposed on each image.

The chemical make–up of the exfoliated graphene flakes was investigated by XPS. The recorded survey spectra (not shown) indicated that carbon was the dominant element for all the samples, as expected, but oxygen and sulphur were also present to a variable extent depending on the specific amphiphile used (see ESI† for further details on XPS analysis). We note that the graphene dispersions employed for the XPS measurements were subjected to a special purification protocol consisting of several cycles of sedimentation via centrifugation and re–suspension in Milli–Q water. This procedure aimed at removing the largest possible amount of amphiphile from the samples, so that the actual oxygen content of the graphene flakes could be properly determined without substantial interference from the sulfonate/sulfate groups of the electrolyte/dispersant. Table 1 lists the oxygen content, expressed as O/C atomic ratio, for the different graphene samples prepared with the successful amphiphiles as well as with SS (0.1 M), the latter serving as a benchmark to afford direct comparisons with an electrolyte commonly used in the anodic exfoliation of graphite. As could be anticipated,

the SS–derived graphene flakes were seen to be significantly oxidized (O/C ratio ~0.11). Similar or even higher levels of oxidation are usually reported for anodically exfoliated graphene,[21,24,25,49,62,63] which are thought to be the result of oxidation reactions inherent to such an exfoliation process carried out in aqueous medium. More specifically, it has been postulated that water molecules are readily oxidized at the graphite anode, giving rise to highly reactive hydroxyl and oxygen radicals that then attack the graphene layers.[32,34] Thus, a more or less extensive oxidation of the resulting graphenes has been generally regarded as an inescapable consequence of the anodic exfoliation approach.[19,20] Because oxidation is almost invariably associated to degradation of the structural quality and properties of graphene, anodically exfoliated graphenes are deemed to have a relatively narrow scope of application compared to that of high quality graphene flakes obtained, e.g., by cathodic exfoliation of graphite in organic solvents or direct exfoliation in the liquid phase via ultrasound or shear forces.

Nevertheless, the present results indicated that graphenes with limited oxidation could be attained with a proper choice of the electrolyte/dispersant. Although some amphiphiles (e.g., SBDS, SBS or SDBS) yielded products with a similar or somewhat lower O/C ratio than that of the SS–derived material (see Table 1), others (e.g., SPTS, SNTS and SNDS) led to graphene samples with significantly reduced levels of oxidation. SNDS was particularly effective in this regard, affording O/C ratios as low as 0.02. To the best of our knowledge, this is by far the lowest degree of oxidation reported to date for any anodically exfoliated graphene, and is even lower than that typical of graphenes obtained by cathodic exfoliation approaches in organic solvents (O/C ratios ~0.04-0.09).[28–31,64] As illustrated in Fig. 3, the extent of oxidation of the graphene lattice was reflected in the shape of the high resolution C 1s core level XPS spectrum. For samples with high O/C ratios, e.g. those obtained with SS (a) and SBDS (b), the C 1s spectrum was dominated by a component centered at ~284.6 eV, which can be attributed to carbon atoms in non-oxidized graphitic environments (C=C species), with an additional significant component located at about 286.5 eV (C-O species in, e.g., hydroxyl or epoxide groups) and a minor one at ~288.5 eV (C=O species; e.g., carbonyls).[44,62] We note that the combined weight of the two latter components was commensurate with the O/C atomic ratio of the corresponding samples as deduced from their survey spectra. On the other hand, the weight of the C–O and C=O components (relative to the C=C component) was seen to decrease substantially for graphene samples with reduced extent of oxidation (e.g., Fig. 3c for SPTS with O/C ratio of 0.06),

and was virtually negligible for the SNDS–derived graphene with O/C ratio ~0.02 (Fig. 3d, black trace). For comparison purposes, the C 1s envelope of a graphene sample prepared by direct exfoliation of graphite powder through sonication in a sodium cholate aqueous solution, which is known to yield essentially pristine, oxide–free flakes,[65] is also shown in Fig. 3d (red trace), being almost identical to that of the SNDS–derived graphene. O/C ratios of ~0.01 were measured for this pristine graphene sample, as well as for both its parent graphite powder and the graphite foil used for anodic exfoliation. These results indicate that oxidation of anodically exfoliated graphene can be largely prevented as long as a suitable electrolyte is used (e.g., SNDS). This is in sharp contrast with what has been usually found for this production method using common electrolytes (e.g., H_2SO_4, K_2SO_4 or SS).

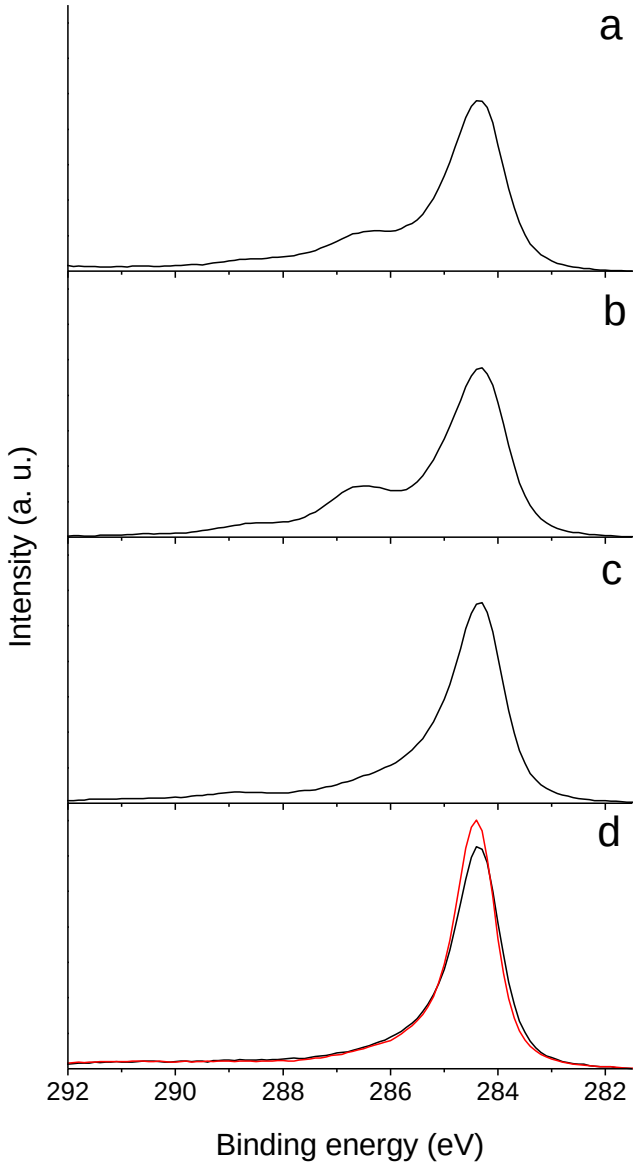

Figure 3. High resolution C 1s core level XPS spectra for graphene obtained with SS **(a)**, SBDS **(b)**, SPTS **(c)**, and SNDS **(d)**. For the sake of comparison, the C 1s spectrum of a sample obtained by direct exfoliation of graphite powder through sonication in a sodium cholate aqueous solution is also shown (red trace).

Further evidence of the high structural quality that could be attained with some of the tested amphiphiles was gathered by Raman spectroscopy. The same aforementioned purification procedure applied to samples for XPS analysis was used here. Some exemplary spectra are presented in Fig. 4 for graphenes anodically exfoliated with SS (a), SBDS (b), SPTS (c) and SNDS (d), as well as the graphene sample prepared by direct exfoliation of graphite in water–isopropanol mixture (e), shown for comparison. The first–order region of the spectra (1100–1700 cm^{-1}) was dominated by the well–

known G and D bands of graphitic materials, located at about 1582 and 1350 cm^{-1}, respectively, while the so–called 2D band (~2700 cm^{-1}) was the main feature observed in the second–order region (2300–3300 cm^{-1}). As noticed from Fig. 4, the intensity of the D band relative to the G band was seen to differ significantly between the different samples. Because the D peak is a defect–related band, whereas the G peak is just associated to the presence of sp^2 carbon atoms, the integrated intensity ratio of the D and G bands (I_D/I_G ratio) is frequently taken as a quantitative measure of the structural disorder in graphite/graphene.[66,67] The I_D/I_G ratio was calculated for the different graphene samples and the results are given in Table 1. As could be expected, graphenes with high O/C ratios tended to exhibit rather high values of I_D/I_G, indicative of carbon lattices with substantial structural disorder, whereas those samples with lower degrees of oxidation possessed correspondingly low I_D/I_G ratios. In particular, the graphene material with the lowest O/C ratio (0.02), prepared using SNDS (0.2 M), exhibited an I_D/I_G value of 0.2, i.e., it was much smaller than that obtained with a standard electrolyte (SS, 1.0) but very similar to that of the graphene sample prepared by direct exfoliation of graphite (~0.2). This is clear indication that extensive introduction of disorder in the graphene lattice is not invariably associated to the anodic exfoliation process in aqueous medium, but graphenes with a very low defect content are also possible under certain preparation conditions (e.g., using appropriate electrolytes in the present case). As a result, materials with attractive characteristics (e.g., a high electrical conductivity) should be attainable using the high quality anodically exfoliated graphenes. For instance, the electrical conductivity of free–standing, paper–like graphene films prepared by vacuum filtration of dispersions derived from SNDS (0.2 M) and SPTS (0.01 M) was 46000 and 45000 S m^{-1} (see ESI† for details on film thickness by FE–SEM), which compares favorably with values previously reported for graphene films obtained by direct exfoliation of graphite via ultrasonication or shear mixing in organic solvents or water–surfactant systems (2000-20000 S m^{-1}).[17,46,47,68–71] We note that, although the results presented here correspond to graphene dispersions prepared from graphite foil, graphene dispersions could also be obtained by anodic exfoliation of other types of graphite in the presence of SNDS, specifically, from HOPG and natural graphite powder (see Fig S13, Table S1 and accompanying text in ESI†).

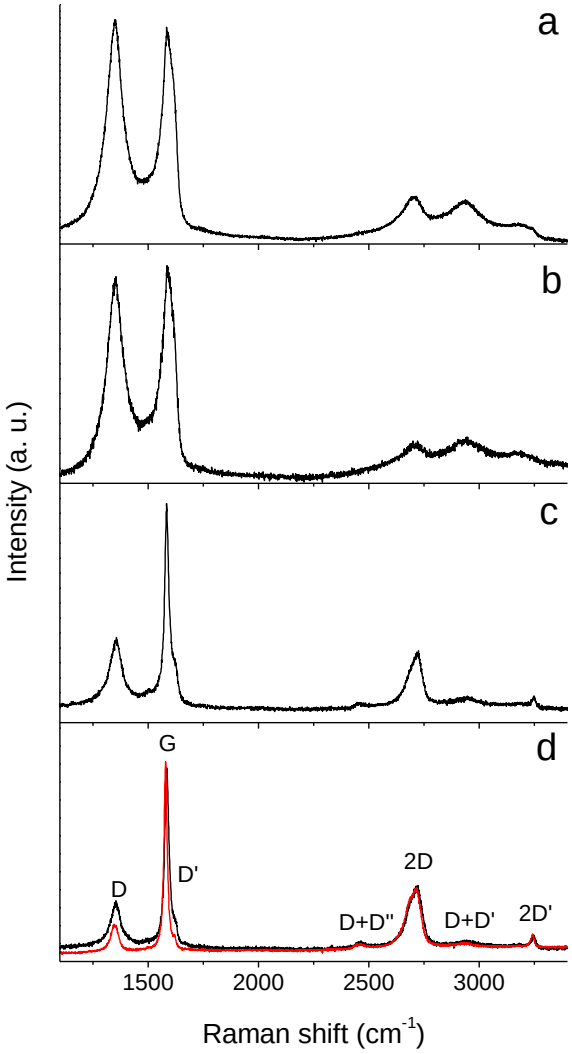

Figure 4. Raman spectra for graphene samples with SS **(a)**, SBDS **(b)**, SPTS **(c)**, and SNDS **(d)**. For the sake of comparison, the spectrum of a sample obtained by direct exfoliation of graphite powder through sonication in a 0.1 mg mL^{-1} sodium cholate aqueous solution is also shown (red trace). The main peaks are labeled for clarity.

3.3. Multifunctional electrolytes for the preparation of oxide–free anodically exfoliated graphene: implications and mechanism

In addition to identifying a number of chemical species that are effective as both electrolyte and dispersant in the anodic preparation of graphene in aqueous medium, the previous results have demonstrated that such a method is able to afford graphene nanosheets with structural and chemical characteristics comparable to those of graphene

flakes produced by direct liquid–phase exfoliation of graphite (i.e., very low oxygen and defect contents). In our opinion, this finding is important for two reasons. First, it has the potential to broaden significantly the scope of application of anodically exfoliated graphenes, which has been deemed to be somewhat limited as a result of the substantial oxidation and relatively low structural quality usually associated to this graphene type.[19,20] Thus, through modulation of its oxygen and defect content, anodic graphene could be targeted either for practical uses that are generally explored with high quality flakes, such as those obtained by direct liquid–phase or cathodic exfoliation approaches (e.g., in applications requiring high electrical or thermal conductivity), or alternatively, for uses where an extensive oxidation of the material, similar to that of graphene oxides, is desirable (e.g., to allow covalent functionalization with biomolecules towards theranostic applications). In addition, aqueous anodic exfoliation boasts significant advantages over other top–down, potentially scalable production methods. For example, it does not require the use of harsh chemicals (compared to the graphite oxide route) or organic solvents (as opposed to cathodic exfoliation), and affords higher yields and degrees of exfoliation (thinner flakes) relative to direct liquid–phase exfoliation.

Second, contrary to previous assumptions,[19,20] the mentioned finding proves that significant oxidation of the graphene layers is neither a strictly required step nor an inevitable consequence of the aqueous anodic exfoliation method. As discussed above, anodic exfoliation is thought to be made possible by pre–expansion of the graphite edges to allow an efficient intercalation of anions from the electrolyte. In turn, such a pre–expansion is believed to be the result of attack of the graphite edges by hydroxyl and oxygen radicals generated through anodic oxidation of water molecules.[32,34] It would then be conceivable that the only stringent requirement for anodic intercalation and exfoliation to take place efficiently is that the edges of the graphene layers, but not their interiors (i.e., their basal planes), become oxidized, even though in practice basal plane oxidation occurs for the highly oxidized anodic graphenes that are usually reported in the literature. Because just a very small fraction of carbon atoms are expected to be located at the edge of graphene nanosheets with lateral sizes of a few hundred nanometers or larger, this implies that anodic exfoliation should be possible with minimal oxidation of the resulting graphenes, as actually demonstrated in the present work with, e.g., SNDS.

The main question to elucidate in connection with these results is why oxidation of the graphene flakes could be largely prevented with some electrolytes, especially SNDS.

To this end, we note that intercalation of anions from the electrolyte within the graphene layers during the anodic process is probably accompanied by the co–intercalation of a number of water molecules surrounding each anion (hydrated anion). Oxidation of these water molecules at the high anodic potential applied (10 V) would generate the hydroxyl and oxygen radicals that in turn oxidize the graphene layers. However, in some cases oxidation of the anion itself would also be expected to take place. For instance, organic compounds and especially polycyclic aromatic hydrocarbons (PAHs), including sulfonated PAHs, are particularly prone to anodic oxidation in aqueous medium as a result of their relatively low oxidation potential.[72–74] In fact, electrolytic oxidation methods have been successfully deployed for the degradation of organic compounds in wastewaters.[75] On this ground, it is reasonable to assume that either (1) preferential anodic oxidation of the PAHs hinders the oxidation of water molecules and hence the generation of hydroxyl/oxygen radicals or, as a more likely possibility, (2) the PAHs do not avert water oxidation but act as scavengers of the resulting hydroxyl/oxygen radicals, leading to their own oxidation (to give, e.g., hydroxylated PAHs). As a result of either of these two processes, oxidation of the graphene layers would be prevented. Therefore, the use of readily oxidizable electrolytes (e.g., SNDS) can be an effective strategy to avoid the oxidation of anodically exfoliated graphenes and thus yield very high quality materials. The actual performance of any given oxidizable electrolyte towards this end is believed to depend on both thermodynamic and kinetic factors, but an analysis in this regard is beyond the scope of the present work. By contrast, non– or hardly oxidizable electrolytes (e.g., SS) will not be able to impede oxidation of the graphene layers, leading to the well–known products of relatively high oxygen content and low structural quality. The main processes thought to be involved in these two situations, as well the as the consequences for the resulting graphene nanosheets, are schematically depicted in Fig. 5. From these results it can be concluded that several of the investigated electrolytes, most significantly SNDS, boast not just a dual but a triple functionality in the anodic preparation of graphene: (1) exfoliating electrolyte, (2) colloidal dispersant and (3) sacrificial agent to prevent oxidation of the flakes.

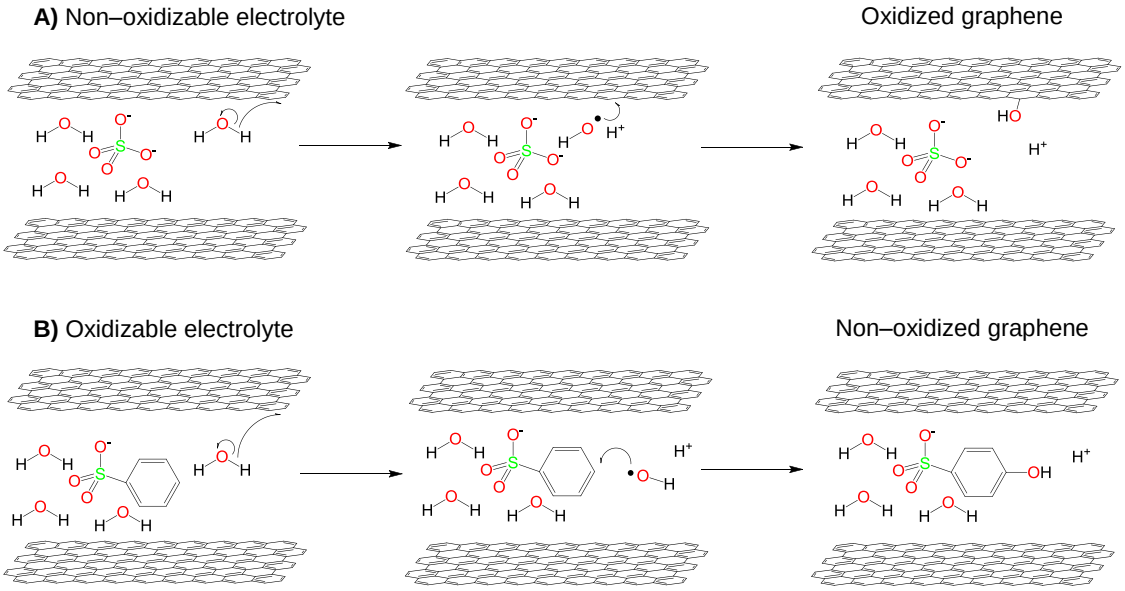

Figure 5. A) When graphite is anodically exfoliated in water in the presence of a non–oxidizable electrolyte such as sodium sulphate (SS), water molecules oxidize at the graphite anode, giving rise to highly reactive hydroxyl and oxygen radicals that then attack the graphene layers. As a result, the SS–derived graphene flakes are significantly oxidized. **B)** In the presence of a readily oxidizable electrolyte (an electrolyte with low oxidation potential), such as sodium benzenesulfonate (SBS), preferential anodic oxidation of electrolyte (to give, e.g., hydroxylated electrolyte) hinders the oxidation of graphene. Thus, the electrolyte acts as sacrificial agent preventing graphene oxidation.

3.4. Synthesis and catalytic activity of anodically exfoliated graphene–Pt NP hybrids

Hybrid nanostructures consisting of metallic and other types of NPs supported onto graphene are currently the focus of intense research efforts due to their strong potential for application in, e.g., catalysis or energy storage.[76] However, the majority of such efforts involve the use of GO nanosheets, whereas other graphene types have received much less attention. This can be attributed to the fact that the oxygen functional groups present in GO at very high densities serve as efficient anchoring sites for the NPs. In the case of electrolytically exfoliated graphene, its combination with NPs to afford functional hybrids has just started to be explored,[63] where polyaniline was employed as a linker to physically couple both components. We attempted the growth of Pt NPs on graphene flakes prepared by electrolytic exfoliation with the non–amphiphilic,

commonly used electrolyte SS, which gives a significantly oxidized product (O/C ratio~0.11, see Table 1). The procedure was based on reduction of a metal salt (K_2PtCl_4) with $NaBH_4$ in a water–isopropanol dispersion of exfoliated flakes. However, TEM imaging (see Fig. S14 of the ESI†) indicated that very few particles were able to associate to the flakes suggesting a lack of efficient anchoring sites for anodically exfoliated graphenes even if there are relatively well oxidized in this case. Thus, for the anodically exfoliated graphenes with very low extent of oxidation prepared here using certain electrolytes/dispersants, the need for a linker to promote NP anchoring to the graphene support appears to be necessary. Rather than resorting to an additional component, we hypothesized that the very same chemical species used as electrolyte, dispersant and sacrificial agent (e.g., SPTS and SNDS) could also play the role of effective linker. These species must be strongly adsorbed on the graphene surface through π–π interactions and their ionic (sulfonate) groups are expected to promote the nucleation and attachment of the NPs by acting as anchors for the precursor metal cationic species. To verify such a hypothesis, we synthesized Pt NPs by reduction of K_2PtCl_4 in an aqueous dispersion of either SPTS– or SNDS–stabilized graphene flakes (see Experimental section for details). As exemplified in Fig. 6a and c for SPTS– and SNDS–based samples, respectively, TEM imaging confirmed the decoration of the anodically exfoliated graphene flakes with large numbers of NPs. An analysis of their size (see histograms in Fig. 6b and d) revealed that they were typically between 1 and 5 nm in diameter, with an average size of 1.9±0.8 (SPTS) and 3±1 (SNDS) nm. No stand–alone NPs were observed in the TEM images, indicating that they were firmly anchored to the graphene support. XPS measurements demonstrated that the NPs were made up of Pt in metallic form. Fig. 6e shows the high resolution Pt 4f core level spectrum for the SNDS–based sample (results for the SPTS-based hybrid were similar and are not shown). The spectrum consisted of two slightly asymmetrical peaks (doublet band) located at binding energies of 71.3 and 74.6 eV, which could be ascribed to the $4f_{7/2}$ and $4f_{5/2}$ levels of Pt^0, respectively.[77] No significant peaks associated to oxidized Pt (e.g., Pt^{4+}) were noticed. The Pt/graphene mass ratio in the hybrids was determined by ICP–MS, yielding values of 4.0% (SPTS) and 7.9% (SNDS).

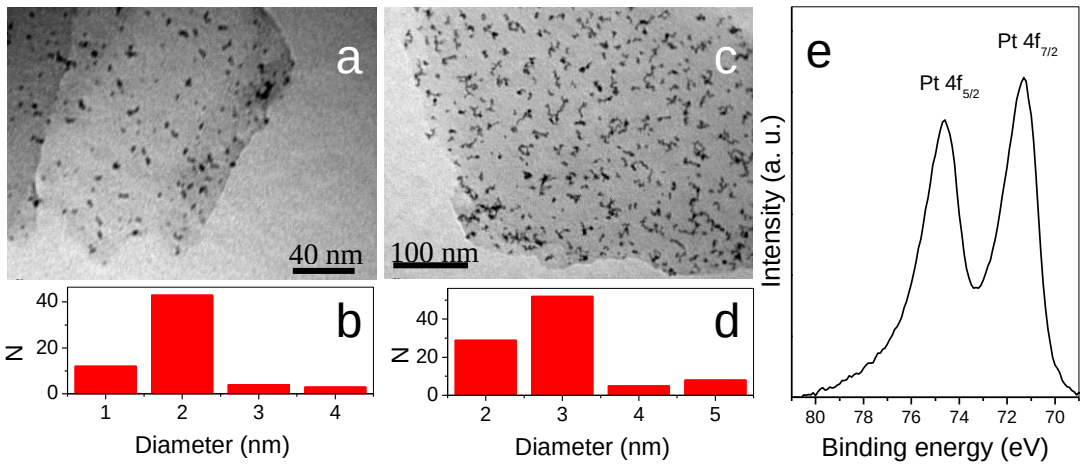

Figure 6. Representative TEM images of anodically exfoliated graphene–Pt NP hybrids obtained with SPTS **(a)** and SNDS **(c).** Histograms of nanoparticle size distribution derived from the TEM images for the graphene–Pt NP hybrids obtained with SPTS **(b)** and SNDS **(d)**. **(e)** Representative high resolution XPS Pt 4f core level spectrum of the anodically exfoliated graphene–Pt NP hybrids.

Among other potential applications, the anodically exfoliated graphene–Pt NP hybrids reported here could find use as catalytic systems. Their catalytic activity was evaluated on the basis of two model reactions carried out in aqueous medium at room temperature, namely the reduction of 4–NP and 4–NA with $NaBH_4$ to yield 4–AP and *p*–PDA, respectively. Both reactions are thermodynamically favorable but their kinetics is restricted by significant activation barriers, so that they need to be catalytically promoted. In addition to their practical relevance in different areas, including the synthesis of pharmaceutical compounds or the management of recalcitrant pollutants, they are commonly studied benchmark reactions in the assessment of metal–based catalysts. [78 , 79] The reaction progress can be readily monitored through UV–vis absorption spectroscopy in both cases. Fig. 7a shows the characteristic absorption spectrum of 4–NP at the slightly acidic pH of deionized water (black trace), which displays a strong band at ~316 nm. In the basic medium generated by the presence of the reductant $NaBH_4$, 4–NP deprotonates to give the 4–nitrophenoxide anion, whose main absorption band is located at ~400 nm (green trace). Reduction of 4–nitrophenoxide with $NaBH_4$ yields the 4–aminophenoxide anion, which exhibits absorption peaks at ~295 nm and below but lacks absorbance at 400 nm (red trace). Therefore, reduction of 4–NP to 4–AP can be kinetically monitored by the decrease in

absorbance at 400 nm. A similar reasoning leads to the selection of absorbance at 380 nm to follow the reduction of 4–NA (Fig. 7b, orange trace) to *p*–PDA (blue trace).

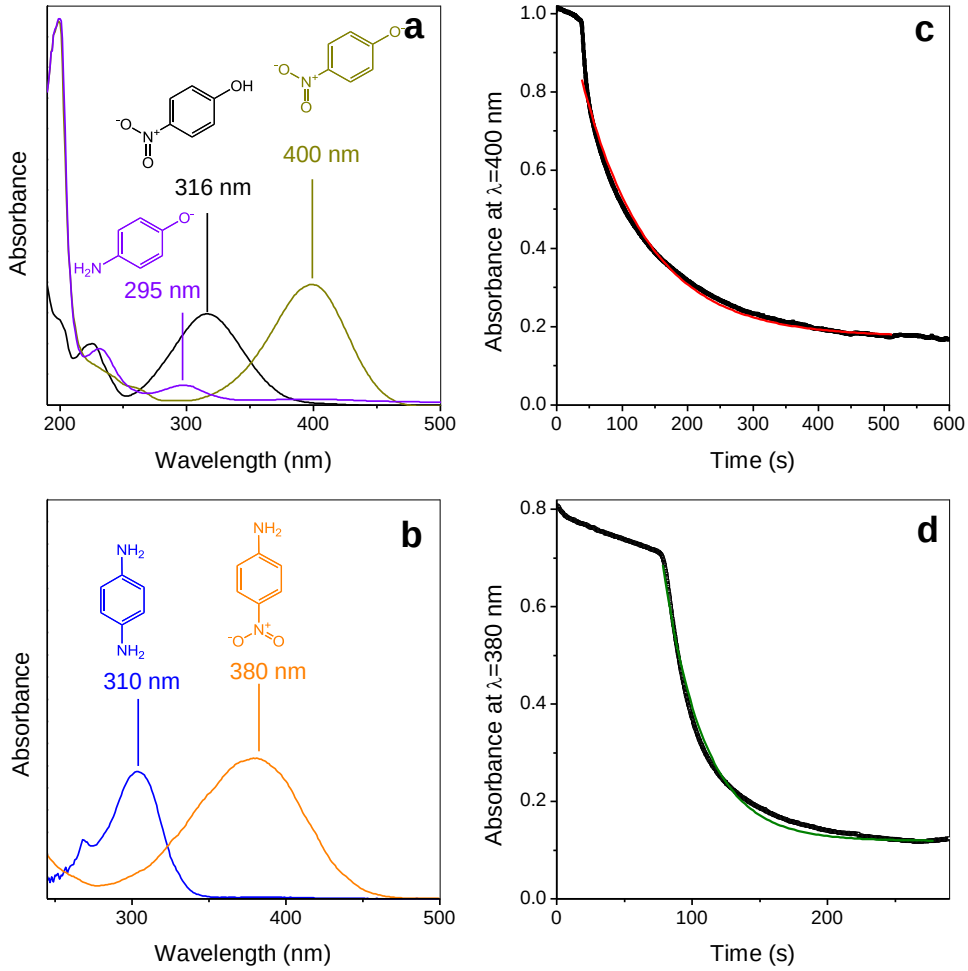

Figure 7. (a) UV–vis absorption spectra of 4-NP (black curve), 4-nitrophenoxide ion (dark yellow), and 4-aminophenoxide ion (violet). The absorption peak at 400 nm of 4-nitrophenoxide is used to monitor its conversion to 4-aminophenoxide by reduction with $NaBH_4$. **(b)** UV–vis absorption spectra of 4-NA (orange trace) and *p*-PDA (blue). The absorption peak at 380 nm of 4-NA is used to monitor the reaction progress. **(c)** Plot of absorbance at 400 nm vs. time for the reduction of 4-nitrophenoxide with $NaBH_4$ in the presence of the anodically exfoliated graphene-Pt NP hybrid obtained with 0.01 M SPTS**.** The experimental kinetic profile could be fitted to an exponential decay function, which is shown as an overlaid red line. **(d)** Plot of absorbance at 380 nm for the reduction of 4-NA with $NaBH_4$ as catalyzed by the anodically exfoliated graphene-Pt NP hybrid obtained with 0.2 M SNDS. The experimental kinetic profiles could be fitted to a straight line which is shown as an overlaid green line.

Figs. 7c and d show typical kinetic curves for the reduction of 4–NP and 4–NA, respectively, in the presence of the anodically exfoliated graphene–Pt NP hybrids. Reaction completion was generally seen to occur in less than 8 min. No significant reduction took place in the absence of the hybrids or in the presence of only the graphene flakes, demonstrating the catalytic role of the metal component. Considering that the experimental kinetic profiles could be fitted to an exponential decay function (see Figs. 7c and d) and that $NaBH_4$ was used to a large excess, so that its concentration could be regarded to remain constant throughout the reaction, the catalyzed reduction was best described by pseudo–first–order kinetics with respect to the substrate (4–NP or 4–NA), i.e.,

$$\frac{d[subs]}{dt} = -k_{app}[subs] \quad (1)$$

, where [subs] is the substrate concentration and k_{app} is the apparent reaction rate constant. Typical values of k_{app} measured for the present hybrids were in the range of 1–2×10^{-2} s^{-1} (4-NP) and 2–6×10^{-2} s^{-1} (4-NA). To allow direct comparisons with other catalysts reported in the literature, the catalytic activity of the hybrids was quantified in terms of turnover frequency (TOF), defined as the number of substrate moles converted per mole of Pt used in the reaction per unit time. The calculated TOF values are given in Table 2, together with those of some of the best performing Pt NP–based catalysts documented beforehand towards 4–NP[46,80–83] and 4–NA[46,84–86] reduction. The catalytic activity of our graphene–Pt NP hybrids was similar (in the case of 4–NP reduction) or even higher (4–NA reduction) than that of the most efficient catalysts developed to date. These results highlight the strong potential of the electrolytically exfoliated graphenes developed here for use as catalyst supports.

Table 2. Comparison of turnover frequency (TOF) values for state-of-the-art Pt-based catalysts used for the reduction of 4-NP and 4-NA with $NaBH_4$ in aqueous medium

Catalyst	TOF (min^{-1})	Reference
Reduction of 4-NP		
Anodically exfoliated graphene (SPTS)-Pt NP hybrid	11	Present work
Anodically exfoliated graphene (SNDS)-Pt NP hybrid	14	Present work
Pt NPs supported on ultrasound-exfoliated graphene	11	46
Surfactant-capped Pt nanocubes	2.5	80
Pt NPs supported on Fe_2O_3/N-doped RGO hybrid	10.8	81

Pt NPs supported on Al_2O_3 microspheres	0.6	82
RGO-supported Pt NPs	10.4	83
Reduction of 4-NA		
Anodically exfoliated graphene (SPTS)-Pt NP hybrid	57	Present work
Anodically exfoliated graphene (SNDS)-Pt NP hybrid	23	Present work
Pt NPs supported on ultrasound-exfoliated graphene	23	46
Bimetallic Pt-Ni NPs	8.7[a]	84
Pt NPs supported on RGO	14.5	85
Pt NPs embedded in RGO aerogel	0.8	86

[a]TOF value calculated considering only the molar amount of Pt present in the bimetallic NPs

4. Conclusions

We have identified a number of chemical species of amphiphilic nature that can be used as multifunctional electrolytes towards the electrolytic (anodic) exfoliation of graphite in water to give graphene flakes with much improved characteristics. First, a pool of amphiphiles (specifically, sulfonate– and sulfate–containing hydrocarbons) with the potential to exhibit a dual role as exfoliating (intercalating) electrolyte and colloidal dispersant in aqueous medium was evaluated. Benchmark tests designed to quantify the overall performance of the amphiphiles in fulfilling such a dual role indicated that successful species possess an appropriate balance between the number of their ionic groups and the size of their hydrophobic component. Second, in addition to acting as electrolyte and dispersant, several of the amphiphiles were also effective in preventing to a large extent the oxidation and structural degradation of the graphene flakes that is usually associated to anodic exfoliation. As a result, hardly oxidized graphenes of a similar quality to that of flakes produced via direct, ultrasound– or shear–induced exfoliation of graphite could be obtained by the anodic route for the first time. This highly relevant characteristic was rationalized on the basis of the ability of some amphiphiles to function as scavengers of the reactive oxygen species that are thought to attack and oxidize the graphene lattice during exfoliation, thus laying down a general strategy to overcome one of the main drawbacks of the anodic approach. Finally, the amphiphiles were also efficient linkers for the anchoring of metal nanoparticles onto the graphene flakes, yielding hybrids that exhibited a very high catalytic activity in the reduction of nitroarenes. We envisage this type of multifunctional electrolytes to be key

enabling elements in the future practical implementation of high quality electrolytically exfoliated graphene.

Acknowledgements

Financial support from the Spanish Ministerio de Economía y Competitividad (MINECO) and the European Regional Development Fund (ERDF) through project MAT2011–26399 is gratefully acknowledged. Partial funding by Plan de Ciencia, Tecnología e Innovación (PCTI) 2013–2017 del Principado de Asturias and the ERDF (project GRUPIN14–056) is also acknowledged. J.M.M. and M.A.-V. are grateful to the Spanish Ministerio de Educación, Cultura y Deporte (MECD) and MINECO, respectively, for their pre-doctoral contracts.

References

1 A. K. Geim, K. S. Novoselov, *Nat. Mater.*, 2007, **6**, 183–191.

2 A. K. Geim, *Science*, 2009, **324**, 1530–1534.

3 K. S. Novoselov, V. I. Fal´ko, L. Colombo, P. R. Gellert, M. G. Schwab, K. Kim, *Nature*, 2012, **490**, 192–200.

4 A. C. Ferrari, F. Bonaccorso, V. I. Fal'ko, K. S. Novoselov, S. Roche, P. Bøggild, S. Borini, F. Koppens, V. Palermo, N. Pugno J. A. Garrido, R. Sordan, A. Bianco, L. Ballerini, M. Prato, E. Lidorikis, J. Kivioja, C. Marinelli, T. Ryhänen, A. Morpurgo, J. N. Coleman, V. Nicolosi, L. Colombo, A. Fert, M. Garcia-Hernandez, A. Bachtold, G. F. Schneider, F. Guinea, C. Dekker, M. Barbone, C. Galiotis, A. Grigorenko, G. Konstantatos, A. Kis, M. Katsnelson, C. W. J. Beenakker, L. Vandersypen, A. Loiseau, V. Morandi, D. Neumaier, E. Treossi, V Pellegrini,M. Polini, A. Tredicucci, G. M. Williams, B. H. Hong, J. H. Ahn, J. M. Kim, H. Zirath, B. J. van Wees, H. van der Zant, L. Occhipinti, A. Di Matteo, I. A. Kinloch, T. Seyller, E. Quesnel, X. Feng, K. Teo, N. Rupesinghe, P. Hakonen, S. R. T. Neil, Q.Tannock, T. Löfwander, J. Kinaret, *Nanoscale*, 2015, **7**, 4598–4810.

5 M. Cai, D. Thorpe, D. H. Adamson, H. C. Schniepp, J. *Mater. Chem.*, 2012, **22**, 24992–25002.

6 F. Bonaccorso, A. Lombardo, T. Hasan, Z. Sun, L. Colombo, A.C. Ferrari, *Mater. Today*, 2012, **15**, 564–589.

7 Y. L. Zhong, Z. Tian, G. P. Simon, D. Li, *Mater. Today*, 2015, **18**, 73–78.

8 S. Park, R. S. Ruoff, *Nat. Nanotechnol.*, 2009, **4**, 217–224.

9 K. P. Loh, Q. Bao, G. Eda, M. Chhowalla, *Nat. Chem.*, 2010, **2**, 1015–1024.

10 L. Feng, L. Wu, X. Qu, *Adv. Mater.*, 2013, **25**, 168–186.

11 V. Chabot, D. Higgins, A. Yu, X. Xiao, Z. Chen, J. Zhang, *Energy Environ. Sci.*, 2014, **7**, 1564–1596.

12 A. Esfandiar, A. Irajizad, O. Akhavan, S. Ghasemi, M. R. Gholami, *Int. J. Hydrogen Energy*, 2014, **39**, 8169–8179.

13 C. Mattevi, G. Eda, S. Agnoli, S. Miller, K.A. Mkhoyan, O. Celik, D. Mastrogiovanni, G. Granozzi, E. Garfunkel, M. Chhowalla, *Adv. Funct. Mater.*, 2009,**19**, 2577–2583.

14 R. Rozada, J. I. Paredes, M. J. López, S. Villar-Rodil, I. Cabria, J. A. Alonso, A. Martínez-Alonso, J. M. D. Tascón, *Nanoscale*, 2015, **7**, 2374–2390.

15 J. N. Coleman, *Acc. Chem. Res.*, 2013, **46**, 14–22.

16 A. Ciesielski, P. Samorì, *Chem. Soc. Rev.*, 2014, **43**, 381–398.

17 K. R. Paton, E. Varrla, C. Backes, R. J. Smith, U: Khan, A. O'Neill, C. Boland, M. Lotya, O. M. Istrate, P. King, T. Higgins, S. Barwich, P. May, P. Puczkarski, I. Ahmed, M. Moebius, H. Pettersson, E. Long, J. Coelho, S. E. O'Brien, E. K. McGuire, B. Mendoza Sanchez, G. S. Duesberg, N. McEvoy, T. J. Pennycook, C. Downing, A. Crossley, V. Nicolosi1, J. N. Coleman, *Nat. Mater.*, 2014, **13**, 624–630.

18 C. T. J. Low, F. C. Walsh, M. H. Chakrabarti, M. A. Hashim, M. A. Hussain, *Carbon*, 2013, **54**, 1–21.

19 H. J. Salavagione, *J. Mater. Chem. A*, 2014, **2**, 7138–7146.

20 A. M. Abdelkader, A. J. Cooper, R. A. W. Dryfe, I. A. Kinloch, Nanoscale, 2015, 7, 6944–6956.

21 J. Liu, M. Notarianni, G. Will, V.T. Tiong, H. Wang, N. Motta, *Langmuir*, 2013, **29**, 13307–13314.

22 Z.-S. Wu, Z. Liu, K. Parvez, X. Feng, K. Müllen, Adv. Mater., 2015, 27, 3669–3675.

23 L. Zhang, H. Huang, H. Yin, Y. Xia, J. Luo, C. Liang, Y. Gan, X. Tao, W. Zhang, *J. Mater. Chem. A*, 2015, **3**, 16513–16519.

24 J. Liu, C. K. Poh, D. Zhan, L. Lai, S. H. Lim, L. Wang, X. Liu, N. G. Sahoo, C. Li, Z. Shen, J. Lin, *Nano Energy*, 2013, **2**, 377–386.

25 K. S. Rao, J. Sentilnathan, H.–W. Cho, J.–J. Wu, M. Yoshimura, *Adv. Funct. Mate*r., 2015, **25**, 298–305.

26 P. Tripathi, Ch. R. P. Patel, A. Dixit, A. P. Singh, P. Kumar, M. A. Shaz, R. Srivastava, G. Gupta, S. K. Dhawan, B. K. Gupta, O. N. Srivastava, *RSC Adv.*, 2015, **5**, 19074–19081.

27 J. Wang, K. K. Manga, Q. Bao, K. P. Loh, *J. Am. Chem. Soc.*, 2011, **133**, 8888–8891.

28 M. Zhou, J. Tang, Q. Cheng, G. Xu, P. Cui, L.-C. Qin, *Chem. Phys. Lett.*, 2013, **572**, 61–65.

29 A. M. Abdelkader, I. A. Kinloch, R. A. W. Dryfe, *ACS Appl. Mater. Interfaces*, 2014, **6**, 1632–1639.

30 A.T. Najafabadi, E. Gyenge, *Carbon*, 2015, **84**, 449–459.

31 M. Zhao, X.-Y. Guo, O. Ambacher, C. E. Nebel, R. Hoffmann, *Carbon*, 2015, **83**, 128–135.

32 J. Lu, J. Yang, J. Wang, A. Lim, S. Wang, K. P. Loh, *ACS Nano*, 2009, **3**, 2367–2375.

33 C.-Y. Su, A.-Y. Lu, Y. Xu, F.-R. Chen, A. N. Khlobystov, L.-J. Li, *ACS Nano*, 2011, **5**, 2332–2339.

34 K. Parvez, Z.-S. Wu, R. Li, X. Liu, R. Graf, X. Feng, K. Müllen, *J. Am. Chem. Soc.*, 2014, **136**, 6083–6091.

35 A. T. Najafabadi, E. Gyenge, *Carbon*, 2014, **71**, 58–69.

36 K. Chen, D. Xue, *J. Colloid Interface Sci.*,2014, 436, 41–46.

37 Y. Hernandez, M. Lotya, D. Rickard, S. D. Bergin, J. N. Coleman, *Langmuir*, 2010 **26**, 3208–3213.

38 S. Park, J. An, I. Jung, R. D. Piner, S. J. An, X. Li, A. Velamakanni, R. S. Ruoff, *Nano Lett.*, 2009, **9**, 1593–1597.

39 S. Villar–Rodil, J. I. Paredes, A. Martínez–Alonso, J. M. D. Tascón, *J. Mater. Chem.*,2009, **19**, 3591–3593.

40 M. Alanyalıoğlu, J. J. Segura, J. Oró-Solè, N. Casañ–Pastor, *Carbon*, 2012, **50**, 142–152.

41 J. P. Mensing, T. Kerdcharoen, C. Sriprachuabwong, A. Wisitsoraat, D. Phokharatkul, T. Lomas, A. Tuantranont, *J. Mater. Chem* , 2012, **22**, 17094–17099.

42 T. Kuila, P. Khanra, N. H. Kim, S. K. Choi, H. J. Yun, J. H. Lee, *Nanotechnology*, 2013, **24**, 365706.

43 C.-H. Chen, S.-W. Yang, M.-C. Chuang, W.-Y. Woon, C.-Y. Su, *Nanoscale*, 2015, **7**, 15362–15373.

44 J. M. Munuera, J. I. Paredes, S. Villar–Rodil, M. Ayán–Varela, A. Pagán, S. D. Aznar–Cervantes, J. L. Cenis, A. Martínez–Alonso, J. M. D. Tascón, *Carbon*, 2015, **94**, 729–739.

45 Z. Sun, J. Masa, Z. Liu, W. Shuhmann, M. Muhler, *Chem. Eur. J.*, 2012, **18**, 6972–6978.

46 M. Ayán–Varela, J. I. Paredes, L. Guardia, S. Villar–Rodil, J. M. Munuera, M. Díaz–González, C. Fernández–Sánchez, A. Martínez–Alonso, J. M. D. Tascón, *ACS Appl. Mater. Interfaces*, 2015, **7**, 10293–10307.

47 L. Guardia, M. J. Fernández–Merino, J. I. Paredes, P. Solís–Fernández, S. Villar–Rodil, A. Martínez–Alonso, J. M. D. Tascón, *Carbon*, 2011, **49**, 1653–1662.

48 M. J. Fernández–Merino, J. I. Paredes, S. Villar–Rodil, L. Guardia, P. Solís–Fernández, D. Salinas–Torres, D. Cazorla–Amorós, E. Morallón, A. Martínez–Alonso, J. M. D. Tascón, *Carbon*, 2012, **50**, 3184–3194.

49 X. Lu, C. Zhao, *Phys. Chem. Chem. Phys*., 2013, **15**, 20005–20009.

50 D. Parviz, S. Das, H. S. T. Ahmed, F. Irin, S. Bhattacharia, M. J. Green, *ACS Nano*, 2012, **6**, 8857–8867.

51 A. Schlierf, H. Yang, E. Gebremedhn, E. Treossi, L. Ortolani, L. Chen, A. Minoia, V. Morandi, P. Samorì, C. Casiraghi, D. Beljonne, V. Palermo, *Nanoscale*, 2013, **5**, 4205–4216.

52 D. Li, M. B. Müller, S. Gilje, R .B. Kaner, G. G. Wallace, *Nat. Nanotech.*, 2008, **3**, 101–105.

53 J.-W. T. Seo, A. A. Green, A. L. Antaris, M. C. Hersam, *J. Phys. Chem. Lett.*, 2011, **2**, 1004–1008.

54 D. A. Skoog, F. J. Holler, T. A. Nieman, *Principles of Instrumental Analysis*, Hartcourt Brace & Company, Philadelphia, 1998, ch. 13.

55 M. Lotya, Y. Hernandez, P. J. King, R. J. Smith, V. Nicolosi, L. S. Karlsson, F. M. Blighe, S. De, Z. Wang, I. T. McGovern, G. S. Duesberg, J. N. Coleman, *J. Am. Chem. Soc.*, 2009, **131**, 3611–3620.

56 H.-J. Butt, K. Graf, M. Kappl, *Physics and Chemistry of Interfaces*, Wiley-VCH, Weinheim, 2003.

57 M. S. Dresselhaus, G. Dresselhaus, *Adv. Phys.*, 1981, **30**, 139–326.

58 M. Noel, R. Santhanam, *J. Power Sources*, 1998, **72**, 53–65.

59 W. Yan, M. M. Lerner, *Carbon*, 2004, **42**, 2981–2987.

60 M. Lotya, P. J. King, U. Khan, S. De, J. N Coleman. *ACS Nano*, 2010, **4**, 3155–3162.

61 Z. Y. Xia, S. Pezzini, E. Treossi, G. Giambastiani, F. Corticelli, V. Morandi, A. Zanelli, V. Bellani, V. Palermo, *Adv. Funct. Mater.*, 2013, **23**, 4684–4693.

62 L. Wu, W. Li, P. Li, S. Liao, S. Qiu, M. Chen, Y. Guo, Q. Li, C. Zhu, L. Liu, *Small*, 2014, **10**, 1421–1429.

63 W. Wei, G. Wang, S. Yang, X. Feng, K. Müllen, *J. Am. Chem. Soc.*, 2015, **137**, 5576–5581.

64 A. J. Cooper, N. R. Wilson, I. A. Kinloch, R. A. W. Dryfe, *Carbon*, 2014, **66**, 340–350.

65 U. Halim, C. R. Zheng, Y. Chen, Z. Lin, S. Jiang, R. Cheng, Y. Huang, X. Duan, *Nat. Commun.*, 2013, **4**, 2213.

66 M. A. Pimenta, G. Dresselhaus, M. S. Dresselhaus, L. G. Cançado, A. Jorio, R. Saito, *Phys. Chem. Chem. Phys.*, 2007, **9**, 1276–1291.

67 A. C. Ferrari, D. M. Basko, *Nat. Nanotechnol.*, 2013, **8**, 235–246.

68 S. De, P. J. King, M. Lotya, A. O´Neill, E. M. Doherty, Y. Hernandez, G. S. Duesberg, J. N. Coleman, *Small*, 2010, **6**, 458–464.

69 U. Khan, A. O´Neill, M. Lotya, S. De, J. N. Coleman, *Small*, 2010, **6**, 864–871.

70 V. Chabot, B. Kim, B. Sloper, C. Tzoganakis, A. Yu, *Sci. Rep.*, 2013, **3**, 1378.

71 L. Zhang, Z. Zhang, C. He, L. Dai, J. Liu, L. Wang, *ACS Nano*, 2014, **8**, 6663–6670.

72 C.A. Martínez–Huitle, S. Ferro, *Chem. Soc. Rev.*, 2006, **35**, 1324–1340.

73 M. Panizza, M. Zolezzi, C. Nicolella, *J. Chem. Technol. Biotechnol.*, 2006, **81**, 225–232.

74 J. Muff, E.G. Søgaard, *Water Sci. Technol.*, 2010, **61**, 2043–2051.

75 C.A. Martínez–Huitle, E. Brillas, *Appl. Catal. B: Environ.*, 2009, **87**, 105–145.

76 M. Khan, M. N. Tahir, S. F. Adil, H. U. Khan, M. R. H. Siddiqui, A. A. Al-warthan, W. Tremel, *J. Mater. Chem. A*, 2015, **3**, 18753–18808.

77 B. V. Crist, *Handbook of Monochromatic XPS Spectra*, *XPS International LLC, Mountain View*, 2004, Vol. 1. The Elements and Native Oxides.

78 T. Aditya, A. Pal, T. Pal, *Chem. Commun.*, 2015, **51**, 9410–9431.

79 H. Hu, J.H. Xin, H. Hu, X. Wang, D. Miao, Y. Liu, *J. Mater. Chem. A*, 2015, **3**, 11157–11182.

80 C. Kim, H. Lee, *Catal. Commun.*, 2009, **10**, 1305–1309.

81 Y. Dai, Y. Chai, Y. Sun, W. Fu, X. Wang, Q. Gu, T. H. Zeng, Y. Sun, *J. Mater. Chem. A*, 2015, **3**, 125–130.

82 E. Kan, L. Kuai, W. Wang, B. Geng, *Chem. Eur. J.*, 2015, **21**, 13291–13296.

83 B. K. Barman, K. K. Nanda, *Appl. Catal. A: Gen.*, 2015, **491**, 45–51.

84 S. K. Ghosh, M. Mandal, S. Kundu, S. Nath, T. Pal, *Appl. Catal. A: Gen.*, 2004, **268**, 61–66.

85 M. M. Raju, D. K. Pattanayak, *RSC Adv.*, 2015, 5, 59541–59549.

86 X. Zhang, D. Liu, L. Yang, L. Zhou, T. You, *J. Mater. Chem. A*, 2015, **3**, 10031–10037.

ARTÍCULO II

Electronic Supplementary Information
for

Electrolytic exfoliation of graphite in water with multifunctional electrolytes: en route towards high quality, oxide–free graphene flakes

J.M. Munuera, J.I. Paredes, S. Villar–Rodil,* M. Ayán–Varela, A. Martínez–Alonso, J.M.D. Tascón

Instituto Nacional del Carbón, INCAR-CSIC, Apartado 73, 33080 Oviedo, Spain

*Corresponding author: E-mail address: silvia@incar.csic.es (S. Villar-Rodil)

Contents

S1. Experimental set–up

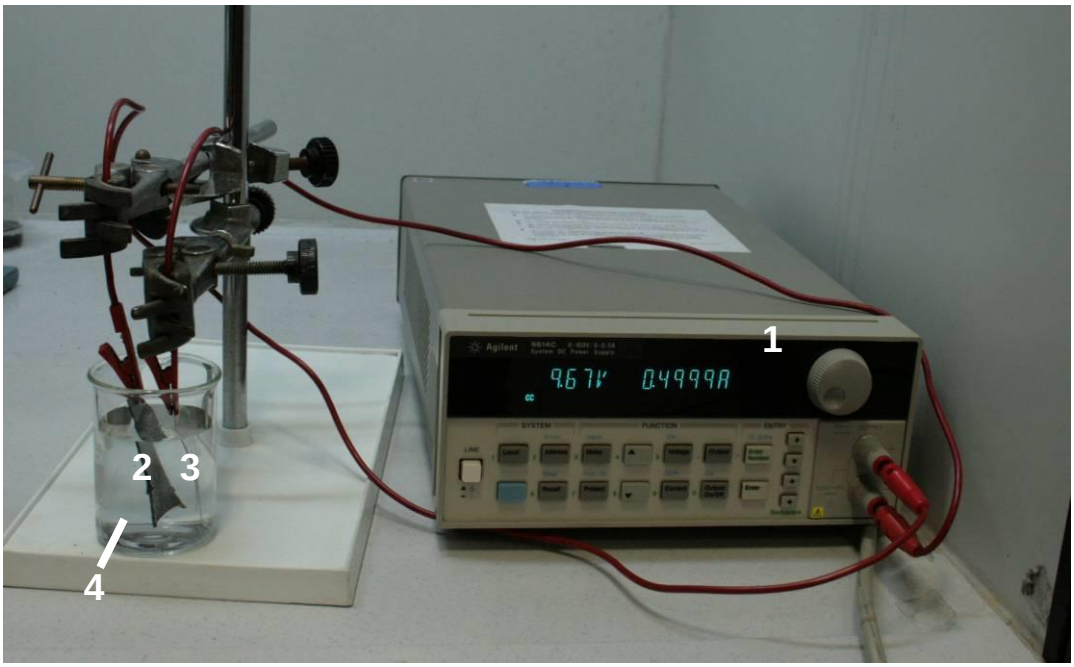

Figure S1. Digital photograph of the experimental set–up for the anodic exfoliation process consisting of an Agilent 6614C DC power supply (1) and two electrodes, namely, a graphite foil piece ($40\times25\times0.5$ mm^3) as working electrode (2), and a platinum wire as counter electrode (3). The platinum wire was placed parallel to the graphite foil surface at a distance of about 2 cm. The two electrodes were immersed in an aqueous solution (20 mL) of a given electrolyte at a certain concentration (4).

S2. Visual and microscopic evidence for the expansion of graphite foil upon anodic treatment

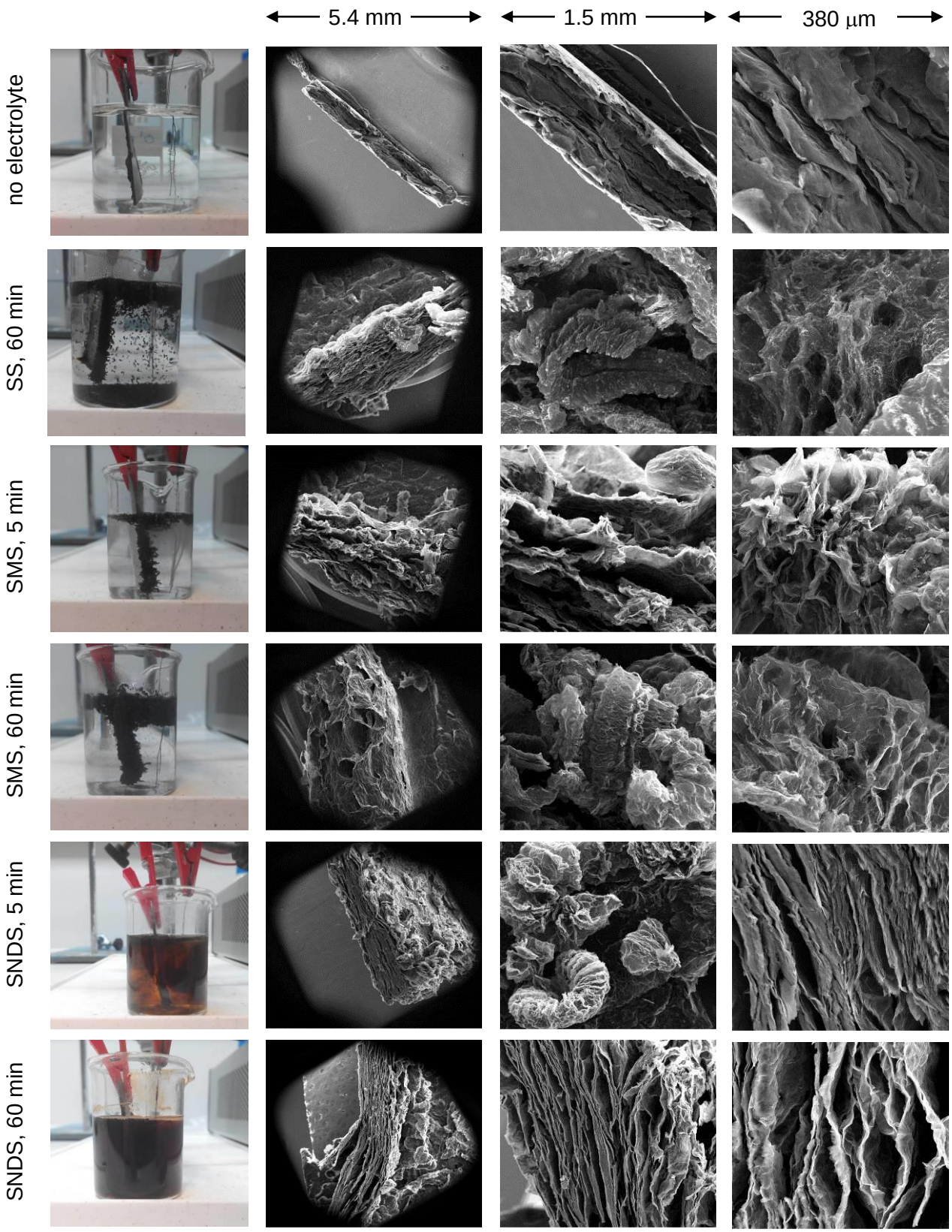

Figure S2. Digital photographs of graphite foil subjected to electrolytic treatment for the indicated periods of time in the presence of different electrolytes, namely, sodium sulfate (SS), sodium

methanesulfonate (SMS), or disodium naphthalene–1,5–disulfonate (SNDS). SEM images of the edge surface of graphite foil at increasing magnification for the different electrolytic treatements are also given.

Application of a positive potential of 10 V to a graphite working electrode in aqueous solutions of the specified electrolytes (see Fig. S1) led to the expansion and detachment of small fragments of material (up to a few millimeters), in line with recent studies on the anodic exfoliation of graphite in aqueous solutions of sulfate–based salts [1,2,3]. The vigorous expansion of the graphite slabs was noticeable even to the naked eye. The first column in Fig. S2 shows digital pictures of the beaker where the electrolytic process takes place in the presence of different electrolytes and for the treatment times indicated. On comparing any of the photographs corresponding to graphite subjected to electrolysis with that corresponding to the starting graphite foil in the absence of any electrolyte, the expansion of the foil becomes apparent. Further evidence for such an expansion could be gathered by examining the morphology of the edge planes of the graphite electrode by FE–SEM. The second, third and forth columns in Fig. S2 gather representative FE–SEM edge plane views of graphite foil at increasing magnification following th indicated electrolytic treatment conditions. The edge plane surface of the starting graphite foil slab (first row in fig. S2) exhibits a rather compact morphology. Anodic treatment in presence of any of the specified electrolytes brings about expanded structures, consisting of thin layers separated by large voids several micrometers wide. In some cases, the expansion takes place in a more or less homogeneous accordion–like fashion. In other cases, detached, worm–like structures of expanded graphite are observed.

S3. Evidence for the electrolytic treatment being the critical step in the exfoliation

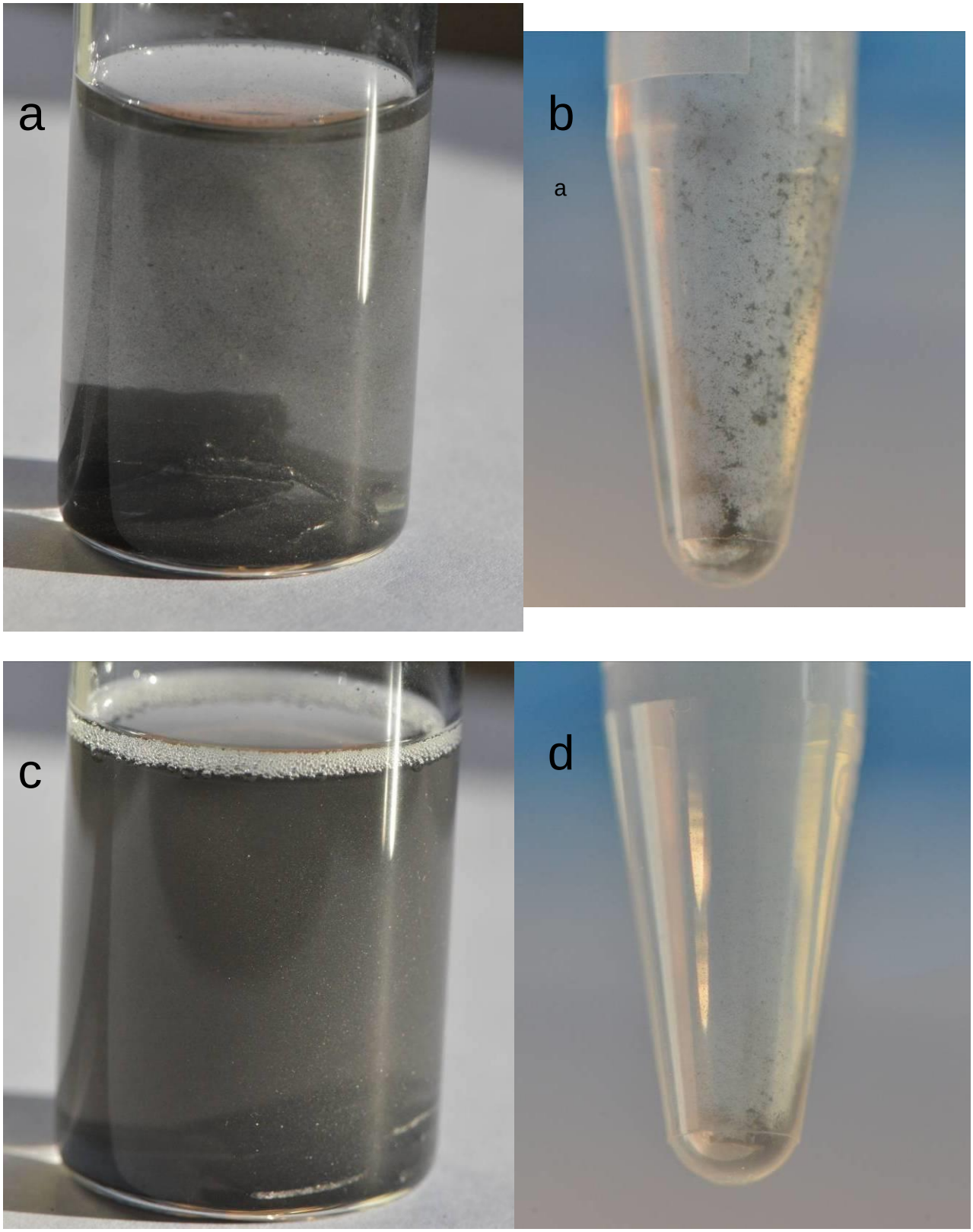

Fig. S3. Digital photograph of the dispersion of graphite foil obtained by ultrasonication for 3 h in the

presence of 1 mg mL^{-1} SNDS before (a), after centrifugation at 50*g* (b); in the presence of 0.1 mg mL^{-1} SC before (c), after centrifugation at 50*g* for 20 min (d).

We have demonstrated in the main text that, through electrolytic treatment with a suitable electrolyte followed by ultrasonication, it is possible to obtain aqueous graphene dispersions from graphite foil, which are colloidally stable for weeks or months. In contrast, when the electrolytic treatment is omitted, and the graphite foil is only sonicated in the presence of the same electrolyte, colloidal dispersions cannot be prepared. For instance, the dispersions prepared in the presence of 1 mg mL^{-1} SNDS consist of quite large particles visible to the naked eye before centrifugation (Fig. S3a). A very mild centrifugation at 50*g* induces complete sedimentation of the particles (Fig. S3b), while the colloidally stable dispersions prepared with a previous electrolytic step withstand centrifugation at 200*g*. The same happens when a reportedly good dispersant for graphite, such as SC, is used (see Figs. S3c, and S3d, right). We interpret that ultrasonication detaches some graphitic fragments from the surface of the foil, but it does not exfoliate it significantly. Thus, the electrolytic step is essential for the effective exfoliation of the material into graphene. In conclusion, in the approach investigated here, the exfoliation process takes place mostly, if not exclusively, during the electrochemical treatment. As previously stated in the literature [4], ultrasonication is only needed to detach the pre–exfoliated material.

If HOPG is used as starting graphite material, ultrasonication alone does not lead to detached graphitic fragments in any significant amount (photographs not shown), as HOPG is a compact, very low surface area material. However, as we have demonstrated in a previous work [4], effective exfoliation of HOPG is possible though electrolytic treatment. Furthermore, in Fig. SX, we demonstrate that colloidally stable graphene dispersions are obtained from HOPG though the same process as that described in the main text for graphite foil.

Of course, as is well known, graphite powder can be effectively exfoliated by ultrasonication only. However, as we previously reported [4], the dispersed amount is higher if a previous electrolytic step is introduced (8–fold when SS is used as electrolyte). Therefore, even in the case of graphite powder, the electrolytic treatment is a major driver for the exfoliation process.

S4. AFM characterization of the samples

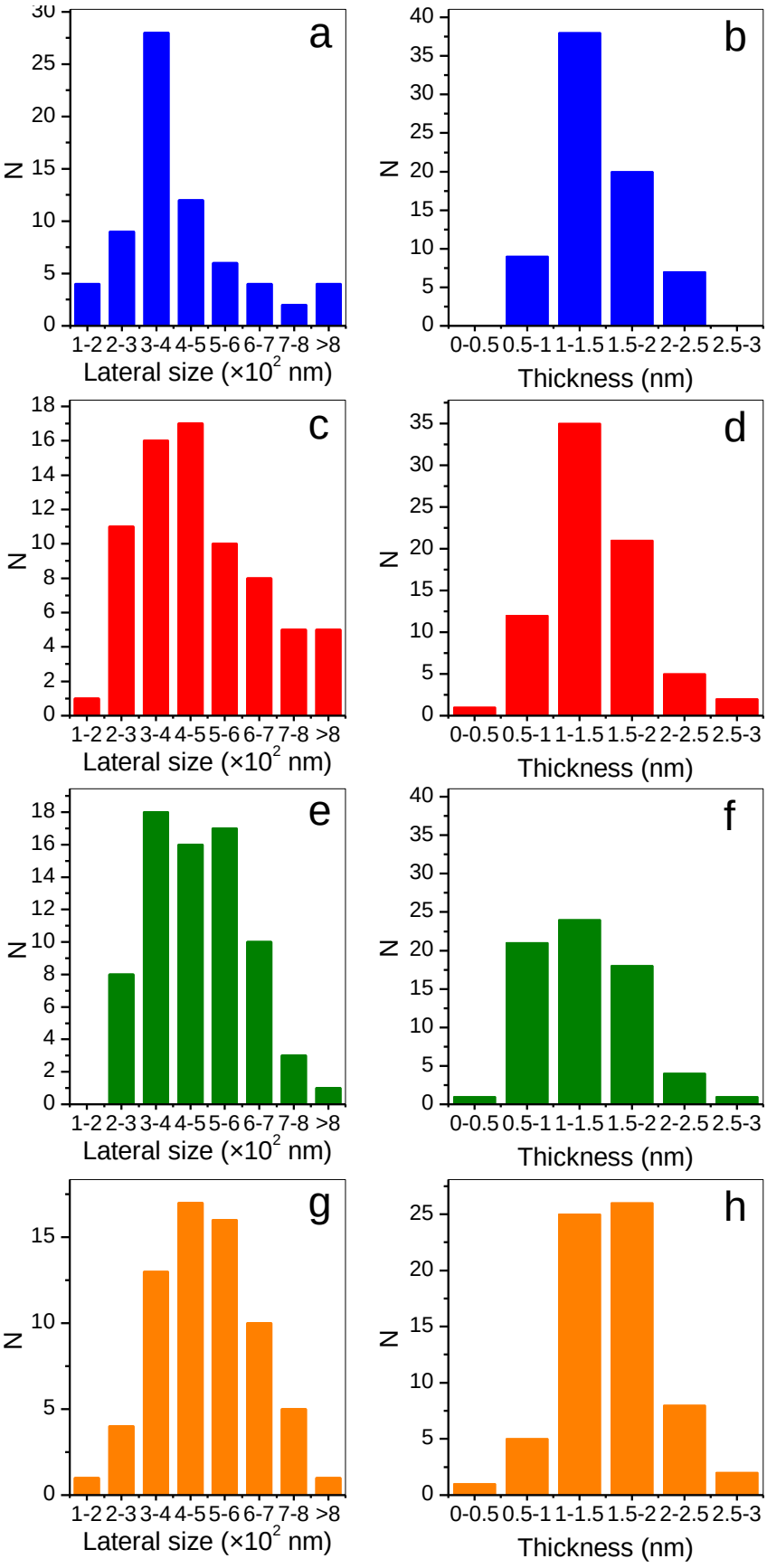

Figure S4. Histograms of flake lateral size (left) and apparent thickness (right) derived from a pool of 75 flakes measured from the AFM images of graphene dispersions obtained with 0.1M ss (blue columns), 0.05 M SBDS (red columns), 0.01 M SPTS (green columns), and 0.2M SNDS (orange columns).

The average apparent thickness for the graphene dispersions obtained with 0.1M SS, 0.05 M SBDS, 0.01 M SPTS, and 0.2M SNDS is 1.3±0.5 nm, 1.5±0.5 nm, 1.5±0.4 nm, 1.6±0.5 nm, respectively. Taking into account that the typical thickness of the patches of amphiphilic molecules adsorbed onto the HOPG surface (see Fig. 2d–f in the main text) was slightly above 1 nm and that these molecules are expected to contribute to the measured thickness of the flakes, we conclude the actual thickness of the flakes to be noticeably lower than that given in the histograms of apparent thickness of Fig. S4, and therefore consistent with the flakes being mostly single– to few(<5) –layered.

S5. XPS characterization of the samples

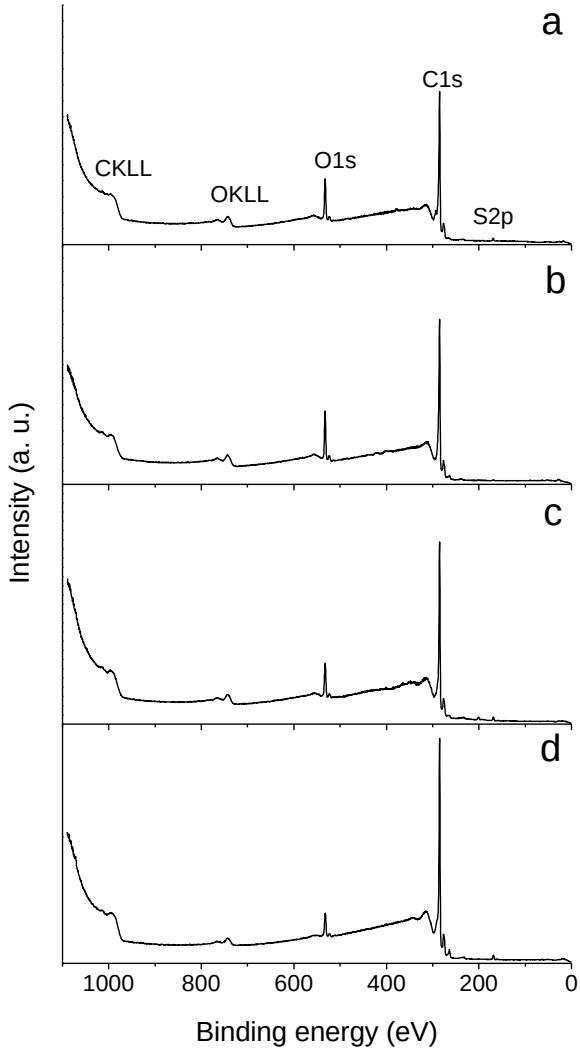

Figure S5. XPS survey spectra for graphene obtained with SS **(a)**, SBDS **(b)**, SPTS **(c)**, and SNDS **(d)**. The main XPS and Auger peaks have been labeled for clarity.

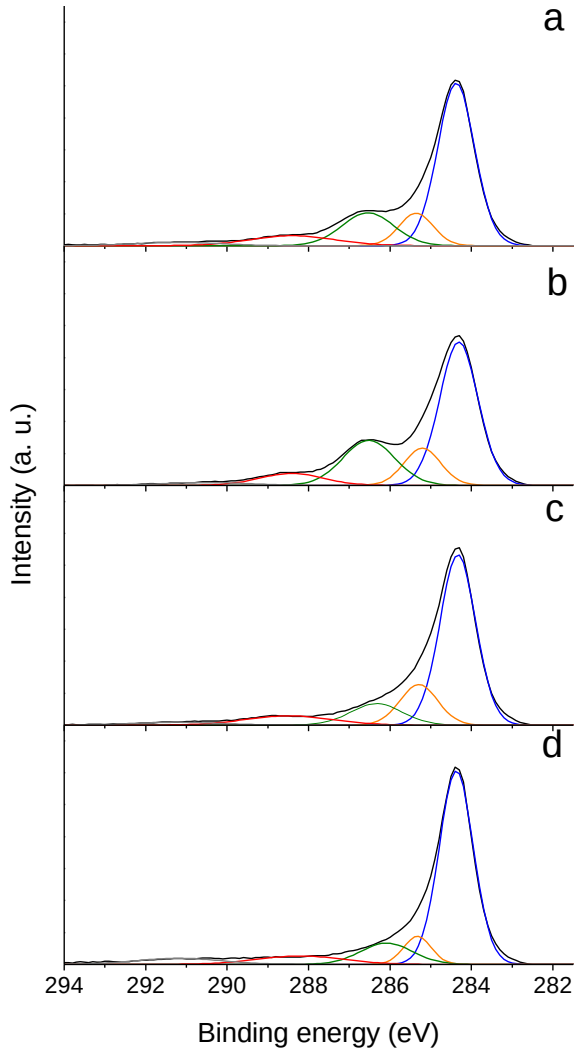

Figure S6. Background–subtracted, normalized, high resolution C 1s core level XPS spectra for graphene obtained with SS **(a)**, SBDS **(b)**, SPTS **(c)**, and SNDS **(d)**. The bands have been deconvoluted into 5 components, namely: graphitic carbon (blue trace); localized alternant hydrocarbon (orange trace); sp^3 carbon and C–O bonds in hydroxyl and epoxy groups (green trace); C=O bonds, carboxyls and $\pi \rightarrow \pi^*$ satellite band of the band at 285.5 eV (red trace); $\pi \rightarrow \pi^*$ satellite band associated to the graphitic carbon band (grey trace).

On deconvoluting the C 1s XPS band, it must be born in mind that the results can only be taken as semi–quantitative. In principle, deconvolution of the high resolution XPS C1s band could yield the type and relative amount of oxygen functionalities from the position of the maxima and the relative areas of the different components, which relate to different chemical environments of the C atom. This process is relatively straightforward for relatively well–defined materials as polymers, where the known formula of a parent, non modified polymer can help with the identification of the different chemical functionalities and give an idea of the expected area ratios. In the case of the relatively ill–defined carbon materials, apart from the lack of a suitable reference, there is the added problem of the metallic character of conducting, graphitic carbon, which is usually the principal component in the C1s envelope of any sp^2–based carbon material. Crystalline, pristine graphite shows an asymmetric C1s band,

with a tail to the high binding energy (BE) side, with an associated π→π* shake–up satellite. Both the band and the satellite correspond to a unique chemical environment – graphitic carbon – and cover a wide BE range from 282 to 296 eV, approximately. Even for perfect graphite, fitting the experimental C1s band to an analytical function is not a trivial task, let alone for carbon materials where there are different chemical environments for its C atoms, which give rise to bands superimposed on the graphitic C band. Furthermore, for a given carbon material, the exact shape of the main component is unknown, having only the C1s envelope of pristine graphite as a reference of an extreme case of maximum asymmetry and minimum FWHM for the band, arising from its highest electrical conductivity and largest homogeneity in the chemical environment, respectively, and maximum intensity of the satellite. A survey of the literature on XPS analysis of carbon materials shows that the issue of the asymmetry in the main component of the C1s band of (conducting) carbon materials is seldom addressed, except for graphite. As a rather unsatisfactory solution, this component is usually fitted with a symmetrical function (Gaussian–Lorentzian), just as any other component of the C1s envelope. However, if the asymmetry of this main component is not taken into account, the rest of the C 1s components will be overestimated [5]. In fact, this is one of the reasons why the oxygen concentrations calculated from the deconvolution of the high resolution C1s spectrum are significantly larger than the O1s/C1s value obtained from the survey spectrum [6,7]. Another reason for this inconsistency in quantitative XPS results for carbon materials is the sometimes ignored existence of a 2nd graphitic band, first suggested by Proctor et *al.* as a β–shift [8] but taken into account by very few authors [9], which is sometimes attributed to sp^3 C, in analogy with amorphous carbons. This 2nd graphitic component has more recently being ascribed to defet alternat hydrocarbon structure, although this assignment is not still widely adopted by the scientific community.

Herein, the C 1s band was allowed to fit to 6 symmetrical components with the following locations and assignments, [9,10]: at ~284.6 eV, graphitic structure whose electrons are extensively delocalized; at around 285.6 eV, defect sp^2 structure having electron delocalization less extensive than the former; at 286.6 eV, sp^3 hybridized free radicals but also C–O in hydroxyl and epoxy groups; at 287.8 eV, C=O bonds but also π→π* satellite band of the band at 285.5 eV; at 288.9, carboxylic groups; at ~291.5 eV, also π→π* satellite band of the band at ~284.6 eV. Note the presence of multiple overlapping bands and the fact that the contribution of oxygen–containing functional groups to the total intensity will increase with the extent of oxidation while the intensity of the π→π* satellite bands associated to conduction will simultaneously decrease in an unknown amount. When the bands were allowed to fit, just five bands were obtained: the bands for C=O and COOH are not resolved, yielding just one band at an intermediate location ~ 288.4 eV. It is noteworthy that the relative intensity of the component ascribed to hydroxyl and/or epoxy groups significantly diminishes when SPTS and SNDS are used as electrolytes, confirming their effectiveness in avoiding the oxidation of the graphene flakes.

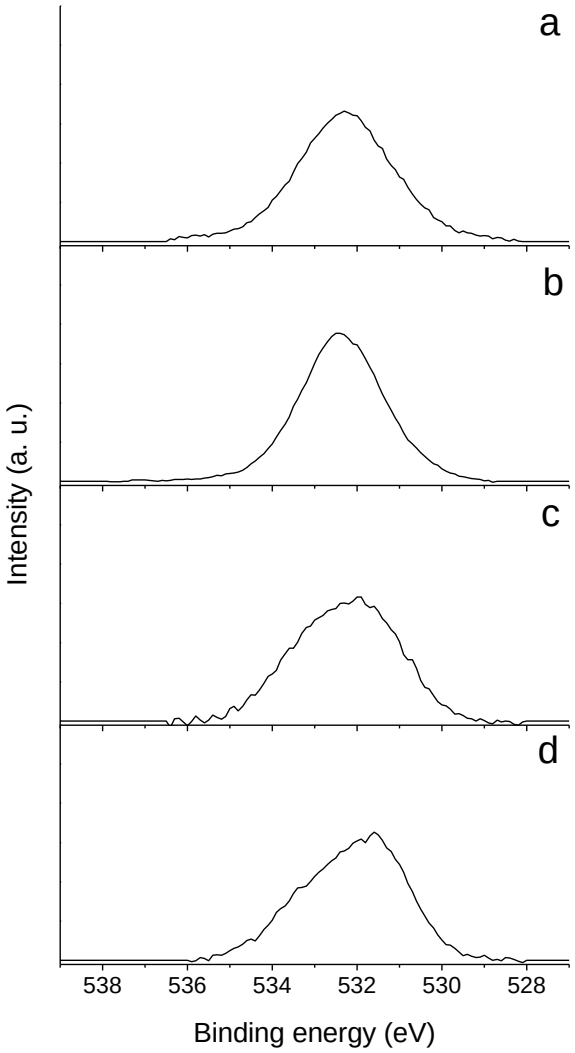

Figure S7. Background–subtracted, normalized high resolution O 1s core level XPS spectra for graphene obtained with SS **(a)**, SBDS **(b)**, SPTS **(c)**, and SNDS **(d)**.

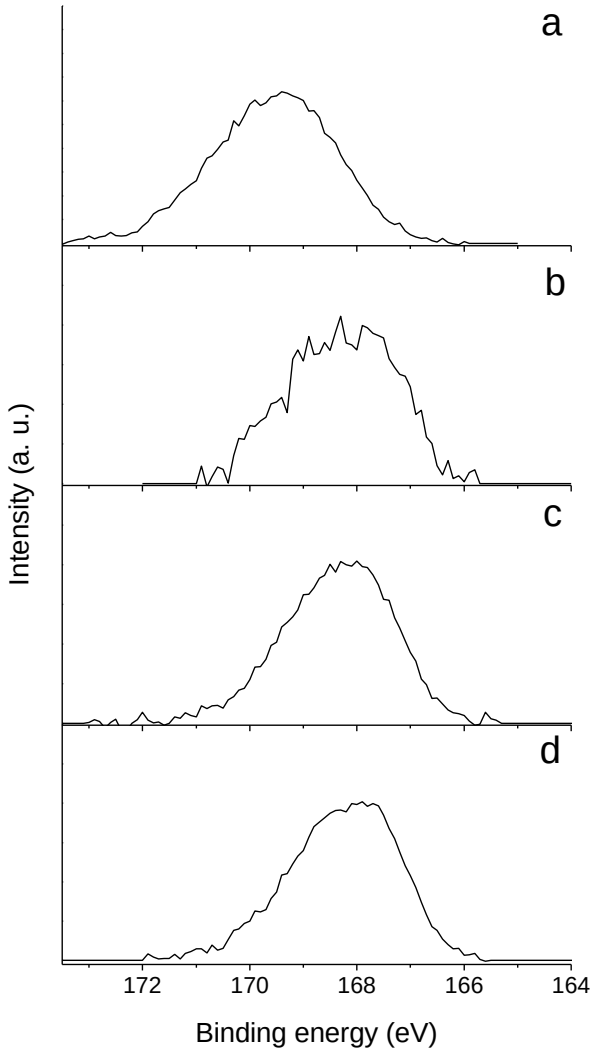

Figure S8. Background–sustracted, normalized high resolution S 2p core level XPS spectra for graphene obtained with SS **(a)**, SBDS **(b)**, SPTS **(c)**, and SNDS **(d)**.

Prior to XPS analysis, the samples were subjected to a special purification protocol to remove the largest possible fraction of amphiphile from the samples. However, a small amount remained. Indeed, some residual sulphur was detected in the samples (see survey spectra in Fig. S5). The high resolution S 2p spectra obtained after extensive accumulation indicate that, as expected, the sulphur present in the sample is of sulfate type in the case of graphene obtained with SS (Fig. S8a) and of sulfonate type for the rest of the samples (e. g., Fig. S8b–d).

S6. Measurement of film thickness by FE–SEM

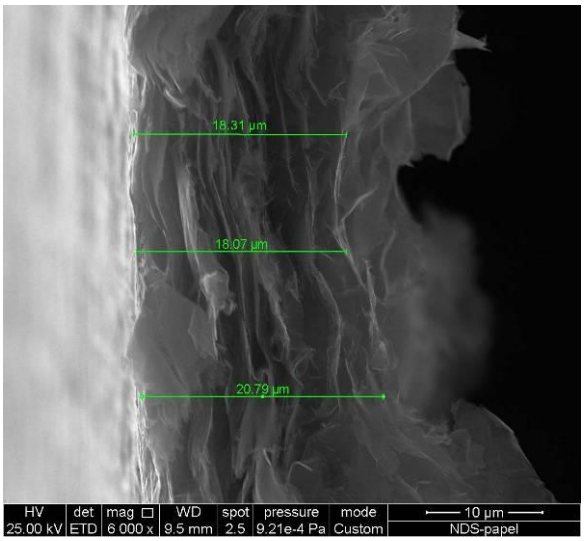

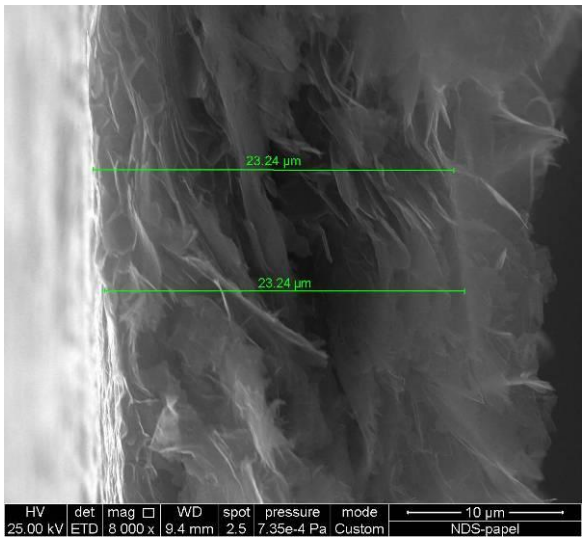

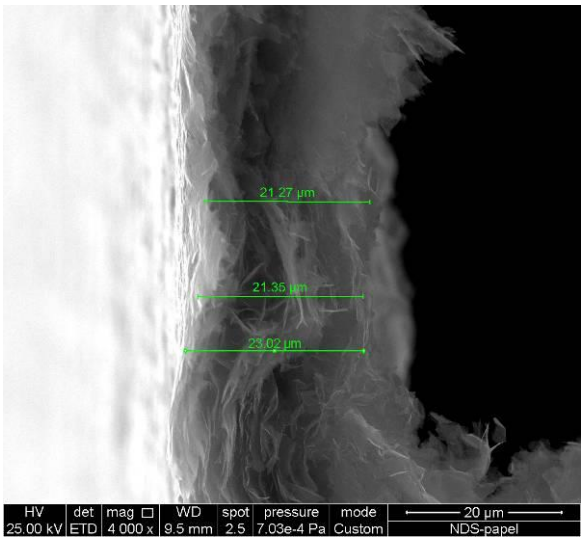

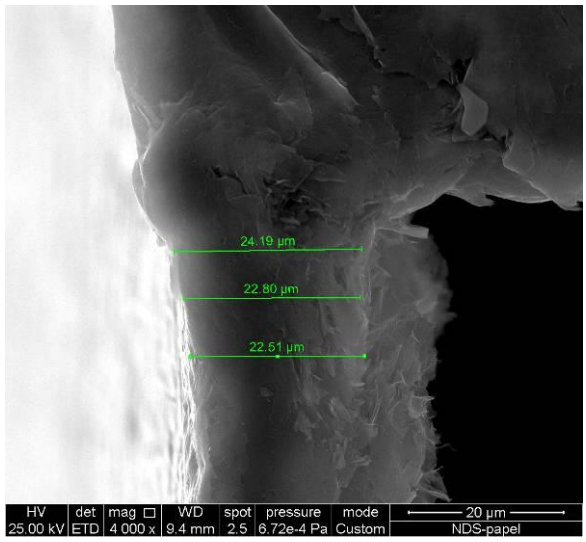

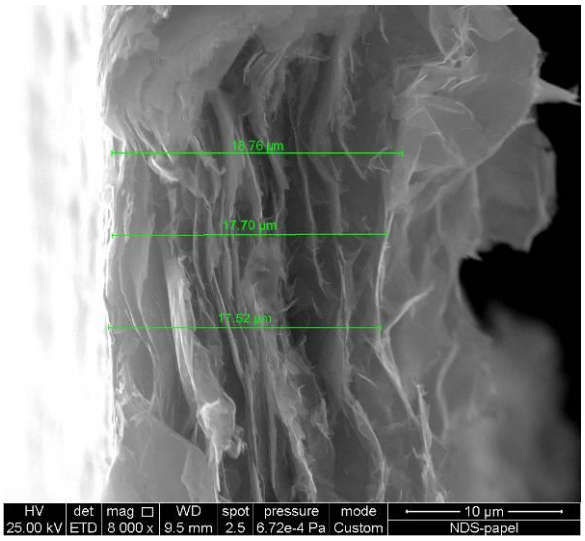

Fig. S9. FE–SEM images of the section of the graphene paper prepared with SNDS on which conductivity measurements were performed. The measurements of film thickness are indicated in green traces on each image. The average value obtained is 21±2 μm.

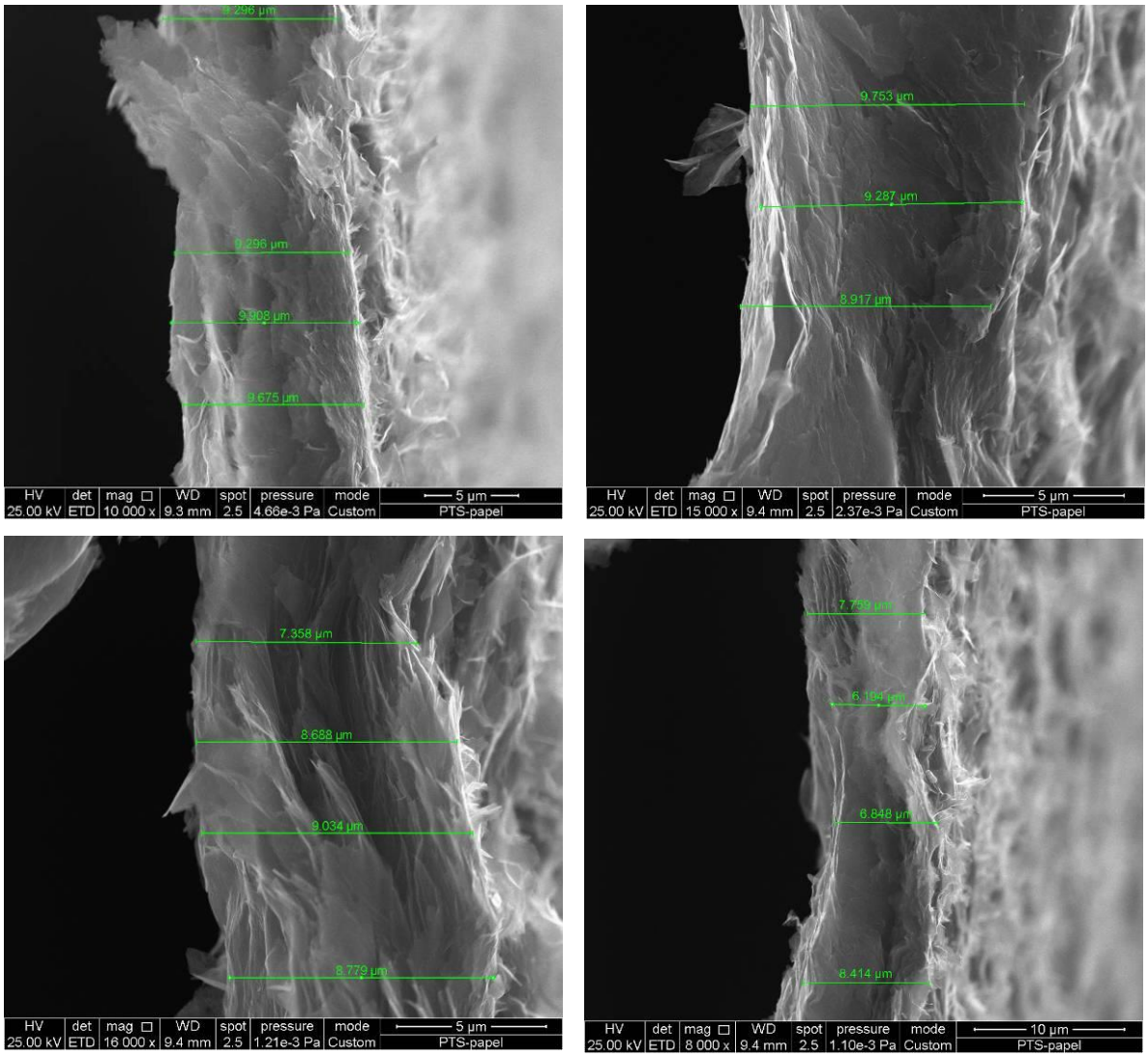

Fig. S10. FE–SEM images of the section of the graphene paper prepared with SPTS on which conductivity measurements were performed. The measurements of film thickness are indicated in green traces on each image. The average value obtained is 9±1 μm.

S7. Derivatization and XPS analysis of the graphene flakes obtained by anodic treatments using SS as electrolyte

A thin graphene film was prepared by drop–casting the graphene sample prepared by anodic exfoliation with SS as electrolyte and subsequently dispersed in water–isopropanol mixture on a pre–heated stainless steel plate. The sample was placed in flasks and introduced in a glove box with dry Ar atmosphere. After tempering for several hours, the sample was immersed in trifluoroacetic anhydride (Sigma–Aldrich) and the flask was closed to avoid the evaporation of the liquid. After 24 h, most of the liquid was removed and the rest was allowed to evaporate. The dry samples were transferred to the XPS equipment for analysis. Figure S11 shows the survey and the high resolution F 1s core level spectra for the treated sample.

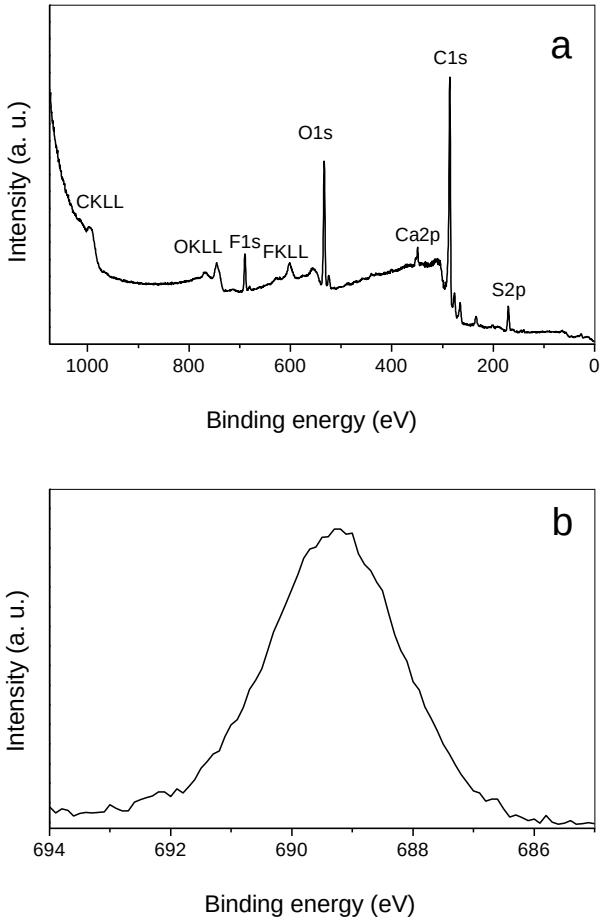

Fig. S11. Survey spectrum **(a)** and high resolution F 1s core level spectrum **(b)** for the graphene material obtained by electrolytic exfoliation with SS after derivatization with trifluoroacetic anhydride.

As seen in Fig. S11, F is incorporated to the sample after the treatment, which means that the derivatization reaction has taken place and confirms that there were indeed hydroxyl groups in graphene prepared with SS [11]. As a result of derivatization, each –OH group is expected to be substituted by O–CO–CF_3. Thus, is all the groups were hydroxyls and they were completely derivatized, 3 F atoms would be incorporated to the structure for each oxygen atom originally present (and one additional O atom for every O atom originally present). Clearly, the amount of F incorporated (~3.5 at. %) is less than thrice the original amount of oxygen in the structure (~11 at. %, see Table 1 in the main text). The additional O

incorporated (~4 at. %) is also less than the original 11 at. %. However, this apparently low extent of derivatization comes partly from the fact that the reaction takes place strictly at the surface of the film, while XPS probes a few nanometers (~3 nm). Hence, the atomic composition yielded by XPS includes both the derivatized outer layers and the non–derivatized inner layers of the film. As the atomic composition is an average over the composition of both types of layers, this ~3.5 at. % of F incorporated to the material reflects a relatively high extent of derivatization and thus a relatively large amount of hydroxyl groups present in the original graphene.

S8. UHPLC/MS of the product of SNDS oxidation

The electrolytic treatment of graphite foil using SNDS as electrolyte was carried out as described in the main text. Then, graphene was precipitated by ultracentrifugation at 20000*g* and the supernatant was subjected to 1:50 dilution in water and analyzed by ultra high performance liquid chromatography/ mass spectrometry (UHPLC/MS). The equipment was a UHPLC Dionex Ultimate 3000 RS liquid chromatograph (Thermo Scientific) equipped with a Bruker Impact II Q-ToF quadrupole–time of flight mass spectrometer (Bruker Daltonics GmbH). The obtained chromatogram is shown in Fig. S12.

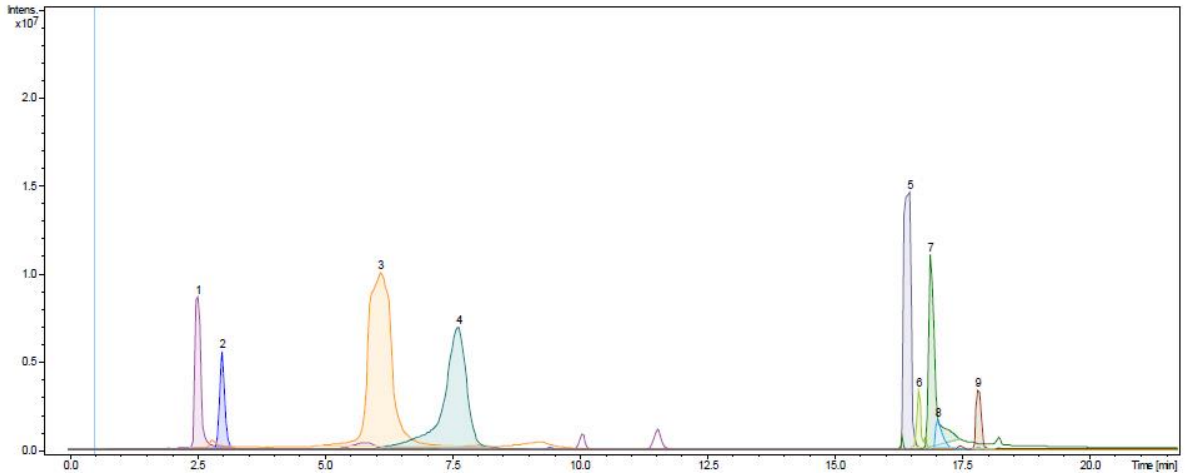

Fig. S12. Chromatograph for the supernatant obtained by precipitation of the graphene dispersion prepared by electrolytic treatment of graphite foil with SNDS.

The chemical formulas determined by MS and the corresponding average, nominal oxidation state for the C atoms of the separated products are the following:

1. $C_{10}H_8O_6S$: -0.2
2. $C_8H_6O_5S$: -0.25
3. $C_{10}H_6O_5S$: -0.2
4. $C_8H_6O_6S$: 0
5. SNDS: -0.6
6. $C_{10}H_{10}O_9S_2$: -0.4
7. $C_{10}H_7O_8S_2$: -0.3
8. undetermined mixture
9. mixture of $C_{10}H_7O_{10}S_2$ (+0.1), $C_{10}H_8O_{10}S_2$)0), and $C_9H_7O_8S_2$ (-0.33).

Oxidation of the sacrificial agent is confirmed by the fact that the average, nominal oxidation state of the C atoms in every detected product is higher than that of the starting substance (SNDS in this case).

S9. Demonstration for starting graphites other than graphite foil

The same protocol established in the main text for graphite foil was assayed for HOPG (grade ZYH, obtained from Advanced Ceramics) and natural graphite powder (grade 2910, from Mersen). For the electrochemical exfoliation experiments, ~10×10×2 mm^3 pieces of HOPG were employed, whereas the graphite powder was pressed into a circular pellet (12 mm in diameter, 2 mm in thickness) by means of a hydraulic press. These two additional graphite types have been treated in exactly the same conditions described in the main text for the electrolytic exfoliation of graphite foil in presence of 0.2 M SNDS, with the exception that in the case of natural graphite powder electrolysis voltage was 3 min instead of 60 min. This short time is due to the quick detachment of the individual graphite particles from their pellet once they start to expand due to intercalation. Indeed, the individual graphite particles in the pelletized working electrode expand very quickly during the electrolytic process due to their small particle size, so that a powder graphite working electrode made up of pressed graphite powder with a mass comparable to that of the HOPG electrode used here (or that of the graphite foil electrode described in the main text) was completely detached in 3 min.

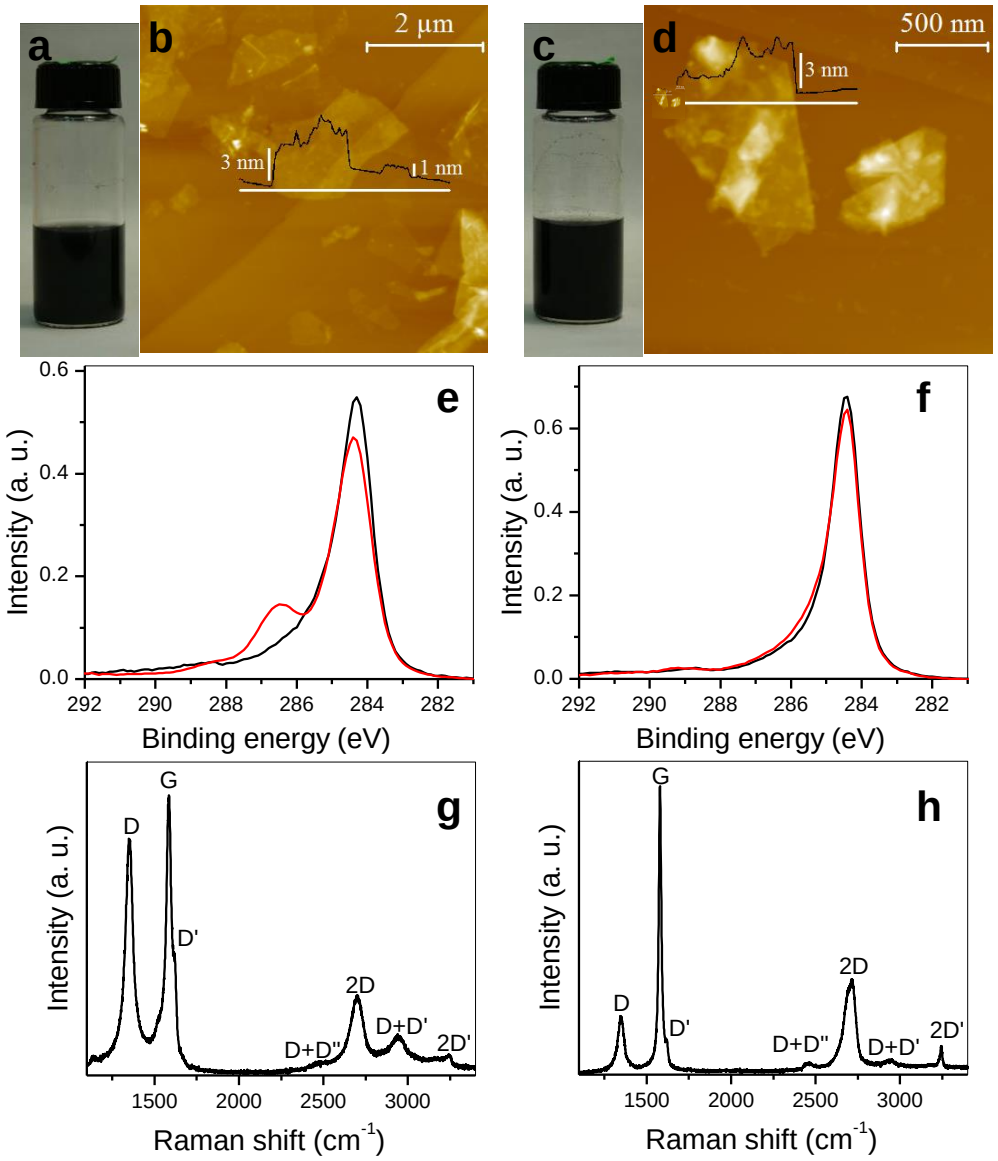

Figure S13. Digital photographs of the dispersions of HOPG **(a)** and natural graphite powder prepared by electrolytic treatment at 10 V in 0.2 M SNDS aqueous solution followed by ultrasonication for 3 h **(c)**. AFM images of the dispersions prepared from HOPG **(b)** and natural graphite powder **(d)** drop–cast onto HOPG substrates. A typical line profile (black trace) taken along the marked white line is shown superimposed on each image. Background–subtracted, normalized, high resolution C 1s core level XPS spectra of the drop–cast dispersions prepared from HOPG **(e)**, and natural graphite powder **(f)** with SNDS. For the sake of comparison, the C 1s spectrum of the drop–cast dispersions obtained with SS are also shown (red trace). Raman spectra of the flakes obtained from HOPG **(g)**, and natural graphite powder **(h)**. The main peaks are labeled.

Table S1. Characteristics of anodically exfoliated graphenes obtained from different types of graphite using sodium sulfate (SS) and sodium naphthalene 1,5–disulfonate (SNDS). The anodic exfoliation time is given in parenthesis.

graphite type	electrolyte	[electrolyte]	[graphene]	Apparent thickness	O/C	I_D/I_G

		(M)	(mg mL^{-1})	(nm)		
Natural graphite powder	SS	0.10		3–4	0.04 [4]	0.2
(3 min)	SNDS	0.20	0.22	3–4	0.04	0.2
Graphite foil (60 min)	SS	0.10	0.66	1–2	0.11 [4]	1.0
	SNDS	0.20	0.84	1–2	0.02	0.2
HOPG (60 min)	SS	0.10		1–2	0.18 [4]	1.2
	SNDS	0.20	0.07	1–2	0.06	0.9

Electrolytic treatment led to homogeneous, opaque black suspensions (see digital photographs of the dispersions in Figs. S13a and S13c), which were colloidally stable for weeks. The effective exfoliation of the starting graphites into thin flakes was evident from the AFM images of the dispersions drop–cast onto HOPG substrates (Figs. S13b and S13d). The flakes showed typical lateral dimensions between a few and several hundred nm, and their apparent thickness, determined as flake height relative to the substrate (see exemplary line profiles in Figs. S13b and S13d), ranged between ~1 and 2 nm for graphene derived from HOPG (although a low proportion of flakes ~3 nm thick were found, see line profile in Fig. S13b), and between ~3 and 4 nm for graphene derived from natural graphite powder. As already found in a previous work [4], where the graphene dispersions obtained by anodic exfoliation of different types of graphite (using a common electrolyte, K_2SO_4) were compared, the exfoliation degree (flake thickness) tended to be better for graphene obtained from compact graphite types, such as HOPG or graphite foil, compared with graphene from particulate graphite types, such as natural graphite flakes and powder. This is due to the fact that the duration of the electrolytic exfoliation process is limited in the case of the particulate forms due to the quick detachment of the individual graphite particles of their pellets.

XPS analysis revealed that, in analogy with the results obtained for graphene from graphite foil, SNDS prevents to a significant extent the oxidation of graphene derived from HOPG compared with the use of a common electrolyte, such as SS. Indeed, the O/C ratios derived from XPS survey spectra (not shown) are 0.06 graphene obtained in the presence of SNDS vs. 0.18 for graphene obtained with SS (see Table 1).

The role of SNDS as a sacrificial agent to prevent graphene oxidation is also evident from the high resolution C 1s core level spectra (black and red trace in Fig. S13e for graphene obtained from HOPG using SNDS and SS, respectively). The significant drop in intensity of the component at ~286.5 eV assigned to carbon in hydroxyl and epoxy groups (C–O bonds) [10] is apparent when using SNDS. In the case of natural graphite powder, the degree of oxidation attained in the presence of common electrolytes, such as SS, is already low (O/C ratio of 0.04, see Table 1). Such low oxidation degree is due to the aforementioned limited duration of the electrolytic treatment (3 min). In this case, the oxidation degree remains unchanged if the electrolyte is changed to SNDS (see Table 1). This is also apparent from the high resolution C 1s core level spectra (Fig. S13f). However, in this case SNDS keeps the dual role of exfoliating electrolyte and colloidal dispersant.

Evidence of the structural quality of the anodically exfoliated graphene flakes was gathered by Raman spectroscopy. Representative Raman spectra of the drop–cast dispersions prepared

from HOPG and natural graphite powder are presented in Figs. S13g and S13h, respectively. The corresponding integrated intensity ratio of the D and G bands (I_D/I_G ratio), which is indicative of the degree of structural quality in graphitic materials, is given in Table 1. Anodically exfoliated natural graphite powder using either SS or SNDS as electrolyte yield I_D/I_G ratio of 0.2 (vs. 0.1 for the starting graphite). As mentioned above, the short electrolytic treatment time limits the extent of oxidation of the flakes. Accordingly, the amount of defects and structural imperfections introduced in the carbon lattice are relatively small. In the case of HOPG, anodic exfoliation significantly increases the structural disorder, the I_D/I_G value increasing from 0 for the starting HOPG to 0.9 for the exfoliated flakes (See Table 1). However, the disorder introduced using SNDS as electrolyte is lower than when SS is used. Again, the presence of a sacrificial agent which diminishes oxidation brings about a lower number of defects.

Therefore, the results discussed in the main text for graphene obtained from graphite foil can be extended to other types of starting graphite. Indeed, with a suitable electrolyte it is possible to directly obtain colloidally stable aqueous graphene dispersions by anodic exfoliation of different types of graphite, with good exfoliation degree and reduced degree of oxidation. These results also confirm the conclusions of our previous work [4] where a comparison between graphene obtained from different starting graphites by electrolytical treatment with potassium sulfate was carried out. In that work it was concluded that graphene flakes with high structural quality and minimized amount of oxygen functional groups can be obtained by selecting appropriate types of graphite, such as graphite foil. A similar conclusion can be reached when using SNDS as electrolyte instead of SS. This behavior was rationalized in our previous work in terms of the specific microstructure of the starting graphite material as well as the general exfoliation mechanism during the anodic process [4].

S10. Growth of Pt NPs on electrolytically exfoliated graphene in the absence of amphiphile electrolyte/dispersants

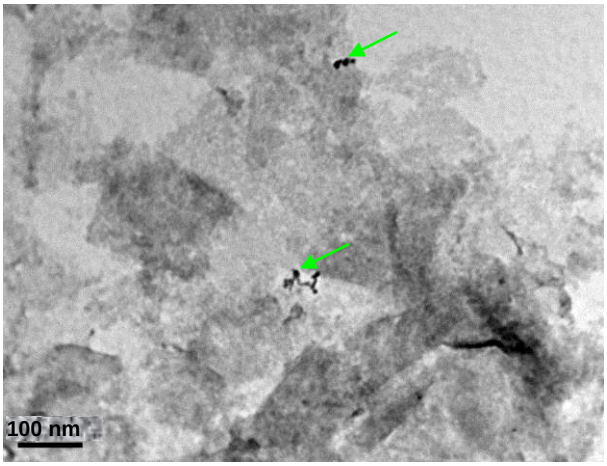

Figure S14. Representative TEM image of graphene–Pt NP hybrid obtained by the same protocol as that described in the main text for graphene–Pt NP hybrids but in the absence of any amphiphilic electrolyte. In this case, graphene was prepared by electrolytic exfoliation of graphite foil with the non–amphiphilic electrolyte SS and dispersion of the exfoliated product in a water–isopropanol mixture. Some NPs are marked by green arrows.

References

[1] K. Parvez, Z.-S. Wu, R. Li, X. Liu, R. Graf, X. Feng, K. Müllen, J. Am. Chem. Soc., 2014, 136, 6083–6091.

[2] K. S. Rao, J. Sentilnathan, H.–W. Cho, J.–J. Wu, M. Yoshimura, Adv. Funct. Mater., 2015, 25, 298–305.

[3] Chen, D. Xue, J. Colloid Interface Sci., 2014, 436, 41–46.

[4] J.M. Munuera, J.I. Paredes, S. Villar–Rodil, M. Ayán–Varela, A. Pagán , S.D. Aznar–Cervantes, J.L. Cenis, A. Martínez–Alonso, J.M.D. Tascón. High quality, low oxygen content and biocompatible graphene nanosheets obtained by anodic exfoliation of different graphite types. Carbon 94 (2015) 729–739.

[5] Dirk Rosenthal, Marina Ruta, Robert Schlögl, Lioubov Kiwi-Minsker. Combined XPS and TPD study of oxygen-functionalized carbon nanofibers grown on sintered metal fibers. Carbon 2010, 48, 1835-1843.

[6] S. Yumitori. Correlation of C1s chemical state intensities with the O1s intensity in the XPS analysis of anodically oxydised glass-like carbon samples. J. Mater. Sci., 2000, 35, 139-146.

[7] E. Papirer, R. Lacroix, J.-B. Donnet, G. Nanse, P. Froux.XPS study of the halogenation of carbon black - part 1. Bromination. E. Papirer, R. Lacroix, J.-B. Donnet, G. Nanse, P. Froux. Carbon 1994, 32, 1341-1358.

[8] A. Proctor, P. M. A. Sherwood. X-Ray photoelectron spectroscopic studies of carbon fibre surfaces-II. The effect of electrochemical treatment. Carbon, 1983, 21, 51-59.

[9] G. Zhang, S. Sun, D. Yang, J.-P. Dodelet, E. Sacher. The surface analytical characterization of carbon fibers functionalized by H_2SO_4/HNO_3 treatment. Carbon 2008, 46, 196-205

[10] D.-Q. Yang, J.-F. Rochette, E. Sacher, Langmuir 21 (2005), 8539-8545.

[11] C. Buono, P. R. Davies, R. J. Davies, T. Jones, J. Kulhav´y, R. Lewis, D. J. Morgan, N. Robinson, D. J. Willock. Spectroscopic and atomic force studies of the functionalisation of carbon surfaces: new insights into the role of the surface topography and specific chemical states. Faraday Discuss., 2014, 173, 257–272.

A simple strategy to improve the yield of graphene nanosheets in the anodic exfoliation of graphite foil

J.M. Munuera*, J.I. Paredes, S. Villar-Rodil, A. Martínez-Alonso, J.M.D. Tascón

Instituto Nacional del Carbón, INCAR-CSIC, Apartado 73, 33080 Oviedo, Spain

Abstract

Strategies that improve the yield of graphene nanosheets in anodic exfoliation processes are desirable for the mass production of this material. Here, a simple pre-treatment of graphite foil with concentrated H_2SO_4 is demonstrated to be such an effective strategy, affording overall exfoliation yields up to ~50 wt% under certain experimental conditions, compared with a baseline value of ~10 wt% for untreated graphite. Filling of inner voids and interstices of the graphite foil with H_2SO_4 molecules was concluded to be responsible for the enhanced exfoliation performance. Additional approaches to further increase the anodic exfoliation yield are also proposed and discussed.

At present, the prospects for the large-scale production of graphene face several hurdles that stand in the path of the widespread practical implementation of this two-dimensional carbon material. Bottom-up production methods (most notably, chemical vapor deposition) can afford monolayer graphene wafers of a high structural quality and large lateral dimensions, but the conditions required for their synthesis are generally not amenable for massive up-scaling [1]. On the other hand, mainstream approaches based on exfoliation of graphite and graphite derivatives (top-down methods) suffer either from a very low crystalline quality of the exfoliated material (e.g., the graphite oxide route) or from low yield (<5 wt%) and incomplete exfoliation (typical flake thickness >3-4 monolayers) of the starting graphites (e.g., direct liquid-phase exfoliation routes reliant on sonication or shear forces) [1,2].

* Corresponding author. Phone number: (+34)985119090. E-mail address: j.munuera@incar.csic.es (Jose Munuera)

In this context, electrochemical exfoliation methods, which rest on ion intercalation of a graphite electrode triggered by an applied DC bias voltage, have recently emerged as a promising alternative [3,4,5,6,7,8]. With the use of proper electrolytes and solvent media, both cathodic and anodic exfoliation is possible, the latter being particularly attractive and more usually deployed because it can be carried out in aqueous solutions of common electrolytes, such as H_2SO_4 or its inorganic salts [4]. Concerning the electrode material for exfoliation, graphite foil is a frequent choice owing to its modest cost (~$10-20 per kilogram) as well as morphological features that are especially conducive to facilitating delamination [9]. However, although graphenes produced by anodic exfoliation tend to possess a higher structural quality than that of their graphite oxide-derived counterparts and are better exfoliated than the typical nanosheets obtained via direct sonication/shear routes, in many cases the overall yield of exfoliation is rather low (e.g., ~10 wt% for graphite foil) [10], with the effect of different process parameters on the yield being seldom investigated [4]. Thus, the development of rational strategies aimed at increasing this yield is needed if anodic exfoliation is to become a truly competitive option for the mass production of graphene. We report here that a simple pre-treatment of graphite foil with concentrated H_2SO_4 is one such effective strategy, as it affords much improved exfoliation yields during the subsequent anodic treatment in aqueous electrolyte. H_2SO_4 is a common and widely used reactive, particularly in the preparation of graphene oxide via the Hummers method and in the anodic exfoliation of graphite into graphene. We also discuss the possible mechanisms responsible for the observed behavior as well as some approaches to further increase the yield.

Treatment of graphite foil pieces ~0.5 mm in thickness with concentrated H_2SO_4 at room temperature for a given period of time [see Electronic Supplementary Material (ESM) for a description of the experimental procedure] afforded highly hygroscopic materials, as visually evidenced by the condensation of water droplets on their surface upon exposure to ambient air. Field emission scanning electron microscopy (FE-SEM) imaging indicated that the graphite foil morphology, which was originally comprised of random stacks of micrometer-sized graphite platelets and exhibited a high density of folds, wrinkles and overlaps with voids and interstitial spaces in-between (Fig. 1a), became slightly rougher and developed a number of dome-like features (blisters) after exposure to H_2SO_4 (Fig. 1b). The latter were ascribed to H_2SO_4 molecules trapped in the voids/interstices of the material. Moreover, prolonged exposure of the graphite foil surface to the electron beam from the FE-SEM apparatus led to the progressive

disappearance of the blisters (images not shown), probably as a result of outward diffusion of the H_2SO_4 molecules induced by a local temperature rise.

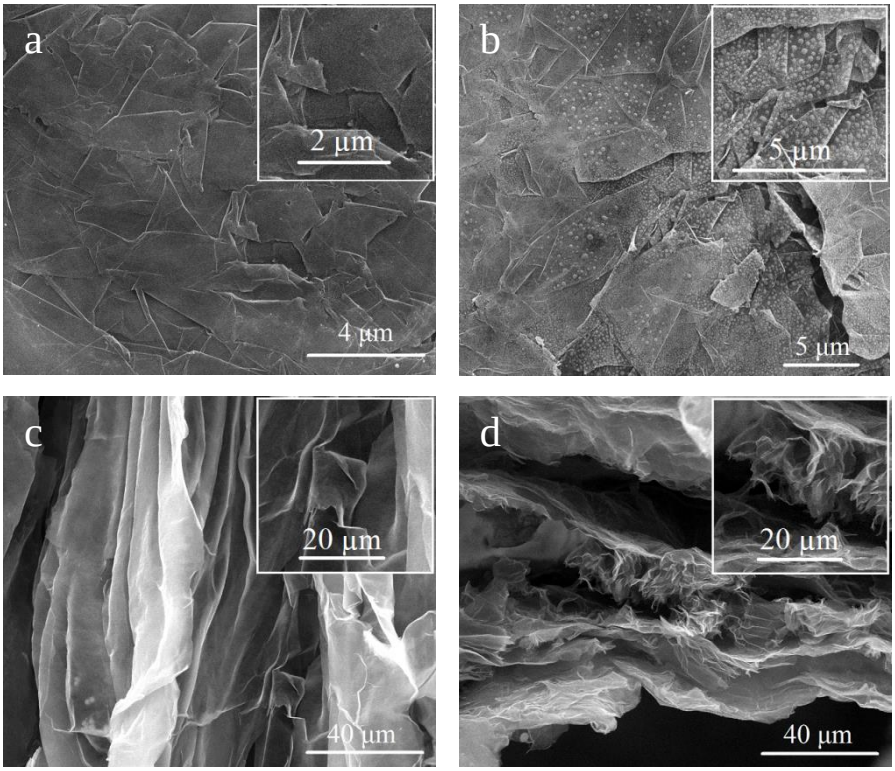

Figure 1. (a,b) Typical FE-SEM images of the surface of (a) untreated and (b) H_2SO_4-treated (6 h) graphite foil. (c,d) FE-SEM images of anodically expanded graphite foil (c) without and (d) with H_2SO_4 pre-treatment (6 h).

The graphite foil samples (both untreated and treated with H_2SO_4 for different periods of time) were then subjected to anodic exfoliation in aqueous 0.1 M K_2SO_4 solution (see ESM for details). In all cases, a significant fraction of the graphite material was seen to expand and detach from the anode, as expected. FE-SEM inspection of the expanded products after extensive washing with deionized water (Fig. 1c and d) provided microscopic evidence of their delamination, revealing very thin, corrugated layers that were separated by submicrometer-/ micrometer-sized voids. Such a type of morphology is characteristic of successful anodic exfoliation processes [10,11]. No significant morphological differences between the untreated (Fig. 1c) and any of the H_2SO_4-treated graphite foil specimens (e.g., Fig. 1d) were apparent after the anodic expansion. However, the net amount of expanded product that was generated from the pre-treated samples was usually much larger than that obtained from their untreated

counterpart, thus providing a first hint of the beneficial effect of such a pre-treatment on exfoliation.

To provide a quantitative measure of the overall yield of exfoliation, the anodically expanded products were bath-sonicated in *N*,*N*-dimethylformamide (DMF), water/isopropanol mixture (65/35 v/v%) or in aqueous solution of flavin mononucleotide (FMN) [9], and then centrifuged to separate the individual, well-exfoliated graphene nanosheets (supernatant) from the incompletely delaminated material (sediment). The exfoliation yield was calculated as the ratio of the amount of graphene nanosheets dispersed in the solvent (estimated by means of UV-vis absorption spectroscopy [10]) to the original mass of the graphite foil electrode. The results obtained for different treatment times of the graphite foil with H_2SO_4 are presented in Fig. 2, where it is apparent that such an approach had a sizable positive impact on the exfoliation yield. Specifically, the yield increased from a baseline value of ~10 wt% attained with untreated graphite foil under the experimental conditions described in the ESM up to ~50 wt% for treatment times longer than ~40 h, i.e., a 5-fold increase in yield was accomplished. However, short treatment times already afforded much enhanced yields (e.g., a ~3-fold increase was observed after 5 h). We note that these yield values exhibited a variance of ~10-20% for different samples prepared under exactly the same conditions, as it is sometimes observed for electrochemically exfoliated graphene. It is important to note that the criterion followed here to determine the exfoliation yield was more stringent than others adopted in the literature. For instance, in some cases the yield has been calculated as the amount of anodically expanded product (before dispersion in any solvent) relative to the starting mass of the graphite anode [11], or as the amount of solvent-dispersed graphene relative to the mass of anodically expanded product (rather than the total mass of the graphite anode) [12]. Likewise, certain process parameters must have a critical effect on the exfoliation yield (e.g., thinner graphite foils are expected to afford higher yields), but in many studies such parameters are not provided. For these reasons, meaningful comparisons with previous yield data from the literature are difficult to make, as such data cannot be taken in absolute terms. Nevertheless, the present results clearly demonstrate that large increases in the anodic exfoliation yield (and thus in the amount of generated graphene per unit time) can be attained just by dipping the graphite foil in concentrated H_2SO_4.

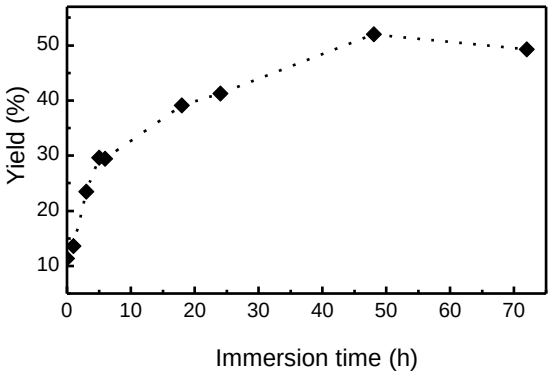

Figure 2. Anodic exfoliation yield of graphite foil as a function of H_2SO_4 pre-treatment time. The yield was determined as the amount of solvent-dispersed graphene nanosheets obtained relative to the initial mass of the graphite foil anode.

Physicochemical characterization of the anodically delaminated products confirmed the generation of graphene nanosheets from H_2SO_4-treated graphite foil. Fig. 3a shows a representative UV-vis absorption spectrum of a colloidal dispersion obtained in water/isopropanol mixture from graphite pre-treated in H_2SO_4 for 24 h (see inset for a digital picture of the dispersion), where a peak at ~268 nm and strong absorbance in the 270-1000 nm range revealed the presence of suspended graphitic material [9]. This spectrum was characteristic of those obtained for graphene dispersions obtained from graphite foil electrodes dipped in H_2SO_4 for different times. Atomic force microscopy (AFM) imaging showed that this material was made up of nanosheets typically between a few and several hundred nanometers in lateral size with an apparent thickness of ~1-1.5 nm (Fig. 3b), consistent with few-layer (< 4) graphene. As revealed by X-ray photoelectron spectroscopy (XPS), pre-treatment with H_2SO_4 led to anodically exfoliated nanosheets having an increased extent of oxidation (Fig. 3c). Indeed, the O/C atomic ratio for graphenes obtained from foils pre-treated for long times was ~0.20, compared with a value of ~0.10 for graphenes derived from untreated graphite foil. However, such a level of oxidation was well within the range of values typically reported for graphenes prepared by anodic exfoliation in H_2SO_4 or sulfate salt electrolytes (O/C ratios ~0.10-0.30) [10,13,14]. Moreover, Raman spectroscopy indicated that the structural quality of the graphene nanosheets was not seriously degraded as a result of pre-treatment of the graphite foil with H_2SO_4, since no significant changes to the D/G band ratios were observed (Fig. 3d). For comparison, the spectrum of hydrazine-reduced graphene oxide exhibited broader D and G Raman bands

[FWHM(G band)~80 cm^{-1} vs. ~50 cm^{-1}, respectively, see inset to Fig. 3d), thus denoting a more disordered carbon lattice. Conductivity measurements were carried out for the samples prepared with a 24h dipping in H_2SO_4, yielding a value of ~35000 S m^{-1}. This value is in the range of conductivities typically measured for good quality electrochemically exfoliated graphene flakes [9,10], suggesting that the structural quality of the flakes has not been diminished to a great extent because of the pre-treatment, in agreement with the Raman data.

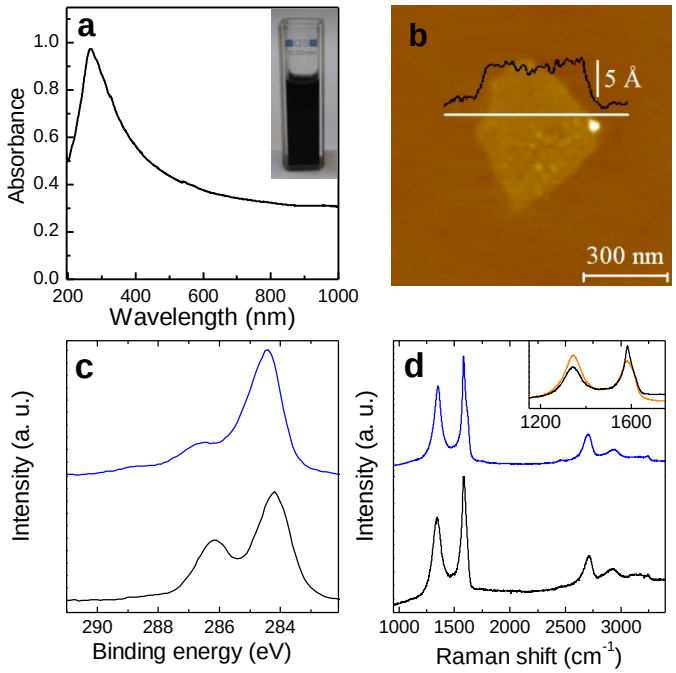

Figure 3. (a) UV-vis absorption spectrum of a colloidal dispersion of anodically exfoliated graphene in water/isopropanol mixture (65/35 v/v%) obtained from a H_2SO_4-treated graphite foil. Inset: digital picture of the dispersion. (b) AFM image of graphene nanosheets anodically exfoliated from graphite foil pre-treated with H_2SO_4 (24 h). A representative line profile (green trace) taken along the marked white line is shown overlaid on the image. (c) High resolution C 1s core level XPS and (d) Raman spectra of graphene nanosheets anodically exfoliated from (i) untreated and (ii) H_2SO_4-treated (24 h) graphite foil. The inset to (d) compares the first-order Raman spectrum of the latter sample (black trace) with that of hydrazine-reduced graphene oxide (orange trace).

To understand the origin of the positive effect of H_2SO_4 pre-treatment on the anodic exfoliation yield of graphite foil, we first note that insufficient intercalation of the graphite anode during the electrolytic process was probably responsible for the limited

exfoliation yield observed with the untreated material. Hence, approaches that boost the extent of ion intercalation should be expected to give rise to increased yields. Second, as noted above, graphite foil incorporates a large number of voids and interstitial spaces in its structure (the density of the material used here was 0.7-1.3 g cm^{-3} vs ~2.26 g cm^{-3} for defect-free, single-crystal graphite [15]). These voids and interstices can be assumed to become progressively filled with H_2SO_4 molecules during exposure to the concentrated acid, thus making the material hygroscopic. When such a pre-filled graphite is subjected to anodic treatment in aqueous electrolyte, the very high local density of SO_4^{2-} anions inside the graphite foil should promote an extensive initial intercalation of the material that would facilitate the further entrance of anions from the aqueous medium, which in turn would result in a more extensive delamination of the anode. We believe void filling to be the only effect of H_2SO_4 pre-treatment, incorporation of the acid in the graphite interlayer spaces to give H_2SO_4-graphite intercalation compounds (GICs) being reasonably ruled out: X-ray diffraction did not support the formation of such GICs (Fig. S1 in the ESM), which generally requires the presence of an oxidizing species in addition to H_2SO_4 [16]. The key role played by the high density of voids/interstices was made apparent in a control experiment in which graphite foil was replaced by a void-free graphite, namely, highly oriented pyrolytic graphite (HOPG; density ~2.25 g cm^{-3}). In this case, pre-treatment of HOPG with H_2SO_4 did not lead to a large increase in the exfoliation yield. A schematic illustration of the proposed effect of H_2SO_4 pre-treatment on the anodic exfoliation of graphite foil is provided in Fig. 4.

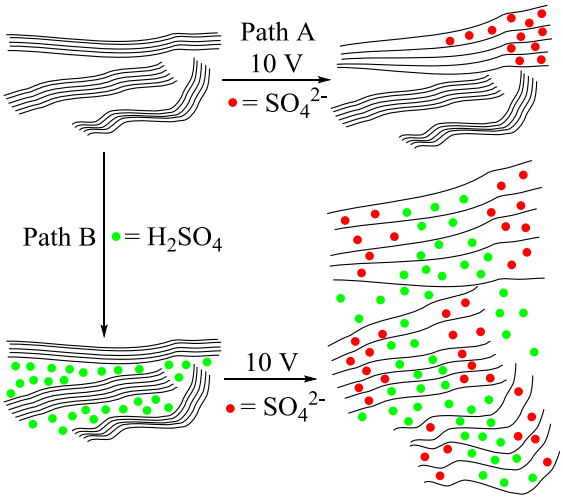

Figure 4. Schematic of the proposed anodic exfoliation process of graphite foil without and with H_2SO_4 pre-treatment. When no pre-treatment is undertaken (path A), limited access of the aqueous anions from the electrolyte (orange circles) to the interior of the foil leads to a low exfoliation yield. When a H_2SO_4 pre-treatment is carried out (path B), the acid molecules filling the inner voids and interstices of the graphite foil (red circles, step B1) promote a more extensive intercalation of the material during the subsequent anodic process, resulting in a higher exfoliation yield (step B2).

We note that simply increasing the aqueous electrolyte concentration as an alternative to the H_2SO_4 pre-treatment is not an effective strategy, as it does not usually lead to higher exfoliation yields [11]. In aqueous medium, access of the electrolyte anions to the inner voids and interstices of the foil is probably restricted by the hydrophobic nature of the material. Such a restriction should be lifted when these voids/interstices become hygroscopic as a result of their filling with H_2SO_4, an effect that would also contribute to increasing the exfoliation yield. On the other hand, dipping the graphite foil in liquid N_2 followed by soaking in ethanol, which created macroscopic cracks and voids in the material, led to a ~2-fold increase in anodic exfoliation yield (up to ~20 wt%). However, combined liquid N_2/H_2SO_4 treatment did not increase the overall exfoliation yield significantly above 50 wt%. Working with lower density versions of graphite foil (densities as low as ~0.05 g cm^{-3} have been produced [17]) should be a better option than the aggressive liquid N_2 treatment, as the higher numbers of small-sized voids and interstices should favor an increased and more uniform filling of the material with H_2SO_4 molecules that would result in higher exfoliation yields. Other process parameters should also bear an influence on the exfoliation yield (e.g., we

have observed that higher electrolyte volume/graphite anode mass ratios as well as thinner foils lead to higher yields), but their effect has not yet been systematically investigated, which should warrant further studies along these lines in the future.

In summary, we have shown that pre-treatment with concentrated H_2SO_4 is an effective strategy to increase the anodic exfoliation yield of graphite foil in aqueous electrolyte. Such an increase was thought to arise from a more extensive intercalation of this material during the electrolytic process due to the filling of its voids/interstices with H_2SO_4 molecules. This simple approach should contribute to making anodic exfoliation a more competitive method for the large-scale production of graphene.

Acknowledgements

Financial support from the Spanish Ministerio de Economía y Competitividad (MINECO) and the European Regional Development Fund (ERDF) through project MAT2015-69844-R is gratefully acknowledged. Partial funding by Plan de Ciencia, Tecnología e Innovación 2013-2017 del Principado de Asturias and the ERDF (project GRUPIN14-056) is also acknowledged. J.M.M. is grateful to the Spanish Ministerio de Educación, Cultura y Deporte (MECD) for his pre-doctoral contract.

References

[1] A.C. Ferrari, F. Bonaccorso, V.I. Fal'ko, K.S. Novoselov, S. Roche, P.Bøggild, et al., Science and technology roadmap for graphene, related two-dimensional crystals, and hybrid systems, Nanoscale 7 (2015), 4598-810.
[2] A. M. Dimiev, G. Ceriotti, A. Metzger, N. D. Kim, J.M. Tour, Chemical mass production of graphene nanoplatelets in ~100% yield, ACS Nano 10, (2016), 274-9
[3] A.M. Abdelkader, A.J. Cooper, R.A.W. Dryfe, I.A. Kinloch, How to get between the sheets: a review of recent works on the electrochemical exfoliation of graphene materials from bulk graphite Nanoscale 7 (2015), 6944-56.
[4] A. J. Cooper, N. R. Wilson, I. A. Kinloch, R. A. W. Dryfe, Single stage electrochemical exfoliation method for the production of few-layer graphene via intercalation of tetraalkylammonium cations, Carbon 66, (2014), 340-50
[5] S. Yang, M.R. Lohe, K. Müllen, X. Feng, New-Generation Graphene from Electrochemical Approaches: Production and Applications, Adv. Mater. 28 (2016), 6213-21.
[6] H. J. Salavagione, Promising alternative routes for graphene production and functionalization, J. Mater. Chem. A, 2, (2014), 7138-46

[7] G.M. Morales, P. Schifani, G. Ellis, C. Ballesteros, G. Martínez, C. Barbero et al, High-quality few layer graphene produced by electrochemical intercalation and microwave-assisted expansion of graphite, Carbon 49, (2011), 2809
[8] A. Ambrosi, M. Pumera, Electrochemically exfoliated graphene and graphene oxide for energy storage and electrochemistry applications, Chem. Eur. J, 22, (2016), 153-9
[9] J.M. Munuera, J.I. Paredes, S. Villar-Rodil, M. Ayán-Varela, A. Pagán, S.D. Aznar-Cervantes, et al., High quality, low oxygen content and biocompatible graphene nanosheets obtained by anodic exfoliation of different graphite types, Carbon 94 (2015), 729-39.
[10] J.M. Munuera, J.I. Paredes, S. Villar-Rodil, M. Ayán-Varela, A. Martínez-Alonso, J.M.D. Tascón, Electrolytic exfoliation of graphite in water with multifunctional electrolytes: en route towards high quality, oxide-free graphene flakes, Nanoscale 8 (2016), 2982-98.
[11] K. Parvez, Z.-S. Wu, R. Li, X. Liu, R. Graf, X. Feng, et al., Exfoliation of Graphite into Graphene in Aqueous Solutions of Inorganic Salts, J. Am. Chem. Soc. 136 (2014), 6083-91.
[12] B.D. Ossonon, D. Bélanger, Functionalization of graphene sheets by the diazonium chemistry during electrochemical exfoliation of graphite, Carbon 111 (2017), 83-93.
[13] J. Liu, M. Notarianni, G. Will, V.T. Tiong, H. Wang, N. Motta, Electrochemically Exfoliated Graphene for Electrode Films: Effect of Graphene Flake Thickness on the Sheet Resistance and Capacitive Properties, Langmuir 29 (2013), 13307-13314.
[14] J. Liu, C.K. Poh, D. Zhan, L. Lai, S.H. Lim, L. Wang, et al, Improved synthesis of graphene flakes from the multiple electrochemical exfoliation of graphite rod, Nano Energy 2 (2013), 377-86.
[15] Papyex Flexible Graphite Technical Guide, https://www.mersen.com/uploads/tx_mersen/12-PAPYEX-flexible-graphite-Mersen_07.pdf, Accessed October 2016.
[16] M.S. Dresselhaus, G. Dresselhaus, Intercalation compounds of graphite, Adv. Phys. 51 (2002), 1-186.
[17] D.D.L. Chung, Exfoliation of graphite, J. Mater. Sci. 22 (1987), 4190-8.

Electronic Supplementary Material for

A simple strategy to improve the yield of graphene nanosheets in the anodic exfoliation of graphite foil

J.M. Munuera, J.I. Paredes, S. Villar-Rodil, A. Martínez-Alonso, J.M.D. Tascón

Instituto Nacional del Carbón, INCAR-CSIC, Apartado 73, 33080 Oviedo, Spain

S1. Materials and reagents

High purity graphite foil (Papyex I980) with a density of 0.7-1.3 g cm^{-3} and a thickness of ~0.5 mm was acquired from Mersen, whereas highly oriented pyrolytic graphite (HOPG; grade ZYH) was obtained from Advanced Ceramics. Concentrated H_2SO_4 (95-98%), K_2SO_4, *N*,*N*-dimethylformamide (DMF), sodium salt of flavin mononucleotide (FMN), isopropanol and ethanol were purchased from Sigma-Aldrich and used as received. Pt wire (diameter: 0.20 mm, purity: 99.99%) was acquired from Goodfellow. Cellulose membranes for dialysis with a molecular weight cutoff of 12000 Da were obtained from Sigma Aldrich. Milli-Q deionized water (resistivity: 18.2 MΩ·cm), from Millipore Corporation, was used throughout the study. Hydrazine-reduced graphene oxide was obtained from graphite oxide by a procedure described elsewhere [1].

S2. H_2SO_4 treatment and anodic exfoliation of graphite foil

Graphite foil was cut into pieces of fixed dimensions (55×30×0.5 mm^3) for use in all the subsequent experiments. The H_2SO_4 treatment was accomplished by immersing a graphite foil piece into 50 mL of the concentrated acid at room temperature for a given period of time, typically ranging from 1 to 72 h. Afterwards, the sample was briefly rinsed with water and allowed to dry under ambient conditions. The anodic exfoliation process was carried out in 80 mL of aqueous 0.1 M K_2SO_4 solution, using a two-electrode configuration that comprised a piece of untreated or H_2SO_4-treated graphite foil as the anode and Pt wire as the cathode. The latter was placed parallel to the graphite foil surface at a distance of about 2 cm. A bias voltage of 10 V was then applied for 1 h by means of an Agilent 6614C DC power supply. The resulting anodically expanded product was collected and washed extensively with water through filter paper. For a more efficient removal of remnants of acids and salts, the washed material was subjected to bath-sonication (JP Selecta Ultrasons system, 40 kHz, ~20 W L^{-1}) for 3 h in a water/isopropanol (65/35 v/v%) mixture and then dialyzed against water (4×2 L) for a total of 72 h. Finally, the resulting wet product was transferred to DMF, water/isopropanol mixture or aqueous FMN solution (1 mg mL^{-1}), bath-sonicated for 1 h and centrifuged at 200 *g* for 20 min (Eppendorf 5424 microcentrifuge) to obtain a colloidal suspension of graphene nanosheets. The concentration of graphene in the suspension was estimated by means of UV-vis absorption spectroscopy, using the Lambert-Beer law: $A/l = \alpha C$, where A is the measured absorbance of the graphene dispersion, l is the length of the optical path, α is the extinction coefficient and C is the graphene concentration. To determine C, the absorbance was measured at a wavelength of 660 nm, for which an extinction coefficient α = 2440 mL mg^{-1} m^{-1} [2,3] was used.

The overall exfoliation yield was calculated as the ratio of the amount of solvent-dispersed graphene nanosheets to the initial mass of the graphite foil piece.

S3. Characterization techniques

UV-vis absorption spectra were recorded on a double-beam Heλios α spectrophotometer, from Thermo Spectronic. Field emission scanning electron microscopy (FE-SEM) images were obtained with a Quanta FEG 650 instrument (FEI Company) operated at 30 kV. Atomic force microscopy (AFM) imaging was carried out in the tapping mode of operation with a Nanoscope IIIa Multimode apparatus (Veeco), using rectangular Si cantilevers with nominal spring constant and resonance frequency of ~40 N m^{-1} and 250-300 kHz, respectively. Samples for AFM were prepared by drop-casting dilute graphene dispersions (~0.05 mg mL^{-1}) onto pre-heated (~50-60 ºC), freshly cleaved HOPG substrates, which were then allowed to dry. X-ray photoelectron spectroscopy (XPS) was accomplished on a SPECS system with a non-monochromatic Mg K_α X-ray source operated at 11.81 kV and 100 W under a pressure of 10^{-7} Pa. Raman spectra were acquired with a Horiba Jobin-Yvon LabRam instrument using a laser excitation wavelength of 532 nm at an incident power of ~2.5 mW. Specimens for both XPS and Raman spectroscopy were prepared by drop-casting solvent-dispersed graphene nanosheets onto a pre-heated (~50-60 ºC), circular stainless steel sample-holder (diameter: 12 mm). X-ray diffraction (XRD) patterns were recorded with a Bruker D8 Advance diffractometer, using Cu K_α (λ = 0.154 nm) at a step size of 0.02º and a step time of 1 s. Electrical conductivity measurements were carried out by the van der Pauw method using a home-built setup (Agilent 6614C DC power supply and Fluke 45 digital multimeter).

S4. XRD of untreated and H_2SO_4-treated graphite foil

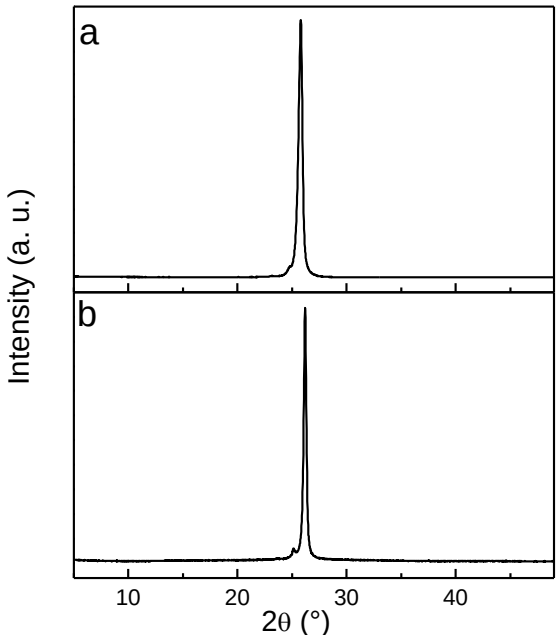

Figure S1. XRD patterns of (a) untreated and (b) H_2SO_4-treated (24 h) graphite foil. No significant differences between the two samples were observed. In particular, no shift of the (002) peak towards lower angles was noticed for the H_2SO_4-treated sample, which would have been indicative of the formation of H_2SO_4-graphite intercalation compounds.

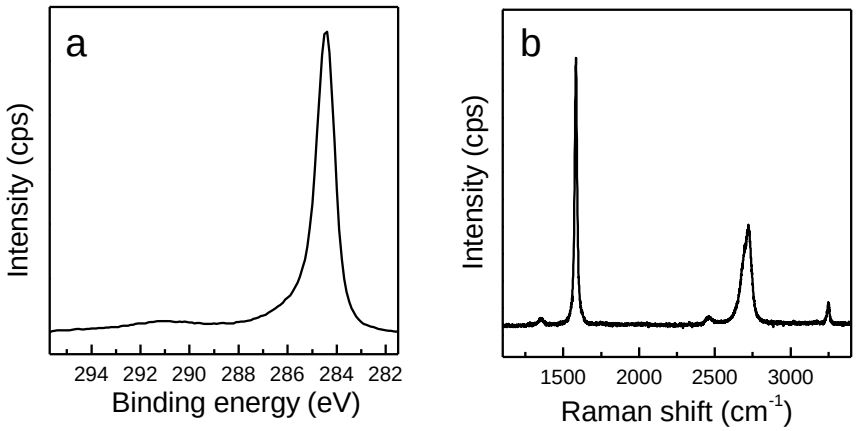

Figure S2. (a) High resolution C 1s core level XPS and (b) Raman spectra of graphite foil.

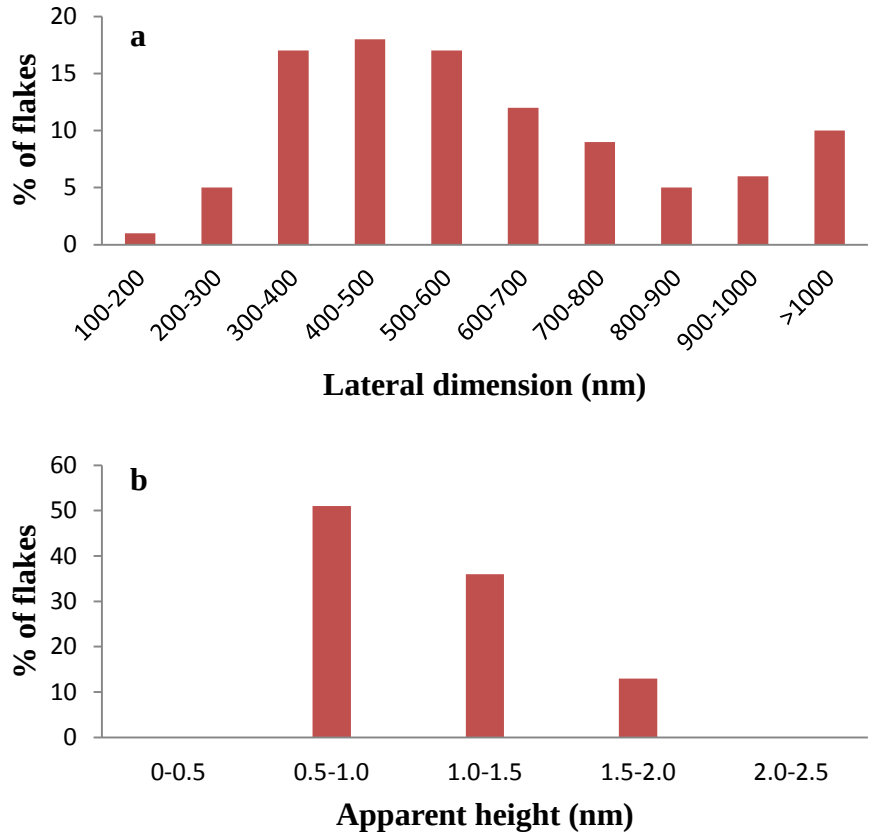

Figure S3. Histograms of (a) lateral dimension and (b) apparent height of 100 graphene flakes measured by AFM.

S5. References

[1] M.J. Fernández-Merino, L. Guardia, J.I. Paredes, S. Villar-Rodil, P. Solís-Fernández, et al., Vitamin C Is an Ideal Substitute for Hydrazine in the Reduction of Graphene Oxide Suspensions J. Phys. Chem. C 114 (2010), 6426-32.

[2] Z. Sun, J. Masa, Z. Liu, W. Shuhmann, M. Muhler, Highly Concentrated Aqueous Dispersions of Graphene Exfoliated by Sodium Taurodeoxycholate: Dispersion Behavior and Potential Application as a Catalyst Support for the Oxygen-Reduction Reaction, Chem. Eur. J. 18 (2012), 6972-8.

[3] M. Ayán-Varela, J.I. Paredes, L. Guardia, S. Villar-Rodil, J.M. Munuera, M. Díaz-González, et al., Achieving Extremely Concentrated Aqueous Dispersions of Graphene Flakes and Catalytically Efficient Graphene-Metal Nanoparticle Hybrids with Flavin Mononucleotide as a High-Performance Stabilizer, ACS Appl. Mater. Interfaces 7 (2015), 10293-307.

Electrochemical exfoliation of graphite in aqueous sodium halide electrolytes towards low oxygen content graphene for energy and environmental applications

J.M. Munuera[a*], J.I. Paredes[a], M. Enterría[b], A. Pagán[c], S. Villar-Rodil[a], M.F.R. Pereira[b], J.I. Martins[d,e], J.L. Figueiredo[b], J.L. Cenis[c], A. Martínez-Alonso[a], J.M.D. Tascón[a]

[a]*Instituto Nacional del Carbón, INCAR-CSIC, Apartado 73, 33080 Oviedo, Spain*
[b]*Laboratório de Processos de Separação e Reacção – Laboratório de Catálise e Materiais (LSRE-LCM), Departamento de Engenharia Química, Faculdade de Engenharia, Universidade do Porto, R. Dr. Roberto Frias s/n, 4200-465 Porto, Portugal*
[c]*Instituto Murciano de Investigación y Desarrollo Agrario y Alimentario (IMIDA), Calle Mayor 1, 30150 La Alberca, Spain*
[d]*Departamento de Engenharia Química, Faculdade de Engenharia, Universidade do Porto, R. Dr. Roberto Frias s/n, 4200-465 Porto, Portugal*
[e]*Universidade do Minho, LAB2PT- Laboratório de Paisagens, Património e Território, Portugal*

Abstract

Graphene and graphene-based materials have shown great promise in many technological applications, but their large-scale production and processing by simple and cost-effective means still constitute significant issues in the path of their widespread implementation. Here, we investigate a straightforward method for the preparation of a ready-to-use and low oxygen content graphene material that is based on electrochemical (anodic) delamination of graphite in aqueous medium with sodium halides as the electrolyte. Contrary to previous conflicting reports on the ability of halide anions to act as efficient exfoliating electrolytes in electrochemical graphene exfoliation, we show that proper choice of both graphite electrode (e.g., graphite foil) and sodium halide concentration readily leads to the generation of large quantities of single-/few-layer graphene nanosheets possessing a degree of oxidation (O/C ratio down to ~0.06) lower than that typical of anodically exfoliated graphenes obtained with commonly used electrolytes. The halide anions are thought to play a role in mitigating the oxidation of the graphene lattice during exfoliation, which is also discussed and rationalized. The as-exfoliated graphene materials exhibited a three-dimensional morphology that was suitable for their

Keywords: graphene, electrochemical exfoliation, supercapacitors, environmental applications, sodium halides

practical use without the need to resort to any kind of post-production processing. When tested as dye adsorbents, they outperformed many previously reported graphene-based materials (e.g., they adsorbed ~920 mg g^{-1} for methyl orange) and were useful sorbents for oils and non-polar organic solvents. Supercapacitor cells assembled directly from the as-exfoliated products delivered energy and power density values (up to 15.3 Wh kg^{-1} and 3220 W kg^{-1}, respectively) competitive with those of many other graphene-based devices, but with the additional advantage of extreme simplicity of preparation.

1. Introduction

Since its first isolation in 2004, graphene has spurred enormous interest in the scientific community due to its excellent electronic, mechanical, thermal and optical properties, as well as to its wide range of potential applications in many fields, including electronics, photonics, energy conversion/storage, catalysis and biomedicine.[1] However, one of the most pressing issues that hinder the actual implementation and widespread use of graphene is that related to its large-scale production. At present, there is no single method that can simultaneously provide high amounts of material of good quality in a reasonable amount of time at a low cost. The existing production methods can be classified into two types: bottom-up and top-down. The former relies on synthesizing graphene sheets from small-molecule precursors, usually following chemical vapor deposition (CVD) methodologies and giving rise to large-area sheets.[2] Top-down methods, on the other hand, rely on the exfoliation of graphitic materials into single- and/or few-layer graphene flakes. Even though there exists a number of exfoliation strategies, the most relevant ones are arguably (i) the graphite oxide route, (ii) the direct liquid-phase exfoliation method and (iii) the electrochemical exfoliation approach.[3,4] The graphite oxide strategy involves harsh oxidation of graphite, causing the oxidized basal planes to be easily exfoliated in polar solvents (including water) into single-layer graphene oxide by sonication or other means.[5] This oxidation can be partially reversed through a reduction process, but the resulting product (reduced graphene oxide) always retains significant amounts of oxygen and structural defects.[6] Direct liquid-phase exfoliation generally circumvents oxidation issues because delamination is directly promoted via, e.g., ultrasound waves or high-shear forces

in a medium that can colloidally stabilize the graphene flakes (organic solvents, aqueous surfactant solutions, etc).[7] The main drawbacks of this method are the predominance of several-layer or even multilayer graphene flakes rather than single- or few-layer (<4) objects, as well as its low production yield (typically below 5 wt%).

On the other hand, electrochemical (or electrolytic) exfoliation methods are based on the intercalation of ions between the layers of a graphite electrode due to the flow of electrical current in an electrolytic cell. [8,9] These ions induce expansion of the interlayer space in graphite and thus facilitate the exfoliation process. There are essentially two approaches to electrochemical exfoliation, namely, the cathodic and the anodic approach. In the former case, graphite acts as the cathode in the electrochemical cell and intercalates cations from the electrolyte. Studies in this area have been typically carried out in organic solvents with lithium or alkylammonium salts,[10,11] as well as molten salts[12,13] and ionic liquids as the electrolyte,[14] and the obtained products are usually few-layer to several-layer graphene flakes of a high structural quality. Anodic exfoliation, on the other hand, takes place with the graphite material as the anode and is typically accomplished in aqueous electrolytes, which is advantageous from an environmental and practical standpoint.[15,16,17,18] Some studies have also reported the possibility of simultaneous anodic and cathodic exfoliation.[19,20,21] One of the main issues regarding aqueous anodic exfoliation, though, is related to the fact that graphite is subjected to a large positive voltage (typically between a few and a few tens of volts).[8] This voltage induces the formation of highly reactive oxygen species (e.g., hydroxyl radicals) from the oxidation of water molecules, which in turn trigger a significant oxidation and structural degradation the carbon lattice.[8,15]

Due to the well-known ability of the sulfate anion to intercalate graphite, sulfuric acid is widely employed as an electrolyte in the preparation of graphene flakes by anodic exfoliation.[16,17,22,23,24] However, the highly acidic nature of this electrolyte is especially conducive to obtaining graphene flakes with a considerable extent of oxidation (typical O/C atomic ratios in the ~0.10-0.25 range). Other protic acids, such as phosphoric, oxalic or perchloric acids have also been explored, with similar results. [23,25] Use of the corresponding inorganic and organic salts of these acids (e.g., sodium sulfate, citrate or perchlorate) as electrolytes has been proposed as a way to mitigate oxidation of the exfoliated graphenes, but these efforts have met with varied success.[17,22,26] More recently, novel strategies to

prevent graphene oxidation during anodic exfoliation have been explored.[27] For example, exfoliation has been accomplished with standard electrolytes (e.g., sulfuric acid) in the presence of certain additives that inhibit graphene oxidation, such as melamine,[28] or the antioxidants sodium borohydride, ascorbic acid and (2,2,6,6-tetramethylpiperidin-1-yl)oxyl (TEMPO).[29] Likewise, some sulfonated aromatic compounds have been simultaneously used as electrolytes and oxidation-preventing agents for the production of low oxygen content graphene flakes.[30] In these cases, graphenes with O/C atomic ratios down to ~0.02-0.04 were attained. However, such methods suffer from some drawbacks, including the use of relatively expensive additives/electrolytes and the difficulty in removing adsorbed additives/electrolytes from the exfoliated products to obtain neat graphenes (the additives can also induce functionalization of the flakes). Thus, the availability of anodic exfoliation methods that make use of very simple and inexpensive electrolytes and at the same time afford low oxygen content and additive-free graphenes would be highly desirable, but for the most part such methods are currently lacking.

We hypothesized that some very simple salts such as sodium halides (NaCl, NaBr, NaI) could be effective, additive-free electrolytes for the anodic exfoliation of graphite into graphene flakes with a limited extent of oxidation. This idea was supported by the fact that graphitic materials can be intercalated with halogens/halides through electrochemical and other means,[31] so that anodic exfoliation of a graphite electrode could in principle be possible in the presence of halide-based electrolytes. Although alkali halides have been previously used as additives in the preparation of graphene via direct ultrasound-induced exfoliation,[32] there are conflicting reports as to the ability of halide anions to act as efficient electrolytes in the aqueous anodic exfoliation of graphite.[16,17,33] We also note that because halide anions are relatively prone to oxidation, these intercalated species could act as sacrificial agents and neutralize the oxygen radicals generated under anodic potential, thus mitigating the oxidation of the graphene flakes in comparison with other commonly used electrolytes, but this point has not yet been demonstrated.

We have thus investigated the use of sodium halides as electrolytes for the aqueous anodic exfoliation of graphite, the results of which are reported here. Significantly, the production of single- and few-layer graphene flakes with a limited degree of oxidation, and thus of a high structural quality, was made possible by chosing an appropiate graphite

material as the anode and carefully testing different electrolyte concentrations in order to find the intermediate range where exfoliation is succesful. Considering the potential scalability of this method together with the use of sustainable and widely available electrolytes, and that no additives are required to limit oxidation, the present work should broaden the prospects of anodic exfoliation as a competitive method for the large-scale production of single-/few-layer graphene flakes towards different applications, particularly in energy- and environment-related fields. Indeed, we demonstrate the use of the halide-derived, as-exfoliated foam-like graphene products as efficient adsorbents for dyes and oils as well as electrodes for supercapacitors. Also, the biocompatibility of these graphene nanosheets is attested.

2. Results and discussion

2.1. Key aspects of the electrochemical exfoliation of graphite in aqueous halide-based electrolytes

We aimed at determining whether some very simple and widely available salts, such as the sodium halides NaCl, NaBr and NaI, could be effectively used as electrolytes towards the anodic exfoliation of graphite in aqueous medium to give graphene flakes with a limited extent of oxidation. Some previous experiments had concluded that the anodic exfoliation of graphite using halide-based electrolytes was not even possible.[16,17] On the other hand, a recent work by Munaiah *et al* has suggested that exfoliated products can be obtained, although they possess a considerable degree of oxidation (O/C atomic ratios of ~0.10-20).[33] On the basis of a suite of tests with the aforementioned sodium halides, we found that single-/few-layer graphene flakes could indeed be produced in considerable quantities. It is important to note, though, that effective exfoliation was found to be critically dependent on two main factors, namely, the type of graphite used as the anode and the concentration of sodium halide used as electrolytic medium. To understand the influence of these two factors, as well as some characteristics of the resulting graphene materials that will be discussed below, the basic mechanism underlying the anodic exfoliation process has to be borne in mind. Such a mechanism has been discussed elsewhere[17] and will just be briefly outlined here: first of all, exfoliation occurring at a graphite anode in the presence of common aqueous electrolytes (e.g., H_2SO_4) under typical bias voltage conditions (5-15 V)

is believed to start with the oxidation of grain boundaries and edges of the graphite crystals due to the presence of oxygen radicals (e.g., hydroxyl species) generated through oxidation of water molecules at the anode. This initial oxidation induces an expansion of the interlayer space at the edges, which in turn facilitates the intercalation of the graphite layers with anions from the electrolyte together with water molecules. Subsequent redox processes involving the intercalated species are thought to give rise to gaseous products that exert strong forces on the layers, leading to the expansion and swelling of the graphite anode. As a result, an expanded graphitic material composed of very weakly attached layers is finally formed, which can then be readily separated into individual single- or few-layer graphene flakes in a proper solvent medium by means of low-power ultrasound or shear forces.[17,18]

In anodic exfoliation tests carried out with sodium halides using three different types of graphite, namely, graphite foil, highly oriented pyrolytic graphite (HOPG) and graphite flakes (+10 V applied to graphite anode for 60 min with platinum foil as a counter electrode; see Experimental section), we observed that well-exfoliated graphitic materials colloidally dispersed either in the organic solvent *N*,*N*-dimethylformamide (DMF) or in water using, e.g., the biomolecule flavin mononucleotide (FMN) as a stabilizer[18,34] could only be obtained with the former graphite type. By contrast, just slightly expanded materials that could not be stably suspended in DMF or water/FMN were attained with both HOPG and graphite flakes. This result suggested that the halide anions failed to extensively intercalate and/or expand the HOPG and graphite flake materials. We believe that the distinct expansion behaviour of graphite foil is a consequence of its particular morphological features and packing configuration. Specifically, the morphology of graphite foil is typically made up of disordered stacks of micrometer-sized graphitic platelets that exhibit many folds, wrinkles and voids in their structure, as noticed from field-emission scanning electron microscopy (FE-SEM) images (Fig. 1a). On the other hand, the HOPG crystals and graphite flakes are comprised of very tightly packed layers with no or very little voids in-between such layers (Fig. 1b and c). The peculiar morphology of graphite foil is a direct result of its production process, which is based on roll compaction of thermally expanded graphite particles and leads to a relatively low density product (~0.7-1.3 g cm^{-3} according to the specifications of the manufacturer, to be compared with a value of ~2.25 g cm^{-3} for HOPG). It is then reasonable to assume that the presence of a large number of

openings and gaps within the layers facilitates the intercalation of chemical species (e.g., halide anions and water molecules) in graphite foil and its subsequent expansion during the anodic treatment, whereas such a relative advantage would be essentially absent from graphites with a more compact morphology (HOPG and graphite flakes). We also note that explorative exfoliation experiments at different bias voltages, both higher and lower than 10 V, were carried out. We observed that the exfoliation process was only successful when using bias voltages above a threshold value of ~4 V, but at such low voltages the flowing current and thus the yield of exfoliated product were lower, whereas the quality of the resulting graphene flakes did not change compared to exfoliation at 10 V. For bias voltages above 10 V, neither the amount of exfoliated product nor its quality changed significantly. Concerning the current profile during exfoliation, generally speaking it was observed to increase at first, probably as a result of the expansion of the graphite anode and the ensuing increase in surface area exposed to the aqueous electrolyte. However, after some time the current tended to reach a plateau. The latter was probably due to the fact that further increases in surface area resulting from exfoliation were counteracted by the loss of expanded graphite fragments that were seen to detach from the anode.

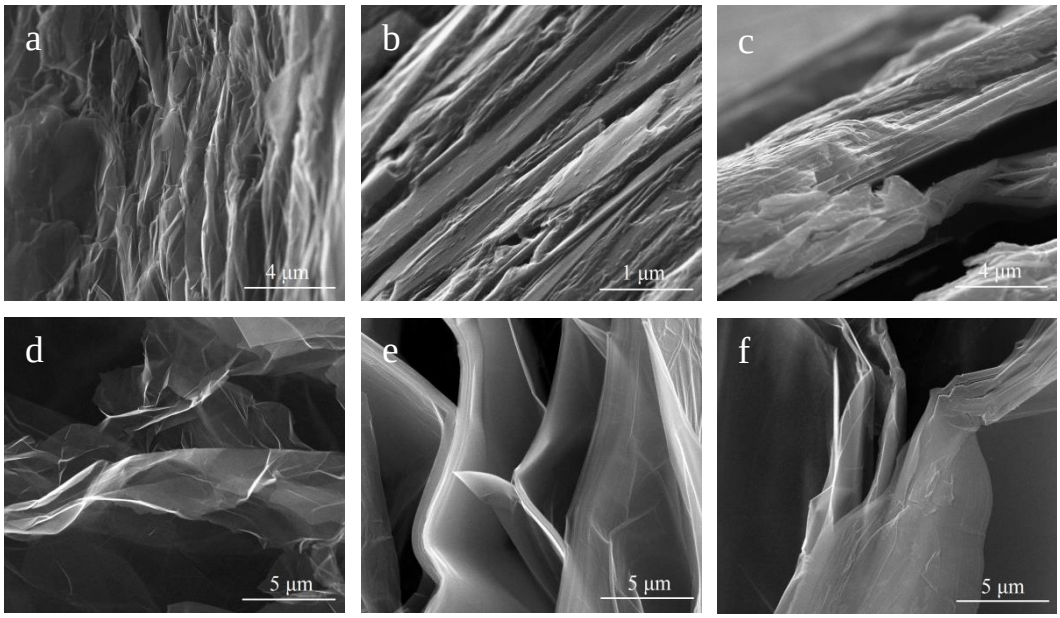

Figure 1. Representative FE-SEM images of graphite foil (a,d), HOPG (b,e) and graphite flakes (c,f) before (a,b,c) and after (d,e, f) electrochemical treatment in 0.05 M NaCl (+10 V, 60 min).

The distinct fate of graphite foil was apparent from the FE-SEM images of the anodically treated materials, as exemplified in Fig. 1d, e, and f using 0.05 M NaCl as the electrolyte. While graphite foil (Fig. 1d) was seen to expand considerably as a result of the anodic process, yielding very thin and well separated layers, a rather limited extent of cleavage was noticed for both HOPG (Fig. 1e) and graphite flakes (Fig. 1f), which exhibited just partially detached graphite platelets of a relatively large thickness. It is thus not surprising that the subsequent mild sonication step was able to complete delamination of the anodically treated graphites into graphene flakes only for the case of graphite foil, but not for the poorly expanded HOPG and graphite flake materials. In line with this result, the effect of compact vs. loose configuration of the graphite anode has been recently highlighted by Yang et al, who reported that a modest pre-expansion of graphite foil prior to the anodic exfoliation step with a sulfate-based electrolyte brings about a considerable increase in the amount of generated single-/few-layer graphene flakes.[29] In the present case, we surmise that the intercalation and/or expansion of graphites using halide-based electrolytes are relatively inefficient processes compared to those associated to the use of commonly employed electrolytes (e.g., sulfate-based ones). Thus, the deployment of graphite types for which the intercalation/expansion process is facilitated due to a suitable morphology (e.g., having a large amount of interlayer openings, voids and gaps) could make a critical difference in attaining a well-expanded product that can then be separated into single-/few-layer graphene flakes, as was actually observed here with graphite foil compared to HOPG and graphite flakes. Consequently, the former graphite type was used exclusively for the remainder of this work. This forced choice of graphite turns out to be quite advantageous with a view to up-scaling the graphene production process, taking into account that graphite foil is a widely available and modestly priced commodity (less than US$0.1 per gram, compared to ~US$100 per gram for HOPG). The fact that virtually no graphene can be obtained with HOPG and graphite flakes does not necessarily mean that the halide anions do not intercalate such graphites at all, but rather that if intercalation takes place, it is too slow and/or limited in extent so as not to allow an efficient exfoliation of these graphite types into graphene. Indeed, the latter are known to be readily intercalated and delaminated by other commonly used anions, such as sulfates.

The second decisive factor for successful anodic exfoliation using sodium halides was the electrolyte concentration. In general terms, for a given applied bias voltage, the anodic process is only able to afford graphene products within a certain range of electrolyte concentrations.[17] We tested the range of concentrations for each electrolyte, and found a range where the exfoliation process is effective for each sodium halide. If the electrolyte concentration is too low, the graphite anode will be poorly intercalated and no or very little expanded product will be obtained. If the concentration is too high, a very vigorous and fast intercalation process will usually take place, so that graphite fragments detach too quickly from the anode without having completed their layer-by-layer expansion. As a result, a large amount of incompletely expanded material will be attained, which cannot be subsequently separated into single-/few-layer graphene flakes via sonication, but gives rise to multilayer graphitic platelets instead, which are unstable in colloidal dispersion and appear as thick (>10 nm) objects in AFM images. However, if an intermediate electrolyte concentration is used, the process is slow enough for the detaching graphite fragments to expand and delaminate to an extent large enough so as to yield graphene nanosheets after sonication. As a result of this behavior, the final concentration of graphene dispersed in solvents as a function of electrolyte concentration is seen to go through a maximum at intermediate electrolyte concentrations (see Table 1 and discussion below). Such a constraint in the useful concentration range was seen to be particularly stringent in the case of sodium halides. To determine the useful concentration ranges for NaCl, NaBr and NaI, pieces of graphite foil of fixed dimensions were subjected to a positive voltage (+10 V, 60 min) in aqueous solutions of the aforementioned salts at different concentrations (see Experimental section for details). The resulting expanded products (if any) were thoroughly rinsed with water and ethanol to remove remnants of salts and other reaction products, and were subsequently dispersed via sonication either in DMF or in water/FMN. This cleaning process was seen to be a vital step for the colloidal stability of the final graphene product, as very small amounts of residual salts will drastically reduce the colloidal stability of the dispersions. After a centrifugation step intended to sediment the non-fully exfoliated fraction of the material, the concentration of the supernatant, which was the final graphene dispersion, was measured using UV-vis absorption spectroscopy. We carried out a control experiment under the same conditions in the absence of any electrolyte (i.e., only in pure

water), in order to test the possible influence of the hydroxide anions present in water. In this case, no change was seen in the graphite anode and no expanded material was obtained.

Table 1 shows the concentration of graphene suspensions in DMF obtained with different concentrations of the sodium halides in the anodic expansion process. The use of water/FMN as a dispersing medium instead of DMF yielded similar results. A graphene concentration value of zero indicates that no significant amount of material could be achieved in the final suspension, either because no anodically expanded product could be generated (at low electrolyte concentrations) or because virtually all the expanded product sedimented after the sonication and centrifugation steps (at high electrolyte concentrations). It can be noticed that NaCl afforded the narrowest useful range of concentrations. Indeed, dispersions of graphitic material were only attained at the tested NaCl concentration of 0.05 M, whereas concentrations of 0.1 M and above as well as 0.01 M and below failed to yield any suspended material. In the case of NaBr, the useful range was seen to be slightly broader, with significant amounts of dispersed graphitic material being obtained at electrolyte concentrations of both 0.05 and 0.1 M. Finally, NaI was determined to perform effectively as an electrolyte in a relatively broad concentration range (between 0.01 and 0.2 M), leading in all cases to very stable, homogeneous dispersions (see inset to Fig. 2 for a digital photograph of representative dispersions in water/FMN obtained with the three sodium halides). As a tentative explanation for this behaviour, we note that the reduction potential of the iodide anion is lower than that of its bromide and chloride counterparts (see below), so that the better exfoliation behavior with iodide can be ascribed to a more extensive formation of the resulting intercalated molecular species (i.e., I_2 in the case of iodide) that can therefore promote layer cleavage to a larger extent than that attained with bromide and chloride. We also note that aqueous chloride anions are not known from the literature to intercalate graphite. This could be an indication that such anions are indeed more difficult to intercalate compared to the case of bromide and iodide anions. We believe that the fact that chloride intercalation of graphite is not generally thought to be possible is due to the very narrow range of concentrations that make the intercalation (and exfoliation) possible, as well as the critical role of the type of graphite material used. As we have demonstrated here, the use of a graphite anode with many interlayer openings and voids in its structure (i.e., graphite foil) is critical to make intercalation and exfoliation possible.

This result suggests that intercalation of chloride anions into graphite is possible provided that it is facilitated through the use of graphites with somewhat increased interlayer spacings. Consequently, we do not believe that the mechanism of chloride intercalation is fundamentally different to that bromide, iodide or other electrolytes; it only needs larger graphite interlayer spacings to proceed.

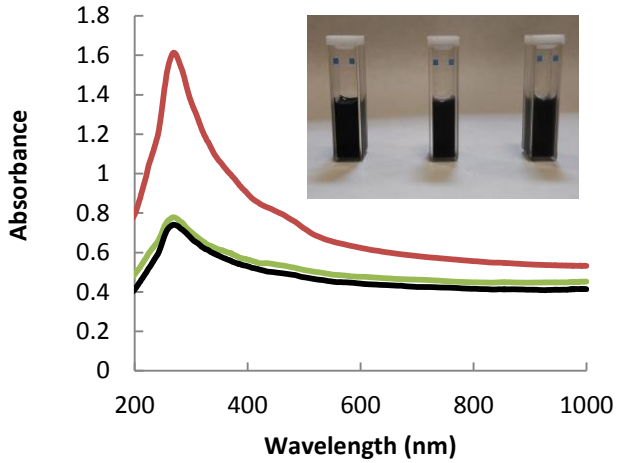

Figure 2. UV-visible absorption spectra of aqueous FMN-stabilized graphene dispersions prepared through anodic exfoliation in 0.05 M NaCl (black trace), 0.1 M NaBr (green trace) and 0.1 M NaI (red trace). Inset: digital photograph of aqueous FMN-stabilized graphene dispersions prepared with 0.05 M NaCl (right), 0.1 M NaBr (middle) and 0.1 M NaI (left).

The graphitic nature of the suspended material was made apparent by UV-vis absorption spectroscopy, as demonstrated in Fig. 2 for dispersions in water/FMN solutions. The spectra were dominated by an absorption peak located at ~265-270 nm together with strong absorbance in the whole wavelength range above 270 nm. These features are characteristic of sp^2-based carbon systems having extended electronically conjugated domains and have been observed, e.g., both on pristine graphene and on well-reduced graphene oxide nanosheets.[35] The very weak, shoulder-like absorption bands noticed at about 250, 375 and 450 nm correspond to absorbance from the FMN stabilizer.[34] As evaluated by this technique, significant amounts of suspended graphitic material (up to ~0.75 mg mL^{-1}) were attained for the as-prepared suspensions following the protocol described in the Experimental section. However, they could be further increased to the range of several milligrams per milliliter through different post-processing concentration strategies, including partial solvent removal using a rotary evaporator or sedimentation of the suspension via high-speed centrifugation and re-dispersion in a smaller solvent

volume.[34] The energy consumption in the anodic exfoliation process is largely due to the current flowing through the cell, and is estimated to be ~0.05 kW h for a usual experiment carried out in our laboratory considering the power consumption of the power supply.

2.2. Characteristics of the exfoliated products and role of the halide anions in the exfoliation process

Having demonstrated that sodium halides can indeed be used in aqueous anodic exfoliation processes to give stable dispersions of graphitic materials, the next step of the investigation focused on determining their physicochemical characteristics. First, the lateral size and exfoliation degree of the dispersed graphitic materials were investigated by means of scanning transmission electron microscopy (STEM) and atomic force microscopy (AFM). Fig. 3 shows typical STEM (a,b,c) and AFM (d,e,f) images recorded from water/FMN dispersions obtained with the three different electrolytes at a given concentration within their respective useful ranges: 0.05 M NaCl (a,d), 0.1 M NaBr (b,e) and 0.1 M NaI (c,f). All the dispersions were comprised of thin nanosheets with mean lateral dimensions of 560±210, 655±390 and 610±260 nm for 0.05 M NaCl, 0.1 M NaBr and 0.1 M NaI respectively, and apparent thickness (derived from AFM height profiles) between ~2 and 3 nm. The apparent thickness values for nanosheets from dispersions obtained at other sodium halide concentrations were very similar and are given in Table 1. The lateral size of the graphene flakes is mainly limited by the sonication step applied to the electrolytically expanded graphite material and it is in the same range as that measured for other electrolytes we have reported before. We also note that in the present work we searched for conditions that allow an efficient delamination of the graphite anode so as to attain very thin graphene nanosheets. In addition to the electrolytic treatment, sonication and centrifugation steps were applied to the electrochemically delaminated material. The main role of these steps, particularly centrifugation, is to select very thin nanosheets generated in the process (if any are generated at all). Therefore, it is not surprising that we obtained similar thickness values for all the samples, because the applied processes were indeed meant to select the thinnest nanosheets. The fact that different halides lead to different amounts of nanosheets ~~was~~ is most probably a result of the different efficiency of the electrolytes in the delamination of the graphite anode. Considering that AFM thickness

measurements of graphene nanosheets on SiO_2/Si and other substrates are affected by a positive offset of ~0.5-1 nm[36] and that FMN molecules adsorbed on both sides of the nanosheets could also contribute to the measured thickness, we conclude the actual thickness of these nanosheets to be not larger than ~0.5-1.5 nm, implying that they are typically comprised between one and four monolayers. Such a result indicates that a high degree of exfoliation could be attained with these electrolytes. For electrolyte concentrations above the useful range, virtually no suspended graphitic material was attained after the sonication and centrifugation steps, as noted above. However, AFM inspection of a sonicated suspension that was allowed to stand undisturbed overnight (no centrifugation) revealed that it was comprised of relatively thick objects (typical apparent thickness above ~10 nm). This observation corroborated the idea that high electrolyte concentrations lead to an inefficient exfoliation of the graphite anode.

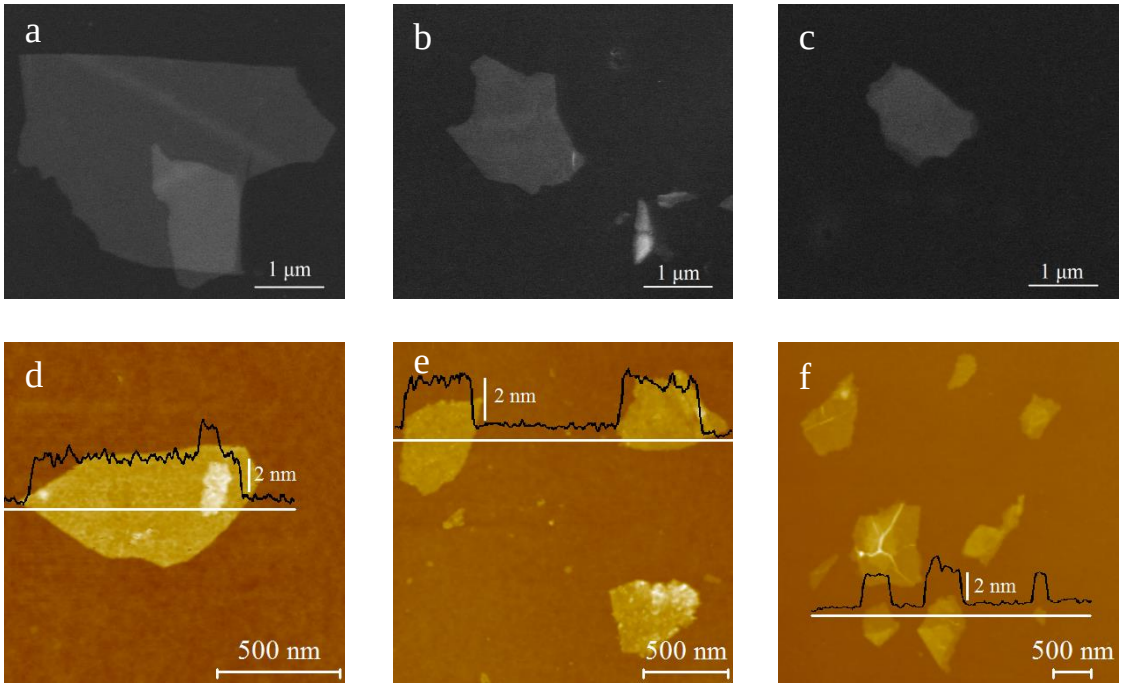

Figure 3. Representative STEM (a,b,c) and AFM (d,e,f) images of graphene nanosheets obtained by aqueous anodic exfoliation of graphite foil in 0.05 M NaCl (a,d), 0.1 M NaBr (b,e) and 0.1 M NaI (c,f). In d, e and f, line profiles (black traces) taken along the marked white lines are shown overlaid on the AFM images.

Chemical analysis of the dispersed materials was carried out by X-ray photoelectron spectroscopy (XPS). Fig. 4 shows survey spectra (a,c,e) as well as high resolution C 1s core level spectra (b,d,f) for graphene dispersions obtained with 0.05 M NaCl (a,b), 0.1 M NaBr (c,d) and 0.1 M NaI (e,f). In all cases carbon was the dominant element, although oxygen was also present to a significant but variable extent depending on the specific electrolyte concentration used for exfoliation. Signals corresponding to the halogen used in the anodic process were not observed, i.e., the amount of halogen present in the graphene samples was below the detection limit of this technique (~0.1 at%), implying that the washing procedure applied to the anodically expanded products was rather effective. This is an advantage over some previously reported electrolytes that cannot be readily removed due to their strong adsorption onto the graphene nanosheets.[30] Another advantage of the present electrolytes is related to their cost: sodium halides are simple, inexpensive and widely available chemicals. The O/C atomic ratios for the different tested electrolyte concentrations are given in Table 1, which were seen to range between 0.06 and 0.11. The high resolution C 1s spectra provided information on the nature of the oxidized carbon species. These spectra comprised a majority component located at ~284.6 eV that could be ascribed to carbon atoms in unoxidized graphitic environments (C=C species) and a minor component at about 286.7 eV, which was attributed to carbon atoms single-bonded to oxygen (C-O species), for example in hydroxyl, ether or epoxy groups.[24] The XPS results thus indicated that the exfoliated graphene nanosheets were oxidized only to a limited extent. Specifically, the O/C atomic ratio of samples prepared with 0.05 M NaCl (0.06) and 0.1 M NaBr (0.07) lay at the lower end of the range of values that have been reported for most graphenes anodically exfoliated using a number of inorganic or organic electrolytes, such as sulfuric acid (O/C ratios ~0.08-0.3),[17,18,22,30,37] sulfate salts (~0.06-0.19),[17,18,22,30,38] phosphoric acid (~0.3),[23] lithium perchlorate (~0.25),[22] sodium methanesulfonate (~0.15)[39] or sodium citrate (~0.13).[25]

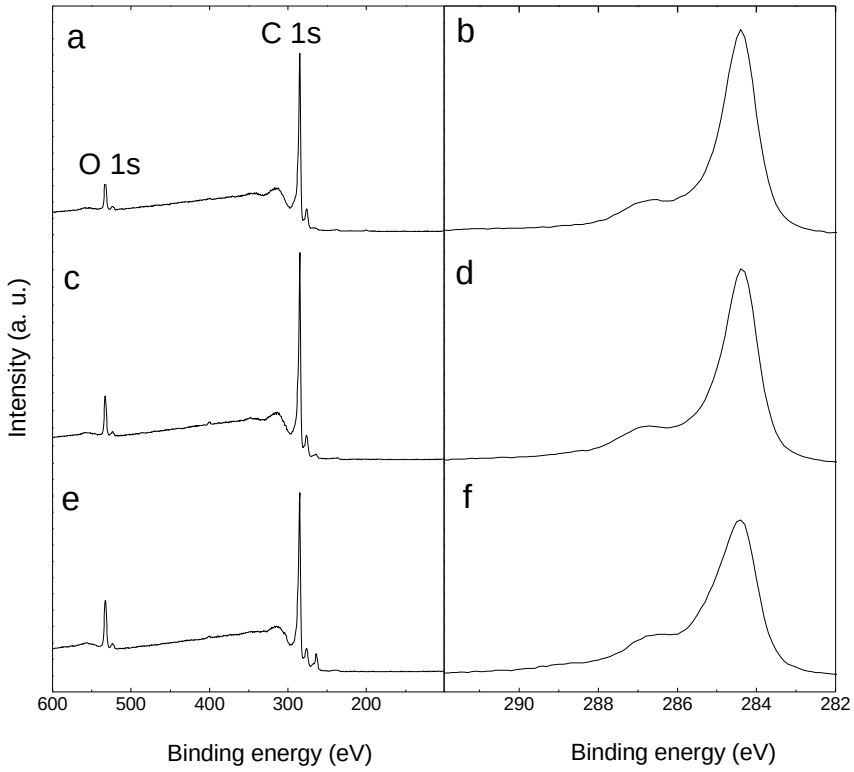

Figure 4. XPS survey spectra (a,c,e) and high resolution C 1s core level spectra (b,d,f) for graphene samples obtained by aqueous anodic exfoliation of graphite foil in 0.05 M NaCl (a,b), 0.1 M NaBr (c,d) and 0.1 M NaI (e,f).

Table 1. Characteristics of the graphene materials obtained by aqueous anodic exfoliation of graphite foil in different concentrations of the sodium halides NaCl, NaBr and NaI. [X^-]: electrolyte concentration in the aqueous anodic system. [Graphene]: concentration of graphene dispersed in DMF after anodic exfoliation, sonication and centrifugation. O/C atomic ratio derived from XPS survey spectra of the samples. Apparent thickness of the nanosheets derived from AFM height data.

Electrolyte	[X^-] (M)	[Graphene] (mg/mL)	O/C ratio	I_D/I_G	Apparent thickness (nm)
NaCl	0.01	0	-	-	-
	0.05	0.21	0.06	0.8	2-3
	0.10	0	-	-	-
	0.20	0	-	-	-
	0.50	0	-	-	-
	1.00	0	-	-	-
NaBr	0.01	0	-	-	-
	0.05	0.05	0.08	0.9	2-3
	0.10	0.26	0.07	1.1	2-3
	0.20	0	-	-	-
NaI	0.01	0.11	0.08	1.3	2-3
	0.05	0.57	0.11	1.4	2-3
	0.10	0.75	0.11	1.4	2-3
	0.20	0.24	0.08	1.2	2-3
	0.50	0	-	-	-

To understand the origin of the limited oxidation degree of the graphene nanosheets exfoliated here with the sodium halides, the possible redox processes involving these electrolytes and the evolution of oxygen species as a result of water oxidation at the graphite anode must be considered. First of all, as outlined above, it is believed that anionic intercalation in general strongly relies on the oxidation of edges and defects of the graphite anode by water molecules from the aqueous electrolyte. This oxidation induces a significant increase in the interlayer spacing of graphite in the local area around the edges. In turn, such a local increase in the interlayer spacing allows even relatively large anions to penetrate the graphitic material at the edges, which thus act as a wedge facilitating the subsequent separation of the graphite layers at regions increasingly farther from the edges. On the basis of this general mechanism, it follows that having a graphite anode with many pre-existing interlayer voids and openings, as it is the case with graphite foil, should clearly facilitate the intercalation and exfoliation of the anode, especially in cases where anion intercalation appears to be generally difficult (e.g., the present halides). Second, we note that halide intercalation in the interlayer spaces at the positively biased graphite electrode should take place most likely in the form of hydrated anions, i.e., halide anions surrounded by a bound shell of water molecules[40,41,42] (see step A in the schematic process chart of Fig. 5). At the high anodic potential used (10 V), oxygen evolution reactions take place and these water molecules are expected to readily oxidize (step B1 in Fig. 5), giving first hydroxyl radicals (·OH) and then oxygen molecules (O_2) through further oxidation[43] (step C1). The build-up of gaseous O_2 in the interlayer spaces should exert a considerable pressure on the graphitic layers and hence contribute to their separation from one another. Additionally, some of the generated ·OH radicals can attack the exfoliated layers (step C2), so that the resulting graphene nanosheets will bear a certain degree of oxidation. Third, it is reasonable to assume that the intercalated halide anion itself also participates in redox processes. In particular, it can be oxidized at the graphite electrode (step B2) to give the corresponding diatomic molecule (e.g., I_2 will be obtained from the anodic oxidation of I^-). As a matter of fact, when using NaBr and NaI as the electrolyte we observed that the aqueous solution progressively turned brown or red-brown around the graphite anode, such a color being characteristic of Br_2 and I_2 dissolved in water. For NaCl no color change was observed: Cl_2 is readily hydrolyzed to give colorless HCl and HClO (or their corresponding

sodium salt forms). In any case, accumulation of the halide oxidation products in the interlayer spaces should also contribute to separate the graphene sheets and therefore to the overall exfoliation process, in a similar way as it has reported to happen when using sulfate salts for the same process.[17]

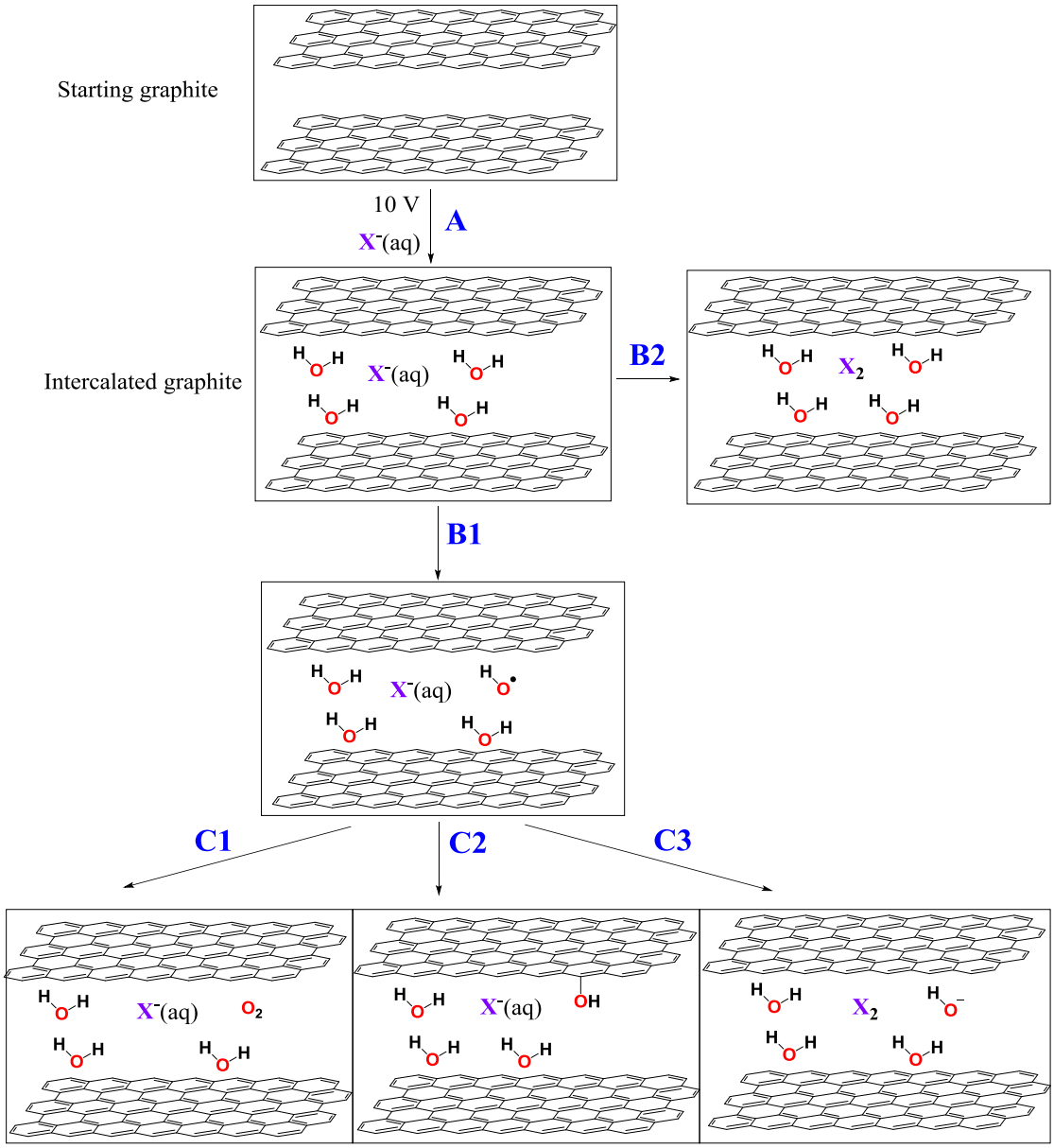

Figure 5. Schematic chart depicting the possible redox processes that take place when halide anions (X^- ≡ Cl^-, Br^- or I^-) are used as electrolyte in the aqueous anodic exfoliation of graphite. Step A: intercalation of hydrated halide [X^-(aq)] anions in the interlayer space of graphite. B1: anodic oxidation of intercalated water molecules to give ·OH radicals. B2: anodic oxidation of intercalated halide anions to give X_2 molecules. C1: further oxidation of ·OH radicals to give O_2 molecules. C2: attack of the graphitic lattice by ·OH radicals to give oxidized graphene materials. C3: neutralization of the highly reactive ·OH radicals by reaction with halide anions.

However, besides reacting directly with the graphite anode, the halide anions can also be oxidized by the generated ·OH radicals (step C3 in Fig. 5). This reaction is thermodynamically feasible for the three halides contemplated here. Indeed, the standard reduction potential of the different halogen/halide pairs in aqueous solution are +1.37 V for Cl_2/Cl^-, +1.09 V for Br_2/Br^- and +0.54 V for I_2/I^-,[44] compared with a value of +1.9 V for the $\cdot OH/OH^-$ pair.43 Furthermore, the oxidation of aqueous Cl^-, Br^- and I^- ions by ·OH radicals has been well investigated in the past,[45,46,47] and such a process is known to involve conversion of the highly oxidizing ·OH radicals to hydroxide anions (OH^-) or water molecules. The reaction of ·OH radicals with halide anions would thus be expected to prevent, at least to some extent, the attack of the graphite electrode by the former species, thus providing a mechanism to mitigate the oxidation of the graphene nanosheets that result from the anodic treatment. On the other hand, this type of reaction is not expected to occur when the electrolyte is comprised of a non-oxidizable anion, such as the sulfate, perchlorate or phosphate anion (for these anions, S, Cl and P are in their corresponding highest possible oxidation state). Hence, under such circumstances the intercalating anions would not be able to curtail the oxidation of the graphene lattice. Based on these considerations, we conclude that the halide anions play a dual role in the anodic exfoliation of graphite to give graphene nanosheets: (1) they act as intercalating electrolyte to promote the exfoliation of graphite, and (2) they mitigate the oxidation of the exfoliated graphene nanosheets by acting as scavengers of the highly reactive oxygen radicals generated during the anodic process. We also note that the presence of voids and openings in the starting graphite foil electrode could contribute to mitigate the oxidation of the resulting graphene nanosheets, as it is expected to make the exfoliation process faster and less reliant on the oxidative opening of the interlayer spaces compared with the use of more compact types of graphite (e.g., graphite rods).[18,33]

In addition to the morphological and chemical analysis, the structural quality of the anodically exfoliated graphenes was probed by Raman spectroscopy, as illustrated in Fig. 6 for samples prepared with 0.05 M NaCl (a), 0.1 M NaBr (b) and 0.1 M NaI (c). In all cases, the well-known G and D bands associated to graphite/graphene-based materials and located at about 1582 and 1350 cm^{-1}, respectively, were seen to dominate the first-order region of the spectra (i.e., the 1100–1700 cm^{-1} region), whereas the main feature observed

in the second-order region (2300–3300 cm^{-1}) was the so-called G´ or 2D band (~2700 cm^{-1}). As noticed from Table 1, the integrated intensity ratio of the D and G bands (I_D/I_G ratio), which is usually taken as a quantitative measure of the structural disorder present in graphite/graphene materials,[48] was seen to differ somewhat between the different graphene samples. Indeed, the I_D/I_G ratio tended to positively correlate with the O/C atomic ratio. Such a result was reasonable considering that anodic oxidation of the graphene nanosheets should be associated to the covalent grafting of oxygen functional groups on the carbon lattice (e.g., hydroxyl groups; see XPS results from Fig. 4), which in turn should convert a fraction of the originally sp^2-hybridized carbon atoms to defect-like sp^3-hybridized species. We note that, in the calculation of the I_G value (integrated intensity of the G band), we explicitly exclude the contribution of the D´ band, which appears as a shoulder on the high wavenumber side of the G band (~1620 cm-1). Because we are calculating the I_D/I_G ratio and not the $I_D/(I_G+I_{D'})$ ratio, we first have to determine the areas associated to the G and D´ bands through a peak-fitting procedure. This implies that the actual area of the G band is obviously smaller than the area of the composite (G+D´) envelope. As a result, the I_D/I_G ratios given in Table 1 might appear to be somewhat larger than the values an observer would guess through direct visual inspection of the spectra shown in Fig. 6. We also measured the electrical conductivity of free-standing, paper-like graphene films obtained through vacuum filtration of the corresponding dispersions in water/FMN. For example, the conductivities of films made up of nanosheets obtained via exfoliation in 0.1 M NaBr (~10 μm thick, as determined by FE-SEM) and 0.1 M NaI (~12 μm thick) were 15220 and 6750 S m^{-1}, respectively. These values were lower by a factor of ~3-6 than those previously reported for films derived from completely defect-free, pristine graphene flakes produced by direct ultrasound-induced exfoliation of graphite in water/FMN solutions,[34] which can be attributed to the somewhat defected nature of the present anodically exfoliated materials. On the other hand, they were similar to the conductivity values measured beforehand for films made up of pristine graphene flakes prepared by ultrasound-exfoliation in water with such stabilizers as sodium dodecylbenzenesulfonate (~1500 S m^{-1}),[49] sodium cholate (~15000 S m^{-1}),[50] sodium taurodeoxycholate (~13000 S m^{-1})[51] or gum Arabic (~10000 S m^{-1})[52]. We note that these prior values could only be obtained after removing at least part of the stabilizer from the as-filtered films through an appropriate treatment (e.g., high

temperature annealing under inert or reducing atmosphere), whereas no post-treatment of the films was required in the present case to achieve similar conductivity results.

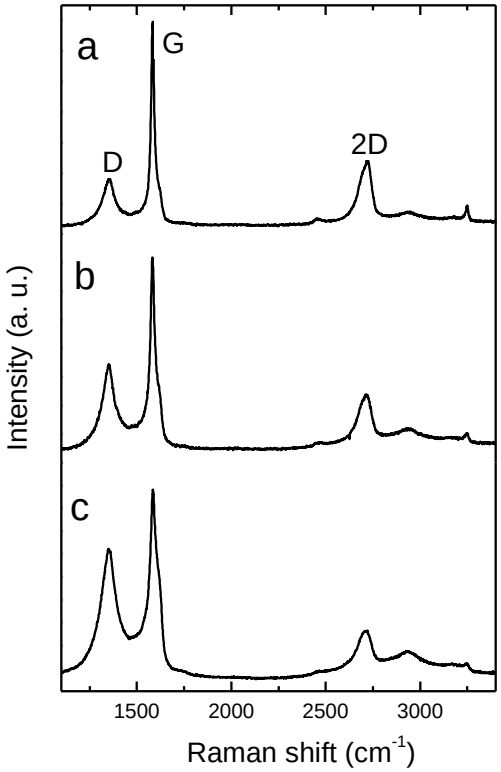

Figure 6. Raman spectra of graphene samples prepared by aqueous anodic exfoliation of graphite foil in 0.05 M NaCl (a), 0.1 M NaBr (b) and 0.1 M NaI (c).

2.3. Use of halide-based anodically exfoliated graphene in energy- and environment-related applications

Owing to their high surface area, good electrical conductivity as well as prominent chemical, mechanical and thermal stability, graphene materials are widely investigated towards their implementation in a number of environment- and energy-related applications, including their use as sorbents for oils and water-soluble organic compounds (e.g., dyes),[53] or as electrodes for supercapacitors and Li-ion batteries.[54] Central to a successful performance in many of these applications is the ability to assemble the graphene sheets into three-dimensional, macroscopic and porous structures in which the accessible area of each individual sheet is retained to the largest possible extent. This has been typically accomplished via appropriate processing of graphene oxide nanosheets or through CVD protocols that make use of metal foams as templates,[55] but such strategies are generally

time-consuming, elaborate and/or costly. As an alternative that could be competitive in terms of both performance and cost, we propose to use the as-exfoliated graphene materials developed here for some of the mentioned applications. Before their dispersion in any solvent via sonication, these materials exhibit a foam-like appearance (Fig. 7a), with an estimated density of ~40-45 mg cm^{-3}, and are comprised of expanded and loosely connected graphene layers having micrometer- to nanometer-sized gaps in-between (Fig. 1d and inset to Fig. 7a). The extremely simple and expeditious nature of their preparation process (just anodic treatment of graphite foil in sodium halide electrolyte) could facilitate the large-scale deployment of such graphene products in many practical uses. Thus, to probe their potential, we examined their performance as adsorbents for dyes and non-polar organic solvents/oils, as well as electrodes for supercapacitors. The material exfoliated in 0.1 M NaI was selected for these studies mainly because it affords the largest amount of graphene products among all the tested electrolytes (see Table 1), which is advantageous from the viewpoint of applications.

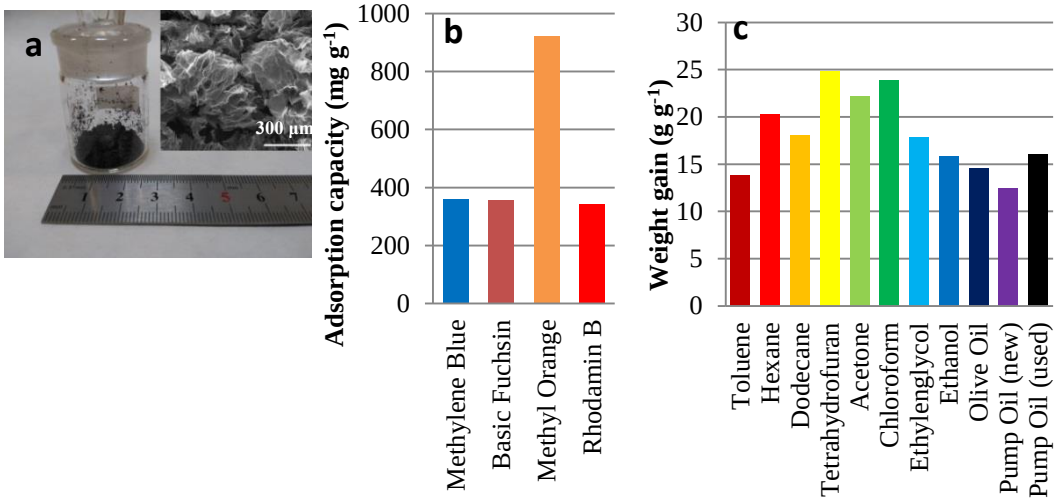

Figure 7. Digital photograph of as-prepared anodically exfoliated graphene using 0.1M NaI as electrolyte (a), SEM image of the same material (inset), adsorption capacities of this material for different dyes (b) and weight gains of the material for different solvents and oils (c).

Fig. 7b shows the adsorption capacity of the as-exfoliated graphene product towards several dyes in aqueous solution, namely, rhodamine B, basic fuchsin, methylene blue and methyl orange, measured at room temperature (295 K) and pH ~6. For the three cationic dyes (i.e., rhodamine B, basic fuchsin and methylene blue), values between 300 and 400 mg g^{-1} were obtained, being comparable to or even higher than those of many graphene-based adsorbent materials that have been previously reported.[7,53,56,57,58] In most prior work, however, the adsorbents typically comprised graphene oxide or reduced graphene oxide nanosheets, which favored adsorption through electrostatic attraction between the positively charged dyes and the negatively charged (ionizable) oxygen functional groups present in the nanosheets (e.g., carboxylates), with π-π stacking probably also playing some role.[53,57] On the other hand, although an electrostatic component could certainly be in place for the present anodically exfoliated materials by virtue of their non-negligible oxidation, we believe dye adsorption to be more reliant on π-π interactions in this case. This is because anodically exfoliated graphenes tend to possess a more graphitic (electronically conjugated) character than that of graphene oxides/reduced graphene oxides with a similar or even smaller extent of oxidation.[59] Furthermore, the adsorption capacity measured for the anionic dye methyl orange was substantially higher than that of its cationic counterparts (~920 mg g^{-1}), a result that is not consistent with a predominance of negatively charged adsorption sites on the graphene sheets. To the best of our knowledge, the adsorbed amount of methyl orange was the highest ever reported for a graphene-based adsorbent. The different adsorption performance of the anodically exfoliated material towards methyl orange and the three other dyes is currently not understood, but we hypothesize that it is related to differences in packing densities of the molecules on the graphene surface. A comparison of dye adsorption capacities of different graphene-based materials from the literature is provided in Table S1 of the Electronic Supplementary Information. Likewise, due to its primarily hydrophobic nature, the anodically exfoliated material was a good sorbent for non-polar organic solvents and oils, such as toluene, hexane, dodecane, tetrahydrofuran, acetone, chloroform, ethylenglycol, ethanol, olive oil or pump oil, with the measured sorption capacities ranging between ~12 and 24 g g^{-1} (Fig. 7c). Although such values are lower than those of lighter graphene and other carbon-based sorbents reported in the literature (e.g., lightweight graphene aerogels), they are comparable to those of sorbents

with a similar density.[7,56,60] Nonetheless, we expect that the oil sorption performance of the anodically exfoliated materials can be significantly improved on the basis of simple strategies, such as working with starting graphite foils of a lower density (densities down to ~0.05 g cm^{-3} have been reported, compared to a value of 0.7-1.3 g cm^{-3} for the foils used here). Because the use of a graphene or any other material in environmental applications could require such material to be non-cytotoxic, we also explored the biocompatibility of the present graphenes. In particular, we investigated the proliferation of murine fibroblasts onto halide-based graphene film substrates. The results (see SI) suggested these materials to be biocompatible.

Finally, the as-exfoliated graphene material was explored as a supercapacitor electrode in aqueous 1 M H_2SO_4 electrolyte (two-electrode configuration). The recorded cyclic voltammetry (CV) curves (Fig. 8a) exhibited an almost rectangular shape with negligible deviation at the limit potentials, even for a voltage window as wide as 1.4 V (CV curves were also obtained in a three-electrode configuration, and are presented and discussed in the Electronic Supplementary Information). This rather unusual, wide operation voltage was further confirmed by charging-discharging the supercapacitor cell at 0.1 A g^{-1}. As noticed from Fig. 8b, the galvanostatic charge-discharge profiles kept a triangular form when the voltage was gradually increased from 1.1 to 1.4 V. We note that the working voltage window of two-electrode symmetric cells using aqueous electrolytes is generally limited by the electrolytic decomposition of water to values ~1 V.[61] In particular, a voltage window of 1.4 V is considerably larger than that usually observed for porous carbon-based aqueous supercapacitors. For conventional porous carbons (e.g., activated carbons), although physisorption can furnish the water molecules with some degree of stability against electrolytic decomposition, the extensive presence of amorphous and/or highly defective structures in their lattice, which act as reactive chemisorption sites, tends to promote water electrolysis. On the other hand, such reactive sites are expected to be much less abundant in the as-exfoliated graphene materials investigated here due to their well-preserved graphitic character (Fig. 6). This feature, together with the particular morphology of voids and pores observed for this material (inset to Fig. 7a), is believed to contribute to a broader voltage window.

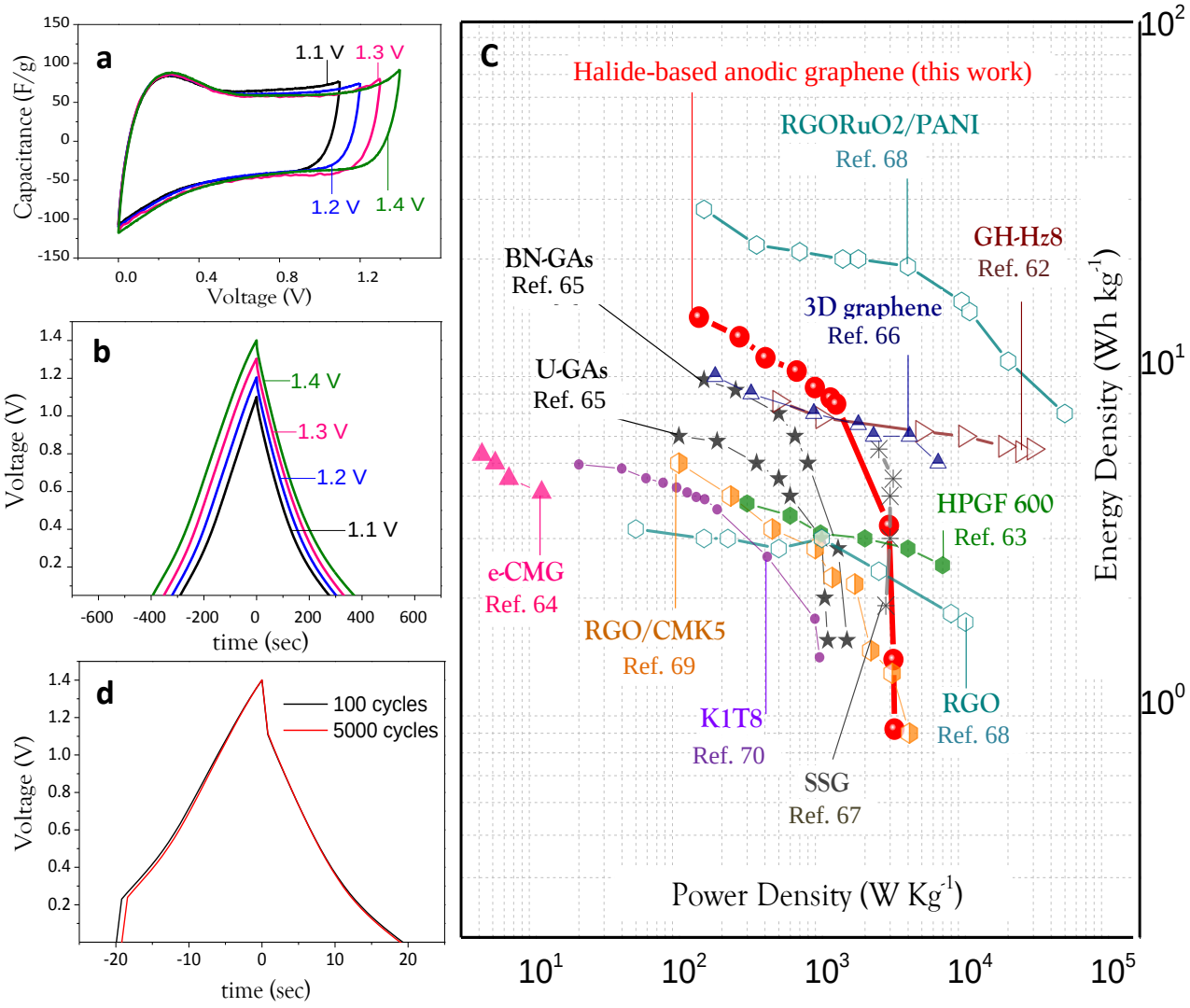

Figure 8. Supercapacitor performance tests for the halide-exfoliated graphite foil (0.1M NaI); a) cyclic voltammetry curves and b)galvanostatic charge-discharge profiles at different potential windows, c) Ragone plot for the exfoliated graphite and for some representative graphene-derived porous structures and d) cycling stability of the symmetric supercapacitor at 1 A/g over 2500 cycles.

The evolution of electrode performance with current density was also investigated on the basis of charge-discharge tests at 1.4 V, and the results were used for the construction of the Ragone plot shown in Fig. 8c. Even though the cells yielded modest values of specific capacitance (e.g., 50 F g^{-1} at 0.1 A g^{-1}), the fact that the device could be operated at a relatively high voltage led to remarkable energy and power density characteristics, with

values up to 15.3 Wh kg^{-1} and 3220 W kg^{-1}, respectively. Such a good capacitive behavior was made apparent by comparison to other similar graphene-based materials that have been previously reported (also given in Fig. 8c). For example, the power and energy densities delivered by the present graphene material were comparable or even higher than those of many three-dimensional graphene structures (such as graphene aerogels),[62,63,64,65,66] graphene films,[67] graphene compounded with electroactive materials (e.g., polyaniline),[68] or graphene/porous carbon hybrids.[69,70] It is important to note that in addition to competitive performance, a critical advantage of the present graphene materials lies in the extreme simplicity and environmental friendliness of their preparation compared with that of other graphene materials that rely on harsh chemical treatments (e.g, those based on graphene oxide), high temperatures and/or complex processing strategies (e.g., supercritical or freeze drying). Additional evidence of the cell stability was demonstrated on the basis of cycling tests (Fig. 8d), which revealed that ~98% of the initial capacitance was retained after 5000 cycles at 1 A g^{-1}. The plots in Fig. 8d suggest a significant internal resistance (IR) drop in the cell, which is discussed in the Supporting Information. In any case, we believe that the approach described here could greatly facilitate the practical implementation of graphene materials towards supercapacitor applications.

3. Conclusions

We have demonstrated that sodium halides (NaCl, NaBr and NaI) are efficient electrolytes in the aqueous anodic exfoliation of graphite, affording single-/few-layer graphene nanosheets of a high structural quality and limited oxygen content. The successful role of these salts as exfoliating electrolytes was seen to rely on two key aspects. First, a proper selection of the graphite source material was required, in particular graphites having many openings, gaps and inner voids in their structure. In this regard, graphite foil (a modestly priced commodity) turned out to be an appropriate choice. Second, identification of an operative range of salt concentrations was also critical towards successful exfoliation. Such a range was seen to be particularly tight in the case of NaCl and NaBr. In addition to their role as exfoliating electrolyte, the halide anions were concluded to act as sacrificial agents that prevented the extensive oxidation of the graphene lattice during anodic exfoliation. Such an oxidation-preventing ability was ascribed to the relatively low redox

potentials of these anions. Significantly, the as-exfoliated graphene materials exhibited a three-dimensional morphology that allowed their direct use in a number of energy- and environment-related applications, thus avoiding the complex processing steps that are usually required for many graphene-based materials. Testing of the halide-derived graphene products as dye adsorbents, as sorbents for oils and non-polar organic solvents, and as electrodes for supercapacitors revealed a performance comparable to or even higher than that frequently reported for different types of graphene (e.g., those obtained from graphite oxide). Cell proliferation tests also indicated a good biocompatibility of the halide-derived graphenes. Overall, we believe that the extremely simple and environmentally friendly nature of the production/processing method of graphene described here, combined with a competitive performance of the material in some relevant applications, constitutes a significant step forward towards the practical implementation of graphene in many real-life applications. Further efforts to improve the performance of the graphene materials in these and other applications along the lines proposed in this work are currently under way.

4. Experimental

4.1. Materials and reagents

Graphite anodes used throughout the study consisted of high purity graphite foil (Papyex I980, acquired from Mersen). For comparison purposes, highly oriented pyrolytic graphite (HOPG; grade ZYH, obtained from Advanced Ceramics) and natural graphite flakes (Sigma-Aldrich, ref. 332461) were also employed. NaCl, NaBr and NaI solutions in Milli-Q water were used as electrolytes. N,N-dimethylformamide (DMF) was used as a dispersing solvent for graphene, and flavin mononucleotide (FMN, riboflavin 5′-monophosphate sodium salt) was used as a stabilizer to colloidally disperse the graphene flakes in aqueous medium. All these chemicals were purchased from Sigma-Aldrich and used as received.

4.2. Aqueous anodic exfoliation of graphite using sodium halides as the electrolyte

The anodic exfoliation process was carried out in a two-electrode configuration, using a piece of graphite foil (dimensions: 40×25×0.5 mm^3) as the anode and a platinum foil (dimensions: 25×25×0.025 mm^3) as the cathode. HOPG pieces and graphite flake pellets

were also used as anodes. In all cases both anode and cathode were held by spring clips connected to the current source. Both electrodes were immersed in an aqueous solution (20 mL) of a sodium halide (NaCl, NaBr or NaI) at a certain concentration (specified below). A positive voltage (10 V) was then applied to the graphite anode for 60 min using an Agilent 6614C DC power supply. The platinum foil cathode was placed parallel to the graphite foil surface at a distance of about 2 cm. During this process, gas bubbles formed in both electrodes, with the graphite anode being typically seen to expand and release graphitic fragments from its surface. After the 60 min electrolysis period, the resulting expanded graphitic product was gently rubbed off from the graphite anode using a spatula, thoroughly rinsed with copious amounts of Milli-Q water and ethanol to remove residual salts as well as other products of the electrochemical reaction and then dried overnight at room temperature under reduced pressure. Subsequently, this expanded material was sonicated in a given volume (20 mL) of either DMF or aqueous FMN solution (1 mg mL^{-1}) for 3 hours (Selecta Ultrasons system, 40 kHz), and then the resulting dispersion was centrifuged at 200 g for 20 min (Eppendorf 5424 microcentrifuge) to sediment insufficiently exfoliated material. The obtained supernatant was collected and stored for further use. In the case of the FMN-stabilized aqueous dispersions, they were further purified (to remove the fraction of free, non-adsorbed FMN from the medium) by two cycles of sedimentation via centrifugation (20000 g, 20 min) and re-suspension in Milli-Q water with a brief sonication step.

4.3. Characterization techniques

Characterization of the graphene samples was carried out by means of UV-vis absorption spectroscopy, Raman spectroscopy, X-ray photoelectron spectroscopy (XPS), field emission scanning electron microscopy (FE-SEM), scanning transmission electron microscopy (STEM), atomic force microscopy (AFM) and measurement of electrical conductivity. UV-vis absorption spectroscopy was carried out with a double-bean Heλios α spectrophotometer, from Thermo Spectronic. Following previous reports,[18,34] the suspension concentration was estimated by means of UV-vis absorption spectroscopy on the basis of the Lambert-Beer law and using a value of 2440 mL mg^{-1} m^{-1} for the extinction coefficient at the measured wavelength of 660 nm. Raman spectra were acquired with a

Horiba Jobin-Yvon LabRam instrument at an incident power of 2.5 mW and using a laser excitation wavelength of 532 nm. XPS measurements were performed on a SPECS apparatus at a pressure of 10^{-7} Pa and using a non-monochromatic Mg K_α X-ray source (11.81 kV, 100 W). Samples for both Raman spectroscopy and XPS were prepared by drop-casting the corresponding aqueous, FMN-stabilized graphene dispersion onto a pre-heated (~50-60 ºC) circular stainless steel sample-holder 12 mm in diameter to give thin, macroscopic graphene films. XPS survey spectra were used to determine the overall elemental composition of the graphene samples in such films. Although XPS is a surface-sensitive technique that only probes the outermost surface layer of materials (a few to several nanometers deep), in the case of graphene samples prepared from colloidal dispersions it can be inferred that the elemental compositions derived from XPS are representative of the whole sample. Because the colloidal graphene suspensions used to prepare the thin films are expected to be spatially homogeneous, there is no reason to believe that the graphene nanosheets constituting the other surface of the formed films are not representative of the whole graphene sample, i.e., the graphene sheets probed in the XPS measurement must be representative of the sample as a whole. Also, because the thickness of the graphene nanosheets is generally comparable to the probing depth of XPS, this technique must probe individual graphene nanosheets in its entirety, and not just the outer surface of nanosheets. Having these two factors in mind, we have to conclude that survey XPS spectra must provide a reasonably accurate picture of the elemental composition of this type of graphene samples. FE-SEM and STEM imaging was accomplished with a Quanta FEG 650 system (FEI Company) operated at 20-30 kV. Specimens for STEM were prepared by mixing a given volume of aqueous graphene suspension with an equal volume of ethanol, and then 40 μL of the resulting water-ethanol dispersion were drop-cast onto copper grids (200 mesh) covered with a thin continuous film of amorphous carbon. AFM images were recorded on a Nanoscope IIIa Multimode apparatus (Veeco Instruments) in the tapping mode of operation under ambient conditions. Rectangular silicon cantilevers with nominal spring constant and resonance frequency values of ~40 N m^{-1} and 250-300 kHz, respectively, were employed. HOPG pieces or SiO_2(300 nm)/Si wafers were used as substrates in the preparation of specimens for AFM. To this end, a small volume (20-40 μL) of the graphene dispersion at a concentration of

~0.05 mg mL^{-1} was drop-cast onto the HOPG or SiO_2/Si substrate pre-heated at ~50-60 ºC and then allowed to dry. For the measurement of electrical conductivity, free-standing paper-like films were prepared from the aqueous graphene dispersions by vacuum filtration through silver membrane filters 25 mm in diameter and 0.2 μm in pore size (Sterlitech Corporation). Conductivity was determined through the van der Pauw method by means of a homemade setup (Agilent 6614C potentiostat and Fluke 45 digital multimeter) with 12×12 mm^2 square pieces that were cut from the free-standing films. The thickness of the films was estimated by FE-SEM.

4.4. Testing of as-prepared anodically exfoliated graphene in energy and environmental applications

The graphene material obtained by anodic exfoliation in 0.1 M NaI was tested as an adsorbent for water-soluble dyes as well as for non-polar organic solvents and oils, and as an electrode for supercapacitors. To this end, the as-exfoliated product, i.e. the material directly generated by the anodic treatment without subsequent sonication (only washed to remove remnants of the electrolyte), was used. For the dye adsorption experiments, ~10 mg of the graphene material was added to 10 mL of an aqueous solution of the dye (rhodamine B, basic fuchsin, methylene blue and methyl orange) at room temperature and pH ~6, which was then gently stirred with a magnetic bar for 48 h to ensure that the adsorption equilibrium was attained. After removal of the graphene component via centrifugation (10000 *g*, 10 min), the concentration of dye remaining in the aqueous solution was determined through UV-vis absorption spectroscopy on the basis of absorption peaks characteristic of each dye (located at ~555 nm for rhodamine B, 540 nm for basic fuchsin, 660 nm for methylene blue and 460 nm for methyl orange), which in turn was used to infer the amount of dye adsorbed on the graphene sample. To estimate maximum adsorption capacities, different starting concentrations of the dye were probed (typically up to 1-2 mg mL^{-1}). For the oil/non-polar organic solvent sorption experiments, a certain amount of the graphene material (~5 mg) was placed in a 1.5 mL centrifuge tube, and then small known volumes of the oil/organic solvent (typically ~80-140 μL) were added in succession. These volumes were quickly absorbed by the graphene sample until a saturation point was reached, which was used to estimate the amount retained by the graphene sorbent. Sorption

assays were carried out with the following compounds: toluene, hexane, dodecane, tetrahydrofuran, acetone, chloroform, ethylenglycol, ethanol, olive oil, new and used pump oil.

For the supercapacitor electrode tests, the as-exfoliated graphene material was hand-ground to obtain a homogeneous powder that was subsequently mixed with polytetrafluoroethylene (PTFE) in absolute ethanol to obtain a carbon paste (graphene:PTFE weight ratio of 8:1). This paste (~7 mg) was pressed in a mould under 1 ton for 15 s to obtain two circular pellets (~0.78 cm^2) with similar mass and thickness. The pellets were degassed at 100 ºC under vacuum for 4h, soaked into the electrolyte (1 M H_2SO_4) for 24 h, and then used as symmetric working electrodes in a two-electrode Swagelok-type with glass microfiber filter (grade 934-AH, from Whatman) acting as the separator. The supercapacitor performance was tested by means of a computer-controlled potentiostat (PGZ 402 Voltalab, from Radiometer Analytical). Cyclic voltammetry (CV) tests were performed at 10 mV s^{-1} and different voltage windows. Galvanostatic charge-discharge profiles were recorded up to different voltages (1.1-1.4 V) and at different current loads (0.1-6 A g^{-1}). Long-term stability tests were carried out by cycling the cell at a constant current density of 1 A g^{-1} for 5000 cycles. The gravimetric capacitance, C_S (F g^{-1}) of a single electrode was calculated on the basis of the following formula:

$$C_S = \frac{2\, I\ \Delta t_d}{m\, \Delta V_d} \qquad (1)$$

, where I is the current (A), Δt_d is the time of discharge at the fixed potential window (s), m is the mass of the active material within the working electrode (g) and ΔV_d is the potential difference (V) between start and finish of the discharge process after omitting the internal resistance (IR) drop. The gravimetric energy density of the electrode, E (Wh kg^{-1}), was calculated through the formula:

$$E = \frac{1}{2} C_{CELL} {\Delta V_d}^2 \qquad (2)$$

, where C_{CELL} is the gravimetric capacitance of the total cell (F g^{-1}). Finally, the gravimetric power density, P (W kg^{-1}), was calculated by applying the following equation:

$$P = \frac{E}{\Delta t_d} \quad (3)$$

Supporting Information

Cell proliferation tests of murine fibroblasts grown onto halide-based graphene substrates. Characterization of as-exfoliated graphene material by N_2 physisorption. Additional XPS data of the exfoliated graphenes. Three electrode characterization of as-prepared anodically exfoliated graphene. Discussion of IR drop contribution to the supercapacitor cell performance. Table comparing adsorption capacities of dyes with different graphene-based materials.

Corresponding Author

*Telephone: (+34) 985 11 90 90. Fax: (+34) 985 29 76 62. Email: j.munuera@incar.csic.es.

Acknowledgements

Financial support from both the Spanish Ministerio de Economía y Competitividad (MINECO) and the European Regional Development Fund (ERDF) through grant MAT2015-69844-R is gratefully acknowledged. We also acknowledge partial funding by both Plan de Ciencia, Tecnología e Innovación 2013-2017 del Principado de Asturias and the ERDF through Project GRUPIN14-056. This work was also partially funded by project "AIProcMat@N2020 - Advanced Industrial Processes and Materials for a Sustainable Northern Region of Portugal 2020" (NORTE-01-0145-FEDER-000006), supported by Norte Portugal Regional Operational Programme (NORTE 2020), under the Portugal 2020 Partnership Agreement, through the European Regional Development Fund (ERDF) and of Project POCI-01-0145-FEDER-006984 – Associate Laboratory LSRE-LCM funded by ERDF through COMPETE2020 - Programa Operacional Competitividade e Internacionalização (POCI) – and by national funds through FCT - Fundação para a Ciência

e a Tecnologia. A.P. thanks her research contract partially supported (80%) by the ERDF/FEDER Operative Programme of the Region of Murcia (Project No. 14-20-01). J.M.M. is grateful to the Spanish Ministerio de Educación, Cultura y Deporte (MECD) for his pre-doctoral contract (FPU14/00792).

References

1 Ferrari, A. C.; Bonaccorso, F.; Fal'ko, V.; Novoselov, K. S.; Roche, S.; Boggild, P.; Borini, S.; Koppens, F. H. L.; Palermo, V.; Pugno, N.; Garrido, J. A.; Sordan, R.; Bianco, A.; Ballerini, L.; Prato, M.; Lidorikis, E.; Kivioja, J.; Marinelli, C.; Ryhanen, T.; Morpurgo, A.; Coleman, J. N.; Nicolosi, V.; Colombo, L.; Fert, A.; Garcia-Hernandez, M.; Bachtold, A.; Schneider, G. F.; Guinea, F.; Dekker, C.; Barbone, M.; Sun, Z.; Galiotis, C.; Grigorenko, A. N.; Konstantatos, G.; Kis, A.; Katsnelson, M.; Vandersypen, L.; Loiseau, A.; Morandi, V.; Neumaier, D.; Treossi, E.; Pellegrini, V.; Polini, M.; Tredicucci, A.; Williams, G. M.; Hee Hong, B.; Ahn, J.-H.; Min Kim, J.; Zirath, H.; van Wees, B. J.; van der Zant, H.; Occhipinti, L.; Di Matteo, A.; Kinloch, I. A.; Seyller, T.; Quesnel, E.; Feng, X.; Teo, K.; Rupesinghe, N.; Hakonen, P.; Neil, S. R. T.; Tannock, Q.; Lofwander, T.; Kinaret, J. Science and Technology Roadmap for Graphene, Related Two-Dimensional Crystals, and Hybrid Systems. *Nanoscale* **2015**, *7*, 4598-4810.

2 Zhang, Y.; Zhang, L.; Zhou, C. Review of Chemical Vapor Deposition of Graphene and Related Applications. *Acc. Chem. Res.* **2013**, *46*, 2329-2339.

3 Zhong, Y. L.; Tian, Z.; Simon, G. P.; Li, D. Scalable Production of Graphene Via Wet Chemistry: Progress and Challenges. *Mater. Today* **2015**, *18*, 73-78.

4 Du, W.; Jiang, X.; Zhu, L. From Graphite to Graphene: Direct Liquid-Phase Exfoliation of Graphite to Produce Single- and Few-Layered Pristine Graphene. *J. Mater. Chem. A* **2013**, *1*, 10592-10606.

5 Chen, L.; Xu, Z.; Li, j.; Li, Y.; Shan, M.; Wang, C.; Wang, Z.; Guo, Q.; Liu, L.; Chen, G.; Qian, X. A Facile Strategy to Prepare Functionalized Graphene Via Intercalation, Grafting and Self-Exfoliation of Graphite Oxide. *J. Mater. Chem.* **2012**, *22*, 13460-13463

6 Pei, S.; Cheng, H.-M. The Reduction of Graphene Oxide. *Carbon* **2012**, *50*, 3210-3228.

7 Niu, L.; Coleman, J. N.; Zhang, H.; Shin, H.; Chhowalla, M.; Zheng, Z. Production of Two-Dimensional Nanomaterials Via Liquid-Based Direct Exfoliation. *Small* **2016**, *12*, 272-293

8 Abdelkader, A. M.; Cooper, A. J.; Dryfe, R. A. W.; Kinloch, I. A. How to Get Between the Sheets: a Review of Recent Works on the Electrochemical Exfoliation of Graphene Materials from Bulk Graphite. *Nanoscale* **2015**, *7*, 6944-6956.

9 Yang, S.; Lohe, M. R.; Müllen, K.; Feng, X. New-Generation Graphene from Electrochemical Approaches: Production and Applications. *Adv. Mater.* **2016**, *28*, 6213-6221.

10 Abdelkader, A. M.; Kinloch, I. A.; Dryfe, R. A. W. Continuous Electrochemical Exfoliation of Micrometer-Sized Graphene Using Synergistic Ion Intercalations and Organic Solvents. *ACS Appl. Mater. Interfaces* **2014**, *6*, 1632-1639.

11 Cooper, A. J.; Wilson, N. R.; Kinloch, I. A.; Dryfe, R. A. W. Single Stage Electrochemical Exfoliation Method for the Production of Few-Layer Graphene Via Intercalation of Tetraalkylammonium Cations. *Carbon* **2014**, *66*, 340-350.

12 Ali Reza Kamali, A. R., Fraya, D. J. Large-Scale Preparation of Graphene by High Temperature Insertion of Hydrogen into Graphite. *Nanoscale*, **2015**, ***7***, 11310-11320

13 Kim, H. K.; Kamali, A. R.; Roh, K. C.; Kim, K. B.; Fray, D. J. Dual Coexisting Interconnected Graphene Nanostructures for High Performance Supercapacitor Applications. *Energy Environ. Sci.* **2016**, *9*, 2249-2256

14 Abdelkader, A. M.; Patten, H. V.; Li, Z.; Chen, Y.; Kinloch, I. A. Electrochemical Exfoliation of Graphite in Quaternary Ammonium-Based Deep Eutectic Solvents: a Route for the Mass Production of Graphane. *Nanoscale*, **2015**, *7*, 11386-11392

15 Lu, J.; Yang, J.-x.; Wang, J.; Lim, A.; Wang, S.; Loh, K. P. One-Pot Synthesis of Fluorescent Carbon Nanoribbons, Nanoparticles, and Graphene by the Exfoliation of Graphite in Ionic Liquids. *ACS Nano* **2009**, *3*, 2367-2375.

16 Su, C.-Y.; Lu, A.-Y.; Xu, Y.; Chen, F.-R.; Khlobystov, A. N.; Li, L.-J. High-Quality Thin Graphene Films from Fast Electrochemical Exfoliation. *ACS Nano* **2011**, *5*, 2332-2339.

17 Parvez, K.; Wu, Z.-S.; Li, R.; Liu, X.; Graf, R.; Feng, X.; Müllen, K. Exfoliation of Graphite into Graphene in Aqueous Solutions of Inorganic Salts. *J. Am. Chem. Soc.* **2014**, *136*, 6083-6091.

18 Munuera, J. M.; Paredes, J. I.; Villar-Rodil, S.; Ayán-Varela, M.; Pagán, A.; Aznar-Cervantes, S. D.; Cenis, J. L.; Martínez-Alonso, A.; Tascón, J. M. D. High Quality, Low Oxygen Content and Biocompatible Graphene Nanosheets Obtained by Anodic Exfoliation of Different Graphite Types. *Carbon* **2015**, *94*, 729-739.

19 Najafabadi, A. T.; Gyenge, E. Synergistic Production of Graphene Microsheets by Simultaneous Anodic and Cathodic Electro-Exfoliation of Graphitic Electrodes in Aprotic Ionic Liquids. *Carbon*, **2015**, *84*, 449-459

20 Najafabadi, A. T.; Ng, N.; Gyenge, E. High-Yield Graphene Production by Electrochemical Exfoliation of Graphite: Novel Ionic liquid (IL)–Acetonitrile Electrolyte With Low IL Content. *Carbon*, **2014**, *71*, 58-69

21 Najafabadi, A. T.; Gyenge, E. Electrochemically Exfoliated Graphene Anodes with Enhanced Biocurrent Production in Single-Chamber Air-Breathing Microbial Fuel Cells. *Biosens. Bioelectron.* **2016**, *81*, 103-110

22 Ambrosi, A.; Pumera, M. Electrochemically Exfoliated Graphene and Graphene Oxide for Energy Storage and Electrochemistry Applications. *Chem. - Eur. J.* **2016**, *22*, 153-159.

23 Liu, J.; Poh, C. K.; Zhan, D.; Lai, L.; Lim, S. H.; Wang, L.; Liu, X.; Gopal Sahoo, N.; Li, C.; Shen, Z.; Lin, J. Improved Synthesis of Graphene Flakes From the Multiple Electrochemical Exfoliation of Graphite Rod. *Nano Energy* **2013**, *2*, 377-386.

24 Wu, L.; Li, W.; Li, P.; Liao, S.; Qiu, S.; Chen, M.; Guo, Y.; Li, Q.; Zhu, C.; Liu, L. Powder, Paper and Foam of Few-Layer Graphene Prepared in High Yield by Electrochemical Intercalation Exfoliation of Expanded Graphite. *Small* **2014**, *10*, 1421-1429.

25 Abdelkader, A. M.; Kinloch, I. A.; Dryfe, R. A. W. High-Yield Electro-Oxidative Preparation of Graphene Oxide. *Chem. Commun*. **2014**, *50*, 8402-8404.

26 Chuang, C.-H.; Su, C.-Y.; Hsu, K.-T.; Chen, C.-H.; Huang, C.-H.; Chu, C.-W.; Liu, W.-R. A Green, Simple and Cost-Effective Approach to Synthesize High Quality Graphene by Electrochemical Exfoliation Via Process Optimization. *RSC Adv.* **2015**, *5*, 54762-54768.

27 Paredes, J. I.; Munuera, J. M. Recent Advances and Energy-Related Applications of High Quality/Chemically Doped Graphenes Obtained by Electrochemical Exfoliation Methods. *J. Mater. Chem. A* **2017**, *5*, 7228-7242.

28 Chen, C.-H.; Yang, S.-W.; Chuang, M.-C.; Woon, W.-Y.; Su, C.-Y. Towards the Continuous Production of High Crystallinity Graphene Via Electrochemical Exfoliation with Molecular In Situ Encapsulation. *Nanoscale* **2015**, *7*, 15362-15373.

29 Yang, S.; Brüller, S.; Wu, Z.-S.; Liu, Z.; Parvez, K.; Dong, R.; Richard, F.; Samorì, P.; Feng, X.; Müllen, K. Organic Radical-Assisted Electrochemical Exfoliation for the Scalable Production of High-Quality Graphene. *J. Am. Chem. Soc.* **2015**, *137*, 13927-13932.

30 Munuera, J. M.; Paredes, J. I.; Villar-Rodil, S.; Ayán-Varela, M.; Martínez-Alonso, A.; Tascón, J. M. D. Electrolytic Exfoliation of Graphite in Water with Multifunctional Electrolytes: En Route Towards High Quality, Oxide-Free Graphene Flakes. *Nanoscale* **2016**, *8*, 2982-2998.

31 Gaier, J. R.; Ditmars, N. F.; Dillon, A. R. Aqueous Electrochemical Intercalation of Bromine into Graphite Fibers. *Carbon* **2005**, *43*, 189-193.

32 Niu, L.; Li, M.; Tao, X.; Xie, Z.; Zhou, X.; Raju, A. P. A.; Young, R. J.; Zheng, Z. Salt-Assisted Direct Exfoliation of Graphite Into High-Quality, Large-Size, Few-Layer Graphene Sheets. *Nanoscale* **2013**, *5*, 7202-7208.

33 Munaiah, Y.; Ragupathy, P.; Pillai, V. K. Single-Step Synthesis of Halogenated Graphene through Electrochemical Exfoliation and Its Utilization as Electrodes for Zinc Bromine Redox Flow Battery. *J. Electrochem. Soc.* **2016**, *163*, A2899-A2910.

34 Ayán-Varela, M.; Paredes, J. I.; Guardia, L.; Villar-Rodil, S.; Munuera, J. M.; Díaz-González, M.; Fernández-Sánchez, C.; Martínez-Alonso, A.; Tascón, J. M. D. Achieving Extremely Concentrated Aqueous Dispersions of Graphene Flakes and Catalytically Efficient Graphene-Metal Nanoparticle Hybrids with Flavin Mononucleotide as a High-Performance Stabilizer. *ACS Appl. Mater. Interfaces* **2015**, *7*, 10293-10307.

35 Guardia, L.; Fernández-Merino, M. J.; Paredes, J. I.; Solís-Fernández, P.; Villar-Rodil, S.; Martínez-Alonso, A.; Tascón, J. M. D. High-Throughput Production of Pristine Graphene in an Aqueous Dispersion Assisted by Non-Ionic Surfactants. *Carbon* **2011**, *49*, 1653-1662.

36 Nemes-Incze, P.; Osváth, Z.; Kamarás, K.; Biró, L. P. Anomalies in Thickness Measurements of Graphene and Few Layer Graphite Crystals by Tapping Mode Atomic Force Microscopy. *Carbon* **2008**, *46*, 1435-1442.

37 Xuhua, H.; Senlin, L.; Zhiqiang, Q.; Wei, Z.; Wei, Y.; Yanyan, F. Low Defect Concentration Few-Layer Graphene Using a Two-Step Electrochemical Exfoliation. *Nanotechnology* **2015**, *26*, 105602-105608

38 Lou, F.; Buan, M. E. M.; Muthuswamy, N.; Walmsley, J. C.; Ronning, M.; Chen, D. One-Step Electrochemical Synthesis of Tunable Nitrogen-Doped Graphene. *J. Mater. Chem. A* **2016**, *4*, 1233-1243.

39 Wei, W.; Wang, G.; Yang, S.; Feng, X.; Müllen, K. Efficient Coupling of Nanoparticles to Electrochemically Exfoliated Graphene. *J. Am. Chem. Soc.* **2015**, *137*, 5576-5581.

40 Mancinelli, R.; Botti, A.; Bruni, F.; Ricci, M. A.; Soper, A. K. Hydration of Sodium, Potassium, and Chloride Ions in Solution and the Concept of Structure Maker/Breaker. *J. Phys. Chem. B* **2007**, *111*, 13570-13577.

41 D'Angelo, P.; Migliorati, V.; Guidoni, L. Hydration Properties of the Bromide Aqua Ion: the Interplay of First Principle and Classical Molecular Dynamics, and X-ray Absorption Spectroscopy. *Inorg. Chem.* **2010**, *49*, 4224-4231.

42 Fulton, J. L.; Schenter, G. K.; Baer, M. D.; Mundy, C. J.; Dang, L. X.; Balasubramanian, M. Probing the Hydration Structure of Polarizable Halides: A Multiedge XAFS and Molecular Dynamics Study of the Iodide Anion. *J. Phys. Chem. B* **2010**, *114*, 12926-12937.

43 Foote, S. C.; Valentine, J. S.; Greenberg, A.; Liebman, J. F. Active Oxygen in Chemistry, 1st ed.; Chapman & Hall: Glasgow, 1995.

44 Vanýsek, P., CRC Handbook of Chemistry and Physics, 93rd ed.; CRC Press: Boca Raton, 2012.

45 Jayson, G. G.; Parsons, B. J.; Swallow, A. J. Some Simple, Highly Reactive, Inorganic Chlorine Derivatives in Aqueous Solution. Their Formation Using Pulses of Radiation and Their Role in the Mechanism of the Fricke Dosimeter. *J. Chem. Soc., Faraday Trans.1* **1973**, *69*, 1597-1607.

46 Zehavi, D.; Rabani, J. Oxidation of Aqueous Bromide Ions by Hydroxyl Radicals. Pulse Radiolytic Investigation. *J. Phys. Chem.* **1972**, *76*, 312-319.

47 Thomas, J. K. Rates of Reaction of the Hydroxyl Radical. *Trans. Faraday Soc.* **1965**, *61*, 702-707.

48 Ferrari, A. C.; Basko, D. M. Raman Spectroscopy as a Versatile Tool for Studying the Properties of Graphene. *Nat. Nanotechnol*. **2013**, *8*, 235-246.

49 Lotya, M.; Hernandez, Y.; King, P. J.; Smith, R. J.; Nicolosi, V.; Karlsson, L. S.; Blighe, F. M.; De, S.; Wang, Z.; McGovern, I. T.; Duesberg, G. S.; Coleman, J. N. Liquid Phase Production of Graphene by Exfoliation of Graphite in Surfactant/Water Solutions. *J. Am. Chem. Soc.* **2009**, *131*, 3611-3620.

50 De, S.; King, P. J.; Lotya, M.; O'Neill, A.; Doherty, E. M.; Hernandez, Y.; Duesberg, G. S.; Coleman, J. N. Flexible, Transparent, Conducting Films of Randomly Stacked Graphene from Surfactant-Stabilized, Oxide-Free Graphene Dispersions. *Small* **2010**, *6*, 458-464.

51 Sun, Z.; Masa, J.; Liu, Z.; Schuhmann, W.; Muhler, M. Highly Concentrated Aqueous Dispersions of Graphene Exfoliated by Sodium Taurodeoxycholate: Dispersion Behavior and Potential Application as a Catalyst Support for the Oxygen-Reduction Reaction. *Chem. - Eur. J.* **2012**, *18*, 6972-6978.

52 Chabot, V.; Kim, B.; Sloper, B.; Tzoganakis, C.; Yu, A. High Yield Production and Purification of Few Layer Graphene by Gum Arabic Assisted Physical Sonication. *Sci. Rep.* **2013**, *3*, 1378-1385

53 Perreault, F.; Fonseca de Faria, A.; Elimelech, M. Environmental Applications of Graphene-Based Nanomaterials. *Chem. Soc. Rev.* **2015**, *44*, 5861-5896.

54 Raccichini, R.; Varzi, A.; Passerini, S.; Scrosati, B. The Role of Graphene for Electrochemical Energy Storage. *Nat. Mater.* **2015**, *14*, 271-279.

55 Sherrell, P. C.; Mattevi, C. Mesoscale Design of Multifunctional 3D Graphene Networks. *Mater. Today* **2016**, *19*, 428-436.

56 Chen, B.; Ma, Q.; Tan, C.; Lim, T.-T.; Huang, L.; Zhang, H. Carbon-Based Sorbents with Three-Dimensional Architectures for Water Remediation. *Small* **2015**, *11*, 3319-3336.

57 Li, F.; Jiang, X.; Zhao, J.; Zhang, S. Graphene Oxide: A Promising Nanomaterial for Energy and Environmental Applications. *Nano Energy* **2015**, *16*, 488-515.

58 Wang, H.; Yuan, X.; Zeng, G.; Wu, Y.; Liu, Y.; Jiang, Q.; Gu, S. Three Dimensional Graphene Based Materials: Synthesis and Applications from Energy Storage and Conversion to Electrochemical Sensor and Environmental Remediation. *Adv. Colloid Interface Sci.* **2015**, *221*, 41-59.

59 Munuera, J. M.; Paredes, J. I.; Villar-Rodil, S.; Martínez-Alonso, A.; Tascón, J. M. D. A Simple Strategy to Improve the Yield of Graphene Nanosheets in the Anodic Exfoliation of Graphite Foil. *Carbon* **2017**, *115*, 625-628.

60 Wan, W.; Lin, Y.; Prakash, A.; Zhou, Y. Three-Dimensional Carbon-Based Architectures for Oil Remediation: From Synthesis and Modification to Functionalization. *J. Mater. Chem. A* **2016**, *4*, 18687-18705.

61 Dai, Z.; Peng, C.; Chae, J. H.; Ng, K. C.; Chen, G. Z. Cell Voltage Versus Electrode Potential Range in Aqueous Supercapacitors. *Sci. Rep.* **2015**, *5*, 9854-9862.

62 Zhang, L.; Shi, G. Preparation of Highly Conductive Graphene Hydrogels for Fabricating Supercapacitors with High Rate Capability. *J. Phys. Chem. C* **2011**, *115*, 17206-17212.

63 Zuo, Z.; Kim, T. Y.; Kholmanov, I.; Li, H.; Chou, H.; Li, Y. Ultra-light Hierarchical Graphene Electrode for Binder-Free Supercapacitors and Lithium-Ion Battery Anodes. *Small* **2015**, *11*, 4922-4930.

64 Choi, B. G.; Yang, M.; Hong, W. H.; Choi, J. W.; Huh, Y. S. 3D Macroporous Graphene Frameworks for Supercapacitors with High Energy and Power Densities. *ACS Nano* **2012**, *6*, 4020-4028.

65 Wu, Z.-S.; Winter, A.; Chen, L.; Sun, Y.; Turchanin, A.; Feng, X.; Müllen, K. Three-Dimensional Nitrogen and Boron Co-doped Graphene for High-Performance All-Solid-State Supercapacitors. *Adv. Mater.* **2012**, *24*, 5130-5135.

66 Ramadoss, A.; Yoon, K.-Y.; Kwak, M.-J.; Kim, S.-I.; Ryu, S.-T.; Jang, J.-H. Fully Flexible, Lightweight, High Performance All-Solid-State Supercapacitor Based on 3-Dimensional-Graphene/Graphite-Paper. *J. Power Sources* **2017**, *337*, 159-165.

67 Yang, X.; Zhu, J.; Qiu, L.; Li, D. Bioinspired Effective Prevention of Restacking in Multilayered Graphene Films: Towards the Next Generation of High-Performance Supercapacitors. *Adv. Mater.* **2011**, *23*, 2833-2838.

68 Zhang, J.; Jiang, J.; Li, H.; Zhao, X. S. A High-Performance Asymmetric Supercapacitor Fabricated with Graphene-Based Electrodes. *Energy Environ. Sci.* **2011**, *4*, 4009-4015.

69 Lei, Z.; Liu, Z.; Wang, H.; Sun, X.; Lu, L.; Zhao, X. S. A High-Energy-Density Supercapacitor with Graphene-CMK-5 as the Electrode and Ionic Liquid as the Electrolyte. *J. Mater. Chem. A* **2013**, *1*, 2313-2321.

70 Enterría, M.; Martín-Jimeno, F. J.; Suárez-García, F.; Paredes, J. I.; Pereira, M. F. R.; Martins, J. I.; Martínez-Alonso, A.; Tascón, J. M. D.; Figueiredo, J. L. Effect of Nanostructure on the Supercapacitor Performance of Activated Carbon Xerogels Obtained from Hydrothermally Carbonized Glucose-Graphene Oxide Hybrids. *Carbon* **2016**, *105*, 474-483.

Supporting Information

Electrochemical exfoliation of graphite in aqueous sodium halide electrolytes towards low oxygen content graphene for energy and environmental applications

J.M. Munuera[a*], J.I. Paredes[a], M. Enterría[b], A. Pagán[c], S. Villar-Rodil[a], M.F.R. Pereira[b], J.I. Martins[d,e], J.L. Figueiredo[b], J.L. Cenis[c], A. Martínez-Alonso[a], J.M.D. Tascón[a]

[a]*Instituto Nacional del Carbón, INCAR-CSIC, Apartado 73, 33080 Oviedo, Spain*
[b]*Laboratório de Processos de Separação e Reacção – Laboratório de Catálise e Materiais (LSRE-LCM), Departamento de Engenharia Química, Faculdade de Engenharia, Universidade do Porto, R. Dr. Roberto Frias s/n, 4200-465 Porto, Portugal*
[c]*Instituto Murciano de Investigación y Desarrollo Agrario y Alimentario (IMIDA), Calle Mayor 1, 30150 La Alberca, Spain*
[d] *Departamento de Engenharia Química, Faculdade de Engenharia, Universidade do Porto, R. Dr. Roberto Frias s/n, 4200-465 Porto, Portugal*
[e] *Universidade do Minho, LAB2PT- Laboratório de Paisagens, Património e Território, Portugal*

[*] j.munuera@incar.csic.es

S1. Biocompatibility of graphene derived from halide-based anodic exfoliation

S1.1 Experimental

To evaluate the biocompatibility of the graphene materials produced by the halide-based anodic exfoliation approach, we investigated the proliferation of murine fibroblasts (L929 cell line, ECACC No. 85011425) seeded onto thin graphene films deposited on polystyrene tissue culture plates. The L929 cell line was chosen for the experiments because it is highly stable, fast-growing and commonly used in cytotoxicity assays. The fibroblasts were initially seeded at a density of 5000 cells per well onto 48-well culture plates, where each well was pre-coated with either 0.25 or 0.5 mg of a given graphene sample drop-cast from its corresponding aqueous dispersion in FMN. For comparison purposes, wells pre-coated with vitamin C-reduced graphene oxide (graphene oxide acquired from Graphenea) were also included in the tests. After fibroblast seeding, the plates were incubated at 37 ºC in a 5% CO_2 atmosphere using Dulbecco´s modified Eagle´s medium (DMEM) supplemented with 10% fetal bovine serum (FBS), penicillin (100 U mL^{-1}) and streptomycin (100 mg mL^{-1}) as the culture medium. This medium was replaced twice a week during the tested cell proliferation period. Cell proliferation was determined at certain time intervals, namely 4, 7 and 10 days after fibroblast seeding, by means of the MTT assay.[1] This assay is based on the enzymatic reduction of the tetrazolium dye 3-(4,5-dimethylthiazol-2-yl)-2,5-diphenyltetrazolium bromide (MTT, acquired from Sigma) to its corresponding purple formazan. To this end, the culture medium was carefully removed from each well and replaced by aqueous MTT solution (1 mg mL^{-1}, 500 μL per well). Following incubation at 37 ºC in 5% CO_2 atmosphere for 4 h, the MTT solution was removed and then dimethyl sulfoxide (200 μL per well) was added to solubilize the water-insoluble purple formazan crystals that could have been formed. Finally, the optical absorbance of the obtained formazan solution was evaluated with a BMG FLUOstar Galaxy microplate reader (MTX Lab Systems, Inc) at 570 nm as well as the 690 nm reference wavelength. For statistically meaningful results, the experiments were performed in hexaplicate, and the statistical analysis was carried out using the SPSS software. When data obeyed the normality and homogeneity of variance requirements, their average was

compared by means of the parametric test ANOVA followed by Bonferroni´s post hoc multiple t-test. The significance level was set to $p < 0.05$.

S1.2. Results

Owing to a number of attractive features, including high mechanical strength, flexibility, chemical inertness and good electrical conductivity, graphene is considered a serious candidate for use as a support or scaffold in tissue engineering applications (e.g., cell growth and differentiation, tissue regeneration, etc).[2,3] To this end, the first and foremost requirement that a graphene material (as well as any prospective biomaterial) must satisfy is that of biocompatibility and non-cytotoxicity. Biocompatibility is also an important issue with a view to using graphene materials in environmental remediation (e.g., water decontamination) applications.[4] While many graphene materials have demonstrated a good biocompatibility towards different mammal cell lines when used as substrates/scaffolds in cell growth and proliferation studies,[5] it has also been recognized that their specific physicochemical characteristics (e.g., nanosheet lateral size and thickness, surface chemistry, presence of impurities, etc) have a strong bearing on their interactions with biological systems.[3] For this reason, graphenes obtained by novel production methods should be tested for biocompatibility on an individual basis. For the anodically exfoliated graphenes developed here using sodium halides as the electrolyte, the presence of even tiny amounts of certain by-products derived from the redox reactions (e.g., such species as I_2, Br_2, Cl_2 or HClO, which possess a strong oxidizing character) could pose an issue with a view to their use in bio-related applications. To shed some light on this question, we carried out a preliminary investigation into the biocompatibility of graphenes produced by the halide-based anodic approach towards the murine fibroblast cell line L929. More specifically, we applied the MTT assay to study the proliferation of fibroblasts seeded onto thin graphene films supported on polystyrene tissue culture plates. We note that the MTT assay and the L929 cell line are commonly employed for the in vitro assessment of cellular toxicity of medical devices[6] and have been previously used in biocompatibility tests of different graphene and graphene-containing materials.[7,8,9,10]

Fig. S1 shows the results of the cell proliferation tests for fibroblasts seeded onto ~1 (a) and 2 (b) μm thick graphene films derived from anodic exfoliation either in 0.05 M NaCl or

in 0.1 M NaI as the electrolyte. The tests were performed 4, 7 and 10 days after seeding the fibroblasts. The ~1 (2) μm thick films were obtained by depositing about 0.25 (0.5) mg of the corresponding graphene nanosheets dispersed in water/FMN per well of the culture plate. The two graphene samples tested for biocompatibility were chosen so as to span the whole range of specimens prepared in this work in terms of their oxidation degree (see Table 1), i.e., we included the graphene product having the lowest O/C ratio (0.06, obtained with 0.05 M NaCl) and a product with the highest ratio (0.11, prepared with 0.1 M NaI). For comparison purposes, a graphene sample with an even larger extent of oxidation (vitamin C-reduced graphene oxide (RGO), O/C ratio ~0.15-0.20) was also tested. For either film thickness, it can be seen that the anodically exfoliated graphenes led to a somewhat lower cell proliferation rate compared to the case of the RGO material, which in turn was slightly lower than the proliferation rate of the control sample (bare plate well). In general, this effect appeared to be more noticeable for the 2 μm thick graphene films (compare panels a and b in Fig. S1), suggesting that some level of cytotoxicity might be present in the halide-based samples. However, the fact that the measured absorbance values distinctly increased with time for the two halide-based samples of either thickness indicated that fibroblast proliferation was not impeded, and therefore that these materials can be considered biocompatible overall. We also note that the differences in proliferation between the halide-based graphenes and RGO could be ascribed, at least in part, to their different oxygen content/hydrophilicity. It is well known that moderately hydrophilic substrates are more convenient for cell growth than their hydrophobic counterparts because they favor cellular adhesion.[8,11,12] The fact that fibroblast proliferation on the graphene samples tended to positively correlate with their oxidation extent (O/C ratio), i.e., it followed the trend 0.05 M NaCl graphene < 0.1 M NaI graphene < RGO, particularly at days 4 and 7, would be consistent with the idea that cell attachment is initially disadvantaged and therefore proliferation delayed on the less oxidized, more hydrophobic graphene surfaces. Nevertheless, for longer culture times (10 days) fibroblast proliferation on the less oxidized graphene substrate (0.05 M NaCl) tended to catch up with that of the 0.1 M NaI graphene and RGO substrates, which would imply that a fast cell growth rate can also be attained on the former once the fibroblasts are able to settle in.

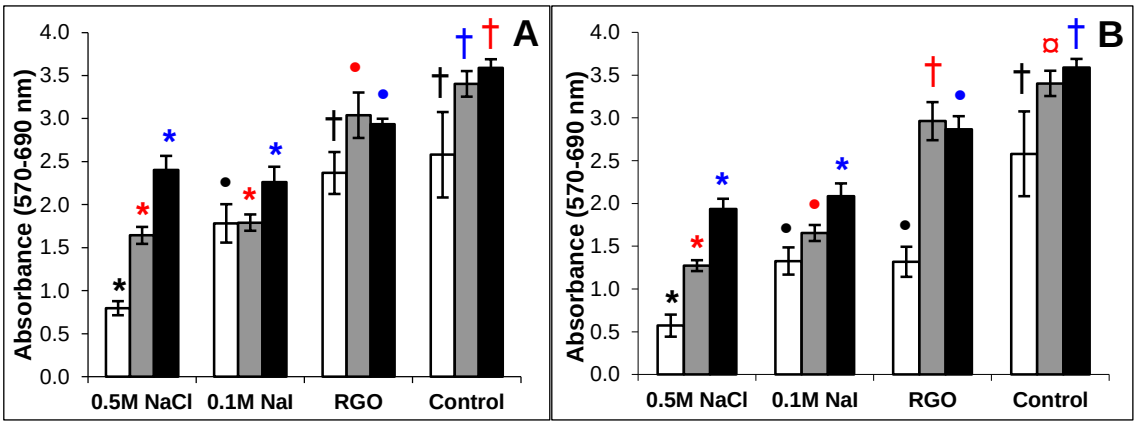

Figure S1. Proliferation of murine fibroblasts (L929 cell line) seeded onto ~1 (a) and 2 (b) μm thick graphene films obtained either from the anodic exfoliation of graphite foil in 0.05 M NaCl and 0.1 M NaI or from the reduction of graphene oxide with vitamin C (RGO) and supported onto polystyrene culture plates. Results for the bare (graphene-free) culture plate are also shown as a control sample. Proliferation was quantified on the basis of the MTT test 4 (white bars), 7 (grey bars) and 10 (black bars) days after fibroblast seeding. For a given testing day, statistically significant differences ($p < 0.05$) between the studied materials are indicated by the use of different symbols (*, † and •). Data are given as average absorbance value (570-690 nm) ± standard deviation ($n = 6$).

S2. N_2 adsorption/desorption isotherm of as-exfoliated graphene

N_2 physisorption for the as-obtained graphene samples exfoliated in 0.1 M NaI was measured in an Autosorb-1 volumetric analyzer (Quantachrome) at -196 ºC in the relative pressure range between 10-7 and 0.99 (Fig. S2). The sample was degassed under vacuum at 125 ºC for 16 h. The BET surface area was determined on the basis of the BET model from the N_2 adsorption branch of the isotherm in the relative pressure range between 0.01 and 0.3, yielding a value of 35 m^2 g^{-1}. The isotherm exhibited significant hysteresis at intermediate relative pressures as well as strong adsorption at relative pressures close to 1, revealing the presence of a large amount of mesoporous and macroporous voids in the sample, as could be anticipated. However, we believe that the BET surface area of the as-exfoliated graphene materials measured through N_2 physisorption does not necessarily reflect the surface area that was actually available in many of the applications tested in the manuscript. For the measurement of N_2 adsorption/desorption isotherms the graphene samples had to be thoroughly dried through the abovementioned procedure, implying that substantial restacking of the expanded graphene layers and thus a reduction in the available surface area was most likely taking place. By contrast, the graphene samples for the application tests were either used in a wet state without drying (e.g., dye adsorption) or were just mildly dried under ambient conditions (e.g., supercapacitor electrodes). In these cases, restacking of the graphene layers was probably avoided to a large extent.

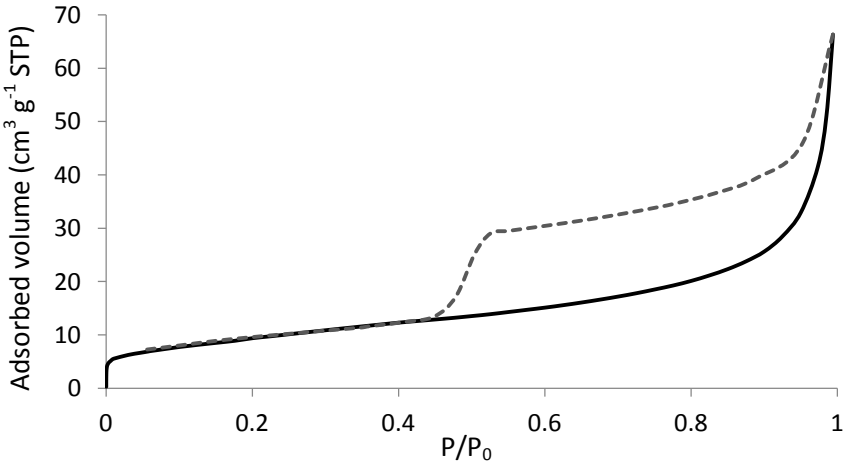

Figure S2. N2 adsorption/desorption isotherm of as-exfoliated graphene prepared by electrochemical exfoliation of graphite foil in 0.1 M NaI. Solid (dashed) line represents adsorption (desorption).

S3. Further XPS characterization of halide-based anodically exfoliated graphenes

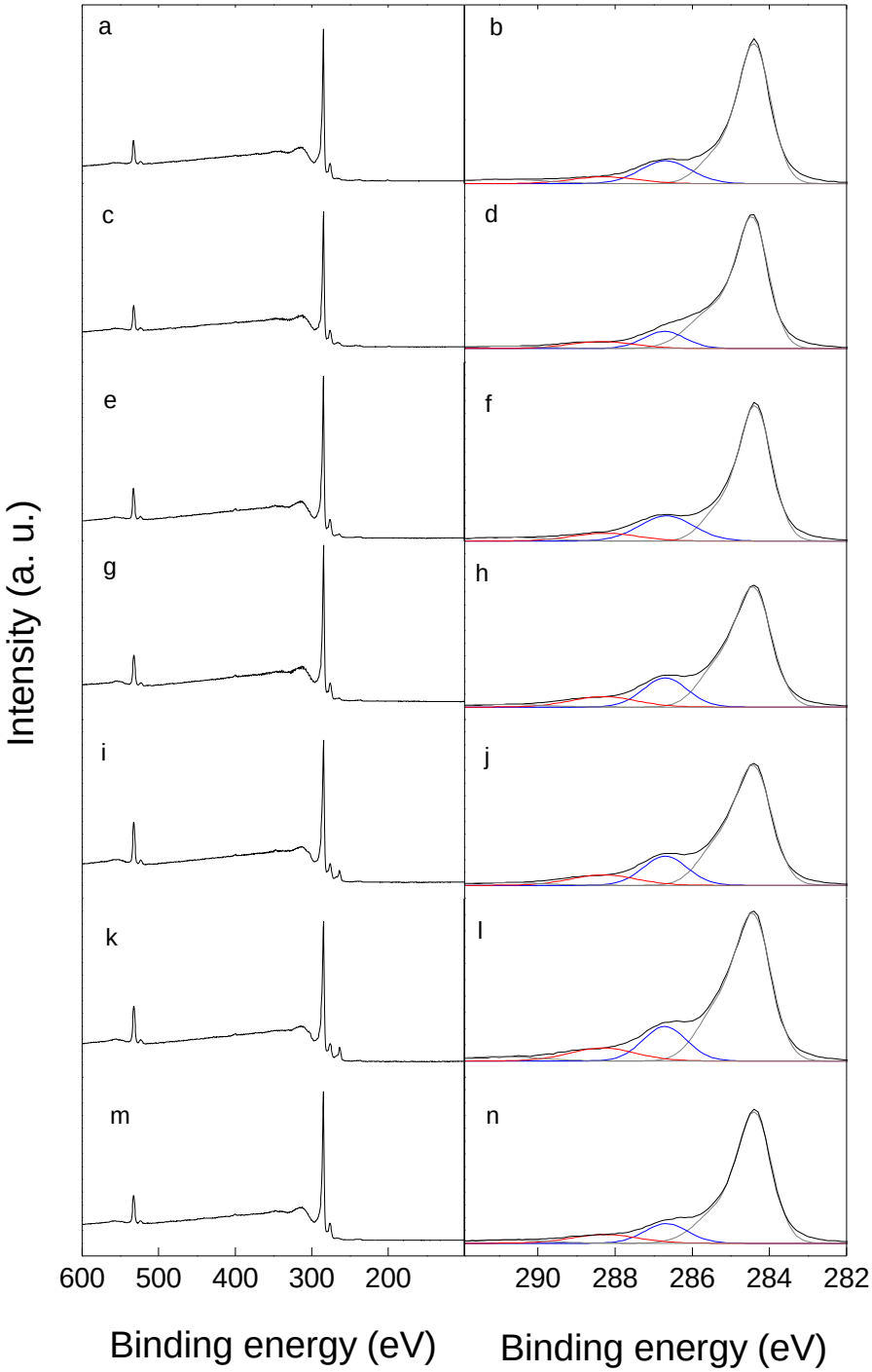

Figure S3. XPS survey spectra (a,c,e,g,i,k,m) and high resolution C 1s core level spectra (b,d,f,h,j,l,n) for graphene samples obtained by aqueous anodic exfoliation of graphite foil in 0.05 M NaCl (a,b), 0.05 M NaBr (c,d) 0.1 M NaBr (e,f), 0.01 M NaI (g,h), 0.05 M NaI (i,j), 0.1 M NaI (k,l), and 0.2 M NaI (m,n).

In Fig. S3, the experimentally obtained high resolution C 1s envelopes (black traces) were peak-fitted into 5 components according to previous work.[13,14] These components were located at about 284.6 eV (carbon atoms in graphitc C=C environments), 285.4 eV (carbon atoms in localized alternant hydrocarbon configurations), 286.7 eV (carbon atoms in oxidation state +1, i.e., carbons single-bonded to oxygen as in hydroxyl and epoxide groups),[15] 288.3 eV (carbon atoms in oxidation state +2, i.e. carbons double-bonded to oxygen, as in carbonyl groups; carbons in oxidation state +3, as in carboxylic groups) and 291.3 ($\pi \rightarrow \pi^*$ shake-up satellite peak for the band centered at 284.6 eV. Although the original peak-fitting scheme allowed for two different components for carbon oxidation states of +2 and +3, only one component was finally retained as they converged during the fitting calculation. The two components assigned to carbon in oxidation state 0 (i.e., those located at 284.6 and 285.4 eV) are shown as a single combined component (gray trace), while those assigned to oxidation states +1 and +2/+3 are shown as blue and red traces, respectively.

S4. Three electrode characterization of as-prepared anodically exfoliated graphene

The NaI-exfoliated graphite foil (0.1 M) was electrochemically characterized in a three-electrode cell in 1 M H_2SO_4 with an Ag/AgCl (1 M KCl) reference electrode. The working electrode was prepared by sandwiching a PTFE/carbon pellet (19 mg of carbon paste composed of 80 wt% as-exfoliated graphene material and 10 wt% PTFE) in a stainless steel mesh and pressing them with 1 ton during 15 s. The counter electrode was prepared in the same manner but using 30 mg of paste prepared with Norit DLC Supra 50® carbon as the active material. The working and counter electrodes were arranged in a stack, separated by filter paper (Whatmann®, qualitative filter paper Grade 1) and connected to two Pt wires as current collectors. Nitrogen gas was bubbled into the electrolyte for 30 min prior to measurement to remove the O_2 present into the electrolyte solution. The obtained voltammetry curves (-0.5 to 0.9 V) displayed two reversible humps centered at 0.3 V (Fig. S4). This pseudofaradaic activity is generally ascribed to the quinone/hydroxyquinone redox pair. The intensity of the observed peaks decreased gradually with increasing scan rate, confirming the pseudocapacive contribution of the surface oxygen functionalities. Hence, the capacitance decreased from 103 to 10 F g^{-1} by increasing the scan rate from 2 to 500 mV s^{-1}.

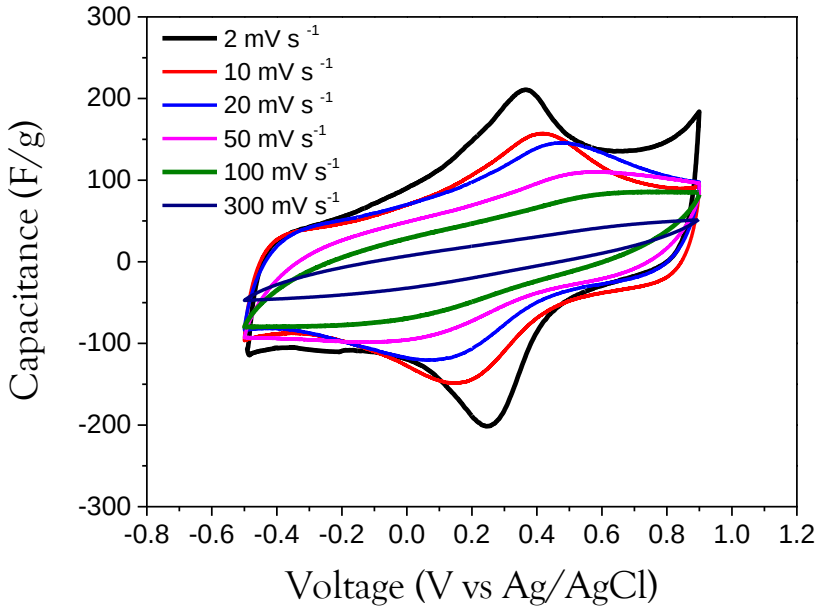

Figure S4. Cyclic voltammetry curves for halide-exfoliated graphite foil (0.1 M NaI) at different scan rates

S5. Discussion of IR drop contribution to the supercapacitor cell performance

Fig. 8d in the main text suggests that the IR drop in the supercapacitor cell is quite high. The operation voltage of a supercapacitor cell is determined by the following equation:[16]

$$E = ETHD + EIR + EH + EO \quad (1)$$

, where ETHD is the thermodynamic term, EIR is the IR drop term, EH is the overpotential for hydrogen gas evolution reaction, and EO is the overpotential for oxygen gas evolution. Both EH and EO, depends largely on the electrode material.[17] The ETHD value for 1 M H2SO4 electrolyte is generally around 0.9 V, sometimes even lower. The EIR was investigated by means of chronopotenciometry and electrochemical impedance spectroscopy (EIS) (see Fig. S5). The IR drop in the cell turned out to be around 0.3 Ω in both cases, which in fact is not too high a value. Indeed, the main component contributing to the electronic resistance was not the IR drop, but the Faradaic activity of the oxygenated species in the electrode surface (ESR, see Fig. S5b).

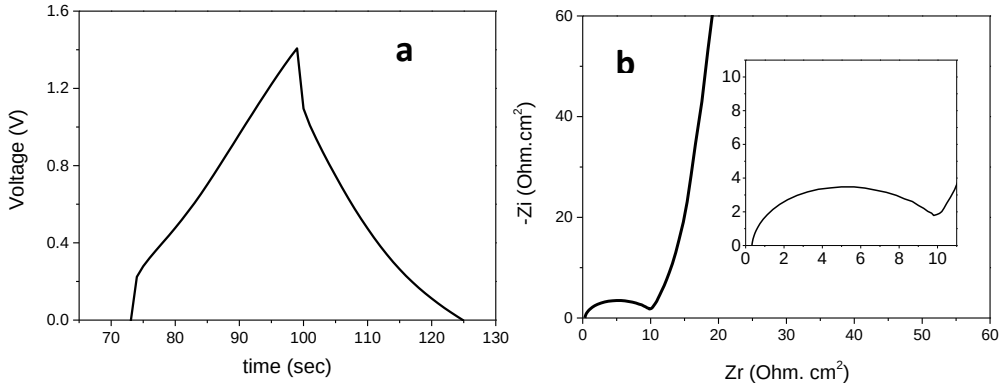

Figure S5. (a) Chronopotentiometry at 1 A mg^{-1} and (b) Nyquist plot extracted from EIS at 0 V of the two-electrode cell.

Based on these results, the potential required for water splitting in this cell, considering the overpotential caused by the IR drop (0.3 Ω * 1A = 0.3 V), would be 1.2 V at most. To get some insight into the EH and EO values, which depend on the electrode nature, we performed some tests in a three-electrode cell using the same electrolyte (Fig. S6). Fig. S6a shows the cyclic voltammetry of the as-prepared graphene material (0.1 M NaI) at 10 mV s^{-}

[1]. The curve not only displayed a clear square shape (good indicator of non-resistive behavior), but also evidence of the formation of O_2 (high-potential limit) or H_2 (low potential limit) was not observed. This capacitive-conductive behavior was also observed in Fig. 8a of the main text. The deviation from a pure capacitive response in the cyclic voltammetry curves (both in two- and three-electrode cells) was probably caused by the presence of some oxygen groups, which are known to be present in the halide-based samples to a limited but non-negligible extent. For example, quinones are highly active redox groups, and even when present in very low amounts they cause a significant Faradaic activity in non-porous conductive carbon-based electrodes.[18] The IR drop calculated by electrochemical impedance spectroscopy in the three-electrode configuration was around 0.2 Ω.

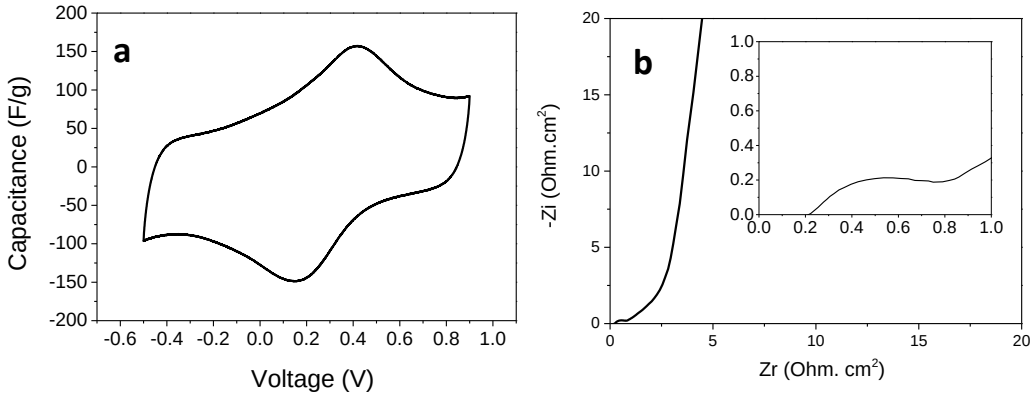

Figure S6. (a) Cyclic voltammetry at 10 mV/s and (b) Nyquist plot (EIS, 0V) for NaI-exfoliated graphene in a three-electrode cell at 10 mV s^{-1} in 1 M H_2SO_4.

On the basis of the previous analysis, we consider that the as-exfoliated graphene material investigated here actually afforded a significant widening of the operation voltage when used as an electrode in a supercapacitor cell. Part of this widening was caused by a quite high IR drop, but the important contribution of the electrode material was also evident. This widening in the operation voltage is believed to arise both from the particular porous morphology of the material and from the relatively defect-free nature of its structure.

Table S1. Adsorption capacities of dyes with different graphene-based materials

Material	**Adsorbate**	**Adsorption capacity ($mg\ g^{-1}$)**	**Ref**
Hemyn/graphene hydrogel	Methyl orange	40	19
Graphene hydrogel	Methyl orange	50	20
Graphene oxide/isophorone diisocyanate	Methyl orange	83	21
Graphene oxide/Ni-Al LDH	Methyl orange	84	22
Graphene oxide/Ni-Cr LDH	Methyl orange	160	23
Graphene oxide/chitosan	Methyl orange	567	24
Halide-based anodic graphene	Methyl orange	923	This work
Hemyn/graphene hydrogel	Methylene blue	100	19
Reduced graphene oxide	Methylene blue	158	25
Graphene oxide/chitosan	Methylene blue	180	26
Graphene oxide/calcium alginate	Methylene blue	182	27
Graphene oxide sponge	Methylene blue	397	28
Graphene oxide	Methylene blue	714	29
Halide-based anodic graphene	Methylene blue	360	This work
Reduced graphene oxide/Fe_2O_4	Rhodamine B	23	30
Graphene oxide/Fe_3O_4	Rhodamine B	50	31
Graphene sponge	Rhodamine B	73	32
Graphene/TiO_2 hydrogel	Rhodamine B	73	33
3D graphene	Rhodamine B	207	34
Hemyn/graphene hydrogel	Rhodamine B	350	19
Halide-based anodic graphene	Rhodamine B	343	This work
Reduced graphene oxide	Basic fuchsin	34	35
Reduced graphene oxide/ PSSMA	Basic fuchsin	388	36
Graphene oxide/polyacrylamide	Basic fuchsin	1034	37
Halide-based anodic graphene	Basic fuchsin	355	This work

References

1 Vistica, D.T.; Skehan, P.; Scudiero, D.; Monks, A.; Pittman, A.; Boyd, M. R. Tetrazolium-based Asays for Celular Viabilty: A Critcal Examination of Selected Parameters Afecting Formazan Production. *Cancer Res.* **1991**, *51*, 2515-2520.

2 Zhang, Y.; Nayak, T. R.; Hong. H; Cai, W. Graphene: a Versatile Nanoplatform for Biomedical Applications. *Nanoscale* **2012**, *4*, 3833-3842.

3 Thompson, B. C.; Murray, E.; Wallace, G. G. Graphite Oxide to Graphene. Biomaterials to Bionics. *Adv. Mater.* **2015**, *27*, 7563-7582.

4 Kemp, K. C.; Seema, H.; Saleh, M.; Le, N. H.; Mahesh, K.; Chandra, K. V.; Kim, K. S. Environmental Applications Using Graphene Composites: Water Remediation and Gas Adsorption. *Nanoscale* **2013**, *5*, 3149-3171.

5 Yang, K.; Li, Y.; Tan, X.; Peng, R.; Liu, Z. Behavior and Toxicity of Graphene and Its Functionalized Derivatives in Biological Systems. *Small* **2013**, *9*, 1492-1503.

6 Biological evaluation of Medical Devices, Part 5: Tests for in vitro cytotoxicity. ISO 10993-5. 2009.

7 Munuera, J. M.; Paredes, J. I.; Villar-Rodil, S.; Ayán-Varela, M.; Pagán, A.; Aznar-Cervantes, S. D.; Cenis, J. L.; Martínez-Alonso, A.; Tascón, J. M. D. High Quality, Low Oxygen Content and Biocompatible Graphene Nanosheets Obtained by Anodic Exfoliation of Different Graphite Types. *Carbon* **2015**, *94*, 729-739.

8 Yan, X.; Chen, J.; Yang, J.; Xue, Q.; Miele, P. Fabrication of Free-Standing, Electrochemically Active, and Biocompatible Graphene Oxide−Polyaniline and Graphene−Polyaniline Hybrid Papers. *ACS Appl. Mater. Interfaces* **2010**, *2*, 2521-2529.

9 Fan, H.; Wang, L.; Zhao, K.; Li, N.; Shi, Z.; Ge, Z.; Jin, Z. Fabrication, Mechanical Properties, and Biocompatibility of Graphene-Reinforced Chitosan Composites. *Biomacromolecules* **2010**, *11*, 2345-2351.

10 Wang, L.; Lu, C.; Zhang, B.; Zhao, Wu, F.; Guan, S. Fabrication and Characterization of Flexible Silk Fibroin Films Reinforced With Graphene Oxide for Biomedical Applications *RSC Adv.* **2014**, *4*, 40312-40320.

11 Masters, K. S.; Anseth, K. S. Cell-Material Interactions. In Advances in Chemical Engineering; Sefton, M., Ed.; Academic Press, 2004, vol. Volume 29, pp. 7-46.

12 O. Akhavan, O.; Ghaderi, E. The Use of Graphene in the Self-Organized Differentiation of Human Neural Stem Cells Into Neurons Under Pulsed Laser Stimulation. *J.*

Mater. Chem. B **2014**, *2*, 5602-5611.

13 Yang, D.-Q.; Rochette, J.-F.; Sacher, E. Controlled Chemical Functionalization of Multiwalled Carbon Nanotubes by Kiloelectronvolt Argon Ion Treatment and Air Exposure *Langmuir* **2005**, *21*, 8539-8545.

14 Yang, D.-Q.; Sacher, E. Carbon 1s X-ray Photoemission Line Shape Analysis of Highly Oriented Pyrolytic Graphite: The Influence of Structural Damage on Peak Asymmetry. *Langmuir* **2006**, *22*, 860-862

15 Wang, Q.; Kaliaguine, S.; Ait-Kadi, A. Catalytic Grafting: A New Technique for Polymer-Fiber Composites. III. Polyethylene-Plasma-Treated Kevlar^{TM} Fibers Composites: Analysis of the Fiber Surface. *J. Appl. Polym. Sci.* **1993**, *48*, 121-148.

16 Iida, T.; Matsushima, H.; Fukunaka, Y. Water Electrolysis under a Magnetic Field. *J. Electrochem. Soc.* **2007**, *154*, E112-E115

17 Zhong, C.; Deng, Y.; Hu, W.; Jinli Qiao, J.; Zhang, L.; Zhang, J. A Review of Electrolyte Materials and Compositions for Electrochemical Supercapacitors. *Chem. Soc. Rev.* **2015**, *44*, 7484—7539.

18 Enterría, M.; Gonçalvesa, A. G.; Pereira, M. F. R.; Martins, J. I.; Figueiredo, J. L. Electrochemical Storage Mechanisms in Non-Stoichiometric Cerium Oxide/Multiwalled Carbon Nanotube Composites. *Electrochim. Acta* **2016**, *209*, 25-35.

19 Zhao, Y.; Zhang, Y.; Liu, A.; Wei, Z.; Liu, S. Construction of Three-Dimensional Hemin-Functionalized Graphene Hydrogel with High Mechanical Stability and Adsorption Capacity for Enhancing Photodegradation of Methylene Blue. *ACS Appl. Mater. Interfaces* **2017**, DOI: 10.1021/acsami.6b10959.

20 Zhang, X.; Liu, D.; Yang, L.; Zhou, L.; You, T. Self-Assembled Three-Dimensional Graphene-Based Materials for Dye Adsorption and Catalysis. *J. Mater. Chem. A* **2015**, *3*, 10031-10037.

21 Yan, J.; Zhu, Y.; Qiu, F.; Zhao, H.; Yang, D.; Wang, J.; Wen, W. Kinetic, Isotherm and Thermodynamic Studies for Removal of Methyl Orange Using a Novel β-Cyclodextrin Functionalized Graphene Oxide-Isophorone Diisocyanate Composites. *Chemical Engineering Research and Design* **2016**, *106*, 168-177.

22 Yang, Z.; Ji, S.; Gao, W.; Zhang, C.; Ren, L.; Tjiu, W. W.; Zhang, Z.; Pan, J.; Liu, T. Magnetic Nanomaterial Derived from Graphene Oxide/Layered Double Hydroxide Hybrid for Efficient Removal of Methyl Orange from Aqueous Solution. *J. Colloid Interface Sci.* **2013**, *408*, 25-32.

23 Ruan, X.; Chen, Y.; Chen, H.; Qian, G.; Frost, R. L. Sorption Behavior of Methyl Orange from Aqueous Solution on Organic Matter and Reduced Graphene Oxides Modified Ni–Cr Layered Double Hydroxides. *Chem. Eng. J.* **2016**, *297*, 295-303.

24 Wang, Y.; Liu, X.; Wang, H.; Xia, G.; Huang, W.; Song, R. Microporous Spongy Chitosan Monoliths Doped with Graphene Oxide as Highly Effective Adsorbent for Methyl Orange and Copper Nitrate (Cu(NO3)2) Ions. *J. Colloid Interface Sci.* **2014**, *416*, 243-251.

25 Chen, L.; Yang, J.; Zeng, X.; Zhang, L.; Yuan, W. Adsorption of Methylene Blue in Water by Reduced Graphene Oxide: Effect of Functional Groups. *Mater. Express* **2013**, *3*, 281-290.

26 Fan, L.; Luo, C.; Sun, M.; Li, X.; Lu, F.; Qiu, H. Preparation of Novel Magnetic Chitosan/Graphene Oxide Composite as Effective Adsorbents Toward Methylene Blue. *Bioresour. Technol.* **2012**, *114*, 703-706.

27 Li, Y.; Du, Q.; Liu, T.; Sun, J.; Wang, Y.; Wu, S.; Wang, Z.; Xia, Y.; Xia, L. Methylene Blue Adsorption on Graphene Oxide/Calcium Alginate Composites. *Carbohydr. Polym.* **2013**, *95*, 501-507.

28 Liu, F.; Chung, S.; Oh, G.; Seo, T. S. Three-Dimensional Graphene Oxide Nanostructure for Fast and Efficient Water-Soluble Dye Removal.*ACS Appl. Mater. Interfaces* **2012**, *4*, 922-927.

29 Yang, S.-T.; Chen, S.; Chang, Y.; Cao, A.; Liu, Y.; Wang, H. Removal of Methylene Blue from Aqueous Solution by Graphene Oxide. *J. Colloid Interface Sci.* **2011**, *359*, 24-29.

30 Bai, S.; Shen, X.; Zhong, X.; Liu, Y.; Zhu, G.; Xu, X.; Chen, K. One-Pot Solvothermal Preparation of Magnetic Reduced Graphene Oxide-Ferrite Hybrids for Organic Dye Removal. *Carbon* **2012**, *50*, 2337-2346.

31 Geng, Z.; Lin, Y.; Yu, X.; Shen, Q.; Ma, L.; Li, Z.; Pan, N.; Wang, X. Highly Efficient Dye Adsorption and Removal: a Functional Hybrid of Reduced Graphene Oxide-Fe3O4 Nanoparticles as an Easily Regenerative Adsorbent. *J. Mater. Chem.* **2012**, *22*, 3527-3535.

32 Zhao, J.; Ren, W.; Cheng, H.-M. Graphene Sponge for Efficient and Repeatable Adsorption and Desorption of Water Contaminations. *J. Mater. Chem.* **2012**, *22*, 20197-20202.

33 Hou, C.; Zhang, Q.; Li, Y.; Wang, H. P25–Graphene Hydrogels: Room-Temperature Synthesis and Application for Removal of Methylene Blue from Aqueous Solution. *J. Hazard. Mater.* **2012**, *205–206*, 229-235.

34 Li, W,; Gao, S.; Wu, L.; Qiu, S.; Guo, Y.; Geng, X.; Chen, M.; Liao, S.; Zhu, C.; Gong, Y.; Long, M.; Xu, J.; Wei, X.; Sun, M.; Liu, L. High-Density Three-Dimension Graphene

Macroscopic Objects for High-Capacity Removal of Heavy Metal Ions. *Sci. Rep.* **2013**, *3*, 2125.

35 Tokalioɨlu, Ş.; Yavuz, E.; Aslantaş, A.; Şahan, H.; Taşkin, F.; Patat, Ş.Spectrophotometric Determination of Basic Fuchsin from Various Water Samples after Vortex Assisted Solid Phase Extraction Using Reduced Graphene Oxide as an Adsorbent. Spectrochim. *Acta Mol. Biomol. Spectrosc.* **2015**, *149*, 378-384.

36 Song, Y.-B.; Song, X.-D.; Cheng, C.-J.; Zhao, Z.-G. Poly(4-Styrenesulfonic Acid-co-Maleic Acid)-Sodium-Modified Magnetic Reduced Graphene Oxide for Enhanced Adsorption Performance Toward Cationic Dyes. *RSC Adv.* **2015**, *5*, 87030-87042.

37 Yang, X.; Li, Y.; Du, Q.; Sun, J.; Chen, L.; Hu, S.; Wang, Z.; Xia, Y.; Xia, L. Highly Effective Removal of Basic Fuchsin from Aqueous Solutions by Anionic Polyacrylamide/Graphene Oxide Aerogels. *J. Colloid Interface Sci.* **2015**, *453*, 107-114.

High quality, low-oxidized graphene via anodic exfoliation with table salt as an efficient oxidation-preventing co-electrolyte for water/oil remediation and capacitive energy storage applications

J.M. Munuera[1], J.I. Paredes[1], S. Villar-Rodil, A. Castro-Muñiz, A. Martínez-Alonso, J.M.D. Tascón

Instituto Nacional del Carbón, INCAR-CSIC, C/Francisco Pintado Fe 26,CP33011 Oviedo, Spain

[1] Corresponding authors.
E-mail addresses: j.munuera@incar.csic.es; paredes@incar.csic.es

Abstract

The production of graphene through anodic exfoliation of graphite in water is regarded as a competitive approach in the efforts to scale-up the manufacturing of this two-dimensional material for different practical uses. However, issues related to oxidative attack of the nanosheets inherent to this delamination process have traditionally precluded the attainment of high quality materials, with the use of proper electrolyte additives as oxidation-preventing agents being proposed as a possible way out. Here we demonstrate that sodium chloride (table salt) can be used as a highly efficient additive (co-electrolyte) of common sulfate-based electrolytes, yielding anodically exfoliated graphene with minimal oxidation (O/C ratio ~0.02-0.03) and thus a high structural quality. As an oxidation-preventing co-electrolyte, sodium chloride clearly outperformed other tested additives, including sodium borohydride, sulfite, citrate, bromide and iodide, ascorbic acid or ethanol, as well as other recently reported chemical species of a more complex nature and/or less readily available. The apparently contradicting ability of the chloride anion to avert oxidation of anodic graphene without negatively interfering with the exfoliation process itself was also discussed and ultimately ascribed to the different chemical reactivity of graphite edges and basal planes. The as-prepared, low-oxidized graphene exhibited a notable adsorption capacity towards organic dyes in aqueous solution (e.g., ~450 mg g^{-1} for methyl orange), a substantial ability to absorb oils and non-polar organic solvents (15-30 g g^{-1}), and displayed a good capacitive energy storage behavior (e.g., ~120 F g^{-1} at 0.1 A g^{-1}), all without the need of any post-processing steps that are so common for graphene-based materials. Overall, the demonstration that low-oxidized anodic graphene can be obtained by resorting only to inexpensive and widely available reagents should facilitate the implementation of this methodology in the industrial manufacturing of high quality graphene for several applications.

Keywords

Graphene

Electrochemical exfoliation

Energy storage

Water remediation

1. Introduction

The electrochemical exfoliation of graphite has emerged in recent years as a very promising approach in the efforts to tackle one of the most pressing issues that hinder the widespread implementation of graphene in real-life applications, namely, its large-scale production [1-5]. Such an approach boasts a number of assets that are not always present in other potentially scalable methods of graphene production, such as simplicity of operation, versatility (e.g., in terms of electrolyte choice), alacrity (short processing times) and cost-effectiveness. The electrochemical process of graphite delamination to give graphene nanosheets can be carried out under either cathodic or anodic conditions [3,4], or by a combination of both [6,7]. Cathodic exfoliation typically makes use of lithium or alkylammonium salts in organic solvents as the electrolytic system, yielding graphene materials of a high structural quality and limited oxidation (O/C atomic ratios of ~0.03-0.08) [8-10]. However, it tends to suffer from low exfoliation degrees (flakes frequently comprising more than 5 monolayers) and yields. Anodic exfoliation, on the other hand, is generally accomplished in water with inorganic acids or their salts as the electrolyte, which is attractive from an environmental and practical point of view [3,4]. Further, the anodic approach is normally more efficient than its cathodic counterpart in terms of both delamination degree (single- to few-layered nanosheets) and yield.

Unfortunately, anodic graphene has a strong tendency to oxidize during exfoliation, due to attack by oxygen radicals generated from the oxidation of water molecules at the graphite anode. For common electrolytes (e.g., sulfuric acid, sulfate salts and others), graphenes with O/C ratios in the 0.10-0.20 range are usually obtained [11-16]. This extent of oxidation compromises the structural quality of the material, and thus constitutes a serious drawback of the anodic approach that limits its wider practical utility. Still, recent studies have provided evidence that such an oxidation is not an unescapable outcome of anodic exfoliation, and that indeed it can be largely avoided by resorting to appropriate electrolytes and/or electrolyte additives [17]. To this day, only a few chemical species have been identified to be useful towards this purpose, specifically (2,2,6,6-tetramethylpiperidin-1-yl)oxyl (TEMPO) [18] and melamine [19] as additives of sulfate-based electrolytes, as well as sulfonated naphthalene as an electrolyte itself [20]. A significant problem of these organic species is that they are relatively complex and expensive compounds, thus hindering their prospects of use in the industrial production of graphene. Moreover, they can strongly adsorb on the resulting graphene product, making purification of the latter difficult [20]. Hence, the identification of

much simpler, readily available, low-cost and easy-to-remove species with a similar or even better oxidation-preventing ability to give high quality, oxide-free anodic graphene nanosheets would be highly desirable, but has so far not been attained.

We report here the finding that a readily available and extremely simple substance, namely NaCl (table salt), is a highly efficient oxidation-preventing additive (co-electrolyte) towards the anodic exfoliation of graphite. The use of NaCl as an additive of sulfate-based electrolytes is shown to afford anodic graphene with the lowest degree of oxidation documented to date (O/C ratio of ~0.02-0.03) and a high structural quality. Indeed, these features are very similar to those typical of pristine graphene flakes obtained by direct, liquid-phase exfoliation of graphite via ultrasound or shear forces, but with the additional advantage of a process that exhibits higher exfoliation yields and degrees. Concerning its potential utility application-wise, the as-obtained graphene product is shown to be an efficient adsorbent of industrial dyes from the aqueous phase as well as of non-polar organic solvents/oils, and also exhibits a good performance as an electrode for capacitive energy storage. Owing to the obvious practical advantage of NaCl over other electrolyte additives, we believe this work will strengthen the position of electrochemical exfoliation as a method of choice in current efforts to industrialize the production of high quality graphene.

2. Results and discussion

2.1. NaCl as an efficient electrolyte additive (co-electrolyte) towards low-oxidized anodic graphene

The aqueous anodic exfoliation of graphite to give graphene nanosheets is generally considered to rely, at least in its early stages, on oxidation processes that assist in the interlayer expansion at edges, grain boundaries and other structural defects of the graphitic lattice, thus facilitating the subsequent intercalation of anions from the electrolyte together with water molecules (hydrated anions) to induce an efficient delamination [4,21]. The oxidative attack of the graphite electrode is triggered by highly reactive oxygen species, such as hydroxyl radicals (·OH), generated from the anodic oxidation of water molecules. Hence, the inclusion of chemical species in the electrolytic medium as additives or co-electrolytes with an ability to neutralize (i.e., reduce) these oxygen radicals could be an effective strategy to curtail the oxidation of the anodically derived graphene nanosheets [17]. Obvious candidates for this role are certain organic and inorganic compounds that are widely employed as reducing agents

or antioxidants in chemical reactions, such as $NaBH_4$ or ascorbic acid. However, their efficacy in preventing oxidative attack during anodic exfoliation could be compromised by kinetic and other factors that are difficult to ascertain, and they could also negatively interfere with the delamination process itself [18]. Alternatively, we hypothesize that chemical species without a well-known ability to act as reductants or antioxidants, but having a reduction potential lower than that of the oxygen radicals generated during the anodic process, could be efficient in averting oxidation of the exfoliated nanosheets. In particular, we focus our attention on NaCl as a potential oxidation-preventing electrolyte additive. NaCl is a very common and low-priced commodity, making its use especially attractive with a view to the scaled-up production of graphene, and the standard reduction potential of the relevant redox pair (i.e., the Cl^-/Cl_2 pair, +1.37 V) is lower than that of the $\cdot OH/OH^-$ pair (+1.9 V) [22,23]. Indeed, oxidation of the Cl^- anion by ·OH radicals in aqueous medium to give OH^- anions or water molecules has been well documented in past studies [24].

As schematically depicted in Fig. 1a, we carried out a series of benchmark exfoliation experiments by which a graphite foil piece (working electrode) was set to a positive voltage (10 V) relative to a platinum foil (counter electrode). The process was conducted in an aqueous solution containing 0.1 M Na_2SO_4 as the main (exfoliating) electrolyte and a given molar concentration of another chemical species (e.g., NaCl) as the prospective oxidation-preventing agent [see Electronic Supplementary Material (ESM) for details on the experimental procedure]. Na_2SO_4 was chosen as the main electrolyte owing to the well-known ability of the sulfate anion to intercalate and expand the interlayer space of graphite under anodic conditions [25-28]. For comparison purposes, additives or co-electrolytes other than NaCl were tested in the exfoliation experiments, including KCl, KBr, KI, $NaBH_4$, Na_2SO_3, sodium citrate, ascorbic acid and ethanol. KBr and KI were selected because the redox potential of the Br^-/Br_2 and I^-/I_2 pairs (+1.09 and +0.54 V, respectively [23]) is also lower than that of the $\cdot OH/OH^-$ pair, while $NaBH_4$, Na_2SO_3, sodium citrate, ascorbic acid and ethanol are common reductants/antioxidants. Upon application of the bias voltage the graphite foil anode was seen to swell and enlarge in thickness, giving rise to exfoliated products in significant quantities (Fig. 1b) made up of worm-like, highly expanded particles (Fig. 1c) with a morphology of very thin, corrugated layers separated by micrometric or even nanometric voids (Fig. 1d). This morphology is characteristic of anodically delaminated graphites [21,29]. The as-exfoliated material was then transferred to the liquid phase

with the aid of a mild sonication step, finally yielding colloidal suspensions of graphene nanosheets in, e.g., water/isopropanol mixture, *N*,*N*-dimethylformamide or water with flavin mononucleotide dispersant that were stable for weeks (Fig. 1e; see ESM for details). The UV-vis absorption spectra of the suspensions in water/isopropanol (Fig. 1f) exhibited a peak centered at ~270 nm together with strong absorbance in the whole measured wavelength range above 270 nm. This result was consistent with the presence of extended, electronically conjugated sp^2-based domains in the dispersed material, as reported previously for graphenes with limited oxidation (e.g., highly reduced graphene oxide and pristine graphene flakes) [30,31].

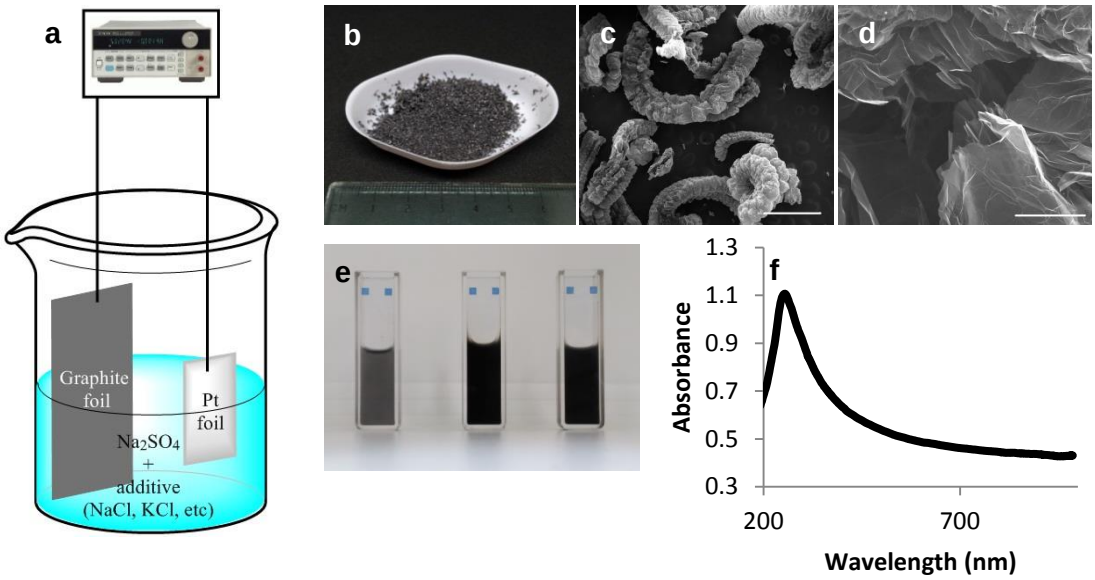

Figure 1. (a) Schematic of the anodic exfoliation of graphite using different compounds as additives (co-electrolytes) of Na_2SO_4 (main electrolyte) in the potential role of oxidation-preventing agents. (b-d) Digital photograph (b) as well as low (c) and high (d) magnification FE-SEM images of the as-prepared graphene product obtained with NaCl as a co-electrolyte with scale bars of 1mm (c) and 20 μm (d). (e) Digital photograph of graphene obtained with NaCl as a co-electrolyte and colloidally dispersed in water/isopropanol mixture (left cuvette), *N*,*N*-dimethylformamide (center) and water with flavin mononucleotide stabilizer (right) after mild sonication of the as-prepared material. (f) UV-vis optical absorption spectrum of the graphene dispersion in water/isopropanol mixture.

To quantify the impact of the abovementioned additives on the extent of oxidation of the exfoliated nanosheets, their corresponding dispersions in water/isopropanol were deposited onto metallic sample holders, forming thin graphene films that were

subsequently investigated by X-ray photoelectron spectroscopy (XPS). Table 1 shows the O/C atomic ratio measured by this technique for anodic graphenes obtained at different molar concentrations of the additives. In the absence of any additive (control sample; only 0.1 M Na_2SO_4 was used as electrolytic medium), this ratio was determined to be ~0.09. It was generally observed that at low molar concentrations (e.g., 0.01-0.02 M), the additives had a detrimental effect on the oxidation of the nanosheets, i.e., the resulting graphenes tended to exhibit O/C ratios higher than that of the control sample (~0.11-0.18 vs 0.09). On the other hand, concentrations around 0.1 M of the NaCl and KCl additives afforded graphenes with a remarkably reduced degree of oxidation, boasting O/C ratios as low as 0.02-0.03. Indeed, the latter figures were among the lowest ever documented for anodically exfoliated graphenes [17-20]. For example, using TEMPO and melamine as additives, O/C ratios around 0.04 were attained [18,19]. but different to the case of these previous reports, the present results were obtained using readily available, very low-priced and environmentally friendly substances in the electrolytic process. The amount of oxygen in these samples was very close to that present in the starting graphite foil material (O/C ratio ~0.01), implying that anodic oxidation of the graphite electrode could be kept to a minimum using the chloride-based additives. Noticeably, for ionic additives incorporating anions other than Cl^-, specifically Br^-, I^- and SO_3^{2-}, as well as for ethanol, the use of concentrations in the order of 0.1 M (or even higher) did not bring about large reductions, if any at all, in the extent of oxidation of the corresponding graphene samples compared to the control one. For some compounds ($NaBH_4$ and ascorbic acid), swelling and expansion of the graphite anode did not even take place to any substantial extent at concentrations of 0.1 M, and thus no exfoliated products were procured. In the case of 0.1 M sodium citrate, only a small amount of exfoliated material could be obtained. We have also determined the yield of graphene material produced both in the absence (control sample) and presence of Cl^- (i.e., 0.1 M Na_2SO_4 plus 0.1 M NaCl or KCl). For graphite foil pieces with a thickness around 500 μm, the measured yields were ~13 and 10 wt% for anodic exfoliation in the absence and presence of Cl^-, respectively. First of all, we note that in general these yield values cannot be directly compared with those reported in the literature by other groups, because exfoliation yields are dependent, among other factors, on the thickness of the graphite piece used in the electrolytic process [28]. Indeed, we have used a graphite foil that is several times thicker than those used in other reports [21], implying that the yield should be several times lower. Second, the yield

values measured here in the absence and presence of Cl^- were of a similar magnitude (somewhat lower for the latter), indicating that the presence of this additive in the electrolyte (at the relevant moderate concentration of 0.1 M) does not hamper the exfoliation process to a very significant extent.

Table 1. O/C atomic ratios determined from XPS data for anodic graphene obtained in the presence of 0.1 M Na_2SO_4 as the main electrolyte and different molar concentrations of a second compound used as an additive (co-electrolyte).

Electrolyte additive	Concentration (M)	O/C ratio
None	0.00	0.09
NaCl	0.01	0.24
	0.05	0.05
	0.10	0.03
	0.20	0.03
	0.50	0.03
KCl	0.01	0.13
	0.05	0.02
	0.10	0.04
	0.25	0.02
NaBr	0.01	0.19
	0.10	0.11
NaI	0.01	0.16
	0.10	0.13
Na_2SO_3	0.01	0.19
	0.10	0.12
Sodium citrate	0.01	0.14
	0.10	0.05
Sodium ascorbate	0.01	0.12
$NaBH_4$	0.01	0.16
Ethanol	0.02	0.20
	0.04	0.21
	0.20	0.24
	0.30	0.23
	0.40	0.24
	0.50	0.09
	0.70	0.06

It is currently unknown why the chloride-based additives perform so efficiently in averting the oxidation of anodic graphene in a certain range of concentrations around 0.1 M, whereas at lower molar concentrations all the tested additives appear to promote graphene oxidation. We can expect a number of different competing processes that arise from complex interactions between the graphite electrode, main electrolyte, additive and water molecules to be in place during the anodic treatment. In turn, such processes and interactions are probably dependent, among other factors, on the electrolyte and additive concentration. This hypothesis was supported by the observation that at sufficiently high additive concentrations (e.g., $NaBH_4$ and ascorbic acid at 0.1 M, but also NaCl and KCl at 1 M, and ethanol at 3 M), exfoliation of the graphite anode did not even take place, suggesting that these compounds could inhibit intercalation of the sulfate anion or, alternatively, certain subsequent reactions that trigger expansion of the interlayer space in the anode. The complexity of the involved mechanisms is also made apparent by noting that the oxidation-preventing ability of the halide-based additives did not correlate directly with the redox potential of the corresponding halide/halogen pair. If such a correlation were indeed in place, we would expect the KBr and KI additives to yield graphenes with a lower oxidation degree than that afforded by the NaCl/KCl additives by virtue of the lower redox potential of the Br^-/Br_2 and I^-/I_2 pairs relative to the Cl^-/Cl_2 pair, but that was not the case. It is thus very likely that kinetic factors play a relevant role in the reactions occurring between different chemical species during intercalation and exfoliation of the graphite anode.

The present results also raise the apparently contradicting question of why the exfoliation yield was not critically affected by the addition of 0.1 M NaCl (or KCl) while at the same time this additive prevented to a large extent the oxidation of the graphite anode, which on the other hand is assumed as a prerequisite for exfoliation to occur. In this regard, a couple of points have to be considered. First, it is quite likely that the only strict requirement for anodic exfoliation to proceed is the oxidation of the graphite edges, but not of its basal planes. This oxidation would locally increase the interlayer spacing at the graphite edge, thus facilitating the penetration of hydrated anions from the electrolyte. Once a number of hydrated anions have been inserted into the interlayer space at the edges, further oxidation of the graphite lattice (i.e., at locations other than the edges) would not be strictly necessary, as the inserted ions and water molecules themselves (or their electrolyzed products) would readily trigger the interlayer expansion (exfoliation) of the material increasingly further away from the

edges by acting as a sort of wedge. Under this scenario, only the edges of the exfoliated graphene nanosheets would have to be necessarily oxidized for anodic exfoliation to take place. Considering that the fraction of edge atoms in graphene nanosheets with sizes in the micrometric and submicrometric range is low (a few percent at most), the overall extent of oxidation in the resulting nanosheets should be correspondingly small, provided that only edges become oxidized. Second, as suggested above, we believe that the oxidation-preventing action of the Cl^- anions must be driven not only by thermodynamic but also by kinetic factors regarding the reactions that take place between Cl^- anions, oxygen radicals and graphite anode. More specifically, it is well known in carbon science that graphite edges and basal planes possess quite different reactivities towards attack by oxygen radicals [32], the former being substantially more reactive than the latter. Such a difference in reactivity should imply a faster attack of the edges by the oxygen radicals compared to basal planes. In the presence of a chemical species, such as the Cl^- anion, with an ability to neutralize (reduce) the oxygen radicals and thus avert attack (oxidation) of the graphite anode, radical neutralization will effectively take place only if the concentration of this chemical species is sufficiently high so that it can reach and neutralize the oxygen radical before the latter can attack the graphite anode. From this reasoning, it follows that the concentration of oxidation-preventing species required to avert attack by oxygen radicals will be higher in the case of graphite edges (faster attack by radicals) than in the case of basal planes (slower attack). Consequently, there should be a range of concentrations below a certain threshold for which oxidative attack is prevented in the basal plane but not at graphite edges. In this case, exfoliation of the graphite anode would be able to take place, giving rise to graphene products with a low extent of oxidation. This was indeed the case of NaCl and KCl at a concentration of 0.1 M. On the other hand, if the concentration of the oxidation-preventing agent in the electrolytic medium is sufficiently high, oxidative attack will also be arrested at the graphite edges, and hence we would expect no exfoliation of the graphite anode at all. As a matter of fact, this was the situation observed for NaCl and KCl at a concentration of 1 M.

Furthermore, we note that graphite foil could be anodically exfoliated using NaCl or KCl as the only electrolyte (i.e., in the absence of Na_2SO_4) [33]. However, in this case the delamination process was somewhat inefficient, yielding comparatively small amounts of graphene, which can be ascribed to a poor ability of the chloride anion to intercalate graphite on its own. Furthermore, exfoliation was possible just in a very

narrow range of chloride concentrations (around 0.05 M, but not at 0.01 and 0.1 M) and the process was substantially less efficient in averting graphene oxidation (O/C ratio of the resulting graphene ~0.06). Hence, the use of NaCl or KCl as an additive (co-electrolyte) of a main electrolyte (Na_2SO_4) is clearly advantageous over their use as the only electrolyte for anodic exfoliation. We surmise that the sulfate anions act as a sort of advance party in the intercalation and exfoliation of the graphite anode, triggering the expansion of the interlayer space to a point where the subsequent entry of the oxidation-preventing chloride anions is greatly facilitated. Likewise, the use of commercial table salt (typically made up of 97-99 wt% NaCl plus some anticaking and other added agents as minor components) as an additive led to anodically exfoliated graphenes with the same characteristics as those of graphenes derived from the pure, analytical-grade NaCl. Particularly, high quality graphene with a very low degree of oxidation could be similarly attained with a proper concentration of table salt, i.e., 6 mg mL^{-1} (amounting to ~0.1 M of its NaCl component). Considering that up-scaling the production of electrochemically exfoliated graphene to the tonne scale is expected in the near future [34], the present results bode well for the industrial implementation of the anodic approach towards high quality, low-oxidized graphene, as only very cheap and abundant source materials are required.

2.2. Further characterization of the low-oxidized anodic graphene

The improved structural quality of the anodic graphenes obtained using NaCl or KCl as an electrolyte additive was confirmed by their high resolution C 1s X-ray photoelectron spectra as well as by Raman spectroscopy. Fig. 2a shows the C 1s photoelectron spectrum of graphene prepared with 0.1 M NaCl additive (red trace). For comparison purposes, the spectra for the starting graphite foil (black trace) and the control sample (graphene exfoliated only with 0.1 M Na_2SO_4, orange trace) are also given. The survey spectra of these three samples are also presented in Fig. S2 of the ESM. In all cases, the C 1s envelope was dominated by a component centered at a binding energy of about 284.6 eV, corresponding to carbon atoms in unoxidized graphitic environments (sp^2-based C=C species). Nonetheless, while the relatively oxidized control sample exhibited significant additional components in the 285-288 eV range, ascribed to carbon atoms in different oxidation states (C-O and C=O species) [7,11,20,29], such components were almost absent from the graphene sample obtained using the NaCl additive, as noticed by comparing its C 1s envelope with that of the starting graphite foil. This result further supports the conclusion that very few carbon

atoms from the graphene lattice become oxidized during anodic exfoliation in the presence of proper amounts of chloride anions. Moreover, the water contact angle for paper-like graphene films (~20-25 μm thick) obtained through vacuum filtration of the NaCl-derived graphene nanosheets dispersed in water/isopropanol was determined to be 116±4º (inset to Fig. 2a), indicating that the material was hydrophobic as expected from its very low oxidation degree. Significantly, this contact angle was much larger than that of its counterpart prepared from graphene nanosheets anodically exfoliated in the absence of NaCl (60±8º; see Fig. S2 in the ESM). Such a result was consistent with the higher hydrophilicity expected for the latter graphene material on account of its substantially larger degree of oxidation relative to graphene prepared in the presence of NaCl as a co-electrolyte. On the other hand, the contact angle measured for the starting graphite foil (60±2º; Fig. S2 in the ESM) was virtually the same as that determined for the graphene film obtained in the absence of NaCl, even though we could have expected it to be more comparable to that of the graphene film obtained in the presence of NaCl due to their similar (very low) extent of oxidation. However, we note that the contact angle of the starting graphite foil cannot be directly compared to that of the anodically exfoliated graphene films, because in addition to surface chemistry, the wettability of surfaces is also known to depend on their morphology/roughness. While the two graphene films can be expected to possess a similar surface morphology (they are made up of graphene nanosheets with similar lateral size and thickness, and assembled using the very same filtration method), the surface morphology of the starting graphite foil should be different, as it is made up of collections of much larger and thicker roll-pressed graphite particles.

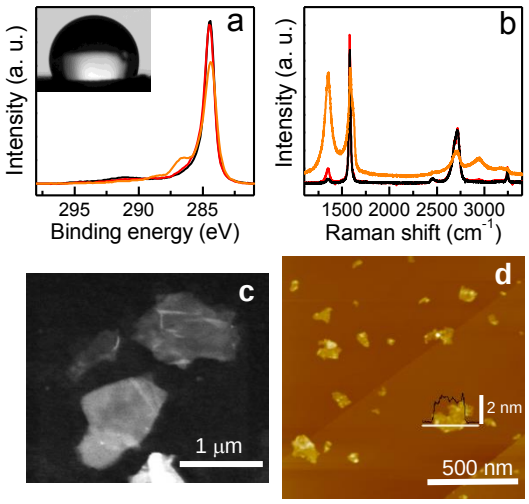

Figure 2. (a,b) High resolution C 1s core-level spectra (a) and Raman spectra (b) of the starting graphite foil (black trace), graphene anodically exfoliated in 0.1 M Na_2SO_4 electrolyte (orange trace) and graphene anodically exfoliated in 0.1 M Na_2SO_4 with 0.1 M NaCl as a co-electrolyte (red trace). Inset to a: digital photograph of a water droplet (~2 μL) deposited onto a vacuum-filtered film of graphene prepared by anodic exfoliation in the presence of NaCl co-electrolyte. (c,d) STEM (c) and AFM (d) images of graphene nanosheets produced by anodic exfoliation with NaCl co-electrolyte. A typical line profile of a nanosheet taken along the marked white line is shown overlaid on the AFM image.

The Raman spectra of graphene obtained with 0.1 M NaCl additive (red trace), starting graphite foil (black) and control sample (orange) are presented in Fig. 2b. Their first-order region (1100-1700 cm^{-1} range) incorporated the well-known G and defect-related D bands characteristic of graphite- and graphene-based materials [35,36], which were located at ~1582 and ~1350 cm^{-1}, respectively. An additional, weaker defect-related band (D´ band) appeared in some cases as a shoulder on the high wavenumber side of the G band at ~1620 cm^{-1}. The second order region (2300-3300 cm^{-1}) was dominated by the 2D band (~2700 cm^{-1}). As a quantitative proxy of structural quality and defect density [36], the integrated intensity ratio of the D and G bands (I_D/I_G ratio) was used to reveal the possible introduction of structural imperfections in the graphene samples upon anodic exfoliation. The I_D/I_G ratio for graphene prepared with 0.1 M NaCl additive was determined to be 0.21±0.06, which was significantly smaller than that of the control sample (1.3±0.2) and consistent with the higher structural quality expected for the former as a result of its lower extent of oxidation. By contrast, the I_D/I_G ratio for the starting graphite foil was a meager 0.03±0.02. Rather than arising from basal plane

defects induced by oxidation, we infer that the significant increase in I_D/I_G ratio observed for the NaCl-derived graphene relative to the starting graphite stems mostly from the presence of a larger fraction of edges in the exfoliated nanosheets, which in turn can be ascribed to their relatively small (micrometric/submicrometric) size. Such a conclusion was supported by measurement of the $I_D/I_{D'}$ ratio, the magnitude of which has been proposed to reflect the type of prevailing defect in graphene materials [37,38]. Specifically, $I_D/I_{D'}$ values around 13, 7 and 3.5 have been associated to graphenes with imperfections dominated by basal plane sp^3-defects, vacancy defects and boundaries/edges, respectively. $I_D/I_{D'}$ was calculated to be ~4.5 for the NaCl-derived graphene, thus suggesting that the increase in I_D/I_G ratio for such a sample relative to the starting graphite foil referred to above was largely due to the generation of exfoliated nanosheets with relatively small sizes (increased fraction of edges). Furthermore, when using the measured I_D/I_G ratio to estimate the average lateral size of the graphene nanosheets (<L>) by way of the formula recently proposed by Backes et al [39], which assumes the intensity of the D band to arise mostly from edges and not from basal plane defects, we obtained <L> values in the range between a few and several hundreds of nanometers. This result was in good agreement with the typical sizes of the nanosheets as imaged by scanning transmission electron microscopy (STEM; Fig. 2c) and atomic force microscopy (AFM; Fig. 2d). By contrast, the values of <L> derived from I_D/I_G for the control sample were substantially smaller (~50-100 nm), even though the actual size of the corresponding nanosheets was very similar to that of their NaCl-derived counterparts (images not shown). Hence, unlike the case of the latter, the nanosheets from the control sample were concluded to possess a significant amount of basal plane defects generated from the anodic delamination process, as could be anticipated on the basis of their substantial oxidation degree.

As illustrated by the line profiles from Fig. 2d, AFM was also used to assess the thickness of the exfoliated nanosheets deposited onto SiO_2/Si substrates. Apparent thickness values were determined to be typically between ~1.5 and 2.5 nm. Taking into account that this technique introduces a positive offset of ~1 nm in the measurement of graphene thickness, as is well known [40-42], we estimated the actual thickness of the nanosheets to be between ~0.5 and 1.5 nm. This result implies that such nanosheets were mostly single- to few-layered (< 5) objects, which in turn indicates that the efficiency of the anodic exfoliation process was not compromised by the use of NaCl as an electrolyte additive. The electrical conductivity (σ) of the paper-like, NaCl-derived

graphene films was measured to further emphasize their high structural quality, yielding σ ~34000 S m^{-1}. This figure was similar to, or even higher than, those previously reported for films of high quality, low-oxidized anodic graphene obtained with other oxidation-preventing electrolytes, such as sulfonated naphthalenes (σ ~46000 S m^{-1}) [20], or electrolyte additives (e.g., TEMPO; σ ~10000 S m^{-1} [18]), and generally higher than those determined for as-prepared (without post-treatment) films of pristine graphene derived from direct, ultrasound- or shear-induced exfoliation in organic solvents (σ ~5400-20000 S m^{-1}) [38-44].

2.3. Applications of the low-oxidized anodic graphene in water/oil remediation and capacitive energy storage

A high quality, low-oxidized graphene produced in large amounts in powder form, like the one developed here by anodic exfoliation with NaCl as an electrolyte additive, could find practical use in water and oil remediation applications, where hydrophobic sorbents are typically required [45-47], and in electrochemical energy storage, where electrodes with a high electrical conductivity are needed [48-50]. Indeed, as discussed above, this graphene material was highly hydrophobic and electrically conductive. To explore such possibilities, we have examined its performance as an adsorbent of dyes from the aqueous phase and as a sorbent for oils and non-polar organic solvents, as well as an electrode for capacitive energy storage (see ESM for details on the experimental procedures). To this end, we used the as-exfoliated product (Fig. 1b), i.e., the material directly obtained from the anodic treatment (only washed with water and dried) that was not submitted to sonication in any solvent to separate individual graphene nanosheets from one another. Such a material was a fluffy, low density powder (~30-40 mg cm^{-3}) that could be manipulated for the intended purposes more conveniently than the individual, solvent-dispersed nanosheets.

Fig. 3a shows the measured adsorption capacities of the graphene product towards five different dyes, namely, rose bengal, methylene green, basic fuchsin, methylene blue and methyl orange. The adsorption values ranged between ~130 mg g^{-1} (for rose bengal) and ~450 mg g^{-1} (for methyl orange). These figures were similar to, or even better than, those of many graphene-based adsorbents previously reported in the literature [45,51,52] (see Table S1 in the ESM for a detailed comparison of adsorption capacities). The good adsorption performance of the present graphene powder can be

ascribed to its characteristic morphology consisting of very thin rippled sheets separated by micrometer- to nanometer-sized voids (Fig. 1d), which in turn should be associated to a large exposed surface area. Indeed, the dye adsorption capacities of the as-exfoliated graphene following a sonication step, whereby many individual graphene nanosheets are physically detached from the bulk powder, were not very different to those determined before sonication, thus suggesting that the surface area available for dye adsorption was already well developed in the as-exfoliated (non-sonicated) material. Concerning the sorption of oils and non-polar organic solvents, the measured capacities were typically between 15 and 30 g g^{-1} (Fig. 3b). Even though these values were relatively modest compared to those obtained with very lightweight graphene-based sorbents [45,47] (a detailed comparison of different sorbents is given in Table S2 of the ESM), they were nonetheless consistent with what could be expected for a material with a density of 30-40 mg cm^{-3}. Moreover, very lightweight graphene-based sorbents are commonly obtained through the production and processing of graphite oxide, which in turn involves time-consuming and relatively complicated procedures [46,47]. By contrast, the anodic graphene material investigated here can be prepared in a short time by a very simple process, thus making its use particularly attractive from an applied perspective.

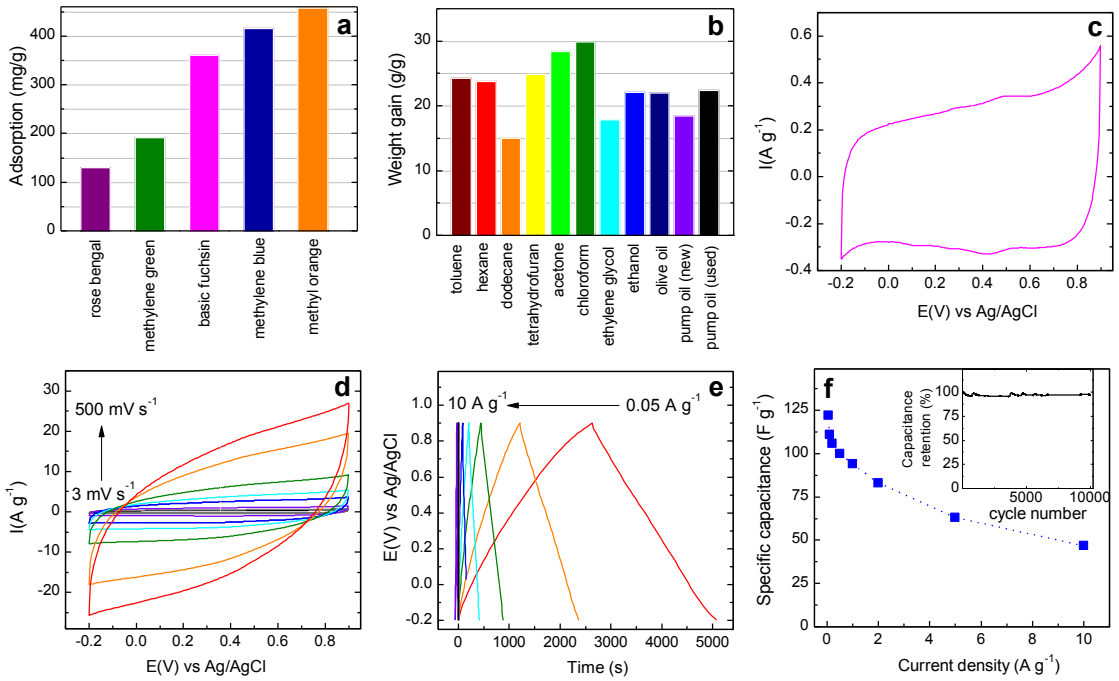

Figure 3. Applications of the as-prepared, low-oxidized anodic graphene obtained with NaCl as a co-electrolyte. (a,b) Histograms showing the adsorption capacity of the material towards different dyes in aqueous solution (a) as well as its sorption capacity towards different oils and non-polar organic solvents (b). (c) Cyclic voltammogram recorded at a potential scan rate of 3 mV s^{-1}. (d) Cyclic voltammograms recorded at potential scan rates between 3 and 500 mV s^{-1}. (e) Galvanostatic charge/discharge curves recorded at different current densities between 0.05 and 10 A g^{-1}. (f) Gravimetric capacitance values determined at different current densities from the discharge curves in e. Inset to f: evolution of capacitance values (in percentage) of the electrode measured at a current density of 2 A g^{-1} for consecutive charge/discharge cycles (up to 10000).

The results of testing the low-oxidized anodic graphene as an electrode for capacitive energy storage are presented in Fig. 3c-f. The measurements were carried out in a three-electrode configuration, using a commercial activated carbon as a counter electrode and Ag/AgCl (3 M KCl) as a reference electrode (see ESM for details). Fig. 3c shows the cyclic voltammogram of the graphene electrode recorded at a potential scan rate of 3 mV s^{-1}. Even at such a low scan rate, the voltammogram exhibited a nearly rectangular shape with no significant redox peaks (except for some slight oxidation/reduction humps at ~0.4-0.5 V vs Ag/AgCl), indicating that charge storage in the electrode was mostly dominated by the formation of an electric double layer with little contribution from Faradaic processes (i.e., pseudocapacitance). This observation was in agreement with the very limited amount of oxygen functional groups (and indeed of any other heteroatoms) detected by XPS for this graphene sample, the presence of

which is generally ascribed to the emergence of pseudocapacitance in carbon materials [48,49]. Furthermore, the rectangular shape of the voltammograms was largely retained upon increasing the voltage scan rate (Fig. 3d), although some degree of distortion became apparent at the highest rates (i.e., 300 and 500 mV s^{-1}). The latter would indicate that access of the electrolyte ions to certain areas of the electrode is somewhat sluggish, which in turn could be due to the particular morphology of the graphene product that is obtained from the anodic process. More specifically, the FE-SEM images of the anodically expanded material (e.g., Fig. 1d) suggest that there could be very narrow voids between parallel sheets at some specific points, creating two-dimensional slit pores where ion adsorption/desorption can take place. Because the anodic treatment does not lead on its own to a complete separation of the graphene layers, we can expect many of these two-dimensional voids to be closed at one of their ends, thus creating cul-de-sac porosities that hamper ionic transport to/from these pores.

Typical galvanostatic charge/discharge curves recorded at different current densities between 0.05 and 10 A g^{-1} are presented in Fig. 3e. The curves displayed mostly triangular and symmetrical shapes, this being again consistent with capacitive processes as the main driving force behind charge storage in the graphene electrode. As shown in Fig. 3f, the gravimetric capacitance values derived from the discharge curves were highest (around 120 F g^{-1}) at the lowest current densities and decreased down to ~50 F g^{-1} at a current density of 10 A g^{-1}. These figures lay within the range of values measured for many graphene-based materials that have previously tested as electrodes for capacitive energy storage [48,50] (see Table S3 in the ESM for a comparative list). However, different to the case of these prior graphene materials, many of which were obtained through complex preparation and processing steps (e.g., via the graphite oxide route, or by chemical vapor deposition for very high quality graphenes), a practical advantage of the present approach was its simplicity of operation and the use of inexpensive, environmentally friendly and widely available reagents. Moreover, the stability of the graphene electrode was demonstrated by noting that about 98% of its initial capacitance could be retained after 10000 consecutive charge/discharge cycles at 2 A g^{-1} (inset to Fig. 3f).

3. Conclusions

We have demonstrated the production of high quality and low-oxidized graphene nanosheets by anodic exfoliation of graphite in water using NaCl (table salt) as an

electrolyte additive (co-electrolyte) with a remarkable efficiency in preventing the oxidation of the nanosheets that is commonly associated to such a process. Different to previous instances, where relatively complex and expensive electrolyte additives were employed to avert the oxidation of anodically exfoliated graphene, the present work has introduced a particularly cheap, straightforward and readily available substance as an alternative oxidation-preventing co-electrolyte. The high efficiency of this additive in curtailing oxidative attack of the exfoliated nanosheets was particularly significant, yielding anodic graphene with the lowest extent of oxidation reported to date (O/C ratio ~0.02-0.03). The as-prepared, low-oxidized graphene material also demonstrated its potential practical utility as a sorbent of dyes and non-polar organic solvents for water/oil remediation processes, as well as an electrode for capacitive energy storage, its simplicity of preparation and processing being an additional asset compared to other graphene-based materials. Finally, because only inexpensive raw materials that are available in large quantities were required for its production, we believe the anodic route is now better positioned as a competitive approach in the efforts to industrialize the manufacturing of high quality graphene for different applications.

Acknowledgements

Funding by the Spanish Ministerio de Economía y Competitividad (MINECO) and the European Regional Development Fund (ERDF) through project MAT2015-69844-R is gratefully acknowledged. We also acknowledge partial funding by Plan de Ciencia, Tecnología e Innovacción 2013-2017 del Principado de Asturias and the ERDF through project GRUPIN14-056. J.M.M. is grateful to the Spanish Ministerio de Educación, Cultura y Deporte (MECD) for his pre-doctoral contract (FPU14/00792).

References

[1] A.C. Ferrari, F. Bonaccorso, V. Fal'ko, K. S. Novoselov, S. Roche, P. Boggild, S. Borini, F. H. L. Koppens, V. Palermo, N. Pugno, J. A. Garrido, R. Sordan, A. Bianco, L. Ballerini, M. Prato, E. Lidorikis, J. Kivioja, C. Marinelli, T. Ryhanen, A. Morpurgo, J. N. Coleman, V. Nicolosi, L. Colombo, A. Fert, M. Garcia-Hernandez, A. Bachtold, G. F. Schneider, F. Guinea, C. Dekker, M. Barbone, Z. Sun, C. Galiotis, A. N. Grigorenko, G. Konstantatos, A. Kis, M. Katsnelson, L. Vandersypen, A. Loiseau, V. Morandi, D. Neumaier, E. Treossi, V. Pellegrini, M. Polini, A. Tredicucci, G. M. Williams, B. Hee Hong, J.-H. Ahn, J. Min Kim, H. Zirath, B. J. van Wees, H. van der Zant, L. Occhipinti, A. Di Matteo, I. A. Kinloch, T. Seyller, E. Quesnel, X. Feng, K. Teo, N. Rupesinghe, P. Hakonen, S. R. T. Neil, Q. Tannock, T. Lofwander, J. Kinaret, Science and technology roadmap for graphene, related two-dimensional crystals, and hybrid systems, Nanoscale 7 (2015), 4598-4810.

[2] H.J. Salavagione, Promising alternative routes for graphene production and functionalization, J. Mater. Chem. A 2 (2014), 7138-7146.

[3] A.M. Abdelkader, A.J. Cooper, R.A.W. Dryfe, I.A. Kinloch, How to get between the sheets: a review of recent works on the electrochemical exfoliation of graphene materials from bulk graphite, Nanoscale 7 (2015), 6944-6956.

[4] S. Yang, M.R. Lohe, K. Müllen, X. Feng, New-generation graphene from electrochemical approaches: production and applications, Adv. Mater. 28 (2016), 6213-6221.

[5] Y.L. Zhong, Z. Tian, G.P. Simon, D. Li, Scalable production of graphene via wet chemistry: progress and challenges, Mater. Today 18 (2015), 73-78.

[6] A.T. Najafabadi, E. Gyenge, Synergistic production of graphene microsheets by simultaneous anodic and cathodic electro-exfoliation of graphitic electrodes in aprotic ionic liquids, Carbon 84 (2015), 449-459.

[7] S. Yang, A.G. Ricciardulli, S. Liu, R. Dong, M.R. Lohe, A. Becker, M.A. Squillaci, P. Samorì, K. Müllen, X. Feng, Ultrafast delamination of graphite into high-quality graphene using alternating currents, Angew. Chem. Int. Ed. 56 (2017), 6669-6675.

[8] A.J. Cooper, N.R. Wilson, I.A. Kinloch, R.A.W. Dryfe, Single stage electrochemical exfoliation method for the production of few-layer graphene via intercalation of tetraalkylammonium cations, Carbon 66 (2014), 340-350.

[9] M. Zhao, X.-Y. Guo, O. Ambacher, C.E. Nebel, R. Hoffmann, Electrochemical generation of hydrogenated graphene flakes, Carbon 83 (2015), 128-135.

[10] Y.R. Leroux, J.-F. Bergamini, S. Ababou, J.-C. Le Breton, P. Hapiot, Synthesis of functionalized few-layer graphene through fast electrochemical expansion of graphite, J. Electroanal. Chem. 753 (2015), 42-46.

[11] J. Liu, M. Notarianni, G. Will, V.T. Tiong, H. Wang, N. Motta, Electrochemically exfoliated graphene for electrode films: effect of graphene flake thickness on the sheet resistance and capacitive properties, Langmuir 29 (2013), 13307-13314.

[12] L. Wu, W. Li, P. Li, S. Liao, S. Qiu, M. Chen, Y. Guo, Q. Li, C. Zhu, L. Liu, Powder, paper and foam of few-layer graphene prepared in high yield by electrochemical intercalation exfoliation of expanded graphite, Small 10 (2014), 1421-1429.

[13] A. Ambrosi, M. Pumera, Electrochemically exfoliated graphene and graphene oxide for energy storage and electrochemistry applications, Chem. Eur. J. 22 (2016), 153-159.

[14] Z. Liu, Z.-S. Wu, S. Yang, R. Dong, X. Feng, K. Müllen, Ultraflexible in-plane micro-supercapacitors by direct printing of solution-processable electrochemically exfoliated graphene, Adv. Mater. 28 (2016), 2217-2222.

[15] P. Khanra, T. Kuila, S. H. Bae, N. H. Kim, J. H. Lee, Electrochemically exfoliated graphene using 9-anthracene carboxylic acid for supercapacitor application, J. Mater. Chem. 22 (2012) 24403–24410.

[16] P. Khanra, C.-N. Lee, T. Kuila, N. H. Kim, M. J. Park, J. H. Lee, 7,7,8,8-Tetracyanoquinodimethane-assisted one step electrochemical exfoliation of graphite and its performance as an electrode material, Nanoscale 6 (2014) 4864–4873.

[17] J.I. Paredes, J.M. Munuera, Recent advances and energy-related applications of high quality/chemically doped graphenes obtained by electrochemical exfoliation methods, J. Mater. Chem. A 5 (2017), 7228-7242.

[18] S. Yang, S. Brüller, Z.-S. Wu, Z. Liu, K. Parvez, R. Dong, F. Richard, P. Samorì, X. Feng, K. Müllen, Organic radical-assisted electrochemical exfoliation for the scalable production of high-quality graphene, J. Am. Chem. Soc. 137 (2015), 13927-13932.

[19] C.-H. Chen, S.-W. Yang, M.-C. Chuang, W.-Y. Woon, C.-Y. Su, Towards the continuous production of high crystallinity graphene via electrochemical exfoliation with molecular in situ encapsulation, Nanoscale 7 (2015), 15362-15373.

[20] J.M. Munuera, J.I. Paredes, S. Villar-Rodil, M. Ayán-Varela, A. Martínez-Alonso, J.M.D. Tascón, Electrolytic exfoliation of graphite in water with multifunctional electrolytes: en route towards high quality, oxide-free graphene flakes, Nanoscale 8 (2016), 2982-2998.

[21] K. Parvez, Z.-S. Wu, R. Li, X. Liu, R. Graf, X. Feng, K. Müllen, Exfoliation of graphite into graphene in aqueous solutions of inorganic salts, J. Am. Chem. Soc. 136 (2014), 6083-6091.

[22] S.C. Foote, J.S. Valentine, A. Greenberg, J.F. Liebman, Active Oxygen in Chemistry, Chapman & Hall, Glasgow, 1995.

[23] P. Vanÿsek, CRC handbook of Chemistry and Physics, 93rd edition, CRC Press, Boca Raton, 2012.

[24] G.G. Jayson, B.J. Parsons, A.J. Swallow, Some simple, highly reactive, inorganic chlorine derivatives in aqueous solution. Their formation using pulses of radiation and their role in the mechanism of the Fricke dosimeter, J. Chem. Soc., Faraday Trans. 1 69 (1973), 1597-1607.

[25] L.B. Ebert, Annu. Intercalation compounds of graphite, Rev. Mater. Sci. 6 (1976), 181-211.

[26] H. Shioyama, R. Fujii, Electrochemical reactions of stage 1 sulfuric acid—Graphite intercalation compound, Carbon 25 (1987), 771-774.

[27] C.-Y. Su, A.-Y. Lu, Y. Xu, F.-R. Chen, A.N. Khlobystov, L.-J. Li, High-quality thin graphene films from fast electrochemical exfoliation, ACS Nano 5 (2011), 2332-2339.

[28] J.M. Munuera, J.I. Paredes, S. Villar-Rodil, A. Martínez-Alonso, J.M.D. Tascón, A simple strategy to improve the yield of graphene nanosheets in the anodic exfoliation of graphite foil, Carbon 115 (2017), 628-632.

[29] J.M. Munuera, J.I. Paredes, S. Villar-Rodil, M. Ayán-Varela, A. Pagán, S.D. Aznar-Cervantes, J.L. Cenis, A. Martínez-Alonso, J.M.D. Tascón, High quality, low oxygen content and biocompatible graphene nanosheets obtained by anodic exfoliation of different graphite types, Carbon 94 (2015), 729-739.

[30] D. Li, M.B. Müller, S. Gilje, R.B. Kaner, G.G. Wallace, Processable aqueous dispersions of graphene nanosheets, Nat. Nanotechnol. 3 (2008), 101-105.

[31] L. Guardia, M.J. Fernández-Merino, J.I. Paredes, P. Solís-Fernández, S. Villar-Rodil, A. Martínez-Alonso, J.M.D. Tascón, High-throughput production of pristine graphene in an aqueous dispersion assisted by non-ionic surfactants, Carbon 49 (2011), 1653-1662.

[32] J.I. Paredes, A. Martínez-Alonso, J.M.D. Tascón, Multiscale imaging and tip-scratch studies reveal insight into the plasma oxidation of graphite, Langmuir 23 (2007), 8932-8943.

[33] J.M. Munuera, J.I. Paredes, M. Enterría, A. Pagán, S. Villar-Rodil, M.F.R. Pereira, J.I. Martins, J.L. Figueiredo, J.L. Cenis, A. Martínez-Alonso, J.M.D. Tascón, Electrochemical exfoliation of graphite in aqueous sodium halide electrolytes toward low oxygen content graphene for energy and environmental applications, ACS Appl. Mater. Interfaces 9 (2017), 24085-24099.

[34] X.-Y. Wang, A. Narita, K. Müllen, Precision synthesis versus bulk-scale fabrication of graphenes, Nat. Rev. Chem. 2 (2017), 00100.

[35] M.A. Pimenta, G. Dresselhaus, M.S. Dresselhaus, L.G. Cançado, A. Jorio, R. Saito, Studying disorder in graphite-based systems by Raman spectroscopy, Phys. Chem. Chem. Phys. 9 (2007), 1276-1291.

[36] A.C. Ferrari, D.M. Basko, Raman spectroscopy as a versatile tool for studying the properties of graphene, Nat. Nanotechnol. 8 (2013), 235-246.

[37] A. Eckmann, A. Felten, A. Mishchenko, L. Britnell, R. Krupke, K.S. Novoselov, C. Casiraghi, Probing the nature of defects in graphene by Raman spectroscopy, Nano Lett. 12 (2012), 3925-3930.

[38] K. R. Paton, E. Varrla, C. Backes, R. J. Smith, U. Khan, A. O'Neill, C. Boland, M. Lotya, O. M. Istrate, P. King, T. Higgins, S. Barwich, P. May, P. Puczkarski, I. Ahmed, M. Moebius, H. Pettersson, E. Long, J. Coelho, S. E. O'Brien, E. K. McGuire, B. Mendoza Sanchez, G. S. Duesberg, N. McEvoy, T. J. Pennycook, C. Downing, A. Crossley, V. Nicolosi, J. N. Coleman, Scalable production of large quantities of defect-free few-layer graphene by shear exfoliation in liquids, Nat. Mater. 13 (2014), 624–630.

[39] C. Backes, K.R. Paton, D. Hanlon, S. Yuan, M.I. Katsnelson, J. Houston, R.J. Smith, D. McCloskey, J.F. Donegan, J.N. Coleman, Spectroscopic metrics allow in situ

measurement of mean size and thickness of liquid-exfoliated few-layer graphene nanosheets, Nanoscale 8 (2016), 4311-4323.

[40] K.S. Novoselov, A.K. Geim, S.V. Morozov, D. Jiang, Y. Zhang, S.V. Dubonos, I.V. Grigorieva, A.A. Firsov, Electric field effect in atomically thin carbon films, Science 306 (2004), 666-669.

[41] P. Nemes-Incze, Z. Osváth, K. Kamarás, L.P. Biró, Anomalies in thickness measurements of graphene and few layer graphite crystals by tapping mode atomic force microscopy, Carbon 46 (2008), 1435-1442.

[42] P. Solís-Fernández, J.I. Paredes, S. Villar-Rodil, A. Martínez-Alonso, J.M.D. Tascón, Determining the thickness of chemically modified graphenes by scanning probe microscopy, Carbon 48 (2010), 2657-2660.

[43] U. Khan, A. O´Neill, M. Lotya, S. De, J.N. Coleman, High-concentration solvent exfoliation of graphene, Small 6 (2010), 864-871.

[44] K.H. Park, B.H. Kim, S.H. Song, J. Kwon, B.S. Kong, K. Kang, S. Jeon, Exfoliation of non-oxidized graphene flakes for scalable conductive film, Nano Lett. 12 (2012), 2871-2876.

[45] Z. Niu, L. Liu, L. Zhang, X. Chen, Porous graphene materials for water remediation, Small 10 (2014), 3434-3441.

[46] B. Chen, Q. Ma, C. Tan, T.-T. Lim, L. Huang, H. Zhang, Carbon-based sorbents with three-dimensional architectures for water remediation, Small 11 (2015), 3319-3336.

[47] W. Wan, Y. Lin, A. Prakash, Y. Zhou, Three-dimensional carbon-based architectures for oil remediation: from synthesis and modification to functionalization, J. Mater. Chem. A 4 (2016), 18687-18705.

[48] J. Chen, C. Li, G. Shi, Graphene materials for electrochemical capacitors, J. Phys. Chem. Lett. 4 (2013), 1244-1253.

[49] R. Raccichini, A. Varzi, S. Passerini, B. Scrosati, The role of graphene for electrochemical energy storage, Nat. Mater. 14 (2015), 271-279.

[50] H. Wu, Y. Zhang, L. Cheng, L. Zheng, Y. Li, W. Yuan, X. Yuan, Graphene based architectures for electrochemical capacitors, Energy Stor. Mater. 5 (2016), 8-32.

[51] F. Li, X. Jiang, J. Zhao, S. Zhang, Graphene oxide: A promising nanomaterial for energy and environmental applications, Nano Energy 16 (2015), 488-515.

[52] H. Wang, X. Yuan, G. Zeng, Y. Wu, Y. Liu, Q. Jiang, S. Gu, Three dimensional graphene based materials: Synthesis and applications from energy storage and conversion to electrochemical sensor and environmental remediation, Adv. Colloid Interface Sci. 221 (2015), 41-59.

Electronic Supplementary Material for

High quality, low-oxidized graphene via anodic exfoliation with table salt as an efficient oxidation-preventing co-electrolyte for water/oil remediation and capacitive energy storage applications

J.M. Munuera, J.I. Paredes, S. Villar-Rodil, A. Castro-Muñiz, A. Martínez-Alonso, J.M.D. Tascón

Instituto Nacional del Carbón, INCAR-CSIC, Apartado 73, 33080 Oviedo, Spain

Contents

S1. Electrochemical exfoliation experiments

Unless otherwise stated, all the materials and chemicals used throughout this study were obtained from Sigma-Aldrich. Milli-Q deionized water (Millipore Corporation; resistivity: 18.2 MΩ·cm) was employed in all the experiments. The electrochemical (anodic) exfoliation experiments were carried out in a two-electrode setup consisting of a high purity graphite foil piece (Papyex I980, acquired from Mersen; dimensions: ~40 × 25 × 0.5 mm^3) as the working electrode and a platinum foil (thickness: 0.025 mm) as the counter electrode. Both electrodes were immersed in an aqueous electrolyte solution (80 mL) incorporating 0.1 M Na_2SO_4 as the main electrolyte and a given molar concentration of another chemical species as the electrolyte additive. Although best results in terms of preventing oxidation of the exfoliated graphene nanosheets were obtained with NaCl, other electrolyte additives tested included KCl, KBr, KI, $NaBH_4$, Na_2SO_3, sodium citrate, vitamin C and ethanol. To trigger its delamination, a positive voltage (10 V) was applied to the graphite foil electrode for 60 min by means of an Agilent 6614C DC power supply, while keeping the platinum counter electrode parallel to the graphite foil surface at a distance of about 2 cm. During the electrolytic process the outer layers of the graphite electrode were seen to swell and expand, giving rise to many millimeter-sized fragments that detached from the electrode and tended to float on the aqueous solution. Subsequently, these fragments as well as the swollen graphitic material that had not yet detached from the electrode (retrieved by gently scraping with a spatula) were collected, rinsed off with copious amounts of water through filter paper and dried overnight at room temperature under reduced pressure. The resulting product was transferred either to a water/isopropanol mixture (65/35 v/v%), to an aqueous solution of the dispersant flavin mononucleotide (FMN, 1 mg mL^{-1}) or to the organic solvent *N*,*N*-dimethylformamide (DMF), sonicated in an ultrasound bath cleaner (J.P. Selecta Ultrasons system, 40 kHz) for 3 h and finally centrifuged at 200 *g* for 20 min (Eppendorf 5424 microcentrifuge) to obtain a colloidal suspension (supernatant) of graphene nanosheets in these solvents.

S2. Characterization techniques

The obtained materials were characterized by field emission scanning electron microscopy (FE-SEM), scanning transmission electron microscopy (STEM), atomic force microscopy (AFM), UV-vis absorption spectroscopy, Raman spectroscopy, X-ray

photoelectron spectroscopy (XPS) and measurement of electrical conductivity and water contact angle. FE-SEM and STEM images were recorded in a Quanta FEG 650 microscope (FEI Company) at 25 kV. Specimens for STEM were prepared by drop-casting ~40 μL of graphene dispersed in water/isopropanol onto copper grids (200 mesh) covered with a thin continuous film of amorphous carbon. AFM imaging of the graphene nanosheets was performed in the tapping mode of operation with a Nanoscope IIIa Multimode apparatus (Veeco Instruments), using rectangular silicon cantilevers (spring constant: ~40 N m^{-1}; resonance frequency: 250-300 kHz). To this end, the nanosheets were deposited onto pre-heated (~50-60 ºC) highly oriented pyrolytic graphite (HOPG) substrates by drop-casting their colloidal dispersion in water/isopropanol. UV-vis absorption spectroscopy was accomplished in a double-beam Heλios α spectrophotometer (Thermo Spectronic). Raman spectra were acquired in a Horiba Jobin-Yvon LabRam instrument at a laser excitation wavelength and incident power of 532 nm and 2 mW, respectively. XPS was carried out on a SPECS apparatus under a pressure of 10^{-7} Pa using a non-monochromatic Al K_α X-ray source (11.81 kV, 100 W). Specimens for both Raman spectroscopy and XPS were prepared by drop-casting graphene dispersions in water/isopropanol onto pre-heated (~50-60 ºC) stainless steel disks 12 mm in diameter until a thin, continuous graphene film with a lustrous gray tone became visible to the naked eye. The electrical conductivity of paper-like graphene films was measured on the basis of the van der Pauw method using a home-made setup consisting of an Agilent 6614C DC power supply and a Fluke 45 digital multimeter. The graphene films were prepared by vacuum filtration of graphene dispersions in water/isopropanol through polycarbonate membrane filters (Whatman; diameter: 25 mm; pore size: 0.2 μm) and were cut into 12 × 12 mm^2 square pieces for the measurements, with their thickness being estimated by both FE-SEM and a high precision electronic caliper (Digimatic Micrometer, model MDC-25PX, from Mitutoyo). Measurement of water contact angles was carried out on the paper-like graphene films by carefully dropping 2 μL of water on the films with a pipette and immediately taking images of the droplet using a standard digital camera attached with a macro lens. Contact angles were determined from the recorded images through analysis with ImageJ software.

S3. Applications of the high quality, anodically exfoliated graphene

To explore their possible applications, the high quality graphene materials developed in this work were tested as adsorbents for water-soluble dyes and as sorbents for non-polar organic solvents and dyes, as well as electrodes for capacitive energy storage. In this case, the as-exfoliated graphene materials, i.e., the products directly obtained from the anodic delamination process without a subsequent sonication step (only washed with water to remove remnants of the electrolyte) were used, as they exhibited a powdery, three-dimensional morphology that was convenient for their manipulation. The dye adsorption tests were carried out by adding ~1.5 mg of graphene material to 1.5 mL of an aqueous solution of a given dye at room temperature and pH ~6, followed by gently stirring with a magnetic bar for 24 h to ensure the attainment of adsorption equilibrium and centrifuging the solution (20000 *g*, 20 min) to sediment the graphene component. The concentration of the dye in the resulting supernatant was then determined by means of UV-vis absorption spectroscopy and contrasted with that of the starting dye solution, which in turn allowed the amount of dye adsorbed on the graphene sample to be estimated. The adsorption experiments were performed with the following dyes (wavelengths given in parenthesis correspond to the position of the absorption peak used to measure the dye concentration): methyl orange (460 nm), methylene blue (660 nm), basic fuchsin (540 nm), methylene green (660 nm) and rose bengal (560 nm). To determine the maximum adsorption capacities of the graphene materials, different starting concentrations of the dye (typically up to 2-3 mg mL^{-1}) were probed in the tests. For the sorption of oils and non-polar solvents, a certain mass of graphene material (typically ~5 mg) was first put into a 1.5 mL centrifuge tube. Then, small known volumes of a given oil/solvent (usually around 100 μL) were successively added to the tube. Such volumes were readily taken up by the graphene sample until a point was reached where the latter became saturated, which in turn allowed to estimate the total volume of oil/solvent retained by the sorbent. Sorption tests were conducted with the following substances: toluene, hexane, dodecane, tetrahydrofuran, acetone, chloroform, ethylene glycol, ethanol, olive oil, as well as unused and used pump oil.

Testing of the high quality anodic graphene as an electrode for capacitive energy storage was accomplished in a three-electrode configuration with a Swagelok-type cell, using a paste based on a commercial activated carbon (ACF A20) as the counter electrode and Ag/AgCl (3M KCl) as the reference electrode in an acidic aqueous electrolyte (1 M H_2SO_4). The counter electrode paste consisted of a mixture of the

activated carbon, polytetrafluoroethylene (PTFE) as a binder and carbon black as a conductive additive in a weight ratio of 90:5:5. The graphene working electrode was prepared by pressing the as-prepared anodic graphene under a moderate force (1 ton for 15 s) onto a graphite foil support by means of a hydraulic press. Two pieces of glass microfiber filter (grade 934-AH, from Whatman) were used as the separator. Prior to assembling the cell, the working electrode, counter electrode and separator were soaked in the electrolyte and vacuum-degassed. The assembled cell with the electrolyte was also vacuum-degassed before the measurements, which were conducted in a Biologic VSP potentiostat. Both cyclic voltammograms at different potential scan rates and galvanostatic charge/discharge curves at different current densities were recorded.

S4. Additional figures

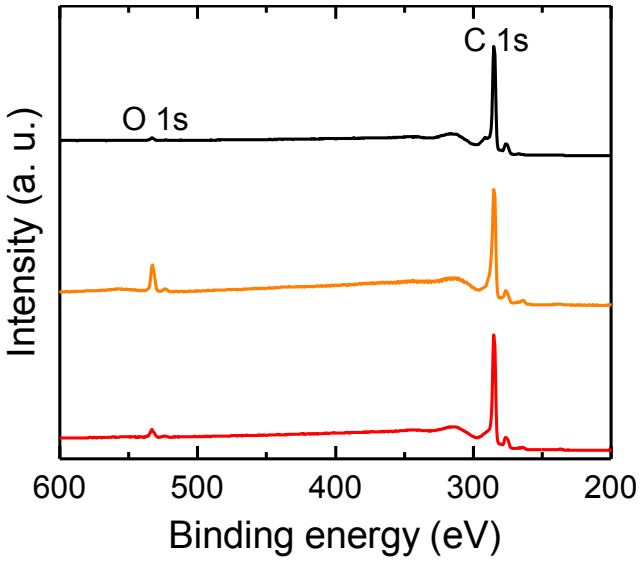

Figure S1. XPS survey spectra of the starting graphite foil (black trace), graphene anodically exfoliated in 0.1 M Na_2SO_4 electrolyte (orange trace) and graphene anodically exfoliated in 0.1 M Na_2SO_4 with 0.1 M NaCl as a co-electrolyte (red trace).

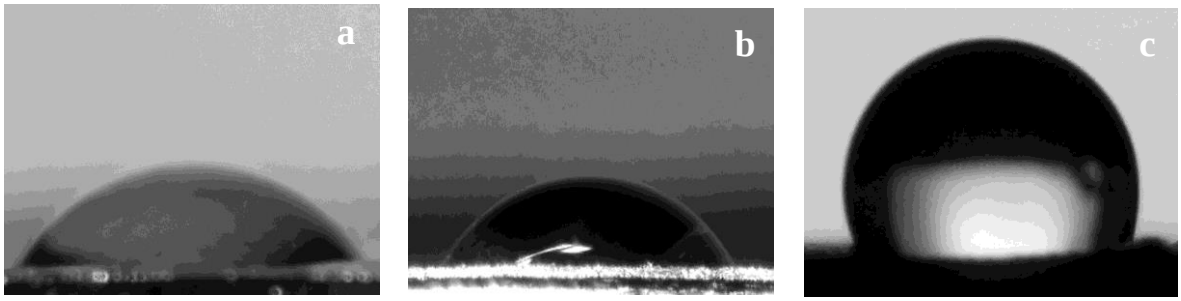

Figure S2. Digital photographs of water droplets (1–2 μL) deposited onto the starting graphite foil (a), and vacuum-filtered films of graphene prepared by anodic exfoliation in the absence (b) and presence (c) of 0.1 M NaCl as a co-electrolyte.

S5. Additional tables

Table S1. Adsorption capacities of different dyes (methyl orange, methylene blue, methylene green, basic fuchsin and rose bengal) with a range of graphene-based materials.

Material	Adsorbate	Adsorption capacity (mg g^{-1})	Ref.
Graphene oxide	Methyl Orange	17	S1
CoFe2O4 functionalized graphene	Methyl orange	72	S2
Graphene oxide/Ni-Al LDH	Methyl orange	84	S3
Graphene oxide/Ni-Cr LDH	Methyl orange	160	S4
Graphene oxide/chitosan	Methyl orange	567	S5
As-prepared anodic graphene	Methyl orange	457	This work
Reduced graphene oxide	Methylene blue	154	S6
Graphene oxide	Methylene blue	244	S7
Citric acid functionalized magnetic graphene oxide	Methylene blue	316	S8
Agar/graphene oxide composite aerogel	Methylene blue	578	S9
Porous graphene oxide/hydrogel nanocomposite	Methylene blue	714	S10
As-prepared anodic graphene	Methylene blue	415	This work
As-prepared anodic graphene	Methylene green	343	This work
Reduced graphene oxide	Basic fuchsin	34	S11
β-cyclodextrin–carboxymethyl cellulose–graphene oxide composite	Basic fuchsin	59	S12
Reduced graphene oxide/ PSSMA	Basic fuchsin	388	S13
Graphene/β-cyclodextrin composite	Basic fuchsin	426	S14
Graphene oxide/polyacrylamide	Basic fuchsin	1034	S15
As-prepared anodic graphene	Basic fuchsin	361	This work
Graphene oxide/sodium alginate/polyacrylamide hydrogel	Rose Bengal	6	S16
Graphene Oxide@PLA@HA Composite Microcapsule	Rose Bengal	53	S17
Graphene sheets/graphene quantum dots	Rose Bengal	587	S18
As-prepared anodic graphene	Rose Bengal	130	This work

Table S2. Range of sorption capacities of different graphene-based materials towards oils and non-polar organic solvents.

Material	**Retention capacity (g/g)**	**Ref.**
Magnetic graphene foam	7-27	S19
Hydrothermal graphene sponge	20-35	S20
Graphene–carbon nanotube aerogel	20-35	S21
GO foam	5-40	S22
N-doped graphene aerogel	40-110	S23
Graphene sponge	80-160	S24
As-prepared anodic graphene	15-30	This work

Table S3. Gravimetric capacitance values of a range of graphene-based materials determined at different current densities.

Material	**Current density (A/g)**	**Capacity (F/g)**	**Ref**
rGO	0.3	57	S25
rGO/carbon black	1	79	S26
rGO	0.5	82	S27
rGO	1	116	S28
rGO foam	5	125	S29
rGO	1	130	S30
graphene hydrogel	1	186	S31
graphene/PANI nanofibers	0.3	210	S25
Highly crumpled N-doped graphene nanosheets	1	246	S32
Anodic graphene	0.3	105	This work
Anodic graphene	0.5	100	This work
Anodic graphene	1	94	This work
Anodic graphene	5	63	This work

S6. References

[S1] D. Robatia, B. Mirzab, M. Rajabic, O. Moradid, I. Tyagie, S. Agarwaleg, V. K. Gupta, Removal of hazardous dyes-BR 12 and methyl orange using graphene oxide as an adsorbent from aqueous phase, Chem. Eng. J. 284 (2016) 687-697.

[S2] N. Li, M. Zheng, X. Chang, G. Ji, H. Lu, L. Xue, L. Pan, J. Cao, Preparation of magnetic CoFe2O4-functionalized graphene sheets via a facile hydrothermal method and their adsorption properties, J. Solid State Chem.184 (2011) 953-958.

[S3] Z. Yang, S. Ji, W. Gao, C. Zhang, L. Ren, W. W. Tjiu, Z. Zhang, J. Pan, T. Liu, Magnetic Nanomaterial Derived from Graphene Oxide/Layered Double Hydroxide Hybrid for Efficient Removal of Methyl Orange from Aqueous Solution, J. Colloid Interface Sci. 408 (2013) 25-32.

[S4] X. Ruan, Y. Chen, H. Chen, G. Qian, R. L. Frost, Sorption Behavior of Methyl Orange from Aqueous Solution on Organic Matter and Reduced Graphene Oxides Modified Ni–Cr Layered Double Hydroxides, Chem. Eng. J. 297 (2016) 295-303.

[S5] Y. Wang, X. Liu, H. Wang, G. Xia, W. Huang, R. Song, Microporous Spongy Chitosan Monoliths Doped with Graphene Oxide as Highly Effective Adsorbent for Methyl Orange and Copper Nitrate (Cu(NO3)2) Ions, J. Colloid Interface Sci. 416 (2014) 243-251.

[S6] T. Liu,Y. Lia, Q. Du. J. Sun, Y. Jiao, G. Yang, Z. Wang, Y. Xia, W. Zhang. K. Wang, H. Zhu, D. Wu, Adsorption of methylene blue from aqueous solution by graphene, Colloids Surf. B 90 (2012) 197-203.

[S7] Y. Li, Q. Du, T. Liu, X. Peng, J. Wang, J. Sun, Y. Wang, S. Wu, Z. Wang, Y. Xia, L. Xia Comparative study of methylene blue dye adsorption onto activated carbon, graphene oxide, and carbon nanotubes, Chem. Eng. Res. Des. 91 (2013) 361-368.

[S8] H. Ge, C. Wang, S. Liu, Z. Huang, Synthesis of citric acid functionalized magnetic graphene oxide coated corn straw for methylene blue adsorption, Bioresour. Technol. 221 (2016) 419-429.

[S9] L.Chen, Y. Li, Q. Du, Z. Wang, Y. Xia, E. Yedinak, J. Lou, L. Ci, High performance agar/graphene oxide composite aerogel for methylene blue removal, Carbohydr. Polym. 155 (2017) 345-353.

[S10] A. Pourjavadi, M. Nazari, B. Kabiri, S. H. Hosseini, C Bennett, Preparation of porous graphene oxide/hydrogel nanocomposites and their ability for efficient adsorption of methylene blue, RSC Adv. 6 (2016) 10430-10437.

[S11] Ş.Tokalioɨlu, E. Yavuz, A. Aslantaş, H. Şahan, F. Taşkin, Ş. Patat, Spectrophotometric Determination of Basic Fuchsin from Various Water Samples after Vortex Assisted Solid Phase Extraction Using Reduced Graphene Oxide as an Adsorbent, Spectrochim. Acta A 149 (2015) 378-384.

[S12] J. Yuan, F. Qiu, P. Li, Synthesis and characterization of β-cyclodextrin–carboxymethyl cellulose–graphene oxide composite materials and its application for removal of basic fuchsin, J. Iran. Chem. Soc. 14 (2017) 1827-1837

[S13] Y.-B. Song, X.-D. Song, C.-J. Cheng, Z.-G. Zhao, Poly(4-Styrenesulfonic Acid-co-Maleic Acid)-Sodium-Modified Magnetic Reduced Graphene Oxide for Enhanced Adsorption Performance Toward Cationic Dyes, RSC Adv. 5 (2015) 87030-87042.

[S14] P. Tan, Y. Hu, Improved synthesis of graphene/β-cyclodextrin composite for highly efficient dye adsorption and removal, J. Mol. Liq. 242 (2017) 181-189.

[S15] X. Yang, Y. Li, Q. Du, J. Sun, L. Chen, S. Hu, Z. Wang, Y. Xia, L. Xia, Highly Effective Removal of Basic Fuchsin from Aqueous Solutions by Anionic Polyacrylamide/Graphene Oxide Aerogels. J. Colloid Interface Sci. 453 (2015) 107-114.

[S16] J. Fan, Z. Shi, M. Lian, H. Li, J. Yin Mechanically strong graphene oxide/sodium alginate/polyacrylamide nanocomposite hydrogel with improved dye adsorption capacity J. Mater. Chem. A, 1 (2013) 7433-7443

[S17] H. Guo, Y. Wang, Y. Huang, F. Huang, S. Li, Y. Shen, M. Zhu, A. Xie, A GO@PLA@HA Composite Microcapsule: Its Preparation and Multistage and Controlled Drug Release, Eur. J. Inorg. Chem. 27 (2017) 3312–3321.

[S18] Y. Ying, P. He, G. Ding, X. Peng, Ultrafast adsorption and selective desorption of aqueous aromatic dyes by graphene sheets modified by graphene quantum dots, Nanotechnology 27 (2016) 245703.

[S19] S.Yang, L. Chen, L. Mu, P.-C. Ma, Magnetic graphene foam for efficient adsorption of oil and organic solvents J. Colloid Interface Sci. 430 (2014) 337-344.

[S20] R.Wu, B.Yu, X. Liu, H.Li, W. Wang, L. Chen, Y. Bai, Z. Ming, S.-T. Yang, One-pot hydrothermal preparation of graphene sponge for the removal of oils and organic solvents Appl. Surf. Sci. 362 (2016) 56-62.

[S21] S. Kabiri, D. N. H. Tran, T. Altalhi, D. Losic, Outstanding adsorption performance of graphene–carbon nanotube aerogels for continuous oil removal, Carbon 80 (2014) 523-533

[S22] Z. Niu , J. Chen , H. H. Hng , J. Ma , X. Chen , A Leavening Strategy to Prepare Reduced Graphene Oxide Foams, Adv. Mater. 24 (2012) 4144-4150.

[S23] H. Ren, X. Shi, J. Zhu, Y. Zhang, Y. Bi, L. Zhang, Facile synthesis of N-doped graphene aerogel and its application for organic solvent adsorption, J. Mater. Sci. 51 (2016) 6419-6427.

[S24] J. Zhao, W. Ren, H.-M. Cheng, Graphene sponge for efficient and repeatable adsorption and desorption of water contaminations J. Mater. Chem. 22 (2012) 20197-20202.

[S25] Q. Wu, Y. X. Xu, Z. Y. Yao, A. R. Liu, G. Q. Shi, Supercapacitors Based on Flexible Graphene/Polyaniline Nanofiber Composite Films, ACS Nano, 4 (2010) 1963–1970.

[S26] Y. Wang, J. Chen, J. Cao, Y. Liu, Y. Zhou, J.-H. Ouyang, D. Jia, Graphene/Carbon Black Hybrid Film for Flexible and High Rate Performance Supercapacitor, J. Power Sources 271 (2014) 269−277.

[S27] J.-Y. Kim, K.-H. Kim, S.-B. Yoon, H.-K. Kim, S.-H. Park, K.-B. Kim, In situ chemical synthesis of ruthenium oxide/reduced graphene oxide nanocomposites for electrochemical capacitor applications, Nanoscale, 5 (2013) 6804–6811.

[S28] Z. F. Li, H. Zhang, Q. Liu, L. Sun, L. Stanciu, J. Xie, Fabrication of High-Surface-Area Graphene/Polyaniline Nanocomposites and Their Application in Supercapacitors, ACS Appl. Mater. Interfaces, 5 (2013) 2685–2691.

[S29] J. Yan, Y. Ding, C. Hu, H. Cheng, N. Chen, Z. Feng, Z. Zhang, L. Qu, Preparation of multifunctional microchannel-network graphene foams, J. Mater. Chem. A, 2 (2014) 16786-16792.

[S30] D. Mhamane, S. M. Unni, A. Suryawanshi, O. Game, C. Rode, B. Hannoyer, S. Kurungot and S. Ogale, Trigol based reduction of graphite oxide to graphene with enhanced charge storage activity, J. Mater. Chem. 22 (2012) 11140–11145.

[S31] Y. Xu, Z. Lin, X. Huang, Y. Liu, Y. Huang, X. Duan, Flexible Solid-State Supercapacitors Based on Three-Dimensional Graphene Hydrogel Films. ACS Nano 7 (2013) 4042−4049.

[S32] Z. H. Wen, X. C. Wang, S. Mao, Z. Bo, H. Kim, S. M. Cui, G. H. Lu, X. L. Feng, J. H. Chen, Crumpled Nitrogen-Doped Graphene Nanosheets with Ultrahigh Pore Volume for High-Performance Supercapacitor, Adv. Mater. 24 (2012) 5610-5616.

5.2 Funcionalización covalente de disulfuro de molibdeno

Artículo VI

Impact of Covalent Functionalization on the Aqueous Processability, Catalytic Activity, and Biocompatibility of Chemically Exfoliated MoS2 Nanosheets, Paredes, J.I., Munuera, J.M., Villar-Rodil, S. , Guardia, L., Ayán-Varela, M., Pagán, A., Aznar-Cervantes, S.D., Cenis, J.L., Martínez-Alonso, A., Tascón, J.M.D., ACS Applied Materials and Interfaces, 2016, 8, 41, 27974-27986.

Aparte del grafeno, el material bidimensional más ampliamente estudiado en los últimos años es el disulfuro de molibdeno (MoS_2). Los métodos de preparación de este material se basan en tres grandes enfoques: depósito en fase vapor, exfoliación directa por ultrasonidos/cizalla y exfoliación química por intercalación de metales alcalinos. Estos dos últimos métodos, ambos llevados a cabo generalmente en fase líquida, presentan grandes diferencias en cuanto a las características del material obtenido. En el caso de ultrasonidos/cizalla, las dispersiones obtenidas están formadas por láminas multicapa de MoS_2, y la fase mayoritaria presente en el material es la 2H (termodinámicamente estable), la misma que en el material *bulk* sin exfoliar. Sin embargo, durante la exfoliación química por reacción con un metal alcalino (normalmente litio) se forman compuestos de intercalación tipo Li_xMoS_2, en los que tiene lugar un cambio de fase de la original 2H a la fase metálica 1T (metaestable). Al reaccionar con agua, estos compuestos de intercalación, al reaccionar con agua dan lugar a la exfoliación, y permiten obtener dispersiones de láminas de disulfuro de molibdeno 1T (denotados como ce-MoS_2) compuestas mayoritariamente por monocapas, que son estables coloidalmente en agua debido al exceso de electrones que produjo la intercalación de litio. No obstante, uno de los mayores problemas que plantean estas dispersiones es su estabilidad coloidal y estructural, ya que, por reacción con el agua, las láminas pierden rápidamente sus electrones en exceso (y por tanto su carga eléctrica) y las dispersiones precipitan irreversiblemente en cuestión de pocas semanas, a la par que la fase 1T va revirtiendo progresivamente a la 2H.

En el **artículo VI** se describe un método de funcionalización de ce-MoS_2 con grupos funcionales de ácido acético, y se estudia su influencia en la estabilidad coloidal a lo largo del tiempo, así como las posibles aplicaciones del material funcionalizado (f-MoS_2) respecto al original. Para la funcionalización, se hizo reaccionar el ce-MoS_2 con

ácido yodoacético en medio ácido, donde tras cinco días tiene lugar una sustitución nucleófila por parte del azufre del ce-MoS_2, que sustituye al átomo de yodo dando como resultado el enlace covalente de las moléculas de ácido acético a las nanoláminas en una proporción de 0.4 moléculas por cada unidad de MoS_2. El primer efecto evidente de la funcionalización es la estabilidad coloidal de las dispersiones. Mientras que las dispersiones de ce-MoS_2 precipitaron irreversiblemente en cuatro semanas, las de f-MoS_2 mantuvieron su estabilidad durante periodos de varios meses sin precipitación irreversible.

Debido a la intercalación de litio, las láminas de ce-MoS_2 están constituidas mayoritariamente por la fase metálica 1T (73% 1T, 27% 2H). Como se comprobó mediante espectroscopías UV-visible y XPS, a pesar de que la reacción elimina el exceso de electrones (y por tanto la conductividad propia de la fase metálica), la fase 1T sigue siendo mayoritaria e incluso aumenta ligeramente su proporción (79%) debido a la funcionalización, que parece tener un efecto estabilizador en la fase 1T.

En vista de la estabilidad coloidal del f-MoS_2, y conociendo la actividad catalítica que presentan las dispersiones de este material en fase 1T, se estudió su uso como catalizador de la reacción de reducción de nitroarenos y la evolución de su eficiencia con el tiempo. En el caso del ce-MoS_2, la actividad catalítica disminuye drásticamente en pocas semanas, mientras que para el material funcionalizado, a pesar de ser menor en inicio, a lo largo del tiempo su disminución es menor, llegando a valores iguales o superiores al material sin funcionalizar. Los valores obtenidos para ambas reacciones catalíticas a los 3 meses de la preparación del f-MoS_2 se encuentran dentro del rango superior de los valores documentado para catalizadores basados en materiales bidimensionales y nanopartículas, siendo solo superados por materiales basados en metales preciosos como platino o paladio.

Si bien existen protocolos conocidos para la conversión de la fase 2H del MoS_2 (la presente en el material sin exfoliar) a la 1T en dispersión acuosa, como el método de exfoliación química, el proceso inverso solo ha sido descrito previamente en disolventes de alto punto de ebullición, y es habitual que los productos obtenidos posean poca estabilidad coloidal. En este trabajo se describe un método hidrotérmico consistente en un calentamiento a 160 ºC de la dispersión de f-MoS_2 que permite la reversión mayoritaria a la fase 2H (81%). Este proceso implica una cierta pérdida de la

funcionalización, bajando de 0.4 a 0.16 moléculas de ácido acético por unidad de MoS_2. Sin embargo, este grado de funcionalización no altera significativamente la estabilidad coloidal de las láminas, manteniéndose las dispersiones acuosas estables durante meses.

Por último, se sometió a los tres materiales [ce-MoS_2, f-MoS_2(1T) y f-MoS_2(2H)] a estudios de biocompatibilidad para evaluar el efecto de la funcionalización y el cambio de fase en las posibles aplicaciones biomédicas de los mismos. En los ensayos de proliferación de células de ratón L929 se aprecia una mejora significativa de la biocompatibilidad en el caso del f-MoS_2(1T), lo que apoya el futuro uso de este material en aplicaciones biológicas.

5. RESÚMENES YARTÍCULOS

Impact of Covalent Functionalization on the Aqueous Processability, Catalytic Activity and Biocompatibility of Chemically Exfoliated MoS_2 Nanosheets

Juan I. Paredes,[a] Jose M. Munuera,[a] Silvia Villar–Rodil,[a,*] Laura Guardia,[a] Miguel Ayán–Varela,[a] Ana Pagán, [b] Salvador Aznar-Cervantes,[b] Jose L. Cenis,[b] Amelia Martínez–Alonso,[a] Juan M.D. Tascón[a]

[a]Instituto Nacional del Carbón, INCAR-CSIC, Apartado 73, 33080 Oviedo, Spain
[b]Instituto Murciano de Investigación y Desarrollo Agrario y Alimentario (IMIDA), Calle Mayor 1, 30150 La Alberca, Spain

*Corresponding author: E-mail address: silvia@incar.csic.es (S. Villar-Rodil)

Abstract

Chemically exfoliated MoS_2 (ce-MoS_2) has emerged in recent years as an attractive two-dimensional material for use in relevant technological applications, but fully exploiting its potential and versatility will most probably require the deployment of appropriate chemical modification strategies. Here, we demonstrate that extensive covalent functionalization of ce-MoS_2 nanosheets with acetic acid groups (~0.4 groups grafted per MoS_2 unit) based on the organoiodide chemistry brings a number of benefits in terms of their processability and functionality. Specifically, the acetic acid-

functionalized nanosheets were furnished with long-term (>6 months) colloidal stability in aqueous medium at relatively high concentrations, exhibited a markedly improved temporal retention of catalytic activity towards the reduction of nitroarenes and could be more effectively coupled with silver nanoparticles to form hybrid nanostructures. Furthermore, in vitro cell proliferation tests carried out with murine fibroblasts suggested that the chemical derivatization had a positive effect on the biocompatibility of ce-MoS_2. A hydrothermal annealing procedure was also implemented to promote the structural conversion of the functionalized nanosheets from the 1T phase that was induced during the chemical exfoliation step to the original 2H phase of the starting bulk material, while retaining at the same time the aqueous colloidal stability afforded by the presence of the acetic acid groups. Overall, by highlighting the benefits of this type of chemical derivatization, the present work should contribute to strengthen the position of ce-MoS_2 as a two-dimensional material of significant practical utility.

Keywords: MoS_2, two-dimensional material, transition metal dichalcogenides (TMDs), colloidal dispersion, functionalization, metal nanoparticles, catalytic reduction.

1. Introduction

Over the last decade, graphene has been the focus of intense research efforts aimed at exploiting the exceptional electronic, mechanical, thermal and optical properties of this two-dimensional (2D) carbon material towards a wide variety of different technological applications.[1] Such an interest has progressively broadened in recent years to include other 2D materials, as it has become increasingly apparent that many of them boast their own share of attractive and frequently unusual physical properties that are distinct from those of their bulk counterparts and complementary to those of graphene.[1,2] At present, one of the most actively investigated 2D materials beyond graphene is arguably MoS_2, which belongs to the larger family of layered transition metal dichalcogenides (TMDs).[3,4] As recent work has demonstrated, single- and few-layer sheets of MoS_2 and other TMDs are very promising platforms for use in, e.g., electronic and optoelectronic devices,[5] catalysis,[6] energy conversion and storage,[7] molecular sensing[8] or biomedicine.[9]

Similar to the case of other 2D materials, it is generally accepted that the successful implementation of atomically thin MoS_2 in real-life applications will first and foremost

depend on the availability of efficient techniques for its production in large quantities. In this regard, three main approaches that show promise towards the mass production of 2D MoS_2 can be currently identified: (1) chemical vapor deposition (CVD) from molybdenum and sulfur precursor species onto appropriate substrates,[10] (2) direct liquid-phase exfoliation of bulk MoS_2 assisted by ultrasound or shear forces,[11,12] and (3) chemical exfoliation based on the intercalation of alkali metals (typically Li) into the bulk parent solid.[13–15] Although bottom-up CVD methods appear ideally suited to attain high quality, large-area wafers of single-/few-layer MoS_2 for use in high-end electronic or photonic applications, top-down exfoliation strategies are probably a better option when large amounts of solution-processable 2D flakes are sought after. Indeed, direct exfoliation of bulk MoS_2 powder in proper organic solvents (e.g., *N*-methyl-2-pyrrolidone) or water/surfactant solutions is known to afford stable colloidal dispersions of 2D flakes.[12] Such dispersions can then be made into useful macroscopic materials, such as thin films, coatings or composites, by straightforward processing techniques (vacuum filtration, spray-coating, solution blending, etc). However, this exfoliation approach suffers from some significant drawbacks, most notably a low exfoliation yield (< 5 wt%) and a population of exfoliated objects dominated by few- and several-layer MoS_2 flakes rather than single-layer ones.[16]

By contrast, chemical exfoliation based on Li intercalation has been reported to afford almost fully delaminated products, both in terms of yield (> 90 wt%) and flake thickness (mostly monolayers).[17] Intercalation is typically carried out by reaction of bulk MoS_2 with an organolithium reagent (e.g., *n*-butyllithium) or by electrochemical means, which involve electron transfer to the host MoS_2 lattice.[13,18] Such a reduction process facilitates the subsequent exfoliation of the intercalated product (Li_xMoS_2) in aqueous medium as well as the colloidal stabilization of the resulting negatively charged, chemically exfoliated MoS_2 (ce-MoS_2) nanosheets, but also triggers a conversion of the MoS_2 structure from the original semiconducting 2H phase to the metallic 1T phase.[17] Albeit this semiconducting-to-metallic phase transition can be detrimental in some cases (e.g., in electronic devices), recent work has demonstrated that 1T-phase ce-MoS_2 outperforms its 2H-phase counterpart when used, for example, as a catalyst and/or co-catalyst in the electrochemical and photocatalytic production of hydrogen[19,20] as well as in aqueous-phase organic reduction reactions,[21] or as an electrode material for supercapacitors.[22] The utility of ce-MoS_2 in biomedicine[23] and sensing[24] has also been demonstrated.

While the potential of ce-MoS_2 as a valuable material towards different applications is now well established, its actual implementation faces several hurdles that require consideration. These hurdles, which mainly concern the processing and manipulation of the exfoliated nanosheets but have ramifications in different areas of interest, include the following. (1) Although Li-intercalated MoS_2 can be exfoliated and dispersed in water, the resulting colloidal dispersions lack long-term stability (< 1 month),[25] which seriously limits their utility as, e.g., aqueous-phase catalytic systems. (2) Conversion of 1T-phase ce-MoS_2 back to the 2H phase directly in water (to give stable aqueous dispersions of 2H-phase nanosheets) would be highly desirable for their broader applicability, but no way to do such a conversion has yet been reported. 1T-to-2H conversion has only been demonstrated for thin ce-MoS_2 films on appropriate substrates[13] or, very recently, for ce-MoS_2 dispersions in high boiling point organic solvents.[26] (3) Combining ce-MoS_2 nanosheets with metallic or semiconducting nanoparticles (NPs) to yield functional hybrids is attractive for a number of applications, but generally difficult to achieve in practice due to the lack of proper chemical handles in the nanosheet surface.[27] (4) ce-MoS_2 nanosheets are attractive platforms for use in biomedical applications, but studies on their biocompatibility as well as on strategies to boost it have received little attention.[28]

We hypothesize that functionalization of ce-MoS_2 with proper chemical groups could provide a unified solution to the abovementioned issues. Over the last few years, a number of functionalization schemes have been explored for both ce-MoS_2 and single-/few-layer MoS_2 obtained by other means.[29,30] Among these, conjugation with thiols relying on the presence of structural defects in the MoS_2 lattice (mainly sulfur vacancies) has been by far the most extensively investigated approach.[25,27,31,] Indeed, such a type of derivatization has been used to partially tackle some, though not all, of these issues.[25,27] Very recently, covalent functionalization of ce-MoS_2 with organic groups through reaction with certain electrophiles (organoiodides[32] and aryldiazonium salts)[33] has been reported. Derivatization with organoiodides, in particular, has been shown to afford very high degrees of functionalization (~0.3 organic groups grafted per MoS_2 unit), making it an especially attractive strategy for tuning the surface characteristics and, consequently, many of the properties of ce-MoS_2. However, the potential of covalent functionalization as a means to address the limitations of ce-MoS_2 towards practical uses remains mostly unexplored.

We report here an investigation on the derivatization of ce-MoS_2 nanosheets with iodoacetic acid. Significantly, an extensive degree of functionalization could be attained (~0.4 acetic acid groups grafted per MoS_2 unit), which afforded a radical change in the long-term aqueous dispersibility of the nanosheets (stable dispersions for more than 6 months were attained) as well as a significantly extended shelf-life of the nanosheet dispersions when used as a catalyst for reduction reactions in water. Furthermore, a hydrothermal method for the conversion of the functionalized, 1T-phase ce-MoS_2 to 2H-phase ce-MoS_2 while retaining the long-term colloidal stability of the nanosheets was implemented, which was previously not possible. Finally, the covalent functionalization of ce-MoS_2 with acetic acid was also seen to be beneficial for the nucleation and growth of Ag NPs onto the nanosheets to form hybrid structures and in enhancing the biocompatibility of the as-prepared nanosheets, as evaluated from cell proliferation studies using murine fibroblasts. Taken together, the present results highlight the benefits of this type of derivatization in improving the processability and functionality of ce-MoS_2 towards a number of uses.

2. Results and discussion

2.1. Covalent functionalization of ce-MoS_2 nanosheets with acetic acid groups

Lithium intercalation of bulk MoS_2 powder based on reaction with *n*-butyllithium and subsequent ultrasound-induced exfoliation of the intercalated product (Li_xMoS_2) in water is well-known to afford colloidal dispersions of ce-MoS_2 nanosheets, which are mostly single-layered objects.[13,17] Although the starting bulk MoS_2 material exhibits the thermodynamically stable, semiconducting 2H phase (trigonal prismatic coordination), charge transfer from the lithium intercalates to the host MoS_2 lattice triggers an extensive (although incomplete) structural transformation in Li_xMoS_2 to the metastable, metallic 1T phase (octahedral coordination) that is carried forward to the ce-MoS_2 nanosheets dispersed in aqueous medium.[17] The excess electron charges present in the nanosheets are also thought to be responsible for their dispersibility in aqueous medium. However, this colloidal stability is generally rather limited, in particular when working at moderately high ce-MoS_2 nanosheet concentrations. For example, aqueous dispersions at a concentration of ~0.8 mg mL^{-1} are seen to precipitate in a matter of just 3 weeks (Supporting Information, Fig. S1), whereas strong agglomeration is already observed after 1 month for ~0.1 mg mL^{-1} suspensions. Precipitation of the ce-MoS_2 nanosheets is an irreversible process, as the sedimented material cannot be successfully

re-dispersed even after sonication for several hours. Such a behavior is likely due to the slow reaction of water molecules with the excess electrons,[34] but in any case it is clearly detrimental to the manipulation and use of ce-MoS_2 towards different applications. We envisaged that covalent derivatization of the nanosheets with proper organoiodides could be a particularly efficient way to overcome this issue, taking into account the extensive degree of functionalization that has been previously achieved using this particular approach for MoS_2 and other TMDs.[32] Organoiodides having ionic or ionizable moieties should be well suited for the intended purpose, as the net charge associated to the covalently grafted groups would be expected to provide the nanosheets with enhanced and enduring colloidal stability. To test this hypothesis, we selected iodoacetic acid and iodomethanesulfonic acid, which possess, respectively, a pH-dependent carboxylate anion and a permanent sulfonate anion.

Addition of iodoacetic acid to a mildly acidic ce-MoS_2 dispersion in water was seen to induce a slight coagulation of the nanosheets within several hours. After being allowed to react for a total of 5 days and thoroughly washed, the nanosheets could be readily re-dispersed in neutral and basic aqueous medium (see Experimental section for details). Evidence for their successful functionalization with acetic acid groups was obtained using a suite of characterization techniques. Fig. 1a (black trace) shows the UV-vis absorption spectrum of the starting, non-functionalized ce-MoS_2 dispersion. Unlike the case of MoS_2 flakes produced by direct exfoliation of the bulk powder, the structure of which is dominated by the semiconducting 2H polymorph,[11,35] no excitonic peaks in the 400-500 and 600-700 nm wavelength ranges were observed for ce-MoS_2. Instead, two absorption bands at ~255 and 300 nm, together with essentially featureless absorbance above 300 nm, were noticed. Such attributes are characteristic of MoS_2 with a predominance of metallic 1T phase, as expected for the as-prepared ce-MoS_2 nanosheets.[13] The two mentioned bands, which are largely absent from 2H-phase MoS_2 flakes, can be ascribed to plasmon resonances associated to the metallic state of ce-MoS_2.[36] By contrast, these plasmon bands tended to disappear after treating the nanosheets with iodoacetic acid, whereas the rest of the spectrum remained essentially unaltered except for the emergence of a shoulder-like feature at about 400 nm (Fig. 1a, green trace). Such a result was indicative of changes to the electronic structure of the nanosheets, which in turn would be consistent with derivatization having taken pace. Furthermore, recent experimental and theoretical work has suggested that the originally metallic nature of the as-prepared ce-MoS_2 nanosheets becomes semiconducting upon

their covalent functionalization with different chemical groups, even though the 1T phase is retained is the process.[32,37] Thus, if the iodoacetic acid treatment was successful towards the covalent modification of ce-MoS_2, its associated plasmon resonances would be expected to disappear as a result of the loss of metallic character, and this is exactly what the absorption spectrum of the treated nanosheets indicated (Fig. 1a).

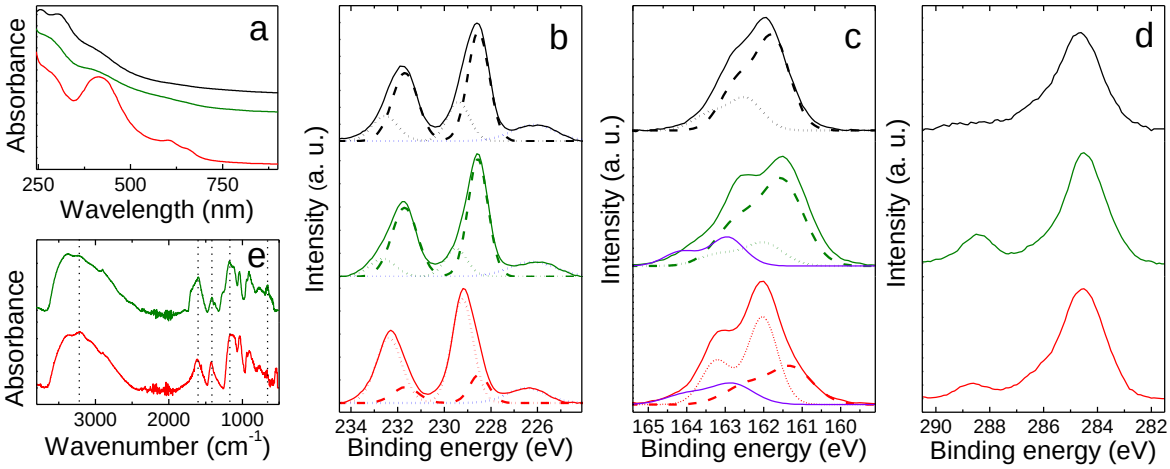

Figure 1. Spectroscopic characterization of the starting, non-functionalized ce-MoS_2 dispersion, (black trace), and the same material after treatment with iodoacetic acid (green trace), and annealing at 160 ºC (red trace): (a) UV-vis absorption spectra, high resolution XPS (b) Mo 3d (and S2s, blue dotted line), (c) S 2p, (d) C1s core level spectra, and (e) ATR-FTIR spectra. Mo3d and S2p XPS core level doublet bands are deconvoluted into two components assigned to the 2H (dotted line) and 1T phases (dashed line). In the S2p core level spectra of the treated samples, an additional doublet component at binding energies of ~163–164 eV (solid violet trace) is assigned to C–S covalent bonds. Dotted lines have been added to the ATR–FTIR spectra to assist in the identification of the main peaks.

Further indication of derivatization of the nanosheets with acetic acid groups was obtained by X-ray photoelectron spectroscopy (XPS). Fig. 1b (top plot) shows the high resolution Mo 3d core level spectrum for the starting ce-MoS_2 material. A doublet band corresponding to the $3d_{3/2}$ (located at ~232 eV) and $3d_{5/2}$ (~229 eV) levels of Mo^{4+} was observed (the weak feature at ~226.5 eV arises from the S 2s level). Following prior work on ce-MoS_2,[13,32] each peak from this doublet band could be fitted to two components that could be associated to the 2H and 1T phases, namely, the components located at ~232.6 and 229.4 eV (dotted traces) arose from Mo atoms in the 2H phase, whereas the components at about 231.8 and 228.6 eV (dashed traces) corresponded to Mo atoms from the 1T phase (i.e, they were downshifted ~0.8 eV relative to their 2H

counterparts). Such a peak-fitting allowed quantification of the percentage of each phase present in the nanosheets, revealing that the 1T polymorph was predominant (~73% 1T phase, ~27% 2H phase). This phase composition was comparable (slightly higher) to that previously reported for ce-MoS_2.[32] Following treatment of the nanosheets with iodocacetic acid, the Mo 3d core level spectrum did not experience very significant changes (Fig. 1b, middle plot), which would be consistent with the idea that organoiodide functionalization takes place through sulfur but not molybdenum atoms of ce-MoS_2.[32] However, a slight but clear increase in the fraction of 1T phase (up to about 79%) was noticed. We interpret this increase to be a consequence of functionalization. It has been recently reported on the basis of theoretical calculations that covalent grafting of MoS_2 with a number of chemical groups (such as –H and $–CH_3$) through its sulfur atoms induces stabilization of the originally metastable 1T phase, so that above a certain threshold coverage of grafted groups (estimated to be ~20% of the sulfur atoms) this phase becomes the thermodynamically stable one.[37] It is therefore not unreasonable to assume that grafting of acetic acid groups triggered a partial conversion of the 2H phase remaining in the ce-MoS_2 nanosheets to the stabilized 1T polymorph.

More direct evidence of the covalent bonding of acetic acid groups to the ce-MoS_2 nanosheets was gathered from the high resolution S 2p core level spectra of the samples. The S 2p band is also a doublet, with peaks located at ~162 ($2p_{1/2}$) and ~163 ($2p_{3/2}$) eV for 2H-phase MoS_2 that are again downshifted by ~0.8 eV in the case of 1T-phase MoS_2.[13,32] As expected, the S 2p spectrum of as-prepared, non-functionalized ce-MoS_2 (Fig. 1c, top plot) could be fitted to four components that can be associated to both the 2H and 1T polymorphs, but with a prevalence of the latter. (For simplicity, the two components of each phase in Fig. 1c are shown as a single line: dotted line for 2H, dashed line for 1T). After treatment with iodoacetic acid, the shape of the S 2p band underwent some noticeable changes (Fig. 1c, middle plot), so that in addition to the 1T- and 2H-related components, a new doublet component appeared at binding energies of ~163-164 eV (solid violet trace). Such additional doublet component can be ascribed to sulfur atoms covalently bonded to carbon,[32] thus constituting direct indication of the grafting of acetic acid groups to the nanosheets. The presence of this chemical group was also made apparent from the C 1s region of the XPS spectra (Fig. 1d). For non-functionalized ce-MoS_2 (top plot), a relatively broad band centered at ~285 eV was observed. This a priori unexpected feature can be assigned to the adventitious carbon (hydrocarbon contamination) that so pervasively comes to light when samples are

investigated by XPS.[38] By contrast, for iodoacetic acid-treated ce-MoS_2 a further component at about 288.4 eV was clearly noticed (Fig. 1d, middle plot), which could be attributed to carbon atoms in carboxylic acids, therefore substantiating the idea that acetic acid groups were incorporated to the ce-MoS_2 nanosheets. Furthermore, Fig. 1e (top plot) shows the ATR-FTIR spectrum of iodoacetic acid-treated ce-MoS_2, which exhibited additional indication of successful functionalization. Specifically, the following features were observed: (1) a sharp peak located at ~655 cm^{-1}, ascribed to S–C stretching vibrations arising from acetic acid groups grafted onto the nanosheets via sulfur atoms), (2) a peak at ~1170 cm^{-1}, attributed to CH_2-S wagging, (3) a peak at ~1420 cm^{-1}, attributed to symmetric C=O stretching of acetate groups, and to a combination of C–O stretch. and O–H deformation vibrations from the carboxylic acid group of acetic acid, (4) a peak at ~1600 cm^{-1} assigned to asymmetric stretching for C=O bonds in acetate groups together with a shoulder on its high wavenumber side (~1680 cm^{-1}) corresponding to C=O stretch. for H–bonded COOH groups, and (5) an intense and broad band (2750–3400 cm^{-1}), which can be associated to O-H stretching vibrations from H–bonded carboxylic acid groups. Thus, the ATR–FTIR spectrum of the iodoacetic acid-treated ce-MoS_2 in the solid phase indicates the presence of both acetate salts and H–bonded COOH groups. Moreover, derivatization with acetic acid groups was not seen to induce significant changes to the morphology of the ce-MoS_2 nanosheets, as evidenced from both transmission electron microscopy (TEM; Fig. 2a and c) and atomic force microscopy (AFM; Fig. 2b and d) imaging. The non-functionalized sample (Fig. 2a and b) was comprised of lamellar objects with typical lateral sizes in the 50–500 nm range and apparent thickness of ~1–2 nm, indicating that they were mainly single-layer ce-MoS_2 nanosheets.[17,21] The acetic acid-functionalized material was 1–2 nm thicker (Fig. 2c and d), which is consistent with the presence of carboxylic acids on both sizes of the nanosheets adding to their thickness.

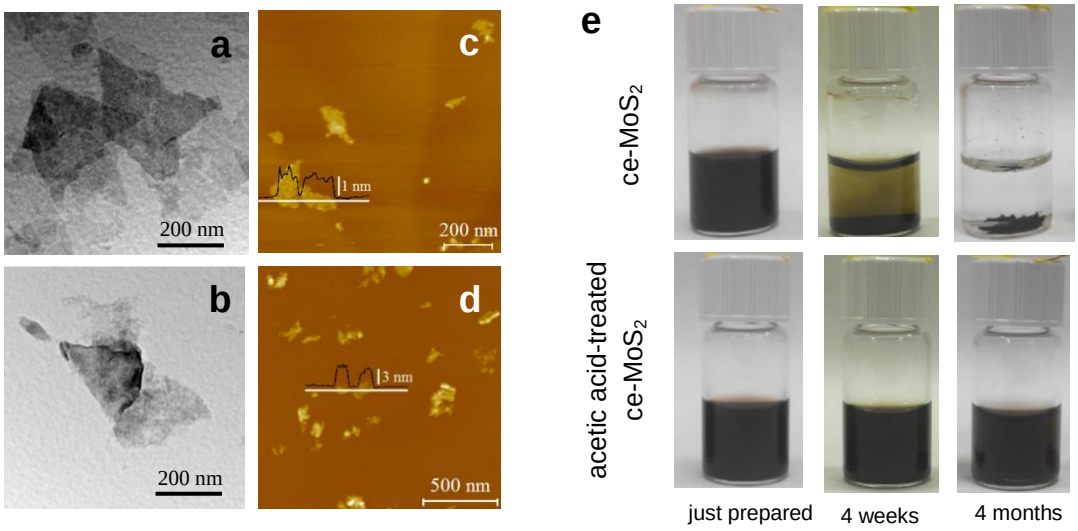

Figure 2. TEM (a,b) and AFM (c,d) images of the starting non-functionalized material (a,c) and the acetic acid-functionalized material (b,d). (e) Digital photographs of ~0.2 mg mL^{-1} dispersions of non-functionalized ce-MoS_2 (top row) and acetic acid-functionalized ce-MoS_2 (bottom row) (left column: just prepared; middle column: after 4 weeks; right column: after 4 months).

We note that iodoacetic acid could not have simply adsorbed on the ce-MoS_2 nanosheets, but instead must have reacted to form covalent bonding with this material. If the former situation had taken place, we would expect to observe the presence of iodine in the XPS survey spectrum (i.e., the I $3d_{5/2}$ band at ~621 eV), feature which is not found (see Supporting Information, Fig. S2b), as well as a component in the C 1s region of the spectrum associated to C–I bonds (spectrum not shown). However, none of these features were noticed, but only the emergence of a component consistent with S–C bonds in the S 2p spectra (Fig. 1c). The XPS data were also used to estimate the degree of functionalization of the nanosheets. This calculation was done by two different, independent ways: (1) determining the amount of carbon atoms present in carboxylic acid groups relative to the amount of either sulfur or molybdenum atoms in the functionalized samples, taking into account that the number of carboxylic acid carbons equals the number of acetic acid groups, and (2) determining the amount of carbon-bonded sulfur atoms relative to the total amount of sulfur in the sample, using the areas of the peak-fitted components from the S 2p spectra and considering that the number of carbon-bonded sulfur atoms equals the number of grafted acetic acid groups. The values derived from these two methods were seen to be consistent with each other, yielding a functionalization degree for the nanosheets in the range of 0.17-0.20 acetic acid groups per sulfur atom, or equivalently, 0.35-0.40 groups per MoS_2 unit. This

extent of derivatization is considerably larger than that reported for other functionalization schemes of ce-MoS_2. For example, covalent grafting of 4-methoxyphenyl groups based on the use of the corresponding diazonium salt has led to a functionalization degree of ~0.2 groups per MoS_2 unit,[33] whereas conjugation with 3-mercaptopropionic acid afforded ~0.1 groups per MoS_2 unit.[27] By comparison, the previous report on functionalization of ce-MoS_2 with organoiodides (2-iodoacetamide) attained 0.29 grafted groups per MoS_2 unit.[32] Treatment of the ce-MoS_2 material prepared in the present work with 2-iodoacetamide yielded a slightly higher derivatization degree (~0.34). We interpret this difference to arise from the somewhat larger extent of 1T fraction present in our nanosheets (73 vs 65%). Considering that the covalent grafting of chemical groups appears to be energetically very favorable on the 1T phase but very weak on the 2H phase,[37] a larger fraction of 1T phase in ce-MoS_2 should be associated to larger numbers of readily available derivatization sites, and consequently to the possibility of higher functionalization degrees.

2.2. Effect of functionalization on the aqueous processability, catalytic activity and use as nanoparticle support of ce-MoS_2

Functionalization with acetic acid groups was seen to drastically improve the dispersibility of the nanosheets in water, particularly in the long term. This point is illustrated in Fig. 2e, which shows digital photographs of dispersions (~0.2 mg mL^{-1}) of both non-functionalized (left column) and acetic acid-functionalized (right column) ce-MoS_2 following different standing times after their preparation (first row: just prepared; second row: 4 weeks; third row: 4 months). It can be noticed that the non-functionalized nanosheets precipitated in a matter of 4 weeks, whereas their acetic acid-derivatized counterparts remained colloidally stable, forming homogeneous suspensions to the naked eye well beyond 4 months (this was observed also for acetic acid-functionalized dispersions at concentrations up to 0.4 mg mL^{-1}). Such a result can be ascribed to the presence of negatively charged, deprotonated carboxylate moieties associated to the grafted acetic acid groups in the functionalized samples, which are expected to furnish the nanosheets with enhanced colloidal stability through electrostatic repulsion. In particular, we note that full deprotonation of the carboxylic acids can be expected to bestow the functionalized nanosheets with a net negative charge of ~0.35-0.40*e* per MoS_2 unit. This figure is larger than the estimated value for the excess charge present in as-prepared ce-MoS_2 nanosheets (~0.15-0.25*e*),[34] although the latter should probably

depend on the particular extent of 2H-to-1T phase conversion attained for each sample in question, which differs considerably in the literature.[13,21,32] Nevertheless, extensive deprotonation of carboxylic acids usually takes place only under basic, neutral and very slightly acidic conditions, but not at lower pH values. In accordance with this, the acetic acid-functionalized nanosheets were seen to be colloidally stable at basic and neutral pH values, whereas they precipitated in acidified media.

In an attempt to make the nanosheets colloidally stable in a wider pH range, we tried to derivatize ce-MoS_2 with iodomethanesulfonic acid instead of iodoacetic acid, as the former organoiodide possesses a more permanent anion (the pK_a value of sulfonic acids is typically around -3). However, analysis of the nanosheets treated with iodomethanesulfonic acid suggested such an attempt to be unsuccessful. For instance, XPS (S 2p region) did not show evidence of the formation of S-C bonds in the nanosheets (spectrum not shown), but rather pointed to the presence of unreacted organoiodide molecules (iodine detected in the survey spectrum; see Supporting Information, Fig. S2a). Furthermore, the colloidal stability of as-prepared ce-MoS_2 was not changed after treatment with iodomethanesulfonic acid, so that dispersions exposed to this reagent also precipitated in 4 weeks. We believe that this functionalization reaction cannot effectively take place due to electrostatic repulsions between the nanosheets and the organoiodide, i.e. the permanent negative charge associated to the sulfonate group prevents the organoiodide from approaching the nanosheets, which are also negatively charged.

The enhanced processability of ce-MoS_2 nanosheets in water after their covalent functionalization with acetic acid groups should have a number of practical benefits. For example, it has been recently demonstrated that ce-MoS_2 is rather efficient as a catalyst in reduction reactions of several organic molecules (including nitroarenes and dyes) carried out in aqueous medium.[21] We can expect this catalytic activity to be strongly dependent on the number of active sites that are readily available for interaction with the reaction medium, and thus to be dependent on the degree of agglomeration of the nanosheets. Therefore, non-functionalized ce-MoS_2 should become a much less effective catalyst after a few weeks as a result of its colloidal instability in water, i.e., the shelf life of this catalyst should be quite limited. On the other hand, although we envisage the catalytic performance of acetic acid-functionalized ce-MoS_2 to be initially lower than that of its non-functionalized counterpart (due to, e.g., steric barriers to reaction associated to the presence of functional groups on the catalytically active 1T

domains),[21] the increased colloidal stability of the former should lead to a less pronounced decline in activity with time. It would thus be conceivable that the functionalized nanosheets exhibit a better catalytic performance in the long run compared to the non-functionalized nanosheets. To test this hypothesis, we compared the reduction of two nitroarenes, namely the reduction of 4-nitrophenol (4-NP) to 4-aminophenol (4-AP) and the reduction of 4-nitroaniline (4-NA) to *p*-phenylenediamine (*p*-PDA), in aqueous medium at room temperature using sodium borohydride as a reductant. In addition to their practical relevance, e.g., as key steps in the synthesis of certain drugs and polymers, these reduction reactions are frequently used to benchmark the activity of different catalytic systems.[39] As detailed in the Experimental section and thoroughly discussed elsewhere,[21,40] both reactions can be readily followed using UV-vis absorption spectroscopy. For the present studies, because some ce-MoS_2 dispersions (specifically, non-functionalized ones) could be found in a precipitated state, we routinely sonicated all the aqueous samples for a few minutes to temporarily re-suspend the catalytic material and be able to perform the catalytic measurements.

Fig. 3 compares the catalytic activity (determined as number of moles of substrate converted per hour per mole of MoS_2 used) of non-functionalized and acetic acid-functionalized ce-MoS_2 in the reduction of 4-NP (a) and 4-NA (b) measured immediately, one month and three months after preparation of the nanosheets. From these results, several points can be noticed. First, the catalytic activity of the nanosheets (either functionalized or non-functionalized) tended to be lower towards reduction of 4-NP compared to 4-NA. This outcome is probably related to the fact that under the basic pH of the reaction medium, electrostatic repulsions between the deprotonated 4-NP molecules (4-nitrophenoxide anions)[40] and the negatively charged nanosheets hinders the approach of the substrate to the active sites on the catalyst. By contrast, such electrostatic barriers are expected to be absent in the case of 4-NA because this substrate lacks a net charge. Second, as expected, the catalytic activity of acetic acid-functionalized ce-MoS_2 immediately after its preparation was lower than that of its non-functionalized counterpart for both 4-NP and 4-NA reduction. However, in relative terms the difference between non-functionalized and functionalized nanosheets was much more significant for the former reaction (~70% reduction in catalytic activity for 4-NP compared to ~30% for 4-NA). Again, electrostatic effects can be invoked to rationalize this result. The catalytically active sites of ce-MoS_2 are thought to be mostly located on its 1T domains,[21] but such domains have been very extensively grafted with

negatively charged acetate groups (~0.45-0.50 groups per MoS_2 unit from the 1T phase according to the data given above and assuming that only this phase can be covalently grafted with chemical moieties).[37] For the electrically neutral 4-NA molecules, the acetate groups would just constitute a steric barrier in their path to the catalytic sites on the nanosheets, but for the deprotonated 4-NP molecules both steric and electrostatic barriers would be expected to be in place at the very location of the active sites, leading to a larger degree of reduction in catalytic activity.

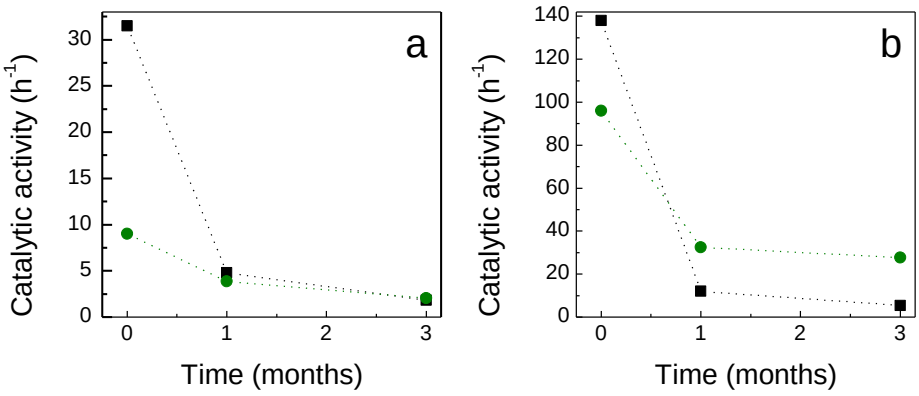

Figure 3. Catalytic activity (determined as number of moles of substrate converted per hour per mole of MoS_2 used) of non-functionalized (black squares) and acetic acid-functionalized (green circles) ce-MoS_2 in the reduction of 4-NP (a) and 4-NA (b) measured immediately, one month and three months after preparation of the nanosheets.

Concerning the time evolution of catalytic activities in Fig. 3, we note that the efficiency of both non-functionalized and acetic acid-functionalized ce-MoS_2 decreased markedly in tests carried out one and three months after their preparation, but the extent of such a decline was seen to be much larger with the former material. For instance, non-functionalized ce-MoS_2 retained just ~6% (4%) of its original catalytic activity in the reduction of 4-NP (4-NA) after three months, whereas the corresponding values for acetic acid-functionalized ce-MoS_2 were ~23% (4-NP) and 29% (4-NA). The origin of the decreased activity for the functionalized nanosheets is currently not understood, as it is apparently not related to colloidal stability issues (no precipitated material was visible to the naked eye after three months), so an in-depth analysis of their partial deactivation is warranted in future studies. In any case, the long-term catalytic activities of functionalized ce-MoS_2 turned out to be either similar (for 4-NP reduction) or much

higher (4-NA) than those of its non-functionalized correlative, suggesting the former to be a more convenient catalyst for extended use. Furthermore, as can be noticed from Table 1, even such decreased, long-term activities were competitive with those reported in the literature in recent years for a considerable number of catalytic systems. For example, the catalytic activity of acetic acid-functionalized ce-MoS_2 towards 4-NP reduction after three months (~2 h^{-1}) lay in the lower range of values typically documented for catalysts based on expensive noble metal (e.g., Pt or Pd) NPs,[41–46] whereas it was similar to or somewhat higher than that of non-noble metal (e.g., Cu) NP-based catalysts[47–50] but much higher than that of novel metal-free catalysts based on heteroatom-containing carbon materials, such as nitrogen-doped reduced graphene oxide.[51–55] In the case of 4-NA reduction, the long-term catalytic activity of the functionalized nanosheets (27.6 h^{-1}) was comparable to the values typically reported with noble metal NP-based catalysts[56–62] and much higher than that of nitrogen-doped reduced graphene oxide[21] (data for catalysts based exclusively on non-noble metal NPs are not available for this reaction in the literature).

Table 1. Comparison of the catalytic activity (defined as number of moles of substrate converted per hour per mole of catalyst used) of non-functionalized and acetic acid-functionalized ce-MoS_2 three months after their preparation with that of other catalysts towards the reduction of 4-NP and 4-NA.

Catalytic system	**Catalytic activity (h^{-1})**	**Ref.**
Reduction of 4-NP		
Non-functionalized ce-MoS_2 (3 months)	1.8	Present work
Acetic acid-functionalized ce-MoS_2 (3 months)	2	Present work
Pt NPs on graphene oxide/PVA/Fe_3O_4 composite gel	3	41
$PtPd_3$ bimetallic NPs	1.8	42
Porous Pd nanoclusters	0.3	43
Dendritic Pd NPs	6	44
Ir NPs	2.4	45
Au NPs supported on poly(ε-caprolactone) nanofibers	0.6	46
Cu NPs supported onto carbon microspheres	0.2	47
Cu and Sn sponges/dendrites	1.2-1.8	48
Cu_2O octahedrons supported on BN nanosheets	0.7	49
Ni NPs supported on MOF-derived mesoporous carbon	0.25	50
N-doped reduced graphene oxide	0.06	51
Hydrothermally reduced graphene oxide	0.05	52
Vitamin C-reduced graphene oxide	0.002	53
N-doped porous carbons derived from different MOFs	0.05-0.25	54,55
Reduction of 4-NA		
Non-functionalized ce-MoS_2 (3 months)	5.4	Present work
Acetic acid-functionalized ce-MoS_2 (3 months)	27.6	Present work
N-doped reduced graphene oxide	0.08	21
Pt NPs supported on graphene aerogel	48	56
Bimetallic Pt-Ni NPs	18	57
$NiFe_2O_4$-Pd NP hybrid	180	58
Polyaniline/Fe_3O_4/Pd NP hybrid	15	59
Pd NPs supported on reduced graphene oxide	25	60
Polyhedral Au NPs	1-6	61
Hollow Ag nanospheres	6	62

The abundant presence of covalently grafted acetate groups on ce-MoS_2 can also be beneficial towards the production of hybrids with metallic or semiconducting NPs, because the carboxylate moieties can act as effective anchoring sites that favor the nucleation and/or attachment of such NPs onto the nanosheets.[27] As a preliminary test of this possibility, we tried to synthesize Ag NPs on both non-functionalized and acetic acid-functionalized ce-MoS_2 by reduction of a metal salt (silver nitrate) with sodium borohydride in an aqueous dispersion of the corresponding nanosheets. We note that Ag^+ ions can be directly reduced to Ag NPs in the presence of as-prepared ce-MoS_2 without the need of a reducing agent, presumably due to the transfer of the excess electrons that are present in the nanosheets. However, very recent work has demonstrated that this approach triggers the over-oxidation and finally disintegration of the nanosheets in a matter of hours.[63] To avoid this outcome, we included the reductant sodium borohydride in our synthetic procedure. Upon mixing the reactants in the presence of the non-functionalized ce-MoS_2 nanosheets, the solution immediately turned dark green, indicative of the formation of Ag NPs. Nonetheless, TEM inspection of the products (Fig. 4a) revealed that very few NPs were actually resting on the nanosheets, whereas stand-alone NPs were frequently observed. By contrast, large numbers of NPs (~10–15 nm in diameter) were seen to be decorating the acetic acid-functionalized nanosheets (Fig. 4b), implying a stronger interaction between the two components in this case. This result suggests the functionalized material to be a superior substrate for the synthesis of hybrids based on ce-MoS_2.

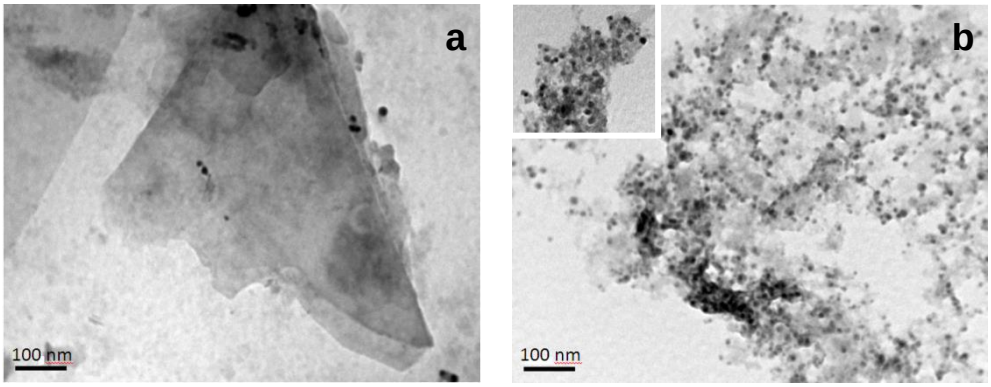

Figure 4. TEM images of hybrids of Ag NPs on both non-functionalized (a) and acetic acid-functionalized ce-MoS_2 (b).

2.3. 1T-to-2H phase transformation of acetic acid-functionalized ce-MoS_2 in aqueous colloidal suspension

As demonstrated above, the covalent functionalization of ce-MoS_2 with acetic acid groups promotes the aqueous dispersibility of the nanosheets, which in turn can bring several advantages when considering the practical use of this material. Nonetheless, similar to the case of its as-prepared, non-functionalized counterpart, the functionalized ce-MoS_2 material incorporates a majority of 1T phase in its structure. It would be desirable to be able to convert ce-MoS_2 back to its original 2H phase while retaining at the same time a good dispersibility of the nanosheets in aqueous medium. In principle, this phase conversion can be achieved by thermal annealing at moderate temperatures (150–300 ºC),[13] so that for nanosheets in aqueous dispersion a hydrothermal treatment could be a convenient way to induce the 1T-to-2H conversion. In this context, successful phase conversion of ce-MoS_2 stably dispersed in non-polar or low-polarity organic solvents has been recently reported after electrostatic binding of oleylamine to the nanosheets,[26] but conversion in water has not yet been achieved. As a matter of fact, we observed that hydrothermal treatment of non-functionalized ce-MoS_2 at relevant temperatures (>100 ºC) led to immediate and irreversible precipitation of the suspensions unless the process was carried out at low nanosheet concentrations (~0.05 mg mL^{-1} and below), and even in the latter case the resulting annealed dispersions tended to precipitate in a matter of several hours to a few days. We note, however, that it was possible to induce conversion of the acetic acid-functionalized ce-MoS_2 nanosheets back to the 2H phase while retaining their aqueous dispersibility to a large degree. To this end, the hydrothermal annealing temperature had to be carefully chosen so as to strike a balance between the extent of phase conversion attained and the degree of defunctionalization that is also associated to the annealing process, the latter being detrimental to the aqueous colloidal stability of the nanosheets.

A suite of hydrothermal annealing experiments revealed a temperature of 160 ºC to be appropriate for the intended purpose. As noticed from Fig. 1a (red trace), absorption features in the 400–500 and 600–700 nm wavelength regions, which can be ascribed to excitonic transitions in 2H-phase MoS_2, were seen to emerge after annealing the functionalized dispersions at 160 ºC. Furthermore, the high resolution Mo 3d core level spectrum of this sample (Fig. 1b, bottom plot) indicated that an extensive (although incomplete) structural conversion to the 2H phase had occurred (81% 2H phase vs 21% for functionalized but non-annealed ce-MoS_2). Such an extent of phase conversion was comparable to that recently reported in non-polar/low-polarity organic solvents.[26] Consistent with the idea that the catalytically active sites in ce-MoS_2 are mostly located

on the 1T phase (some non-negligible contribution from the nanosheet edges is also expected to be in place),[21] the catalytic activity of the hydrothermally annealed nanosheets immediately after their preparation was seen to decrease by a factor of 3 to 5 in the reduction of 4-NP and 4-NA compared to their non-annealed counterpart (results not shown). In parallel to the phase conversion, we observed by XPS a decrease in the amount of acetic acid groups grafted onto the nanosheets, i.e., a less intense S-C component in the S 2p region (Fig. 1c, bottom plot) as well as a weaker feature at ~288.4 eV related to carboxylic acids in the C 1s region (Fig. 1d, bottom plot). This conclusion was supported by ATR-FTIR spectroscopy (Fig. 1e, bottom plot), as the peak associated to S–C stretching vibrations became clearly less intense compared to that of the non-annealed sample (top plot).

XPS-based quantification of the functionalization degree for the dispersions annealed at 160 ºC yielded a value of about 0.16 acetic acid groups grafted per MoS_2 unit. This figure was significantly lower than that estimated for the non-annealed nanosheets (0.35-0.40; see above) but nonetheless comparable to the values reported for non-annealed nanosheets functionalized via thiol conjugation or reaction with aryldiazonium salts (~0.1-0.2).[27,33] We also note that such a degree of functionalization is consistent with the fraction of 1T phase remaining in the annealed nanosheets (19%). If the covalent attachment of chemical moieties is strongly favored at sulfur atoms from the 1T phase relative to the 2H phase,[37] then we would expect the degree of functionalization of the annealed sample not to be higher than 0.19 grafted groups per MoS_2 unit, which was in agreement with the actual data derived from the XPS measurements. In any case, the decreased extent of functionalization associated to the annealed nanosheets was still sufficient to afford their aqueous dispersibility at significant concentrations (e.g., 0.2–0.4 mg mL^{-1}) for reasonable periods of time. Even though the annealed suspensions tended to precipitate before then non–annealed ones, they could be re-dispersed by a simple hand-shaking procedure. We also note that different annealing temperatures either failed to induce a considerable 1T-to-2H phase conversion (<160 ºC) or led to colloidally unstable products that agglomerated immediately due to extensive defunctionalization (>160 ºC), so that a temperature of 160 ºC constituted a reasonable compromise between these two opposing requirements.

2.4. Biocompatibility of acetic acid-functionalized ce-MoS_2

Finally, we carried out a preliminary investigation on the biocompatibility of acetic acid-functionalized ce-MoS_2. 2D materials, including MoS_2, are currently the focus of intense research activities towards their prospective application in biomedicine, e.g., as drug carriers in different therapies or as contrast agents in diagnostic imaging.[9] In the particular case of ce-MoS_2 nanosheets, previous work has explored their use as photothermal agents[23] or as drug carriers in combined photothermal, photodynamic and chemotherapy of cancer.[64] For these and other bio-related applications, it is obvious that the nanosheets need to be highly biocompatible and non-cytotoxic, and so studies on their biological interactions are highly relevant.[65] Although 2D MoS_2 (including ce-MoS_2) nanosheets are generally regarded to exhibit low toxicity towards mammalian cell lines,[65,66] it is also known that their specific toxicity profile is affected by a number of physicochemical parameters associated to the material, such as its exfoliation degree, aggregation state or electrical conductivity.[28,66] Similar to the case of graphene,[67] we also expect the biocompatibility/cytotoxicity of the ce-MoS_2 nanosheets to be modulated by their surface chemistry, and therefore to be sensitive to functionalization treatments, but such a point has not yet been investigated. To shed light on this question, we explored and compared the biocompatibility of the different ce-MoS_2 materials prepared here towards murine fibroblasts (L929 cell line) on the basis of the MTT assay. The L929 cell line is generally used as a benchmark in the biocompatibility assessment of medical devices.

Fig. 5 summarizes the results of L929 cell proliferation tests carried out on polystyrene culture plates 24 h after having seeded the cells at an initial density of 5500 cells cm^{-2}, in the presence of different concentrations of ce-MoS_2 materials in the culture medium. For comparison purposes, tests with graphene oxide nanosheets were also performed. At the lowest nanosheet concentration (10 μg mL^{-1}), all the ce-MoS_2 materials, i.e. the non-functionalized, acetic acid-functionalized as well as functionalized and 160 ºC annealed samples, displayed somewhat reduced cell proliferation values compared with the control test (no nanosheets in the culture medium, 100% proliferation), although the reduction was more significant for the two latter samples. As the nanosheet concentration was progressively increased up to 100 μg mL^{-1}, cell proliferation values tended to decrease a bit in the presence of non-functionalized ce-MoS_2, whereas they increased slightly for the functionalized and annealed material. By contrast, the functionalized nanosheets (i.e., without annealing)

afforded significantly enhanced proliferation. Such a result suggests that the extensive grafting of acetic acid moieties (0.35-0.40 groups per MoS_2 unit in the functionalized material compared to ~0.16 after annealing at 160 ºC) has a clearly beneficial effect on the biocompatibility of the nanosheets. We also note that the performance of the functionalized material paralleled that of the graphene oxide nanosheets, as both appeared to stimulate substantially the proliferation of L929 cells with increasing concentration of the 2D material. On the other hand, at the highest nanosheet concentration (150 μg mL^{-1}), both non-functionalized and functionalized/annealed ce-MoS_2 became remarkably cytotoxic (~70-90% reduction in proliferation compared to the control test), while proliferation in the presence of the functionalized material was also seen to decrease relative to lower concentrations, but nonetheless kept pace with that of the control. This behavior was not observed with graphene oxide, which seemingly induced further cellular proliferation at the concentration of 150 μg mL^{-1}.

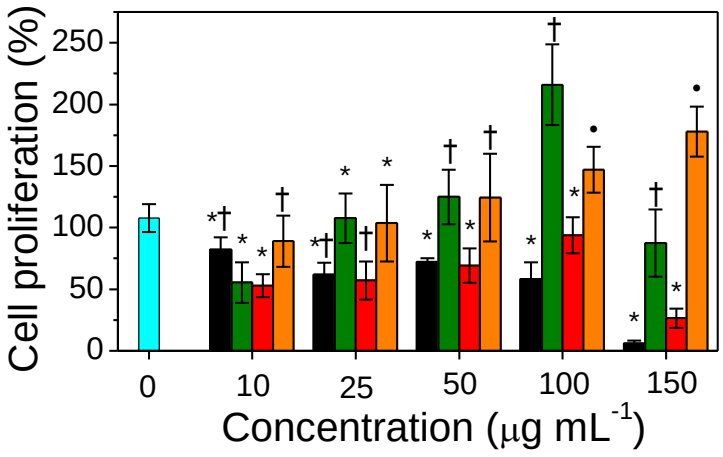

Figure 5. Results of L929 cell proliferation tests, based on the MTT assay, for aqueous dispersions of ce-MoS_2 (black), acetic acid-functionalized ce-MoS_2 (green), hydrothermically treated acetic acid-functionalized ce-MoS_2 (red), and graphene oxide (orange) at different concentrations. The light blue bar corresponds to the blank experiment. Significant statistical differences between the different materials according to the concentration data groups are indicated by the use of the different symbols *, † and •.

Overall, the L929 cell proliferation studies suggested the presence of acetic acid groups on the surface of the functionalized ce-MoS_2 nanosheets, and more specifically their associated carboxylic acid groups, to be a major driver in boosting the

biocompatibility of this material. This conclusion would be in line with previous results obtained using other nanostructured materials. For example, comparison between unreduced and reduced forms of graphene oxide, which only differ in the amount of oxygen functional groups (hydroxyl, epoxy, carboxylic) grafted onto the carbon lattice, revealed that the unreduced, heavily functionalized nanosheets were more biocompatible towards L929 cells than their reduced counterparts.[67] Similarly, functionalization of carbon nanotubes with either carboxylic or sulfonic acid groups was demonstrated to drastically reduce their in vitro cytotoxicity towards human dermal fibroblasts.[68] Despite the very different chemical composition and structure of the starting material in question, the present results indicate that covalent functionalization can be an effective strategy to improve the biocompatibility also in the case of ce-MoS_2.

3. Conclusions

In conclusion, the extensive covalent derivatization of chemically exfoliated MoS_2 (ce-MoS_2) nanosheets with acetic acid groups has been made possible based on reaction of the nanosheets with the corresponding organoiodide (i.e., iodoacetic acid). Analysis of the resulting products indicated that a high degree of functionalization can be attained with this approach (0.35-0.40 acetic acid groups grafted per MoS_2 unit). The ensuing presence of a very high density of carboxylic acid groups on the surface of the functionalized ce-MoS_2 nanosheets has demonstrated a number of practical benefits regarding the processing and practical use of this two-dimensional material. More to the point, the functionalized nanosheets exhibited greatly improved long-term (>6 months) colloidal dispersibility in aqueous medium, a much higher temporal retention of catalytic activity towards the reduction of nitroarenes as well as an enhanced ability to anchor silver nanoparticles and form hybrid structures in comparison with their non-functionalized counterpart. Likewise, hydrothermal treatment of the acetic acid-functionalized, 1T-phase ce-MoS_2 material at an appropriate temperature (160 ºC) afforded its extensive conversion to the original 2H phase while retaining at the same time a significant aqueous colloidal dispersibility in the phase-reversed nanosheets, which was not previously possible. Functionalization with acetic acid groups was also seen to significantly improve the in vitro biocompatibility of the ce-MoS_2 nanosheets, as evaluated by cell proliferation tests using murine fibroblasts. Finally, we anticipate that the abundant presence of carboxylic acid moieties on this functionalized material can be exploited, e.g., towards the covalent attachment of biomolecules (DNA, proteins, etc)

on the ce-MoS_2 nanosheets through well-developed chemistries, giving rise to hybrid structures with potential utility in biomedicine or biosensing.

4. Experimental

4.1. Materials and reagents

The following chemicals were obtained from Sigma-Aldrich and used as received: MoS_2 powder, *n*-hexane, 1.6 M *n*-butyllithium solution in *n*-hexane, 2-iodoacetamide, iodoacetic acid, iodomethanesulfonic acid, isopropanol, ethanol, silver nitrate, 4-nitrophenol, 4-nitroaniline, sodium borohydride and sodium hydroxide. Cellulose ester dialysis membranes (molecular weight cutoff: 14000 Da) were also acquired from Sigma-Aldrich, whereas alumina membrane filters (pore size: 0.2 μm; diameter: 25 mm) were purchased from Whatman. Milli-Q water (resistivity: 18.2 MΩ cm) was used throughout the studies.

4.2. Preparation of ce-MoS_2 nanosheets

The method originally described by Morrison and co-workers,[69] based on the intercalation of MoS_2 through reaction with *n*-butyllithium, was used for the preparation of ce-MoS_2 nanosheets. Caution must be exercised in dealing with such a highly pyrophoric reagent such as *n*-butyllithium. Specifically, a solution of *n*-butyllithium in *n*-hexane (1.6 M, 3 mL) was poured into MoS_2 powder (300 mg) in an argon-filled glovebox, and the mixture was left to stand for 48 h at room temperature under static conditions to obtain a lithium-intercalated product (Li_xMoS_2). The latter was then washed with *n*-hexane (60 mL) through filter paper to remove unreacted *n*-butyllithium as well as residues from its reaction with MoS_2, and immediately dispersed in water under bath sonication (JP Selecta Ultrasons system, frequency: 40 kHz, ultrasound power: 22 W L^{-1}) for 1 h to exfoliate the Li_xMoS_2 powder into individual nanosheets. The resulting aqueous dispersion of ce-MoS_2 nanosheets was purified by dialyzing it against water for 2 days and subsequently stored for further use. The concentration of the as-prepared ce-MoS_2 suspensions was estimated by UV-vis absorption spectroscopy on the basis of the Lambert-Beer law ($A/l = \alpha C$), where, A/l is the absorbance per unit length of optical path, C is the concentration and α is the extinction coefficient. The measurements were carried out at a wavelength of 450 nm, for which the extinction coefficient of ce-MoS_2 had been previously determined (α_{450} = 5045 m^{-1} g^{-1} L).[21]

4.3. Covalent functionalization of ce-MoS_2 nanosheets with acetic acid groups

Derivatization of ce-MoS_2 nanosheets with acetic acid groups was accomplished through a slight modification of the general scheme recently developed by Voiry *et al* for functionalization with acetamide and methyl groups, which is based on reaction of the nanosheets with the corresponding electrophilic organoiodides.[32] More to the point, iodoacetic acid (1.1×10^{-3} mol) was added to a mildly acidic (pH~ 4) aqueous dispersion of ce-MoS_2 nanosheets (40 mL, 0.44 mg mL^{-1}), and the mixture was left to stand for 5 days at room temperature. Afterwards, the dispersion was washed consecutively with isopropanol, ethanol and water via repeated cycles of sedimentation via centrifugation (1743*g*, 30 min) and re-suspension in the corresponding solvent (3 cycles for each solvent). Following completion of this washing procedure, the functionalized nanosheets were obtained in aqueous dispersion, which was dialyzed for 2 days against water to further remove unreacted species. For comparison purposes, treatment of ce-MoS_2 with either 2-iodoacetamide or iodomethanesulfonic acid instead of iodoacetic acid was also carried out, using the same molar amounts in all cases.

4.4. 1T-to-2H phase conversion of acetic acid-functionalized ce-MoS_2 nanosheets in aqueous dispersion

A hydrothermal treatment was implemented to induce conversion of the acetic acid-functionalized ce-MoS_2 from the 1T phase that was brought about by the lithium intercalation step back to the original 2H phase, while attaining at the same time a long-term colloidal stability in water of the converted nanosheets. Briefly, an aqueous dispersion of acetic acid-functionalized, 1T-phase ce-MoS_2 (20 mL, 0.2 mg mL^{-1}) was first purged with an argon flow (45 mL min^{-1}) for 30 min and then transferred to a Teflon-lined stainless steel autoclave (50 mL in capacity), where it was heated at 160 ºC for 4 h. After cooling down to room temperature, the dispersion was collected and its pH was adjusted to ~8 with addition of NH_3 to promote the colloidal stability of the nanosheets.

4.5. Testing of the catalytic activity of non-functionalized and acetic acid-functionalized ce-MoS_2 nanosheets

The catalytic activity of non-functionalized and acetic acid-functionalized ce-MoS_2 was evaluated on the basis of two reduction reactions, namely, the reduction of 4-

nitrophenol (4-NP) and 4-nitroaniline (4-NA) to 4-aminophenol (4-AP) and *p*-phenylenediamine (*p*-PDA), respectively, carried out with sodium borohydride as a reducing agent at room temperature. It has been previously shown that as-prepared ce-MoS_2 nanosheets are rather efficient catalysts for both reactions.[21] To this end, an aqueous mixed solution (2.5 mL) containing either non-functionalized or acetic acid-functionalized ce-MoS_2 nanosheets (concentration of ce-MoS_2 component: ~0.015 mg mL^{-1}), either 4-NP (0.12 mM) or 4-NA (0.11 mM), as well as sodium borohydride [72 mM (for 4-NP) or 110 mM (for 4-NA)] was prepared and then the reaction progress was monitored through UV-vis absorption spectroscopy by measuring the intensity of the peak located either at ~400 nm (characteristic of 4-NP) or at ~382 nm (characteristic of 4-NA).

4.6. Growth of Ag NPs onto non-functionalized and acetic acid-functionalized ce-MoS_2 nanosheets

The growth of Ag NPs onto ce-MoS_2 nanosheets was carried out in the aqueous phase and was based on the reduction of a metal precursor (silver nitrate) with sodium borohydride in the presence of the nanosheets. Specifically, mixed aqueous solutions containing 0.5 mM silver nitrate, 22.5 mM sodium borohydride and 0.1 mg mL^{-1} ce-MoS_2 were prepared and left to react undisturbed for 2 h. Subsequently, the reacted product was purified by two cycles of sedimentation through centrifugation (20000 *g*, 20 min) and re-dispersion in water.

4.7. Biocompatibility testing of ce-MoS_2 materials

Murine fibroblasts (L929 cell line, ECACC 85011425) were chosen to evaluate the biocompatibility of the different ce-MoS_2 materials, as these fibroblasts are highly stable, fast-growing and commonly used in cell culture studies for cytotoxicity assessment. The fibroblasts were seeded at a density of 5500 cells cm^{-2} onto 96-well tissue culture polystyrene plates. The culture medium used was Dulbecco's modified Eagle's medium (DMEM) supplemented with 10% fetal bovine serum (FBS), penicillin (100 U mL^{-1}), and streptomycin (100 mg mL^{-1}), and incubation was carried out at 37 °C in a 5% CO_2 atmosphere. 72 hours after seeding, the culture medium was replaced by fresh medium that also contained a given type of ce-MoS_2 (non-functionalized, acetic acid-functionalized as well as functionalized and hydrothermally treated) at different concentrations: 10, 25, 50, 100 and 150 μg mL^{-1}. For comparison purposes, graphene

oxide (obtained from Graphenea) was also assayed at the same concentrations. The cell proliferation tests were carried out 24 h after addition of the MoS_2-containing media by means of the MTT assay (Sigma-Aldrich). This assay is based on the enzymatic reduction of the tetrazolium dye 3-(4,5-dimethylthiazol-2-yl)-2,5-diphenyltetrazolium bromide (MTT) to its water-insoluble formazan derivative.[70] To this end, the MoS_2-containing culture medium was taken out from each seeded well and then 200 μL of aqueous MTT solution (1 mg mL^{-1}) were added to each well. To exclude interference of the MoS_2 material on the MTT assay, special emphasis was placed on thoroughly removing the MoS_2-containing medium from the wells. After incubation at 37 °C under 5% CO_2 atmosphere for 4 h, the MTT solution was carefully removed, 100 μL of dimethyl sulfoxide were added to solubilize the generated formazan crystals and finally the absorbance of this reaction product was measured with a BMG FLUOstar Galaxy microplate reader (MTX Lab Systems, Inc.) at 570 nm and the reference wavelength of 690 nm. Statistical analysis of the results was performed with the SPSS Statistics software. When data followed the normality and homogeneity of variance requirements, their means were compared by the parametric test ANOVA followed by Bonferroni's post hoc multiple *t*-test. The significance level was set to a p-value < 0.05.

4.8. Characterization techniques

The different ce-MoS_2 materials were characterized by UV-vis absorption spectroscopy, X-ray photoelectron spectroscopy (XPS), attenuated total reflection Fourier transform infrared (ATR-FTIR) spectroscopy, atomic force microscopy (AFM) and transmission electron microscopy (TEM). UV-vis absorption spectra were recorded on a double-beam Heλios α spectrophotometer (Thermo Spectronics). XPS was carried out with a SPECS system at a pressure of 10^{-7} Pa with a non-monochromatic Mg K_α X-ray source operated at a power of 100 W. The high resolution spectra were taken at pass energy of 10 eV with an energy step of 0.1 eV. The binding energy scale of all spectra was referenced to the maximum of the C1s band for adventitious carbon. ATR-FTIR spectroscopy was accomplished on a Nicolet 8700 spectrometer (Thermo Scientific) with a diamond ATR crystal. Specimens for XPS and ATR-FTIR spectroscopy were prepared in the form of free-standing, paper-like films by vacuum-filtering aqueous dispersions of the corresponding ce-MoS_2 sample (60 mL, 0.1 mg mL^{-1}) through anodic alumina membrane filters. AFM imaging of the ce-MoS_2 nanosheets was performed

with a Nanoscope IIIa Multimode apparatus (Veeco Instruments) in the tapping mode of operation, using silicon cantilevers (spring constant ~40 N m^{-1}; resonance frequency ~250-300 kHz). To this end, a small volume of a diluted aqueous dispersion of the nanosheets (~10 μL, ~0.05 mg mL^{-1}) was drop-cast onto a freshly cleaved mica substrate and allowed to dry under ambient conditions. TEM images were recorded on a JEOL 2000 EX-II microscope operated at 160 kV. In this case, the aqueous ce-MoS_2 dispersion was diluted with an equal volume of ethanol, and then 50 μL of the resulting suspension were drop-cast onto a copper grid (200 mesh) covered with a continuous amorphous carbon film and allowed to dry under ambient conditions.

Supporting Information. Evidence for the limited colloidal stability of as–prepared aqueous dispersions of ce-MoS_2; survey XPS spectra of ce–MoS_2 treated with iodomethanesulfonic and iodoacetic acid.

Acknowledgements

Financial support from the Spanish Ministerio de Economía y Competitividad (MINECO) and the European Regional Development Fund (FEDER) through project MAT2015-69844-R is gratefully acknowledged, as well as partial support of the ERDF/FEDER. Operative Program of the Región de Murcia 2007–2013. We also acknowledge partial funding by Plan de Ciencia, Tecnología e Innovación 2013-2017 del Principado de Asturias and FEDER through grant GRUPIN14-056. M.A-V. and J.M.M. are thankful to MINECO and the Spanish Ministerio de Educación, Cultura y Deporte (MECD), respectively, for their pre-doctoral contracts.

References

(1) Ferrari, A.C.; Bonaccorso, F.; Falko, V.; Novoselov, K. S.; Roche, S.; Bøggild, P.; Borini, S.; Koppens, F.; Palermo, V.; Pugno N.; Garrido, J. A.; Sordan, R.; Bianco, A.; Ballerini, L.; Prato, M.; Lidorikis, E.; Kivioja, J.; Marinelli, C.; Ryhänen, T.; Morpurgo, A.; Coleman, J. N.; Nicolosi, V.; Colombo, L.; Fert, A.; Garcia-Hernandez, M.; Bachtold, A.; Schneider, G. F.; Guinea, F.; Dekker, C.; Barbone, M.; Galiotis, C.; Grigorenko, A.; Konstantatos, G.; Kis, A.; Katsnelson, M.; Beenakker, C. W. J.; Vandersypen, L.; Loiseau, A.; Morandi, V.; Neumaier, D.; Treossi, E.; Pellegrini, V.;

Polini, M.; Tredicucci, A.; Williams, G. M.; Hong, B. H.; Ahn, J. H.; Kim, J. M.; Zirath, H.; van Wees, B. J.; van der Zant, H.; Occhipinti, L.; Di Matteo, A.; Kinloch, I. A.; Seyller, T.; Quesnel, E.; Feng, X.; Teo, K.; Rupesinghe, N.; Hakonen, P.; Neil, S. R. T.; Tannock, Q.; Löfwander, T.; Kinaret, J. Science and Technology Roadmap for Graphene, Related Two-Dimensional Crystals, and Hybrid Systems. *Nanoscale* **2015**, *7*, 4598–4810.

(2) Bhimanapati, G. R.; Lin, Z.; Meunier, V.; Jung, Y.; Cha, J.; Das, S; Xiao, D.; Son, Y.; Strano, M. S.; Cooper, V. R.; Liang, L.; Louie, S. G.; Ringe, E.; Zhou, W.; Kim, S. S.; Naik, R. R.; Sumpter, B. G.; Terrones, H.; Xia, F.; Wang, Y.; Zhu, J.; Akinwande, D.; Alem, N.; Schuller, J. A.; Schaak, R. E. Terrones, M.; Robinson, J. A. Recent Advances in Two-Dimensional Materials beyond Graphene. *ACS Nano* **2015**, *9*, 11509–11539.

(3) Lv, R.; Robinson, J.A.; Schaak, R.E.; Sun, D.; Sun, Y.; Mallouk, T.E.; Terrones, M. Transition Metal Dichalcogenides and Beyond: Synthesis, Properties, and Applications of Single- and Few-Layer Nanosheets. *Acc. Chem. Res.* **2015**, *48*, 56–64.

(4) Subbaiah, Y.P.V.; Saji, K.J.; Tiwari, A. Atomically Thin MoS2: A Versatile Nongraphene 2D Material. *Adv. Funct. Mater.* **2016**, *26*, 2046–2069.

(5) Wang, Q.H.; Kalantar-Zadeh, K.; Kis, A.; Coleman, J.N.; Strano, M.S. Electronics and Optoelectronics of Two-Dimensional Transition Metal Dichalcogenides. *Nat. Nanotechnol.* **2012**, *7*, 699–712.

(6) Lu, Q.; Yu, Y.; Ma, Q.; Chen, B.; Zhang, H. 2D Transition-Metal-Dichalcogenide-Nanosheet-Based Composites for Photocatalytic and Electrocatalytic Hydrogen Evolution Reactions. *Adv. Mater.* **2016**, *28*, 1917–1933.

(7) Latorre-Sánchez, M.; Esteve-Adell, I.; Primo, A.; García, H. Innovative Preparation of MoS_2–graphene Heterostructures Based on Alginate Containing $(NH_4)_2MoS_4$ and their Photocatalytic Activity for H_2 Generation. *Carbon* **2015**, *81*, 587–596.

(8) Huang, Y.; Guo, J.; Kang, Y.; Ai, Y.; Li, C.M. Two Dimensional Atomically Thin MoS_2 Nanosheets and their Sensing Applications. *Nanoscale* **2015**, *7*, 19358–19376.

(9) Chimene, D.; Alge, D.L.; Gaharwar, A.K. Two-Dimensional Nanomaterials for Biomedical Applications: Emerging Trends and Future Prospects. *Adv. Mater.* **2015**, *27*, 7261–7284.

(10) Shi, Y.; Li, H.; Li, L.-J. Recent Advances in Controlled Synthesis of Two-Dimensional Transition Metal Dichalcogenides via Vapour Deposition Techniques. *Chem. Soc. Rev.* **2015**, *44*, 2744–2756.

(11) Varrla, E.; Backes, C.; Paton, K.R.; Harvey, A.; Gholamvand, Z.; McCauley, J. Coleman, J.N. Large-Scale Production of Size-Controlled MoS_2 Nanosheets by Shear Exfoliation. *Chem. Mater*. **2015**, *27*, 1129–1139.

(12) Quinn, M. D. J.; Ho, N. H.; Notley, S. M. Aqueous Dispersions of Exfoliated Molybdenum Disulfide for Use in Visible-Light Photocatalysis. *ACS Appl. Mater. Interfaces* **2013**, *5*, 12751−12756.

(13) Eda, G.; Yamaguchi, H.; Voiry, D.; Fujita, T.; Chen, M.; Chhowalla, M. Photoluminiscence from Chemically Exfoliated MoS_2. *Nano Lett.* **2011**, *11*, 5111–5116.

(14) Zheng, J.; Zhang, H.; Dong, S.; Liu, Y.; Nai, C.T.; Shin, H.S.; Jeong, H.Y., Liu, B. Loh, K.P. High Yield Exfoliation of Two-Dimensional Chalcogenides Using Sodium Naphthalenide *Nat. Commun.* **2014**, *5*, 2995.

(15) Jeffery, A. A.; Nethravathi, C.; Rajamathi, M. Two-Dimensional Nanosheets and Layered Hybrids of MoS_2 and WS_2 through Exfoliation of Ammoniated MS_2 (M = Mo,W). *J. Phys. Chem. C* **2014**, 118, 1386–1396.

(16) Niu, L.; Coleman, J.N.; Zhang, H.; Shin, H.; Chhowalla, M.; Zheng, Z. Production of Two-Dimensional Nanomaterials via Liquid-Based Direct Exfoliation. *Small* **2016**, *12*, 272–293.

(17) Chhowalla, M.; Shin, H.S.; Eda, G.; Li, L.-J.; Loh, K.P.; Zhang, H. The Chemistry of Two-Dimensional Layered Transition Metal Dichalcogenide Nanosheets. *Nat. Chem.* **2013**, *5*, 263–275.

(18) Zeng, Z.; Yin, Z.; Huang, X.; Li, H.; He, Q.; Lu, G.; Boey, F.; Zhang, H. Single-Layer Semiconducting Nanosheets: High-Yield Preparation and Device Fabrication *Angew. Chem. Int. Ed.* **2011**, *50*, 11093–11097.

(19) Lukowski, M.A.; Daniel, A.S.; Meng, F.; Forticaux, A.; Li, L.; Jin, S. Enhanced Hydrogen Evolution Catalysis from Chemically Exfoliated Metallic MoS_2 Nanosheets. *J. Am. Chem. Soc.* **2013**, *135*, 10274–10277.

(20) Bai, S.; Wang, L.; Chen, X.; Du, J.; Xiong, Y. Chemically Exfoliated Metallic MoS_2 Nanosheets: A Promising Supporting Co-Catalyst for Enhancing the Photocatalytic Performance of TiO_2 Nanocrystals. *Nano Res.* **2015**, *8*, 175–183.

(21) Guardia, L.; Paredes, J.I.; Munuera, J.M.; Villar-Rodil, S.; Ayán-Varela, M.; Martínez-Alonso, A.; Tascón, J.M.D. Chemically Exfoliated MoS_2 Nanosheets as an Efficient Catalyst for Reduction Reactions in the Aqueous Phase. *ACS Appl. Mater. Interfaces* **2014**, *6*, 21702–21710.

(22) Acerce, M.; Voiry, D.; Chhowalla, M. Metallic 1T Phase MoS_2 Nanosheets as Supercapacitor Electrode Materials. *Nat. Nanotechnol.* **2015**, *10*, 313–318.

(23) Chou, S.C.; Kaehr, B.; Kim, J.; Foley, B.M.; De, M.; Hopkins, P.E.; Huang, J.; Brinker, C.J.; Dravid, V.P. Chemically Exfoliated MoS_2 as Near-Infrared Photothermal Agents. *Angew. Chem. Int. Ed.* **2013**, *52*, 4160–4164.

(24) Ge, J.; Ou, E.-C.; Yu, R.-Q.; Chu, X. A Novel Aptameric Nanobiosensor Based on the Self-assembled DNA–MoS_2 Nanosheet Architecture for Biomolecule Detection. *J. Mater. Chem. B* **2014**, *2*, 625–628.

(25) Chou, S.S.; De, M.; Kim, J.; Byun, S.; Dykstra, C.; Yu, J.; Huang, J.; Dravid, V.P. Ligand Conjugation of Chemically Exfoliated MoS_2. *J. Am. Chem. Soc.* **2013**, *135*, 4584–4587.

(26) Chou, S.S.; Huang, Y.-K.; Kim, J.; Kaehr, B.; Foley, B.M.; Lu, P.; Dykstra, C.; Hopkins, P.E.; Brinker, C.J.; Huang, J.; Dravid, V.P. Controlling the Metal to Semiconductor Transition of MoS_2 and WS_2 in Solution. *J. Am. Chem. Soc.* **2015**, *137*, 1742–1745.

(27) Cheng, Z.; He, B.; Zhou, L. A General One-Step Approach for in Situ Decoration of MoS_2 Nanosheets with Inorganic Nanoparticles. *J. Mater. Chem. A* **2015**, *3*, 1042–1048.

(28) Chng, E.L.; Sofer, Z.; Pumera, M. MoS_2 Exhibits Stronger Toxicity with Increased Exfoliation. *Nanoscale* **2014**, *6*, 14412–14418.

(29) Presolski, S.; Pumera, M. Covalent Functionalization of MoS_2. *Mater. Today* **2016**, *19*, 140–145.

(30) Chen, X.; McDonald, A.R. Functionalization of Two-Dimensional Transition-Metal Dichalcogenides. *Adv. Mater.* **2016**, *28*, 5738–5746.

(31) Cho, K.; Min, M.; Kim, T.-Y.; Jeong, H.; Pak, J.; Kim, J.-K.; Jang, J.; Yun, S.J. Lee, Y.H.; Hong, W.-K.; Lee, T. Electrical and Optical Characterization of MoS_2 with Sulfur Vacancy Passivation by Treatment with Alkanethiol Molecules. *ACS Nano* **2015**, *9*, 8044–8053.

(32) Voiry, D.; Goswami, A.; Kappera, R.; Silva, C.D.C.E.; Kaplan, D.; Fujita, T.; Chen, M.; Asefa, T.; Chhowalla, M. Covalent Functionalization of Monolayered Transition Metal Dichalcogenides by Phase Engineering. *Nat. Chem.* **2015**, *7*, 45–49.

(33) Knirsch, K.C.; Berner, N.C.; Nerl, H.C.; Cucinotta, C.S.; Gholamvand, Z.; McEvoy, N.; Wang, Z.; Abramovic, I.; Vecera, P.; Halik, M.; Sanvito, S.; Duesberg, G.S.; Nicolosi, V.; Hauke, F.; Hirsch, A.; Coleman, J.N.; Backes, C. Basal-Plane Functionalization of Chemically Exfoliated Molybdenum Disulfide by Diazonium Salts. *ACS Nano* **2015**, *9*, 6018–6030.

(34) Heising, J.; Kanatzidis, M.G. Exfoliated and Restacked MoS_2 and WS_2: Ionic or Neutral Species? Encapsulation and Ordering of Hard Electropositive Cations. *J. Am. Chem. Soc.* **1999**, *121*, 11720–11732.

(35) Guardia, L.; Paredes, J.I.; Rozada, R.; Villar-Rodil, S.; Martínez-Alonso, A.; Tascón, J.M.D. Production of Aqueous Dispersions of Inorganic Graphene Analogues by Exfoliation and Stabilization with Non-Ionic Surfactants. *RSC Adv.* **2014**, *4*, 14115–14127.

(36) Wang, Y.; Ou, J.Z.; Chrimes, A.F.; Carey, B.J.; Daeneke, T.; Alsaif, M.M.Y.A.; Mortazavi, M.; Zhuiykov, S.; Medhekar, N.; Bhaskaran, M.; Friend, J.R.; Strano, M.S. Kalantar-Zadeh, K. Plasmon Resonances of Highly Doped Two-Dimensional MoS_2. *Nano Lett.* **2015**, *15*, 883–890.

(37) Tang, Q.; Jiang, D. Stabilization and Band-Gap Tuning of the 1T-MoS_2 Monolayer by Covalent Functionalization. *Chem. Mater.* **2015**, *27*, 3743–3748.

(38) P. Swift. Adventitious Carbon-The Panacea for Energy Referencing? *Surf. Interface Anal.* **1982**, *4*, 47–51.

(39) Hu, H.; Xin, J.H.; Hu, H.; Wang, X.; Miao, D.; Liu, Y. Synthesis and Stabilization of Metal Nanocatalysts for Reduction Reactions – a Review. *J. Mater. Chem. A* **2015**, *3*, 11157–11182.

(40) Ayán-Varela, M.; Paredes, J.I.; Guardia, L.; Villar-Rodil, S.; Munuera, J.M.; Díaz-González, M.; Fernández-Sánchez, C.; Martínez-Alonso, A.; Tascón, J.M.D. Achieving Extremely Concentrated Aqueous Dispersions of Graphene Flakes and Catalytically Efficient Graphene-Metal Nanoparticle Hybrids with Flavin Mononucleotide as a High-Performance Stabilizer. *ACS Appl. Mater. Interfaces* **2015**, *7*, 10293–10307.

(41) Cheng, Z.; Liao, J.; He, B.; Zhang, F.; Zhang, F.; Huang, X.; Zhou, L. One-Step Fabrication of Graphene Oxide Enhanced Magnetic Composite Gel for Highly Efficient Dye Adsorption and Catalysis. *ACS Sustainable Chem. Eng.* **2015**, *3*, 1677–1685.

(42) Zhang, B.; Zhan, X.; Zhao, P.; Li, Z. Ionic Liquid-Mediated Synthesis of Unique PtPd Bimetallic Particles with Tiny Subunits for Efficient Electrocatalytic and Catalytic Applications. *RSC Adv.* **2015**, *5*, 57640–57646.

(43) Halder, A.; Patra, S.; Viswanath, B.; Munichandraiah, N.; Ravishankar, N. Porous, Catalytically Active Palladium Nanostructures by Tuning Nanoparticle Interactions in an Organic Medium. *Nanoscale* **2011**, *3*, 725–730.

(44) Premkumar, T.; Geckeler, K.E. Palladium Nanostructures: Solvent-Less, One-Pot Mechano-Chemical Synthesis Using Poly(vinylpyrolidone) and Catalytic Activity. *Colloids Surf. A* **2014**, *456*, 49–54.

(45) Xu, D.; Diao, P.; Jin, T.; Wu, Q.; Liu, X.; Guo, X.; Gong, H.; Li, F.; Xiang, M.; Ronghai, Y. Iridium Oxide Nanoparticles and Iridium/Iridium Oxide Nanocomposites: Photochemical Fabrication and Application in Catalytic Reduction of 4-Nitrophenol. *ACS Appl. Mater. Interfaces* **2015**, *7*, 16738–16749.

(46) Kim, I.; Son, H.Y.; Yang, M.Y.; Nam, Y.S. Bioinspired Design of an Immobilization Interface for Highly Stable, Recyclable Nanosized Catalysts. *ACS Appl. Mater. Interfaces* **2015**, *7*, 14415–14422.

(47) Cheng, X.; Fu, A.; Li, H.; Wang, Y.; Guo, P.; Liu, J.; Zhang, J.; Zhao, X.S. Sustainable Preparation of Copper Particles Decorated Carbon Microspheres and Studies on Their Bactericidal Activity and Catalytic Properties. *ACS Sustainable Chem. Eng.* **2015**, *3*, 2414–2422.

(48) Barman, B.K.; Nanda, K.K. Uninterrupted Galvanic Reaction for Scalable and Rapid Synthesis of Metallic and Bimetallic Sponges/Dendrites as Efficient Catalysts for 4-Nitrophenol Reduction. *Dalton Trans.* **2015**, *44*, 4215–4222.

(49) Huang, C.; Ye, W.; Liu, Q.; Qiu, X. Dispersed Cu_2O Octahedrons on h-BN Nanosheets for p-Nitrophenol Reduction. *ACS Appl. Mater. Interfaces* **2014**, *6*, 14469–14476.

(50) Zuo, W.; Yu, G.; Dong, Z. A MOF-Derived Nickel Based N-Doped Mesoporous Carbon Catalyst with High Catalytic Activity for the Reduction of Nitroarenes. *RSC Adv.* **2016**, *6*, 11749–11753.

(51) Kong, X.; Sun, Z.; Chen, M.; Chen, C.; Chen, Q. Metal-Free Catalytic Reduction of 4-Nitrophenol to 4-Aminophenol by N-Doped Graphene. *Energy Environ. Sci.* **2013**, *6*, 3260–3266.

(52) Kong, X.; Chen, Q.; Lun, Z. Probing the Influence of Different Oxygenated Groups on Graphene Oxide's Catalytic Performance. *J. Mater. Chem. A* **2014**, *2*, 610–613.

(53) Hu, H.; Xin, J.H.; Hu, H.; Wang, X. Structural and Mechanistic Understanding of an Active and Durable Graphene Carbocatalyst for Reduction of 4-Nitrophenol at Room Temperature. *Nano Res.* **2015**, *8*, 3992–4006.

(54) Yang, Y.; Zhang, W.; Ma, X.; Zhao, H.; Zhang, X. Facile Construction of Mesoporous N-Doped Carbons as Highly Efficient 4-Nitrophenol Reduction Catalysts. *ChemCatChem* **2015**, *7*, 3454–3459.

(55) Huang, G.; Yang, L.; Ma, X.; Jiang, J.; Yu, S.-H.; Jiang, H.-L. Metal–Organic Framework-Templated Porous Carbon for Highly Efficient Catalysis: The Critical Role of Pyrrolic Nitrogen Species. *Chem. Eur. J.* **2016**, *22*, 3470–3477.

(56) Zhang, X.; Liu, D.; Yang, L.; Zhou, L.; You, T. Self-Assembled Three-Dimensional Graphene-Based Materials for Dye Adsorption and Catalysis. *J. Mater. Chem. A* **2015**, *3*, 10031–10037.

(57) Ghosh, S.K.; Mandal, M.; Kundu, S.; Nath, S.; Pal, T. Bimetallic Pt–Ni Nanoparticles Can Catalyze Reduction of Aromatic Nitro Compounds by Sodium Borohydride in Aqueous Solution. *Appl. Catal. A* **2004**, *268*, 61–66.

(58) Karaoġlu, E.; Özel, U.; Caner, C.; Baykal, A.; Summak, M.M.; Sözeri, H. Synthesis and Characterization of $NiFe_2O_4$–Pd Magnetically Recyclable Catalyst for Hydrogenation Reaction. *Mater. Res. Bull.* **2012**, *47*, 4316–4321.

(59) Kong, L.; Lu, X.; Jin, E.; Jiang, S.; Bian, X.; Zhang, W.; Wang, C. Constructing Magnetic Polyaniline/Metal Hybrid Nanostructures Using Polyaniline/Fe_3O_4 Composite Hollow Spheres as Supports. *J. Solid State Chem.* **2009**, *182*, 2081–2087.

(60) Yang, M.-Q.; Pan, X.; Zhang, N.; Xu, Y.-J. A Facile One-Step Way to Anchor Noble Metal (Au, Ag, Pd) Nanoparticles on a Reduced Graphene Oxide Mat with Catalytic Activity for Selective Reduction of Nitroaromatic Compounds. *CrystEngComm* **2013**, *15*, 6819–6828.

(61) Chiu, C.-Y.; Chung, P.-J.; Lao, K.-U.; Liao, C.-W.; Huang, M.H. Facet-Dependent Catalytic Activity of Gold Nanocubes, Octahedra, and Rhombic Dodecahedra toward 4-Nitroaniline Reduction. *J. Phys. Chem. C* **2012**, *116*, 23757–23763.

(62) Vadakkekara, R.; Chakraborty, M.; Parikh, P.A. Reduction of Aromatic Nitro Compounds on Colloidal Hollow Silver Nanospheres. *Colloids Surf. A* **2012**, *399*, 11–17.

(63) Mondal, B.; Som, A.; Chakraborty, I.; Baksi, A.; Sarkar, D.; Pradeep, T. Unusual Reactivity of MoS_2 Nanosheets. *Nanoscale* **2016**, *8*, 10282–10290.

(64) Liu, T.; Wang, C.; Gu, X.; Gong, H.; Cheng, L.; Shi, X.; Feng, L.; Sun, B.; Liu, Z. Drug Delivery with PEGylated MoS_2 Nano-sheets for Combined Photothermal and Chemotherapy of Cancer. *Adv. Mater.* **2014**, *26*, 3433–3440.

(65) Wang, Z.; Zhu, W.; Qiu, Y.; Yi, X.; von dem Bussche, A.; Kane, A.; Gao, H.; Koski, K.; Hurt, R. Biological and Environmental Interactions of Emerging Two-Dimensional Nanomaterials. *Chem. Soc. Rev.* **2016**, *45*, 1750–1780.

(66) Wang, X.; Mansukhani, N.D.; Guiney, L.M.; Ji, Z.; Chang, C.H.; Wang, M.; Liao, Y.-P.; Song, T.-B.; Sun, B.; Li, R.; Xia, T.; Hersam, M.C.; Nel, A.E. Differences in the Toxicological Potential of 2D versus Aggregated Molybdenum Disulfide in the Lung. *Small* **2015**, *11*, 5079–5087.

(67) Wojtoniszak, M.; Chen, X.; Kalenczuk, R.J.; Wajda, A.; Łapczuk, J.; Kurzewski, M.; Drozdzik, M.; Chu, P.K.; Borowiak-Palen, E. Synthesis, Dispersion, and Cytocompatibility of Graphene Oxide and Reduced Graphene Oxide. *Colloid Surf. B* **2012**, *89*, 79–85.

(68) Sayes, C.M.; Liang, F.; Hudson, J.L.; Mendez, J.; Guo, W.; Beach, J.M.; Moore, V.C.; Doyle, C.D.; West, J.L.; Billups, W.E.; Ausman, K.D.; Colvin, V.L. Functionalization Density Dependence of Single-Walled Carbon Nanotubes Cytotoxicity In Vitro. *Toxicol. Lett.* **2006**, *161*, 135–142.

(69) Joensen, P.; Frindt, R.F.; Morrison, S.R. Single-Layer MoS_2. *Mater. Res. Bull.* **1986**, *21*, 457–461.

(70) Vistica, D.T.; Skehan, P.; Scudiero, D.; Monks, A.; Pittman, A.; Boyd, M.R. Tetrazolium-based Assays for Cellular Viability: A Critical Examination of Selected Parameters Affecting Formazan Production. *Cancer Res.* **1991**, *51*, 2515–2520.

Supporting Information

for

Impact of Covalent Functionalization on the Aqueous Processability, Catalytic Activity and Biocompatibility of Chemically Exfoliated MoS_2 Nanosheets

Juan I. Paredes,[a] Jose M. Munuera,[a] Silvia Villar–Rodil,[a,*] Laura Guardia,[a] Miguel Ayán–Varela,[a] Ana Pagán, [b] Salvador Aznar-Cervantes,[b] Jose L. Cenis,[b] Amelia Martínez–Alonso,[a] Juan M.D. Tascón[a]

[a]Instituto Nacional del Carbón, INCAR-CSIC, Apartado 73, 33080 Oviedo, Spain

[b]Instituto Murciano de Investigación y Desarrollo Agrario y Alimentario (IMIDA), Calle Mayor 1, 30150 La Alberca, Spain

*Corresponding author: E-mail address: silvia@incar.csic.es (S. Villar-Rodil)

Contents

S1. Evidence for the limited colloidal stability of as–prepared aqueous dispersions of ce-MoS_2

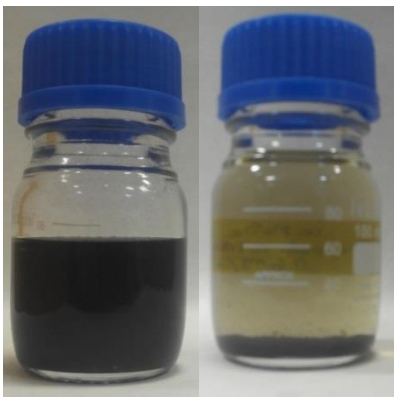

Figure S1. Digital photographs of an aqueous dispersion of ce-MoS_2 at a concentration of ~0.8 mg mL^{-1} just prepared (left) and 3 weeks after its preparation (right).

S2. Survey XPS spectra of ce–MoS_2 treated with iodomethanesulfonic and iodoacetic acid

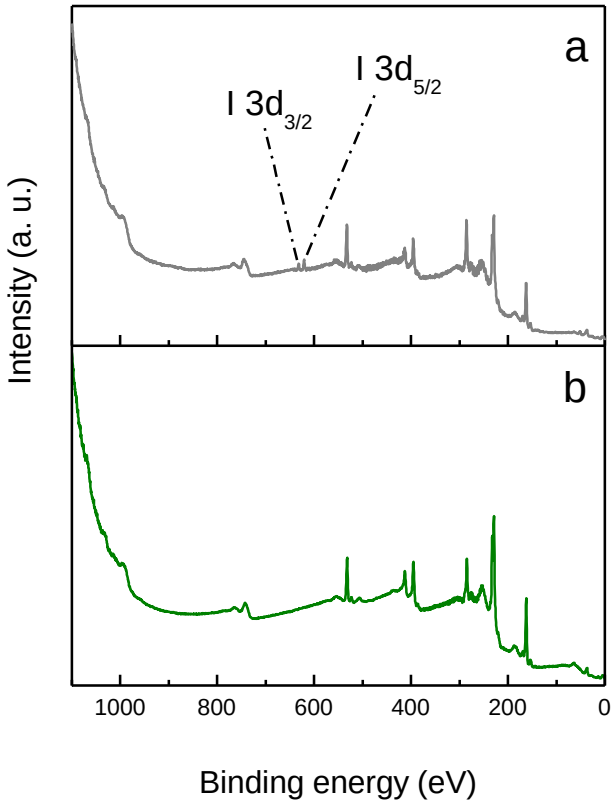

Figure S2. XPS survey spectra of ce–MoS_2 treated with (a) iodomethanesulfonic acid and with (b) iodoacetic acid.

ARTÍCULO VI

5.3 Síntesis y aplicaciones de óxido de cobalto

Artículo VII

A direct route to activated two-dimensional cobalt oxide nanosheets for electrochemical energy storage, catalytic and environmental applications, Munuera, J. M.; Paredes, J. I.; Villar-Rodil, S.; García-Dalí, S.; Castro-Muñiz, A.; Martínez-Alonso, A.; Tascón J. M. D., Journal of Colloid and Interface Science 2019, 539, 263–276.

Dentro del campo de los materiales bidimensionales, una de las familias que está despertando interés de la comunidad científica es la de los materiales bidimensionales no laminares, como pueden ser los óxidos TiO_2, SnO_2, α-Fe_2O_3 y Co_3O_4, entre otros. Éstos, a diferencia de los materiales bidimensionales laminares, no possen una estructura laminar en su forma *bulk* tridimensional, sino que poseen una estructura cristalina con enlaces fuertes en las tres direcciones espaciales. Para obtener láminas delgadas de estos materiales, generalmente se utilizan metodologías ascendentes (bottom-up), en las que se utilizan precursores moleculares que se ensamblan por la acción de surfactantes en fase líquida. Estos materiales bidimensionales no laminares han despertado interés porque, al igual que otros materiales bidimensionales, su morfología laminar implica un aumento de su superficie específica y su reactividad, y abre la posibilidad de utilizarlos en aplicaciones relacionadas con el almacenamiento y conversión de energía y la catálisis. Entre ellos, el Co_3O_4, por su bajo coste, baja toxicidad y alta estabilidad, ha despertado interés como catalizador de la reacción de evolución de oxígeno, y como electrodo de supercondensadores y de baterías de litio. Los métodos convencionales para la preparación de óxidos de cobalto bidimensionales ricos en centros de Co(II) activos consisten habitualmente en la obtención de Co_3O_4 mediante calcinación a alta temperatura de precursores, para posteriormente activar el material mediante un proceso de reducción. Estos procesos son típicamente ineficientes, por lo que es conveniente desarrollar métodos de preparación más directos de los materiales activados, en los que no sea necesario una etapa de reducción.

En el **artículo VII** se detalla un método de preparación de láminas de óxido de cobalto activado y sus aplicaciones como electrodos para almacenamiento de carga eléctrica, como catalizador de la reducción de nitroarenos y como adsorbente de colorantes en agua.

La preparación del material consiste en un primer paso hidrotérmico de formación de láminas de CoO amorfo a 170 ºC a partir de acetato de cobalto (II). Mediante la adición de un surfactante que forma una fase micelar inversa de tipo laminar, se genera un sólido (CoO amorfo) con morfología laminar. A continuación, este óxido se calcinó a temperaturas de 250, 350 y 450 ºC para así obtener láminas de Co_3O_4 activado. Esta activación del óxido, cuantificada en base a la relación Co(II)/Co(III), es muy relevante de cara a las aplicaciones del material, ya que el número de centros catalíticos y electroactivos está directamente relacionado con los centros de Co(II). Además, uno de los factores limitantes de la aplicación en almacenamiento de energía es la conductividad, y ésta depende directamente tanto del grado de cristalinidad como del grado de activación. El análisis de los materiales mediante difracción de rayos X de polvo y XPS permite confirmar la naturaleza nanocristalina de las muestras, así como evaluar su proporción de Co(II)/Co(III), que resulta ser de ~1.4 para los óxidos calcinados a 250 y 350 ºC y de ~1.3 para el calcinado a 450 ºC. Los óxidos se estudiaron también mediante microscopía electrónica de barrido por transmisión (STEM) y AFM, y gracias a estas técnicas se observó el efecto del tratamiento térmico en la morfología de las láminas. El material sin calcinar está formado por láminas lisas y delgadas, mientras que la calcinación produce que las láminas cristalicen, haciéndose más gruesas y dando lugar a la aparición de poros.

Los materiales preparados por este método (sin calcinar y calcinados a diferentes temperaturas) se estudiaron como electrodos en almacenamiento electroquímico de carga eléctrica. Todos los materiales presentan voltamogramas con intensos picos de oxidación y reducción, es decir, una respuesta de tipo batería. Los cuatro materiales tienen comportamientos cualitativamente similares debido a su naturaleza. Sin embargo, el calcinado a 350ºC, debido a que una buena combinación de entre su conductividad eléctrica (que aumenta al aumentar la temperatura de calcinación) y proporción Co(II)/Co(III) (que disminuye al aumentar esa temperatura), es el que presenta los mejores resultados, con una capacidad de ~293 mA h g^{-1} medida a 1 A g^{-1}. Este valor está entre los mejores obtenidos para materiales de Co_3O_4 nanoestructurados, con la ventaja de tener un método de preparación relativamente sencillo.

Los cuatro materiales se utilizaron también como catalizadores para la reducción de 4-nitrofenol y 4-nitroanilina con borohidruro de sodio. En este caso, la conductividad no es un factor tan relevante como lo son el número de centros de Co(II) y el área

superficial de las láminas. Los mejores resultados los presentan las láminas sin calcinar y calcinadas a 250ºC, con valores de actividad catalítica comparables y en la mayoría de casos superiores a los de materiales derivados de óxidos de cobalto, otros óxidos metálicos y nanopartículas metálicas que no estén basados en metales nobles.

Debido a su morfología laminar y la facilidad de procesado, los materiales se utilizaron también como adsorbentes de colorantes (naranja de metilo y azul de metileno), para así estudiar su potencial aplicación en el tratamiento de aguas residuales. Los materiales calcinados muestran capacidades de adsorción del orden de pocos cientos de mg g^{-1}, superiores a las documentadas en la literatura. No obstante, el óxido sin calcinar demostró ser un excelente adsorbente de ambos colorantes, con capacidades de más de 900 mg g^{-1}, muy superior a cualquier otro óxido metálico documentado hasta la fecha. Esta diferencia parece deberse a la morfología de los materiales antes y después de la calcinación, ya que el óxido sin calcinar está formado por láminas delgadas de material amorfo, mientras que la calcinación provoca una cristalización que engrosa sensiblemente las láminas y reduce proporcionalmente su superficie.

5. RESÚMENES Y ARTÍCULOS

A direct route to activated two-dimensional cobalt oxide nanosheets for electrochemical energy storage, catalytic and environmental applications

J.M. Munuera,* J.I. Paredes,* S. Villar-Rodil, S. García-Dalí, A. Castro-Muñiz, A. Martínez-Alonso, J.M.D. Tascón

Instituto Nacional del Carbón, INCAR-CSIC, C/Francisco Pintado Fe 26, 33011 Oviedo, Spain

* Corresponding author: j.munuera@incar.csic.es

* Corresponding author: paredes@incar.csic.es

Abstract

Two-dimensional Co_3O_4 nanosheets have emerged as attractive materials for use in a number of relevant technological applications. To exhibit a competitive performance in such uses, however, their structure needs to be activated, which is frequently accomplished via post-synthesis reduction strategies that introduce oxygen vacancies and increase the number of active Co(II) sites. Here, we investigate a direct route for the synthesis of activated Co_3O_4 nanosheets that avoids reduction post-treatments, yielding materials with a high potential towards energy- and environment-related applications. The synthesis relied on an interim amorphous cobalt oxide material with nanosheet morphology, which upon calcination afforded Co_3O_4 nanosheets having Co(II) sites in quantities similar to those usually found for Co_3O_4 nanostructures activated by reduction post-treatments. When tested as electrodes for charge, the nanosheets demonstrated a competitive behavior in terms of both capacity and rate capability, e.g., a gravimetric capacity of ~293 mAh g^{-1} at 1 A g^{-1} with 57% retention at 60 A g^{-1} was measured for nanosheets calcined at 350 ºC. The materials were shown to be efficient catalysts for the reduction of nitroarenes (4-nitrophenol and 4-nitroaniline), outperforming other Co_3O_4 nanostructures, as well as effective adsorbents for the removal of organic dyes (methyl orange, methylene blue) from water.

Keywords: two-dimensional (2D) material, non–layered material, cobalt oxide, electrochemical charge storage, catalysis, dye adsorption.

1. Introduction

Spurred by the impressive advances in both fundamental and applied research on graphene and other two-dimensional (2D) materials of a layered nature (e.g., transition metal dichalcogenides such as MoS_2 and WS_2, hexagonal boron nitride, phosphorene or MXenes), the field of 2D materials has been continually evolving and maturing during the past decade.[1-5] In this regard, one of the most significant trends of the last few years has been arguably the surge of activity in a vast, relatively unexplored subset of materials from this family, namely the subset of non-layered 2D materials.[6–8] The latter can be defined as materials with a 2D morphology (nanosheets, atomically thin films, etc) the bulk, 3D counterparts of which do not possess a lamellar structure of weakly interacting (e.g., van der Waals type) atomic layers, but exhibit strong chemical bonds in the three spatial directions instead. Thus, in addition to boasting the general attractions of 2D materials, such as increased surface areas for interaction with the environment or distinct electronic properties derived from electron confinement, non-layered 2D materials (unlike layered ones) tend to possess sizable amounts of low-coordinated surface atoms, which makes them intrinsically more reactive and hence potentially useful in applications that rely on, e.g., redox reactions relevant in the areas of catalysis and energy conversion/storage.[8,9] The range of non-layered 2D materials currently under scientific scrutiny mainly includes transition and post-transition metal oxides (TiO_2, SnO_2, α-Fe_2O_3, Co_3O_4, etc) and hydroxides, noble and non-noble metals and their alloys (Au, Ag, Pd, Cu, etc), metal chalcogenides (e.g., Co_3S_4, CuS or CdSe), as well as perovskites.[6-8,10–12]

Among non-layered metal oxides in 2D form, Co_3O_4 has received in recent years significant attention with a view to practical applications, due to the low cost and toxicity, earth abundance and high corrosion stability of this oxide.[8,10,13] Furthermore, thin (typically <10–20 nm) Co_3O_4 nanosheets exhibit large fractions of surface and near-surface metal sites with different oxidation states and high activities towards a number of redox and catalytic processes, making them an attractive material for use, e.g., as electrocatalysts for the oxygen evolution reaction[8,14–16] or as electrodes for supercapacitors[10,17–21] and Li-ion batteries.[10,22–25] Nonetheless, as is usually the case with many metal oxides, the performance of 2D Co_3O_4 nanosheets, and indeed of virtually any nanostructured form of Co_3O_4, in these and other applications is substantially limited by their poor electrical conductivity.[26,27] To address this issue, researchers have traditionally resorted to electrically conductive scaffolds of different

types as supporting substrates of the metal oxides. Typical scaffolds include metal (Ni, Cu, etc.) foams and wires/nanowires, as well as graphitic carbon materials (carbon fibers, nanofibers and nanotubes, or graphene).[10,16,17,19,25,28–31] However, more recent efforts have targeted the intrinsic characteristics of the metal oxide, and thus have sought to finely tune its atomic-scale structure as a means of activating it towards the intended practical purpose, for instance through the introduction of defects or dopants, which includes the synthesis of mixed metal oxides based on cobalt (i.e., MCo_2O_4).[27,32–34] Also of particular relevance within this kind of strategy is the activation of Co_3O_4 nanosheets and other nanostructures (as well as many other nanostructured metal oxides) by post-synthesis reduction treatments that generate oxygen vacancies in the lattice and convert a fraction of the original Co(III) sites to the more (electro)catalytically active Co(II).[16,20,26,35–39] As a testament of its practical benefits, such an activation has led to Co_3O_4 nanosheets with much improved performance when used as, e.g., supercapacitor electrodes[20] or electrocatalysts for the oxygen evolution reaction.[16,39]

Although highly effective in enhancing the performance of 2D Co_3O_4 nanosheets, the aforementioned post-treatments are probably not the ideal option for activating this material with a view to its large-scale manufacturing and practical implementation, as they involve additional processing steps that require high temperatures and/or reducing agents. Furthermore, from an atom-economy perspective, a synthesis strategy whereby a large number of active Co(II) sites are originally present in the Co_3O_4 material is more attractive than one by which a full-fledged Co_3O_4 lattice is first generated only to remove a fraction of its oxygen atoms in a subsequent reduction step to increase the amount of Co(II). In this regard, we hypothesized that activated, i.e. Co(II)-rich, Co_3O_4 nanosheets could be directly accessed via appropriate synthesis routes without the need to resort to any kind of reduction post-treatment. Such a hypothesis was founded on the idea that in the bottom-up production of metal oxides from atomic/molecular precursors, the actual characteristics of the final (as well as intermediate) products should be determined to a significant extent by a number of synthesis parameters, such as the nature and amount of the precursors and solvents, the use of certain additives (e.g., surfactants), or the temperature and pH of the reaction medium.[40]

Following this line of exploration, we report here that activated 2D Co_3O_4 nanosheets with a remarkable performance towards several applications can be readily synthesized through a suitable procedure that obviates the need for any activation

(reduction) post-treatment. The reported strategy is based on a general procedure recently developed by Sun *et al.*[41] and relies on the use of an interim material with nanosheet morphology that can be viewed as an amorphous cobalt oxide having an almost complete dominance of Co(II) sites. Subsequent calcination of this material at properly chosen temperatures afforded nanocrystalline Co_3O_4 nanosheets that retained a high fraction of Co(II) sites. When tested as electrodes for electrochemical charge storage, the activated nanosheets outperformed many other activated and non-activated Co_3O_4 nanomaterials that have been previously studied for such a purpose, and they also exhibited a competitive performance as non-noble metal-based catalysts for the reduction of nitroarenes and as adsorbents for organic pollutants (dyes) from the aqueous phase. Such results demonstrate the potential advantages of these activated Co_3O_4 nanosheets application-wise.

2. Results and discussion

2.1. Rationale of the proposed route and characteristics of the starting solvothermal nanosheets

Fig. 1 shows a schematic representation of the rationale behind the proposed strategy for directly accessing activated Co_3O_4 nanosheets, avoiding the need for activation (reduction) post-treatments. The bottom-up synthesis of 2D Co_3O_4 nanosheets, as well as of Co_3O_4 in other nanostructured forms (e.g., 0D nanoparticles or 1D nanorods) generally relies on a solvothermal step carried out at a moderately low temperature (usually < 150 ºC), whereby a molecular or ionic cobalt precursor species is converted under basic conditions to α- or β-phase cobalt hydroxide (path A in Fig. 1).[40] The latter is then transformed to cobalt oxide through calcination at typical temperatures in the 250–500 ºC range. This process normally affords Co_3O_4 materials with a limited concentration of active sites, i.e., Co(II) centers that are frequently associated to oxygen vacancies in the lattice, so that a subsequent reduction post-treatment is required to attain a substantial amount of such active sites.[16,20,35,36,42,43] Typical reduction strategies include high temperature annealing in a hydrogen-containing atmosphere or the use of proper reducing agents, such as $NaBH_4$, in the liquid phase. On the other hand, it has been suggested that cobalt oxide already starts to form at temperatures around 150 ºC or even lower, although this depends on the specific synthesis conditions.[44–47] For example, the presence of a small amount of water in the solvothermal medium has been shown to trigger the structural evolution from the hydroxide to the oxide phase at

moderate temperatures.[48] Therefore, we surmised that conducting the solvothermal step under appropriate conditions (e.g., temperature slightly above 150 ºC in the presence of a small amount of water) could allow the cobalt precursors to react and develop past the hydroxide stage into an incipient cobalt oxide material (path B in Fig. 1).[48,49] Due to the relatively low temperature of the solvothermal step, such an oxide (before calcination) should possess a highly disordered or even amorphous structure, and thus should exhibit a large concentration of active (defect) sites. Upon calcination, the solvothermal oxide should evolve towards (nano)crystalline Co_3O_4. However, owing to its expected higher stability relative to the hydroxide phase, the structural evolution of this oxide (and in particular, the healing of its defect sites) could be somewhat limited, especially at moderate calcination temperatures. As a result, the final Co_3O_4 material would retain a large number of the defect sites originally present in the solvothermal oxide and hence would be directly obtained in an activated state, hence circumventing the need for any activation post-treatments.

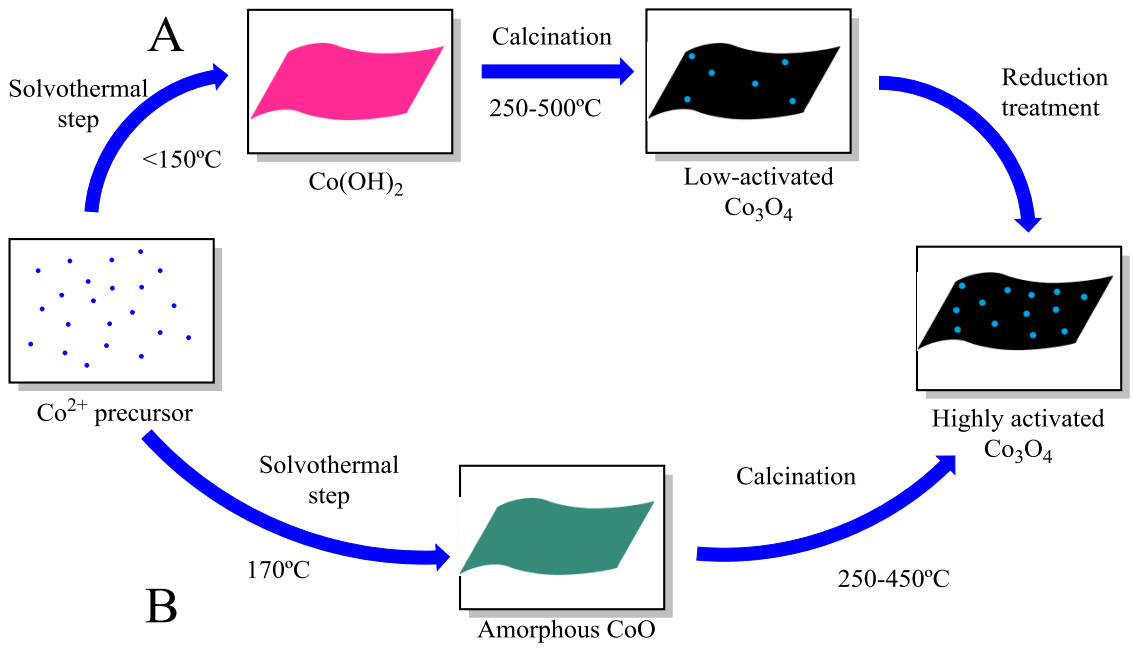

Figure 1. Schematic chart depicting two different strategies to access activated Co3O4 nanosheets, namely, through a post-synthesis reduction treatment (path A) or via a direct route that avoids reduction post-treatments (path B).

Building on this idea, we synthesized 2D Co_3O_4 nanosheets using a solvothermal route at a relatively high temperature (170 ºC) that yielded an interim cobalt oxide, which was then calcined at different temperatures (250, 350 and 450 ºC) to give a range

of final Co_3O_4 materials having a substantial degree of activation. The solvothermal step was based on a general procedure recently developed by Sun *et al.*[41] and was carried out in a mixed ethanol/water solvent with cobalt (II) acetate tetrahydrate as the precursor and hexamethylenetetramine as a base, in the presence of the polymeric surfactant Pluronic P123 as well as ethylene glycol as a co-surfactant (see Experimental section for details). It was reported that with the assistance of ethylene glycol, the Pluronic P123 surfactant forms an inverse micellar phase of a lamellar structure, which confines the oligomerization and assembly of the cobalt precursor in a 2D space and thus promotes the formation of a product with nanosheet morphology.[41,50] In the work by Sun *et al.*[41] the synthesis of Co_3O_4 nanosheets is reported amidst several examples in the more general framework of transition metal oxide. As long as cobalt oxide is concerned, the focus is on the characteristics of the final, calcined product at a particular temperature (400° C), no information being provided on the characteristics of the non-calcined solvothermal product or the calcined products obtained in intermediate stages of the process. Such an information is reported here in detail. As illustrated in Fig. 2a, the solvothermal method developed by Sun *et al.*[41] yielded a pale green powdery solid (left) that could be readily dispersed in water by means of a mild sonication step (right). Field emission scanning electron microscopy (FE-SEM) indicated that the as-prepared solid was a collection of large (up to several hundreds of micrometers) and relatively thin (~5–10 μm) plates (Fig. 2b). Closer inspection of their edges revealed that the plates were of a highly stratified nature (Fig. 2c), this being consistent with the formation of the solid within the confinement of a lamellar micellar phase. Individual nanosheets could be readily detached from the plates in large numbers through mild sonication, the 2D character of which was made apparent by imaging them with scanning transmission electron microscopy (STEM). Nanosheets that were highly transparent to the electron beam and exhibited many wrinkles and folds could be noticed (Fig. 2d). Apart from these morphological features, these nanosheets did not display any internal structure and appeared essentially featureless in the images, with their typical lateral sizes ranging between several hundreds of nanometers and a few micrometers. Furthermore, atomic force microscopy (AFM) indicated that their thickness was typically ~3–5 nm (Fig. 2e).

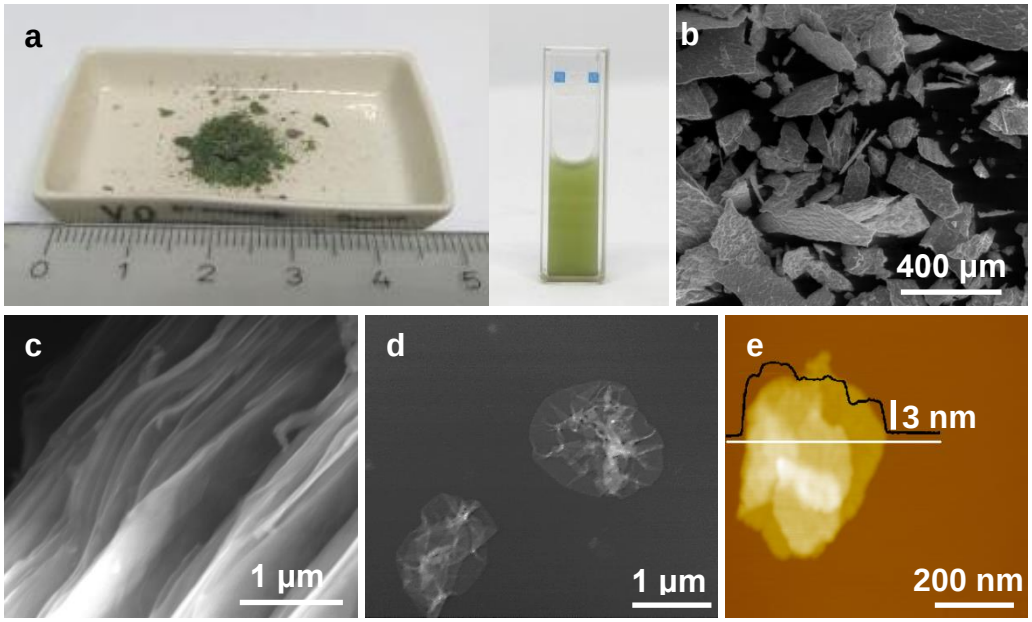

Figure 2. (a) Digital photograph of the as-prepared solvothermal product (left) and the same product after being dispersed in water by mild sonication (right). (b,c) FE-SEM images of the as-prepared solvothermal solid highlighting its stratified nature. (d,e) STEM (d) and AFM (e) images of individual nanosheets detached from the solvothermal solid. In (e), a line profile taken along the marked white line is shown in black color superimposed on the AFM image.

The solvothermally obtained pale green nanosheets could not be assigned to a cobalt hydroxide phase. α- and β-phase cobalt hydroxides, which are generally associated to dark green (or deep blue) and pink solids (see Fig. S1 in the Supporting Information), respectively. In fact, their color was that characteristic of cobalt oxide with the metal in the divalent state (CoO).[51] Of course, these colored substances can be distiguished on the basis of their optical absorption spectra. Specifically, α-$Co(OH)_2$ displays a strong doublet band in the 600–700 nm wavelength range, arising from Co(II) in tetrahedral coordination with hydroxide anions, together with an additional, relatively weak band in the 450–550 nm region [Co(II) in octahedral coordination], whereas only the latter is present in β-$Co(OH)_2$.[52–55] Such bands were completely absent from the UV-vis absorption spectrum of the solvothermal product (Fig. 3a), which was characterized by a sharp peak at around 200 nm along with a relatively broad shoulder in the 300–450 nm region. Indeed, these features were very similar to those previously reported by other authors for several cobalt oxide nanostructures (including nanosheets),[56,57] suggesting that the present solvothermal solid was also a cobalt oxide

predominantly in an oxidation state of +2. It must be noted that although α-$Co(OH)_2$ has been included in this discussion for completeness, it is not strictly $Co(OH)_2$ as it contains layers of anions other than hydroxide (such as nitrate, carbonate, chloride…) [58]. Consequently, during the synthesis of our materials, in the absence of such anions, such substance could not possibly have formed.

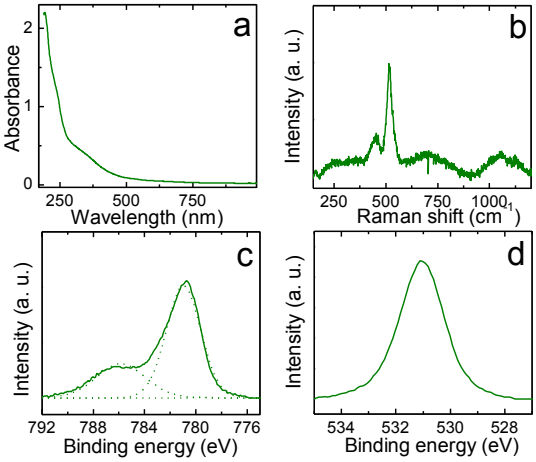

Figure 3. Spectroscopic characterization of the as-prepared solvothermal nanosheets: (a) UV-vis absorption spectrum of the nanosheets dispersed in water, (b) Raman spectrum, and (c,d) high resolution XPS Co $2p_{3/2}$ (c) and O 1s (d) core-level spectra.

The X-ray diffraction (XRD) pattern of the solvothermal material (not shown) was completely featureless, pointing to a poorly crystalline or even amorphous structure. On the other hand, its Raman spectrum (Fig. 3b) was dominated by an intense peak located at ~515 cm^{-1}, a relatively weak peak at around 450 cm^{-1} and two broad bands at ~690 and 1060 cm^{-1}. Collectively, these Raman features could not be unequivocally assigned to any crystalline, pristine cobalt oxide (CoO, Co_3O_4) or hydroxide phase,[59-62] or even to amorphous cobalt hydroxide.[63] Still, they were consistent with the presence of a highly defective oxide in which cobalt was mostly found in an oxidation state of +2. More specifically, it is known that the Raman spectrum of single-crystal, defect-free CoO only incorporates a broad and relatively weak band located at ~1060 cm^{-1}, which is ascribed to a second-order, two-phonon scattering process, while first-order processes are forbidden due to symmetry considerations.[61] In the presence of structural disorder in the CoO lattice, however, a number of first-order bands may appear in the 450–700 cm^{-1} region of the spectrum, in particular bands at ~510–540 and 450–480 cm^{-1},[61,64,65] this

being similar to what was obtained with the solvothermal solid investigated here (Fig. 3b). We note that a sharp peak located around 670–690 cm^{-1} has also been frequently reported in the literature for CoO materials, but such a peak has been recently ascribed to Co_3O_4 generated by the partial oxidation of CoO due to laser-induced heating during the Raman measurement.[61] In our case, the solvothermal nanosheets exhibited a broad, weak band at ~690 cm^{-1}, suggesting that Co(III) was only present to a minimal extent in the solid. This result was consistent with the fact that the solvothermal synthesis was carried out at a moderate temperature (< 200 ºC) in a closed autoclave (i.e., with a limited supply of oxygen), so that conversion of the Co(II) precursor species to higher oxidation states should be difficult to come about.

X-ray photoelectron spectroscopy (XPS) provided further support to the aforementioned conclusion. The survey spectrum of the solvothermally derived nanosheets (see Fig. S2a in the Electronic Supplementary Material) revealed the presence of only cobalt, oxygen and carbon. The latter was mainly ascribed to the well-known hydrocarbon contamination of surfaces (adventitious carbon) that so pervasively comes to light in XPS in the form of a C 1s band located at a binding energy of ~285 eV (Fig. S2b).[66] The high resolution Co 2p and O 1s core-level spectra of the sample are presented in Fig. 3c and d, respectively. We note that the Co 2p band is indeed a doublet, corresponding to Co $2p_{1/2}$ and Co $2p_{3/2}$ levels. However, both components contain the same information, so only the Co $2p_{3/2}$ region is shown in Fig. 3c for simplicity. The Co $2p_{3/2}$ band comprised a main peak located at a binding energy of ~780 eV, which in principle contains contributions from cobalt species in different oxidation states [including Co(III) at ~779.6 eV and Co(II) at ~780.9 eV], and a second, less intense peak at around 786 eV, which has been identified as a satellite band arising exclusively from Co(II) species[67] (see Fig. S3 in the Supporting Information). Fitting of the main peak with potential contributions from both Co(III) and Co(II) components led to a negligible contribution from the former species, indicating that cobalt was mostly (if not exclusively) present in an oxidation state of +2 in the solvothermal nanosheets. The O 1s band exhibited a rather symmetrical shape, suggesting that all the oxygen species in the material were essentially of the same type. Further, the position of this band (~531 eV) was consistent with that expected for oxygen in defective locations of cobalt oxides.[68] Therefore, taken together, the characterization results described above indicated that the solvothermal nanosheets synthesized by general procedure developed

by Sun *et al.*[41] were essentially a highly defective or even amorphous Co(II) oxide with little, if any, contribution from Co(III) species.

2.2. Conversion of the solvothermal nanosheets to activated Co_3O_4 nanosheets

To convert the highly defective, solvothermal Co(II) oxide nanosheets to an activated Co_3O_4 phase, i.e., to Co_3O_4 nanosheets that retain a substantial amount of Co(II) sites, the former were subjected to calcination under static air conditions at moderate temperatures (250, 350 and 450 ºC). In all cases, the pale green color of the starting solid changed to a blackish tone upon calcination, consistent with the emergence of the Co_3O_4 phase. Fig. 4 shows FE-SEM images of the products calcined at 250 (a), 350 (b) and 450 ºC (c). Unlike their non-calcined counterpart (Fig. 2b), these materials were made up of relatively loose clumps of randomly arranged, thin nanosheets. Furthermore, a closer inspection of individual nanosheets by STEM [Fig. 4d and g (250 ºC), e and h (350 ºC), f and i (450 ºC)] revealed substantial differences between the calcined and non-calcined samples. First, although the lateral size of the individual nanosheets did not appear to change significantly upon calcination, the calcined objects were much less transparent to the electron beam of the microscope and appeared to exhibit less wrinkles and folds (Fig. 4d-f). These features were clearly indicative of thicker and more rigid nanosheets. Indeed, AFM measurements (see inset to Fig. 4e) revealed the thickness of the calcined nanosheets to range typically between 5 and 15 nm. Second, the calcined nanosheets possessed a distinct internal structure, consisting of a more or less compact assembly of nanometric grains with scattered holes in-between, the latter becoming somewhat larger but less abundant at higher calcination temperatures (Fig. 4g-i). The grain size (generally ~8–15 nm, but tending to increase slightly with calcination temperature) was similar to the thickness of the nanosheets determined by AFM, suggesting that each individual nanosheet was made up of just one monolayer of grains.

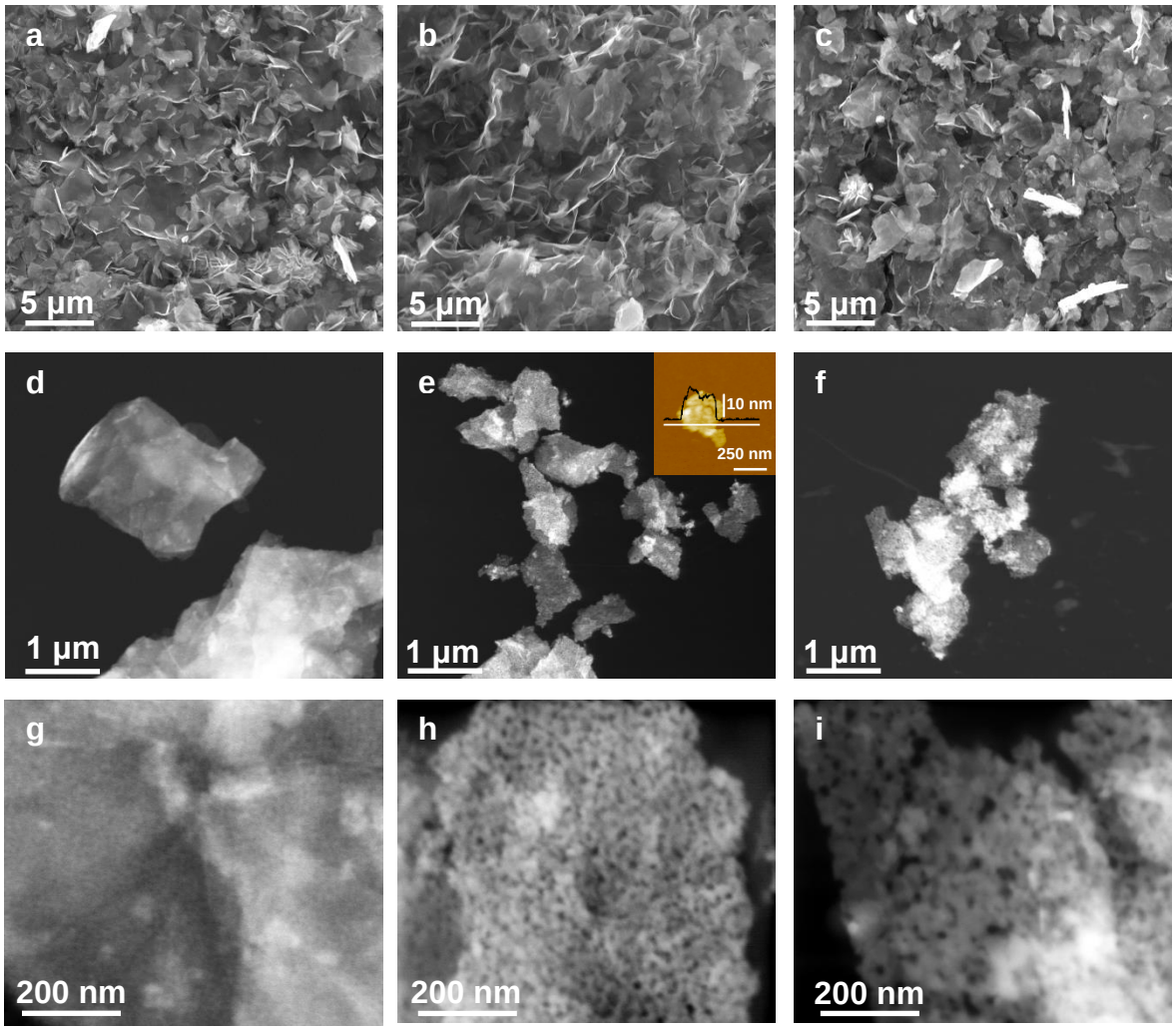

Figure 4. FE-SEM (a-c) and STEM (d-i) images of the solvothermal nanosheets after calcination at 250 (a,d,g) 350 (b,e,h) and 450 ºC (c,f,i).

We interpret the grainy structure of the calcined nanosheets to be a result of localized crystallization events taking place in the starting, amorphous solvothermal nanosheets during the heat treatment. In this process, Co_3O_4 nuclei would be initially generated at many random locations throughout the nanosheet, with their surrounding amorphous phase acting as the source material for the growth of these nuclei into nanometer-sized grains. Owing to the isotropic, non-layered nature of the Co_3O_4 lattice, the individual nanocrystals should be expected to grow at similar rates along the three spatial directions, and in particular their growth along the direction perpendicular to the nanosheet should not be confined to the very small thickness (~3−5 nm) of the starting amorphous nanosheet. At the same time, however, this very small thickness should

prevent the formation of multiple grains along the direction perpendicular to the nanosheet, because there would be a limited supply of source material along that direction. In consequence, the amorphous solvothermal nanosheet would be converted to a monolayer of interconnected Co_3O_4 nanocrystals, yielding nanosheets that could be thicker than their corresponding solvothermal oxide precursors, as it was indeed the case. The transformation of the amorphous solvothermal nanosheets into a thicker, monolayered assembly of nanometer-sized grains should also lead to the appearance of voids (holes) in the resulting nanosheets, which was observed in the STEM images as well.

Direct evidence for the crystallization of the solvothermal nanosheets upon calcination was obtained by XRD (Fig. 5a). Unlike the case of the starting nanosheets, the XRD pattern of which was completely featureless, the diffractogram of the calcined materials exhibited a peak located at ~36º (2θ), which could be assigned to the (311) reflection of the Co_3O_4 lattice (standard XRD data for Co_3O_4 are shown in Fig. S4).[16,36,69,70] The intensity of the (311) reflection, which is generally the most intense XRD peak observed in Co_3O_4 materials, rose with the calcination temperature, which was ascribed to a corresponding increase of crystallinity. However, the fact that other, rather intense peaks [e.g., (220) at ~31º, (511) at ~59º or (440) at ~66º] could not be clearly made out from the background noise pointed to a relatively limited crystallization of the solvothermal nanosheets upon calcination. Nonetheless, the conversion of the latter to Co_3O_4 was corroborated by the emergence of the Raman signature peaks of the spinel phase (Fig. 5b). More specifically, the Raman spectra of the calcined nanosheets displayed five well–defined bands located at ~192, 470, 515, 610 and 672 cm^{-1}, which could be ascribed to three F_{2g}, one E_g and one A_{1g} vibrational modes of Co_3O_4.[59,65,69] It is worth noting that the position of these bands appeared somewhat downshifted (a few to several cm^{-1}) relative to what is commonly found for bulk and nanostructured Co_3O_4, a result that can be put down to the relatively poor crystallinity of the present calcined nanosheets.[20,70,71] The trend with calcination temperature of such downshift was that expected from the above results on cristallinity, i. e., the lower the calcination temperature, the larger the downshift. The UV-vis absorption spectrum of all the calcined samples (Fig. 5c) was also in agreement with that expected for Co_3O_4, which is mainly characterized by two broad bands centered at about 470 and 770 nm.[37,69] No clear trends with calcination temperature were found in this case.

To provide quantitative estimates of the degree of activation of these Co_3O_4 nanosheets, which is determined by the relative abundance of Co(II) sites, the XPS technique was employed. Fig. 5d shows the high resolution Co $2p_{3/2}$ core-level spectra for the samples calcined at the different temperatures. As could be anticipated, the intensity of the Co(II)-associated satellite band relative to the main peak at ~786 eV decreased significantly after calcination (compare with the spectrum of the non-calcined material in Fig. 3c), strongly suggesting that Co(II) was no longer the only cobalt species present in the nanosheets. In point of fact, as can be seen from Fig. 5d, the main peak could be fitted with a combination of Co(II) and Co(III) components. In the fitted spectra, the full width at half maximum of the former component was substantially larger than that of its Co(III) counterpart (2.7 vs 1.7 eV), a result whose physical origin is grounded on the fact that Co(II) is an unresolved spin-triplet system, whereas Co(III) is a spin-singlet.[68] The Co(II)/Co(III) molar ratio of the samples, which is taken as a quantitative proxy of the degree of activation of Co_3O_4, was evaluated on the basis of the area of the corresponding cobalt components in the spectra, yielding values of ~1.4 for the nanosheets calcined at 250 and 350 ºC and ~1.3 for those calcined at 450 ºC, the degree of activation shows a slightly diminishing trend with calcination temperature. For ideal, stoichiometric Co_3O_4, a Co(II)/Co(III) ratio of 0.5 is expected. Nevertheless, the actual ratios determined in real Co_3O_4 materials synthesized using calcination temperatures below 500 ºC tend to be higher, with typical values lying in the 0.6–1.0 range.[16,20,42,71–73] On the other hand, activation of these materials through reduction post-treatments has been shown to further increase the Co(II)/Co(III) ratio to the 1.2–1.7 range.[16,20,42] Such results indicate that the Co_3O_4 nanosheets investigated here boasted a substantial degree of activation, even though no reduction post-treatment was applied to them, and therefore demonstrate a direct, simplified route to access this type of active material.

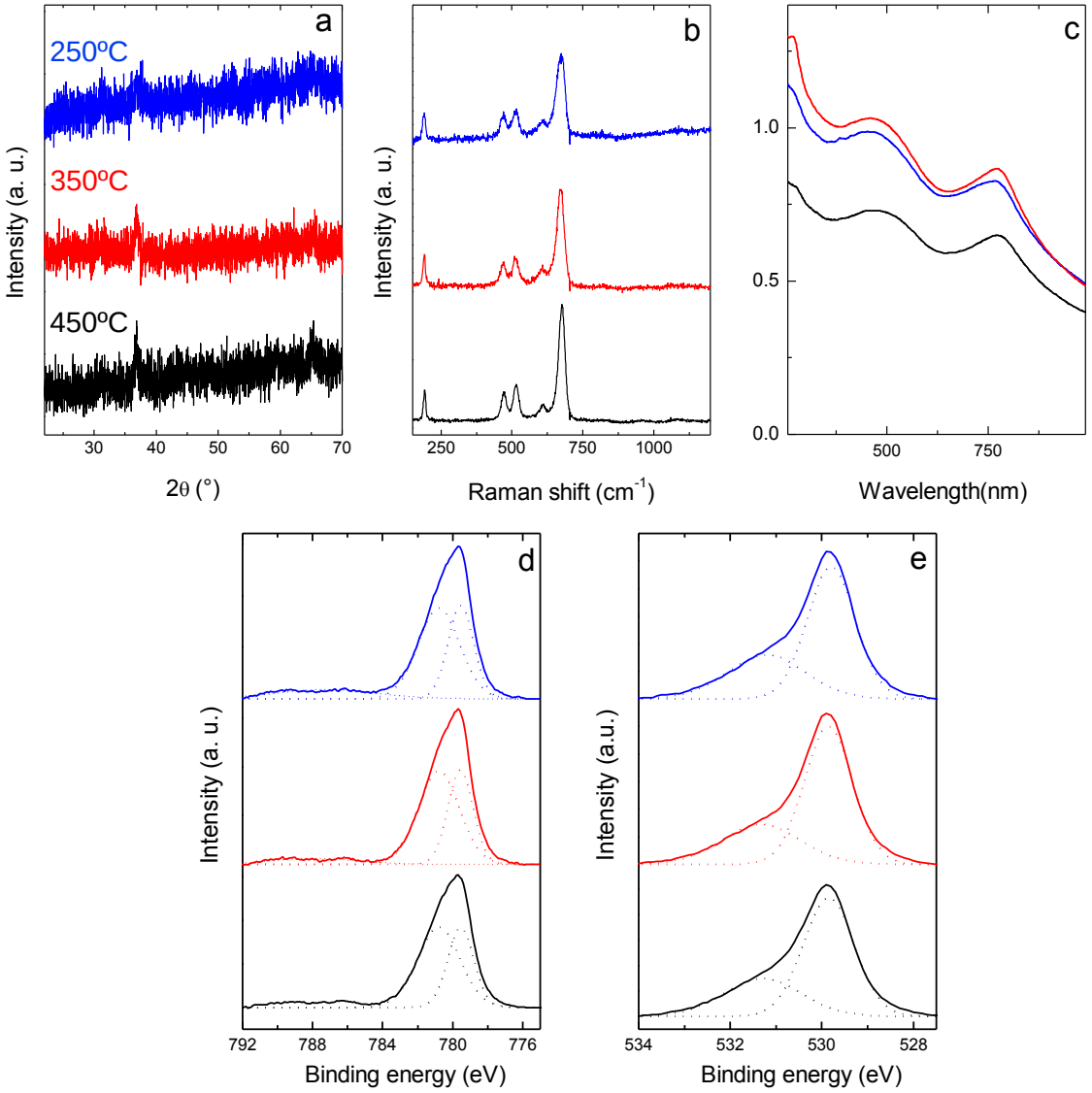

Figure 5. Structural and spectroscopic characterization of the calcined nanosheets: (a) X-ray diffractograms, (b) Raman spectra, (c) UV-vis absorption spectra, and (d,e) high resolution XPS Co $2p_{3/2}$ (d) and O 1s (e) core-level spectra.

An increased fraction of Co(II) sites in Co_3O_4 should be associated to the presence of significant numbers of oxygen vacancies in the lattice. The latter can be indirectly detected in the XPS O 1s band of the sample, as the binding energy of 1s electrons from oxygen atoms neighboring oxygen vacancies (i.e., defect oxygen; ~531 eV) is known to be different to that from oxygen atoms located in unaltered regions of the lattice (i.e., lattice oxygen; ~529.5 eV).[67,68] Fig. 5e shows the high resolution O 1s core-level spectra of the calcined nanosheets, which revealed the presence of a significant amount of oxygen species of the former type, in addition to the expected Co_3O_4 lattice oxygen. We

note, however, that a direct correlation between the area of the component associated to defect oxygen in the O 1s band and the concentration of oxygen vacancies in the material cannot be possibly made. This is because the number of defect oxygen atoms that contribute to such a component should most likely be determined not only by the overall density of oxygen vacancies, but also by their specific spatial distribution (e.g., isolated vs clustered vacancies), which should be highly dependent on the history of the material.

2.3. Applications of the activated Co_3O_4 nanosheets

It is known that having an increased fraction of Co(II) sites in nanostructured Co_3O_4 materials can bring a number of advantages with a view to their use in practical applications. For instance, Co(II) centers associated to oxygen vacancies increase the electrical conductivity of Co_3O_4 through n-type doping of the lattice, which can be highly beneficial when used as an electrode in electrochemical energy storage and conversion devices,[35,39,42] and they have been identified as the main active site towards different (electro)catalytic reactions, such as the oxygen evolution reaction,[74] the electroreduction of CO_2[70] or the reduction of nitroarenes.[36] Furthermore, because extra Co(II) sites are associated to a local increase in electron density,[35] those sites present on the Co_3O_4 surface should exhibit enhanced interaction with certain foreign chemical species (e.g., molecules with electron-deficient groups), so that activated Co_3O_4 with high surface area (nanoparticles, nanosheets, etc) could also be an attractive material in adsorption processes. To explore the potential of the activated Co_3O_4 nanosheets investigated here in these application areas, we have examined their performance towards three specific uses, namely (1) as electrodes for electrochemical charge storage, (2) as catalysts for the reduction of nitroarenes (4-nitrophenol and 4-nitroaniline), and (3) as adsorbents of dyes (methyl orange and methylene blue) from the aqueous phase.

2.3.1 Electrochemical energy storage

The electrochemical charge storage experiments were carried out in a three-electrode configuration using the cobalt oxide samples supported onto graphite foil as the working electrode, a commercial activated carbon as the counter electrode and Hg/HgO as the reference electrode, with aqueous 6 M KOH as the electrolytic medium (see Experimental section for details).

Fig. 6a shows typical cyclic voltammograms (CVs) recorded at a potential scan rate of 10 mV s^{-1} for the non-calcined nanosheets as well as their counterparts calcined at different temperatures. The evolution of the CVs of the sample calcined at 350 ºC with increasing scan rate between 3 and 500 mV s^{-1} is presented in Fig. 6b, whereas the corresponding results for the other three samples are given in Fig. S6 of the Electronic Supplementary Material. Similar to what has been reported in the literature for Co_3O_4 materials,[75] the obtained CVs were dominated by intense oxidation and reduction peaks, indicative of a charge storage mechanism that is mostly reliant on Faradaic redox reactions occurring at the metal centers of the oxide. This type of behavior allowed us to categorize the present materials as having a battery-type response rather than a capacitor-type one,[75–77] where charge storage is mostly based on ionic intercalation into the electrode and not on the formation of an electrical double layer on its surface. Such a conclusion was further substantiated by the observation that the magnitude of the measured current for the oxidation peak located at 0.42–0.46 V vs Hg/HgO was directly proportional to the square root of the potential scan rate (i.e., $I \sim \nu^{1/2}$, where I is the oxidation peak current and ν is the scan rate), as can be seen in the inset to Fig. 6b. This square root dependence implied that the electrode capacity was controlled by diffusion of the electrolyte ions into the material, which in turn was consistent with a battery-type behavior.[76]

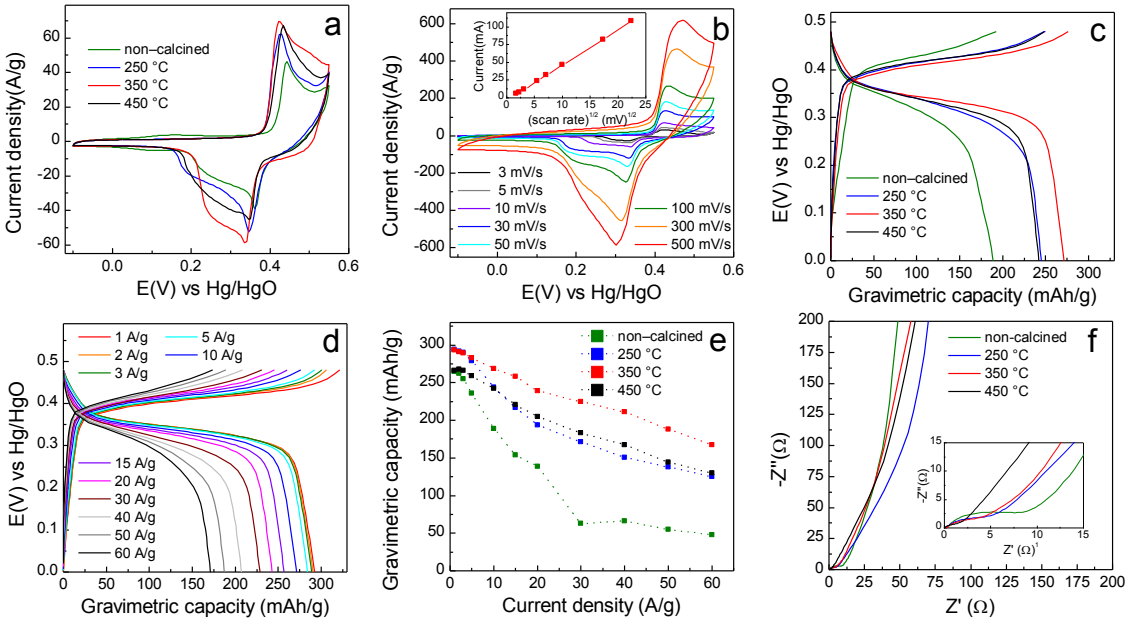

Figure 6. Electrochemical testing of the nanosheets in 6 M KOH electrolyte: (a) cyclic voltammograms recorded at a potential scan rate of 10 mV s^{-1} for the non-calcined and calcined nanosheets, (b) cyclic voltammograms recorded at different scan rates between 3 and 500 mV s^{-1} for the nanosheets calcined at 350 ºC (inset: magnitude of the oxidation peak current vs square root of the potential scan rate), (c) galvanostatic charge-discharge curves recorded at a current density of 10 A g^{-1} for the non-calcined and calcined nanosheets, (d) galvanostatic charge-discharge curves recorded at different current densities between 1 and 60 A g^{-1} for the nanosheets calcined at 350 ºC, (e) gravimetric capacity of the non-calcined and calcined nanosheets measured as a function of current density, and (f) electrochemical impedance spectra of the non-calcined and calcined nanosheets (inset: detailed view of the high frequency region of the spectra).

Representative galvanostatic charge-discharge curves, in the form of voltage vs gravimetric capacity plots, recorded for the different cobalt oxide nanosheet samples at a current density of 10 A g^{-1} are shown in Fig. 6c, while charge-discharge curves for the sample calcined at 350 ºC measured at current densities between 1 and 60 A g^{-1} are presented in Fig. 6d. Charge-discharge curves for the other three materials can be found in Fig. S7 of the Electronic Supplementary Material. As expected for battery-type electrodes, the galvanostatic curves were highly non-linear, exhibiting large regions of slowly varying potential, i.e., plateaus. For example, the plateaus in the discharge curves of Fig. 6d were located in the 0.3–0.4 V range (vs Hg/HgO), which was consistent with the potential at which reduction of the cobalt centers took place as deduced from the reduction peaks in the CVs of this sample (Fig. 6b). From the

discharge curves we determined the gravimetric capacity delivered by the materials, the values of which are plotted in Fig. 6e as a function of current density. At low current densities, all the samples (both calcined and non-calcined) were seen to deliver similar capacities (e.g., between 265 and 295 mAh g^{-1} at 1 A g^{-1}). However, significant differences emerged in terms of their rate capability, with the non-calcined nanosheets displaying the poorest performance. More to the point, the capacity values for the latter dropped markedly with increasing current density (particularly in the range up to 30 A g^{-1}), yielding a capacity retention of only ~18% at the highest current density of 60 A g^{-1}. By contrast, the reductions in capacity for the calcined nanosheets were much more moderate, with retention values of about 43, 57 and 49% at 60 A g^{-1} for the materials calcined at 250, 350 and 450 ºC, respectively. Moreover, the coulombic efficiency of the nanosheets, defined as the ratio between the charge delivered in a discharge cycle and the charge stored during a charging cycle, was ~85–90% at a current density of 1 A g^{-1} and approached 100% at 60 A g^{-1}. Furthermore, their stability as electrodes was tested by recording consecutive galvanostatic charge/discharge cycles. After 3000 cycles, ~95% of the initial capacity of the electrodes was retained with the nanosheets calcined at 350 °C and 450 °C, whereas the capacity retention was around 105% for the material calcined at 250 °C and 115% for the non-calcined material (Fig. S8 in the Electronic Supplementary Material). Such increases in capacity with cycling are not unusual in electrochemical energy storage devices of metal oxides, and can be ascribed to the conditioning of the materials upon the charge-discharge cycles, especially those with a poorer crystalline structure (i.e., non calcined sample and samples calcined at lower temperatures in our case) [20,21,71]

It is concluded from Fig. 6e that the nanosheets calcined at 350 ºC boasted the best performance, as they demonstrated the highest capacities across the whole current density range together with the best rate capability. Table S1 in the Electronic Supplementary Material compares the gravimetric capacity values obtained from this sample at several selected current densities with literature data documented for other Co_3O_4 nanomaterials. Concerning the collection of these data, we note that although in a strict sense the concept of capacitance is not applicable to electrodes with a battery-type behavior,[75,76] in many instances capacitance (rather than capacity) values are given for electrodes based on Co_3O_4 materials tested in basic electrolytes, which fall into such a category. However, in these cases capacity values can be readily derived from the reported capacitance data if the potential window is provided, which is most frequently

the norm. Overall, it is apparent from Table S1 that the present activated nanosheets exhibited a rather competitive performance, not only in terms of the capacity values themselves but also as regards their retention at high current densities. In particular, they compared favorably with oxygen vacancy-rich Co_3O_4 nanosheets and reduced mesoporous Co_3O_4 nanowires reported previously, the electrochemical performance of which had been substantially boosted through activation by reduction post-treatment with $NaBH_4$. For example, the capacity of the nanosheets calcined at 350 ºC was 291 mA h g^{-1} at 2 A g^{-1}, compared with values of ~227 and 136 mA h g^{-1} for the oxygen vacancy-rich nanosheets and the reduced mesoporous nanowires, respectively, and their capacity retention was ~92% at 10 A g^{-1} (compared to ~50% for the reduced mesoporous nanowires) and ~88% at 15 A g^{-1} (compared to ~80% for the oxygen vacancy-rich nanosheets).[20,35] These results demonstrate that the direct route proposed here for the preparation of Co_3O_4 nanosheets can afford activated materials with comparable or even better performance than that of similar Co_3O_4 nanomaterials that were activated post-synthesis, which can be beneficial when considering their practical use.

It is reasonable to assume that the different rate capabilities of the investigated materials, as noticed in Fig. 6e, arise from their distinct abilities to allow the conduction of electrons and the (de)intercalation of ions, which are the two basic processes accounting for their charge storage behavior. For example, the highly disordered or even amorphous nature of the non-calcined nanosheets could lead to a poorer rate capability relative to that of their calcined counterparts, as the amorphous structure would be expected to hamper electron conduction in the lattice. To investigate this question, the electrodes were analyzed by the electrochemical impedance spectroscopy (EIS) technique. Fig. 6f shows Nyquist plots derived from the EIS data recorded in the frequency range between 100 kHz and 10 mHz for the different cobalt oxide nanosheet samples, with the inset providing a closer view of the high frequency region of the plots. The latter was characterized by a semicircle profile, the diameter of which [i.e., the equivalent series resistance (ESR) parameter] provided a measure of the electronic conduction in the materials. As anticipated, the ESR value for the non-calcined nanosheets (7.8 Ω) was larger than those determined for the calcined nanosheets (5.3, 4.5 and 1.8 Ω for the samples calcined at 250, 350 and 450 ºC, respectively), indicative of a relatively impaired electronic conduction in the former material. Having similar numbers of Co(II) sites, the difference in conductivity between the calcined nanosheets

can be ascribed to differences in crystallinity due to the calcination process (the higher the calcination temperature, the more structured the samples become and therefore the higher the electrical conductivity). On the other hand, from the lower frequency region of the Nyquist plots we notice that the non-calcined material boasted the most vertical line of all the samples, suggesting a better efficiency towards ion insertion.[37] This result can be understood on the basis of the smaller thickness of the non-calcined nanosheets (~3–5 nm) relative to that of their calcined counterparts (around 10 nm), which implies the former to be more accessible to ion intercalation. Among the activated Co_3O_4 nanosheets, the sample prepared by calcination at 350 ºC exhibited the most vertical line in the higher frequency range, followed by the sample calcined at 450 ºC. Therefore, even though the 350 ºC sample possessed neither the highest electronic conductivity nor the best ion diffusion ability, it probably struck a proper balance between these two key characteristics (it was the second best sample for both), finally resulting in the material with the best overall performance in terms of capacity and rate capability.

2.3.2 Catalytic reduction of nitroarenes

The cobalt oxide nanosheets were also evaluated as catalysts for the reduction of the nitroarenes 4-nitrophenol (4-NP) and 4-nitroaniline (4-NA) to 4-aminophenol (4-AP) and *p*-phenylenediamine (*p*-PDA), respectively, with $NaBH_4$ as the reducing agent, which are reactions of practical relevance in, e.g., the synthesis of certain analgesic drugs (paracetamol) or dyes.[78,79] Both reactions are thermodynamically feasible but kinetically hindered by substantial activation barriers, thus requiring the use of proper catalysts to make them proceed at significant rates. Although catalysts based on noble metals (Au, Ag, Pt, Pd, etc) have been intensively investigated for this purpose, a recent move towards more abundant and cost-effective alternatives, such as those relying on non-noble metals (e.g., Ni or Cu), has been gaining momentum.[79] In this context, nanostructured Co_3O_4 has been proposed as a suitable non-noble metal-based catalyst for nitroarene reduction, with its activity being mostly attributed to additional Co(II) centers (usually associated to oxygen vacancies in the lattice).[72,80] Having an abundance of the latter, the present nanosheets (both calcined and non-calcined) could be particularly efficient catalysts for such reactions. Their performance was tested by following the evolution of the intensity of optical absorption peaks characteristic of the nitroarenes (see Fig. S9 of the Electronic Supplementary Material).[72,81] Specifically, in the case of 4-NP we monitored the evolution of the peak located at ~400 nm, which is associated to the deprotonated form of this molecule (i.e., the nitrophenoxide anion,

generated in the basic medium of $NaBH_4$) and is not present in its reduced counterpart (aminophenoxide anion; Fig. S9a). For 4-NA, we followed its signature peak at ~380 nm, which is absent from *p*-PDA (Fig. S9b). As the intensity of these absorption peaks reflects the concentration of their respective substrate molecules in the reaction medium, it can be used to plot kinetic profiles of the reaction progress.

Representative examples of the kinetic curves recorded for the cobalt oxide nanosheets are given in Fig. 7a (4-NP) and b (4-NA). The profiles were generally seen to decay in an exponential fashion (after an induction period), hence suggesting the reduction reactions to obey a pseudo-first-order kinetic behavior with respect to the substrate concentration.[81] As expected, no reaction was observed to occur in the absence of the nanosheets, i.e., when the nanosheet dispersion added to the reaction medium was replaced either by pure water or by the supernatant liquid obtained after sedimentation of the dispersed nanosheets through centrifugation, thus confirming their role as the catalytically active component. As shown in Fig. S9, the reaction products (4-AP and *p*-PDA) were detected by UV-vis absorption spectroscopy. Indeed, calibration of their concentration by this technique indicated an aproximatley one-to-one conversion of reagent to the corresponding expected product. To quantify the catalytic activity of the nanosheets, we determined the number of moles of substrate (4-NP or 4-NA) converted per unit time per mole of cobalt present in the nanosheets, the results of which are shown in Fig. 7c. In the calculations, we assumed CoO and Co_3O_4 as the approximate stoichiometric formulas for the non-calcined and calcined samples, respectively. There were not very large differences in activity between the different materials, although the values for the non-calcined nanosheets tended to be somewhat higher than those of their calcined counterparts. This result can be probably ascribed to (1) the smaller thickness of the former, which implies that more surface active sites are potentially available for reaction per unit mass of catalyst, and/or (2) the fact that Co(II) centers, which are assumed to be the catalytically active sites, are relatively more abundant in the non-calcined nanosheets [~100%, almost no Co(III) centers] than in the calcined samples [~55-60% Co(II) and ~40−45% Co(III)]. Nonetheless, concerning the latter possibility we note that the actual catalytic activity of the Co(II) centers in the amorphous lattice of the non-calcined nanosheets could be distinct to that of their counterparts in the (more nanocrystalline) calcined nanosheets, but this point is currently unknown. It could also be argued that the in-situ treatment of the nanosheets with $NaBH_4$ during the catalytic

reaction of the nitroarenes could be activating the nanosheets themselves (particularly the calcined ones). However, XPS measurements (data not shown) of nanosheets treated with $NaBH_4$ showed no significant change in their Co(II)/Co(III) ratios, so we conclude that the materials do not become further activated during the catalytic reaction. The reason for this could be that because the as-prepared nanosheets are already substantially activated, the remaining Co(III) sites could be hard to reduce to Co(II) by a chemical species with a relatively limited reducing ability. At any rate, the nanosheets boasted a competitive performance when compared with previously reported cobalt oxide nanomaterials as well as other materials made up of non-noble metals and/or their oxides, as noticed from catalytic activity data on 4-NP shown in Table S2 of the Electronic Supplementary Material (data on 4-NA with similar catalysts are much less abundant). In most cases, the activity of the nanosheets was significantly higher than that of other nanostructured cobalt oxide catalysts. In particular, it was similar or even higher than that of Co_3O_4 nanoplates of comparable thickness that were activated through a common reduction post-treatment.[72]Also, it is worth noting that the materials could be reused through centrifugation of the suspension and then redispersion of the nanosheets in water. Again, these results bear testament to the efficiency of the present strategy in accessing activated Co_3O_4 without any post-treatment but at the same time exhibiting improved performance towards practical uses. The fact that the non-calcined sample performed better in these experiments than their calcined counterparts (unlike the case of the electrochemical tests) can be ascribed to the relevance of different factors, such as the electrical conductivity or the Co(II) content, that play a role in their behavior towards different uses, While a good electrical conductuvity is key to the nanosheet performance in electrochemical applications, the same is not expected to be the case for the catalytic reactions, where a large number of active Co(II) centers should be the most relevant single factor that determines nanosheet performance. Under such circumstances, the non-calcined nanosheets should possess the better catalytic activity because they possessed the larger amount of Co(II) sites, as was indeed observed.

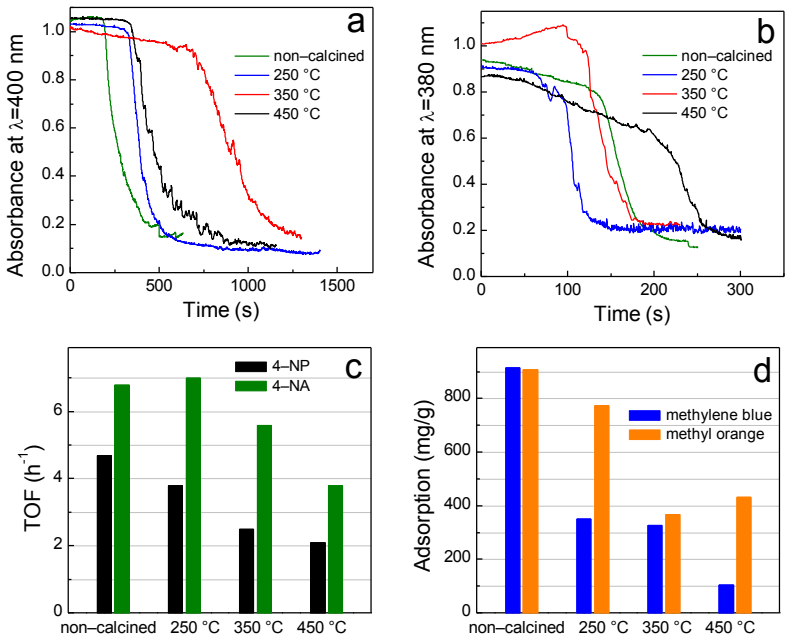

Figure 7. (a,b) Kinetic profiles recorded for the reduction of 4-NP (a) and 4-NA (b) with $NaBH_4$ using the non-calcined and calcined nanosheets catalysts. (c) Catalytic activities of the non-calcined and calcined nanosheets towards 4-NP (black columns) and 4-NA reduction with $NaBH_4$ (green columns), determined as the number of moles of substrate (4-NP or 4-NA) converted per unit time per mole of cobalt present in the nanosheets. (d) Measured adsorption capacities of the non-calcined and calcined nanosheets towards methylene blue (blue columns) and methyl orange (orange columns) from the aqueous phase.

2.3.3 Dye adsorption

Finally, owing to their small thickness and hence large surface area, the nanosheets could also act as efficient adsorbents for, e.g., the decontamination of polluted water. To explore such a possibility, we have preliminarily tested the aqueous-phase adsorption of two dyes (methylene blue and methyl orange) onto the cobalt oxide materials. These are charged molecules, which can therefore be favorably adsorbed on the polar surface of the nanosheets through charge-dipole interactions. Fig. 7d shows the corresponding adsorption capacities measured for both the non-calcined and the calcined samples. In most cases, the adsorbed amounts were found to be substantial (~300–900 mg g^{-1}), suggesting that these nanosheets could make good adsorbents for environmental applications. However, as could have probably been expected, the best results were obtained for the non-calcined nanosheets (adsorption capacities around 900 mg g^{-1}), which could be ascribed to their smaller thickness relative to that of their calcined

counterparts. Like we noted for the catalysis tests, the nanosheets could be reused, through several centrifugation and redispersion steps in ethanol in order to desorb the dyes. To put these figures into context, they are compared in Table S3 of the Electronic Supplementary Material with adsorption data taken from the literature for a number of metal oxides, including several in nanostructured form, with the same two dyes (we note that data for Co_3O_4 materials could not be found). Overall, the present nanosheets exhibited the best performance from this set of metal oxide materials in terms of the amount of dye that can be taken up, which should warrant more detailed studies in the future to disclose their full potential in this application area.

3. Conclusions

We have demonstrated that activated Co_3O_4 nanosheets having substantial amounts of Co(II) sites can be obtained through a direct synthesis route that circumvents the need of activation (reduction) post-treatments. The strategy based on a general procedure recently developed by Sun *et al.*[41] and relied on an intermediate cobalt oxide material with nanosheet morphology and a highly disordered structure, the calcination of which afforded Co_3O_4 nanosheets boasting Co(II)/Co(III) ratios of ~1.3–1.4, i.e., similar to those achieved for Co_3O_4 nanomaterials activated by reduction post-treatments. These activated nanosheets demonstrated a good potential for use in a number of energy- and environment-related applications. Specifically, they exhibited a competitive performance in their role as an electrode for charge storage in alkaline electrolyte, surpassing many other nanostructured Co_3O_4 materials in terms of both gravimetric capacity and rate capability (including those materials activated post-synthesis). Furthermore, the activated nanosheets were shown to be effective catalysts in the reduction of nitroarenes, with their activity comparing favorably to that of other catalysts based on non-noble metals and/or their oxides, and were also promising adsorbents of dye pollutants from the aqueous phase. For these two latter applications where electrical conductivity is not an issue, the solvothermal nanosheets prepared without any calcination post-treatment, which were thinner and displayed almost exclusively Co(II) sites, offered the best performance. Finally, the present results suggest that the use of these nanosheets in other relevant applications where nanostructured Co_3O_4 is known to have good prospects for development, such as electrocatalysts for the oxygen evolution reaction or electrodes for Li-ion batteries, will be worth exploring in the future.

4. Experimental

4.1. Chemicals and reagents

The following chemicals and reagents were acquired from Sigma-Aldrich and used as received: ethylene glycol, ethanol, hexamethylenetetramine, sodium borohydride, potassium hydroxide, the surfactant Pluronic P123, the dyes methyl orange and methylene blue, the nitroarenes 4-nitrophenol and 4-nitroaniline. Cobalt (II) acetate tetrahydrate was obtained from Alfa Aesar. Ultrapure water (Milli-Q; resistivity: 18.2 MΩ·cm) was used throughout the work.

4.2 Synthesis of activated 2D Co_3O_4 nanosheets

Activated Co_3O_4 nanosheets were prepared by first synthesizing amorphous cobalt oxide nanosheets in the confined 2D space of inverse lamellar micelles of the non-ionic surfactant Pluronic P123 in ethanol/water medium, followed by controlled calcination at a given target temperature.[41] To obtain the amorphous nanosheets, 200 mg of Pluronic P123 were dissolved in 14 mL of a mixed ethanol/water (33/2, v/v) solvent under stirring. Subsequently, 125 mg of cobalt (II) acetate tetrahydrate and 70 mg of hexamethylenetetramine were added to the resulting mixture. After 15 min, a purple-colored solution was obtained, into which 13 mL of ethylene glycol were poured. Under continuous stirring, the purple solution became transparent in about 30 min, following which it was allowed to statically age for 24 h. The aged solution was then transferred to a Teflon-lined autoclave (capacity: 40 mL) and heat-treated at 170 ºC for 2 h. The resulting greenish solid product was thoroughly washed by repeated cycles of centrifugation (2000 *g* for 20 min, J.P. Selecta Meditronic centrifuge in 30 mL tubes) and re-suspension in water and ethanol (3 cycles for each solvent), and finally dried at room temperature under a vacuum. Calcination of this product was accomplished by heating at different temperatures, namely 250, 350 and 450 ºC, for 2 h under static air conditions (Thermolyne muffle furnace, from Thermo Scientific).

4.3 Characterization techniques

The samples were characterized by UV-vis absorption spectroscopy, field-emission scanning electron microscopy (FE-SEM), scanning transmission electron microscopy (STEM), atomic force microscopy (AFM), X-ray diffraction (XRD), Raman spectroscopy and X-ray photoelectron spectroscopy (XPS). UV-vis absorption spectra

were obtained with a double-beam Heλios α spectrophotometer (Thermo Spectronic). FE-SEM and STEM images were recorded on a Quanta FEG 650 apparatus (FEI Company) working at a voltage of 30 kV. Specimens for FE-SEM were directly mounted onto metallic sample holders using double-sided carbon adhesive tape, whereas for STEM the samples were first dispersed in water by bath-sonication for 20 min (J.P. Selecta Ultrasons system, 40 kHz, power ~20 W L^{-1}) and then drop-cast (~10 μL) onto a copper grid (200 square mesh) covered with a thin, continuous carbon film (Electron Microscopy Sciences). AFM imaging was carried out in the tapping mode of operation with a Nanoscope IIIa Multimode microscope (Veeco), using silicon cantilevers with nominal spring constant and resonance frequency of ~40 N m^{-1} and 250-300 kHz, respectively. SiO_2 (300 nm)/Si was employed as a supporting substrate for AFM, onto which an aqueous dispersion of the sample (prepared by bath-sonication) was deposited by drop-casting. XRD patterns were recorded with a D5000 diffractometer (Siemens) at angles (2θ) between 20 and 70º, using Cu K_α radiation (λ = 0.1504 nm) at a step size of 0.02º and time per step of 1 s. Raman spectroscopy was conducted in a LabRam apparatus (Horiba Jobin Yvon) with a laser excitation wavelength of 532 nm. To prevent damage to the samples, a low incident laser power (0.5 mW) was applied. For XPS, a SPECS apparatus working at a pressure of 10^{-7} Pa and using a non-monochromatic Mg K_α X-ray source (11.81 kV, 100 W) was employed. Specimens for Raman spectroscopy and XPS were prepared in the form of thin films supported onto silver membrane filters (0.2 μm in pore size, 25 mm in diameter, from Sterlitech Corporation), which were prepared by vacuum filtration of the samples dispersed in aqueous medium.

4.4. Applications of the highly activated 2D Co_3O_4 nanosheets

The activated Co_3O_4 nanosheets were tested as electrodes for electrochemical charge storage, as catalysts for the reduction of nitroarenes and as adsorbents for dyes from the aqueous phase.

4.4.1 Electrochemical energy storage

The electrochemical energy storage experiments were carried out in a three-electrode configuration with a Swagelok-type cell, using the Co_3O_4 materials as the working electrode, a commercial activated carbon fiber as the counter electrode, Hg/HgO (1 M NaOH) as the reference electrode and aqueous 6 M KOH as the electrolyte. The

working electrode was prepared by drop-casting aqueous dispersions (0.5 mg mL^{-1}) of the activated nanosheets onto circular (~0.8 cm in diameter) graphite foil pieces, which were then allowed to dry under ambient conditions. Typical nanosheet loadings onto the graphite foil support were in the 0.3–0.4 mg cm^{-2} range. The counter electrode was obtained in the form of a paste that incorporated, in addition to the activated carbon fiber, polytetrafluoroethylene as a binder and carbon black as a conductive additive, in a weight ratio of 90:5:5. A circular piece (~1.3 cm in diameter) of nylon membrane filter (0.45 μm of pore size, from Whatman) was used as a separator for the working and counter electrodes. Before the cell was assembled, the working and counter electrodes as well as the separator were individually soaked in 6 M KOH and vacuum-degassed. Prior to measurements, the assembled cell with the electrolyte was also vacuum-degassed. The measurements were carried out in a VSP potentiostat (Bio-Logic Science Instruments), recording both cyclic voltammograms at different voltage scan rates and galvanostatic charge/discharge curves at different current densities.

4.4.2 Catalytic reduction of nitroarenes

The catalytic activity of the cobalt oxide nanosheets was evaluated in the reduction of two nitroarenes, namely, 4-nitrophenol (4-NP) and 4-nitroaniline (4-NA), in aqueous medium with $NaBH_4$ as the reducing agent. To this end, aqueous solutions (2.105 mL) containing either 4-NP (0.06 mM) or 4-NA (0.06 mM), a certain amount of the nanosheets (typically ~14-24 mg mL^{-1}) and $NaBH_4$ (36 mM) were prepared and immediately transferred to an UV-vis absorption spectrophotometer. Kinetic profiles of the reaction progress were then recorded by monitoring the intensity of an absorption peak characteristic of the substrate molecule (i.e., the peak located at a wavelength of ~400 nm for 4-NP and ~380 nm for 4-NA) over a certain period of time.

4.4.3 Dye adsorption

For the dye adsorption tests, aqueous solutions of the dyes (methylene blue or methyl orange) were mixed with a colloidal suspension of the nanosheets that was obtained by sonicating the as-prepared powder in water, so that the final concentration of the latter in the mixed solution was ~4 mg mL^{-1}. After being gently stirred with a magnetic bar for 24 h, the nanosheets were separated from the solution by centrifugation (20000 *g*, 20 min). This long adsorption time was selected only to ensure the attainment of adsorption equilibrium and allow the determination of maximum adsorbed concentrations, although in actual applications much shorter times would probably suffice (kinetic tests were beyond the scope of this work). Subsequently, the concentration of dye remaining

in the supernatant was determined by UV-vis absorption spectroscopy and compared with that of the starting solution before adsorption, so that the amount of dye taken up by the nanosheets could be finally derived. Dye concentrations were estimated by measuring the intensity of absorption peaks characteristic of the dyes, namely, the peak located at a wavelength of ~660 nm for methylene blue and ~460 nm for methyl orange. To assess the maximum adsorption capacities of the cobalt oxide nanosheets, the starting concentrations of the dyes in the mixed solutions were purposefully chosen to be high, typically between 1 and 4 mg mL^{-1}.

Acknowledgements

Funding by the Spanish Ministerio de Economía y Competitividad (MINECO) and the European Regional Development Fund (ERDF) through project MAT2015-69844-R is gratefully acknowledged. We are also grateful to Plan de Ciencia, Tecnología e Innovación 2013-2017 del Principado de Asturias and the ERDF for partial funding through project GRUPIN14-056. J.M.M. and S.G-D. are grateful to the Spanish Ministerio de Educación, Cultura y Deporte (MECD) and MINECO, respectively, for their pre-doctoral contracts (FPU14/00792 and BES/2016 077830, respectively).

Electronic Supplementary Material: Supplementary material on the mechanism of formation of the cobalt oxides, digital photograph of pure cobalt hydroxide, additional XPS characterization of the materials, standard powder diffraction pattern of crystalline Co_3O_4, BET surface and total pore volume of the materials as calculated form N_2 adsorption isotherms acquired at -196 °C, on electrochemical charge storage experiments for the non-calcined nanosheets and the nanosheets calcined at 250 and 450 ºC, as well as the UV-vis absorption spectra of the reactants and the products of the catalytic reduction of nitroarenes assayed in this work, and data from the literature on the performance of similar materials in the different applications assayed in this work to put our results into context is available.

References

[1] Ferrari, A. C.; Bonaccorso, F.; Fal'ko, V.; Novoselov, K. S.; Roche, S.; Boggild, P.; Borini, S.; Koppens, F. H. L.; Palermo, V.; Pugno, N. et al. Science and technology roadmap for graphene, related two-dimensional crystals, and hybrid systems. *Nanoscale* **2015**, *7*, 4598-4810.

[2] Ng, V.M.H.; Huang, H.; Zhou, K.; Lee, P. S.; Que, W.; Xu, J.Z.; Kong, L.B. Recent progress in layered transition metal carbides and/or nitrides (Mxenes) and their composites: synthesis and applications. *J. Mater. Chem. A* **2017**, *5*, 3039-3068.

[3] Zhang, K.; Feng, Y.; Wang, F.; Yang, Z.; Wang, J. Two dimensional hexagonal boron nitride (2D-hBN): synthesis, properties and applications. *J. Mater. Chem. C* **2017**, *5*, 11992-12022.

[4] Samadi, M.; Sarikhani, N.; Zirak, M.; Zhang, H.; Zhang, H.-L.; Moshfegh, A. Z. Group 6 transition metal dichalcogenide nanomaterials: synthesis, applications and future perspectives. *Nanoscale Horiz.* **2018**, *3*, 90-204.

[5] Zhang, S.; Guo, S.; Chen, Z.; Wang, Y.; Gao, H.; Gómez-Herrero, J.; Ares, P.; Zamora, F.; Zhu, Z.; Zeng, H. Recent progress in 2D group-VA semiconductors: from theory to experiment. *Chem. Soc. Rev.* **2018**, *47*, 982-1021.

[6] Tan, C.; Zhang, H. Wet-chemical synthesis and applications of non-layer structured two-dimensional nanomaterials. *Nat. Commun.* **2015**, *6*, 7873.

[7] Wang, F.; Wang, Z.; Shifa, T. A.; Wen, Y.; Wang, F.; Zhan, X.; Wang, Q.; Xu, K.; Huang, Y.; Yin, L. et al. Two-dimensional non-layered materials: synthesis, properties and applications. *Adv. Funct. Mater.* **2017**, *27*, 1603254.

[8] Dou, Y.; Zhang, L.; Xu, X.; Sun, Z.; Liao, T.; Dou, S. X. Atomically thin non-layered nanomaterials for energy storage and conversion. *Chem. Soc. Rev.* **2017**, *46*, 7338-7373.

[9] Yang, W.; Zhang, X.; Xie, Y. Advances and challenges in chemistry of two-dimensional nanosheets. *Nano Today* **2016**, *11*, 793-816.

[10] Tan, H. T.; Sun, W.; Wang, L.; Yan, Q. 2D transition metal oxides/hydroxides for energy-storage applications. *ChemNanoMat* **2015**, *2*, 562-577.

[11] Chen, P.-Y.; Liu, M.; Valentin, T. M.; Wang, Z.; Steinberg, R. S.; Sodhi, J.; Wong, I. Y.; Hurt, R. H. Hierarchical metal oxide topographies replicated from highly textured graphene oxide by intercalation templating. *ACS Nano* **2016**, *10*, 10869-10879.

[12] Kong, X.; Liu, Q.; Zhang, C.; Peng, Z.; Chen, Q. Elemental two-dimensional nanosheets beyond graphene. *Chem. Soc. Rev.* **2017**, *46*, 2127-2157.

[13] Liu, M.; Chen, P.-Y.; Hurt, R. H. Graphene inks as versatile templates for printing tiled metal oxide crystalline films. *Adv. Mater.* **2018**, *30*, 1705080.

[14] Sun, Y.; Gao, S.; Lei, F.; Liu, J.; Liang, L.; Xie, Y. Atomically-thin non-layered cobalt oxide porous sheets for highly efficient oxygen-evolving electrocatalysts. *Chem. Sci.* **2014**, *5*, 3976-3982.

[15] Du, S.; Ren, Z.; Qu, Y.; Wu, J.; Xi, W.; Zhu, J.; Fu, H. Co_3O_4 Nanosheets as a high-performance catalyst for oxygen evolution proceeding via a double two-electron process. *Chem. Commun*. **2016**, *52*, 6705-6708.

[16] Cai, Z.; Bi, Y.; Hu, E.; Liu, W.; Dwarica, N.; Tian, Y.; Li, X.; Kuang, Y.; Li, Y.; Yang, X.-Q et al. Single-crystalline ultrathin Co_3O_4 nanosheets with massive vacancy defects for enhanced electrocatalysis. *Adv. Energy Mater*. **2018**, *8*, 1701694.

[17] Yuan, C.; Yang, L.; Hou, L.; Shen, L.; Zhang, X.; Lou, X. W. Growth of ultrathin mesoporous Co_3O_4 nanosheet arrays on Ni foam for high-performance electrochemical capacitors. *Energy Environ. Sci.* **2012**, *5*, 7883-7887.

[18] Feng, C.; Zhang, J.; He, Y.; Zhong, C.; Hu, W.; Liu, L.; Deng, Y. Sub-3 nm Co_3O_4 nanofilms with enhanced supercapacitor properties. *ACS Nano* **2015**, *9*, 1730-1739.

[19] Fan, H.; Quan, L.; Yuan, M.; Zhu, S.; Wang, K.; Zhong, Y.; Chang, L.; Shao, H.; Wang, J.; Zhang, J. et al. Thin Co_3O_4 nanosheet array on 3D porous graphene/nickel foam as a binder-free electrode for high-performance supercapacitors. *Electrochim. Acta* **2016**, *188*, 222-229.

[20] Xiang, K.; Xu, Z.; Qu, T.; Tian, Z.; Zhang, Y.; Wang, Y.; Xie, M.; Guo, X.; Ding, W.; Guo, X. Two dimensional oxygen-vacancy-rich Co_3O_4 nanosheets with excellent supercapacitor performances. *Chem. Commun.* **2017**, *53*, 12410-12413.

[21] Xiao, Z.; Fan, L.; Xu, B.; Zhang, S.; Kang, W.; Kang, Z.; Lin, H.; Liu, X.; Zhang, S.; Sun, D. Metal–organic framework-derived metal oxide embedded in nitrogen-doped graphene network for high-performance lithium-ion batteries. *ACS Appl. Mater. Interfaces* **2017**, *9*, 41827-41836.

[22] Son, M. Y.; Kim, J. H.; Kang, Y. C. Study of Co_3O_4 mesoporous nanosheets prepared by a simple spray-drying process and their electrochemical properties as anode material for lithium secondary batteries. *Electrochim. Acta* **2014**, *116*, 44-50.

[23] Wang, B.; Lu, X.-Y.; Tang, Y.; Ben, W. General polyethyleneimine-mediated synthesis of ultrathin hexagonal Co_3O_4 nanosheets with reactive facets for lithium-ion batteries. *ChemElectroChem* **2016**, *3*, 55-65.

[24] AbdelHamid, A. A.; Yu, Y.; Yang, J.; Ying, J. Y. Generalized synthesis of metal oxide nanosheets and their application as Li-ion battery anodes. *Adv. Mater.* **2017**, *29*, 1701427.

[25] Yao, Y.; Zhu, Y.; Zhao, S.; Shen, J.; Yang, X.; Li, C. Magnetic electrodeposition of hierarchical cobalt oxide nanostructure from spent lithium-ion batteries: its application as supercapacitor electrode. *ACS Appl. Energy Mater.* **2018**, *1*, 1239-1251.

[26] Wang, G.; Yang, Y.; Han, D.; Li, Y. Oxygen defective metal oxides for energy conversion and storage. *Nano Today* **2017**, *13*, 23-39.

[27] Kou, T.; Yao, B.; Liu, T.; Li, Y. Recent advances in chemical methods for activating carbon and metal oxide based electrodes for supercapacitors. *J. Mater. Chem. A* **2017**, *5*, 17151-17173.

[28] Kalantar-zadeh, K.; Ou, J. Z.; Daeneke, T.; Mitchell, A.; Sasaki, T.; Fuhrer, M. S. Two dimensional and layered transition metal oxides. *Appl. Mater. Today* **2016**, *5*, 73-89.

[29] Zhang, G.; Xiao, X.; Li, B.; Gu, P.; Xue, H.; Pang, H. transition metal oxides with one-dimensional/one-dimensional-analogue nanostructures for advanced supercapacitors. *J. Mater. Chem. A* **2017**, *5*, 8155-8186.

[30] Kong, D.; Ren, W.; Cheng, C.; Wang, Y.; Huang, Z.; Yang, H. Y. Three–dimensional $NiCo_2O_4$@polypyrrole coaxial nanowire arrays on carbon textiles for high-performance flexible asymmetric solid–state supercapacitor. *ACS Appl. Mater. Interfaces* **2015**, *7*, 21334−21346.

[31] Sahoo, S.; Shim, J.-J. Facile synthesis of three-dimensional ternary $ZnCo_2O_4$/reduced graphene oxide/NiO composite film on nickel foam for next generation supercapacitor electrodes. *ACS Sustainable Chem. Eng.* **2017**, *5*, 241−251.

[32] Young, C.; Salunkhe, R. R.; Alshehri, S. M.; Ahamad, T.; Huang, Z.; Henzie, J.; Yamauchi, Y. High energy density supercapacitors composed of nickel cobalt oxide

nanosheets on nanoporous carbon nanoarchitectures. *J. Mater. Chem. A* **2017**, *5*, 11834-11839.

[33] Kaneti, Y. V.; Salunkhe, R. R.; Septiani, N.L.W.; Young, C.; Jiang, X. C.; He, Y. B.; Kang, Y. M.; Sugahara, Y.; Yamauchi, Y. General template-free strategy for fabricating mesoporous two-dimensional mixed oxide nanosheets via self-deconstruction/reconstruction of monodispersed metal glycerate nanospheres. *J. Mater. Chem. A* **2018**, *6*, 5971-5983.

[34] Li, X.; Wang, L.; Shi, J.; Du, N.; He, G. Multishelled nickel−cobalt oxide hollow microspheres with optimized compositions and shell porosity for high-performance pseudocapacitors. *ACS Appl. Mater. Interfaces* **2016**, *8*, 17276−17283.

[35] Wang, Y.; Zhou, T.; Jiang, K.; Da, P.; Peng, Z.; Tang, J.; Kong, B.; Cai, W.-B.; Yang, Z.; Zheng, G. Reduced mesoporous Co_3O_4 nanowires as efficient water oxidation electrocatalysts and supercapacitor electrodes. *Adv. Energy Mater.* **2014**, *4*, 1400696.

[36] Chen, H.; Yang, M.; Tao, S.; Chen, G. Oxygen vacancy enhanced catalytic activity of reduced Co_3O_4 towards p-nitrophenol reduction. *Appl. Catal. B: Environ.* **2017**, *209*, 648-656.

[37] Yang, S.; Liu, Y.; Hao, Y.; Yang, X.; Goddard, W. A.; Zhang, X. L.; Cao, B. Oxygen-vacancy abundant ultrafine Co_3O_4/graphene composites for high-rate supercapacitor electrodes. *Adv. Sci.* **2018**, *5*, 1700659.

[38] Yang, M.-Q.; Wang, J.; Wu, H.; Ho, G. W. Noble metal-free nanocatalysts with vacancies for electrochemical water splitting. *Small* **2018**, *14*, 1703323.

[39] Wei, R.; Fang, M.; Dong, G.; Lan, C.; Shu, L.; Zhang, H.; Bu, X.; Ho, J. C. High-index faceted porous Co_3O_4 nanosheets with oxygen vacancies for highly efficient water oxidation. *ACS Appl. Mater. Interfaces* **2018**, *10*, 7079-7086.

[40] Qiao, L.; Swihart, M. T. Solution-phase synthesis of transition metal oxide nanocrystals: morphologies, formulae, and mechanisms. *Adv. Colloid Interface Sci.* **2017**, *244*, 199-266.

[41] Sun, Z.; Liao, T.; Dou, Y.; Hwang, S. M.; Park, M.-S.; Jiang, L.; Kim, J. H.; Dou, S. X. Generalized self-assembly of scalable two-dimensional transition metal oxide nanosheets. *Nat. Commun.* **2014**, *5*, 3813.

[42] Xu, L.; Jiang, Q.; Xiao, Z.; Li, X.; Huo, J.; Wang, S.; Dai, L. Plasma-engraved Co_3O_4 nanosheets with oxygen vacancies and high surface area for the oxygen evolution reaction. *Angew. Chem. Int. Ed.* **2016**, *55*, 5277-5281.

[43] Zhou, Y.; C.-K. Dong, C.-K.; L.-L. Han, L.-L.; J. Yang, J.; X.-W. Du, X.-D. Top-down preparation of active cobalt oxide catalyst. *ACS Catal.* **2016**, *6*, 6699-6703.

[44] Shim, H.-S.; Shinde, V. R.; Kim, H. J.; Sung, Y.-E.; Kim, W. B. Porous cobalt oxide thin films from low temperature solution phase synthesis for electrochromic electrode. *Thin Solid Films* **2008**, *516*, 8573-8578.

[45] Farhadi, S.; Safabakhsh, J.; Zaringhadam, P. Synthesis, Characterization, and investigation of optical and magnetic properties of cobalt oxide (Co_3O_4) nanoparticles. *J. Nanostruct. Chem.* **2013**, *3*, 69.

[46] Kang, M.; Zhou, H. Facile synthesis and structural characterization of Co_3O_4 nanocubes. *AIMS Mater. Sci.* **2015**, *2*, 16-27.

[47] Samal, R.; Dash, B.; Sarangi, C. K.; Sanjay, K.; Subbaiah, T.; Senanayake, G.; Minakshi, M. Influence of synthesis temperature on the growth and surface morphology of Co_3O_4 nanocubes for supercapacitor applications. *Nanomaterials* **2017**, *7*, 356.

[48] Ma, K.; Liu, F.; Yuan, Y. F.; Liu, X. Q.; Wang, J.; Xie, J.; Cheng, J. P. CoO microspheres and metallic Co evolved from Hexagonal α-$Co(OH)_2$ plates in a

hydrothermal process for lithium storage and magnetic applications. *Phys. Chem. Chem. Phys.* **2018**, *20*, 595-604.

[49] Nethravathi, C.; Sen, S.; Ravishankar, N.; Rajamathi, M.; Pietzonka, C.; Harbrecht, B. Ferrimagnetic nanogranular Co_3O_4 through solvothermal decomposition of colloidally dispersed monolayers of α-cobalt hydroxide. *J. Phys. Chem. B* **2005**, *109*, 11468-11472.

[50] Dou, Y.; Zhang, L.; Xu, J.; He, C.-T.; Xu, X.; Sun, Z.; Liao, T.; Nagy, B.; Liu, P.; Dou, S. X. Manipulating the architecture of atomically thin transition metal (hydr)oxides for enhanced oxygen evolution catalysis. *ACS Nano* **2018**, *12*, 1878−1886.

[51] N. N. Greenwood, A. Earnshaw. Chemistry of the elements. Ch. 26: Cobalt, rhodium and iridium., p. 1296. Pergamon Press. Oxford, 1984.

[52] Ma, R.; Liu, Z.; Takada, K.; Fukuda, K.; Ebina, Y.; Bando, Y.; Sasaki, T. Tetrahedral Co(II) coordination in α-type cobalt hydroxide: Rietveld refinement and X-ray absorption spectroscopy. *Inorg. Chem.* **2006**, *45*, 3964-3969.

[53] Al-Ghoul, M.; El-Rassy, H.; Coradin, T.; Mokalled, T. Reaction–diffusion based co-synthesis of stable α- and β-cobalt hydroxide in bio-organic gels. *J. Cryst. Growth* **2010**, *312*, 856-862.

[54] Schneiderová, B.; Demel, J.; Pleštil, J.; Tarábková, H.; Bohuslav, J.; Lang, K. Electrochemical performance of cobalt hydroxide nanosheets formed by the delamination of layered cobalt hydroxide in water. *Dalton Trans.* **2014**, *43*, 10484-10491.

[55] Lyu, F.; Bai, Y.; Wang, Q.; Wang, L.; Zhang, X.; Yin, Y. Phase-controllable synthesis of cobalt hydroxide for electrocatalytic oxygen evolution. *Dalton Trans.* **2017**, *46*, 10545-10548.

[56] Kim, T. W.; Oh, E.-J.; Jee, A.-Y.; Lim, S. T.; Park, D. H.; Lee, M.; Hyun, S.-H.; Choy, J.-H.; Hwang, S.-J. Soft-Chemical exfoliation route to layered cobalt oxide monolayers and its application for film deposition and nanoparticle synthesis. *Chem. Eur. J.* **2009**, *15*, 10752-10761.

[57] Kundu, S.; Jayachandran, M. Shape-selective synthesis of non-micellar cobalt oxide (CoO) nanomaterials by microwave irradiations. *J. Nanopart. Res.* **2013**, *15*, 1543.

[58] Ma, R.; Liu, Z.; Takada, K.; Fukuda, K.; Ebina, Y.; Bando, Y.; Sasaki, T. Tetrahedral Co(II) Coordination in α-type Cobalt Hydroxide: Rietveld Refinement and X-Ray Absorption Spectroscopy. *Inorg. Chem.* **2006**, *45*, 3964-3969.

[59] Gallant, D.; Pézolet, M.; Simard, S. Optical and physical properties of cobalt oxide films electrogenerated in bicarbonate aqueous media. *J. Phys. Chem. B* **2006**, *110*, 6871-6880.

[60] Alrehaily, L. M.; Joseph, J. M.; Wren, J. C. Radiation-induced formation of Co_3O_4 nanoparticles from Co^{2+}(aq): Probing the Kinetics Using Radical Scavengers. *Phys. Chem. Chem. Phys.* **2015**, *17*, 24138-24150.

[61] Li, Y.; Qiu, W.; Qin, F.; Fang, H.; Hadjiev, V. G.; Litvinov, D.; Bao, J. Identification of cobalt oxides with Raman scattering and Fourier transform infrared spectroscopy. *J. Phys. Chem. C* **2016**, *120*, 4511-4516.

[62] Rivas-Murias, B.; Salgueiriño, V. Thermodynamic CoO– Co_3O_4 crossover using Raman spectroscopy in magnetic octahedron-shaped nanocrystals. *J. Raman Spectrosc.* **2017**, *48*, 837-841.

[63] Li, H. B.; Yu, M. H.; Lu, X. H.; Liu, P.; Liang, Y.; Xiao, J.; Tong, Y. X.; Yang, G. W. Amorphous cobalt hydroxide with superior pseudocapacitive performance. *ACS Appl. Mater. Interfaces* **2014**, *6*, 745-749.

[64] Choi, H. C.; Jung, Y. M.; Noda, I.; Kim, S. B. A Study of the mechanism of the electrochemical reaction of lithium with CoO by two-dimensional soft X-ray absorption spectroscopy (2D XAS), 2D Raman, and 2D heterospectral XAS−Raman correlation analysis. *J. Phys. Chem. B* **2003**, *107*, 5806-5811.

[65] Ravindra, A. V.; Behera, B. C.; Padhan, P. Laser induced structural phase transformation of cobalt oxides nanostructures. *J. Nanosci. Nanotechnol.* **2014**, *14*, 5591-5595.

[66] Johansson, G.; Hedman, J.; Berndtsson, A.; Klasson, M.; Nilsson, R. Calibration of electron spectra. *J. Electron Spectrosc.* **1973**, *2*, 295.

[67] Cochran, S. J.; Larkins, F. P. Surface reduction of some transition-metal oxides. an X-Ray photoelectron spectroscopic study of iron, cobalt, nickel and zinc oxides. *J. Chem. Soc., Faraday Trans. 1*, **1985**, *81*, 2179-2190

[68] Chuang, T. J.; Bridle, C. R.; Rice, D. W. Interpretation of the X-Ray photoemission spectra of cobalt oxides and cobalt oxide surfaces. *Surface Science* **1976**, *59*, 413-429.

[69] Wang, G.; Shen, X.; Horvat, J.; Wang, B.; Liu, H.; Wexler, D.; Yao, J. Hydrothermal synthesis and optical, magnetic, and supercapacitance properties of nanoporous cobalt oxide nanorods. *J. Phys. Chem. C* **2009**, *113*, 4357-4361.

[70] Gao, S.; Sun, Z.; Liu, W.; Jiao, X.; Zu, X.; Hu, Q.; Sun, Y.; Yao, T.; Zhang, W.; Wei, S. et al. atomic layer confined vacancies for atomic-level insights into carbon dioxide electroreduction. *Nat. Commun*. **2017**, *8*, 14503.

[71] Cheng, G.; Kou, T.; Zhang, J.; Si, C.; Gao, H.; Zhang, Z. O_2^{2-}/O^- functionalized oxygen-deficient Co_3O_4 Nanorods as high performance supercapacitor electrodes and electrocatalysts towards water splitting. *Nano Energy* **2017**, *38*, 155-166.

[72] Tian, X.; Sun, X.; Jiang, Z.; Jiang, Z.-J.; Hao, X.; Shao, D.; Maiyalagan, T. Exploration of the active center structure of nitrogen-doped graphene for control over the growth of Co_3O_4 for a high-performance supercapacitor. *ACS Appl. Energy Mater.* **2018**, *1*, 143-153.

[73] Yan, K.-L.; Qin, J.-F.; Lin, J.-H.; Dong, B.; Chi, J.-Q.; Liu, Z.-Z.; Dai, F.-N.; Chai, Y.-M.; Liu, C.-G. Probing the active sites of Co_3O_4 for the acidic oxygen evolution reaction by modulating the Co^{2+}/Co^{3+} ratio. *J. Mater. Chem. A* **2018**, *6*, 5678-5686.

[74] Wang, H.-Y.; Hung, S.-F.; Chen, H.-Y.; Chan, T.-S.; Chen, H. M.; Liu, B. In operando identification of geometrical-site-dependent water oxidation activity of spinel Co_3O_4. *J. Am. Chem. Soc.* **2016**, *138*, 36-39.

[75] Brousse, T.; Bélanger, D.; Long, J. W. To be or not to be pseudocapacitive? *J. Electrochem. Soc.* **2015**, *162*, A5185-A5189.

[76] Gogotsi, Y.; Penner, R. M. Energy storage in nanomaterials – capacitive, pseudocapacitive, or battery-like? *ACS Nano* **2018**, *12*, 2081-2983.

[77] Tan, H.; Liu, Z.; Chao, D.; Hao, P.; Jia, D.; Sang, Y.; Liu, H.; Fan, H. J. Partial nitridation-induced electrochemistry enhancement of ternary oxide nanosheets for fiber energy storage device. *Adv. Energy Mater.* **2018**, *8*, 1800685.

[78] Aditya, T.; Pal, A.; Pal, T. Nitroarene reduction: a trusted model reaction to test nanoparticle catalysts. *Chem. Commun.* **2015**, *51*, 9410-9431.

[79] Hu, H.; Xin, J. H.; Hu, H.; Wang, X.; Miao, D.; Liu, Y. Synthesis and stabilization of metal nanocatalysts for reduction reactions – a review. *J. Mater. Chem. A* **2015**, *3*, 11157-11182.

[80] Mandlimath, T. R.; Gopal, B. Catalytic activity of first row transition metal oxides in the conversion of p-nitrophenol to p-aminophenol. *J. Mol. Catal. A: Chem.* **2011**, *350*, 9-15.

[81] Ayán-Varela, M.; Paredes, J. I.; Guardia, L.; Villar-Rodil, S.; Munuera, J. M.; Díaz- González, M.; Fernández-Sánchez, C.; Martínez-Alonso, A.; Tascón, J. M. D. Achieving Extremely Concentrated Aqueous Dispersions of Graphene Flakes and Catalytically Efficient Graphene-Metal Nanoparticle Hybrids with Flavin Mononucleotide as a High Performance Stabilizer. *ACS Appl. Mater. Interfaces* **2015**, *7*, 10293-10307.

Supporting Information for

A direct route to activated two-dimensional cobalt oxide nanosheets for electrochemical energy storage, catalytic and environmental applications

J.M. Munuera, J.I. Paredes, S. Villar-Rodil, S. García-Dalí, A. Castro-Muñiz, A. Martínez-Alonso, J.M.D. Tascón
Instituto Nacional del Carbón, INCAR-CSIC, C/Fracisco Pintado Fe 26, 33011 Oviedo, Spain

Contents

S1. Reaction mechanism for the formation of cobalt oxides

Firstly, the hydrolysis of cobalt acetate itself results in the formation of OH^- ions (Eq. 1), which provide a basic environment for the formation of cobalt hydroxide:

$$CH_3COO^- + H_2O \rightarrow CH_3COOH + OH^- \quad (1)$$

Also the hydrolysis of hexamethylene tetramine ($C_6H_{12}N_4$) generates ammonia which in turn releases OH^- ions into the solution [1] according to Eqs. (2) and (3):

$$C_6H_{12}N_4 + 6\ H_2O \rightarrow 6\ HCHO + 4\ NH_3 \quad (2)$$

$$NH_3 + H_2O \rightarrow NH_4^+ + OH^- \quad (3)$$

Hydroxide anion reacts with Co^{2+}, which results in the formation of $Co(OH)_2$ nanosheets Eq. (4):

$$Co^{2+} + 2\ OH^- \rightarrow Co(OH)_2 \quad (4)$$

Both the presence of a small amount of water and the fact that the temperature is 170 °C, which is above that typical for synthesizing cobalt hydroxide (< 150 °C), could allow cobalt precursor to develop past the hydroxide stage into cobalt oxide [2]. Indeed, dehydration of the hydroxide will be favored under such conditions Eq. (5):

$$Co(OH)_2 \rightarrow CoO + H_2O \quad (5)$$

Ethylene glycol can act as reducing agent, keeping cobalt in divalent state [3].

Finally, CoO is oxidized to Co_3O_4 by calcination with O_2at 250–450 °C, which is shown in Eq. (6):

$$3CoO + ½\ O_2 \rightarrow Co_3O_4 \quad (6)$$

S2. Additional information on the characterization of the materials

Figure S1. Digital photograph of pure $Co(OH)_2$ as received from Sigma-Aldrich.

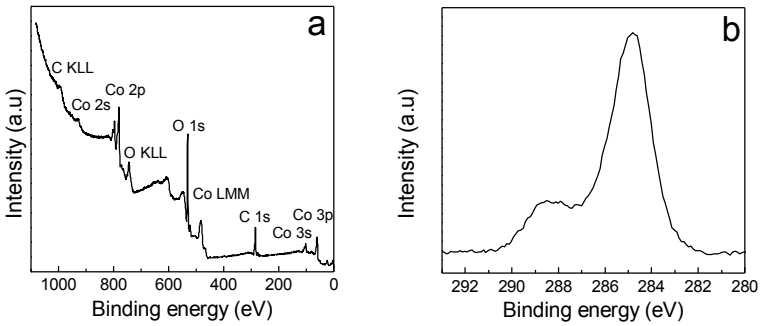

Figure S2. XPS survey spectrum (a) and high resolution XPS C 1s core-level spectrum of the as-prepared solvothermal nanosheets.

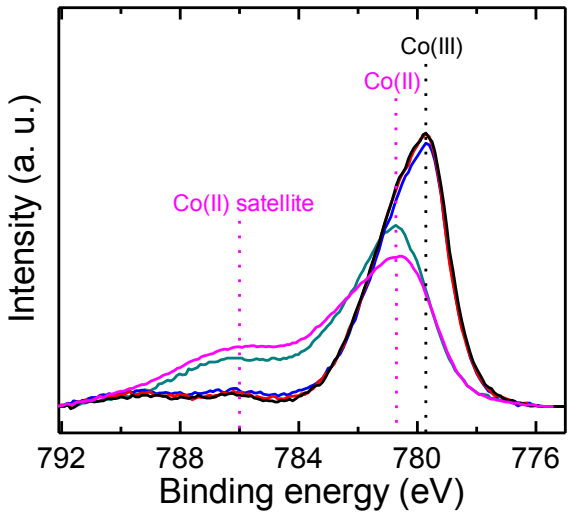

Figure S3. Background-subtracted, normalized Co $2p_{3/2}$ XPS spectra for all the materials prepared here: as-prepared solvothermal nanosheets (green trace) and nanosheets calcined at 250 °C (blue trace), 350 °C (red trace) and 450 °C (black trace). The spectra of pure $Co(OH)_2$ (magenta trace) has been added as a reference. The location of the main features of the spectra is indicated by the dotted lines. Specifically, Co(III) peak is located at ~779.6 eV, while Co(II) displays both a main band at ~780.9 eV and a satellite at ~786 eV.

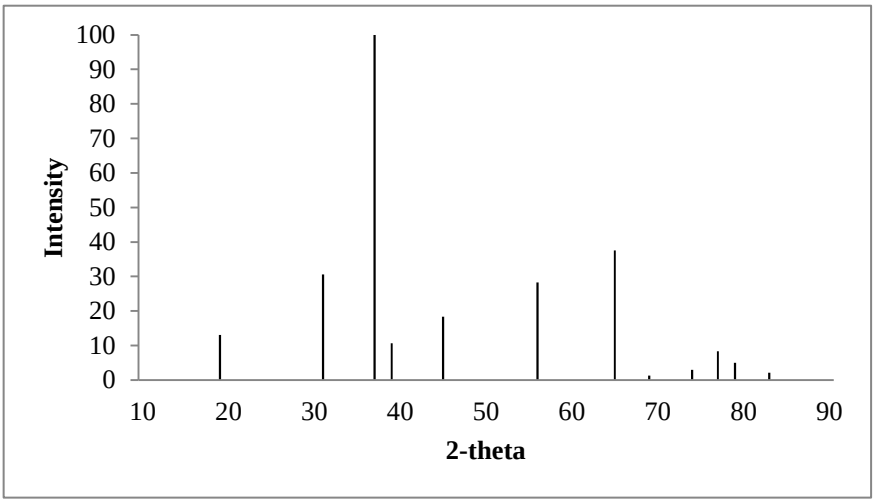

Figure S4. Powder Co_3O_4 diffraction pattern

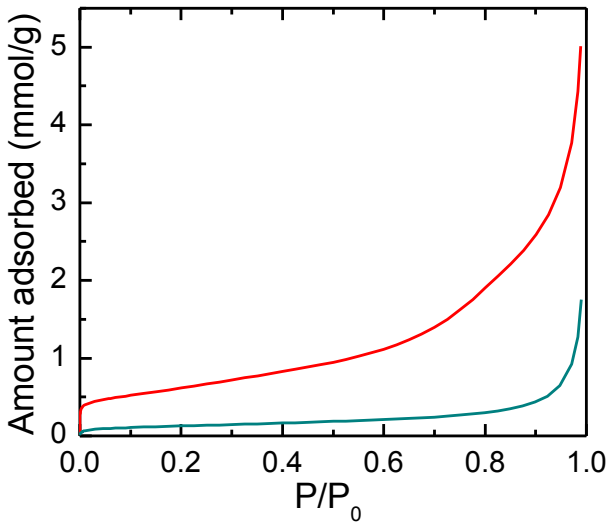

Figure S5. N_2 adsorption isotherms recorded at -196° on a volumetric apparatus (ASAP, from Micromeritics) for the non-calcined material (green trace) and that calcined at 350° C (red trace). Prior to the analysis, the samples were outgassed overnight at 150° C under vacuum. The BET surface areas were calculated according to the BET model from the nitrogen isotherms in the relative pressure range 0.05–0.35 and were 10 and 50 m^2 g^{-1} for the non-calcined and calcined material, respectively. The total pore volumes were calculated as the amount of N_2 adsorbed at the relative pressure of 0.95, yielding values of 0.02 and 0.11 cm^3 g^{-1} for the non-calcined and the calcined material, respectively.

S3. Additional information on the application of the materials

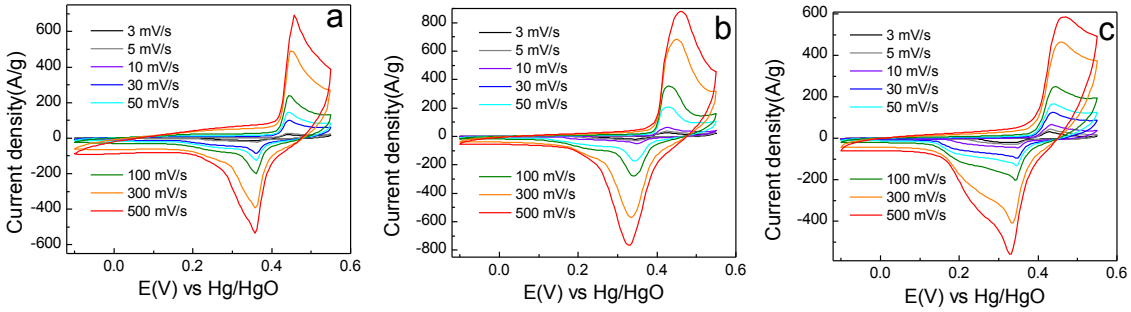

Figure S6. Cyclic voltammograms recorded at different potential scan rates between 3 and 500 mV s^{-1} for the non-calcined nanosheets (a) as well as nanosheets calcined at 250 (b) and 450 ºC (c).

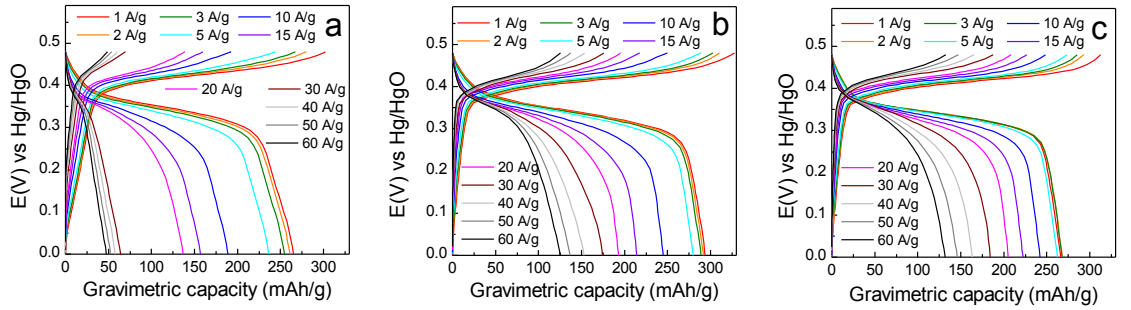

Figure S7. Galvanostatic charge-discharge curves recorded at different current densities between 1 and 60 A g^{-1} for the non-calcined nanosheets (a) as well as nanosheets calcined at 250 (b) and 450 ºC (c).

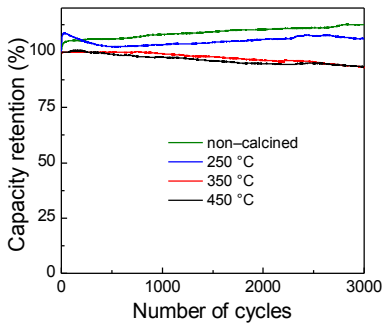

Figure S8. Capacity retention (in percentage) of the non-calcined and calcined nanosheets as a function of the number of charge/discharge cycles (cycle 1 = 100%).

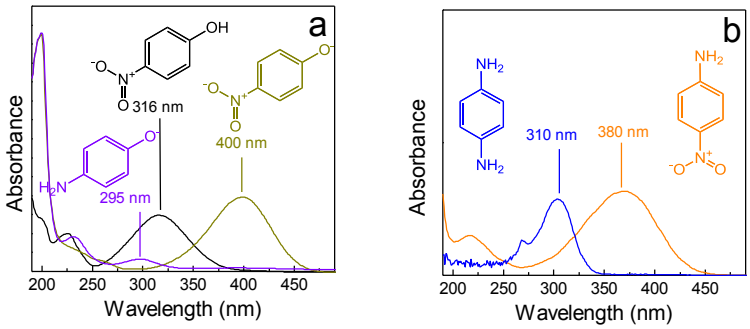

Figure S9. (a) UV-vis absorption spectra of 4-NP (black curve), its corresponding 4-nitrophenoxide anion (green) and the reduced anion 4-aminophenoxide (violet). (b) UV-vis absorption spectra of 4-nitroaniline (orange curve) and its reduced form *p*-phenylenediamine (blue).

Table S1. Gravimetric capacity values of a range of nanostructured Co_3O_4 materials measured in three-electrode configuration and alkaline electrolyte at different current densities.

Material	**Gravimetric capacity (mAh g^{-1})**	**Current density (A g^{-1})**	**Electrolyte**	**Reference**
Activated Co_3O_4 nanosheets (calcined at 350º)	293 291 283 269 258 225	1 2 5 10 15 30	6 M KOH	This work
Co_3O_4 nanorods	89.6 89.0 87.9 85.6 83.9 77.3	4.1 6.8 9.1 13.6 18.2 27.3	2 M KOH	S4
Co_3O_4 nanofilms	182.8 179.6 174.9 166.6	1 2 4 8	2 M KOH	S5
Co_3O_4 thin sheets	166.7 143.4 129.7 110.3 92.0	1 2 3 5 10	2 M KOH	S6
Mesoporous Co_3O_4 nanosheets on Ni foam	243.8 219.0 201.6 173.6 148.4 133.1	1 2 3 5 10 15	1 M KOH	S7
Reduced mesoporous Co_3O_4 nanowires	135.8 133.9 121.0 106.9 97.4 82.1 67.2	2 3 4 5 6 8 10	1 M KOH	S8
Oxygen-vacancy-rich Co_3O_4 nanosheets	243.9 226.6 221.1 203.8 182.1 176.8	1 2 4 8 16 32	6 M KOH	S9
Ultrathin Co_3O_4 Nanosheets	171.3 133.4	1 25	6 M KOH	S10
Co_3O_4 nanosheet arrays	222.8	1.8	2 M KOH	S11

Mesoporous Co_3O_4 nanosheet arrays	341.9 315.4 274.9 238.9 221.0 198.3 183.9	2 3 4 5 6 8 10	2 M KOH	S12
Phosphate ion functionalized Co_3O_4 ultrathin nanosheets	286.0	4.5	6 M KOH	S13
3D Co_3O_4 twinspheres	86.8 83.8 77.8 74.4 67.9	0.5 1 2 4 8	6 M KOH	S14
Co_3O_4 nanosheets	39.3 34.7	1 10	2 M KOH	S15
CoO/Co_3O_4 nanocomposite	50.1 43.2 39.2 36.2 34.2	1 5 10 15 20	3 M KOH	S16
Mesoporous Co_3O_4 nanowire	161.1 138.3 122.8 119.6 113.9	2 5 10 15 20	6 M KOH	S17
Macro-/ mesoporous Co_3O_4	103.1 56.1	0.5 20	2 M KOH	S18

Table S2. Catalytic activities of Co_3O_4 nanomaterials, as well as other materials based on non-noble metals and/or their oxides, in the reduction of 4-NP with $NaBH_4$. The catalytic activity is calculated as the number of moles of 4-NP converted per unit time per mole of metal in the catalyst. Acronyms: NP (nanoparticle), MOF (metal-organic framework), RGO (reduced graphene oxide).

Catalyst	TOF 4-nitrophenol (h^{-1}; relative to molar amount of Co)	TOF 4-nitroaniline (h^{-1}; relative to molar amount of Co)	Reference
Non-calcined nanosheets	4.7	6.8	This work
Calcined at 250 ºC	3.8	7.0	This work
Calcined at 350 ºC	2.5	5.6	This work
Calcined at 450 ºC	2.1	3.8	This work
Co3O4 nanoplates activated through reduction post-treatment	0.8-2.1		S19
Co3O4 nanowires	1.8		S20
Co3O4 powder	0.7		S21
CuO powder	0.7		S21
Fe2O3 powder	0.6		S21
NiO powder	0.05		S21
Mesoporous Co3O4 NPs	0.05		S22
Ca-doped mesoporous Co3O4 NPs	0.06		S23
CoOx clusters embedded in N-doped carbon derived from MOF	9.9		S24
Cu NPs supported onto carbon spheres	0.2		S25
Submicrometric Cu particles supported onto carbon spheres	0.05-0.2		S25
Co@BN nanoparticles	0.4		S26
CuNi alloy NPs	12.0		S27
Cu nanocrystals supported onto RGO	0.6		S28
Hexagonal Ni plates supported onto RGO	0.4		S29
Hollow porous Cu particles	3.0		S30
Co NPs embedded in MOF-derived nanoporous carbon	18.0		S31
Co NPs embedded in ordered mesoporous carbon	7.8		S32
Ni NPs supported onto RGO	0.1		S33
Cu NPs supported onto mesoporous carbon	9.6		S34
Ni NPs supported onto silica nanotubes	1.8		S35
Ni NPs supported onto MOF-derived mesoporous carbon	0.25		S36
Hollow CuO nanospheres	4.2		S37
Hollow NiO nanospheres	3.0		S37

Table S3. Adsorption capacities of different metal oxides towards methylene blue and methyl orange from the aqueous phase.

Material	**Adsorbate**	**Adsorption capacity (mg/g)**	**Reference**
Co_3O_4 nanosheets	Methyl orange	909.3	This work
Mg-Al mixed metal oxides	Methyl orange	182.8	S38
Zn-Al mixed metal oxides	Methyl orange	178.6	S39
CuO_2 particles	Methyl orange	96.42	S40
Fe_3O_4/ZnCr-layered double hydroxide	Methyl orange	240.16	S41
Co_3O_4 nanosheets	Methylene blue	916.2	This work
MgO-urea	Methylene blue	19.2	S42
$CoFe_2O_4$	Methylene blue	26.4	S43
Co_3O_4/SiO_2	Methylene blue	53.87	S44
Manganese Oxide Nanostructures	Methylene blue	68.4	S45
γ-MnOOH nanorods	Methylene blue	50.0	S46

S4. References

[S1] X. Wang, H. Xia, Xiuqin Wang, J. Gao, B. Shi, Y. Fang. Facile synthesis ultrathin mesoporous Co_3O_4 nanosheets for high-energy asymmetric supercapacitor. J. Alloys Comp. 2016, 686, 969–975.

[S2] Ma, K.; Liu, F.; Yuan, Y. F.; Liu, X. Q.; Wang, J.; Xie, J.; Cheng, J. P. CoO microspheres and metallic Co evolved from Hexagonal α-Co(OH)2 plates in a hydrothermal process for lithium storage and magnetic applications. Phys. Chem. Chem. Phys. 2018, 20, 595-604.

[S3] Li-Xia Yang, Ying-Jie Zhu, Liang Li, Ling Zhang, Hua Tong, Wei-Wei Wang, Guo-Feng Cheng, and Jie-Fang Zhu.A Facile Hydrothermal Route to Flower-Like Cobalt Hydroxide and Oxide. Eur. J. Inorg. Chem. 2006, 4787–4792.

[S4] Cheng, G.; Koub, T.; Zhang, J., Si, C.; Gao, H.; Zhang, Z. O22-/O- functionalized oxygen-deficient Co_3O_4 nanorods as high performance supercapacitor electrodes and electrocatalysts towards water splitting. *Nano Energy* **2017**, *38*, 155–166.

[S5] Feng, C.; Zhang, J.; He, Y.; Zhong, C.; Hu, W.; Liu, L.; Deng, Y. Sub‑3 nm Co_3O_4 nanofilms with enhanced supercapacitor properties. *ACS Nano* **2015**, *9*, 1730-1739.

[S6] Jiang, Y.; Chen, L.; Zhang, H.; Zhang, Q.; Chen, W.; Zhu, J.; Song, D. Two-dimensional Co_3O_4 thin sheets assembled by 3D interconnected nanoflake array framework structures with enhanced supercapacitor performance derived from coordination complexes. *Chem. Eng. J.* **2016**, *292*, 1–12.

[S7] Qiu, K.; Lu, Y.; Cheng, J.; Yan, H.; Hou, X.; Zhang, D.; Lu, M.; Liu, X.; Luo, Y. Ultrathin mesoporous Co_3O_4 nanosheets on Ni foam for high-performance supercapacitors. *Electrochim. Acta* **2015**, *157*, 62–68.

[S8] Wang, Y.; Zhou, T.; Jiang, K.; Da, P.; Peng, Z.; Tang, J.; Kong, B.; Cai, W.; Yang, Z.; Zheng, G. Reduced mesoporous Co_3O_4 nanowires as efficient water oxidation electrocatalysts and supercapacitor electrodes. *Adv. Energy Mater.* **2014**, *4*, 1400696.

[S9] Xiang, K.; Xu, Z.; Qu, T.; Tian, Z.; Zhang, Y.; Wang, Y.; Xie, M.; Guo, X.; Ding, W.; Guo, X. Two dimensional oxygen-vacancy-rich Co_3O_4 nanosheets with excellent supercapacitor performances. *Chem. Commun.* **2017**, *53*, 12410-12413.

[S10] Xiao, Z.; Fan, L.; Xu, B.; Zhang, S.; Kang, W.; Kang, Z.; Lin, H.; Liu, X.; Zhang, S.; Sun, D. Green fabrication of ultrathin Co_3O_4 nanosheets from metal−organic framework for robust high-rate supercapacitors. *ACS Appl. Mater. Interfaces* **2017**, *9*, 41827−41836.

[S11] Yang, Q.; Lu, Z.; Sun, X.; Liu, J. Ultrathin Co_3O_4 nanosheet arrays with high supercapacitive performance. *Sci. Rep.* **2013**, *3*, 3537.

[S12] Yuan, C.; Yang, L.; Hou, L.; Shen, L.; Zhang, X.; Lou, X. W. Growth of ultrathin mesoporous Co_3O_4 nanosheet arrays on Ni foam for high-performance electrochemical capacitors. *Energy Environ. Sci.* **2012**, *5*, 7883–7887.

[S13] Zhai, T.; Wan, L.; Sun, S.; Chen, Q.; Sun, J.; Xia, Q.; Xia, H. Phosphate ion functionalized Co_3O_4 ultrathin nanosheets with greatly improved surface reactivity for high performance pseudocapacitors. *Adv. Mater.* **2016**, 1604167.

[S14] Xiao, Y.; Liu, S.; Li, F.; Zhang, A.; Zhao, J.; Fang, S.; Jia, D. 3D hierarchical Co_3O_4 twin-spheres with an urchin-like structure: large-scale synthesis, multistep-splitting growth, and electrochemical pseudocapacitors. *Adv. Funct. Mater.* **2012**, *22*, 4052.

[S15] Wang, Y.; Zhong, Z.; Chen, Y.; Ng, C. T.; Lin, J. Controllable Synthesis of Co_3O_4 from Nanosize to Microsize with Large-Scale Exposure of Active Crystal Planes and Their Excellent Rate Capability in Supercapacitors Based on the Crystal Plane Effect. *Nano Res.* **2011**, *7*, 695–704.

[S16] Pang, M.; Long, G.; Jiang, S.; Ji, Y.; Han, W.; Wang, B.; Liu, X.; Xi, Y.; Wang, D.; Xu, F. Ethanol-assisted solvothermal synthesis of porous nanostructured cobalt oxides (CoO/Co_3O_4) for high-performance supercapacitors. *Chem. Eng. J.* **2015**, *280*, 377–384.
[S17] Zhang, Z.; Yuan, C.; Lu, X.; Zhang, L.; Che, Q.; Zhang, X. Facile growth of mesoporous Co_3O_4 nanowire arrays on Ni foam for high performance electrochemical capacitors. *J. Power Sources* **2012**, *203*, 250–256.
[S18] Wang, X.; Sumboja, A.; Khoo, E.; Yan, C.; Lee, P. S. Cryogel Synthesis of hierarchical interconnected macro-/mesoporous Co_3O_4 with superb electrochemical energy storage. *J. Phys. Chem. C* **2012**, *116*, 4930−4935.
[S19] Chen, H.; Yang, M.; Tao, S.; Chen, G. Oxygen vacancy enhanced catalytic activity of reduced Co3O4 towards p-nitrophenol reduction. *Appl. Catal. B: Environ.* **2017**, *209*, 648-656.
[S20]Huang, X.; Wu, D.; Cheng, D. Porous Co_2P nanowires as high efficient bifunctional catalysts for 4-nitrophenol reduction and sodium borohydride hydrolysis. *J. Colloid Interface Sci.* **2017**, *507*, 429–436.
[S21] Triveni Rajashekhar Mandlimath, T. R.; Buvaneswari Gopal, B. Catalytic activity of first row transition metal oxides in the conversion of p-nitrophenol to p-aminophenol. *J. Mol. Catal. A: Chem.* **2011**, *350*, 9–15.
[S22]Mogudi, B. M.; Ncube, P.; Meijboom, R. Catalytic activity of mesoporous cobalt oxides with controlled porosity and crystallite sizes: Evaluation using the reduction of 4-nitrophenol. *Appl. Catal., B* **2016**, *198*, 74–82.
[S23]Mogudi, B. M.; Ncube, P.; Bingwa, N.; Mawila, N.; Mathebula, S.; Meijboom, R. Promotion effects of alkali- and alkaline earth metals on catalytic activity of mesoporous Co_3O_4 for 4-nitrophenol reduction. *Appl. Catal., B* **2017**, *218*, 240–248.
[S24]Zhang, X.; Wang, N.; Geng, L.; Fu, J.; Hua, H.; Zhang, D.; Zhu, B.; Carozza, J.; Han, H. Facile synthesis of ultrafine cobalt oxides embedded into N-doped carbon with superior activity in hydrogenation of 4-nitrophenol. *J. Colloid Interface Sci.* **2018**, *512*, 844–852.
[S25]Cheng, X.; Fu, A.; Li, H.; Wang, Y.; Guo, P.; Liu, J.; Zhang, J.; Zhao, X. S. Sustainable preparation of copper particles decorated carbon microspheres and studies on their bactericidal activity and catalytic properties. *ACS Sustainable Chem. Eng.* **2015**, *10*, 2414-2422.
[S26] Du, M.; Liu, Q.; Huang, C.; Qiu, X. One-step synthesis of magnetically recyclable Co@BN core–shell nanocatalysts for catalytic reduction of nitroarenes. *RSC Adv.*, **2017**, *7*, 35451–35459.
[S27]Fang, H.; Wen, M.; Chen, H.; Wu, Q.; Li, W. Graphene stabilized ultra-small CuNi nanocomposite with high activity and recyclability toward catalysing the reduction of aromatic nitro-compounds. *Nanoscale*, **2016**, *8*, 536-542.
[S28]Guo, M.; Zhao, Y.; Zhang, F.; Xu, L.; Yang, H.; Song, X.; Bu, Y. Reduced graphene oxide-stabilized copper nanocrystals with enhanced catalytic activity and SERS properties. *RSC Adv.*, **2016**, *6*, 50587–50594.
[S29]Ji, Z.; Wang, Y.; Shen, X.; Ma, H.; Yang, J.; Yuan, A.; Zhou, H. Facile synthesis and enhanced catalytic performance of reduced graphene oxide decorated with hexagonal structure Ni nanoparticles. *J. Colloid Interface Sci.***2017**, *487*, 223–230.

[S30]Jiang, J.; Lim, Y. S.; Park, S.; Kim, S.-H.; Yoon, S.; Piao, L. Hollow porous Cu particles from silica-encapsulated Cu_2O nanoparticle aggregates effectively catalyze 4-nitrophenol reduction. *Nanoscale*, **2017**, *9*, 3873-3880.
[S31]Li, X.; Zeng, C.; Jiang, J.; Ai, L. Magnetic cobalt nanoparticles embedded in hierarchically porous nitrogen-doped carbon frameworks for highly efficient and well-recyclable catalysis. *J. Mater. Chem. A*, **2016**, *4*, 7476-7482
[S32]Liu, J.; Wang, Z.; Yan, X.; Jian, P. Metallic cobalt nanoparticles imbedded into ordered mesoporous carbon: A non-precious metal catalyst with excellent hydrogenation performance. *J. Colloid Interface Sci.***2017**, *505*, 789–795.
[S33]Qiu, H.; Qiu, F.; Han, X.; Li, J.; Yang, J. Microwave-irradiated preparation of reduced graphene oxide-Ni nanostructures and their enhanced performance for catalytic reduction of 4-nitrophenol. *Appl. Surf. Sci.* **2017**, *407*, 509–517.
[S34]Rath, P. C.; Saikia, D.; Mishra, M.; Kao, H.-M. Exceptional catalytic performance of ultrafine Cu_2O nanoparticles confined in cubic mesoporous carbon for 4-nitrophenol reduction. *Appl. Surf. Sci.* **2018**, *427*, 1217–1226.
[S35]Zhang, S.; Gai, S.; He, F.; Ding, S.; Lia, L.; Yang, P. In situ assembly of well-dispersed Ni nanoparticles on silica nanotubes and excellent catalytic activity in 4-nitrophenol reduction. *Nanoscale*, **2014**, *6*, 11181-11188.
[S36] Zuo, W.; Yu, G.; Dong, Z. A MOF-derived nickel based N-doped mesoporous carbon catalyst with high catalytic activity for the reduction of nitroarenes. *RSC Adv.* **2016**, *6*, 11749–11753.
[S37] Wu, G.; Liang, X.; Zhang, L.; Tang, Z.; Al-Mamun, M.; Zhao, H.; Su, X. Fabrication of highly stable metal oxide hollow nanospheres and their catalytic activity toward 4‑nitrophenol reduction. *ACS Appl. Mater. Interfaces*, **2017**, *21*, 18207–18214.
[S38] Gao, L.; Li, Q.; Hu, X.; Wang, X.; Song, H.; Yan, L.; Xiao, H. One-pot synthesis of biomorphic Mg-Al mixed metal oxides with enhanced methyl orange adsorption properties. *Appl. Clay Sci.* **2016**, *126*, 299–305.
[S39] Ni, Z.-M.; Xia, S.-J.; Wang, L.-G.; Xing, F.-F.; Pan, G.-X. Treatment of methyl orange by calcined layered double hydroxides in aqueous solution: adsorption property and kinetic studies. *J. Colloid Interface Sci.* **2007**, *316*, 284–291.
[S40] Ho, W. C. J.; Tay, Q.; Qi, H.; Huang, Z.; Li, J.; Chen, Z. Photocatalytic and adsorption performances of faceted cuprous oxide (Cu_2O) particles for the removal of methyl orange (MO) from aqueous media. *Molecules* **2017**, *22*, 677.
[S41] Chena, D.; Li, Y.; Zhang, J.; Li, W.; Zhou, J.; Shao, L.; Qian, G. Efficient removal of dyes by a novel magnetic Fe_3O_4/ZnCr-layered double hydroxide adsorbent from heavy metal wastewater. *J. Hazard. Mater.* **2012**, *243*, 152–160.
[S42] Wanchanthuek, R.; Nunrung, W. The adsorption study of methylene blue onto MgO from various preparation methods. *J. Environ. Sci. Technol.* **2011**, *5*, 534-542.
[S43] Jacob, N. M.; Kuruva, P.; Madras, G.; Thomas, T. Purifying water containing both anionic and cationic species using a (Zn, Cu)O, ZnO, and cobalt ferrite based multiphase adsorbent system. *Ind. Eng. Chem. Res.* **2013**, *52*, 16384−16395.
[S44] Ghafar, H. H. A.; Ali, G. A. M.; Fouad, O. A.; Makhlouf, S. A. Enhancement of adsorption efficiency of methylene blue on Co_3O_4/SiO2 nanocomposite. *Desalin. Water Treat.* **2015**, *53*, 2980-2989.
[S45] Chen, H.; He, J. Facile synthesis of monodisperse manganese oxide nanostructures and their application in water treatment. *J. Phys. Chem. C* **2008**, *112*, 17540–17545.

[S46] Varghese, S. P.; Babu, A. T.; Babu, B.; Antony, R. γ-MnOOH nanorods: Efficient adsorbent for removal of methylene blue from aqueous solutions. *Journal of Water Process Engineering* **2017**, *19*, 1–7.

6. Conclusiones

Los resultados obtenidos en esta tesis y recogidos en la presente memoria permiten extraer las siguientes conclusiones:

- El tipo de grafito usado en la exfoliación electroquímica anódica influye en las características del grafeno obtenido; los grafitos no particulados permiten un mayor grado y rendimiento de exfoliación, pero producen grafeno más oxidado. En conjunto, el grafito flexible permite obtener el compromiso más satisfactorio entre todas estas características.
- Es posible utilizar sulfonatos aromáticos como electrolitos en la exfoliación anódica. Estas moléculas cumplen simultáneamente la función de agente intercalante, estabilizador coloidal, agente antioxidante y centro de anclaje para la formación de híbridos. Es posible obtener así grafeno de muy alta calidad estructural funcionalizado y dispersable en agua.
- Un pretratamiento del grafito flexible con ácido sulfúrico permite aumentar el rendimiento del proceso de exfoliación anódica, aunque con un aumento en el grado de oxidación del grafeno resultante.
- Es posible obtener grafeno exfoliado anódicamente utilizando como electrolitos halogenuros de sodio en base a elegir cuidadosamente su concentración y el grafito de partida. Los grafenos obtenidos muestran contenidos de oxígeno similares o inferiores a los preparados con electrolitos estándar (sulfatos).
- El anión cloruro es un aditivo de electrolito con función antioxidante eficiente en la exfoliación anódica de grafeno, permitiendo obtener un grafeno de muy alta calidad estructural y muy bajo grado de oxidación.
- El MoS_2 exfoliado por intercalación de litio puede ser funcionalizado covalentemente con grupos de ácido acético, lo que permite extender su estabilidad coloidal y su actividad catalítica.
- Es posible obtener láminas de Co_3O_4 activado sin necesidad de post tratamiento mediante un proceso solvotérmico dirigido por fases micelares laminares. Este material posee un gran potencial como electrodo de almacenamiento de carga, así como en aplicaciones en catálisis y eliminación de contaminantes del agua.

Conclusions

The results obtained during this thesis and presented along this document allow to draw the following conclusions:

- The type of graphite used in the electrochemical anodic exfoliation is key to the properties of the obtained graphene. Non-particulate graphites allow a higher degree and yield of exfoliation, however they yield a more oxidized graphene. Graphite foil allows the best compromise within these characteristics.
- Aromatic sulfonates can be used as electrolytes in the anodic exfoliation. These molecules play simultaneously the role of intercalating agent, colloidal stabilizer, antioxidant and anchoring center for the preparation of hybrids. This way it is possible to obtain high quality, water dispersible functionalized graphene.
- Pretreatment of the graphite foil with sulfuric acid can increase the yield of the anodic exfoliation, but with an increase in the oxidation of the resulting graphene.
- It is possible to obtain anodically exfoliated graphene using sodium halides as electrolytes, choosing carefully their concentration and the starting graphite. Graphenes obtained this way show similar or lower oxygen contents than those prepared using standard electrolytes (sulfates).
- Chloride anion is an efficient electrolyte additive with the role of antioxidant, allowing to obtain graphene with very high structural quality and very low oxidation degree.
- MoS_2 prepared through lithium intercalation can be covalently functionalized with acetic acid groups, so its colloidal stability and catalytic activity can be extended.
- It's possible to obtain activated Co_3O_4 nanosheets through a micellar phase directed solvothermal method without any post-processing treatment. This material has a great potential as a charge storage electrode, as well as in applications in catalysis and removal of pollutants from water.

Anexo

Durante la realización de la tesis doctoral se generaron una serie de publicaciones no incluidas en esta memoria, aunque de temática íntimamente relacionada:

1. Guardia, L.; Paredes, J. I.; Munuera, J. M.; Villar-Rodil, S.; Ayán-Varela, M.; Martínez-Alonso, A.; Tascón, J. M. D. Chemically exfoliated MoS_2 nanosheets as an efficient catalyst for reduction reactions in the aqueous phase. *ACS Appl. Mater. Interfaces*, **2014**, 6, 21702−21710.
2. Ayán-Varela, A.; Paredes, J. I.; Guardia, L.; Villar-Rodil, S.; Munuera, J. M.; Díaz-González, M.; Fernández-Sánchez, C.; Martínez-Alonso, A.; Tascón, J. M. D. Achieving extremely concentrated aqueous dispersions of graphene flakes and catalytically efficient graphene-metal nanoparticle hybrids with flavin mononucleotide as a high-performance stabilizer. *ACS Appl. Mater. Interfaces*, **2015**, 7, 10293−10307.
3. Ayán-Varela, M.; Villar-Rodil, S.; Paredes, J. I.; Munuera, J. M.; Pagán, A.; Lozano-Pérez, A. A.; Cenis, J. L.; Martínez-Alonso, A.; Tascón J. M. D. Investigating the dispersion behavior in solvents, biocompatibility, and use as support for highly efficient metal catalysts of exfoliated graphitic carbon nitride. *ACS Appl. Mater. Interfaces*, **2015**, 7, 24032−24045.
4. Paredes, J. I.; Munuera, J. M. Recent advances and energy-related applications of high quality/chemically doped graphenes obtained by electrochemical exfoliation methods. *J. Mater. Chem. A*, **2017**, 5, 7228-7242.
5. Ayán-Varela, M.; Pérez-Vidal, O.; Paredes, J. I.; Munuera, J. M.; Villar-Rodil, S.; Díaz-González, M.; Fernández-Sánchez, C.; Silva, V. S.; Cicuéndez, M.; Vila, M.; Martínez-Alonso, A.; Tascón, J. M. D. Aqueous exfoliation of transition metal dichalcogenides assisted by DNA/RNA nucleotides: catalytically active and biocompatible nanosheets stabilized by acid−base interactions. *ACS Appl. Mater. Interfaces*, **2017**, 9, 2835−2845.
6. García-Dalí, S.; Paredes, J. I.; Munuera, J. M.; Villar-Rodil, S.; Martínez-Alonso, A.; Tascón, J. M. D. An aqueous cathodic delamination route towards high quality graphene flakes for oil sorption and electrochemical charge storage applications. *Chem. Eng. J.*, **2019**, 372, 1226-1239.

7. García-Dalí, S.; Paredes, J. I.; Munuera, J. M.; Villar-Rodil, S.; Adawy, A.; Martinez-Alonso, A.; Tascon, J. M. D. An aqueous cathodic exfoliation strategy towards solution-processable and phase-preserved MoS2 nanosheets for energy storage and catalytic applications. Enviado para su publicación.
8. Munuera, J. M.; Paredes, J. I.; Enterría, M.; Villar-Rodil, S.; Kelly, A. G.; Nalawade, Y.; Coleman, J. N.; Rojo, T.; Ortiz-Vitoriano, N.; Martínez-Alonso, A.; Tascón, J. M. D. High performance Na-O2 batteries and printed micro-supercapacitors based on water-processable, biomolecule-assisted anodic graphene. Enviado para su publicación.

Participaciones en congresos:

1. Díaz-González, M.; Fernández-Sánchez, C.; Ayán-Varela, M.; Paredes, J.I.; Guardia, L.; Villar-Rodil, S.; Munuera, J. M.; Martínez-Alonso, A.; Tascón, J. M. D. Flavin mononucleotide-stabilized graphene-metal nanoparticle hybrids with high catalytic activity toward O2 electroreduction. ICREA Workshop on Graphene Nanobiosensors, Barcelona, España, 25/05/2015. Póster.
2. Munuera, J. M.; Paredes, J.I.; Villar-Rodil, S.; Ayán-Varela, M.; Martínez-Alonso, A.; Tascón, J. M. D. Towards High Quality Graphene Flakes by Electrochemical Exfoliation of Graphite With Multifunctional Electrolytes. European Graphene Forum, París, Francia, 01/06/2016. Comunicación oral, presentada por J. M. Munuera
3. Ayán-Varela, M.; Paredes, J.I.; Guardia, L.; Villar-Rodil, S.; Munuera, J. M.; Díaz-González, M.; Fernández-Sánchez, C.; Martínez-Alonso, A.; Tascón, J. M. D. Preparation of Few-Layer Graphene and Transition Metal Dichalcogenide Flakes in Aqueous Dispersion through Flavin Mononucleotide-Assisted Liquid-Phase Exfoliation. ANM2016, Universidad de Aveiro, 25/07/2016. Comunicación oral, presentada por M. Ayán-Varela.
4. Paredes, J. I.; Munuera, J. M.; Villar-Rodil, S.; Guardia, L.; Ayán-Varela, M.; Pagán, A.; Aznar-Cervantes, S. D.; Cenis, J. L.; Martínez-Alonso, A.; Tascón, J. M. D. Covalent functionalization of chemically exfoliated MoS_2 nanosheets to control their aqueous processability, catalytic activity, and biocompatibility. European Graphene Forum, París, Francia, 28/04/2017. Comunicación oral, presentada por J. M. Munuera.

5. Munuera, J. M.; Paredes, J. I.; Enterría, M.; Pagán, A.; Villar-Rodil, S.; Pereira, M. F. R.; Martins, J. I.; Figueiredo, J. L.; Cenis, J. L.; Martínez-Alonso, A.; Tascón, J. M. D. Just add water and table salt: electrochemical exfoliation of graphite in sodium halide electrolytes towards high quality graphene for energy and environmental applications. Graphene 2018. Dresden, Alemania, 26/06/2018. Comunicación oral, presentada por J. M. Munuera.
6. Munuera, J. M.; Paredes, J. I.; Enterría, M.; Pagán, A.; Villar-Rodil, S.; Pereira, M. F. R.; Martins, J. I.; Figueiredo, J. L.; Cenis, J. L.; Martínez-Alonso, A.; Tascón, J. M. D. Just add water and table salt: new perspectives on the electrochemical exfoliation of high quality graphene. Carbon 2018, Madrid, España, 02/07/2018. Keynote, presentada por J. M. Munuera.
7. Munuera, J. M.; Paredes, J. I.; Enterría, M.; Pagán, A.; Villar-Rodil, S.; Pereira, M. F. R.; Martins, J. I.; Figueiredo, J. L.; Cenis, J. L.; Martínez-Alonso, A.; Tascón, J. M. D. Just add water and table salt: new perspectives on the electrochemical exfoliation of high quality graphene. Grapchina 2018, Xi'an, China, 19/09/2018. Keynote invitada, presentada por J. M. Munuera.
8. Munuera, J. M.; Paredes, J. I.; Enterría, M.; Villar-Rodil, S.; Kelly, A. G.; Nalawade, Y.; Coleman, J. N.; Rojo, T.; Ortiz-Vitoriano, N.; Martínez-Alonso, A.; Tascón, J. M. D. Graphene 2019, Roma, Italia, 25/06/2019. Comunicación oral, presentada por J. M. Munuera.

ANEXO